DISCLAIMER NOTICE

UNCLASSIFIED
Technical
Report

Defense
Technical
Information
Center

DTIC

UNCLASSIFIED

THIS DOCUMENT IS BEST QUALITY AVAILABLE. THE COPY FURNISHED TO DTIC CONTAINED A SIGNIFICANT NUMBER OF PAGES WHICH DO NOT REPRODUCE LEGIBLY.

March 1962

Report No. 0411-10F

STUDY OF MECHANICAL PROPERTIES
OF SOLID ROCKET PROPELLANTS

Contract AF 33(600)-40314 S. A. No. 1

Period Covered:

30 January 1961 through 30 January 1962

Aerojet-General CORPORATION

SOLID ROCKET PLANT • SACRAMENTO, CALIFORNIA

COPY NO.

March 1962

Report No. 0411-10F

STUDY OF MECHANICAL PROPERTIES
OF SOLID ROCKET PROPELLANTS

Contract AF 33(600)-40314 S. A. No. 1

Period Covered: 30 January 1961 through 30 January 1962

Project Engineer

James H. Wiegand

James H. Wiegand, Manager
Mechanical and Ballistic
Properties Laboratory

Aerojet-General CORPORATION

SOLID ROCKET PLANT   .   SACRAMENTO, CALIFORNIA

ABSTRACT

A one year integrated program of research was performed on improved methods of measuring the mechanical properties of composite solid propellant, analyzing the response behavior for values essential to stress analysis, performing theoretical and experimental stress analysis on simple tubular grains, establishing failure criteria for such grains, and developing a method of integrating such experimental and theoretical processes with the grain design and propellant development functions to give an optimum method of grain design for reliable solid propellant motors. The problem of variability in tensile measurement was attacked through improved sample preparation by milling on a vacuum holding fixture, and through study of humidity effects. The role of humidity was found important in the dilatation produced by "dewetting" of the oxidizer-binder bond, and in the embrittlement produced by storage at temperatures of $0°F$, an effect related to the use of ammonium perchlorate as demonstrated by the absence of embrittlement with salt. Compressibility measurements on both inert and live propellants showed significant effects of small void contents at low pressures, the compressibility decreasing with pressure and approaching that of void free propellant. A classification system of propellant behavior is proposed based upon degree and localization of dewetting: Class 4, failure with no dewetting; Class 3, a single localized band of dewetting; Class 2, several bands; and Class 1, general dewetting with no localized bands The interpretation of test data in terms of local strain is different for each and pronounced differences in failure behavior are observed. Description of the mechanical property response behavior by linear viscoelastic descriptions apparently requires at least five parameter models, and a more suitable description in view of the problems of dewetting may be that using strain invariants and strain energy functions which can include change of volume Empirically it was found that the first and second strain invariants for uniaxial and biaxial tensile are linearly related by a constant M, which appears to be a basic material constant. Differentiation of the strain energy function gives the stress strain curve and reasonable agreement was obtained with uniaxial and biaxial data.

Temperature cycling of small tubular, case-bonded cylinders of propellant in heavy walled steel tubes was accomplished with continuous strain measurements for B/A ratios to 12.5 and to temperatures as low as -100°F. The observed strains agreed well with those predicted from an elastic incompressible analysis, and were independent of all properties except coefficient of thermal expansion. Pressurization of inert and live propellant cylinders encased in metal tubes was accomplished under plane strain conditions to 300 psi and the observed strains varied only with the compressibility of the propellant.

Photoelastic experiments on cycling stesses were made using a resin which shrinks on cure to study local strains in flat plates containing bonded or released metal cylinders arranged in square array, simulating in two-dimensions the stress-strain distribution caused by binder-filled interaction. The technique was also used to confirm the stress-strain distribution calculated by infinitesimal elastic analysis in a temperature cycled tubular grain. Photoelastic analysis of a grain sector externally strained showed that it simulated closely th stress distribution of a full grain section under pressurization or cycling.

A study of strain measuring devices resulted in a simple clip gauge and confirmed the value of the Moiré fringe technique. Embedded transducers gave experimental difficulties and require further work.

Computer solution was used for stress-strain calculations, based on stress functions and classical elasticity, and using finite difference methods of calculation. Some calculations were also performed using the displacement equations of equilibrium. General computer programs were written for finite difference solutions of ordinary differential equations with boundary conditions specified at more than one point and of partial differential equations of elliptic type. These equations cover the forms of equations being studied in stress analysis and provide mechanized construction for particular cases. A nomographic method of stress analysis for pressurized grains was also developed, based on finite deformation theory, which predicts significantly higher strains than does

infinitesimal elasticity. Analytical studies were also carried out on the general problem of anisotropic and nonlinear solids under loading conditions of rocket motors.

The variability of propellant failure elongations between and within batches was studied as related to small motor, temperature cycling failure. The relative ordering of failure behavior between batches correlated well for one propellant formulation from 180 to 0°F, moderately well to -40°F, but with no correlation at -75°F. The values at -75°F do correlate well with failure incidence of cycling tubular motors at -75°F in terms of ratio of failure elongation to maximum motor bore strain; no failures being observed above a ratio of 1.8 and all motors failing below 0.85; an exception was observed in one batch of unaged dry propellant which subsequently agreed with the criterion after several weeks of ambient humidity exposure.

The correlation of failure data in uniaxial tension from -75° to 180°F, and from 0.074 to 1000 min.$^{-1}$ through a modified Williams, Landel, Ferry shift for polyurethane propellant, has been accomplished by allowing a vertical shift for temperatures below 80°F. An alternate method of correlation using a temperature shift technique has also been obtained in conjunction with a vertical shift depending on the rate of extension. Failure data at constant rates down to 0.0005 min.$^{-1}$ can be obtained in the newly developed very-low-rate tester, which, together with available high-rate test equipment, covers the full range of strain rates observed in motors from firing down to temperature cycling.

A review of the literature on tear testing was performed and experiments were conducted on several types of samples. The binder-filler interaction was found to strongly affect the tear energy as expected. The desirability of a narrow distribution of molecular chain lengths was shown as well as the adverse effect of clumping to give regions of high and of low cross link density. A theoretical analysis also showed that the failure of filled rocket fuels depends on the failure of the filler-particle bond, first in individual regions and later in larger regions which may be concentrated in discontinuous sheets. From

a stress analysis of the ligaments where filler particles are almost in contact, the stiffness and the load for a critical fracture stress were determined. The resulting fracture locus indicates that the maximum normal stress should decrease linearly with increasing mean normal (hydrostatic) pressure.

Analysis of the grain design problem through the structural interrelations of a PERT network focuses attention on the close integration required in all phases of activity. Computer calculation procedures are sufficiently well advanced in meeting ballistic requirements that it is possible to conceive of computer analysis of preselected critical design features in terms of the actual propellants being considered. Although there are many unsolved structural problems encountered in solid propellant charges, the progress made in relating propellant properties to structural analysis should be reflected in incorporation of these factors in optimization through an integrated design approach.

FOREWORD

The program covered by this report covers specific experiments and theoretical studies at both the Sacramento and Azusa facilities of Aerojet-General Corporation, at the University of California in Berkeley, at the Massachusetts Institute of Technology, and at the Catholic University. This report also includes data taken on various motor development projects, where such data support or extend this program, and attempts to present a relatively complete overall picture of progress made to integrate all of the important factors affecting the structural behavior of solid propellant rocket motor grains. The literature cited here supplements the comprehensive literature review of the Final CALCIT report of M. L. Williams, P. J. Blatz, and R. A. Schapery.

The research work in Azusa was coordinated by K. H. Sweeny and K. W. Bills, Jr., and included work on response and failure properties by K. W. Bills, Jr., F. H. Brock, and W. D. Hart; on basic polymer behavior by H. R. Lubowitz; and on cylinder deformation under pressure by F.S. Salcedo and G. D. Nesheim. In Sacramento, the variability of failure properties and improvement of testing methods was studied by I. G. Hazelton, R. D. Steele, L. W. Martin, and F. H. Davidson, under the direction of H. P. Briar. The change of volume under strain and the related studies on embrittlement were performed by P. C. Colodny and G. J. Svob. The study of bulk modulus of propellant was performed by C. C. Surland and W. T. Milloway. Strain measurements in motors were carried out by R. B. Farnham, D. J. Dougherty, and R. D. Steele. Theoretical analysis of stress and strain in finite elastic cylinders was performed by J. D. McConnell, R. E. Leary, J. Ulrich, and A. Messner, with the alternative solution of tubular and star grain configurations by H. Hilton, P. N. Murthy, A. F. Fraser, C. A. Wagner, R. Toms, and J. E. Vinson. The use of photoelastic analysis was carried out by R. C. Sampson. The development of clip gages and new methods of measuring strain was carried out by R. K. Steel and T. W. Smith, Jr., and at the Catholic University by Dr. A. J. Durelli and V. J. Parks. The study of numerical

FOREWORD (cont.)

computer methods of solving stress analysis problems was performed by
R. Glauz, E. Bender, and H. Bader. The correlation of motor and propellant
failure data was performed by J. H. Wiegand, H. P. Briar, and W. T.
Milloway. The failure studies under combined loading under subcontract to
the Massachusetts Institute of Technology were performed by G. Leon under the
direction of Professors Norman C. Dahl and Frank A. McClintock. Studies on
anisotropic elasticity, viscoelasticity, and nonlinear elasticity at the University
of California were performed by S. B. Dong, L. R. Hermann, and R. L. Taylor
under the direction of Dr. Karl S. Pister. The analysis of the PERT network
for propellant development was done by J. Gellmann and J. H. Wiegand, with
the related problem of grain design studied by J. S. Billheimer.

TABLE OF CONTENTS

TABLE OF CONTENTS (cont.)

TABLE LIST

TABLE LIST (cont.)

FIGURE LIST

FIGURE LIST (cont.)

FIGURE LIST (cont.)

FIGURE LIST (cont.)

FIGURE LIST (cont.)

FIGURE LIST (cont.)

FIGURE LIST (cont.)

FIGURE LIST (cont.)

FIGURE LIST (cont.)

FIGURE LIST (cont.)

APPENDIXES

(Submitted in Separate Volume)

I.   INTRODUCTION

The importance of establishing a rational method of relating laboratory
data on mechanical properties to the structural behavior of solid propellant
charges has been recognized since early in World War II. The relation of the
mechanical properties of solid propellants to the structural behavior of solid
propellant charges in motors has not yet been established quantitatively, though
general property relationships have been used qualitatively as guides by propel-
lant development chemists and the designers of charge configurations. The use
of mechanical property values as acceptance criteria is rare, though rejection
for defects, lack of cure, and unsatisfactory ballistic performance are customary.
This same problem exists in general in the plastics and elastomer field and
reflects the complexity of the mechanical property behavior with time and
temperature of such materials, as well as the difficulty of stress analysis for
either linear or nonlinear viscoelastic materials.

Recent progress in analytical procedures, coupled with the capacity for
high-speed numerical computation in large IBM calculators, has brought some
of these problems facing the stress analyst within reach of solution. It was
proposed for this program that a concerted attack be made on the problem
by empirical and theoretical methods, using the newer methods of measuring
pertinent properties. The results would be confirmed by cycling and pressuri-
zation experiments on simple tubular case-bonded charges of solid propellant.
If the methods proved applicable, the more complex case of star perforations
would then be attempted, but it was not expected that complete structural de-
sign procedures for solid propellant charges would be developed within a one
year program. It was hoped, rather, that a basic approach could be developed
towards more effective utilization of the skills of the grain designer, the stress
analyst, the propellant development chemist, and the rheologist; in short, an
integrated development method for solid propellant charges.

During the program, the importance of an integrated approach became
more evident, since the increasing complexity of each of the fields is becom-
ing less intelligible to those in the related fields. As a result, significant

I, Introduction (cont.)

advances in one field may not be exploited in the related fields because of a lack of understanding unless a positive integration method is in effect. At the same time, certain parts of the overall problem were found to be simpler than expected and allowed the use of simple concepts for solutions. Thus, the strains observed in thermal cycling can be closely estimated by analysis based on the linear infinitesimal elasticity of an incompressible material. The strains so calculated, which are essentially independent of all propellant properties except thermal coefficient of expansion, generally produce low temperature cycling failure when they exceed one half of the simple elongation at break on the JANAF tensile test at the low temperature. This simple conclusion is of direct value to the propellant development chemist screening new formulations, to the grain designer optimizing a configuration, and to the production process man controlling propellant quality. Although applying directly only to the case of low temperature failure, the results suggest an approach to other types of failure and offer the hope that similar simple correlations for other critical conditions may be developed through an integrated development approach.

The program was basic in concept and attempted also to break new ground for further later study on methods of measuring mechanical property response and failure behavior, on analytical methods for anistropic and non-linear materials, on new methods of measuring and observing strain in motors, and on improved methods of correlating the response and failure properties of composite solid propellants. Although polyurethane binders with inert salts and with ammonium perchlorate as fillers were studied in the program, the more general conclusions are believed applicable to other cast composite propellant systems.

In this report, the integrated approach to the problem will be followed. The next four sections present the work on the four phases pertinent to

I, Introduction (cont.)

structural design, followed by a section on the fifth phase that describes the integration of such design procedures with propellant development and charge configurational analysis. The longer analytical derivations and detailed graphs from a computer study are summarized in the body of the report and presented in detail in the appendices.

II.   PHASE 1 -- MECHANICAL PROPERTY DETERMINATION

The broad objective of this phase was to measure the response behavior in terms of properties necessary to structural analysis. Specifically, several batches of live and inert propellants were studied over a wide range of strains, strain rates, and loads at a wide range of temperatures under both uniaxial and multiaxial conditions. Improvements in apparatus and technique were made to give measurements of the desired accuracy, and to allow assessment of the variability of the propellant. Measurements of this type give insight into the causes of behavior, provide the numerical values needed in structural analysis, and provide the parametric relations, with their chemical and physical interpretations, which are pertinent either to currently produced propellant materials or to totally bonded and totally dewetted propellant materials. The behavior of the material has largely dictated the requirements for successful techniques.

A.   MEASUREMENT OF RESPONSE BEHAVIOR

Testing of mechanical properties of solid propellants provides an adequate tool for the determination of material parameters required for solid propellant research and development. It is known, however, that the mechanical properties response behavior of the propellant in the large motor is not simulated under these test conditions. Methods, therefore, must be developed to determine dimensional relationships for which the mechanical properties of solid propellant are independent of sample size.

II, A, Measurement of Response Behavior (cont.)

1.   Tensile Measurements Under Superimposed Hydrostatic
Pressure

One of the factors which affects the dewetting process is
pressure. Under superimposed hydrostatic pressure, which simulates the
effect of motor pressure on the dewetting process, the failure level of inert
propellant (DP-16) was found to be considerably raised for specimens tested
in simple tension in the presence of hydrostatic pressure, confirming the data
of Vernon (1). The tensile strain at nominal maximum stress was more than
doubled when the test pressure was raised from atmospheric to 250 psig at
77°F. The nominal maximum stress was raised from 120 psi to 180 psi under
the same conditions. The initial elastic response of the inert composite did
not seem to be appreciably changed by superimposed hydrostatic pressure.
That is, the Young's Modulus of Elasticity calculated from the initial slope of
the stress-strain curve was essentially constant regardless of the pressure
of testing. This would be expected at the low strains before dewetting of the
oxidizer has occurred.

Four live polyurethane propellants, showing Class 2 be-
havior as discussed in Phase 2, were also tested in the same way and an
analysis made of the effect of hydrostatic pressure on nominal stress at break
and elongation at break. The results, shown in Figures 1 and 2, suggest a
consistent effect of pressure on failure stress but not on failure strain.

The pronounced effect of superimposed hydrostatic pressure
on the tensile behavior of solid propellants appears to be related to the sup-
pression of void formation that occurs on extension. The prototype pres-
surized tensile tester used in these tests was adapted, therefore, to the
measurement of volume changes during extension. A spring clip gage
monitors the lateral dimension of the tensile specimen during extension.
Volume change can be indirectly assessed from the lateral dimensions of
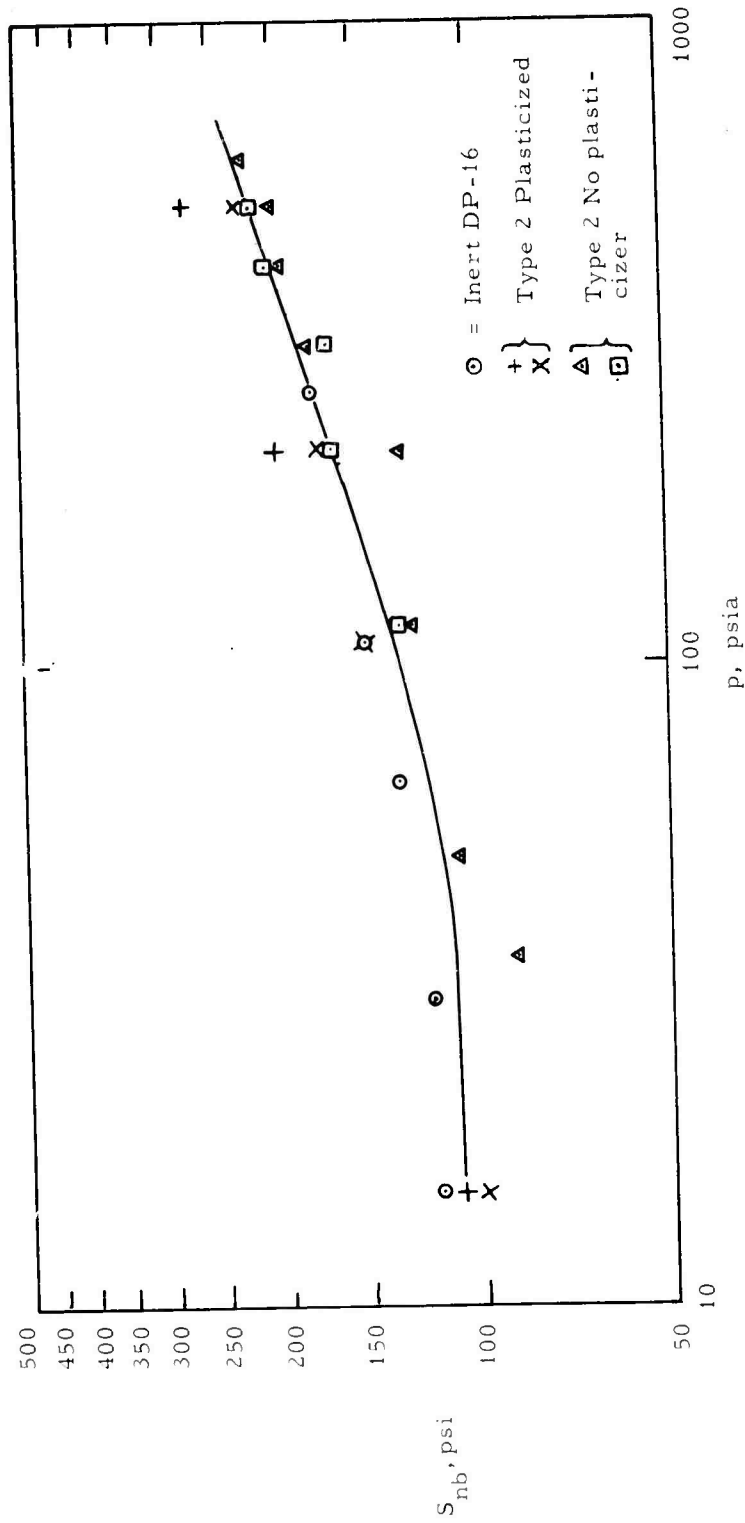
Figure 1. Effect of Pressure on Nominal Stress at Failure
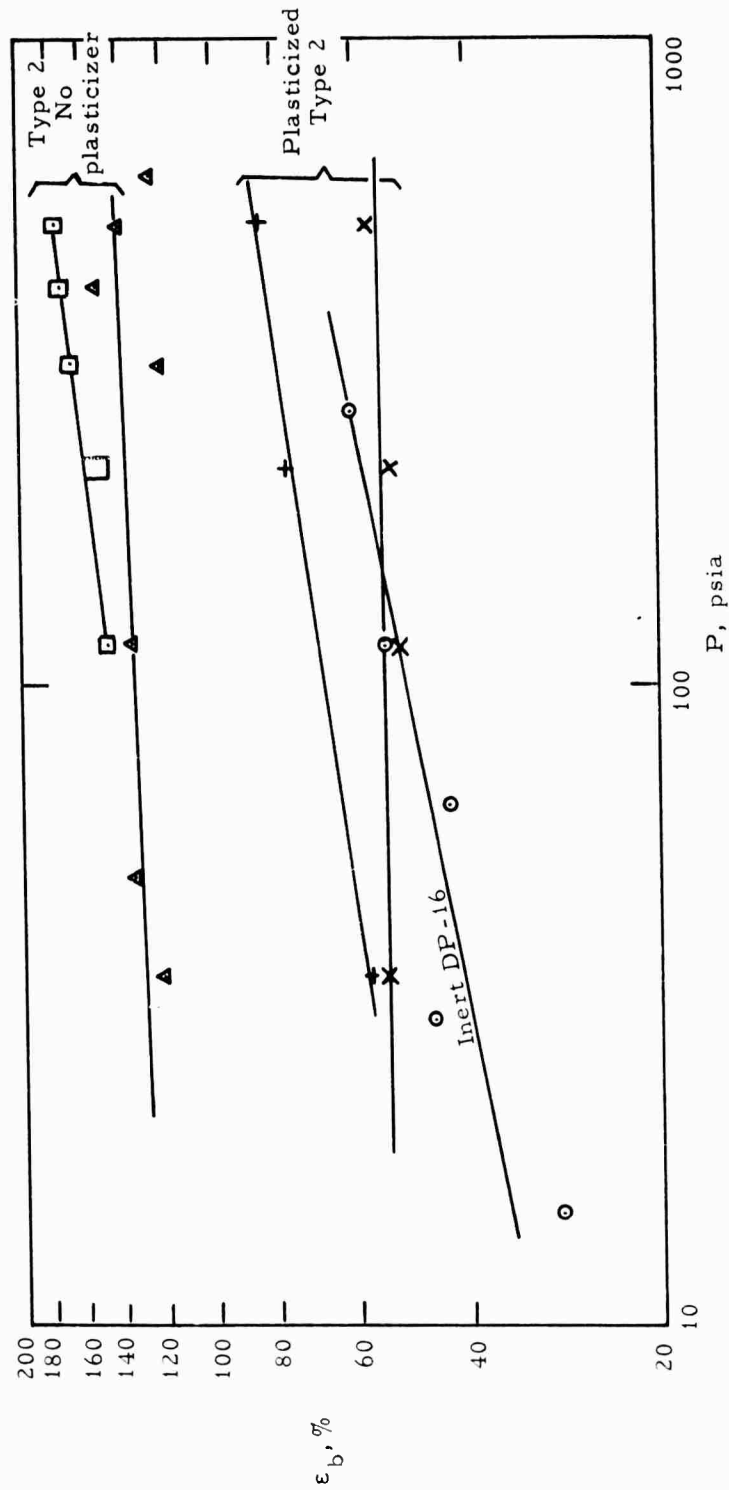
Figure 2.   Effect of Pressure on Elongation at Failure

II, A, Measurement of Response Behavior (cont.)

the specimen and the tensile strain in the region of the clip gage -- to the extent that the lateral strain measured by the clip gage is representative of the behavior in the gage section of the specimen, and that the tensile strain can be interpreted in terms of jaw separation.

Typical results at two pressures for uniaxial extension with standard JANAF tensile specimens of propellants having 65% volume fraction solids at 40 and 515 psia are shown as load-deflection curves in Figure 3. The solid curves are the average of a set of five specimens; the range of variability within each set is indicated by the dashed curves. The ordinate of the plots is the tensile component of the load only, so the combined stress including the hydrostatic pressure failure even for the 515 psia data was compressive.

Lateral contraction data obtained from the clip gage records for these tests are shown in Figure 4. Both stress and lateral contraction were obtained by simultaneous X-Y recordings of these parameters as a function of jaw separation.

The initial slope of the load deflection curves of Figure 3 are typically independent of the superimposed pressure. This would be expected from a linear infinitesimal stress analysis applied to the unit specimen subjected to the stresses indicated in Figure 5.
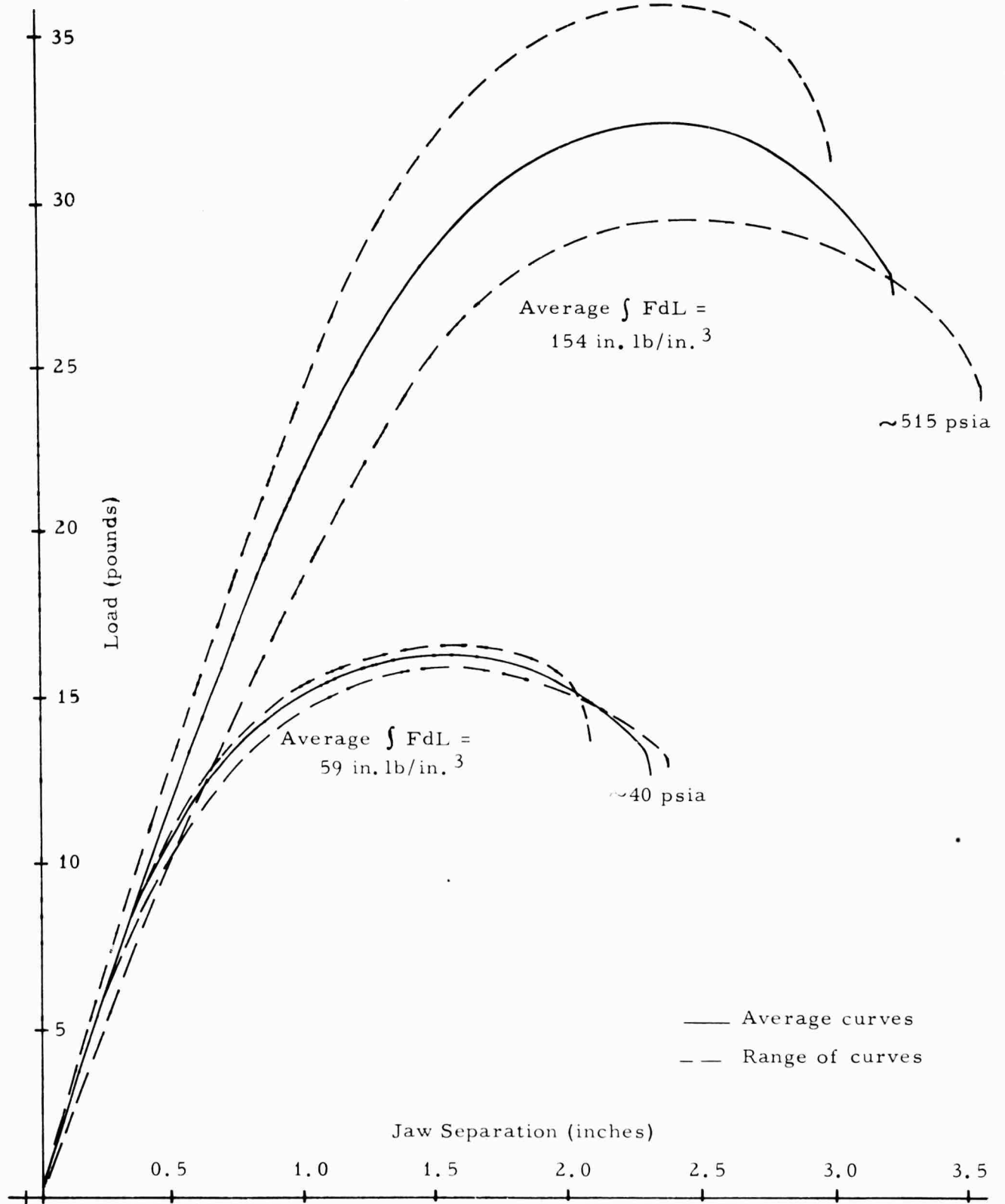
Figure 3. Stress-Strain Curves of 65 Vol % Loading Propellants Tested at Constant Pressures of ~40 and ~515 psia
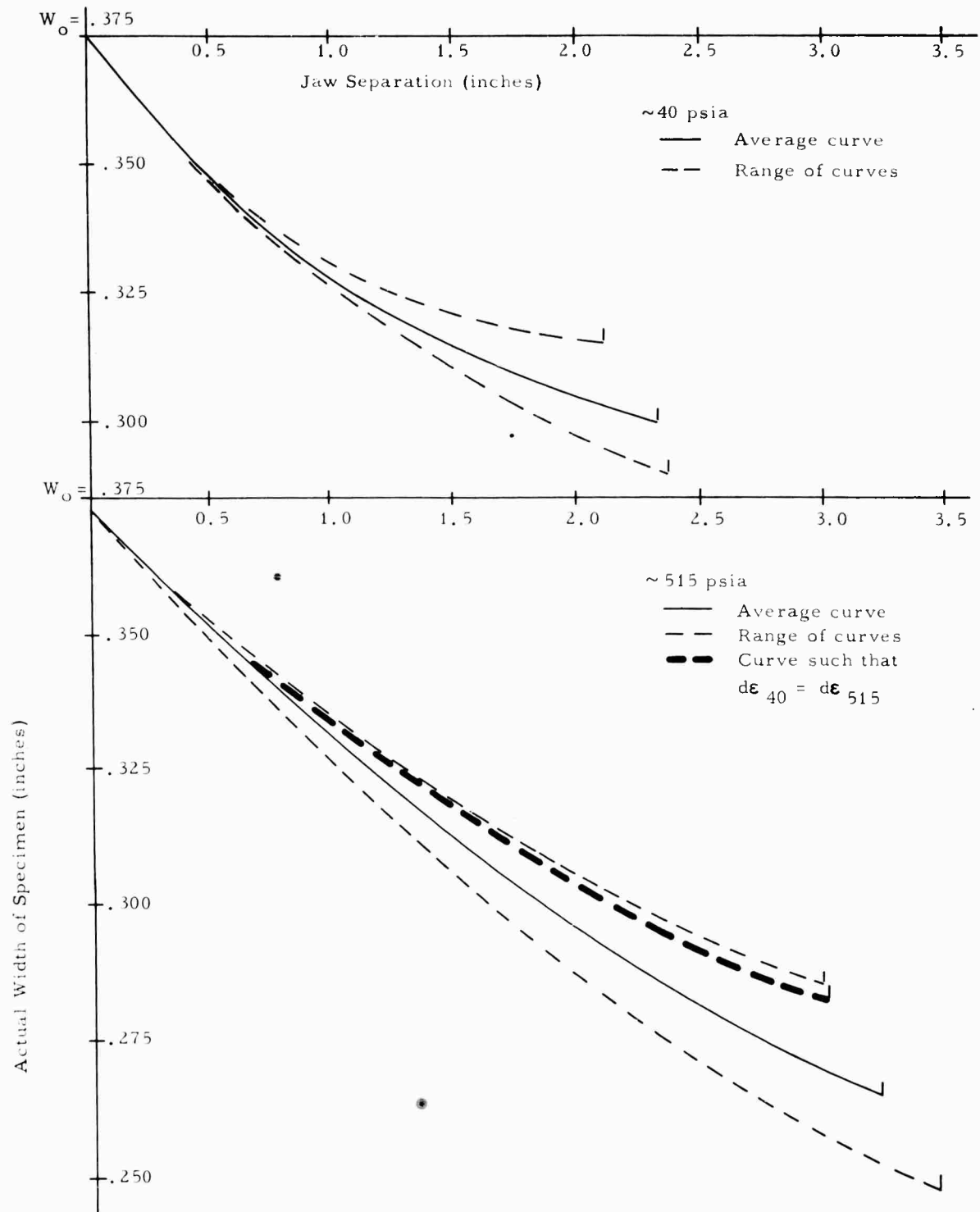
Figure 4. Lateral Contraction - Jaw Separation Data Taken During Constant-Pressure Experiments

II, A, Measurement of Response Behavior (cont.)
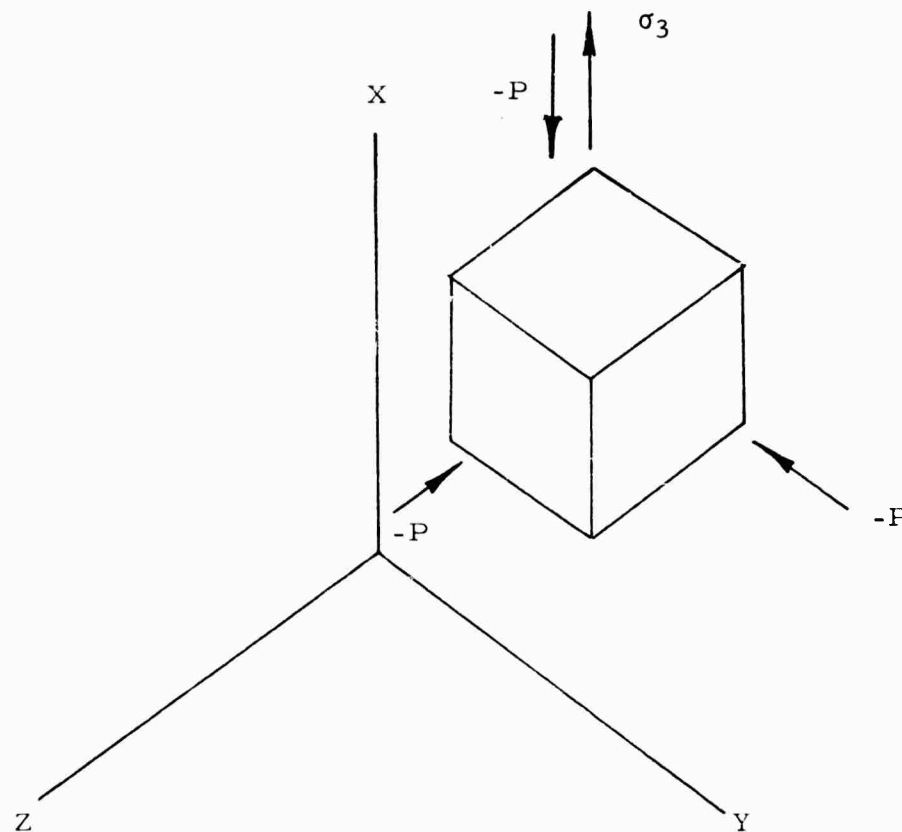
Figure 5. Stress Conditions for Pressurized Uniaxial Tensile Test

For this case, we can write

$$\varepsilon_x = \frac{1}{E} \left(\sigma_x - \nu \sigma_y - \nu \sigma_z \right) \tag{1}$$

which gives the relation between Young's Modulus (E), the stress (σ) and strain (ε) in the X direction, and Poisson's Ratio (ν). The combined tensile and

II, A, Measurement of Response Behavior (cont.)

stress τ_x is then,

$$\tau_x = \tau_3 - P = \frac{F}{A} - P \tag{2}$$

and the lateral stresses are

$$\sigma_y = \sigma_z = -P \tag{3}$$

so that

$$E\varepsilon_x = \tau_x + 2\nu P \tag{4}$$

For extension under constant hydrostatic pressure, E will be independent of pressure if ν is constant.

Figure 6 shows the tensile behavior of a specimen where sudden changes in the pressure level were introduced during extension. These data should be considered in conjunction with Figure 7 which shows the corresponding changes in the lateral dimensions of the specimen or the void suppression effect. These data show the effect of pressure to be essentially reversible.

2. Effect of Microscopic Voids on Propellant Bulk Modulus Values

The microscopic voids were estimated from bulk modulus and volumetric compliance measurements of specimens taken from positions
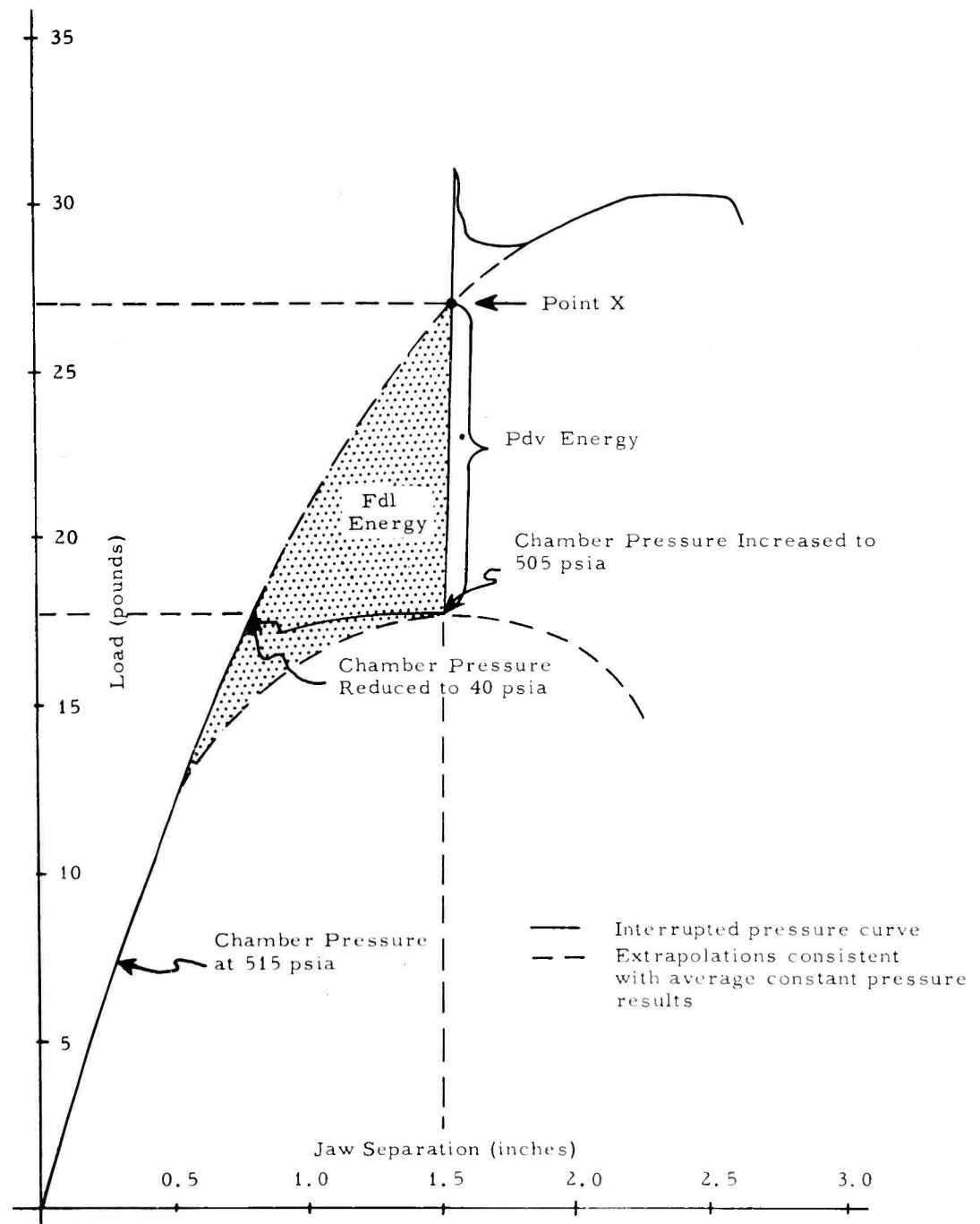
Figure 6. Stress-Strain Curve for Propellant Specimen Subjected to Several Pressure Levels
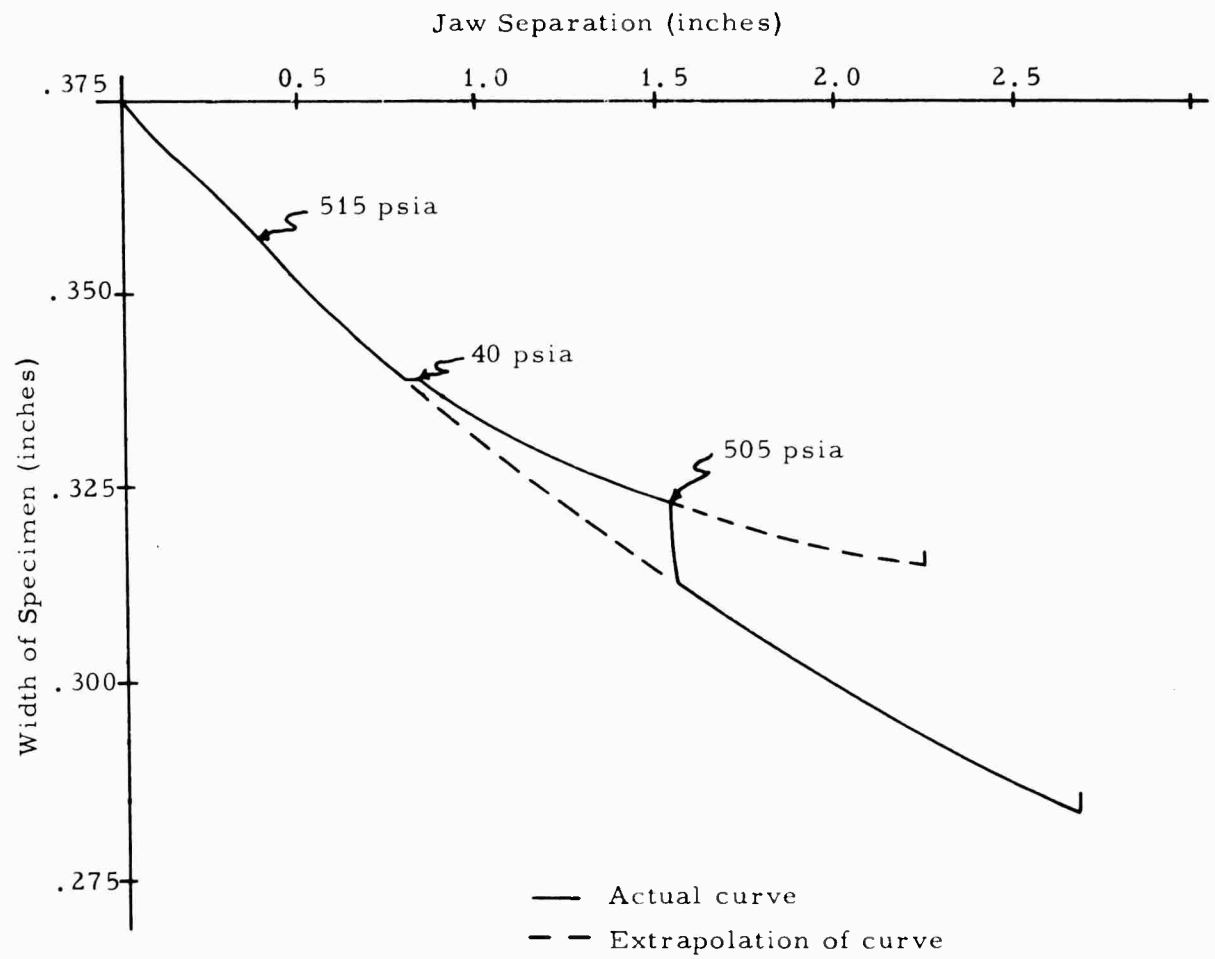
Figure 7. Lateral Contraction - Jaw Separation Curve for Propellant Specimen
Subjected to Several Pressure Levels

II, A, Measurement of Response Behavior (cont.)

along the orthogonal diameters of a one-gallon carton casting of DP-16 inert
propellant. The calculated void content values show a marked inhomogeneity
with respect to initially included voids existing in a regular radial pattern in
gallon-carton castings of DP-16 inert propellant. This pattern of inhomogeneity
is suggestive of the filling pattern during casting of a propellant. The void con-
tent values were verified by precise density measurements. Although the in-
homogeneity observed amounted to only 0.3% by weight, entailing negligible
difference in density, this variability of void content was found to cause a varia-
tion in excess of 50% in the bulk modulus, i.e., 0.595×10^6 to 0.265×10^6 psi.
Such a variation in actual motors could result in the circumferential strain in the
propellant at the bore being significantly higher, on pressurization, than that
expected from stress analysis using a constant propellant bulk modulus
characteristic of void-free propellant.

Figure 8 shows diagramatically the radial location of 17
rectangular bulk modulus specimens of nominal dimensions $1/2 \times 3/8 \times 6$ in.
taken from positions along the orthogonal diameters of the gallon carton.
Typical pressure-deflection curves for selected specimens are shown in
Figure 9. The average bulk modulus of the 17 specimens is 0.424×10^6 psi.
The void-free bulk modulus of DP-16 inert propellant calculated from
$K_{binder} = 0.28 \times 10^6$ psi and $K_{filler} = 2.6 \times 10^6$ psi for 40 vol % binder,
60 vol % filler is 0.60×10^6 psi. Tests on large specimens of DP-16 propel-
lant, comparable in size to gallon cartons repeatedly show values of 0.52×10^6
psi for the bulk modulus. A volume of .025% initial included voids, com-
pletely compressed at this pressure, would explain the variation between cal-
culated and measured bulk modulus values for large specimens of DP-16 inert
propellant. The bulk moduli were determined for each specimen from the slope
of the semi-linear portion of the pressure-compliance test records in the
hydrostatic pressure region from 600 to 900 psi. The measurements reported
are essentially adiabatic as the rate of pressurization exceeds the thermal
relaxation time.
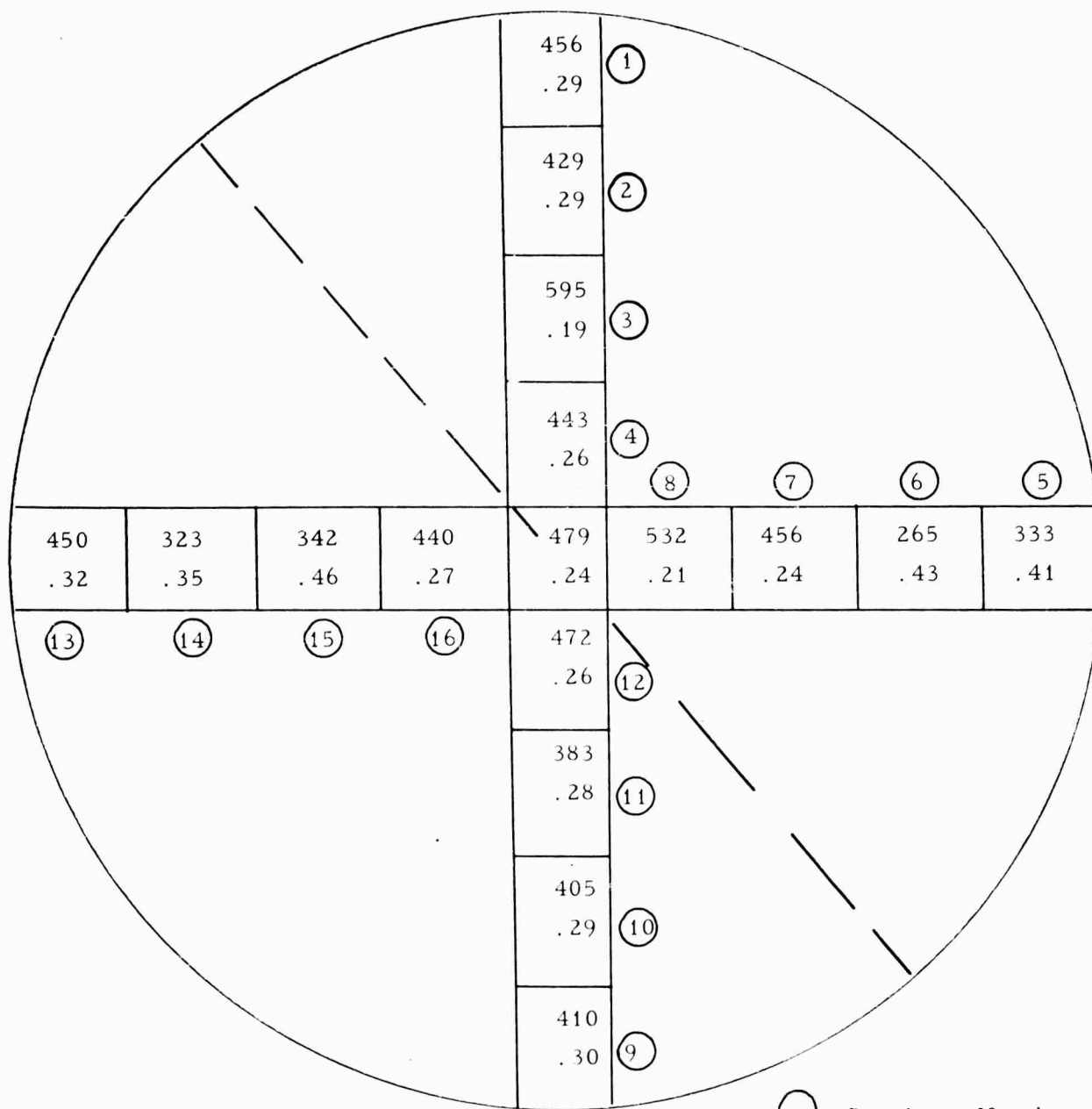
Figure 8. Radial Location of Bulk Modulus Specimens of DP-16 Inert Propellant from Gallon Casting
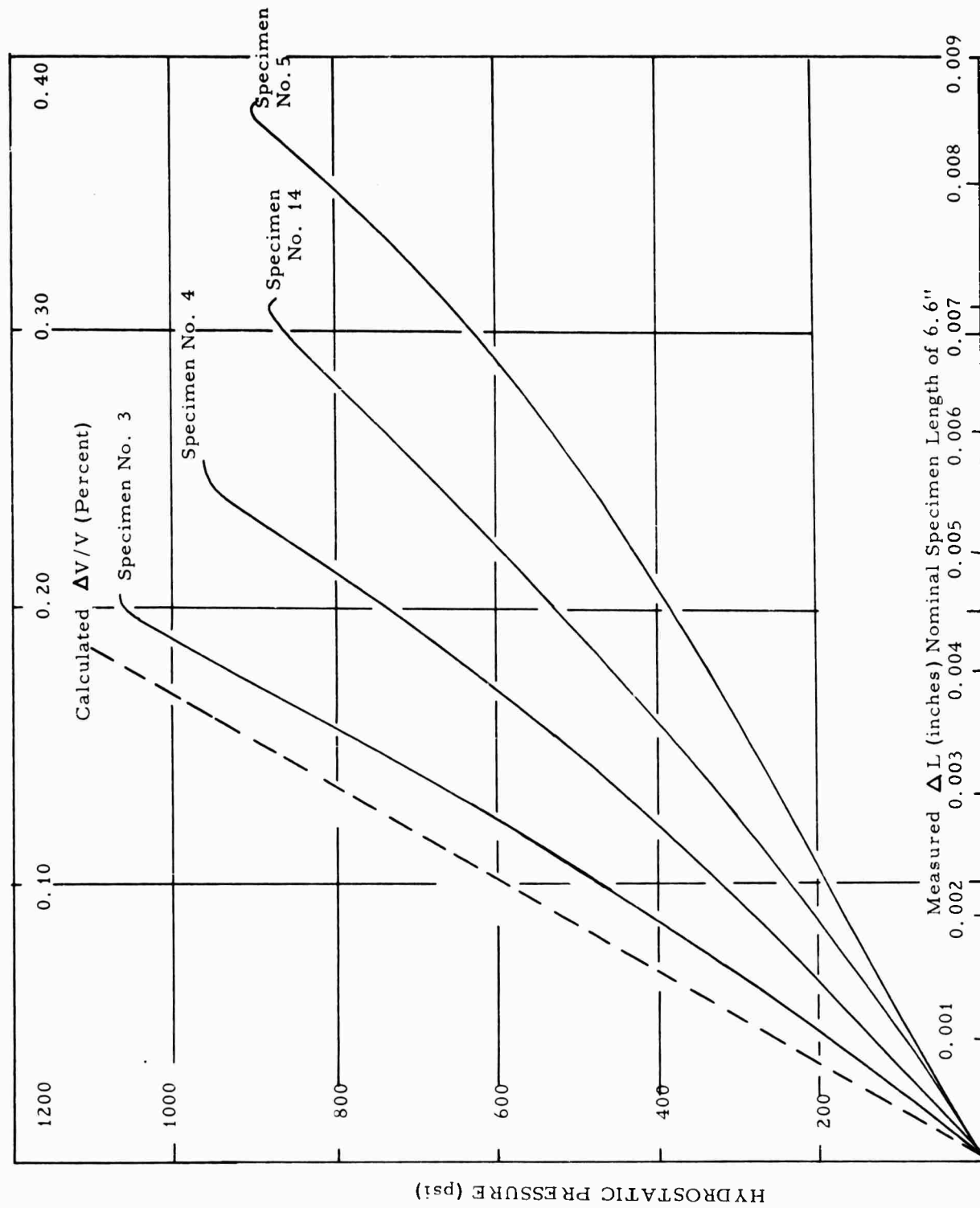
Figure 9. Uniaxial Pressure-Deflection Records Showing Compliance Over Range of Pressurization

II, A, Measurement of Response Behavior (cont.)

To examine radial inhomogeneity, an arbitrary topographic division of the one-gallon sample was made as shown by the dashed line of Figure 8. An analysis of variance for the bulk moduli measured for the two regions showed significantly different compressibility in the pressure range from 700 to 1000 psi at the 95% confidence level, using Student's t-test.

The nominal specific gravity of DP-16 propellant is 1.6500. A weight percentage difference of .041% should exist between void-free materials and materials containing .025% initially included voids, which would be reflected in specific gravity determinations as a change of about 7 parts in the fourth decimal place. Using precision density measurements, specimens No. 4 (bulk modulus 0.60×10^6 psi) and No. 14 (0.323×10^6 psi) were found to have specific gravities of 1.6555 and 1.6500, respectively, equivalent to a difference of 0.33% in initial void volume between these specimens. The measurements suggest that about 72% of the initial void volume in specimen No. 14 remains uncompressed at 1000 psi pressure. The technique used is analogous to that used for large cylindrical specimens (2).

The bulk modulus based on the definition

$$K = (\partial P / \partial V)_s \tag{5}$$

can be assessed for unit volume from the slope of the pressure compliance records. When a linear behavior between P and V exists, the calculated value for the modulus typifies the material over the range of pressure for which this is true. For isotropic materials and small strains, the relation between the volumetric compliance, J_V, and the orthogonal compliances $J_x = J_y = J_z = J_L$, is approximately

$$J_V = 3 J_L \tag{6}$$

II, A, Measurement of Response Behavior (cont.)

In all cases the time of pressurization was reasonably short compared with the thermal relaxation time of the specimen, so that the compliance behavior and calculated bulk modulus values are all for the adiabatic case.

Propellants or composites containing voids were presumed to behave as homogeneous externally pressurized thick-wall hollow spheres. The expression for the radial displacement and stresses for the hollow sphere under hydrostatic pressure is:

$$\frac{U}{r} = \frac{\left(P_b - P_a\right)\left(\dfrac{b^3}{b^3 - a^3}\right) - P_a}{3K} + \frac{\left(\dfrac{P_b - P_a}{4\mu}\right)\dfrac{a^3 b^3}{b^3 - a^3}}{r^3} \qquad (7)$$

where: U = radial displacement at radius r

a = internal radius

b = external radius

P = stress

μ = shear modulus

K = bulk modulus

If $P_b = P_a + dP$ and $P_a = 0$ then

$$\frac{U}{r} = \frac{dP\left(\dfrac{b^3}{b^3 - a^3}\right)}{3K} + \frac{\dfrac{dP}{4\mu}\left(\dfrac{a^3 b^3}{b^3 - a^3}\right)}{r^3} \qquad (8)$$

This equation evaluated at the inner radius, a, and outer radius, b, gives the simultaneous equations

II, A, Measurement of Response Behavior (cont.)

$$dP = \frac{\frac{da}{a}}{\left(\frac{1}{3K} + \frac{1}{4\mu}\right) \cdot \left(\frac{b^3}{b^3 - a^3}\right)} \tag{9}$$

$$dP = \frac{\frac{db}{b}}{\left(\frac{1}{3K} + \frac{a^3}{4\mu b^3}\right) \left(\frac{b^3}{b^3 - a^3}\right)} \tag{10}$$

The solution for Equations (9) and (10) with $P_a = 0$ and evaluated from $P_b = 0$ to $P_b = P$ and from b_o to b is

$$\frac{b^3}{b_o^3} = \frac{V}{V_o} = \frac{e^{-\frac{P}{K}}}{\left(\frac{1 - \delta e^{-\frac{3P}{4\mu}}}{1 - \delta}\right)^{\left(\frac{4\mu}{3K} + 1\right)}} \tag{11}$$

where $\delta = \frac{a_o^3}{b_o^3}$, the volume fraction voids.

Equation (11) can be simplified for $p \gg K$ and when the ratio of shear modulus to bulk modulus is small to

$$\frac{1}{K^*} = \frac{1}{K(1 - \delta)} + \frac{\delta}{(1 - \delta)P} (1 - e^{-3P/4\mu}) \tag{12}$$

II, A, Measurement of Response Behavior (cont.)

which reduces when δ is small to

$$\frac{1}{K^*} = \frac{1}{K} + \frac{\delta}{P} \left[1 - e^{-3P/4\delta} \right] \tag{13}$$

where $K^* = \Delta P/(\Delta V/V_o)$

and K is the bulk modulus for void free material defined by the equation

$$\frac{V}{V_o} = e^{-\frac{P}{K}} \quad \text{or} \quad K = V \left(\frac{\partial P}{\partial V} \right)_S \cong V_o \left(\frac{\partial P}{\partial V} \right)_S \tag{14}$$

Data for five specimens which represent the range of variation in bulk modulus for the specimen set were plotted as points in the pressure versus percent volume change graph of Figure 10. Smooth curves generated from Equation (13) were also drawn to compare with the experimental results. A shear modulus of 390 psi, obtained from torsion measurements of the composite, and a theoretical value of 0.6×10^6 psi for the bulk modulus of void free propellant were used. The theoretical bulk modulus was used to plot the line for zero voids in Figure 10. The experimental data for Specimens #3, #4, #14, #6, and #15 are given as calculated volume change and hydrostatic pressure in Table 1.
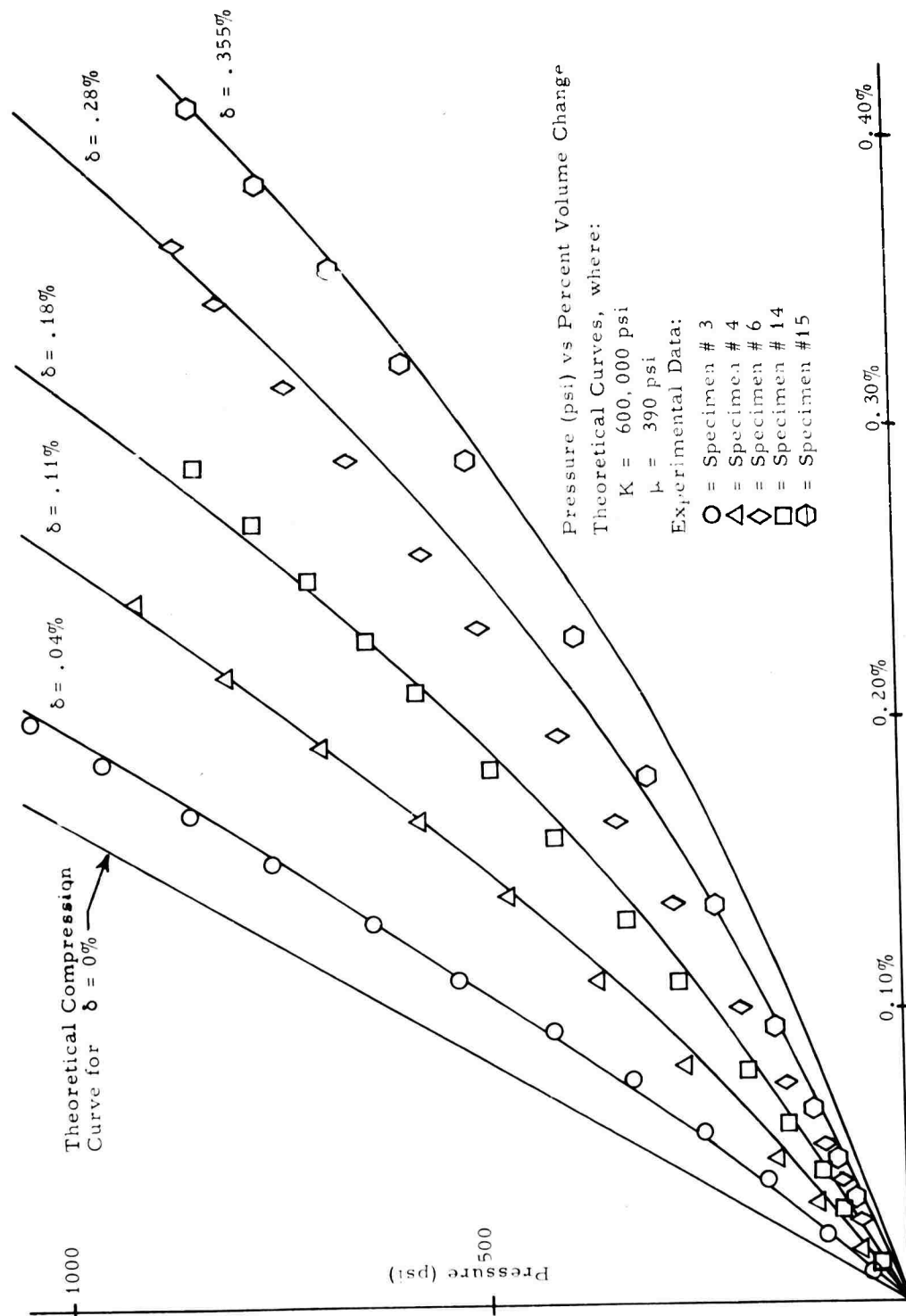
Figure 10. Comparison of Experimental and Theoretical Pressure Volume Behavior for a Composite

II, A, Measurement of Response Behavior (cont.)

TABLE 1

PRESSURE-VOLUME CHANGE DATA

Specimen No.	3	6	14	15	4
Pressure	V/V_o	V/V_o			
0	0	0			
100	.025	.052	.045	.061	.034
200	.050	.105	.088	.125	.066
300	.072	.148	.126	.184	.097
400	.091	.195	.157	.241	.125
500	.111	.238	.191	.291	.152
600	.130	.277	.222	.335	.175
700	.147	.320	.253	.377	.197
800	.166	.355	.283	.409	.221
900	.185	.390		.437	.244
1000	.200	.430			

The theoretical bulk modulus of $K = 0.6 \times 10^6$ psi for the void free composite was calculated from the equation,

$$J \text{ composite} = (V.F.)_A J_A + (V.F.)_B J_B + (V.F.)_C J_C + \text{etc.} \tag{15}$$

where $\frac{1}{J}$ = Bulk modulus

and $(V.F.)_A$ = Volume fraction of ingredient A, etc.

The approximate composition of the composite with experimental bulk moduli from the literature are given in Table 2.

II, A, Measurement of Response Behavior (cont.)

TABLE 2

APPROXIMATE COMPOSITION OF INERT COMPOSITE DP-16

Ingredient	Volume Fraction (percent)	Bulk Modulus (10^6 psi)
Binder (Polyurethane Rubber)	40	0.28
Salt (KCL)	50	2.60
Aluminum (Powder)	9.5	10.6
Miscellaneous	0.5 est'd.	2.0

Equation (11) predicts that at sufficiently high pressures the void compression will become negligible in comparison with that of the void free material, and all curves are expected to have slopes of pressure-volume change corresponding to that of the void free material. Such behavior is shown by the experimental data for Specimen No. 3 having the lowest initial void content of 0.04%. The experimental compliance curves of Figure 10 show good agreement with the curves derived from Equation (13) for low initial void content and less exact correspondence for high initial void content. This might be expected in view of the simple premises on which the equation is based and the many complications which could occur with high initial void content. Void shape and size, distribution, instability of shape, and many other factors undoubtedly become more important with increasing void content.

Work of an exploratory nature was completed on the hydro-static compressibility of a cellular plastic with nominal initial void content of 89%. Compression behavior of the foam was measured to extend and test the applicability of Equation (13) for composites having high void content such as that which occurs on uniaxial extension of propellants. The data are presented in Table 3 and Figure 11. The mechanical properties of the solid material could be determined only crudely from pressed foam specimens. The shear

TABLE 3

HYDROSTATIC COMPRESSION OF A PLASTIC FOAM 89% VOID CONTENT,

DATA AND CALCULATIONS, INCLUDING THEORETICAL CALCULATIONS

Pressure (psi)	Experimental data: $\frac{\Delta V}{V_o}$	Theoretical Calculations	
		$\frac{\Delta V}{V_o}$; where: $\mu = 417$ psi	$\frac{\Delta V}{V_o}$; where: $\mu = 177$ psi
1	0.04217	0.014283	0.03306
2	0.07965	0.028186	0.06447
3	0.11191	0.041570	0.09249
4	0.14009	0.054673	0.11903
5	0.16338	0.067576	0.14465
6	0.18448	0.079668	0.16883
7	0.20422	0.091831	0.19167
8	0.22090	0.103384	0.21177
9	0.23689	0.114647	0.23283
10	0.25110	0.125899	0.25137

For theoretical calculations:

$k = 300,000$ psi

$\delta = 89\%$

$\mu = 417$ psi and 177 psi
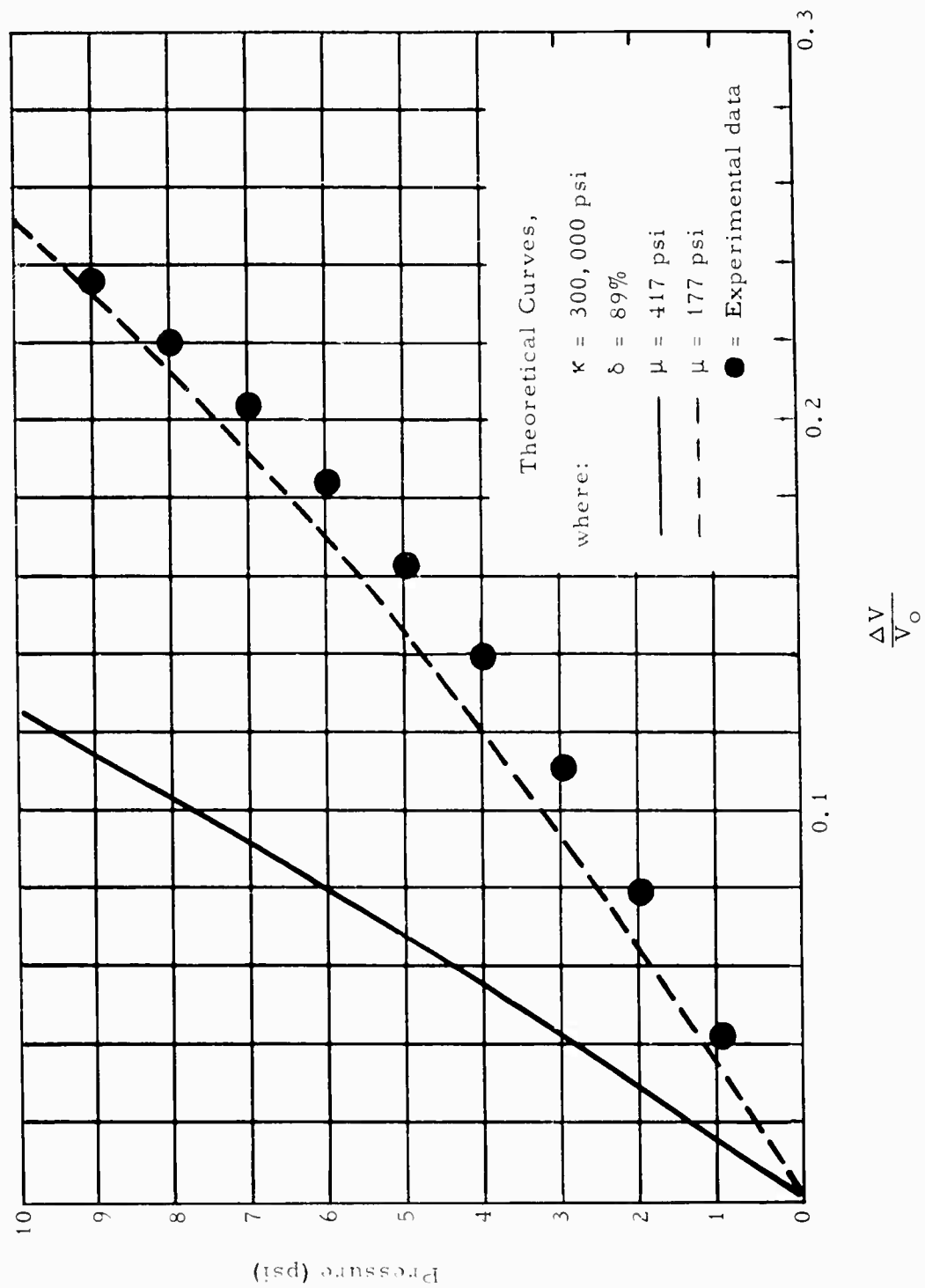
Figure 11. Hydrostatic Compression of a Plastic Foam of 89% Void Content

II, A, Measurement of Response Behavior (cont.)

modulus was estimated to be 417 psi from tensile tests on pressed foam speci-
mens. This value of the shear modulus is presumed to be somewhat too high
because of probable plasticizer loss caused by the heat and pressure used in
solidifying the foam. The behavior that would be predicted for this material
from Equation (13), using the measured shear modulus value of 417 psi for the
solid portion of the foam, is shown in Figure 11 as the solid curve. A close fit
of Equation (13) to the observed data required the working shear modulus in the
solid portion of the foam to be 177 psi, as shown by the dashed curve on
Figure 11.

3. Improved Preparation of JANAF Tensile Specimen

A widely used method of sample preparation for the JANAF
Instron sample uses a die cutter pressed hydraulically through a precut slab of
propellant. This is a fast and simple method of sample preparation, but it
gives several undesirable effects.

a. Nonparallel faces in the gage section of the bar make the
sample trapezoid shaped, and because of this it is extremely difficult to measure
cross sectional area with less than 3 to 5% variation. The trapezoid shape of
the shoulders of the specimen also causes it to bow in the fixtures while testing,
resulting in a nonuniaxial test and a strain rate gradient throughout the cross
section of the specimen. Further, the trapezoid shape of the specimen in the
shoulder and gage sections causes the strain rate to be non-linear due to seat-
ing effects and irregular area changes, resulting in inaccurate strain readings
and low modulus readings.

b. The sample must undergo considerable compressive
stresses and strains while being cut.

II, A, Measurement of Response Behavior (cont.)

c.   The surface of the sample is often rough and scarred as though it was torn and not cut which may cause premature failure.

d.   The gross irregularities in the specimen combine to produce high variances in the data so that many samples have to be tested before obtaining values that have significant meaning statistically.

A method of machining Instron specimens using a fly cutter had been tried here. Good quality specimens were obtained with a significant reduction of variance of the measured parameters. Although such methods for machining samples have been available, no adequate methods for holding the material while it was being machined were available except for limited production. Vise-type gripping fixtures with abrasive surfaces work adequately if great caution is used by the operator. With this type of holding mechanism, the sample must undergo considerable compressive forces and strains in order to be held rigidly enough for milling. and because of the low flexure modulus of most propellants, the material tends to bulge making it difficult to machine specimens within good tolerances. Vise-gripping of the material also minimizes the surface one can machine.

It was decided to hold the material with vacuum while machining. A fixture was designed using several vacuum ports with a machined aluminum section to support the gage section. Grit cloth over the vacuum ports provides an abrasive surface at the propellant-fixture interface resulting in high shear between the propellant and the fixture. The fixture is mounted on a mill, and a water aspirator, with a vacuum reservoir to act as a surge tank. is incorporated to provide a means of displacing the free air in the fixture. Reducing the air pressure in the fixture and surge tank to 5 inches of Hg provides adequate holding force for milling without producing more than 0.0000.

II, A, Measurement of Response Behavior (cont.)

reduction in thickness of the specimen because of atmospheric pressure. The
machining of the first face of the specimen section is shown in Figure 12, the
reverse face is then machined while the specimen section is held on top of the
machined fillet, as shown in Figure 13. After both faces have been completed,
the section is sliced into individual bars on a Do-All saw.

Approximately 200 samples have been prepared in this
manner and the width of the specimen has a range of 0.006 in., equivalent to a
range of area values of 1.6%.

Machining of standard JANAF tensile specimens
improves the quality of the data, but this type of sample produces different
strains in the test section than are calculated from crosshead motion due to
the extrusion of the sample into the jaws, as shown in Figure 14. The effect
is partially compensated for by using an average gage length, nominally 2.7 in.,
at Aerojet-General Corporation. However, use of an average gage length pro-
duces errors, particularly at low strain values, and the true rate of deformation
in the gage section is not constant at constant crosshead speeds.

No matter how the sample is held or what the shape,
direct measurement of deformation in the test section appears to be required
for precise work. If end-bonded specimens are used, then the strain distribu-
tion at the bond is not the same as in the test section. A dog-bone specimen
has been used at Thiokol Chemical Corporation (3), which is gripped beyond
the wide ends of the specimen to provide a uniform strain distribution in the
test section. Bonding to a relatively rigid plastic or to steel at the ends of a
rectangular specimen usually produces non-normal failure behavior and one
solution is to use the standard JANAF shape but replace some part of the wide
tag end with rigid plastic. An experiment was performed using the standard
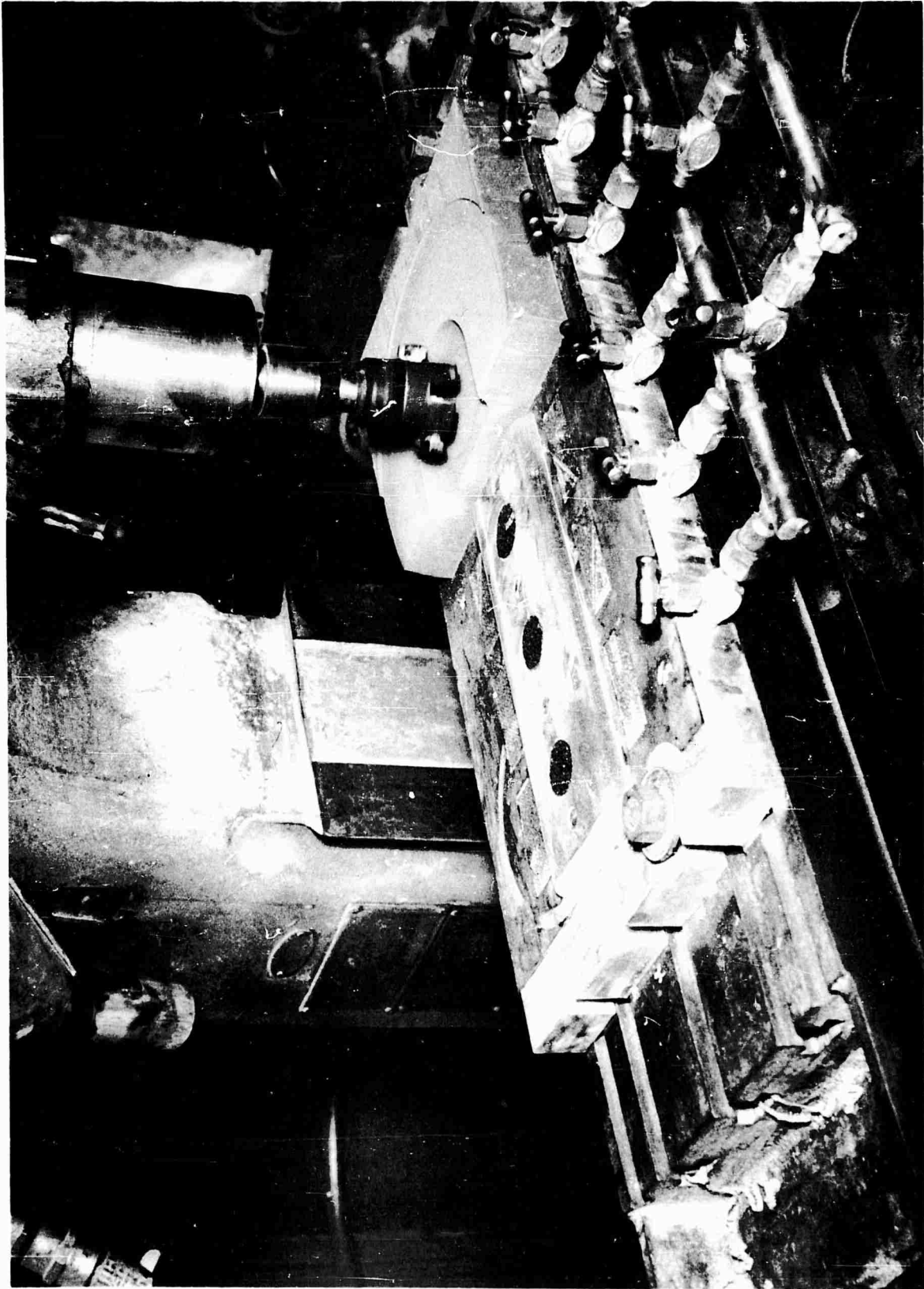
Figure 12.   Machining of First Side of Block of Propellant Using Vacuum to Hold
Block in Place
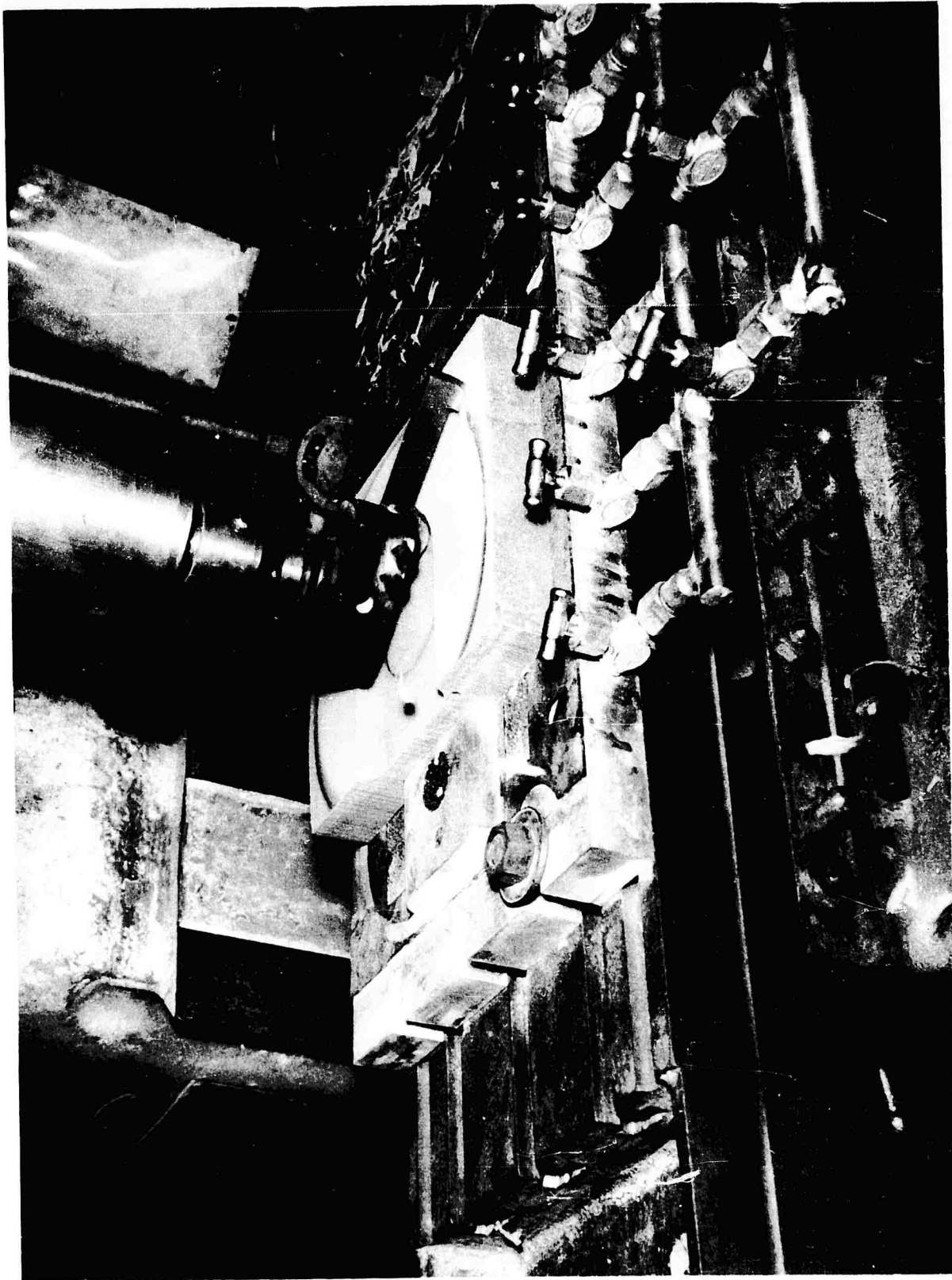
Figure 13. Machining Other Face of Propellant Block Using Vacuum to Hold First Machined Surface on Formed Aluminum Section

A. Unstrained Tensile Specimen
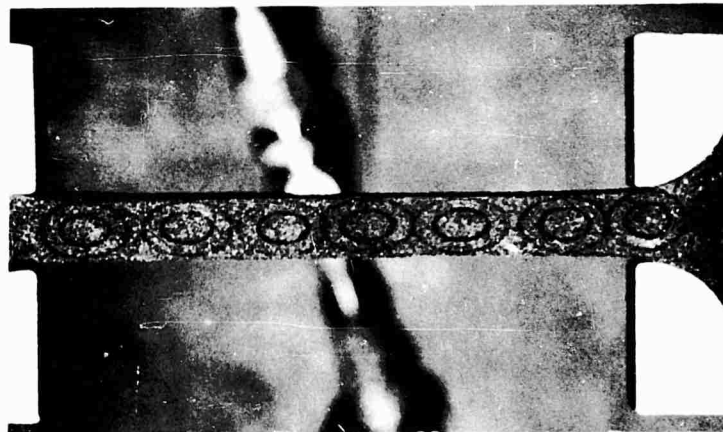
. Strained Tensile Specimen

Figure 14.   Distortion of Circular Grid Due to Straining Specimen, Showing
Extrusion from the Jaws

II, A, Measurement of Response Behavior (cont.)

shape with epoxy bonded to the end of the tabs, and with the same plastic bonded tangent to the 1/2 in. radii at each end. The plastic pieces were held in turn at their ends in an adapter on the Instron testing machine. The strain, measured from photographs taken of bench marks within the gage section (1.5 to 1.8 in. between bench marks), did not vary linearly with crosshead separation. The jaw separation was, however, proportional to $\ln \lambda$, the proportionality constant for a normal specimen with no plastic attached being 3.3, and 2.9 to 3.0 in. for both types of plastic attachment.

A study was made of the effect of milling specimens on the variability of tensile data for a Class 2 propellant. Batches were selected which were enough different in their overall properties to present a reasonable cross section of the production. One part of each carton was sent through to be stamped immediately. The remainder was divided two ways. One half was cut and stamped and the other half was cut into slabs in preparation for the milling operation. The samples then went together to the milling operation so as to have exactly the same conditioning history time, temperature, and exposure to moisture. When the samples were ready for testing, a further subdivision was made into a part which was conditioned for two weeks at 20% RH and a part which was tested immediately.

The data of the experiment are tabulated in Table 4. A variance analysis of the results is contained in Table 5 which shows that a significantly higher maximum stress was obtained on milled bars when a direct comparison was made between the two methods on tensile bars with equivalent conditioning histories prior to testing. Neither the modulus nor the strain at maximum stress were significantly different when tested by either method.

TABLE 4

VARIABILITY DATA BATCHES FOR TWO CLASS 2 PROPELLANTS TESTED AT 77°F AND 2 IN./MIN CROSSHEAD RATE

Batch No.	Preparation Method	History	S_{nm}	ϵ_m	S_{nb}	ϵ_b	E	n
1	Stamped	Uncontrolled	183	26	159	35	1410	4
	Stamped	Same	150	21	128	30	1420	4
	Milled	Uncontrolled History	163	20	136	29	1510	4
	Stamped	20% RH 2 weeks	151	22	132	31	1300	4
	Milled	20% RH 2 weeks	158	21	118	34	1390	4
2	Stamped	Uncontrolled	134	55	123	73	459	4
	Stamped	Same	111	52	98	72	412	4
	Milled	Uncontrolled History	122	54	113	69	418	4
	Stamped	20% RH 2 weeks	110	52	98	69	417	4
	Milled	20% RH 2 weeks	118	52	108	68	458	4
3	Stamped	Uncontrolled	152	49	141	64	526	4
	Stamped	Same	125	48	112	62	486	4
	Milled	Uncontrolled History	149	46	134	63	537	4
	Stamped	20% RH 2 weeks	118	46	108	61	471	4
	Milled	20% RH 2 weeks	134	47	124	60	490	4
4	Stamped	Uncontrolled	155	46	144	55	532	4
	Stamped	Same	126	47	116	57	503	4
	Milled	Uncontrolled History	154	45	142	58	605	4
	Stamped	20% RH 2 weeks	120	41	111	50	596	4
	Milled	20% RH 2 weeks	145	43	136	53	554	4
5	Stamped	Uncontrolled	165	37	150	49	632	4
	Stamped	Same	153	37	133	49	627	4
	Milled	Uncontrolled History	139	36	126	46	647	4
	Stamped	20% RH 2 weeks	130	35	117	45	603	4
	Milled	20% RH 2 weeks	136	35	123	46	663	4

TABLE 5

VARIANCE ANALYSIS OF THE FIVE BATCHES OF TABLE 1

Factor	Sum of Square	F Ratio	Significance	Variance	Coefficient of Variation
		Variance of S_{nm} Values			
Between lots	291	6.6	.999	247	10.0%
20% RH vs Ambient	84	1.9	.9	40	4.6%
Stamp vs Mill	181	4.1	.99	137	8.6%
Replicates	44	-	-	44	4.8%
		Variance of ϵ_b Values			
Between lots	154	56	.999	150	31.0%
20% RH vs Ambient	6.2	1.7	.8	1.6	4.0%
Stamp vs Mill	4.4	1.2	-	-	-
Replicates	3.7	-	-	3.7	4.8%
		Variance of E Values			
Between lots	164,000	34	.999	520	74%
20% RH vs Ambient	5,230	1.08	-	-	-
Stamp vs Mill	5,190	1.07	-	-	-
Replicates	4,830	-	-	-	9.8%

II, A. Measurement of Response Behavior (cont.)

A 4 to 4.6% coefficient of variation was observed in the five batches analyzed between the 20% controlled RH and the uncontrolled ambient. This difference is probably low. Five different batches just preceeding those analyzed showed similar changes, but in the opposite direction. That is, the first five batches showed S_{nm} and ε_m increasing when conditioned for one week at 20% RH. The next five batches which were tested several weeks later and on which the variance analysis was made showed S_{nm} and ε_m decreasing when conditioned for two weeks at 20% RH. If the 20% RH for two weeks conditioning is to be used as a reference, then one can expect that uncontrolled fluctuations in external ambient % RH can contribute at least a variability of 4%, but higher as the time period is extended.

The variance analysis of the modulus values for the five lots contains one very high set of values. These high values probably washed out any other information on the humidity and milling factors.

4. Multiple Position Sample Holder

Efforts were made to increase the information gained from a given experiment and reduce the complexity of the data reduction procedure. The availability of precisely machined tensile specimens have led to several new test techniques of interest.

The testing of large numbers of specimens on the Very Low Rate Tester described later in the report suggested a similar procedure for use on the Instron testing machine. A set of special tensile grips were prepared using the standard shape but thick enough to hold four specimens at once. The holder is shown with three specimens in place in Figure 15. Data are shown below for a typical propellant at 77°F and 2 in./min. crosshead rate.
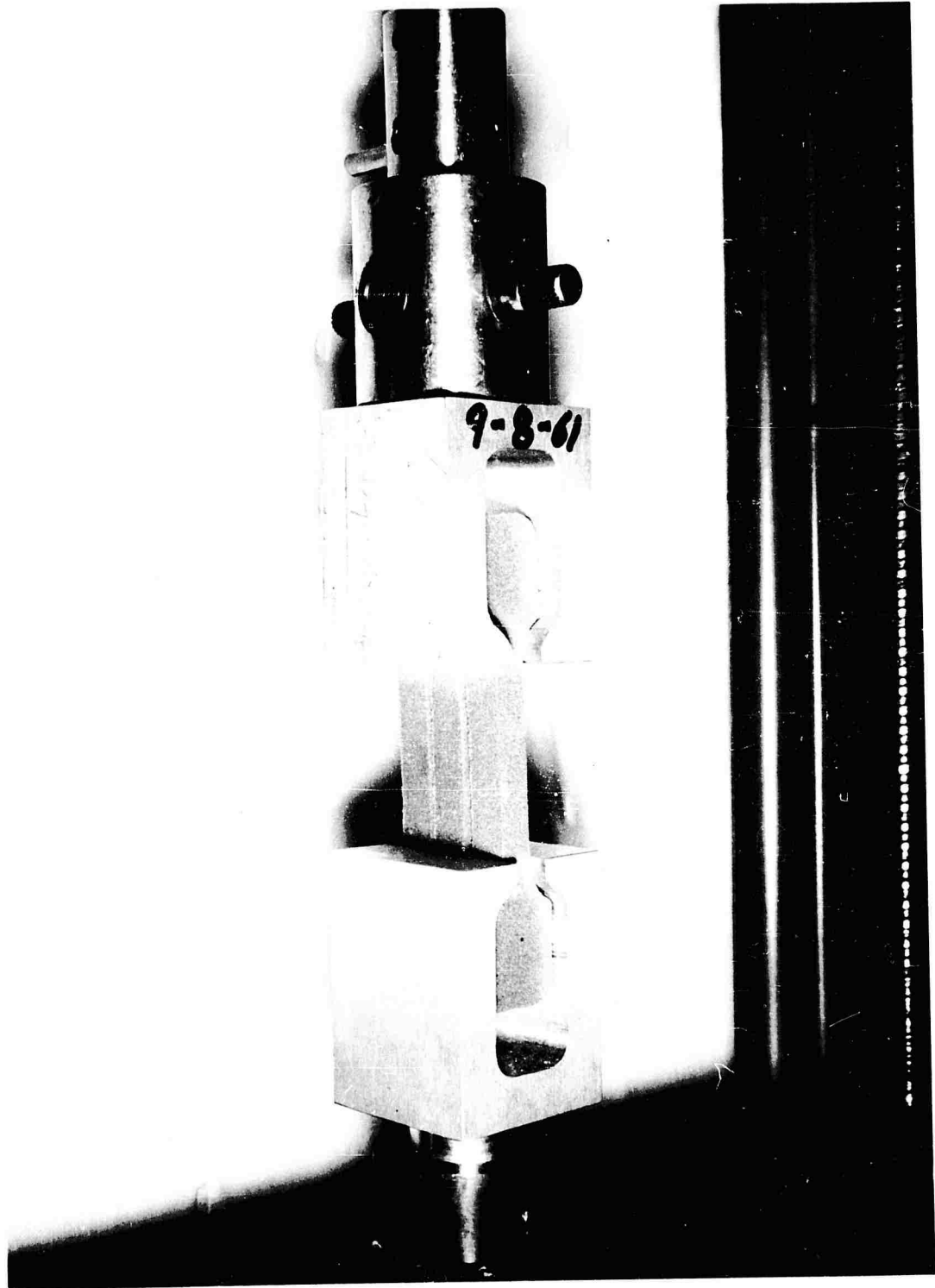
Figure 15.   Multiple Sample Holders for Use on Instron Shown With Three Milled
JANAF Specimens in Place (9-61S 23348)

II, A, Measurement of Response Behavior (cont.)

	S_{nm}	S_{nb}	ε_m	ε_b	E
3 at once	106	102	50	60	395
3 singly #1	109	104	50	62	380
#2	103	98	46	58	435
#3	109	107	50	58	380
Average	107	104	49	59	395

The method of machining test specimens allows the samples for this fixture to
be made as wide as the fixture if desired, a capability useful in a study of scale
effect. The method does not give satisfactory failure data in low temperature
testing where the high modulus produces forces which tilt the jaws when one of
the outside specimens remains after failure of the other two. This difficulty
can be overcome by using support bars similar to those of the Very Low Rate
Tester.

Use of several samples in one test gives an average value of
E, S_{nm}, and ε_m directly while giving separate values of ε_b and S_{nb}. The direct
reading of the average value is facilitated by a divider circuit developed for the
Instron tester, which divides the load cell output by the specimen width and
thickness to give psi. The divider circuit consists of two analog computer grade,
chopper stabilized, differential amplifiers. Connections are made in such a
manner as to use the full amplifier gain in an inverse feedback network to main-
tain the differential inputs at the same potential. When this condition exists, the
input is a null or summing point around which the analog computations are made.

II, A, Measurement of Response Behavior (cont.)

A simplified diagram of one unit of the system is:
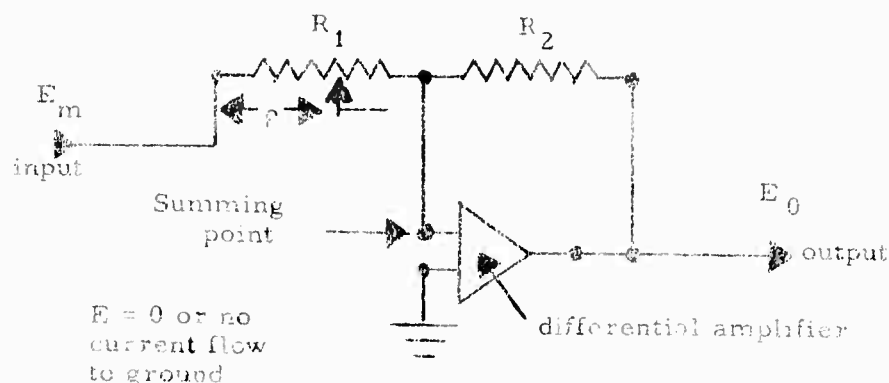
R_1 is a 10-turn potentiometer with a 10-turn dial graduated in 1000 parts, so the output voltage is proportional to the input voltage divided by the 10-turn potentiometer shaft rotation. Calibration is a simple matter of selecting the proper resistors to bring the device in the appropriate range and providing a calibrating point for fine adjustment.

5. Effect of Sample Size

An attempt was made to analyze the mechanical response behavior of oversize specimens of inert polyurethane propellants containing NaCl and KCl fillers. Specimens were milled, barbell shape, 0.5 in thick, with a 0.50 in. radius at the shoulder. The general formulation was filler: 74 wt %, fuel additives: 1 wt %, and polyurethane fuel: 25 wt %. Duplicate specimens were run. The tensile data were obtained from tests in which the ratio of specimen cross sectional area to gage length was held constant regardless of gage length. These comprised all combinations of three different gage lengths and two different area-to-gage ratios. Three specimens of each

II, A, Measurement of Response Behavior (cont.)

configuration were to have been listed, but poor specimen behavior reduced
the specimens to two for two of the six configurations. Discarding one value
chosen at random from the other sets allowed an analysis to be performed.
The values measured are tabulated in Table 6 with the values discarded shown
in parenthesis. The statistical calculations confirmed a visual examination of
the data that no statistically significant effects have been shown. The small
number of observations and the large variability of the data appear responsible
for the lack of definite statistical conclusions.

It is significant to note that the manner in which the Class 2
propellant tensile parameters react to changes in area and gage does not follow
the behavior noted in unfilled systems. The large variability in test data is
not attributed to experimental technique, but rather to non-uniform deformation
of the test specimen on formation of local areas of dewetting. Confirmation of
this phenomenon is seen in an analysis of the stress-strain behavior observed in
different locations within the same test specimen.

Prior to tensile testing, each set of specimens in this series
was marked with a grid system and a series of circles. The number of circles
were dependent upon specimen size. Measurements of dimensional change
within and adjacent to each circle as a function of overall stress were deter-
mined from photographic films. Representative observed behavior of the
stress-strain relations is shown in Figure 16. It is seen that a difference of
as much as 40% strain is observed between areas on the same specimen at
failure. The effect of this non-uniformity is profound in the failure behavior
of Class 2 and Class 3 propellants and will be discussed further in this report.

TABLE 6

MEASUREMENTS FOR STATISTICAL STUDY OF SPECIMEN SIZE EFFECTS UPON THE UNIAXIAL TENSILE BEHAVIOR OF A CLASS 2 PROPELLANT

Gage, in.		Area/Gage Ratio					
		0.65			1.89		
1.35	$\varepsilon_m\%$	77	63	68	64	72	61
	$\varepsilon_b\%$	206	155	184	152	162	174
	σ_m(psi)	85.9	81.4	77.5	84.7	81.0	87.5
	σ_b(psi)	33.2	53.8	46.5	25.1	47.5	51.8
	E (psi)	352	352	352	421	365	365
	$\varepsilon_m\%$	58	60		87	63	70
	$\varepsilon_b\%$	153	177		222	119	136
2.68	σ_m(psi)	114.5	83.3		66.0	74.0	74.6
	σ_b(psi)	88.5	53.5		48.5	63.1	58.6
	E (psi)	580	410		350	407	407
	$\varepsilon_m\%$	57	57	62	43	41	
	$\varepsilon_b\%$	148	132	165	68.0	63.9	
4.00	σ_m(psi)	101	100	92.0	91.0	92.9	
	σ_b(psi)	71.8	64.0	65.0	44.9	33.2	
	E (psi)	433	410	389	461	515	

1.6" x 1.6" x 1.35" gage
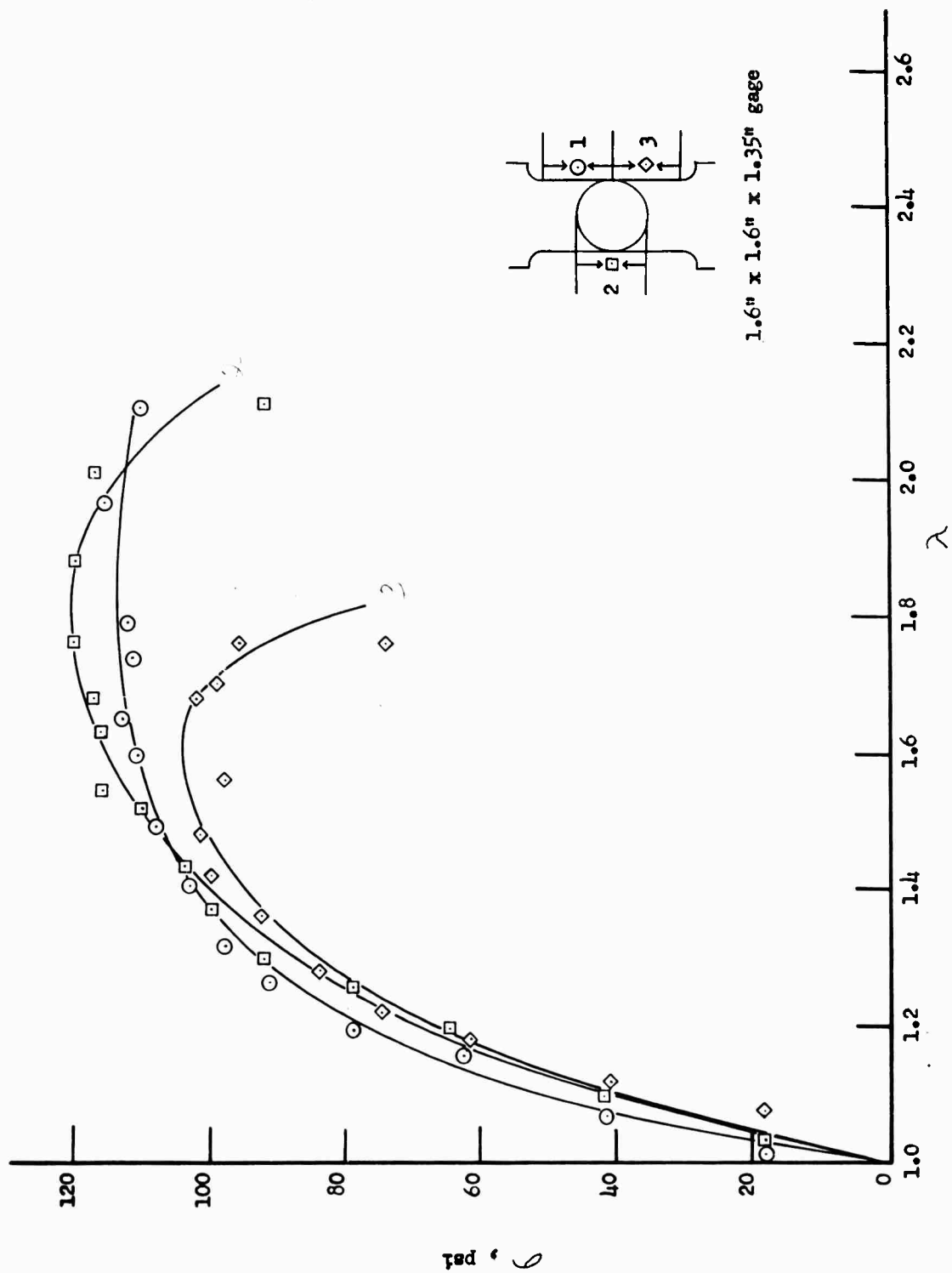
Figure 16. Effect of Nonuniform Dewetting on the Strain Behavior of an Oversize
Tensile Prepared From a Class 2 Inert Propellant

II, Phase 1 -- Mechanical Property Determination (cont.)

B.   THE BINDER-OXIDIZER BOND

The application of a tensile deformation to a propellant specimen results in an increase in volume of the specimen due to the rupturing of adhesive bonds between the binder and oxidizer with the subsequent formation of voids. A knowledge of the extent of volume increase and the strain at which it begins is important to the understanding of the stress-strain behavior of the propellant in question.

1.   Dilatation Technique

In the past, volume change measurements have been made using a dilatometer (4) or a modified hydrometer device (5). In addition to requiring an elaborate apparatus, these techniques are susceptible to errors produced by small temperature fluctuations and are limited in their sensitivity. The method described here was developed with the aim of circumventing these difficulties and providing a simple, accurate technique for the routine measurement of volume changes as a function of strain.

The test specimen consists of a small propellant sample (1/4" x 1/2" x 2") coated with a thin layer of polyurethane rubber and bonded endwise between rectangular shaped pieces of acrylic plastic, one of which has been drilled and tapped in two places to accept 1/8" calibrated screws, Figure 17. The specimen is suspended from the pan of an analytical balance by a thin nylon monofilament into a liquid of known temperature and density contained in a dewar flask. A strain is applied stepwise by turning the calibrated screws a given number of revolutions thus forcing the end pieces apart. The immersed weight is measured at strain intervals of about 0.5% until failure. For a sample having an initial volume of 5 cc, a volume change of 0.004% can be detected.

2-1/2"

P
R
O
P.
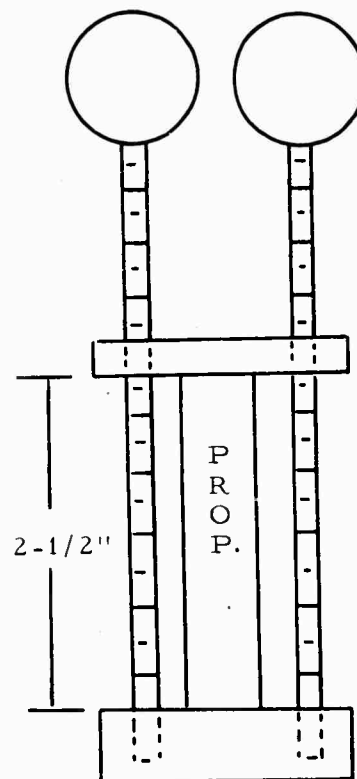
Figure 17.   Dilatation Specimen

II, B, The Binder-Oxidizer Bond (cont.)

The volume changes are calculated from the following relation-
ship:

$$\Delta V = \Delta W / \rho_1 \tag{16}$$

where ΔV = volume, V, at extension, 1, minus initial volume, V_o

ΔW = initial immersed weight, minus immersed weight at
extension, 1.

ρ_1 = liquid density at temperature of measurement

The ratio of the deformed volume can be expressed by the
product of the three principal extension ratios. If we assume that the strain
is isotropic, the volume ratio can be given by the product of the linear exten-
sion ratio and the square of the lateral extension ratio. If we express this in
terms of logarithmic strain and differentiate with respect to the logarithmic
extension ratio, the following relationship of Smith (4) is obtained:

$$\frac{d \ln V/V_o}{d \ln\lambda_1} = 1 + 2 \frac{d \ln\lambda_2}{d \ln\lambda_1} \tag{17}$$

It is sometimes convenient to define Poisson's ratio, ν, as follows:

$$\nu = - \frac{d \ln\lambda_2}{d \ln\lambda_1} \tag{18}$$

so that the slope of a plot of $\ln V/V_o$ versus $\ln\lambda_1$ is equal to $1 - 2\nu$ and ν is
easily obtained.

It should be noted that the above method of calculation of ΔV
assumes that the volume change occurs uniformly throughout the sample. This

II, B, The Binder-Oxidizer Bond (cont.)

is not always the case. Some propellants have a tendency to yield in localized bands. Since practically all of the volume change occurs in these yielded areas, the number of bands formed and thus the sample size become extremely important.

2. Glass Bead-Filled Polyurethane Elastomer

For initial studies using this technique, an idealized system of a polyurethane elastomer containing glass beads was selected. Figure 18 shows volume increase and corresponding Poisson's ratio for the pure elastomer and composites containing 40.8, 50.7, and 58 volume percent filler. As would be expected, the pure rubber showed no measurable volume change corresponding to a Poisson's ratio of 0.500. The extrapolation of the linear portion of the log plot, V/V_o, gives a value defined by Smith (4) as the yield strain. He reports that the relationship between yield strain and volume fraction of filler for this type of system may be represented by the equation:

$$\varepsilon_c = \varepsilon_{r,c}(1 - 1.05 \, V_f^{1/3}) \tag{19}$$

where ε_c = observed yield strain

$\varepsilon_{r,c}$ = strain in the binder between adjacent filler particles just prior to failure of the adhesive bond

V_f = volume fraction of glass beads

A plot of ε_c versus $1 - 1.05 \, V_f^{1/3}$ is presented in Figure 19. The slope, which equals $\varepsilon_{r,c}$ is 0.37, or 37% strain. From the stress-strain curve for the unfilled binder, Figure 20, it can be seen that this strain corresponds to a stress of about 50 psi. These data indicate that the bond strength between binder and filler in these samples is quite low.
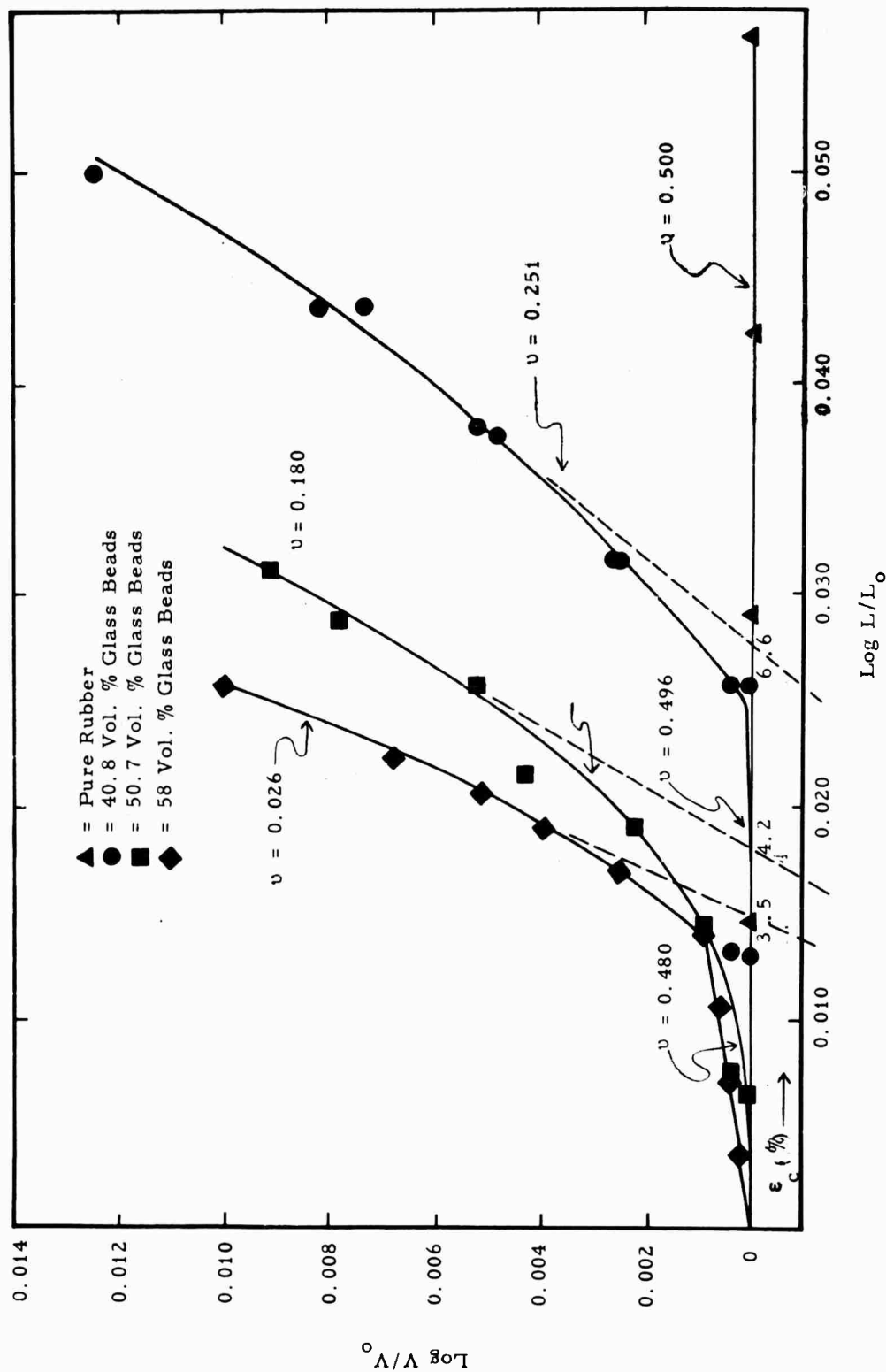
Figure 18. Log Volume Change vs Log Extension Ratio for Several Glass
Bead-Polyurethane Composites

$$\varepsilon_{c, r} = \frac{.074}{0.20} = 0.37$$

$$1 - 1.105 \, V_f^{1/3}$$
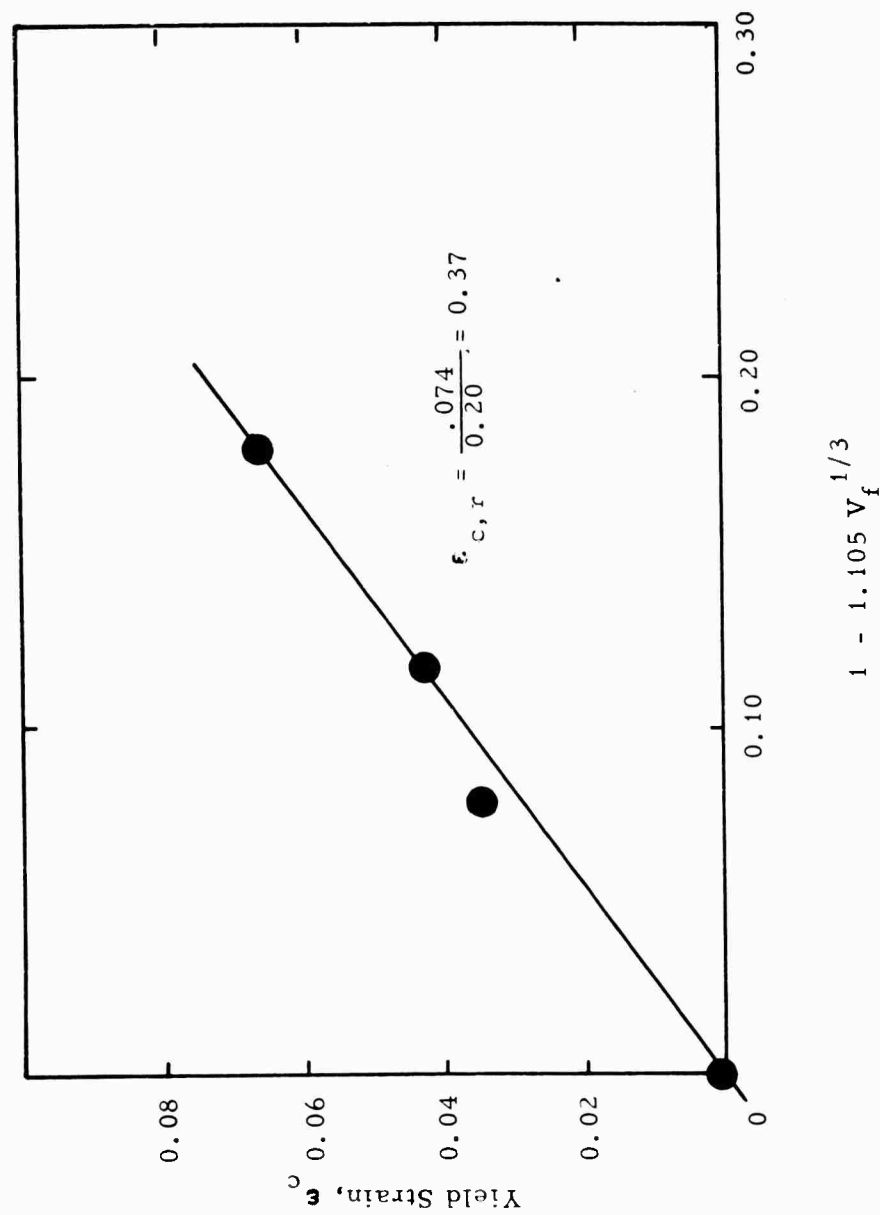
Yield Strain, ε_c

Figure 19.   Variation of Yield Strain With Volume Fraction of Glass Bead

STRAIN RATE 1 min. $^{-1}$
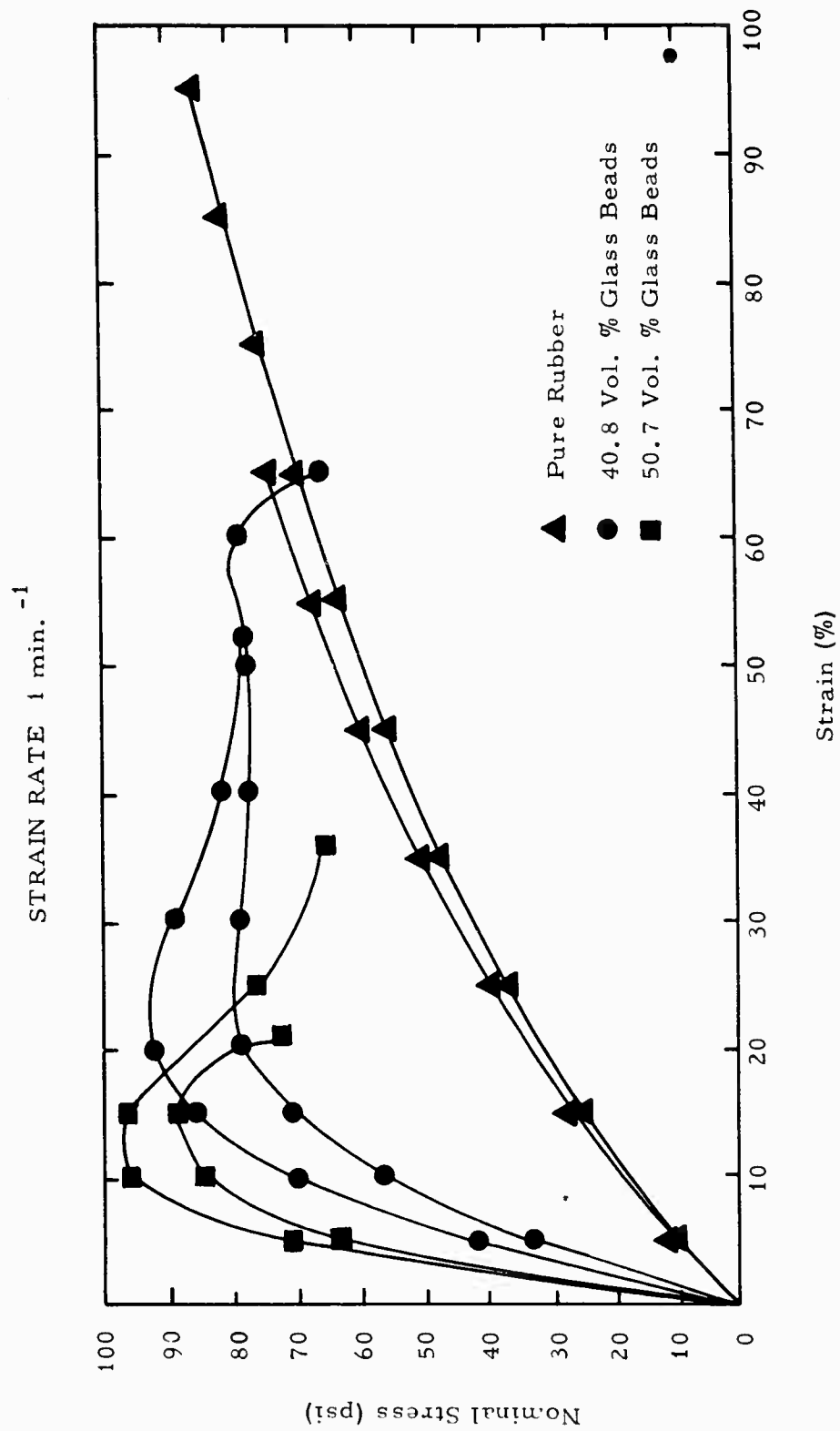
Figure 20. Uniaxial Stress vs Strain Glass Bead - Polyurethane Composites

- ▲ Pure Rubber
- ● 40.8 Vol. % Glass Beads
- ■ 50.7 Vol. % Glass Beads

Strain (%)

Nominal Stress (psi)

II, B, The Binder--Oxidizer Bond (cont.)

The dewetting, or release behavior of the binder-filler bond, appears to be the dominant factor in response behavior of composite propellants. Further information on the nature of this bond is provided by examining volume change behavior on repeated loading of specimens.

Figure 21 shows the log V/V_o versus log L/L_o plots for the specimen containing 50.7 volume percent glass beads cycled three times between 0 and 11% strain. In going from cycle 1 to 3, it should be noted that the "forward" halves of the cycle approximate more closely the "recovery" halves, in which Poisson's ratio is independent of extension. This behavior may be explained by assuming that initially there exists a mechanical bond between the binder and filler particles and a certain critical strain level must be reached before these bonds begin to rupture with the formation of voids around the glass beads. As the strain is increased, more voids form and those already formed increase in size. When the applied strain is reduced, the volume uniformly decreases as the voids become smaller analogous to the behavior of a foam.

A similar plot for a sample containing 40.8 volume percent glass beads cycled to increasingly higher strains is presented in Figure 22. The path of the volume change retraced itself up to a critical strain of about 6%. At that point a sharp change in slope was observed and the recovery curve followed a different path. The immediate and almost complete reversibility noted in the first portion of the curve is further evidence that the initial volume increase is due to inherent voids and unbonded areas.

3.   Testing in Water

Figure 23 shows a plot of ΔV versus strain for a Class 2 polyurethane propellant. It is obvious that the volume begins to increase immediately upon the application of strain. Up to about 15% strain the volume
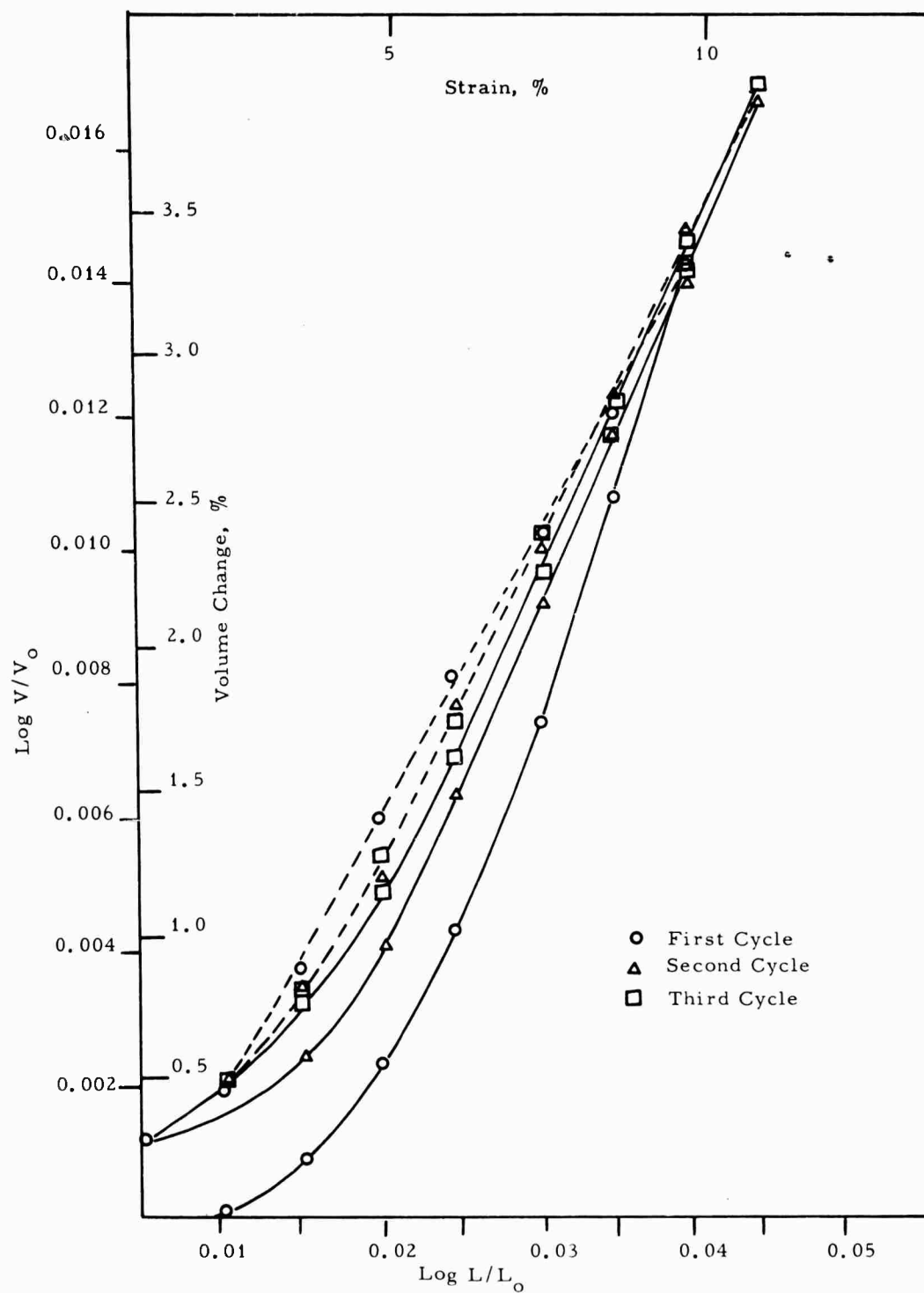
Figure 21. Log Volume Change vs Log Extension Ratio, 50 Volume % Glass Bead-Polyurethane Composite
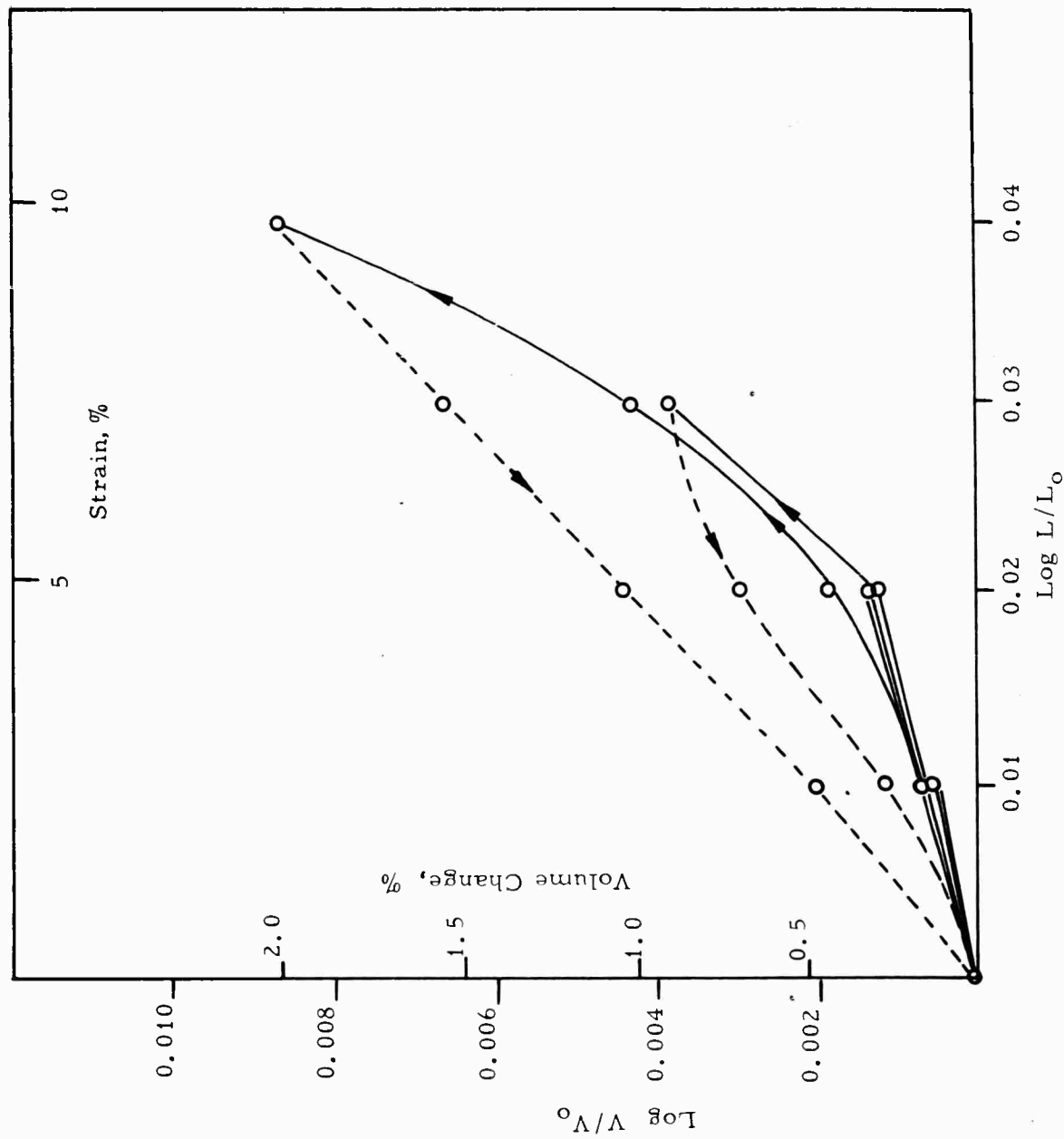
Figure 22. Log Volume Change vs Log Extension Ratio, 40 Volume % Glass Bead-Polyurethane Composite
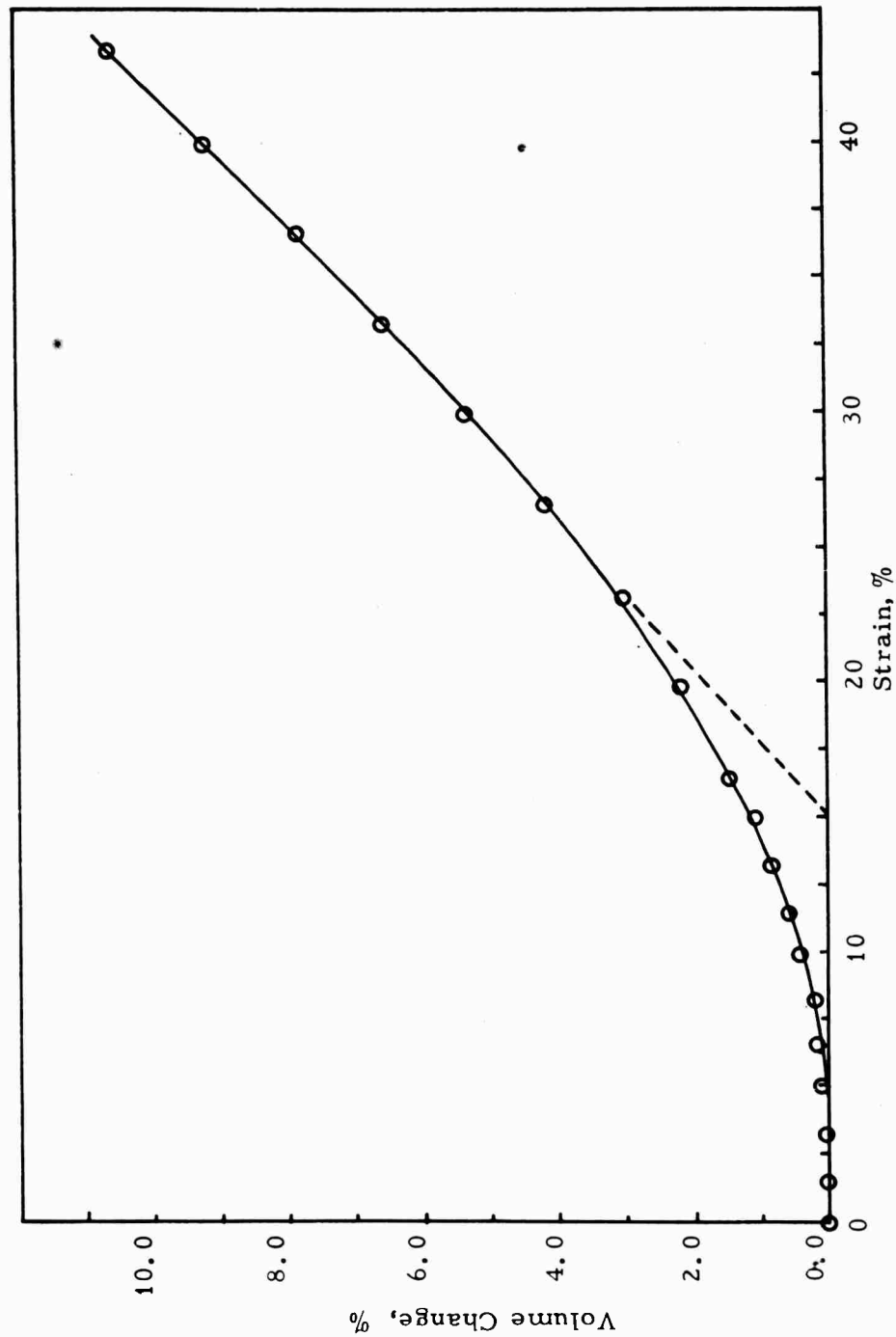
Figure 23. Volume Change vs Strain for a Class 2 Polyurethane Propellant at 77°F

II, B, The Binder-Oxidizer Bond (cont.)

changes slowly. However, above 15% strain the rate of volume change increases markedly. Figure 24 shows uniaxial tensile curves obtained from samples of this same propellant tested at the standard rate of 0.74 min^{-1} in air and while submerged in water. It can be seen that the initial moduli are identical, but at about 15% strain the curve representing the sample tested under water departs from the standard test curve and the sample fails at lower values of stress and elongation. A similar test performed with the sample submerged in silicone oil gave results identical to those obtained from the standard test in air. Tests were also performed in which samples were cycled to continuously higher strain levels while in contact with air, water and silicone oil. In the air and silicone oil tests, the curves obtained from each cycle up to strains approaching ε_m were practically identical to the original except for a small amount of relaxation. In the case of the test under water, however, after a strain of 15% was exceeded, succeeding cycles exhibited a drastic decrease in modulus. Tensile tests performed approximately two weeks after cycling in air to strains well past ε_m have shown that the original properties were almost completely recovered. This is perhaps indicative that little or no tearing occurs within the binder during repeated straining in air.

A so-called "Water Drop Test" has been developed in which tensile specimens are extended and held at various strain levels after which a drop of water is placed anywhere along the gage section and the time to failure recorded. At strain levels above the critical strain the water reduces the time to failure by a factor of several thousand. At strain levels below the critical strain, the water has little effect immediately but produces blanching after several hours.
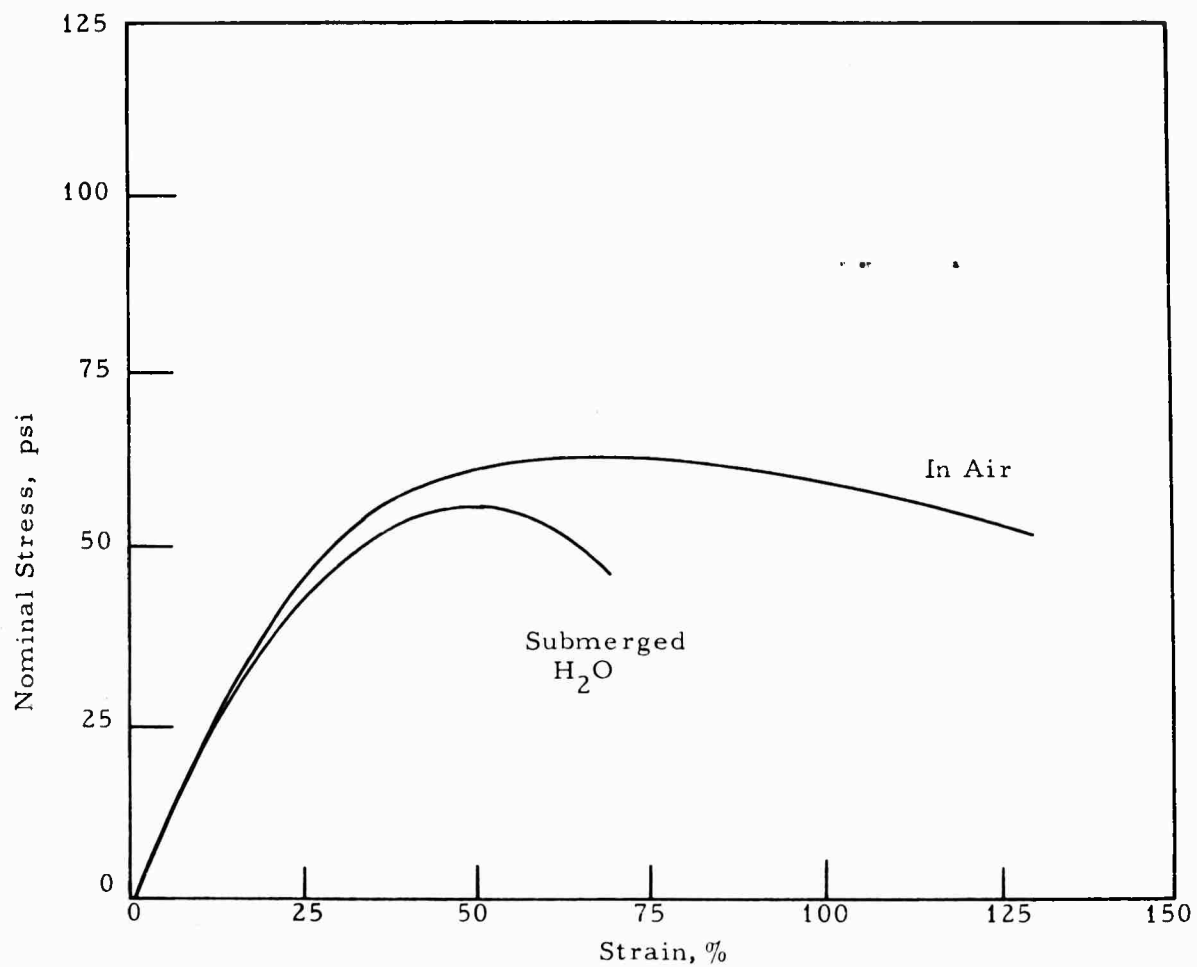
Figure 24. Stress vs Strain for Unaged Class 2 Polyurethane Propellant at 77°F and a Strain Rate of 0.74 min.$^{-1}$

II, B, The Binder-Oxidizer Bond (cont.)

From these observations, the following mechanism for the dewetting process is proposed. In the first portion of the ΔV versus extension curve, Figure 23, the volume change is the result of the enlargement of existing voids and the formation of a small number of additional voids in areas where no bond exists between the binder and oxidizer. As the strain approaches some critical level (15% in the sample cited) the stress exerted on the binder-oxidizer bonds in the vicinity of the vacuoles formed initially becomes sufficient to cause rupture of these bonds. As these bonds break, the stress on neighboring particles is increased and further dewetting occurs. This process continues until complete dewetting or failure is the result. When a sample in contact with water is extended beyond the critical strain, the water is sucked into the voids formed near the propellant surface and because of its solvating effect weakens the binder between oxidizer particles, thus initiating tearing with an accompanying reduction in retractive force and early failure.

4.   Effect of Humidity on Dilatation

The dilatation technique was also used to study binder-oxidizer interaction over a wide temperature range on humidity controlled samples. Figure 25 presents a plot of volume change versus strain for samples of another Class 2 polyurethane propellant dried over P_2O_5 at 77°F and then tested at 77°, 20°, 0°, -20°, and -40°F. Figure 26 shows the results for samples conditioned at 80% relative humidity. In general, for a given test temperature and strain level, the sample conditioned at 80% R.H. exhibits a significantly greater volume increase than the corresponding dried sample. This is illustrated in Figure 27 where the volume increase at 10% strain is plotted as a function of temperature. The maximum volume changes in the dry and wet samples occur at -20° and 0°F, respectively. The cause of this behavior is not yet understood but it may possibly be the result of a simultaneous weakening of the binder-oxidizer bond and stiffening of the propellant binder.
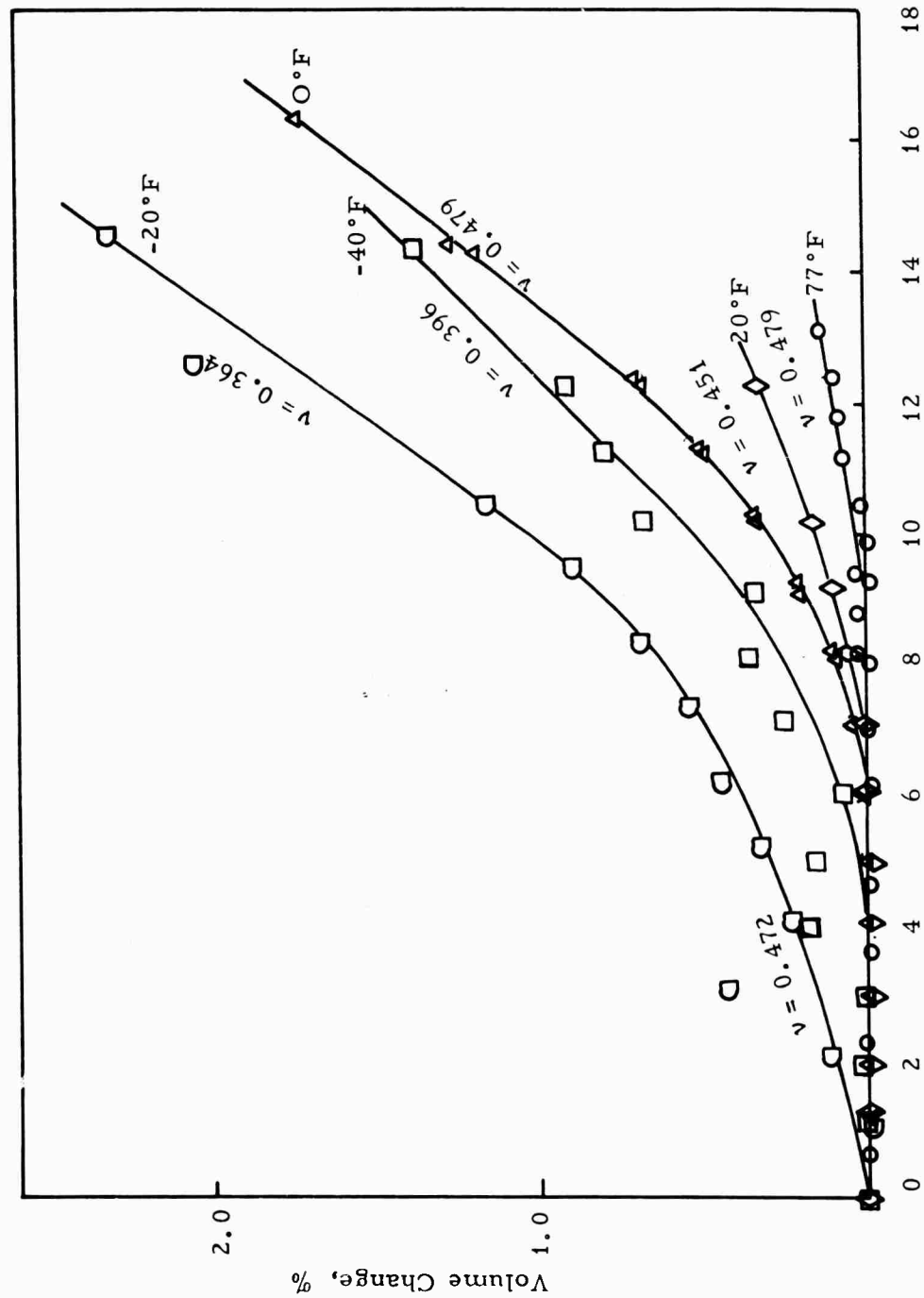
Figure 25. Volume Change vs Strain for Class 2 Polyurethane Propellant
Conditioned Over P_2O_5 Prior to Test at Several Temperatures
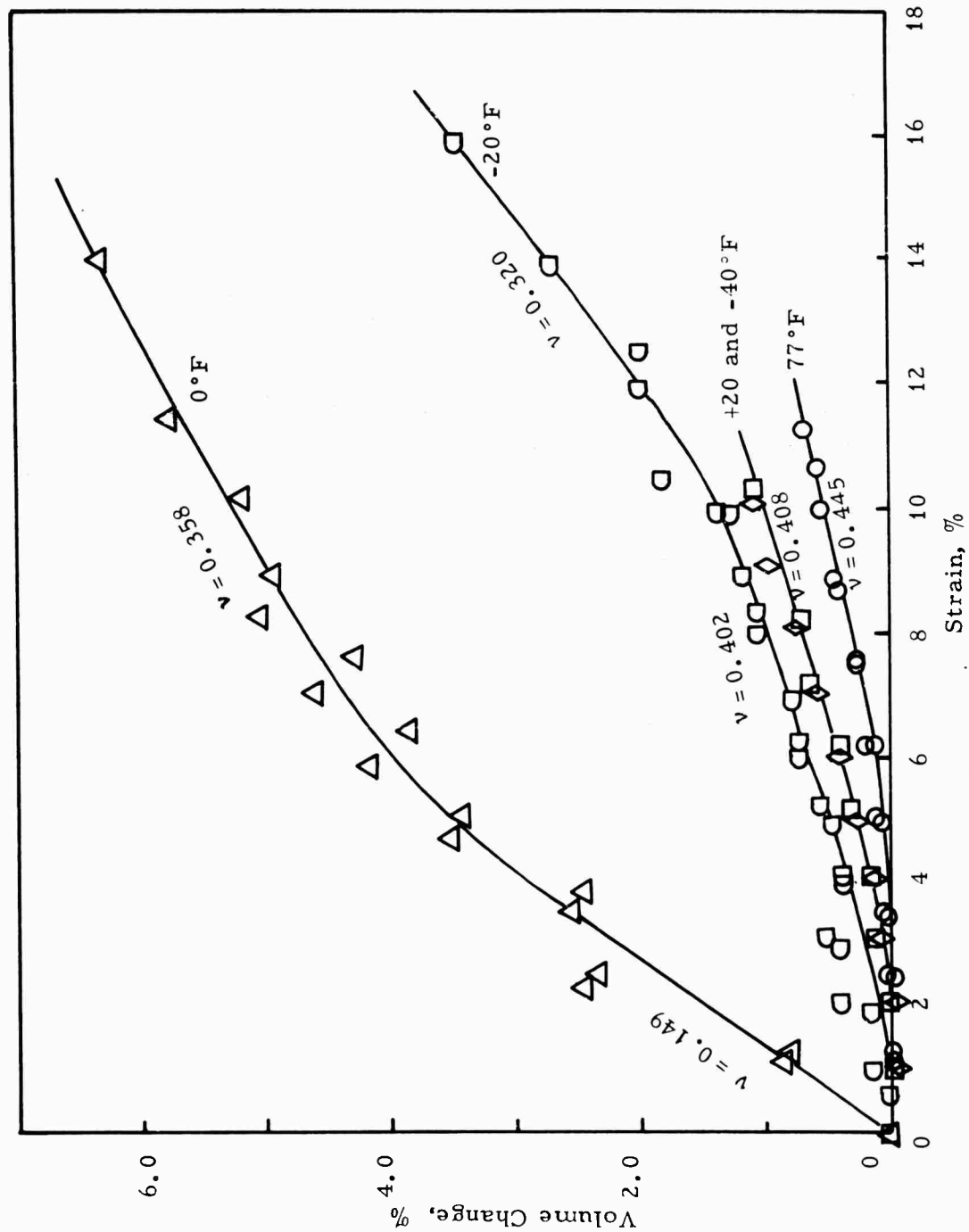
Figure 26. Volume Change vs Strain for a Class 2 Polyurethane Propellant Conditioned at 80% RH Prior to Test at Several Temperatures
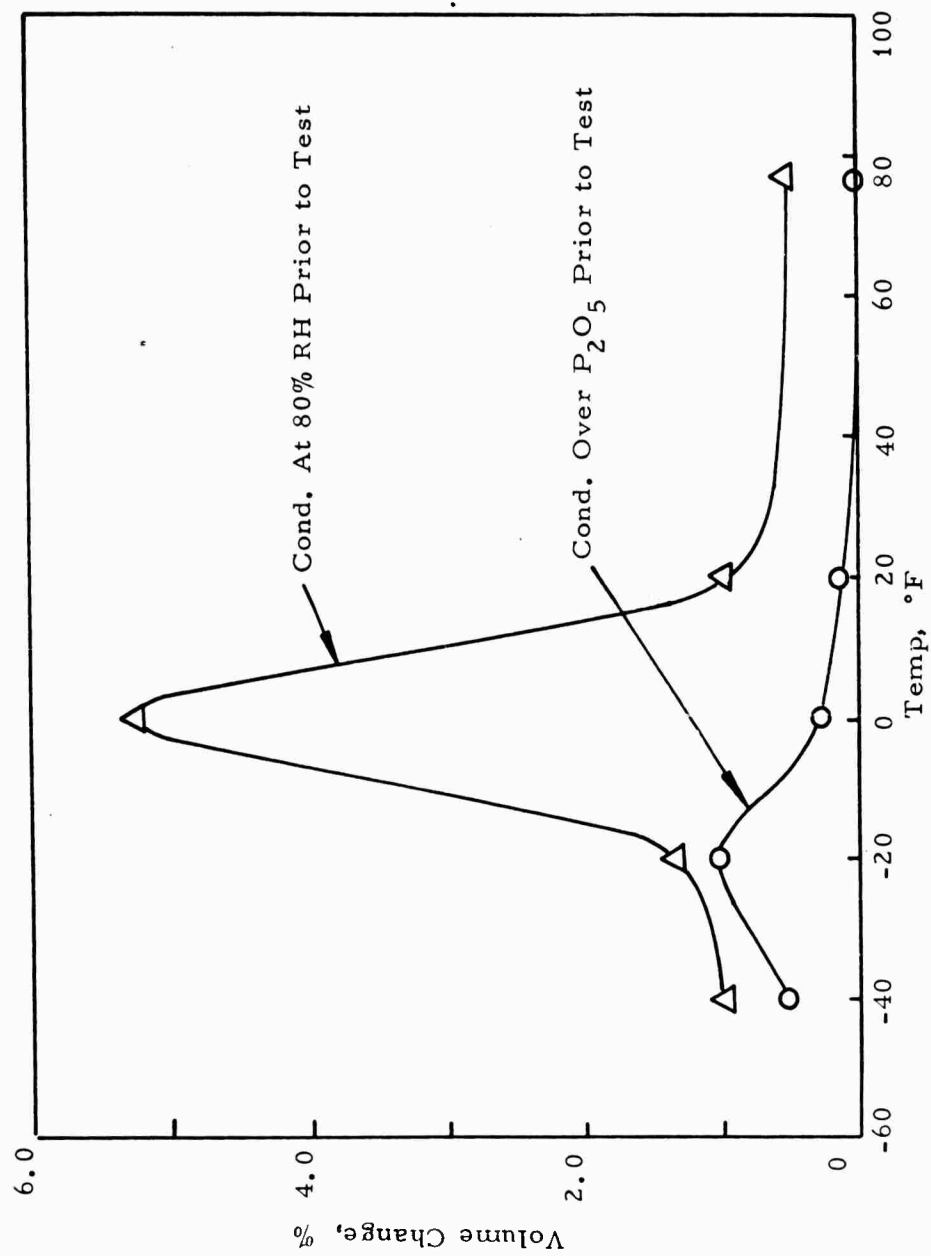
Figure 27. Volume Change at 10% Strain vs Temperature

II, B, The Binder-Oxidizer Bond (cont.)

5. Effect of Embrittlement* on Dilatation

The effect of embrittlement at high humidity levels upon the dilatational behavior of a Class 2 polyurethane propellant is shown in Figure 28. The volume change at 0°F shortly after the samples were removed from 0 or 80% R.H. conditioning at 77°F is compared with data for samples subjected to similar humidity conditioning before being further conditioned for two weeks at 0°F prior to test. The curves are similar in slope but it appears that the volume change is noticeably reduced by the embrittlement phenomenon.

The behavior described above does not appear to be general for all polyurethane propellants even for those showing one class of behavior. Some data for another Class 2 polyurethane propellant at 0 and 80% R.H. and 0°F is shown in Figure 29. The behavior at 0°F at the high humidity is completely different from that shown in Figure 28; the curve from Figure 28 for two weeks at 0°F after P_2O_5 drying is also shown in Figure 29. The cause for this difference is not understood but it is interesting that while the first propellant undergoes embrittlement at a very high rate at 0°F, the second does this to a much lesser extent.

Dilatation data for inert propellant DP-31** at 0°F previously conditioned at 0 and 80% R.H. at 77°F are presented in Figure 30. These data differ appreciably from both of the Class 2 propellants containing NH_4ClO_4, as conditioning the samples for two weeks at 0°F has no effect upon the dilatation behavior. This is in agreement with the absence of embrittlement observed

---

* Embrittlement is a term for the increase of modulus and decrease of elongation as the result of storage at about 0°F for extended times. A more extensive discussion is given by Goldhagen (7).

** DP-31 is an inert propellant containing 55 wt. % KCl, 10 wt, % $(NH_4)_2SO_4$, 17 wt. % Al, and 18 wt. % polyurethane binder containing 10% of the binder as plasticizer.
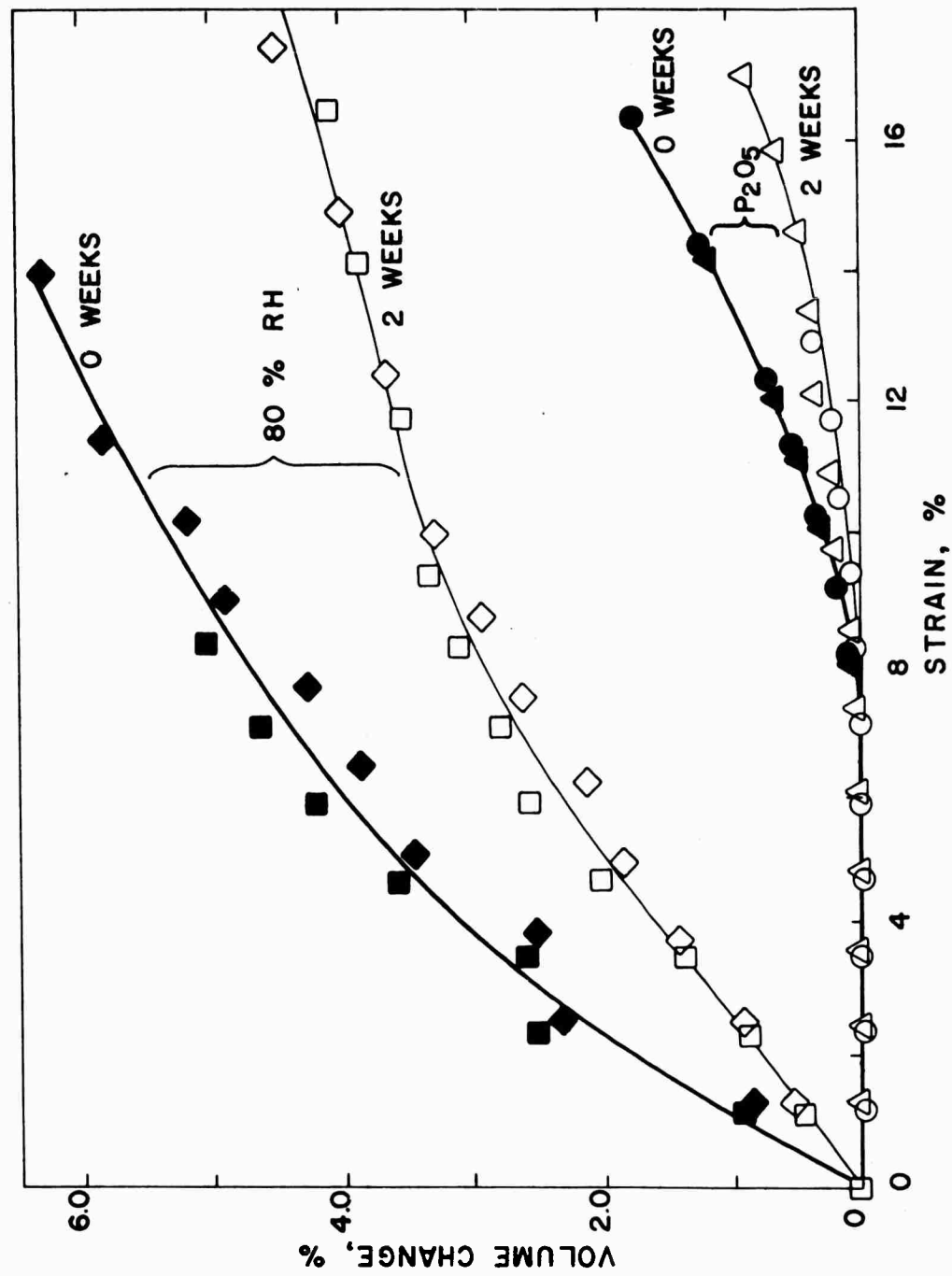
Figure 28. Volume Change vs Strain for a Class 2 Polyurethane Propellant Tested at 0°F After 0 or 2 Weeks Storage at 0°F Following Drying Over P_2O_5 at 77°F or Conditioned at 80% RH at 77°F
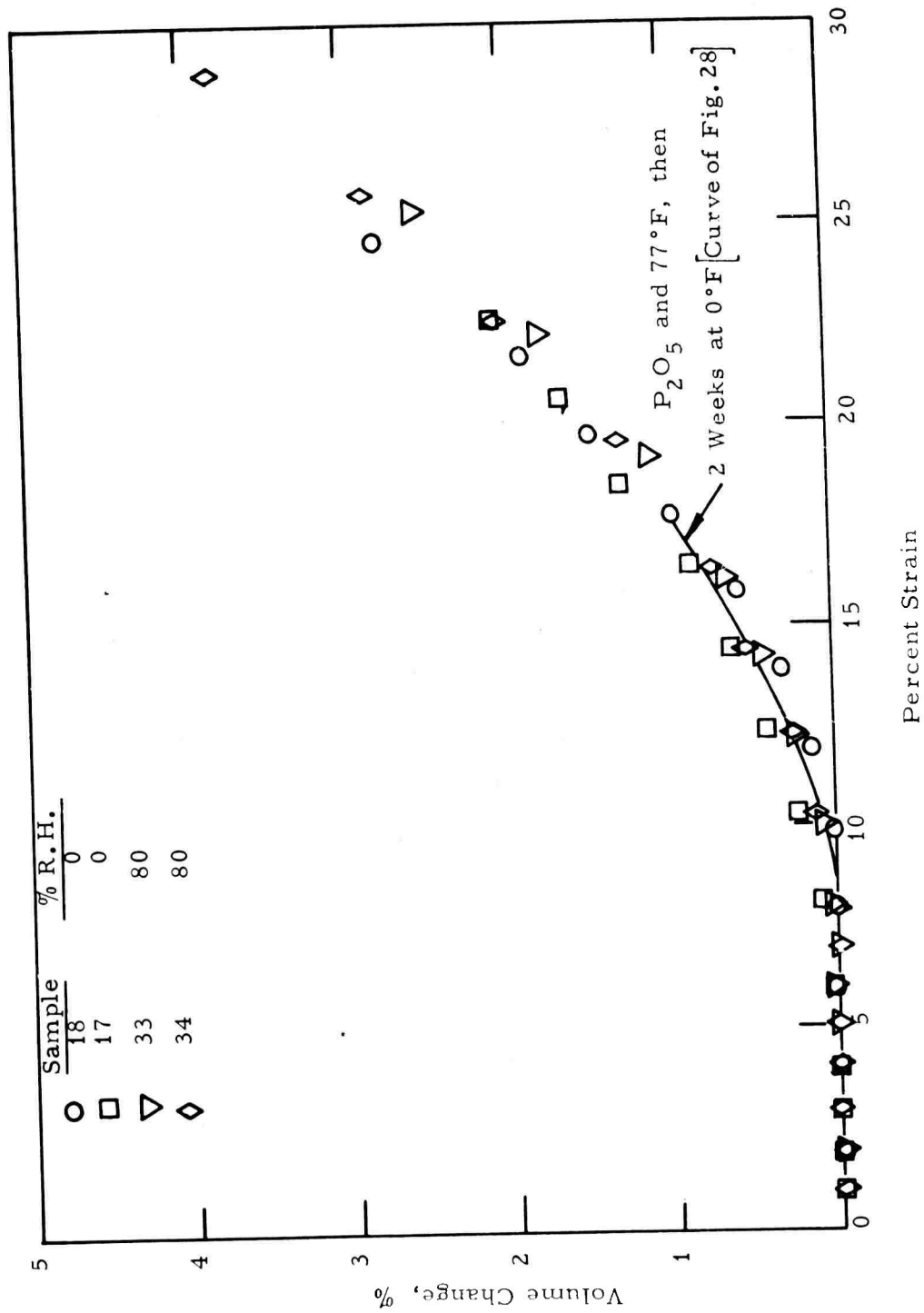
Figure 29. Volume Change vs Strain for Another Class 2 Polyurethane Propellant
Tested at 0°F
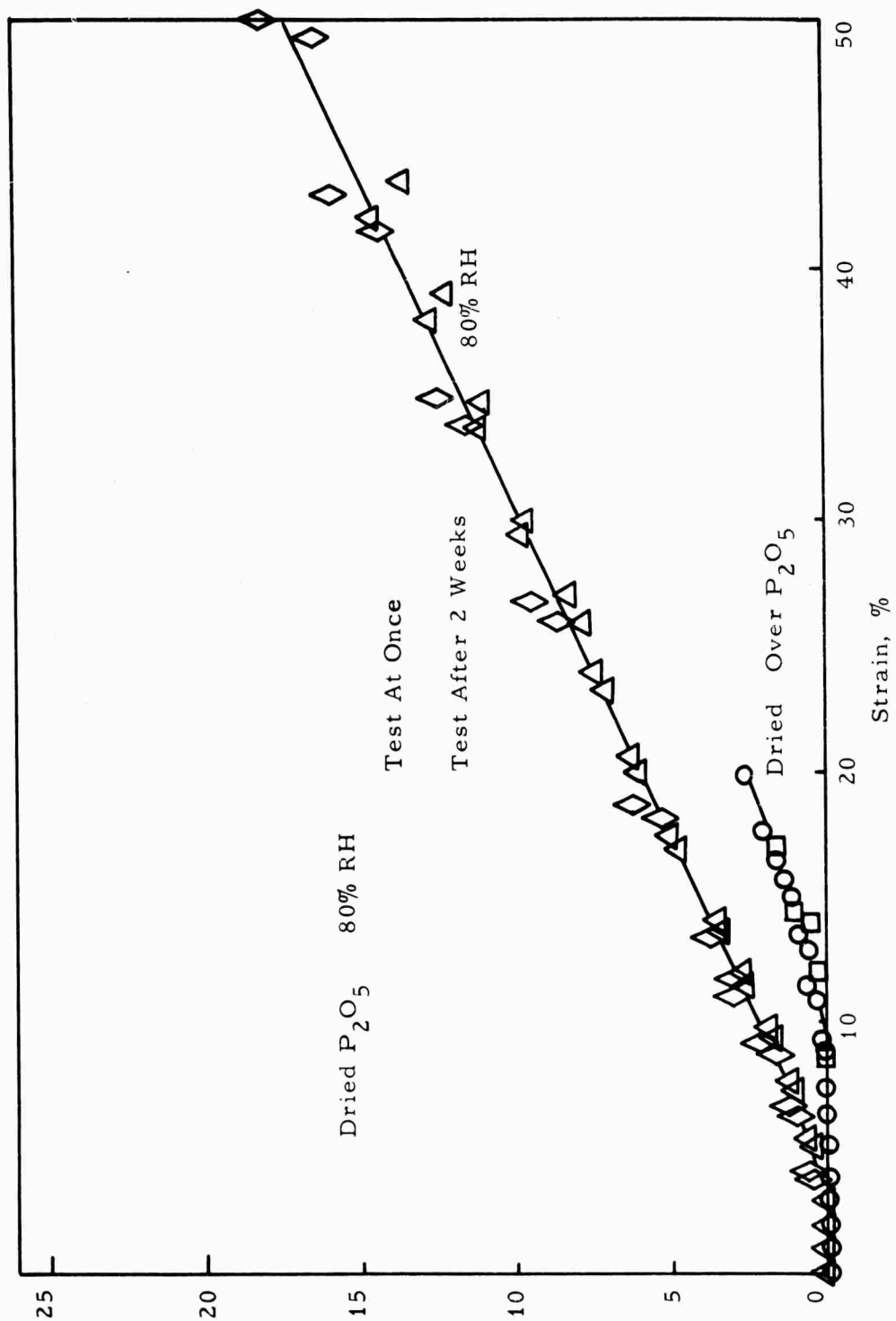
Figure 30.   Volume Change vs Strain for DP-31 Inert Propellant Tested at 0°F

II, B, The Binder-Oxidizer Bond (cont.)

with this material. Also, the humidified samples have a much greater elongation in that they softened considerably and could be strained to the limit of the apparatus without failure.

Dilatation studies of a Class 1 polyurethane propellant were completed at -40°, 0°, and 77°F and at 0 and 80% R.H. and are presented in Figures 31 and 32. The behavior at -40° and 77°F is similar to that shown for a Class 2 propellant in Figures 25 and 26, except for the unusual effect shown at 0°F and 80% R.H. in Figure 26. Figure 33 shows dilatation data for this Class 1 propellant at 0°F and 80% R.H. as a function of gage length. It can be seen that the variation of data with sample size is random and seems to be of similar magnitude to the usual sample-to-sample variation.

Since water plays a role in the embrittlement process, experiments were conducted on the effects of exposure of JANAF tensile specimens of a Class 2 propellant, which had been dried over P_2O_5 and others conditioned at 95% R.H., to vapors of CCl_4, CH_2ClCH_2Cl, CS_2, C_6H_5OH, $C_6H_5NO_2$, $(C_2H_5)_2NH$, o-$C_6H_4Cl_2$, $(C_2H_5)_3N$, $C_6H_5NH_2$, $(C_2H_5)_2O$, CH_3OH, C_6H_6, CH_2Cl_2, and C_5H_5N. These specimens were then conditioned for one week at 0°F and tested at -40°F. The dried samples showed considerable embrittlement after treatment with C_5H_5N and $(C_2H_5)_2NH$ and embrittlement to a lesser degree after exposure to $(C_2H_5)_3N$, C_6H_5OH, $C_6H_5NO_2$, $C_6H_5NH_2$, and o-$C_6H_4Cl_2$. These same reagents caused an increase in the embrittling tendency of the high-humidity tested samples. It is of interest to note that these same compounds would also tend to increase the solubility of ammonium perchlorate in the propellant binder.

Inert propellants (DP 16 and DP 31), which do not undergo embrittlement after exposure to high humidity, exhibited no embrittlement after exposure to the vapors of $(C_2H_5)_3N$ and C_5H_5N for 24 hours at 77°F.
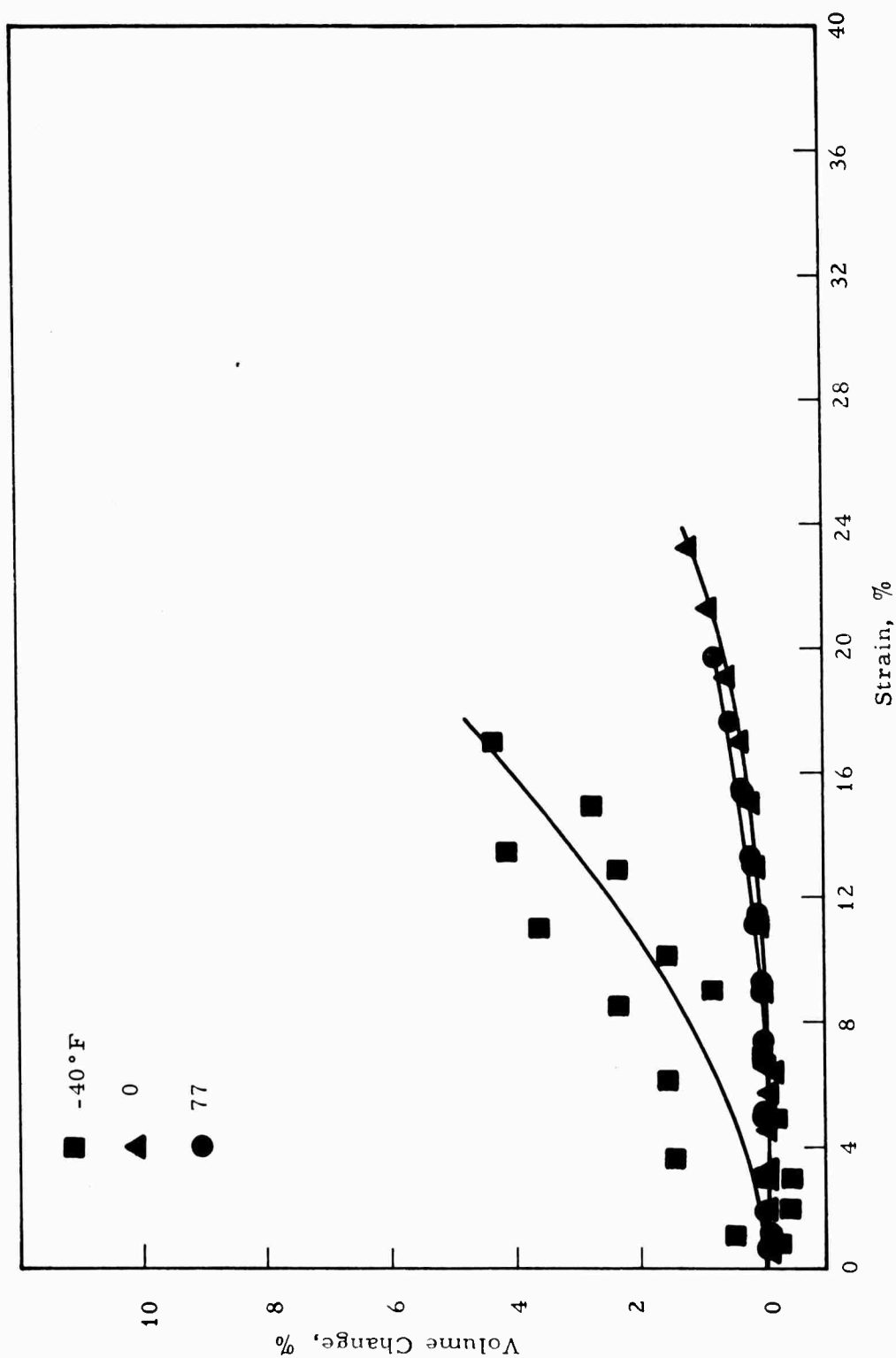
Figure 31. Effect of Temperature on the Volume Change of a Class 1 Polyurethane Propellant After Drying over P_2O_5 at 77°F
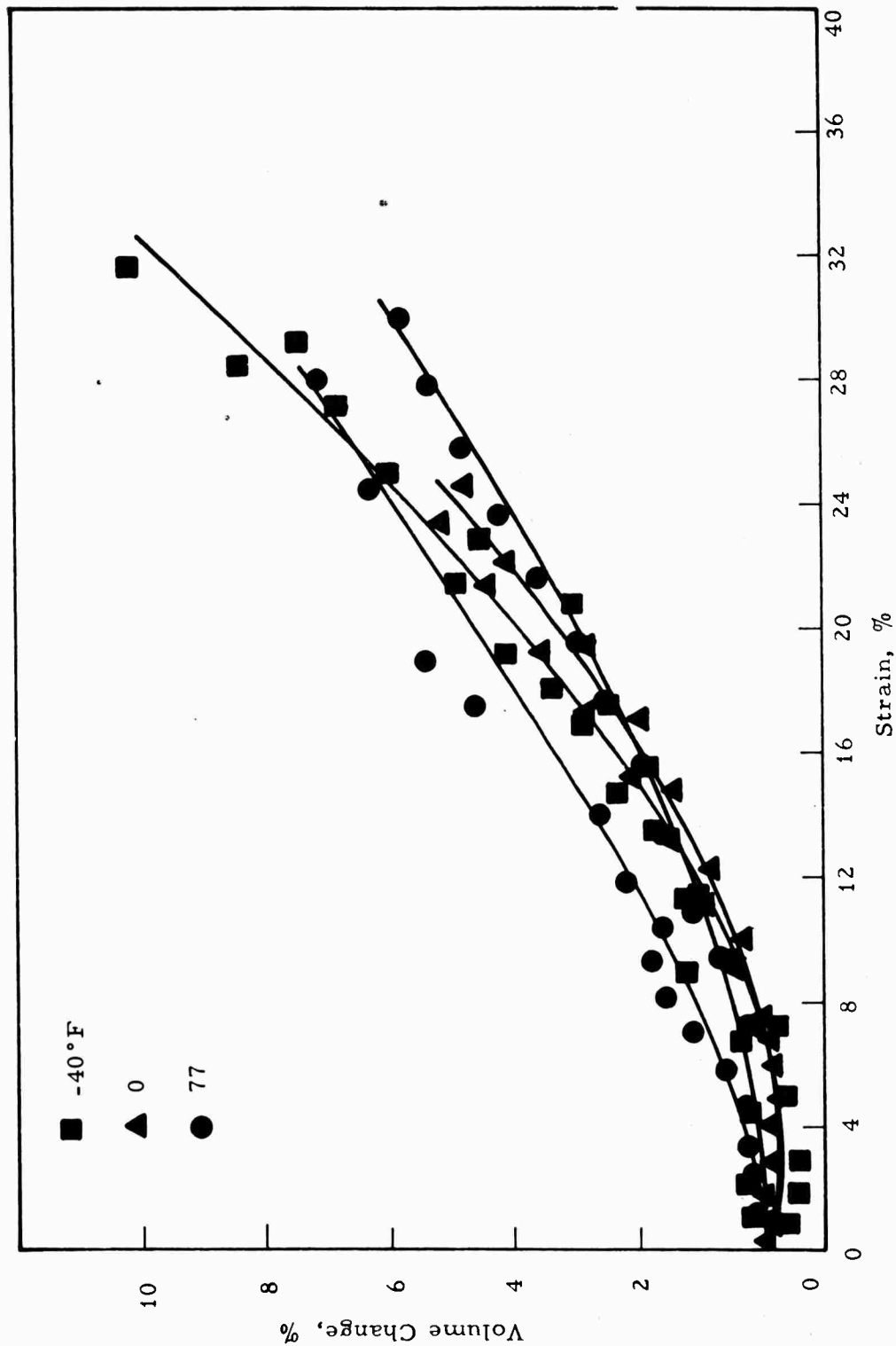
Figure 32. Effect of Temperature on the Volume Change of a Class 1 Polyurethane Propellant After Conditioning at 80% RH and 77°F
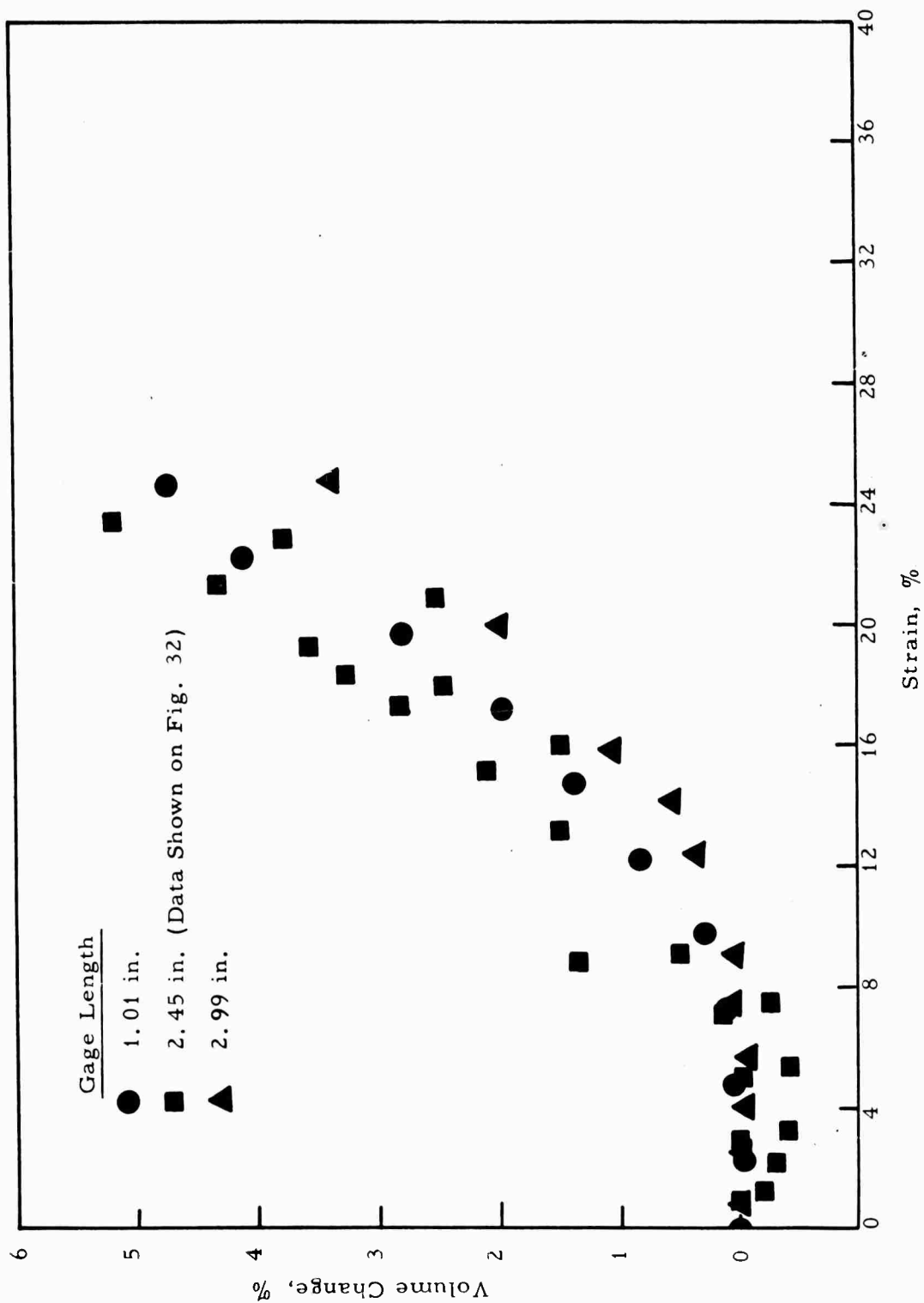
Figure 33. Volume Change vs Strain of a Class 1 Polyurethane Propellant for Three Gas Lengths After Conditioning at 80% RH and Testing at 0°F

II, B, The Binder-Oxidizer Bond (cont.)

6. Rehealing of the Bond

A phenomenon of "rehealing of the bond between the binder and the filler particles is observed as illustrated in Figure 34. A Class 2 polyurethane propellant was repeatedly strained at 77°F at a rate of 0.74 min.[-1] to about 30% strain, reversing the Instron to remove the load after each cycle. The first eleven runs were performed on one day, after which the specimen rested for 13 days before the 12th run. The essential recovery of initial properties suggests that the filler-binder bond was reestablished, or "rehealed".

Measurements were made of the rate of "rehealing" of a Class 2 propellant, which had been previously tensile cycled until an equilibrium modulus was reached, as a function of temperature. In this experiment Instron bars of the propellant conditioned for two weeks at 0% R.H. at ambient temperature were cycled at 77°F and 0.74 min.[-1] to a strain of 30%, well below the nominal maximum stress, until the initial modulus, E_i, reached an equilibrium value, E. These bars were then placed for varying lengths of time at -40, 0, 77 and 110°F, but still at 0% R.H., to "reheal". The moduli, E_3, of bars at various times of rehealing, t, were then measured at 77°F.

If the decrease in initial modulus is due to the cleavage of binder-oxidizer bonds, then $(E_1 - E)$, the difference between the initial and final equilibrium moduli after cycling, would be proportional to the number of bonds still not rehealed after time, t, of conditioning. Assuming that the rate of rehealing is proportional to the number of broken bonds, n, or that first order kinetics if followed, we have

$$- \frac{dn}{dt} = kn. \tag{20}$$
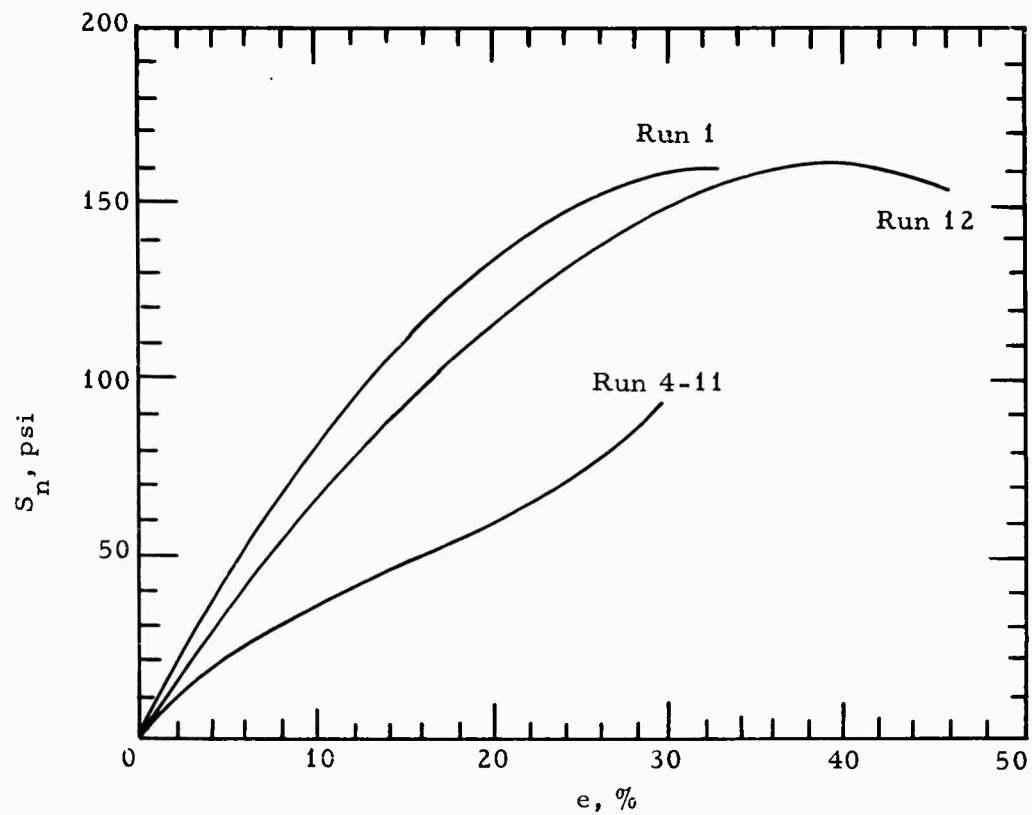
Figure 34. Stress-Strain Behavior of Class 2 Propellant at a Test Temperature of 77°F and a Strain Rate of 0.74 min^{-1} for Repeated Cycles With Rest of 13 Days After Run No. 11

II, B, The Binder-Oxidizer Bond (cont.)

Upon integrating and proper substitution we get

$$\log \frac{E_1 - E_3}{E_1 - E} = \frac{-kt}{2.303} \tag{21}$$

For convenience, the data have been plotted in the form $2 + \log \frac{E_1 - E_3}{E_1 - E}$ vs t in Figure 35. Considerable scatter exists in the data except for those at 110°F. Nevertheless, with the use of imagination, straight lines were drawn for each temperature and the rate constants calculated from the slopes. These rate constants, in turn, have been plotted vs 1/T in Figure 36 so that the activation energy may be calculated. A value of approximately 7 kcal/mole was determined for the overall "rehealing" process.

As these data showed the greatest scatter in the samples "rehealed" at low temperatures, it was felt that the scatter might be caused by conditioning at 77°F prior to measurement of E_3. The experiment was repeated using 40°F as the cycling and reference temperature. Specimens were dried over P_2O_5 at 150°F, tensile cycled this time at 40°F, and placed at 40°, 77°, 110°, and 150°F for rehealing. The data in Figure 37 showed somewhat less scatter and the values of k are plotted also in Figure 36. The activation energy for the "rehealing" process was calculated to be about 8.5 kcal/mole, in reasonable agreement with the previous experiment. The scatter of the data prevents a decision on whether the cycling temperature affects the activation energy.

These compare to a value of 22 kcal/mole for the case of rubber filled with carbon black reported by Bueche (6). Our low value for the activation energy of "rehealing" is indicative of a van der Weals' type interaction compared to a checmical or chemisorption phenomenon reported by Bueche for rubber.
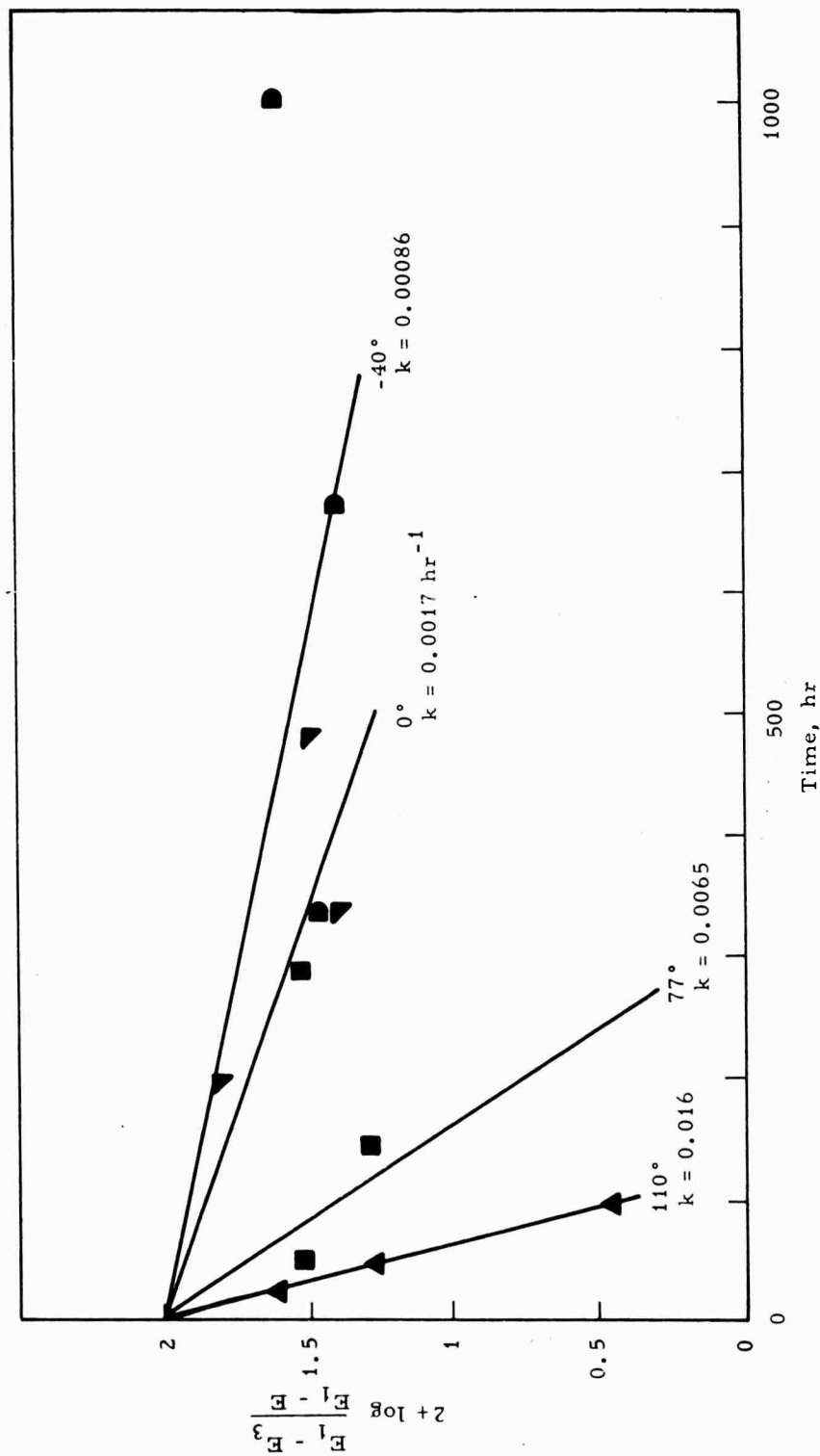
Figure 35. Rate of Rehealing of a Class 2 Polyurethane Propellant at 0% RH and Several Temperatures After Cycling at 77°F and 0% RH
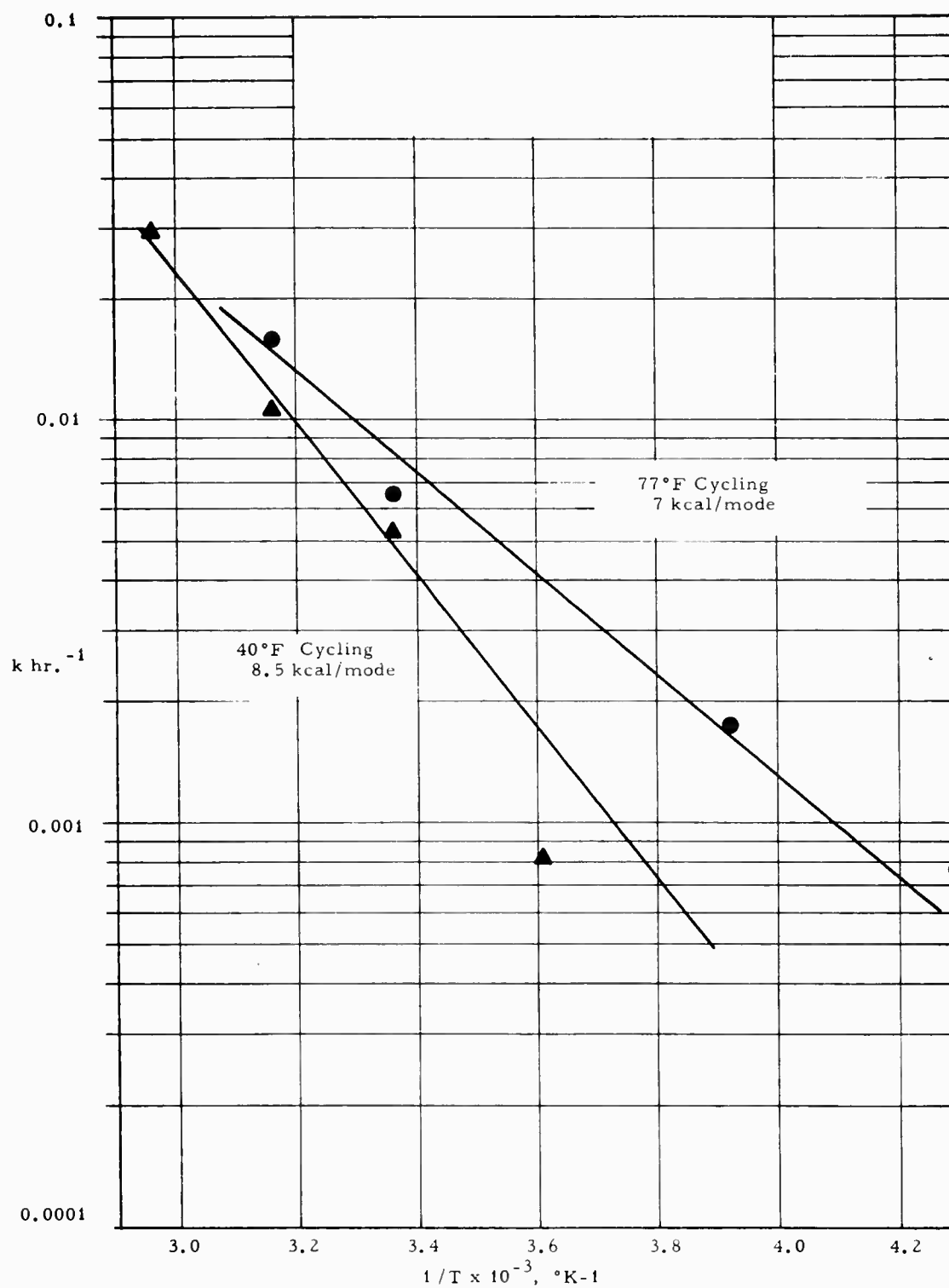
Figure 36. Determination of Activation Energy for Rehealing
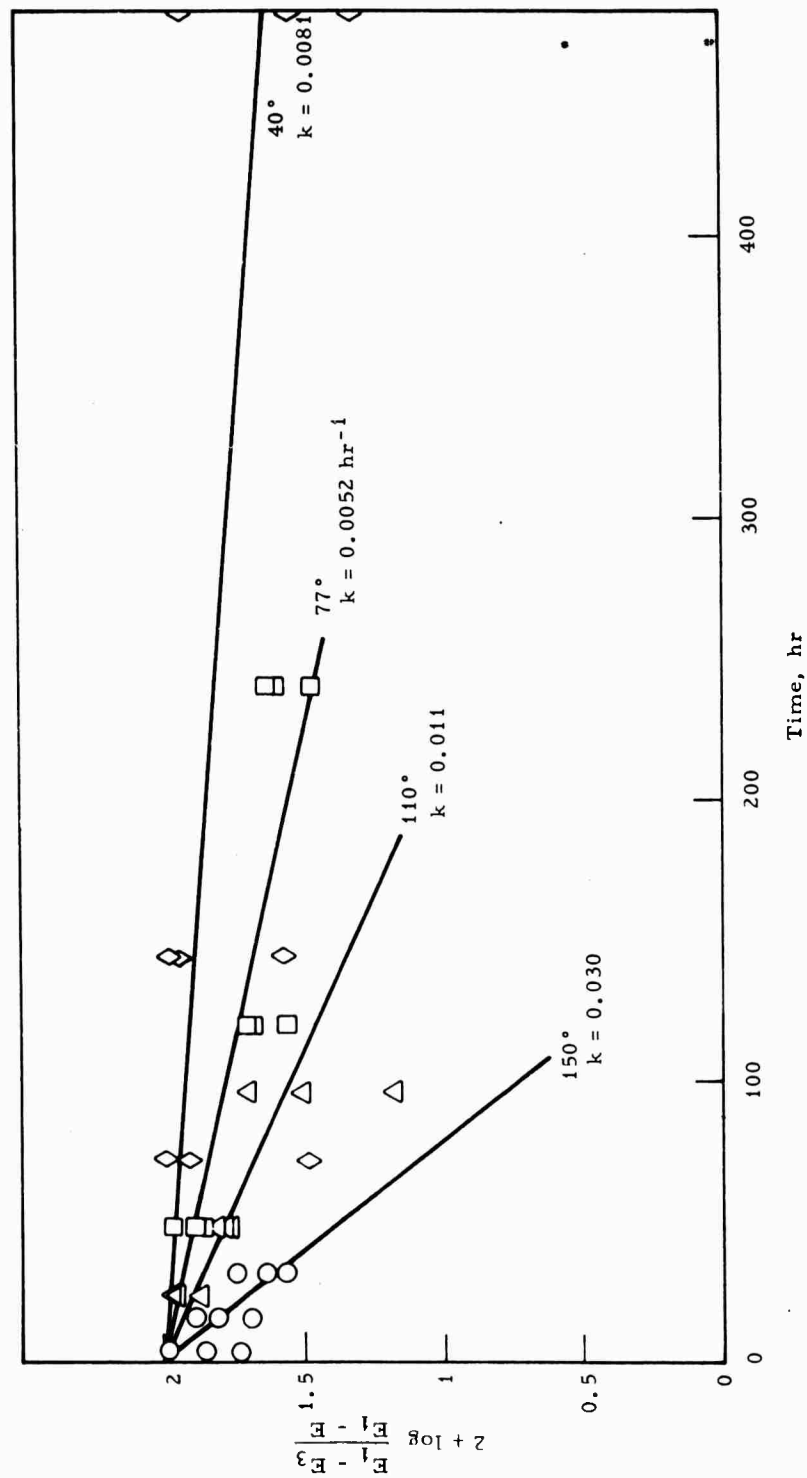
Figure 37. Rate of Rehealing at 0% RH and Several Temperatures After Cycling at 40°F and 0% RH

III. PHASE 2 - MATHEMATICAL REPRESENTATION OF MECHANICAL BEHAVIOR

The objectives of this phase were to systematize the methods for correlating results from the various experimental tasks, and to find the mathematical relationships which best approximate the observed mechanical behavior of solid propellants. This phase was concerned, then, with the real properties of the propellant, as distinguished from the idealized properties required by the limitations of present stress analysis methods. Although some of the real properties affect the accuracy of predictions of maximum stresses and strains in simple motors, their largest effect is evident in the failure behavior of motors.

A. CHARACTERISTIC BEHAVIOR AND PROPELLANT CLASSIFICATION

Before describing the results of current research studies, a review of the characteristic mechanical behavior of castable solid propellants containing more than 50 vol% filler is essential, since these real characteristics affect both the experimental apparatus and the results.

1. Summary of Characteristic Behavior

	Characteristic	Description
a.	Dewetting of the filler-binder bond	A failure of the adhesive bond between the binder and the filler.
	(1) "Work softening"	Produced by any manner of deformation of the material. This deformation destroys (at least temporarily) filler-to-binder bonds. The resulting material is softer because of the loss of structural reinforcement by the filler.

III, A, Characteristic Behavior and Propellant Classification (cont.)

Characteristic	Description
(2) "localized yielding"	Any tensile strain in a specimen will produce local regions where a majority of the binder-to-filler bonds have failed. These local regions have been "work softened". Hence, they elongate readily to very large deformations, while the nonyielded material experiences negligible elongations. Even the essentially nonyield regions exhibit local sites where the adhesive bonds have been severed.
(3) Volume change on straining	The dewetting of the filler permits the polymer about it to extend away from the particle so as to create cavities whose size depends upon the axial and lateral elongation. Volume increases in the cavities in the range of 100% of the filler particle volume are readily observed at 100% axial elongation. Dewetting is observed at strains as small as 1% in some cases.

III, A, Characteristic Behavior and Propellant Classification (cont.)

Characteristic	Description
(4) Size dependency	Because of the nature of the localized dewetting in solid propellants, it is found that most of the results of mechanical testing must be referred to the dimensions of the test specimen: length, width and thickness. An especially critical feature of this behavior is noted when considering alternate layers of "locally-yielded" and non-yielded materials. The harder nonyielded materials act as reinforcing structures preventing the lateral contraction of the "locally-yield" regions. However, when the specimen cross-section becomes sufficiently small the lateral contraction is not prevented. Hence, a marked contrast in the mechanical behavior is noted between specimens of small and of large cross-sections.

III, A, Characteristic Behavior and Propellant Classification (cont.)

	Characteristic	Description
b.	Test temperature effects	The effect of temperature upon the mechanical behavior of solid propellant produces a series of competing effects which are not adequately understood. As the temperature decreases the strength of the filler-to-polymer bond increases, the polymer strength increases, and the polymer contracts about the filler. The net effect is a maximum in the ε_m and ε_b plots versus temperature, while E, S_{nm} and S_{nb} increase continuously with decreasing temperature.
c.	Strain rate effects	Strain rate changes produce results very similar to those obtained from changes in the test temperature. To the extent that the polymeric binder receives equivalent loading conditions this inter-relation with temperature should hold. However, once "localized yielding" is initiated, the loading factors in the dewetted region may

III, A, Characteristic Behavior and Propellant Classification (cont.)

Characteristic	Description
	not possess this equivalence and the results may differ greatly.
d. Humidity effects	The effects of storage at various humidity levels produce marked changes in the propellant mechanical behavior. The effects are crudely analogous to changes in the strain rate or test temperature.
e. Specimen defects	Within a given batch of material marked differences in mechanical performance are frequently observed.
(1) Locally non-uniform cure	Undercured or overcured regions may occur in patches, spots, or in thin layers. Many such regions are overlooked in routine evaluations. These regions are frequently at the sites of tensile failures in routine testing.

III, A, Characteristic Behavior and Propellant Classification (cont.)

Characteristic	Description

(2) Casting bubbles — Flaws in the form of gas bubbles may vary in size from microscopic dimensions to an inch in diameter. The former are numerous, the latter are few in number. In testing, the deformations and stresses around these flaws change the fundamental mechanical behavior of the propellant. Usually the propellant experiences premature failure as a result of their presence.

(3) Filler agglomerates — Layers or clumps of non-uniformly blended filler materials weaken the propellant causing premature failure.

(4) Microvoids — The presence of a very small percentage of sub-microscopic voids (less than 1%) in a solid propellant produces a marked change in its multiaxial behavior.

III, A, Characteristic Behavior and Propellant Classification (cont.)

	Characteristic	Description
f.	Embrittlement	In the temperature region from -20° to +20°F, ammonium perchlorate propellants frequently become progressively harder with storage time. This phenomenon appears to be related to the quantity of water contained within the propellant.

This listing is only partially complete. However, it serves the purpose of calling attention to complex behavior of composite propellant. To this complexity must be added the batch-to-batch variability, and the gross errors met in testing and specimen preparation.

The development of a systematic means for classifying and correlating experimental results requires an analysis of the causes of the mechanical behavior observed in solid propellants. Consideration of these factors leads to a rational classification system.

2. Particle Packing

The problem of particle packing in solid propellant results from loadings in excess of 50 volume percent filler, frequently as high as 67 volume percent or more, used in most solid propellants. As seen in Figure 38 for the special case of a bimodal system, the filler particles are seen as small nodules on the left of the figure. This complex and nonhomogeneous character of solid propellant suggests that the mechanical distortion of this material, involving in turn relative movement of these particles with

SCHEMATIC OF LARGE
PARTICLE PACKING
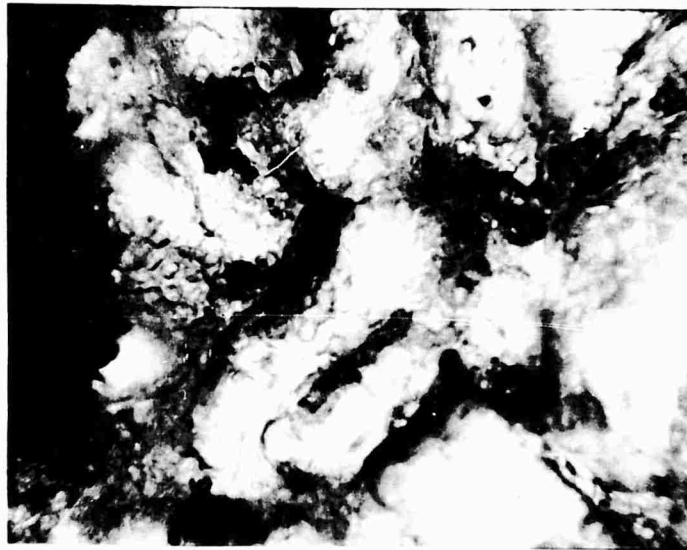
PHOTO SHOWING DEWETTING

× 48 VOL. %   470 - 500 μ

17 VOL. %   45 - 55 μ

Figure 38. Photograph and Derived Sketch of Dewetting in Bimodal Packing System
(461 1239)

III, A, Characteristic Behavior and Propellant Classification (cont.)

respect to one another, should reflect this close packing and nonuniform character. A study was made of this problem using the specimen shown in Figure 38. Points on two of the large particles were used to determine the angle of intersection of lines extending through these points. The angles were measured at various tensile strain levels and compared with calculated values obtained on the assumption of a homogeneous incompressible material. The results are:

Strain, %	Angle of Intersection, degrees	
	Measured	Calculated
1	44.7	44.7 (starting point)
3	42.9	44.15
6	36.1	42.88
8	34.9	42.05

One of the particles chosen for this measurement was closely aligned to the direction of straining. The reduction in the angle of intersection with strain indicates that the second particle is being moved nonuniformly leading to an exaggerated rotation. Examination of the behavior of other particles shows that the degree of rotation experienced is affected by many factors, such as shape, influence of adjacent particles, and orientation.

3.   Dewetting Phenomenon

The effect of particle rotation on strain is to produce a re-packing of the particles which leads to the formation of voids within the medium resulting from the failure, or dewetting, of the bond between the binder and the filler.

III, A, Characteristic Behavior and Propellant Classification (cont.)

The behavior of highly filled elastomers will vary greatly
with changes in bond strength between the filler particles and polymeric
matrix. For zero bond strength, the filler-polymer bond fails immediately
upon straining and small voids are created next to a particle. Since there is
no physical reinforcement, this type of material is weak and highly extensive.
Alternatively, if the bonds are strong, the filled material exhibits a relatively
high modulus with considerable reduction in the ultimate elongation.

It is in those systems where the adhesive bond is of inter-
mediate value that the problem of localized failure appears. As the specimen
undergoes tensile loading, the weakest bond strengths are first exceeded. The
filler particles thus released, transmit a higher stress to the neighboring
polymer-particle bonds, resulting in a band of released particles perpendicular
to the direction of strain. If the applied load occurring after this phenomenon
does not exceed the bond strength of the remaining intact bonds, the polymer
along this line experiences very high strains and eventually fails. The impli-
cation of the above behavior is that the stress-strain data in simple tension ob-
tained after localized yielding occurs can no longer be related to the overall
behavior of the material.

The extremely localized behavior of the dewetting process is
well exemplified in Figure 39. This localized effect is not easily seen by the
naked eye at low strain levels. Measurement of the grid shows that between
34.5 and 49% strain the uppermost portion of the specimen exhibits numerous
white bands which permit the elongation while the three bottom portions of the
specimen grid show no change in dimension.

4. Nature of the Yield Band

The contribution of the yield band to the behavior of the pro-
pellant is demonstrated by the following experiment. Consider tensile speci-
mens which have been machined through one-half of their cross section to pro-
vide various radii at the tips of the machined notch. The specimens were

ϵ=29.4

ϵ=39.5

ϵ=0%
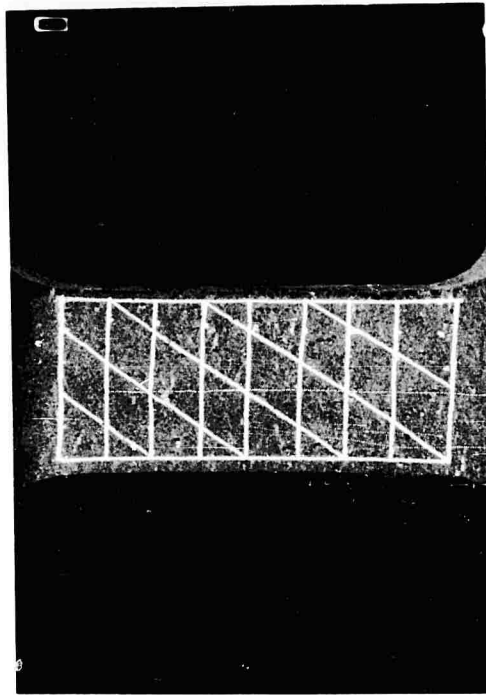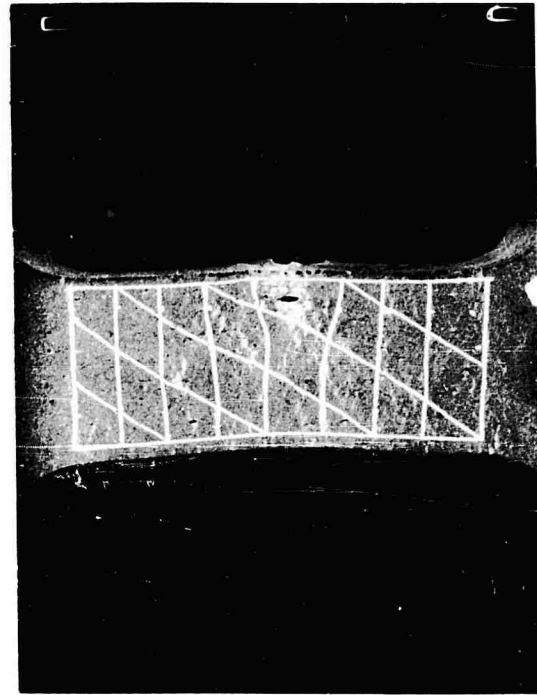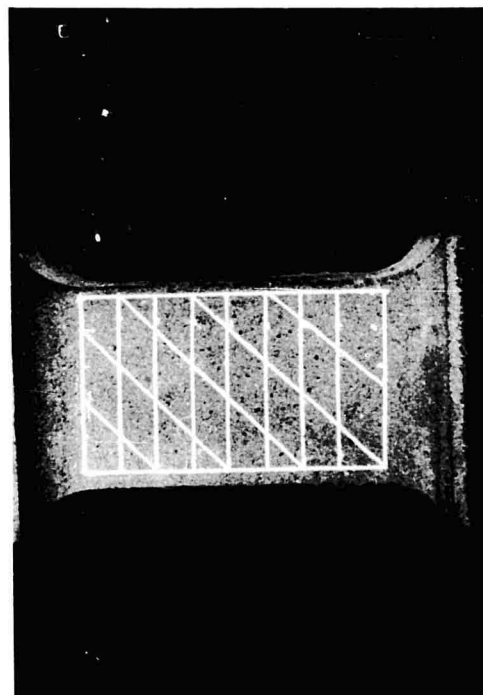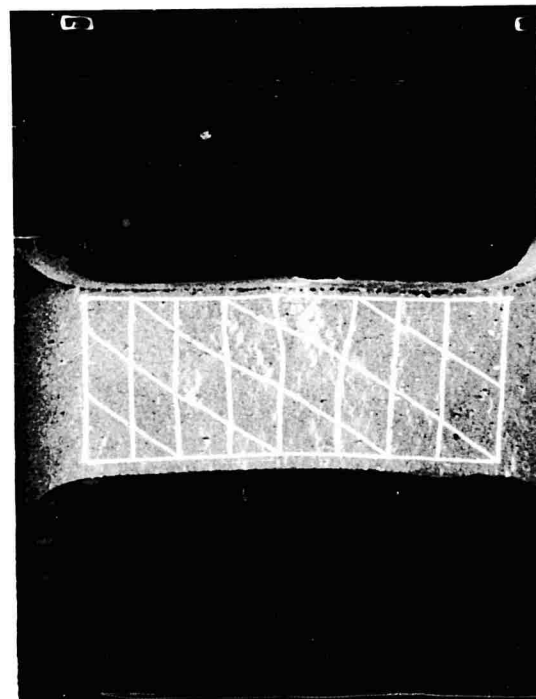
ϵ=36.6

Figure 39. Dewetting in Propellant (461 1238)

III, A, Characteristic Behavior and Propellant Classification (cont.)

clamped to give uniform loading and pulled in tension at constant rate. The re-
duction of the cross section to one-half ensures that negligibly small deforma-
tions will be obtained except at the end of the notch. It was expected that the
narrowest cross section of the specimen would produce just one yield band, in
which case the elongation required to break the specimen would be nearly
independent of the radius at the tip of the notch. The data of Table 7 confirm
this expectation for the two propellants shown. The data suggest further that
these two propellants normally produce three yield bands. A statistical test
of differences of average values for the two propellants gave $t = 0.679$, not
significant, for the $\Delta L_o / \Delta L$ values, and $t = 5.13$, which is significant at the
95% level, for S_{nb} / S_{nbo}.

The first conclusions to be drawn from this experiment is
that the elongation to break of the standard specimen (2.7 in. gage) is equivalent
to about three times the elongation of one yield band, thus emphasizing the high
elongation capabilities of locally yielded material. The second conclusion is
that the elongation at failure is essentially controlled by the nature and amount
of the dewetted material.

The data available on these highly filled systems suggest
that only propellant structures capable of considerable dewetting can produce
large deformations and offer a practical means for benefiting from the superior
characteristics of some binder systems. This is illustrated in the photomicro-
graphs of Figure 40 of a strained propellant exhibiting a high degree of dewett-
ing. The photomicrographs show that the dewetting can be made to increase
quite uniformly with elongations.

III, A, Characteristic Behavior and Propellant Classification (cont.)

TABLE 7

THE STRESS AT BREAK FOR NOTCHED PROPELLANT SPECIMENS TESTED AT 80°F

Radius at tip of cut, in. *	Propellant A				Propellant B			
	Δl	$\dfrac{\Delta l_o}{\Delta l}$ **	S_{nb}', psi	$\dfrac{S_{nb}}{S_{nbo}}$ ***	Δl	$\dfrac{\Delta l_o}{\Delta l}$ **	S_{nb}', psi	$\dfrac{S_{nb}}{S_{nbo}}$ ***
0.01	0.51	3.5	115	1.09	0.15	4.4	125	0.68
0.094	0.605	3.0	109	1.04	0.20	3.3	143	0.77
0.115	0.67	2.7	107	1.02	0.20	3.3	159	0.86
0.125	0.665	2.7	111	1.06	0.20	3.3	178	0.96
0.145	0.71	2.5	109	1.04	0.22	3.0	157	0.85
0.165	0.625	2.9	107	1.02	0.215	3.1	159	0.86
0.190	0.67	2.8	118	1.12	0.215	3.1	174	0.94
0.220	0.665	2.8	109	1.04	0.345	1.9	185	1.00
0.245	0.685	2.6	115	1.09	0.37	1.8	175	0.95
Av.		2.83		1.057		3.02		0.874
Std. Dev.		0.29		0.035		0.78		0.102
Std. Estimate of Error, %		10.3		3.3		25.9		11.6

* radius, in. ←width = 0.375 in.
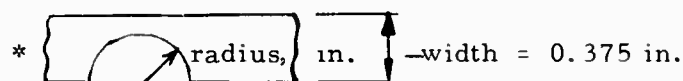
** Δl_o = elongation at failure of unnotched specimen

= 1.8 in. for Prop. A; = 0.66 in. for Prop. B

*** S_{nbo} = nominal stress at break of unnotched specimen

= 105 psi (av. of range 100-110) for Prop. A

= 185 psi (av. of range 170-200) for Prop. B

MAGNIFICATION 44 DIAMETERS
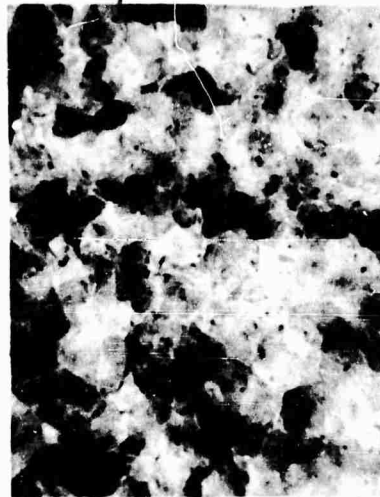
25% STRAIN

50 % STRAIN
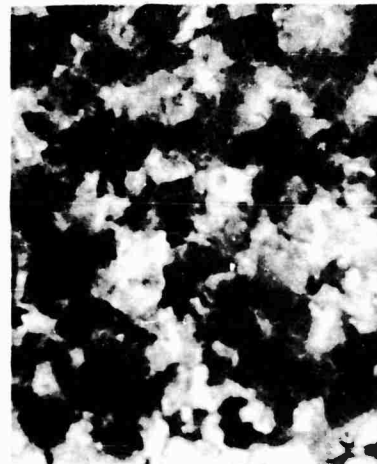
75% STRAIN

DARK AREAS INDICATE THE FORMATION OF
CAVITIES ABOUT WHITE OXIDIZER PARTICLES

Figure 40. Dewetting in a Class 1 Solid Propellant (10-61S 27779)

III, A, Characteristic Behavior and Propellant Classification (cont.)

5. Classification System

The classification proposed for composite propellants is based upon dewetting behavior. Four classes of propellants are proposed as follows:

Class	Description	Mathematical Relation
1	Essentially complete dewetting is observed as the break point is reached. (Figure 40 shows typical Class 1 behavior.)	For the special case where dewetting may be considered complete at all points of strain, the finite deformation relations of Blatz (10) offer a good first approximation. Mathematical description by strain energy functions appears to be the most promising approach.
2	Dewetting occurs in two or more bands throughout the gage length of the specimen. Local sites of dewetting occur generally throughout the specimen. (Figure 39 shows characteristic Class 2 behavior.)	Mathematical description by strain energy functions appears to be the most promising approach.
3	Dewetting occurs generally in one narrow band only.	Mathematical description by strain energy functions appears to be the most promising approach.
4	No dewetting occurs up to the break point, typical of propellants below their glassy temperature.	The classical theory of elasticity applies quite well to these materials.

III, Phase 2 - Mathematical Representation of Mechanical Behavior (cont.)

B.   ANALYTICAL DETERMINATION OF GENERALIZED, LINEAR
     VISCOELASTIC STRESS-STRAIN RELATIONS

A number of commonly used materials exhibit inelastic properties
such as creep and relaxation at normal operating temperatures. A case in point
is the solid rocket propellant grain where elastic analyses are inadequate for
relatively long time conditions, such as thermal cycling and storage, and for
extremely short time dynamic conditions, such as impact and sudden accelera-
tions.   Techniques for linear viscoelastic analysis in terms of integral trans-
forms and integral stress-strain relations have been established (12 to 21).
In order to use the results of such analyses, viscoelastic properties for a given
material under various temperature conditions must be known.

Admittedly, solid propellant grains may behave nonlinearly at
large operating strains. However, if the accuracy and applicability of linear
analysis is to be evaluated, then the suitability of representation of actual ma-
terial properties by linear viscoelastic stress-strain laws must first be es-
tablished.

It is the purpose of the analysis shown in Appendix A to formulate
analytical relations and procedures for the determination of linear visco-
elastic stress-strain relations from actual creep and relaxation test data,
neglecting the effects produced by dewetting. Conditions for uniaxial, biaxial,
and triaxial experiments were investigated in terms of generalized linear
viscoelastic models and their associated stress-strain relations. While in
many cases it might be preferable to conduct dynamic tests to determine ma-
terial properties, these are generally found difficult to execute due to the ex-
treme flexibility of solid propellants. However, the types of stress-strain
relations discussed in Appendix A are general enough to be extendable to dy-
namic behavior, provided a model with a sufficient number of parameters is
chosen for the viscoelastic behavior and provided that the material can be ade-
quately characterized or approximated by linear relations.

III, B, Analytical Determination of Generalized, Linear Viscoelastic
Stress-Strain Relations (cont.)

It must also be emphasized that the determination of any and all
properties is predicated on being able to conduct experiments with sufficient
ease, accuracy, and duplicability to be meaningful, and being able to produce
a reasonably accurate analysis for the state of stress and strain in the geometry
of test specimen under stipulated approximations that are not over restrictive.
Consequently, experiments must be conducted with simple types of loading
that are still general enough to be representative of multiaxial behavior, but
that are not so complex as to defy accurate analysis. With this purpose in mind
the commonly used uniaxial, biaxial, and triaxial types of tests are investigated.

In addition to evaluating viscoelastic behavior, an important by-
product of the present analysis of test results is the determination of the elastic
Young's and shear moduli from creep and relaxation data. While equivalent
elastic solutions form the initial conditions for most viscoelastic problems, the
associated elastic material properties can be determined accurately only from
viscoelastic analyses and experiments.

In order to illustrate and evaluate the various approaches presented
in Appendix A, a number of uniaxial relaxation tests were interpreted in terms
of four, five, and six parameter viscoelastic models. Some of the results for
incompressible material characterization are presented in Tables 8 and 9 and
in Figures 41 and 42. The computations for the two tables were based on the
previously derived expressions and a curve fit at a discrete number of points
executed on an LGP-30 computer. These computations were carried out to com-
pare four and five parameter models for accuracy of characterization and to in-
vestigate the influence of the selection of points on the curve fitting. Since the
time that these computations have been made, new computer programs have
been written for the LGP-30 which allow for a least-square fit of the data and,
therefore, eliminate the arbitrary selection of points for curve fitting purposes.

TABLE 8

SOLID PROPELLANT VISCOELASTIC PROPERTIES

(Based on Step Function Approximation)

Type of Relaxa- tion Test	Propellant	Model	E_0	α_1	α_2	β_1	β_2
Uniaxial at 77°F 10% strain $t_0 = 0.15$ min	ANP 2864HG MOD-1	Incompres- sible four parameter Model B (N = 1)	586.400	0.263 087	4.237 29	1.696.99	
Uniaxial at 77°F 10% strain $t_0 = 0.15$ min	ANP 2864HG MOD-1	Incompres- sible five parameter Model A (N = 2)	586.400 586.400	0.198 787 5.672 37	2.551 02 0.308 525	0.967 628 2.639 39	0.196 488
			586.400	4.849 00	0.252 516	2.131 83	0.169 855

TABLE 9

SOLID PROPELLANT VISCOELASTIC PROPERTIES

(Based on Ramp Function Characterization)

Type of Relaxation Test	Propellant	Model	E_o	α_1	α_2	α_3	β_1	β_2
Uniaxial at 77°F 10% strain $t_o = 0.15$ min	ANP 2864HG	Incompressible five parameter Model A (N = 2)	635.434	5.67237	0.308525		2.42074	0.199726
Uniaxial at 110°F 15% strain $t_o = 0.205$ min	ANP 2816CD3	Incompressible five parameter Model A (N = 2)	879.415	5.09830	0.252693		2.77125	0.189656
Uniaxial at 110°F 15% strain $t_o = 0.205$ min	ANP 2816CD3	Incompressible six parameter Model B (N = 2)	892.217	9.82855	0.940393	0.013301	5.65987	0.76468
Biaxial at 80°F 20% strain $t_o = 0.005$ min	ANP 2639AF	Incompressible six parameter Model B (N = 2)	186.003	2.31770	0.052798	9.64×10^{-6}	0.88096	0.05335
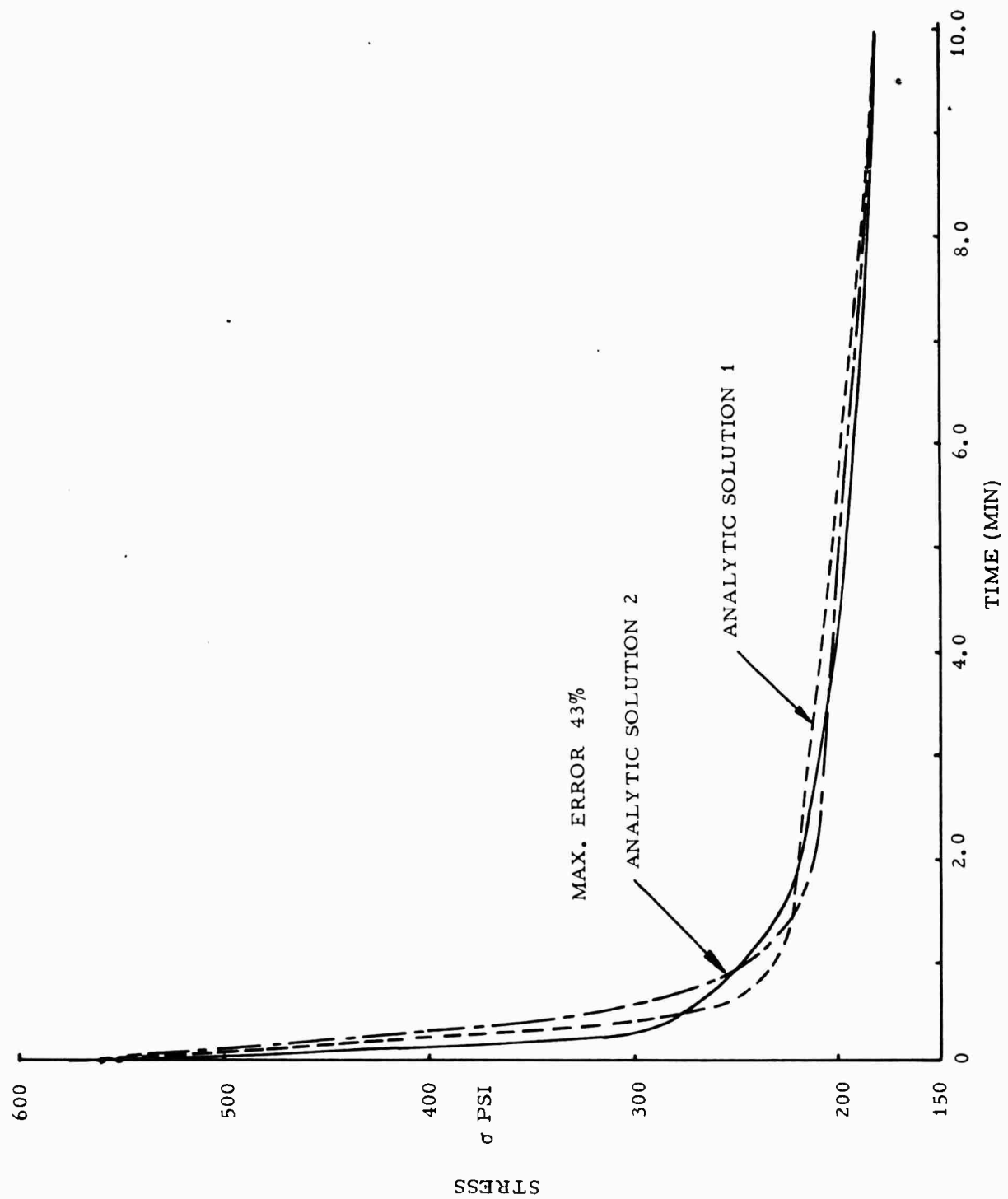
Figure 41. Uniaxial Stress-Relaxation Curve Fit - Four Parameter Model
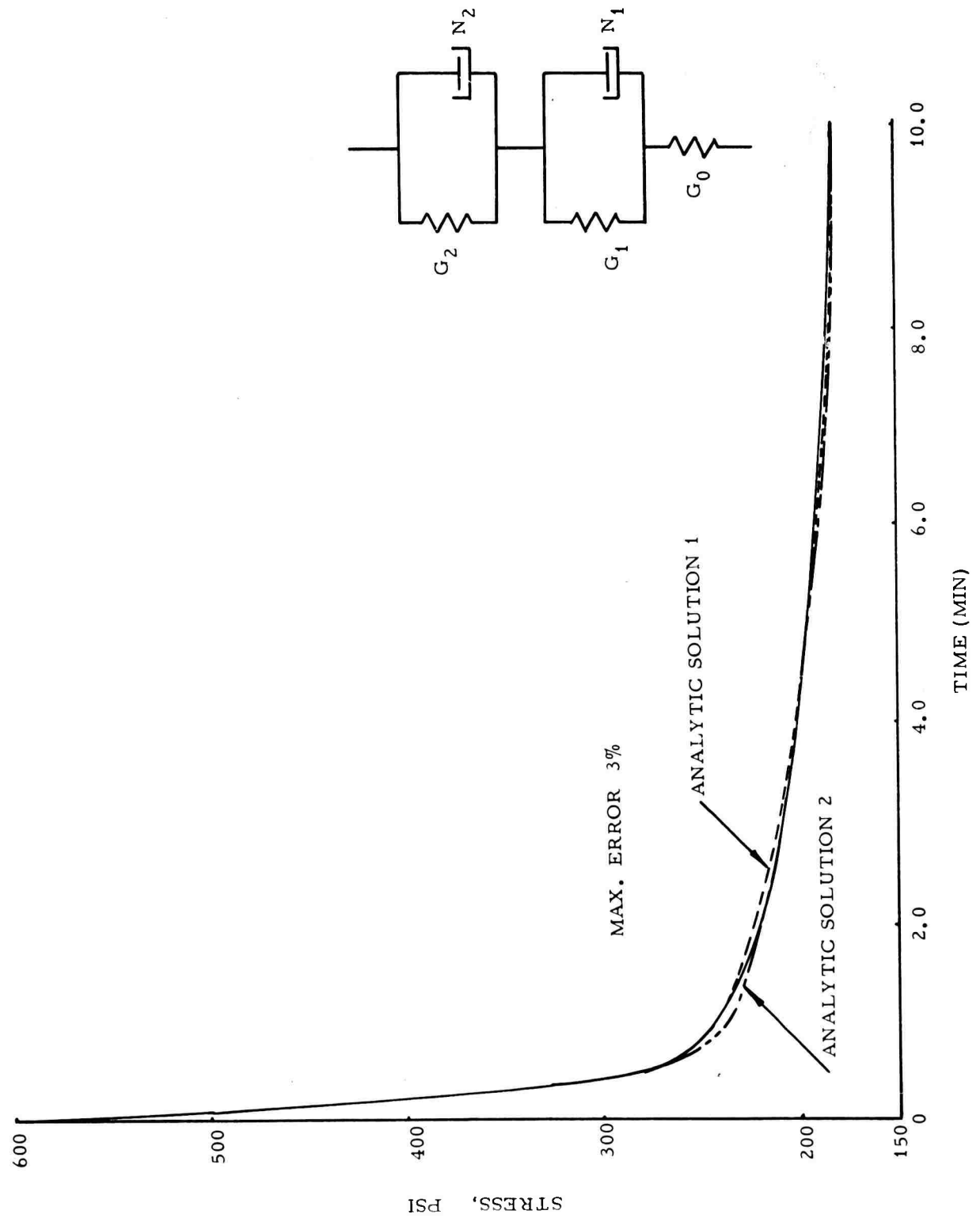
Figure 42.   Uniaxial Stress-Relaxation Curve Fit - Five Parameter Model

III, B, Analytical Determination of Generalized, Linear Viscoelastic
Stress-Strain Relations (cont.)

Table 8 and Figure 41 show the results of a four-parameter Model
B (N = 1) fit using two arbitrary sets of four points. It is seen that there is wide
variation between the three curves and it is felt that this four-parameter model
is not general enough to adequately represent the data since this approximation
results in a maximum error of 43% in stress values. Figure 42 illustrates a
five parameter Model A (N = 2) characterization of the same uniaxial relaxation
test data. Here the maximum error is only 3% and the curves based on two
different sets of five points are very coincident with each other except in the
region of maximum error. It is very doubtful whether the actual experimental
data is reproducible with as small a deviation, and, therefore, this five para-
meter representation seems reasonable, pending the interpretation of future
creep data.

All the characterizations in Table 8 and Figures 41 and 42 were
based on the simplification of representing the strain equations by a step func-
tion, even though the experiments were conducted with strain ramp function.
This simplification was undertaken to evaluate qualitatively its effect on the
characterization. The values in Table 9 were computed by using the proper
strain ramp function and a comparison of the five parameter Model A represen-
tations of Table 8 and 9 shows that the major effect of the neglect of strain-
build-up in the analysis is to lower the computed value of the initial Young's
modulus. This result is not surprising since the analysis based on a strain
step function does not take into account the actual creep which takes place
prior to the leveling off of strain and, therefore, results in apparent E_o values
which are lower than the actual ones. In the present example, where
$t_o = 0.15$ min, the reduction of E_o was about 7.7% of the true value and it is
felt that such error is too large to neglect the strain build-up in the analysis.
Consequently, the values in Table 9 should be regarded as more nearly repre-
sentative of actual material properties.

III, B, Analytical Determination of Generalized, Linear Viscoelastic
Stress-Strain Relations (cont.)

Since uniaxial and multiaxial experiments are generally conducted
under conditions which do not lead to either pure volumetric or pure deviatoric
deformations, care must be taken to properly interpret such test results in
terms of the fundamental properties. Furthermore, when stress-strain rela-
tions for compressible isotropic materials are to be obtained from uniaxial
and/or multiaxial tests, it is necessary to conduct additional experiments to
determine volumetric properties.

The analysis shows that it is possible to determine all linear visco-
elastic properties in terms of complex moduli reduced to partial fractions from
curve fitting creep and/or relaxation data. This approach seems relatively
simpler than the one used by Jones, Daniel, and Johnson (23) where the co-
efficients of the differential operators were determined from the solution of
simultaneous algebraic equations. For stress analysis purposes it is im-
material whether the differential operator, integral relations or complex
moduli are known since these are all equivalent characterizations and any one
can be derived from another.

The amount of experimental data gathered to date on the mechanical
properties of solid propellants is insufficient to determine whether or not linear
viscoelastic representation is an adequate approximation or whether it is neces-
sary to use nonlinear characterization such as that discussed by Freudenthal
(24). Once uniaxial or multiaxial creep and relaxation data at various strain,
stress and temperature levels becomes available, it will be possible to compare
the stress-strain relations obtained from different types of loading and decide
on the minimum number of parameters in a model and the suitability of linear
viscoelastic characterization. Even if materials show excessive nonlinear
characteristics, it may be possible to represent their behavior by linear rela-
tions with the various material properties defined as different average constant
values over given stress, strain, etc., intervals.

III, Phase 2 - Mathematical Representation of Mechanical Behavior (cont.)

C. CORRELATION OF REAL PROPERTIES

The chief difficulty in a mathematical approach lies in the complexity of behavior. Empirical correlation of data, however, shows that each class of propellant is quite consistent in its behavior. As an alternative to fitting classical models for viscoelasticity, usually composed of spring and dashpot elements, work has been initiated on methods of using descriptions of real behavior following the approach suggested by Rivlin and presented clearly in a recent series of lectures. (8)

Rivlin has shown for simple rubbers that the generalized work function may be expressed simply in terms of three strain functions, I_1, I_2, and I_3, called the strain invariants. It is expected that the elastomerically based solid propellants should also be describable by strain invariants. The filler particle-particle interactions and the polymer-filler interactions act to change the basic character of the propellant according to the extent and conditions of loading and deformation. Hence, the usual concepts of moduli as being constants must be challenged for the case of propellants. The moduli for solid propellants are expected to be deformation dependent, in addition to the usually accepted viscoelastic effects of time- and temperature-dependence. The study of actual behavior has not yet been advanced sufficiently to allow a straightforward, theoretical approach to the problem, so that initially the study has been basically empirical.

In the discussion to follow, the work is divided into the empirical and semi-empirical approaches. However, since both efforts employ terms derived from Rivlin's work on the theory of finite elasticity, some of the terminology is defined first. The work required to deform a specimen in a **finite** strain field must be related to the principal extension ratios, λ_1, λ_2, and λ_3, since these are the only parameters defining the deformation. However, studies of the basic relations of finite elasticity lead to three new variables which serve to simplify the considerations required for defining the work of deformation. These new variables are called strain invariants since their

III, C, Correlation of Real Properties (cont.)

numerical values, at any stage in the deformation, do not change with a rotation of the reference coordinate axes. The three strain invariants are given in symmetrical functions of the three principal extension ratios as follows:

$$I_1 = \lambda_1{}^2 + \lambda_2{}^2 + \lambda_3{}^2 \tag{22}$$

$$I_2 = \lambda_1{}^2 \lambda_2{}^2 + \lambda_2{}^2 \lambda_3{}^2 + \lambda_3{}^2 \lambda_1{}^2 \tag{23}$$

$$I_3 = \lambda_1{}^2 \lambda_2{}^2 \lambda_3{}^2 = V^2 \tag{24}$$

In the undeformed state the λ's are equal to one. Therefore, the practical use of the strain invariants requires that they be handled in the forms $I_1 - 3$, $I_2 - 3$, and $I_3 - 1$. In these forms the variables reduce to zero as the specimen returns to the unstrained state.

The uniaxial and biaxial tests, with and without hydrostatic pressure, and the triaxial test have specific conditions which allow simplification of the general equations for the invariants. For uniaxial tensile, $\lambda_2 = \lambda_3$, so we can write

$$I_1 - 3 = (\lambda_1{}^2 - 1) + 2(\lambda_2{}^2 - 1) \tag{25}$$

$$I_2 - 3 = 2(\lambda_1{}^2 \lambda_2{}^2 - 1) + (\lambda_2{}^4 - 1) \tag{26}$$

$$I_3 - 1 = (\lambda_1{}^2 \lambda_2{}^4 - 1) \tag{27}$$

For biaxial tension on specimens restrained in length but not thickness, $\lambda_3 = 1$

$$I_1 - 3 = (\lambda_1{}^2 - 1) + (\lambda_2{}^2 - 1) \tag{28}$$

III, C, Correlation of Real Properties (cont.)

$$I_2 - 3 = (\lambda_1^2 \lambda_2^2 - 1) + (\lambda_1^2 - 1) + (\lambda_2^2 - 1) \tag{29}$$

$$I_3 - 1 = \lambda_1^2 \lambda_2^2 - 1 \tag{30}$$

from which

$$(I_2 - 3) = (I_1 - 3) + (I_3 - 1) \tag{31}$$

For triaxial tension, $\lambda_2 = \lambda_3 = 1$, and we have

$$I_1 - 3 = \lambda_1^2 - 1 \tag{32}$$

$$I_2 - 3 = 2(\lambda_1^2 - 1) \tag{33}$$

$$I_3 - 1 = \lambda_1^2 - 1 \tag{34}$$

from which we obtain Equation (31) also, as well as

$$(I_2 - 3) = 2(I_1 - 3) = 2(I_3 - 1) \tag{35}$$

Thus for triaxial tension, only one of the strain invariants need be used in correlation, for biaxial any two, but for uniaxial, all three are needed. Therefore, empirical relations defining the behavior of a propellant would be useful which generally related the strain invariants to each other for the uniaxial and biaxial cases.

For the most general case, Equations (22), (23), and (24) can be combined to give

$$\lambda_1^6 - I_1 \lambda_1^4 + I_2 \lambda_1^2 - I_3 = 0 \tag{36}$$

III, C, Correlation of Real Properties (cont.)

$$\lambda_2^6 - I_1 \lambda_2^4 + I_2 \lambda_2^2 - I_3 = 0 \qquad (37)$$

$$\lambda_3^6 - I_1 \lambda_3^4 + I_2 \lambda_3^2 - I_3 = 0 \qquad (38)$$

from which it can be seen that for biaxial tension, $\lambda_3 = 1$, Equation (38) becomes Equation (31). Similarly, for triaxial tension, both Equations (37) and (38) reduce to Equation (31), e.g., $\lambda_3 = \lambda_2 = 1$. For the uniaxial case, no simplification of Equation (36) results.

1. Uniaxial Tensile Loading

Dilation measurements were made in a liquid dilatometer designed to provide volume change measurements of a specimen while it is being uniaxially strained at a constant rate. This apparatus was designed for use with specimens of the following dimensions: $3/4 \times 3/4 \times 2.9$ in. gage length. The apparatus is a modification of the one designed by H. C. Jones and H. A. Yiengst (11). Graphs of I_1 vs I_2 were made from typical data on a Class 3 propellant as shown in Figure 43 for aged, unaged, and solvent swollen samples.

$$(I_1 - 3) = M(I_2' - 3) \qquad (39)$$

Further confirmation was obtained for Equation (39) from data reported by Thor Smith (4). In these studies a polyvinyl chloride binder was filled with glass beads at four filler loadings, 13.7, 32.2, 41.5, and 52.5 vol. %. Test specimens were prepared into an elongated ring 3.48 cm in length by 0.98 cm in width by 0.30 cm in thickness. A dilatometric device similar to the one of Jones and Yiengst was used. Testing was conducted at temperatures from -19° to 50°C.

The results of testing, when inserted into the I_1 and I_2 relations, are demonstrated for a typical case in Figure 44. These data show linearity between I_1 and I_2 at low strains with marked departures at the higher values. It is noteworthy that the linearity improves with increasing filler
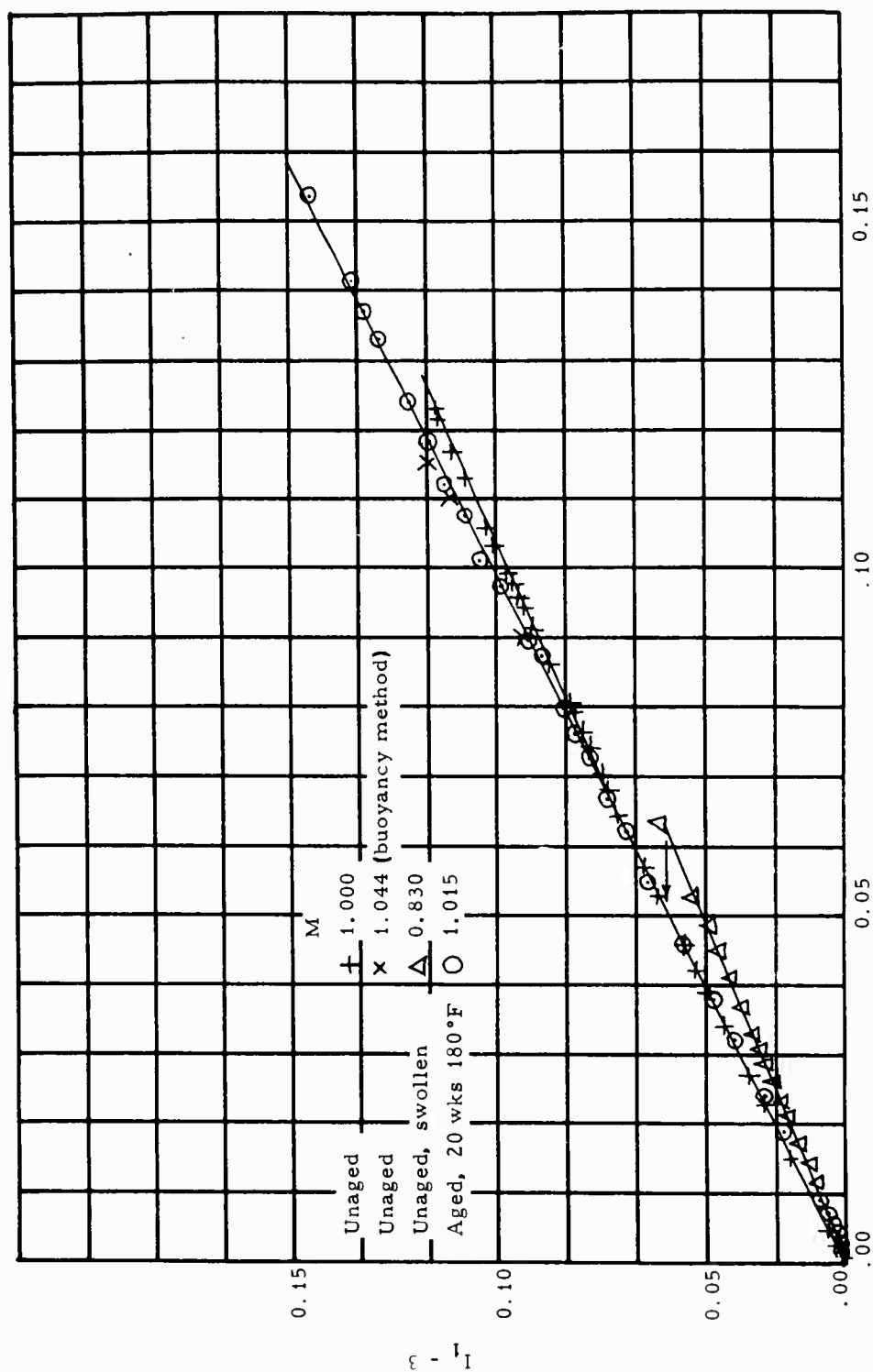
Figure 43.   Correlation of First and Second Strain Invariants for Class 2
Polyurethane Propellant
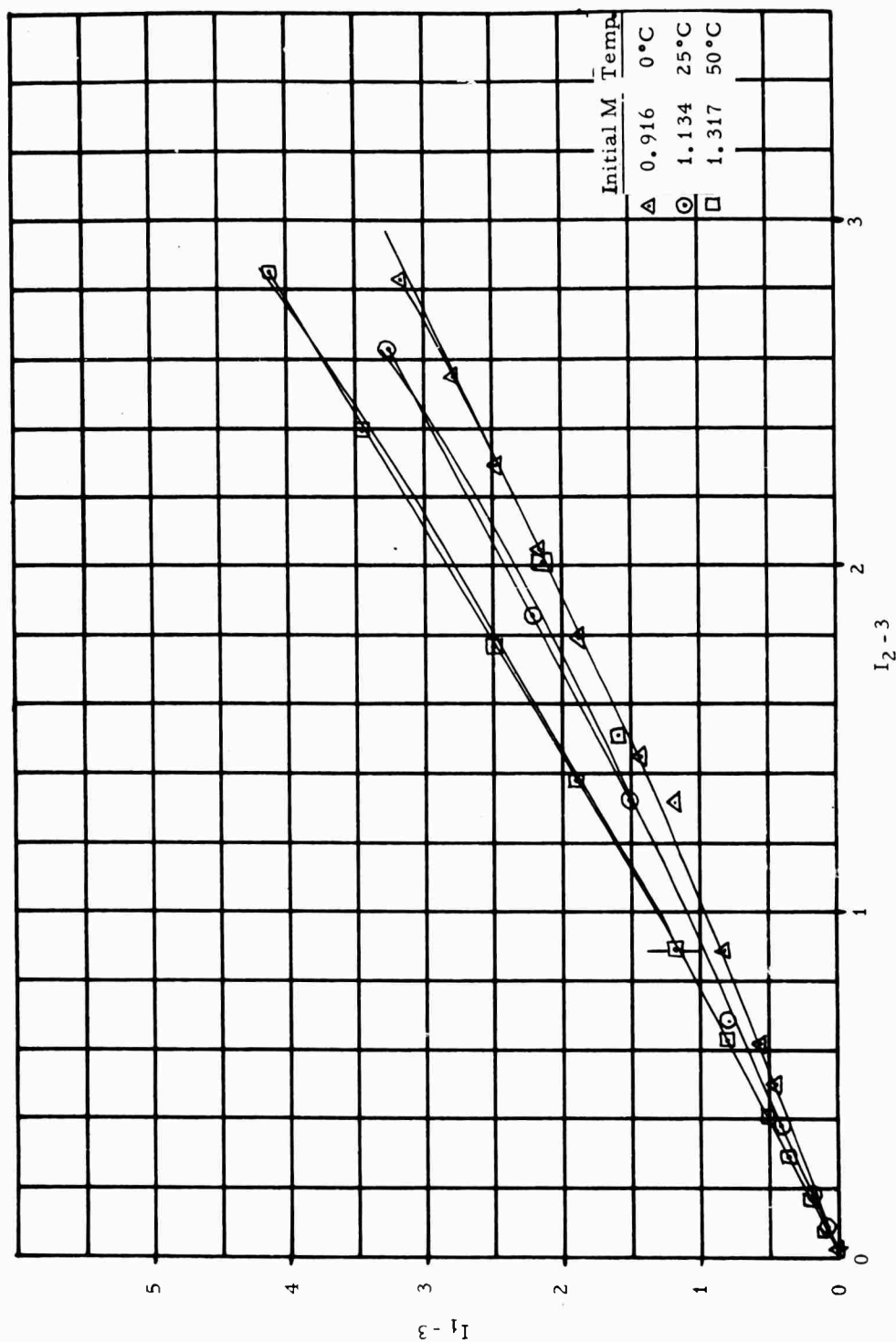
Figure 44. Relation Between the First and Second Strain Invariants for 32.2 Volume Percent of Glass Beads in Polyvinyl Chloride

III, C, Correlation of Real Properties (cont.)

content. For the limited region of I_2 between 3 and 4, the region of interest for
propellants, the linearity between I_1 and I_2 is satisfactory for all temperatures
and filler contents. The effect of test temperature and filler content upon the
constant, M, is shown in the following tabulation.

Volume percent Glass Beads	Test Temp °C	M	
		Observed	Calculated Eq. 40
52.5	50	0.97	0.92
	25	0.81	0.79
41.5	50	1.11	1.13
	25	0.91	0.94
	0	0.86	0.76
	-19	0.71	0.62
32.2	50	1.32	1.32
	25	1.13	1.07
	0	0.92	0.83
13.7	25	1.28	1.33
	0	1.07	0.98

It has been found empirically that the values of M for this sys-
tem obey the following relation

$$M = 0.5 + C(T - 239) (.74 - v_2) \tag{40}$$

where   C is an empirical constant

T is the test temperature, °K

v_2 is the volume fraction of filler employed.

The constant 239 is the reference temperature for polyvinyl chloride taken from
the WLF equation (35), while the value 0.74 was chosen equal to the volume
fraction of solids in closest packing of monodisperse spheres (hexagonal close
packing). The value of C was calculated from the experimental value of M at

III, C, Correlation of Real Properties (cont.)

32.2% loading, 50°C test temperature. Values of M were calculated using this value of C $(0.0231 \ °K^{-1})$, and are shown in the tabulation above.

A further confirmation of the linear relation shown in Equation (39) was provided in work by Bryant and Bisset (25). Their studies were made on a pale crepe with whiting filler. The values of M obtained for these materials are given below.

Filled System	Filler Concentration, Volume Percent	M
Whiting in Pale Crepe	30	1.32
	35	1.16
	40	0.99
	45	1.04

2. Volume Change Under Uniaxial Loading

The relative volume, V, can be obtained from Equation (39) in terms of the axial extension, $\lambda = \lambda_1$, and the material constant, M, by substituting for $I_1 - 3$ and $I_2 - 3$ from Equations (25) and (26), and then substituting the relation $\lambda_2^2 = V/\lambda$, to give

$$V = \lambda \left[\frac{1}{M} - \lambda^2 + \sqrt{(\lambda^2 - \frac{1}{2M})^2 + 3(1 - \frac{1}{2M})^2} \right] = \lambda_1 \lambda_2 \lambda_3 = \sqrt{I_3} \qquad (41)$$

The correlation between the calculated and experimental values for V are shown in Figure 45. These results show good correlations, after taking into account the experimental errors in the observed data. Better correlations between the calculated and observed volumes are shown for the glass bead-polyvinyl chloride system data of Smith (4) for extension ratios below 1.8 in Figure 46.
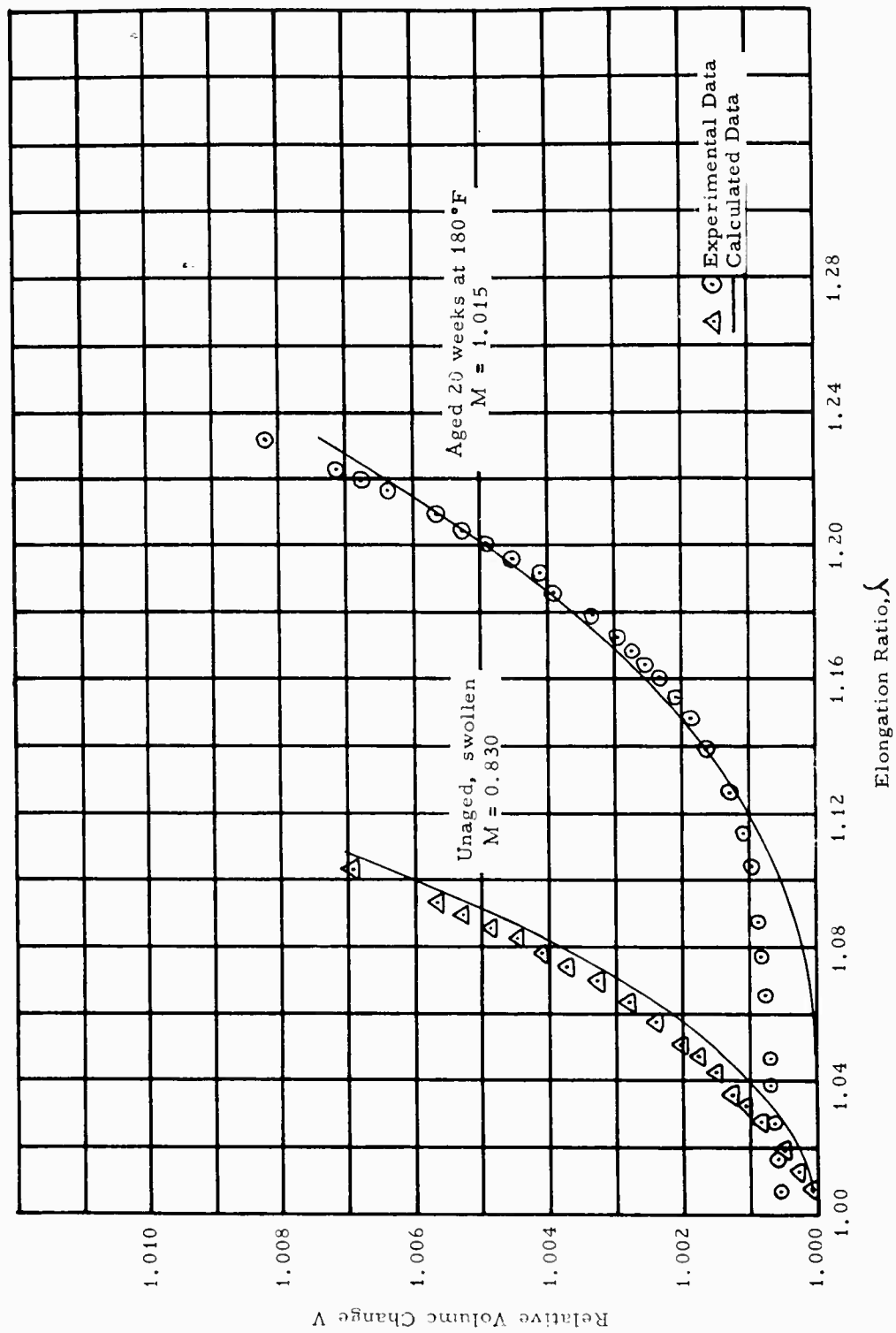
Figure 45. Observed Volume Change vs Elongation Ratio for Class 3
Polyurethane Propellant
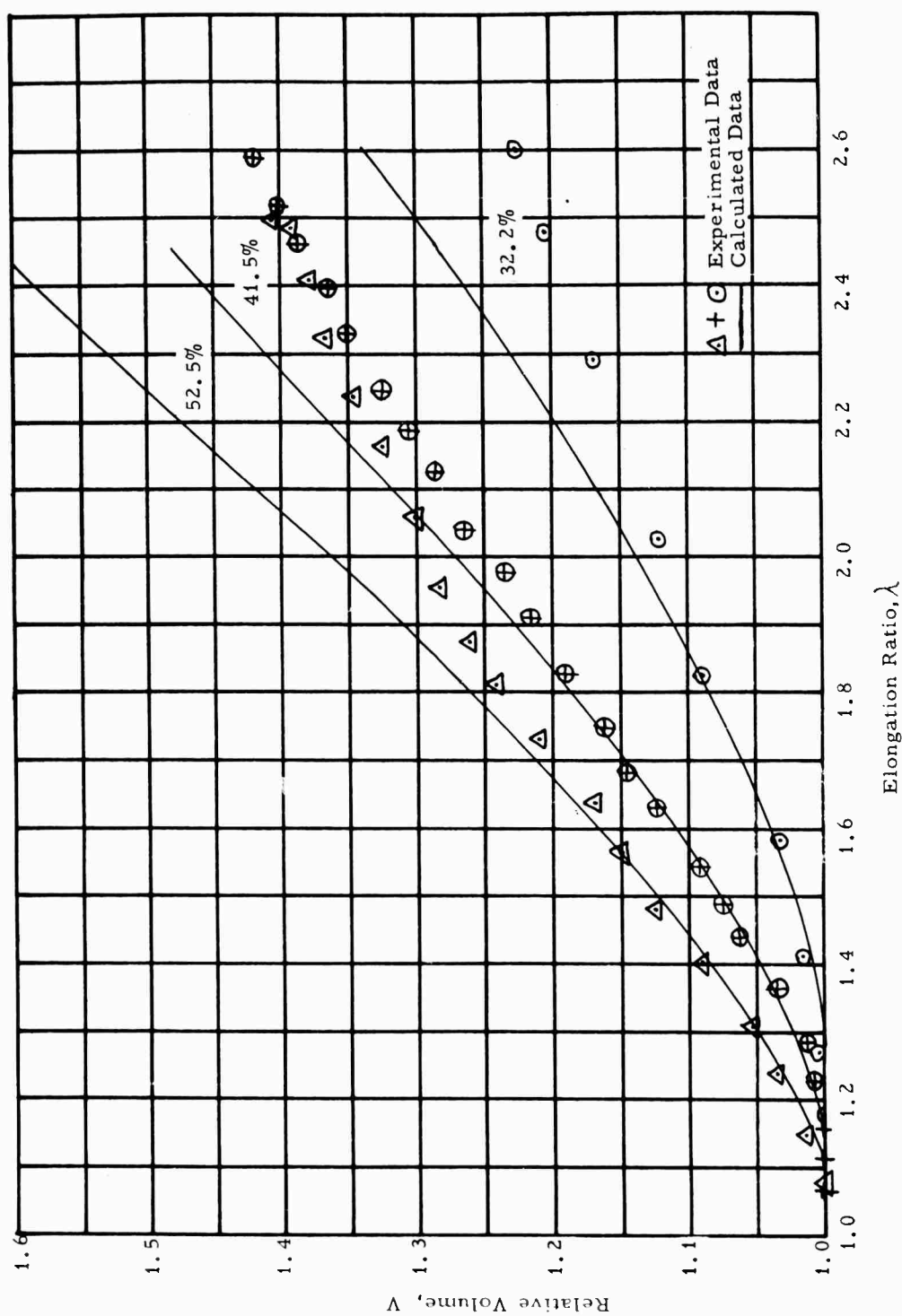
Figure 46. Relative Volume vs Elongation Ratio for Several Volume Percents
of Glass Beads in Polyvinyl Chloride at 25°C

III, C, Correlation of Real Properties (cont.)

3. Biaxial Tensile Loading

The relation between the first and second strain invariants was examined further using data obtained on specimens measured in a biaxial loading field. The specimens were $0.25 \times 7.0 \times 1.0$ in. gage length. The mode of testing was such as to restrain the specimen in one dimension ($\lambda_3 = 1$) while tensile straining it in a second ($\lambda_1 = \lambda$) and allowing it to deform as required in the third direction, λ_2.

A test of the linearity between $I_1 - 3$ and $I_2 - 3$ for biaxial conditions was made as shown in Figure 47 for a Class 1 propellant. The correlation is good and is further confirmed by plotting data on the same specimens in the form of $I_1 - 3$ vs $I_3 - 1$, as shown in Figure 48, where the slope gives $M/(M - 1)$. This can be seen by substituting for $I_2 - 3$ in Equation (31) from Equation (39) to give

$$I_1 - 3 = (I_3 - 1) \, M/(1 - M) \qquad (42)$$

As can be seen, the values of M derived from Figure 48 agree closely with those from Figure 47.

The unique correlation found to exist between the first and second strain invariants has many possible applications. Prime among these may be the smaller number of independent parameters required to define the deformation of a given system. In the classical theory of elasticity, a simple relation between the lateral and axial strains gives rise to Poisson's ratio. Likewise in the theories of rubber elasticity under finite deformations, the principle strains are limited by the requirement of zero volume change in the deformation. Now, as a result of the experimentation described here, a similar type of simplifying relationship useful for solid composite propellants and other highly filled materials appears possible.
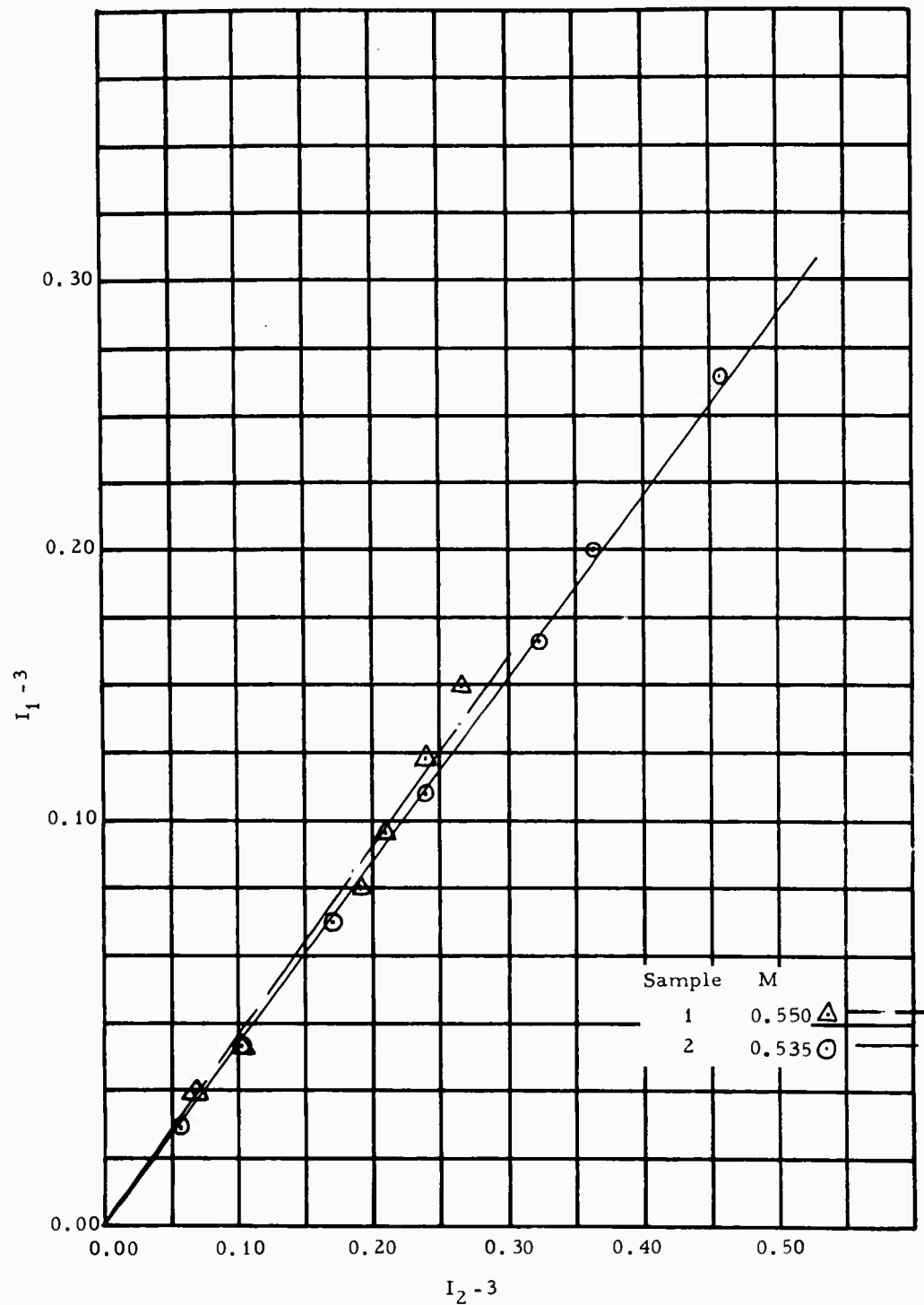
Figure 47. Relation Between the First and Second Strain Invariants for Class 1 Propellant in Biaxial Tension
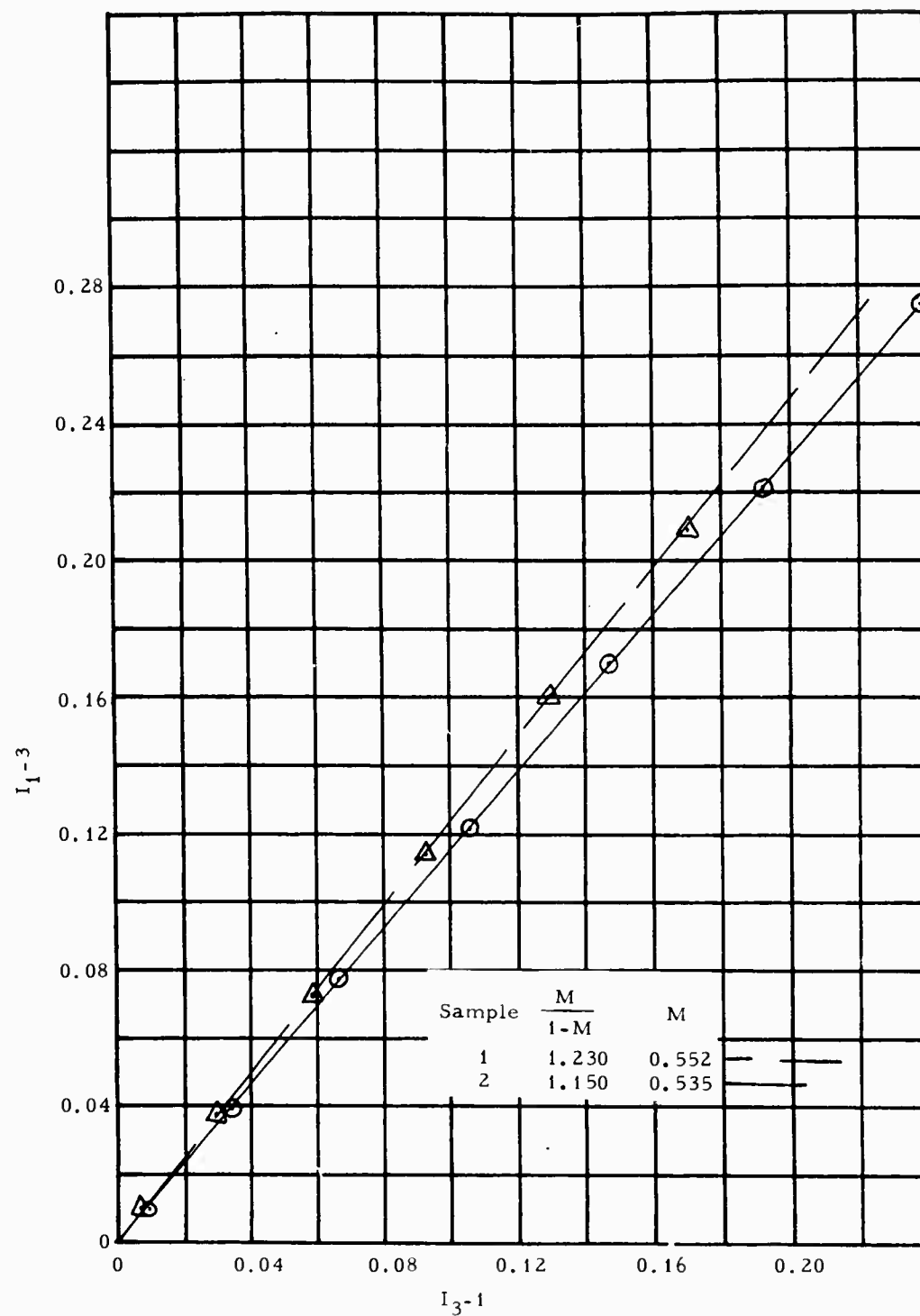
Figure 48. Relation Between the First and Third Strain Invariants for Class 1
Polyurethane Propellant in Biaxial Tension

III, C, Correlation of Real Properties (cont.)

4.   Stored Energy Function

A useful concept in dealing with experimental stress-strain data through strain invariants is that of the stored energy function. One method is discussed here. For uniaxial tension, $\lambda_1 = \lambda$, $\lambda_2 = \lambda_3$, $\lambda_2^2 = (V/V_o)/\lambda$ and we have

$$I_1 = \lambda^2 + \frac{2}{\lambda} \left(\frac{V}{V_o}\right) \tag{43}$$

and for biaxial tension, $\lambda_3 = 1$, $\lambda_2 = (V/V_o)/\lambda$,

$$I_1 = \lambda^2 + \frac{1}{\lambda^2} \left(\frac{V}{V_o}\right)^2 + 1 \tag{44}$$

The value of $\frac{V}{V_o}$ is essentially unity at $\lambda \approx 1$, but increases with increasing λ. However, the coefficient of $\frac{V}{V_o}$ in uniaxial tension, or of $\left(\frac{V}{V_o}\right)^2$ in biaxial tension, decreases as $\frac{1}{\lambda}$ or as $\frac{1}{\lambda^2}$, respectively, so that the contribution of the volume correction term to the value of I_1 is not great even at high elongations.

Voids are formed on straining filled binders, and consequently the strain invariants and the stored energy function should be corrected to take volume changes into account. However, incompressible strain invariants were defined as if no volume changes take place. These incompressible strain invariants were designated as Q_1. Then for uniaxial strain we have

$$Q_1 = \lambda^2 + \frac{2}{\lambda} \tag{45}$$

III, C, Correlation of Real Properties (cont.)

and for biaxial strain

$$Q_1 = \lambda^2 + \frac{1}{\lambda^2} + 1 \tag{46}$$

In terms of the strain invariants, the stored energy function, W, or the energy of deformation per unit volume, is expressed by

$$W = \sum_{i=0}^{\infty} \sum_{j=0}^{\infty} \sum_{k=0}^{\infty} (I_1 - 3)^i (I_2 - 3)^j (I_3 - 1)^k \tag{47}$$

This expression reduces to the Mooney Equation for incompressible materials when $i = 1$, $j = 0$, $k = 0$, and $i = 0$, $j = 1$, $k = 0$; e.g., $I_3 = 1$;

$$W = C_1 (I_1 - 3) + C_2 (I_2 - 3) \tag{48}$$

When $C_2 = 0$, Equation (48) reduces to the ideal rubber relationship given by the kinetic theory of elasticity.

The stored energy function per unit volume is related to the stress, $\sigma(\lambda_i)$, by

$$W = \int_{\lambda_i} \sigma(\lambda_i) \, d\lambda_i \tag{49}$$

so the value of W is given by the area under the experimental stress-strain curve. Values of the stored energy function were determined for both unaxial and biaxial tension covering a wide range of temperature, strain rate, and

III, C, Correlation of Real Properties (cont.)

type of filled system. The experimental values of W were plotted against
$(Q_1 - 3)$. It was found that W was represented by the general equation
(except for a poor fit at very low strains).

$$W = A(1 - e^{-B(Q_1 - 3)}) \underset{\lambda = 1}{=} AB(Q_1 - 3) \tag{50}$$

where A and B are constants. A is the value which W is approaching ex-
ponentially and B is a measure of the rate of increase of W. From the
definition of W, it follows that

$$\frac{dW}{d\lambda} = \sigma(\lambda) \tag{51}$$

Differentiation of Equation (5) with the value of Q_1 from Equation (23) gives the
uniaxial stress-strain equation,

$$\sigma(\lambda) = 2AB(\lambda - \frac{1}{\lambda^2}) \, e^{-B(\lambda^2 + \frac{2}{\lambda} - 3)} \tag{52}$$

whereas the biaxial stress-strain equation using Equation (25) is given by

$$\sigma(\lambda) = 2AB(\lambda - \frac{1}{\lambda^3}) e^{-B(\lambda^2 + \frac{1}{\lambda^2} - 2)} \tag{53}$$

III, C, Correlation of Real Properties (cont.)

The modulus, or initial slope of the stress-strain curves, is obtained from the differential $d\sigma(\lambda)/d\lambda$ at $\lambda = 1$, which is 6AB from Equation (52) for uniaxial and 8AB from Equation (53) for biaxial.

The value of A was determined by successive approximations Reasonable values of A were chosen and log $(1 - \frac{W}{A})$ was plotted against $(Q_{ij} - 3)$ until the resulting plot was linear. Generally, the value of A could be found in one or two trials. The value of B was calculated from the slope of this linear plot. In several graphs, small deviations from linearity were observed at very low elongations and also the semi-log plots had an intercept slightly different from 1 so that Equation (50) becomes

$$W = A(1 - Ce^{-B(Q_1 - 3)}) \tag{54}$$

where C is the value of the intercept, generally ranging from 0.95 to 1.02. These intercepts appeared in many cases to be due to experimental errors. In other cases, C deviates from unity when the stress-strain curve has a very steep initial slope followed by a markedly different slope. The effect of C is also to make the modulus equal to 6ABC and 8ABC, for uniaxial and biaxial, respectively.

Uniaxial tensile testing was performed with standard JANAF specimens with a nominal gage length of 2.7 in. The biaxial specimens were 7 in. long and 0.25 in. thick with 0.5 in. gage length. Two polyurethane propellants were tested under biaxial conditions; the data are given in Table 10. In order to compare the uniaxial and biaxial data of specimens obtained from the same batches, a 10-lb. mix of inert polyurethane propellant, DP-16, designated as System III and containing 59 wt% salt and 15% aluminum powder

TABLE 10

REDUCED BIAXIAL STRESS-STRAIN DATA FOR TWO POLYURETHANE PROPELLANTS

Propellant I

Temp °F	$\dot{\varepsilon}$ Min^{-1}	λ_b	W_b	A	B	C	W_b/A
20	20	2.82	913.10	1200	0.22	0.94	0.76
	40	1.62	322.10	450	1.18	0.94	0.72
60	20	4.02	389.55	500	0.10	0.91	0.78
	40	5.31	649.50	800	0.056	0.88	0.81
80	20	3.49	253.49	80	0.19	0.94	0.90
	40	3.30	243.04	300	0.17	0.95	0.81
	200	2.90	312.00	420	0.20	0.96	0.74
	1,000	2.50	375.58	500	0.29	0.91	0.75
	2,000	1.80	288.48	350	0.80	0.96	0.80
	10,000	1.68	261.32	340	1.17	0.96	0.82
110	20	2.50	128.15	180	0.28	0.97	0.71
	40	2.66	134.86	180	0.26	0.96	0.75

Propellant II

Temp °F	$\dot{\varepsilon}$ Min^{-1}	λ_b	W_b	A	B	C	W_b/A
40	40	1.83	131.91	220	0.53	0.96	0.60
80	20	1.75	53.87	80	0.82	1.00	0.67
	40	1.84	67.82	100	0.65	1.00	0.68
110	20	1.64	36.47	70	0.71	1.00	0.52
	40	1.61	44.27	80	0.82	1.00	0.55

III, C, Correlation of Real Properties (cont.)

of 15 µ dia. and a 10-lb. mix of System IV, containing 65 wt% glass beads of 114 µ dia. were prepared. Both uniaxial and biaxial specimens were tested over a wide range of strain rate and temperature, i.e., 0.1 to 10,000 $\min^{-1}$ from 40°F to 110°F for the biaxial tests, and at 0.074 to 740 $\min^{-1}$ from -40 to 110°F for the uniaxial tests. The resulting data are listed in Tables 11 and 12.

Typical graphs used in these computations are presented in Figures 49 and 50, which show, respectively, a typical plot of W vs $(Q_1 - 3)$, and the corresponding semi-log plot of $(1 - \frac{W}{A})$ vs $(Q_1 - 3)$ for polyurethane propellant II.

The stress-strain Equation (52) is similar in form to the equation proposed by Martin, Roth, and Stiehler (26).

$$\sigma_o = E(\lambda^{-1} - \lambda^{-2}) \, e^{A(\lambda - \lambda^{-1})} \tag{55}$$

where σ_o is the stress based on the initial cross section and A is a constant, found to be 0.38 for pure gum vulcanizates of Hevea, GR-S, GR-1, and Neoprene rubbers subjected to constant tensile loads. The form of equation has been found to describe well the behavior of some composite propellants essentially to failure under constant rate, uniaxial tensile test (27).

The shapes of curves predicted by Equation (52) and by the MRS Equation (55) are shown in Figure 51 for values of A = 0.38, 0, and -0.38, and values of B of 0 and 0.38. Differentiation of the MRS equation shows that maximum stress values are obtained only for $A \lessgtr 0.157$, as the value of A determines the maximum in the nominal stress-strain curve. At A = 0, $\lambda_m = 2$, which is high for composite propellants and one can expect values of A less than one to be required. Similarly, useful values of B are greater than zero. It can be seen that for A = -0.38, and B = 0.38, the typical downward trend of stress following λ_m is represented.

TABLE 11

REDUCED STRESS-STRAIN DATA OF INERT PROPELLANT III

Biaxial

Tsmp °F	$\frac{\epsilon}{Min}-1$	$\lambda_b \%$	W_b	E_{psi}	A	B	C	W_b/A	Linsar Slope	E(calc)
40	0.1	12.9	6.34	994	12	13.3	1.02	0.53	——	1300
40	740	56	205	2941	260	1.8	1.00	0.79	——	3740
40	10,000	54	251	3500	350	1.65	1.02	0.72	——	4710
80	0.1	11.5	4.51	742	---	----	----	----	97.5	780
80	0.1	8.5	3.29	1010	---	---	---	---	127	1020
80	10	11.0	8.53	1705	----	----	----	----	199	1590
80	10	10.7	7.50	1370	----	----	----	----	189	1510
80	740	32.0	92.5	4000	120	4.56	1.00	0.88	——	4380
80	2000	33.0	107.5	2900	200	2.37	1.00	0.54	——	3790
80	2000	28.0	108	5100	160	4.47	1.00	0.68	——	5720
80	10,000	36.0	133	3000	20C	2.88	1.03	0.67	——	4750
110	0.1	9.6	4.6	1100	----	----	----	----	137	1090
110	0.1	9.52	4.1	1000	----	----	----	----	124	992
110	10,000	58.0	125	1680	150	1.80	1.02	0.83	——	2200

Uniaxial

Tsmp °F	$\frac{\epsilon}{Min}-1$	$\lambda_b \%$	W_b	E_{psi}	A	B	C	W_b/A	Linsar Slope	E(calc)
-40	740	9.26	106	55,000	130	66.0	1.00	0.82	——	51,500
80	0.074	34.6	14.8	405	22	3.72	1.00	0.67	——	491
80	7.4	26.9	28.5	1990	35	8.56	1.00	0.81	——	1800
80	740	35.2	67.5	3090	80	5.68	1.00	0.84	——	2730
110	0.074	12.6	6.9	948	----	----	----	----	157	942

        Included in ths tablss are columns of ths extsnsion ratios at break, λ_b; ths work to brsak, W_b; (assuming incomprsssibility) ths modulus calculatsd from ths slops of ths stress-strain curvss and the computed values of the constants A, B and C. The slopes of ths linear plots of W vs $(Q_{1j} - 3)$ are given in the column titled "Linsar Slopes". Valuss of the initial moduli, calculatsd by uss of the constants A, B, C, or from the valuss listed undsr "Linear Slopes" by means of Eq. (34) or (37), are listed in ths last column under E (calc.).

TABLE 12

REDUCED STRESS-STRAIN DATA OF SYSTEM IV, CONTAINING 65 VOL% GLASS BEADS

Biaxial

Temp $^\circ$F	$\dot{\varepsilon}$ Min^{-1}	λ_b%	W_b	E_{psi}	A	B	C	W_b/A	Linear Slope	E(calc)
40	0.1	12.2	4.00	618	---	---	---	---	79.0	632
40	740	22.0	78.7	3650	---	---	---	---	481	3850
40	10,000	22.0	86.8	4480	---	---	---	---	585	4680
80	0.1	7.52	1.72	852	2.5	53.3	1.02	0.69	---	1090
80	10	7.83	3.30	1450	---	---	---	---	145	1160
80	740	54.0	66.0	1070	80	1.85	1.00	0.83	---	1180
80	2,000	28.0	35.5	3740	120	4.84	1.01	0.71	---	4690
80	10,000	28.0	83.0	3200	120	4.68	1.02	0.69	---	4580
110	0.1	6.12	1.06	620	---	---	---	---	78.6	629
110	10,000	36.0	63.8	2640	80	3.69	1.02	0.80	---	2410

Uniaxial

Temp $^\circ$F	$\dot{\varepsilon}$ Min^{-1}	λ_b%	W_b	E_{psi}	A	B	C	W_b/A	Linear Slope	E(calc)
-40	740	7.41	116.6	53,600	180	59.7	1.02	0.65	---	66,000
40	740	14.4	30.7	6,100	40	24.7	1.02	0.77	---	6050
80	0.074	14.3	3.07	355	---	---	---	---	60.4	362
80	7.4	12.6	7.75	1930	10	32.5	1.01	0.78	---	1970
80	740	20.0	23.8	2430	30	13.9	1.00	0.80	---	2490
110	0.074	5.48	1.05	940	---	---	---	---	146	876
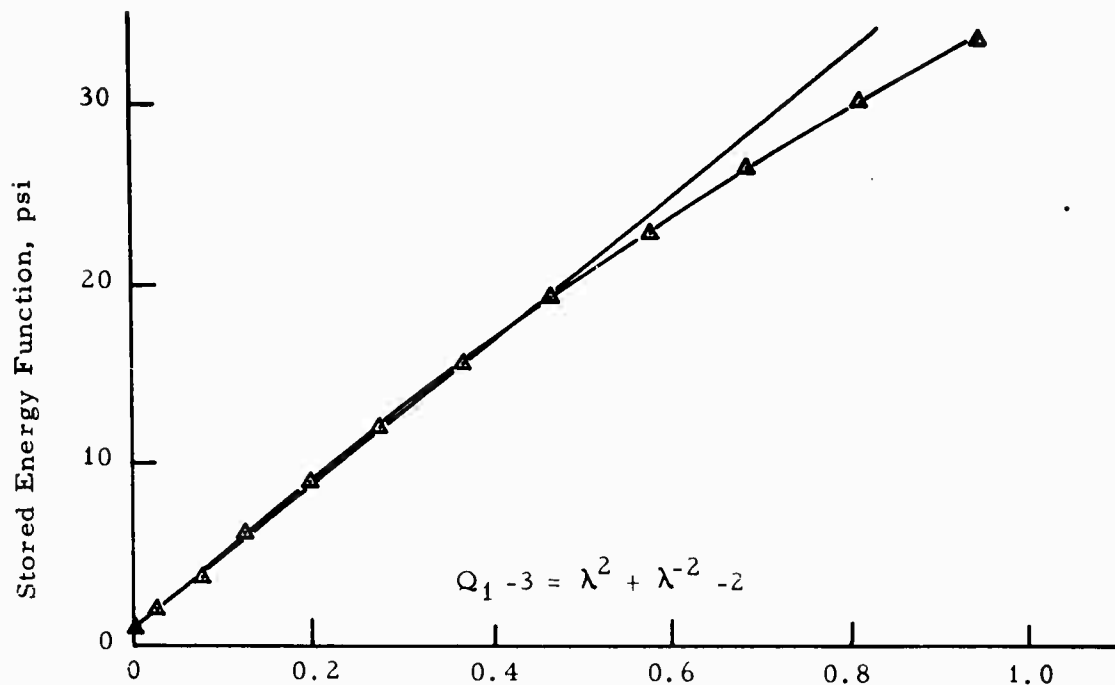
Figure 49. Plot of Stored Energy Function in Biaxial Tension for Propellant System II. Test Temperature: 110°F, Strain Rate: 20 min^{-1}

$$Q_1 - 3 = \lambda^2 + \lambda^{-2} - 2$$
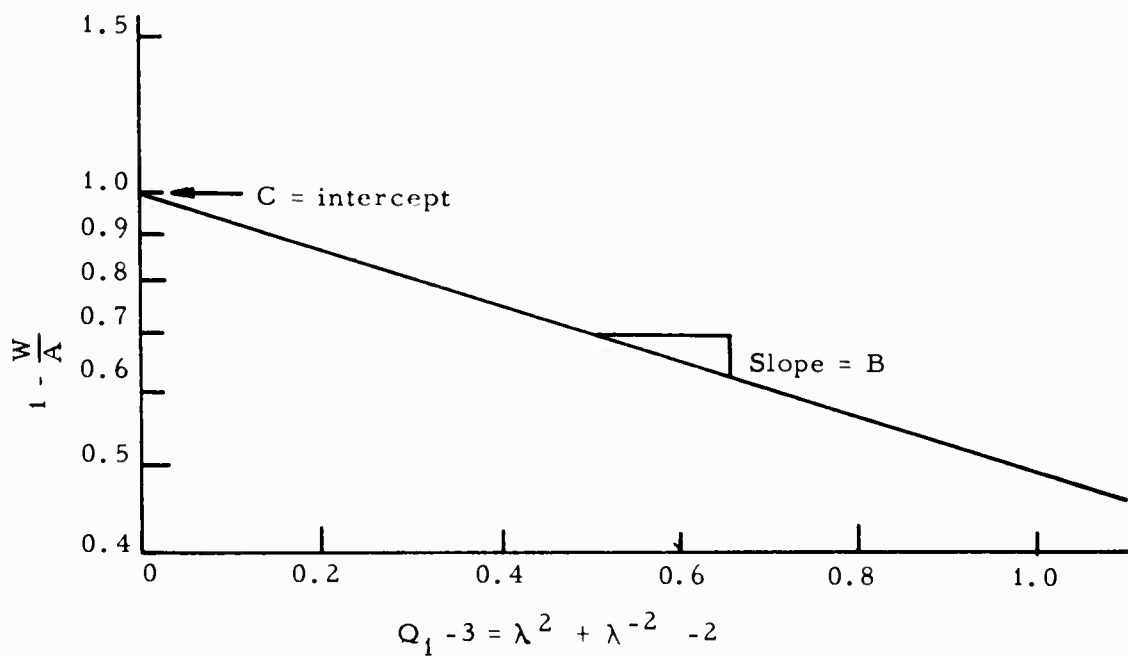
Figure 50. Graph for Determination of Constants A and B, for Propellant System II. Test Temperature: 110°F, Strain Rate: 20 min^{-1}

$$Q_1 - 3 = \lambda^2 + \lambda^{-2} - 2$$

Page 117
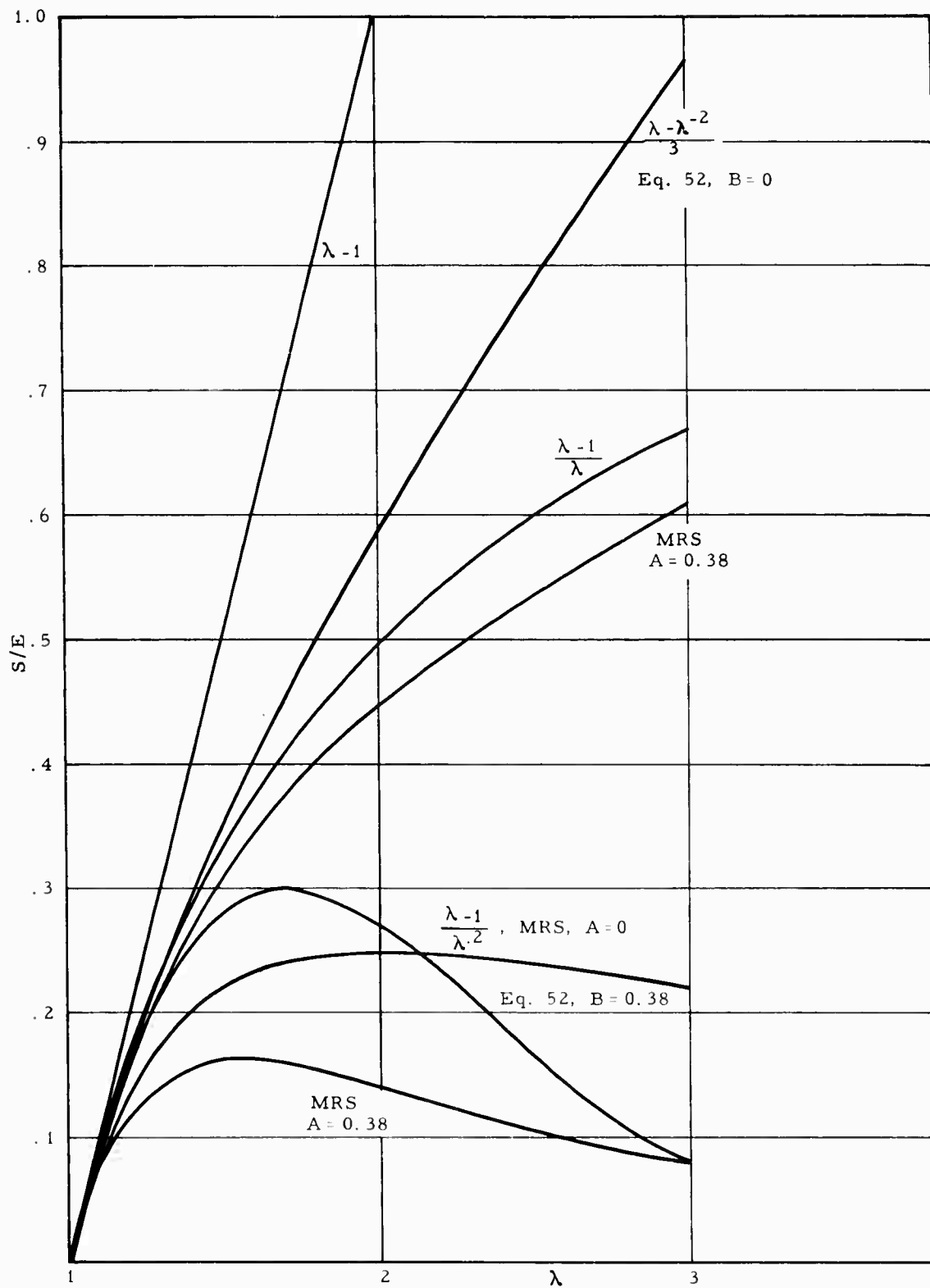
Figure 51. Comparison of S/E Curves for Several Functions of λ

IV. PHASE 3 -- THEORETICAL AND EXPERIMENTAL STRESS ANALYSIS

The objective of this phase was originally to use the data representations of Phase 2 for the calculation of strains in a simple tubular configuration, and observe experimentally the strains experienced under the same boundary conditions used in the analysis. As the studies developed, it became evident that for pressurization and thermal cycling, the observed strains agreed closely with those calculated for a simple elastic, incompressible material, whose modulus had little effect, except for weak motor cases, and whose pertinent properties appeared to be only the thermal coefficient of expansion for temperature cycling and the bulk modulus for pressurization. An exception appeared to be the volume change produced at higher strains caused by dewetting, but later data showed this to be a minor factor and the movement of free grain ends played a larger role. A reservation must be made, however, that because the cycling studies to produce high strains were made in tubular grains which produce a symmetrical strain distribution, the role played by local dilatation at star points cannot be stated as yet. Strain measurement at star tips was not accomplished in the program; the embedded gages using a wire helix cast in propellant appeared promising for local strains but could not be developed beyond 25% strain capability, which is marginal for research use though satisfactory for many grain designs in use if certain connection and calibration problems can be solved. Visual observations of strain still appears to be the most satisfactory method, and the Moire fringe technique is a valuable tool. Star point study through use of a sector offers an important new technique for the visual study of strain distribution in this case of non-uniform strain distribution, and was shown to agree closely with the strain results by the classical technique of pressurization of photoelastic sections of the configuration.

The solution of more complex stress cases, such as creep at higher temperature, where the nonlinear and viscoelastic properties of the propellant become important, were attacked during the program but the complexity of such problems did not allow as significant advances in those areas.

IV, Phase 3 -- Theoretical and Experimental Stress Analysis (cont.)

The discussions of this phase are divided into the experimental and the theoretical areas of work.

A. EXPERIMENTAL STUDIES OF STRESSES AND STRAINS IN SUB-SCALE GRAINS

Experiments were performed on tubular cylinders of small size under conditions of temperature cycling and pressurization. The temperature cycling was performed with grains whose ends were free to move except at the wall, since the grains were case bonded. The pressurization experiments were on grains restrained by an aluminum case, though not bonded to it, with plane strain introduced by rigid containment of the ends by transparent walls.

1. Experimental Temperature Cycling of Propellant Cylinders

It has been observed that the maximum bore strains measured for B/A ratios greater than 8 were essentially constant. Two possible explanations suggested were excess movement of the free unbonded motor ends, or dewetting of the propellant. Calculations by the stress function technique (31) of the computer program, discussed later in this phase, show that the observed results are expected due to the interplay between the free ends and the propellant center. Figure 52 shows the calculated maximum strains for various B/A and L/B ratios and the actual observed points from temperature cycling experiments performed over the past year. The calculated strains for the heavy motor case used are tabulated in Table 13, together with values used in the calculation. The experimental values of maximum strain are given in Table 14, together with the initial increase of strain with decrease of temperature. The agreement between the theoretical and measured is surprisingly good considering the variation in the results from individual grain tests. However, the general pattern of very little increase in ε_{mm} for B/A ratios greater than 8 is predicted and observed for length to outer radius ratios, L/B, as low as 3.
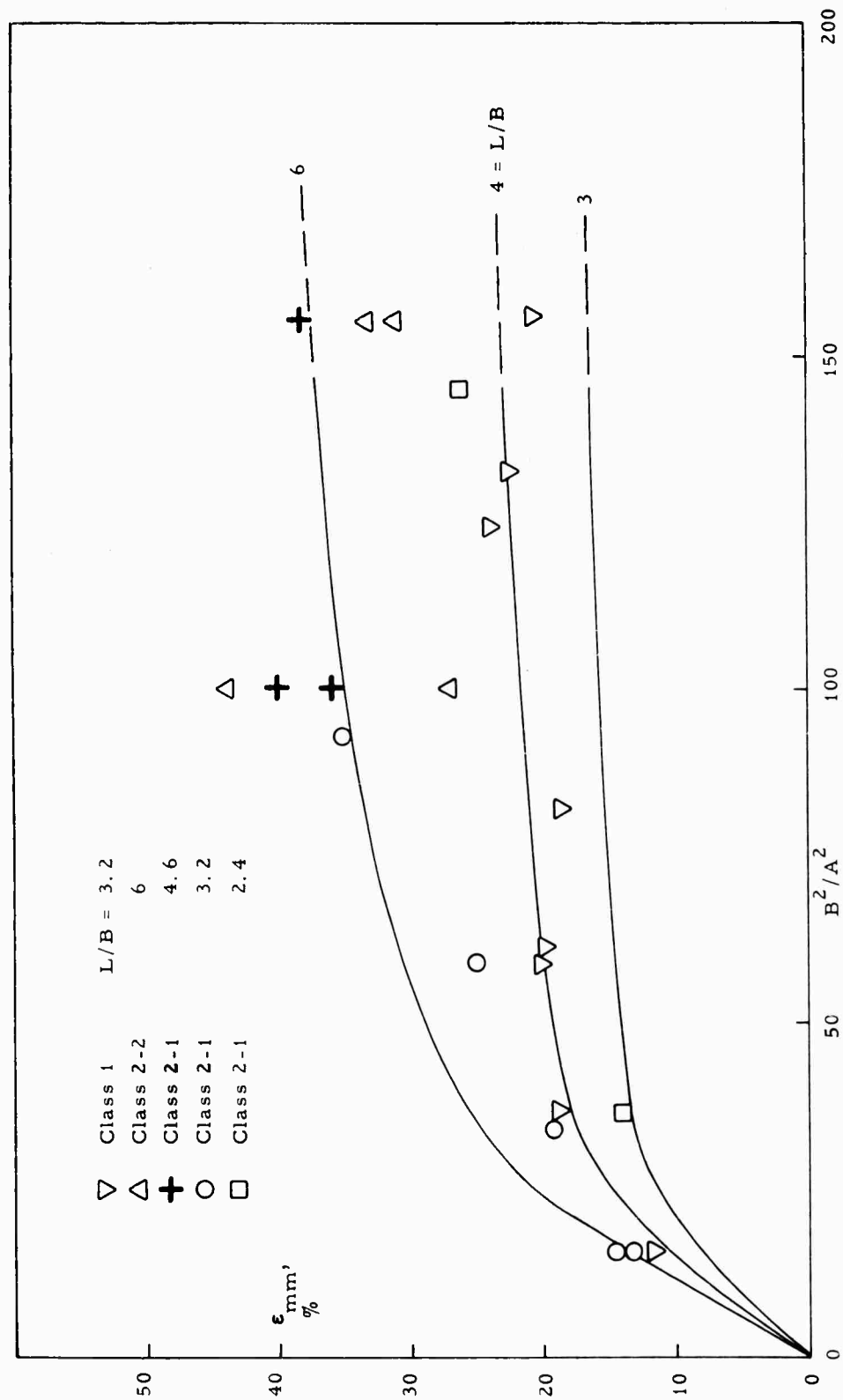
Figure 52. Comparison of Predicted and Observed Maximum Strains in the Bore
of Tubular Grain on Cycling to -75°F

TABLE 13

MAXIMUM INNER BORE HOOP STRAIN CALCULATED FOR EXPERIMENTAL MOTORS

$\frac{L}{B}$	$\frac{B}{A}$	STRAIN
	6	25.8
6	10	34.6
	12	37.1
	6	17.9
4	10	21.7
	12	22.7
	6	13.6
3	10	15.6
	12	16.2

MECHANICAL PROPERTIES USED IN ANALYSIS

Poisson's Ratio of Propellant $\qquad$ $V_p = .5$

Poisson's Ratio of Case $\qquad$ $V_o = .3$

Modulus of Elasticity of Propellant $\qquad$ $E_p = 50000$ psi

Modulus of Elasticity of Case $\qquad$ $E_o = 30 \times 10^6$ psi

Linear Coefficient of Thermal Expansion for Propellant $\qquad$ $\alpha_p = 630 \times 10^{-7} \frac{in}{in \cdot \degree F}$

Linear Coefficient of Thermal Expansion for Case $\qquad$ $\alpha_o = 589 \times 10^{-8} \frac{in}{in \cdot \degree F}$

Temperature Difference used in Analysis $\qquad$ $\Delta T = -185 \degree F$

CONFIGURATION OF GEOMETRY ANALYZED

L = 15-in.
B = 5-in.
C = 5.50-in.
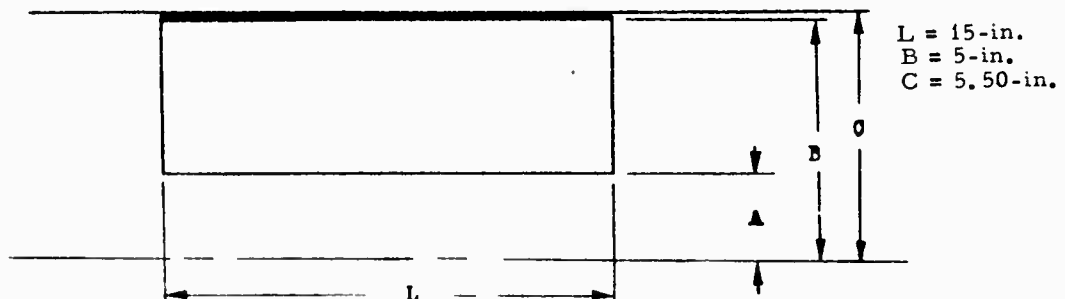
TABLE 14

EXPERIMENTAL VALUES OF MAXIMUM BORE STRAIN

110°F BORE, IN	B^2/A^2	Initial** Strain Increase %/°F	Strain -75°F	
1.25		0.45	12.8	
		0.46	12.8	
		0.48	13.0	
		0.53	13.2	
		0.54	15.0	
		0.75	15.2	
1.035	23.3	0.076	12.7*	
		0.067	9.6*	
		0.051	11.0*	
0.860	33.8	0.103	21.4*	
0.860	33.8	0.103	16.0*	
0.865	33.4	0.114	17.0*	
0.635	62	0.181	25.4*	
0.657	58	0.172	25.3*	
0.662	57	0.156	22.5*	
0.510	96	0.201	37.5*	
0.526	90	0.191	35.5*	
0.518	93	0.200 - 6"	29.0	6" from end of 14.75 motor
0.517	93	0.135 - 2"	27.5	2" from end
0.389	165	0.250	39.3	
0.423	140	0.212	38.5	
0.416	145	0.175	30.5	6" from end of 15 motor, strain
0.412	147	0.175	38	3" from end

*Extrapolated
**Taken from the starting temperature over an interval of 50°F.

IV, A, Experimental Studies of Stresses and Strains in Subscale Grains (cont.)

The continuous monitoring of bore strains in subscale grains was performed at selected points as a function of temperatue and longitudinal bore strain profiles were also taken at selected temperatures. Not all of the instrumented records were successful but sufficient data was obtained to give adequate knowledge of the motor behavior during temperature cycling. Continuous records were made of the inner bore diameter as a function of temperature with strain gages cemented to modified cantilever beams. The gage design which produced adequate and successful records is shown in Figure 53. To improve the accuracy calibration, runs were made with the gages inserted in holes drilled and reamed in a metal block. Nonlinear least squares fitting of this calibration data was then made to obtain a formula

$$ y = A_0 + A_1\ T + A_2\ T^2 + A_3\ T^3 + A_4\ T\ M\ + A_5\ M + A_6\ M^2 + A_7\ M^3 \quad (56) $$

where

y = bore diameter

T = temperature in °F, and

M = millivolt output of gage

while all A's are empirically determined constants obtained by a statistical least squares fit. Accuracy was established as about $\pm$ .003" which was within the limits of accuracy of the carrier amplifying system used.

The experiments with the electronic measuring gages were carried out in a small cold box of suitable size to hold six motors at one time. The cooling method was the injection of CO_2 gas from a tank of
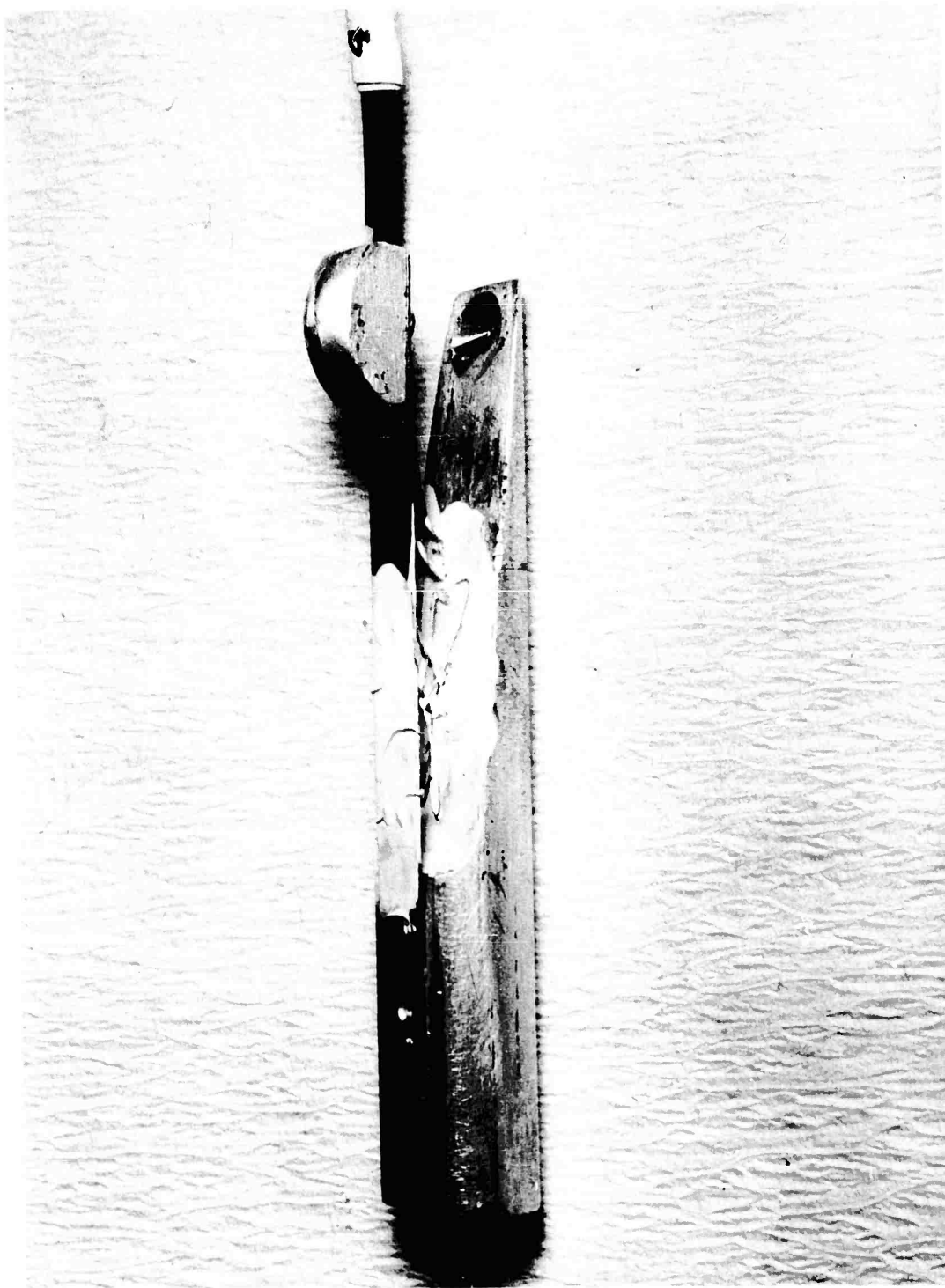
Figure 53. Experimental Bore Measuring Gage for 0.4-in. Bore. The Strain Gages can be seen on the Beam, Deflected by the Button at the End of the Beam when in a Bore (3-62S 08208)

IV, A, Experimental Studies of Stresses and Strains in Subscale Grains (cont.)

liquid CO_2. Two methods of dropping the temperature were used; a slow steady dropping of the temperature by hand regulation and a sharp drop of the control knob. It was found difficult to get smoothly changing temperature time curves by hand control, and adequate temperature control requires an automatic temperature programmer.

Mechanical bore measurements were made also with inside micrometers suited to the bore diameter being measured. In the case of mechanical measurements, the determinations were made in a refrigerated walk-in chamber. Operators wearing protective clothing went inside the chamber with the motors and made the measurements. Equipment available for these measurements was adequate and accurate in the 0.8 to 1.5" measurement range, with an accuracy of $\pm$ .002". Mechanical measurements at smaller diameters require improved measuring equipment, as the results from 0.4" to 0.8" were not accurate. The electronic gages, on the other hand, were best in the 0.4" to 0.6" range in the design used. Electronic gages suitable for measurement over all the ranges necessary can be developed.

Dewetting in thermally cycled grains was studied with buoyancy measurements made in liquid baths in which an entire small motor was suspended. The results of this experiment are tabulated in Table 15. The buoyancy measurements were made at 110°F and at 0°F on motors covered with a binder coating for leakproofing. If 1/3 the volume change observed in the buoyancy experiment is used to estimate the linear dimension changes, then the differences between calculated and observed values of strain caused by dilatation should only be of the order of 2% to 3% at -75°F. Scatter in the motor measurements is larger than this so confirmation from motor data is not expected.

Studies of all of the records and observation of the motors after the experiments indicates that the dimensional record can show a radial

TABLE 15

VOLUME CHANGE IN 3KS-1000 MOTORS MEASURED BY BUOYANCY

AT 110°F AND AT 0°F

	Class 2 Propellant #1[*]			Class 2 Propellant #2[**]		
Bore Diameter	.400"	.625"	1.25"	.400"	.625"	1.25"
% Volume Change Observed	-1.40	-1.12	-1.05	-0.56	-0.82	-1.28
Volume Change Expected in an Unbonded Grain	-3.13	-3.13	-3.13	-3.44	-3.44	-3.44
Effective % Volume Increase at 0°F	+1.73	+2.01	+2.08	+2.88	+2.62	+2.16

---

[*] Some end release was noted on this set.
    Only one end on these motors was machined.

[**] Both ends of these motors were machined and no
    separation from the wall was noted.

IV, A, Experimental Studies of Stresses and Strains in Subscale Grains (cont.)

release failure at the grain end on cracking. Figures 54 and 55 show evidence
of failure during a cycling experiment. In each case, the bore strains were
subsequently seen to fall away to zero over time periods from one to sixteen
hours. During this period, visual evidence of a crack was not noted, but
any subsequent manipulation of the motors developed the visual evidence.
During the period the crack is developing, the inner bore dimensions are
shifting from some complex function of the dimensions to the simple linear
expansion of a free grain of propellant. The strain will fall very nearly to
zero finally if the crack is large and pronounced.

Figure 56 is a record of three polybutadiene propellant
grains thermally cycled with mechanical measurements. From 150°F down
to 0°F, the measurements were made at 24-hour intervals after a 24-hour
conditioning period at each temperature. After the 0°F measurement, the
motors were all placed in a -75°F box and the measurements and failure
observations recorded on a 2-hour basis. Grain #34, which cracked, clearly
shows the abrupt drop in strain to a low strain value during a 2-hour period.
Grains #35 and #36 were slowly separating by radial release at the ends during
an 8-hour period. The center bore strains of #34 dropped to zero while the
strains of #35 and #36 dropped to intermediate levels.

Figure 57 shows the calculated strain vs length profile for
two Class 2 propellant #2 motors, #26 and #27 at -75°F; the maximum values
are those shown in Table 13. These motors were both cooled slowly over a
16-hour period during which a reasonable linear time-temperature curve was
achieved from about 110°F down to -75°F. Figure 58 shows the time, tempera-
ture, strain record of this experiment. Each motor had two measuring gages
in the bore at the indicated points. Figures 59 to 62 show the calculated linear
strain temperature curve using the -75°F strain for the gage position from the
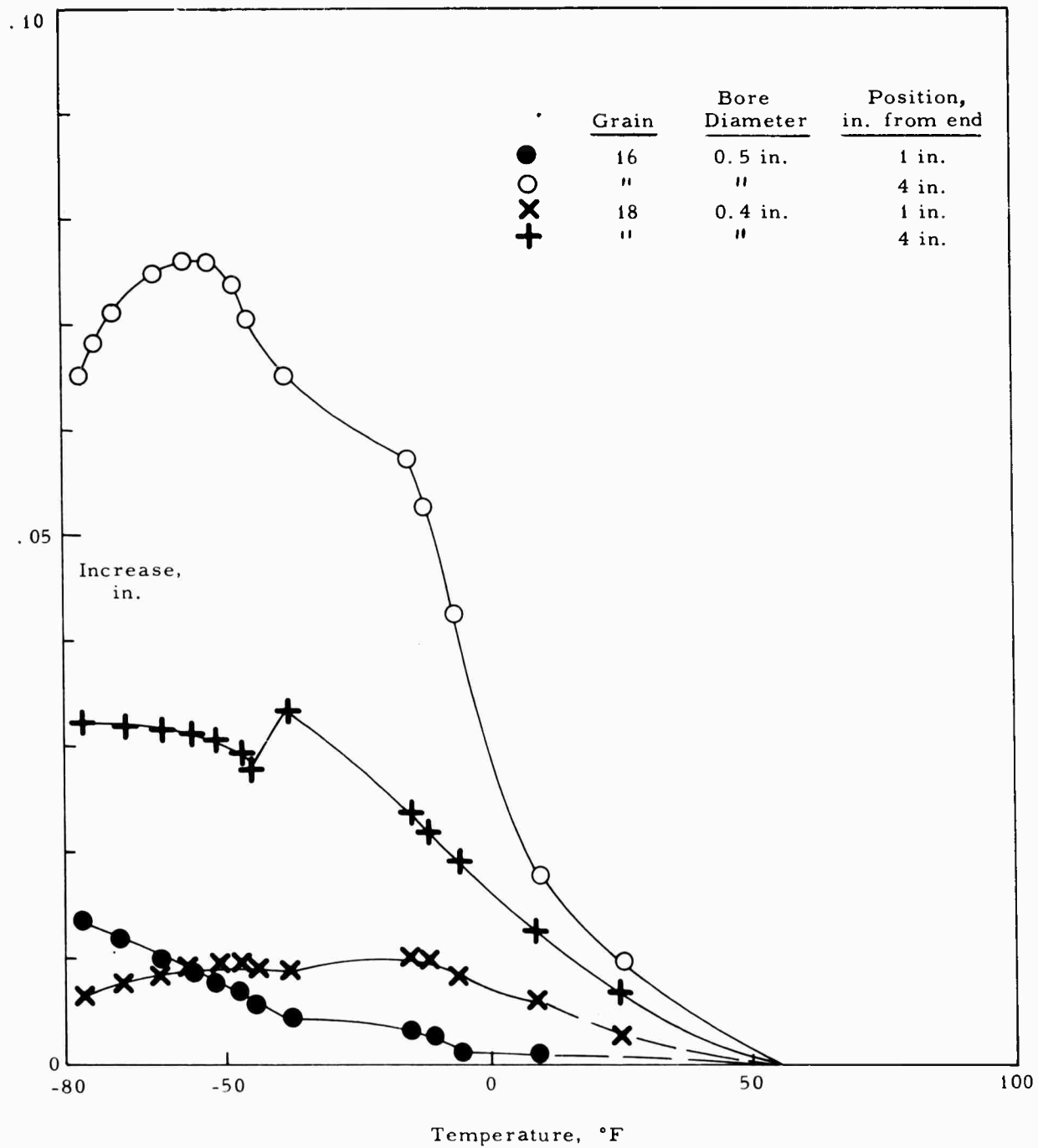
Figure 54. Effect of Temperature on Bore Increase Above 54°F Reading on First
Cycle of Two Motors
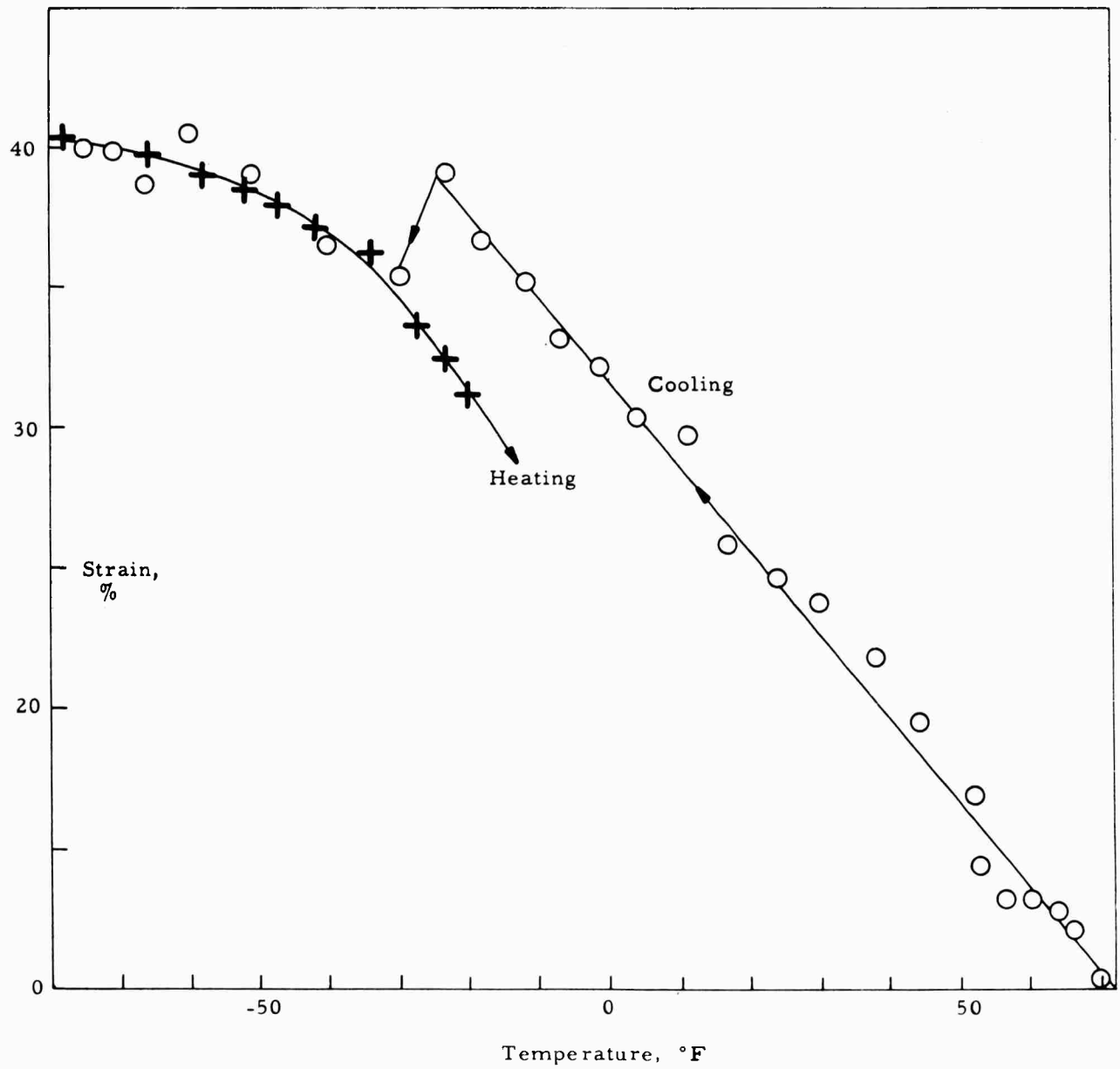
Figure 55. Cooling and Heating of Grain No. 13 Showing Bore Strain Based on 70°F Value for Class 2 Propellant No. 1. Reading Taken 4.75-in. From End of Grain
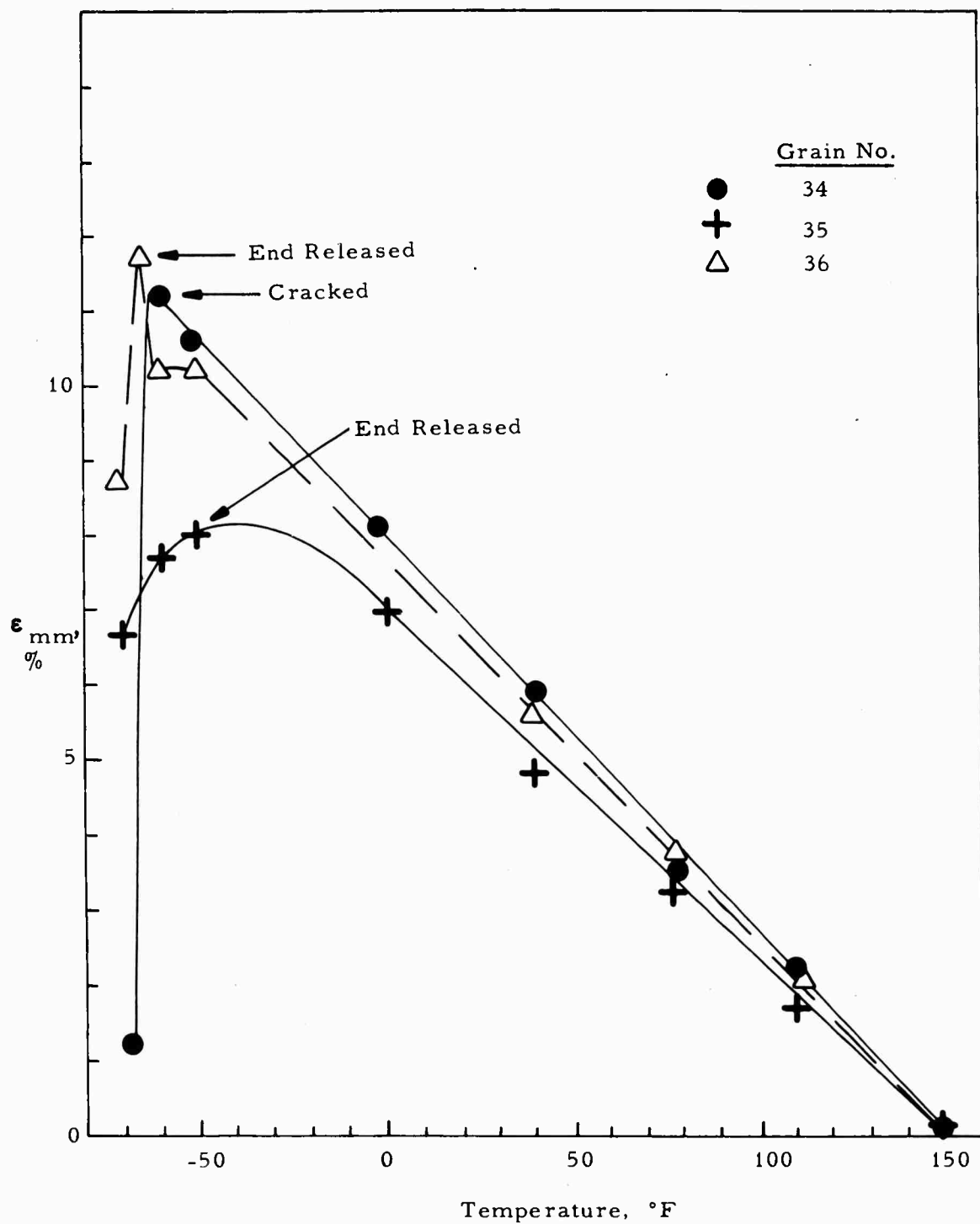
Figure 56. The Effect of Temperature on Maximum Bore Strain for PDB Propellant
at B/A = 4, L/B = 3.2
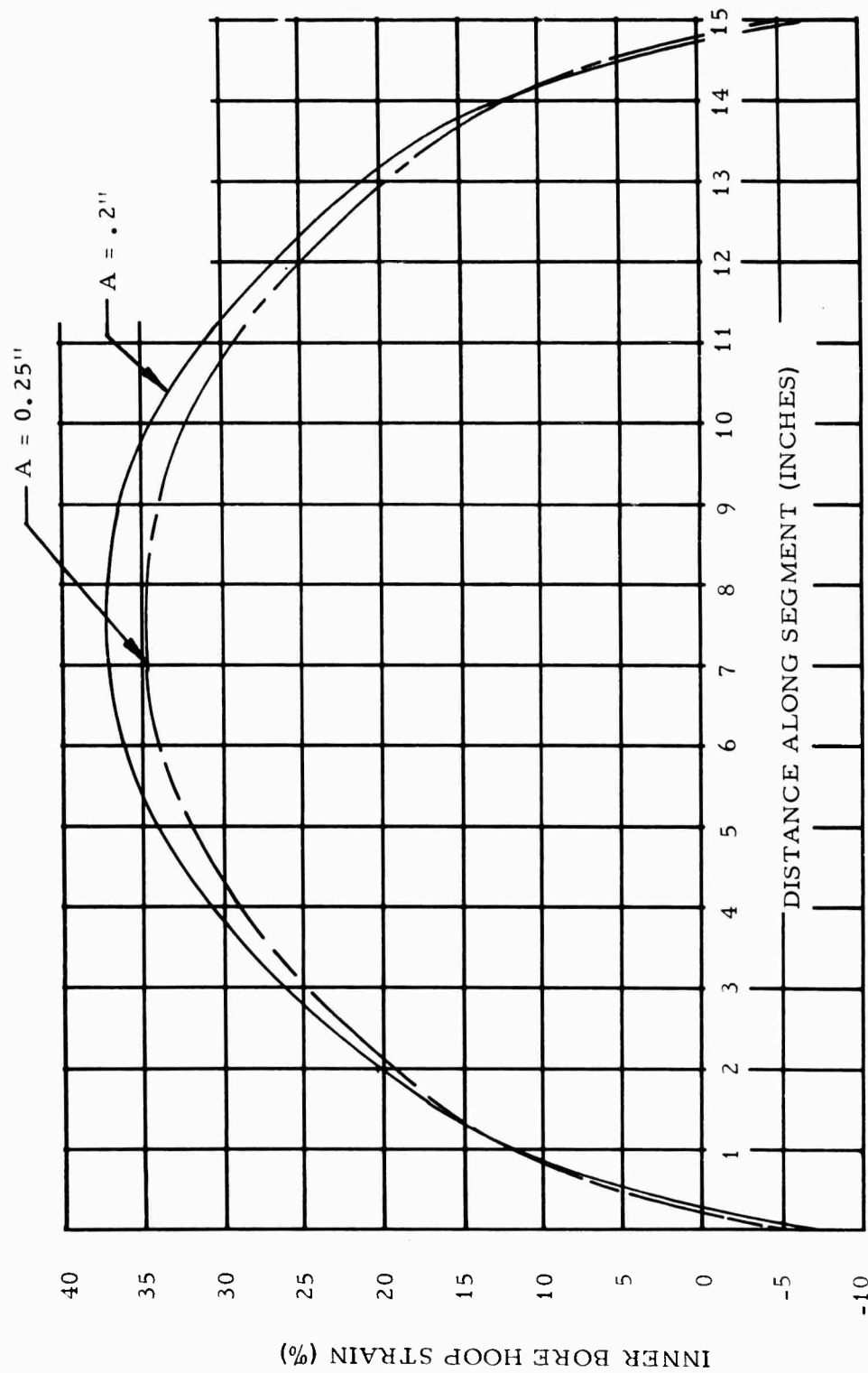
Figure 57. Analytical Solution of Inner Bore Hoop Strain for a Motor Where L = 15 in. and B = 2.5 in. with no End Bonding Under Temperature Cycling ΔT = -185°F
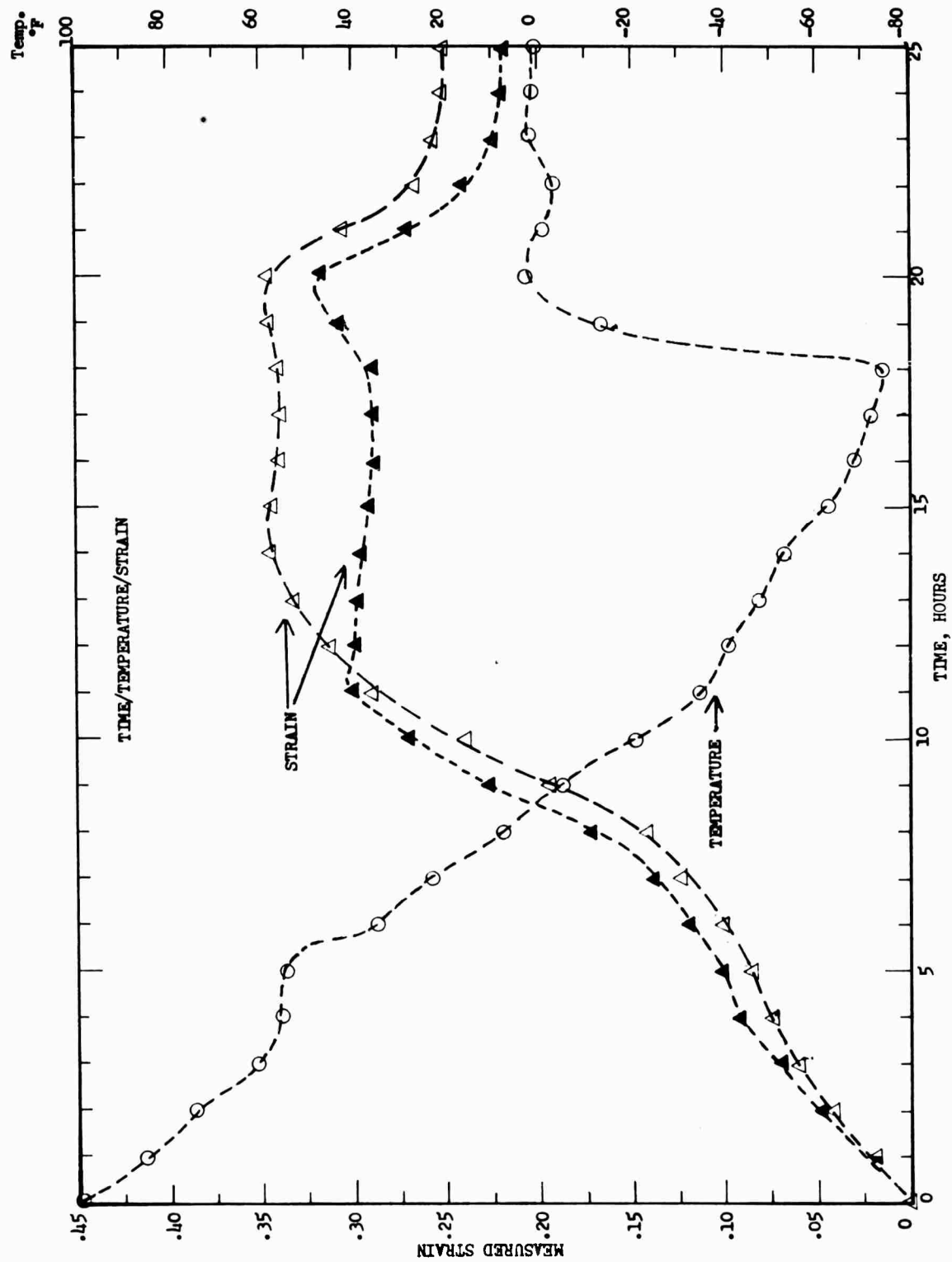
Figure 58. Temperature-Time Curve for Cooling of Motors 26 and 27
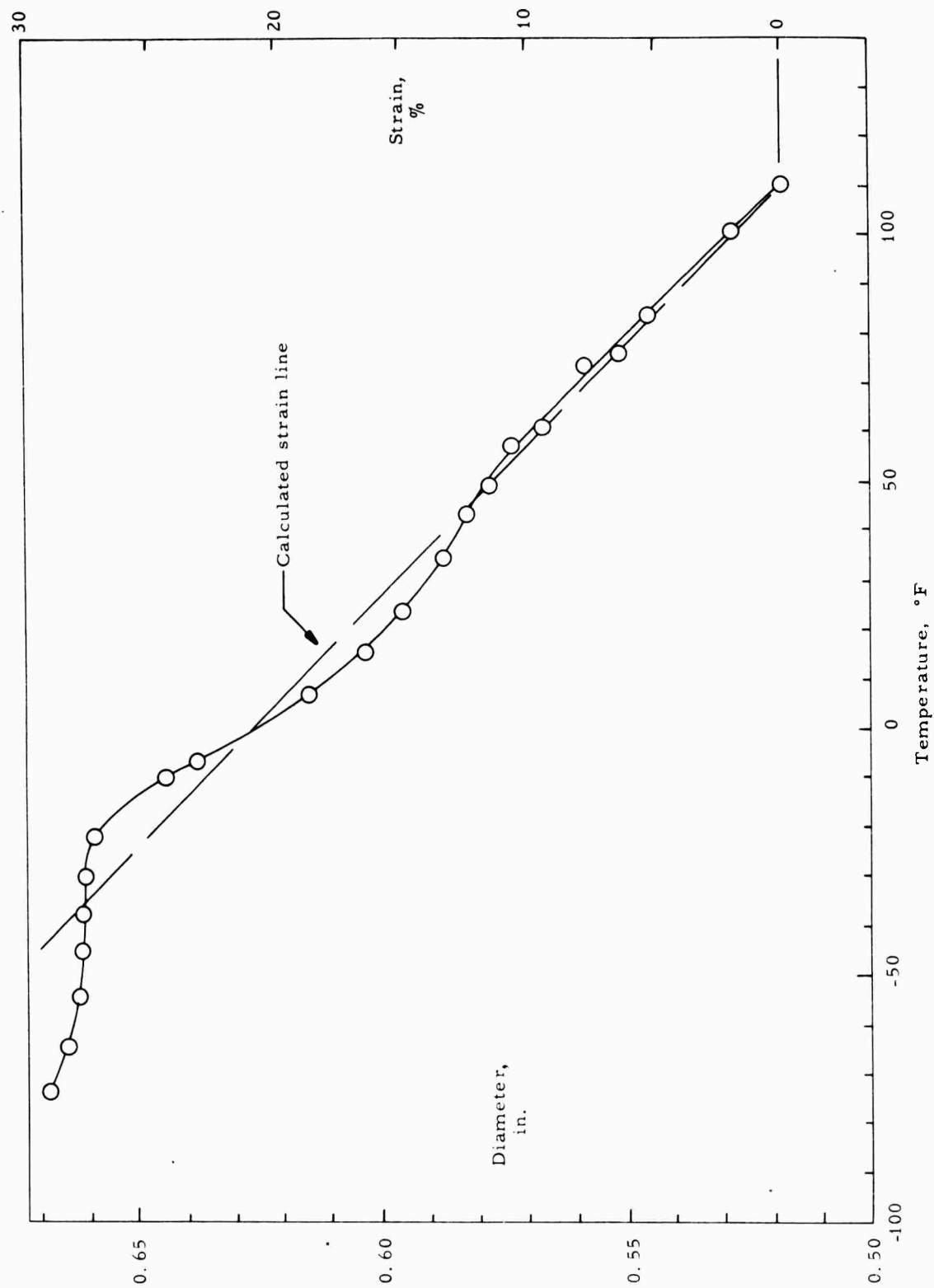
Figure 59. First Cycle Cooling Curve of Grain 27, Taken 1.5-in. From Center of 0.5-in. Bore for Class 2 Propellant No. 2
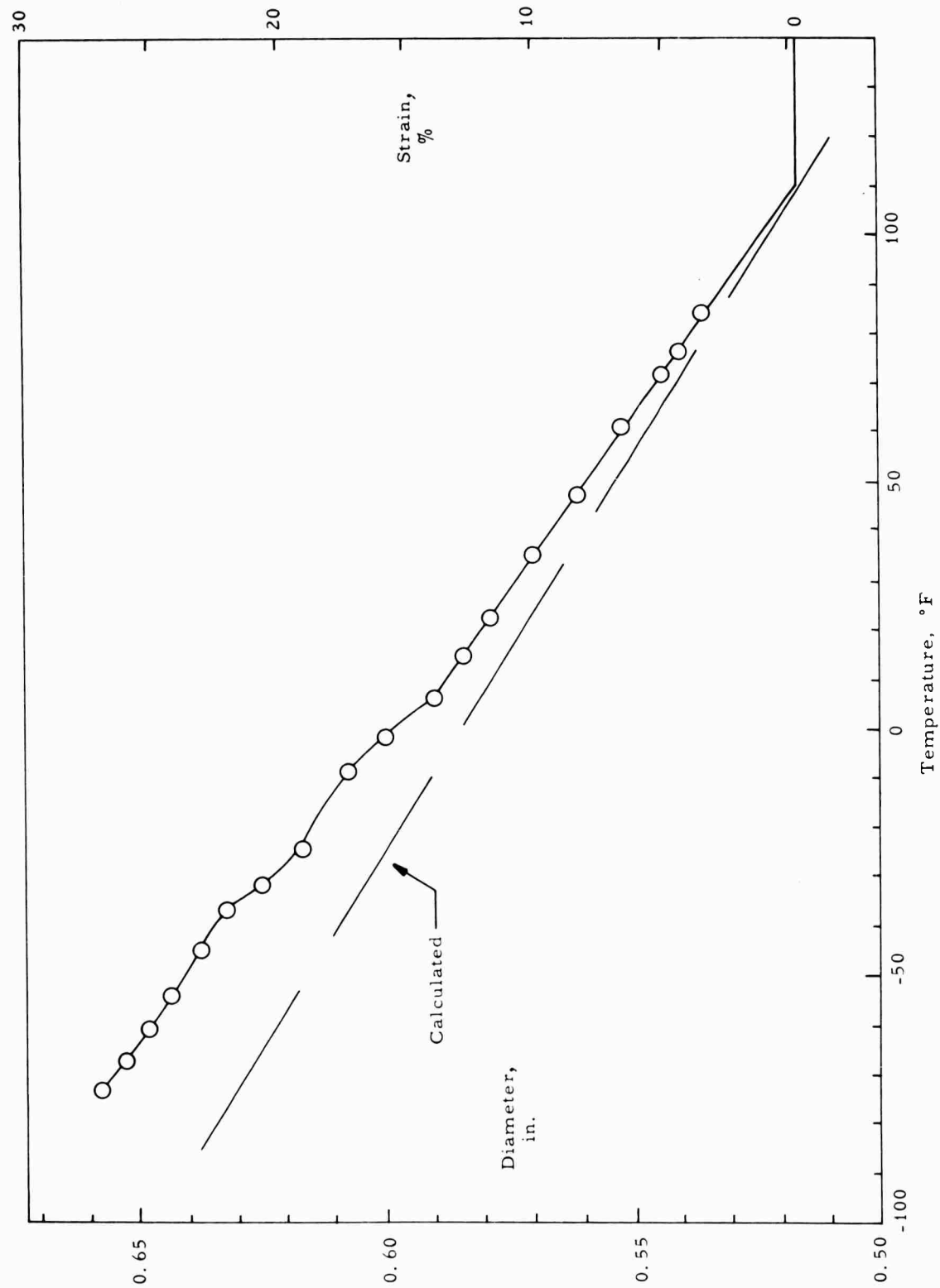
Figure 60. First Cycle Cooling Curve of Grain 27, Taken 2-in. From End of
0.5-in. Bore for Class 2 Propellant No. 2
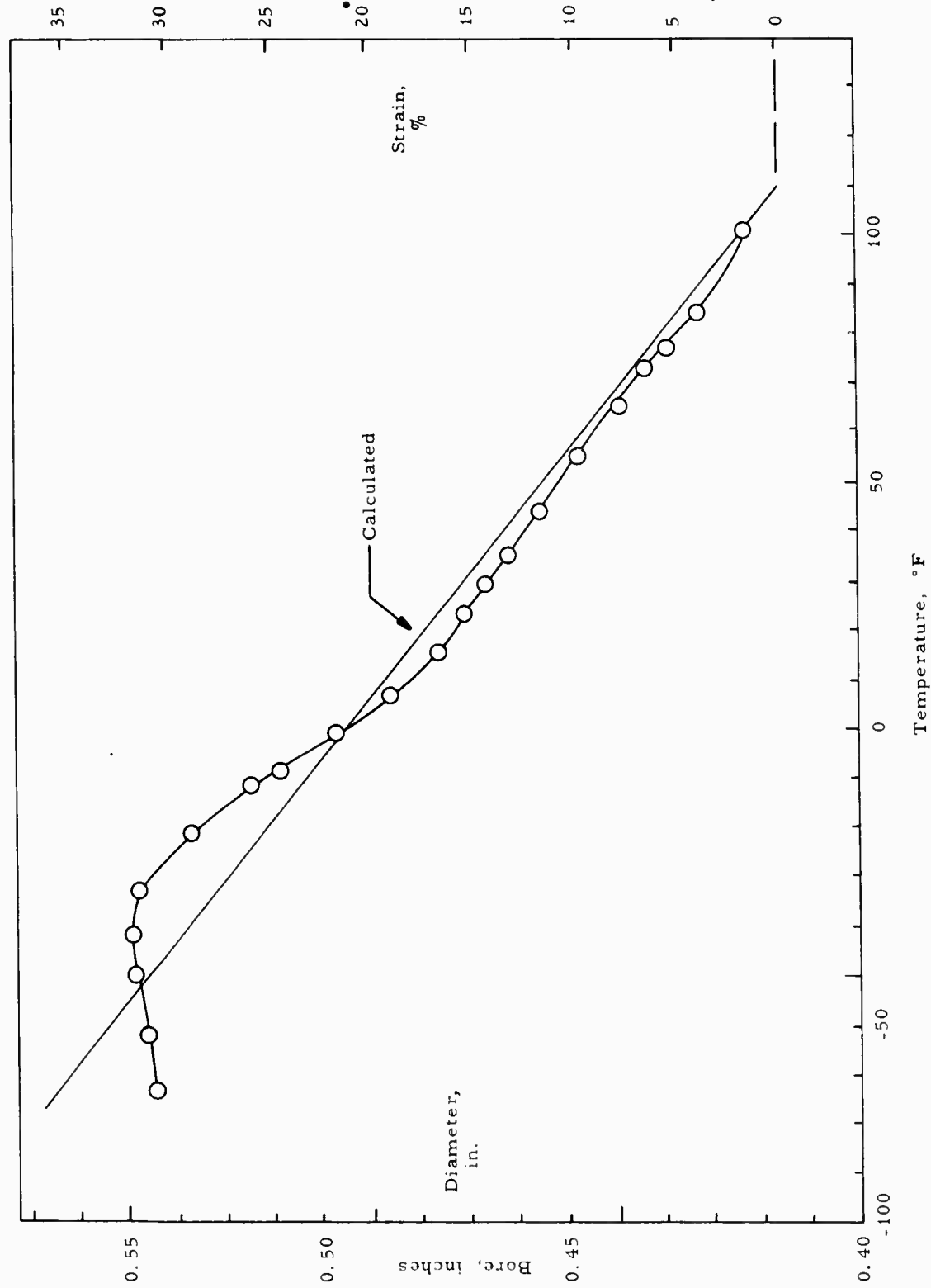
Figure 61. Cooling Curve of Grain 26 Showing Strain 1.5-in. From Center of
0.4-in. Bore of Class 2 Propellant No. 2
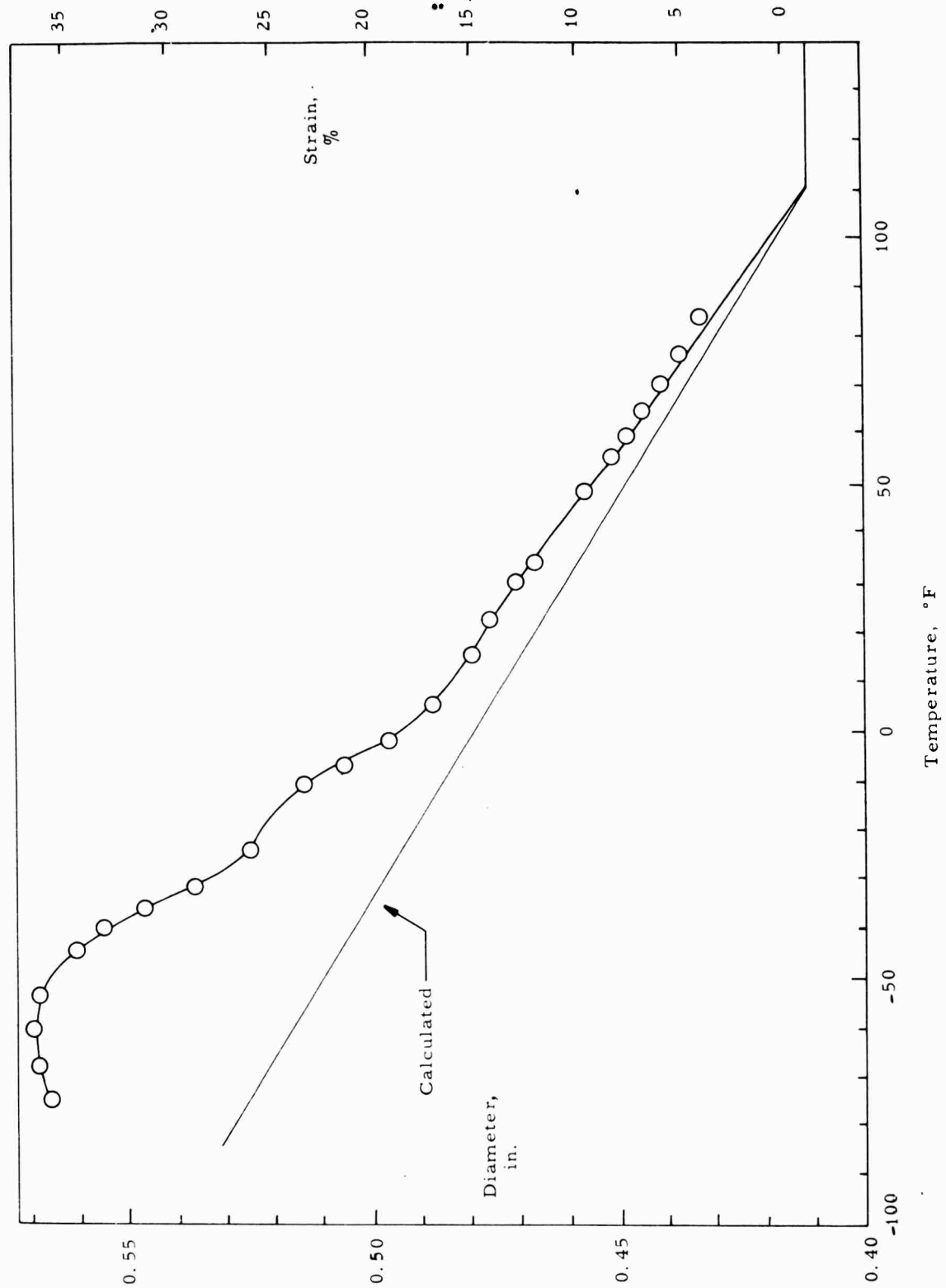
Figure 62. Cooling Curve of Grain 26 Showing Strain 3-in. From End of 0.4-in. Bore of Class 2 Propellant No. 2

IV, A, Experimental Studies of Stresses and Strains in Subscale Grains (cont.)

calculated profile of Figure 57. Gages which were near the center of the
motor gave the best agreement with the calculated strains as in Figure 59
and 61, where the gages 1.5" from the center of the motors show very nearly
precise agreement down to -25°F, though with some wandering on both sides
of the calculated line. Below -25°F, either dewetting or some sort of internal
failure appears to have been taking place, although there was no visible failure
on examination of the motors.

Figures 60 and 62, which were nearer the grain ends, tend
to show somewhat higher strains than calculated. Unfortunately no measured
profile for these small bores could be made due to equipment difficulties.

Figures 63 and 64 show the measured strain temperature
records for rapid temperature drops. These temperature drops were equiva-
lent to shifting the small motors directly from 110°F to -75°F. Some 2 to 4
hours were required to reach 95% of equilibrium at the new temperature.
Strong thermal gradients no doubt existed across the propellant grains. The
hysteresis effect noted with this type of rapid temperature drop is usually
conductive to higher strains than calculated on the return to the high temperature.

2.   Experimental Pressurization of Subscale Propellant Cylinders

The behavior of a cylindrical tubular grain encased in an
aluminum tube under plane strain pressurization was studied to develop the
technique and see what data were obtained with real propellant. First, an
inert propellant was used in a circular configuration, and second, an oval
configuration with live propellant. In both cases the strains were larger
than expected and were not predicted by available calculation procedures.
There are two significant observations that can be made from the test data.
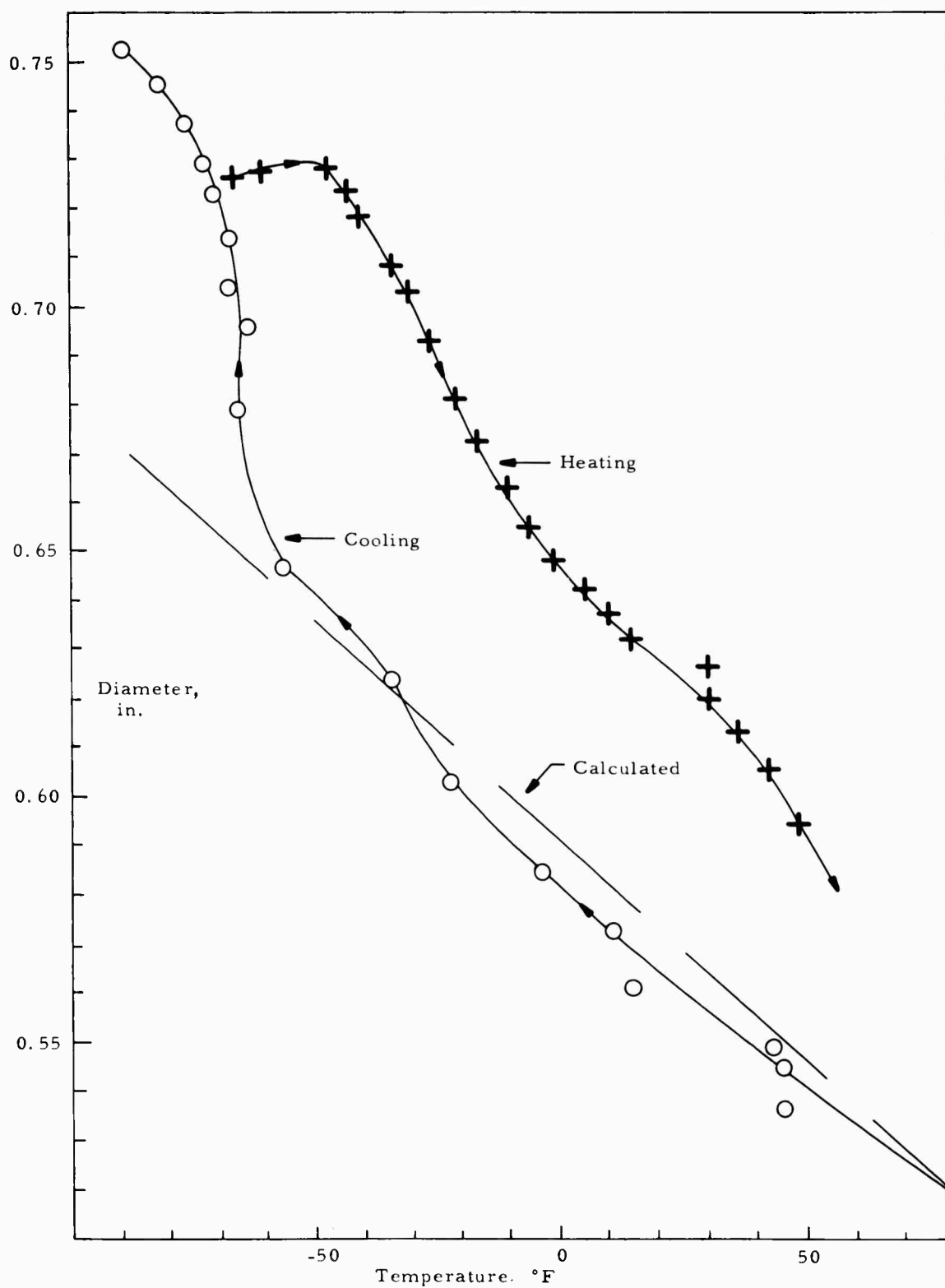
Figure 63. Rapid Cooling and Heating Curve of Grain 32, 4-in. From End of Grain
of 0.5-in. Bore
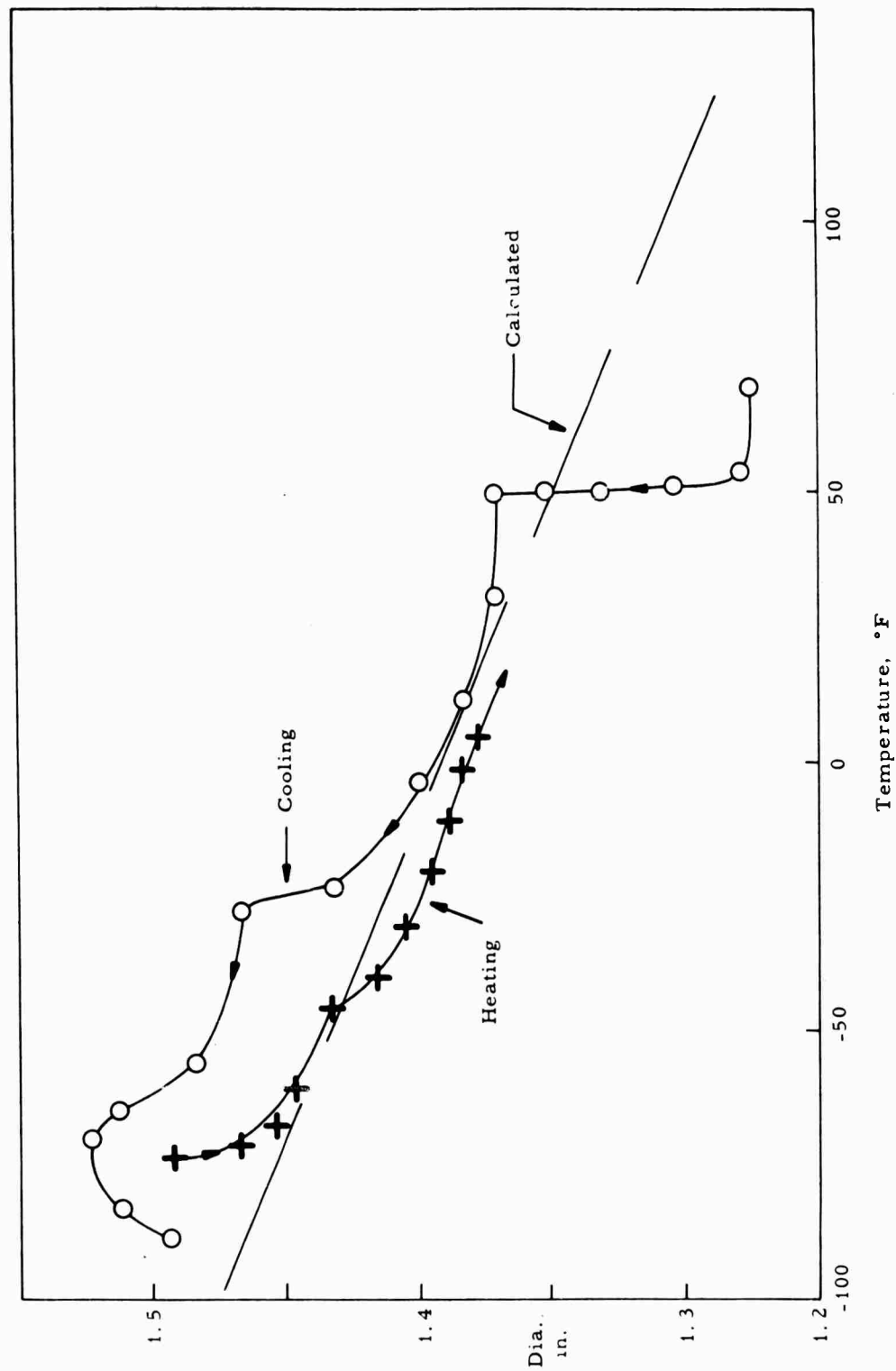
Figure 64. Rapid Cooling and Subsequent Heating of Grain 32

IV, A, Experimental Studies of Stresses and Strains in Subscale Grains (cont.)

First, it is apparent that the magnitude of the strains observed at and near the inner radius of the propellant cylinder was large. Second, the variation of this strain with radius was large, particularly in the region near the inner radius. It would be expected that the stress would exhibit a corresponding variation. In addition to high void content, the material is well known to have a non-linear stress-strain relationship particularly at large strain levels. Both volumetric changes and shear deformations can be expected to exhibit extreme strain dependency under load. Since a large part of these property variations can be attributed to the progressive breaking of the bonds between oxidizer particles and the filler material, it will be difficult to easily express the non-linearity in an algebraic form.

The test measurements included direct measurement of internal pressure by a pressure gage, measurement of hoop strain in the metal case by strain gages, measurement of the change in the volume enclosed by the inner bore of the specimen by means of water volume measurements on the supply reservoir, and direct measurements of radial deformation of the end of the specimen made through a transparent end plate. The accuracy of the internal pressure measurement is dependent on the reliability of the gages and should easily fall within two or three percent of the true values. Similar accuracy is predicted for the strain gage readings on the outer case. However, since a possibility of non-uniformity of deformation at different points along the axis exists, three strain gages located an inch apart were used. The readings of these gages compared closely. Since the elastic properties of the metal case are well known, the external pressure on the specimen can easily and accurately be calculated from the case strains. The severest limitations on accuracy of measurement lies in determining the tangential strain at the inner bore and in the region near the inner bore. Internal strain at low pressure, as deduced from volumetric change, will tend to be high at low pressures, since the rubber

IV, A, Experimental Studies of Stresses and Strains in Subscale Grains (cont.)

bladder used to pressurize the bore does not completely fill the void in the specimen at low pressures, but at higher pressures (in excess of 100 psi), should be accurate to within 2%. Friction between the propellant cylinder and the lucite plate was assumed negligible, since the propellant surface was coated with a silicone grease to provide uniform radial deformation.

The first test was conducted on DP-16 inert propellant. A hollow cylinder of propellant was tested to an internal pressure of 300 psi. A cylinder of 1.00 in. inner diameter, 6.00 in. outer diameter, and 6 in. long was a slip fit into an aluminum case of 0.060 in. wall thickness. The internal radius measurements were made from photographs of the end of the sample through a 1-1/2 in. thick lucite plate. Photographs at zero and 300 psig are shown in Figures 65 and 66. The reduced data are given in Table 16. The tangential strains at the inside boundary measured from the grid photographs and from the change of volume of fluid in the bore, and at the outside boundary calculated from the strain gage measurements are shown in Figure 67. The use of volume change by water displacement gave difficulties caused by a leak in the system and the volume data, even corrected for the leak, were higher than the grid as expected. The strain at the inside boundary was approximately 44% at 300 psi pressure. The corresponding tangential strain at the outside boundary at 300 psi was 0.1%. Figure 68 shows the distribution of strains through the cylinder at various pressures, obtained by measuring the photographs of the grid painted on top the propellant with respect to the grid on the lucite. These data appear to be linear when plotted against $1/r^2$.

Figure 69 shows the relation between the internal pressure and the pressure at the propellant-case interface calculated for a case modulus of 10^7. Percentage of the internal pressure transferred to the case is also shown in the figure. The large non-linearity below 50 psi in case pressure can probably be attributed to the propellant expanding to fill the case.
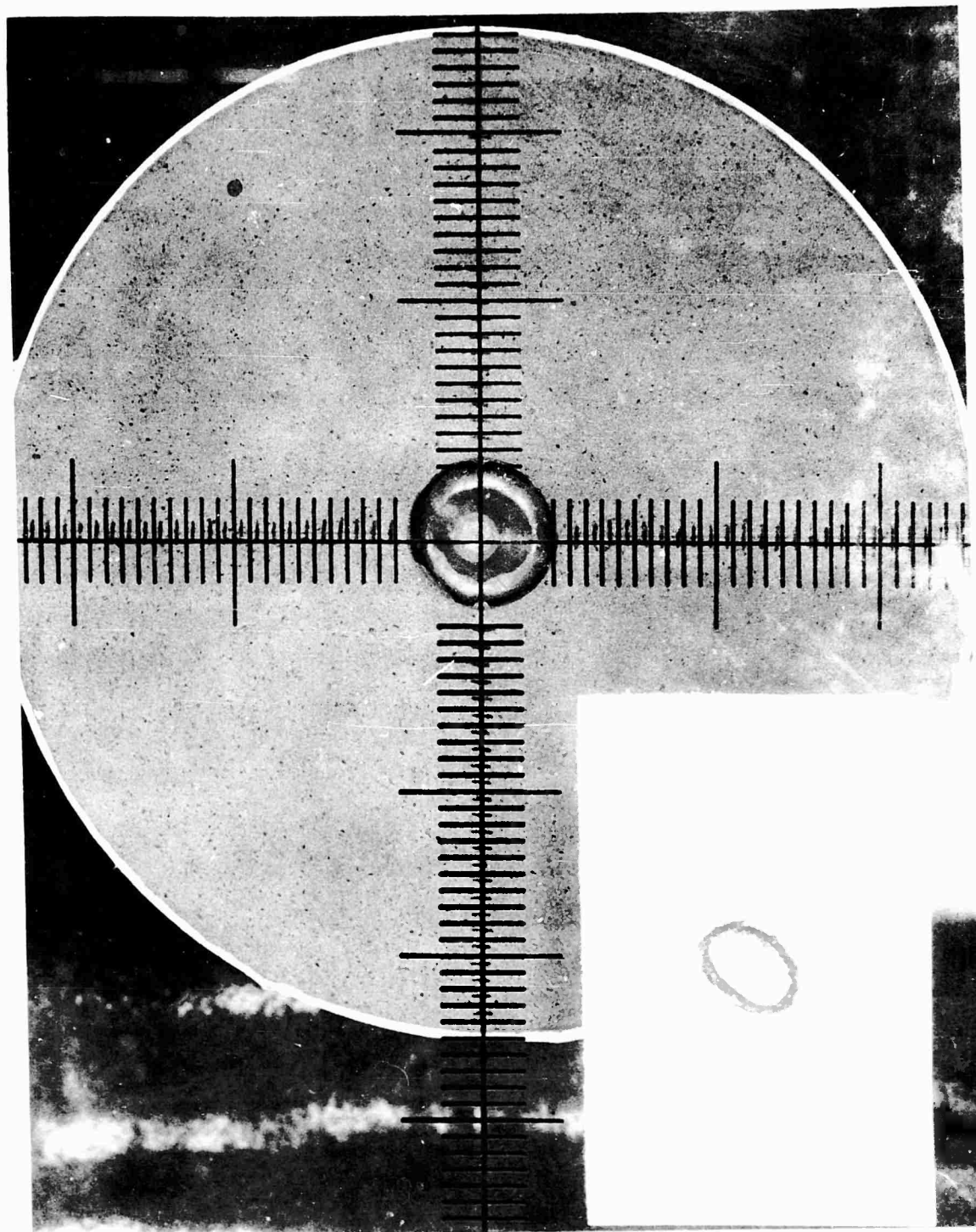
Figure 65. End of Grain at Zero Pressure as Seen Through 1.5-in. Thick
Lucite Plate Showing Grids on the Plate and on the End of the Grain
(461 0229)
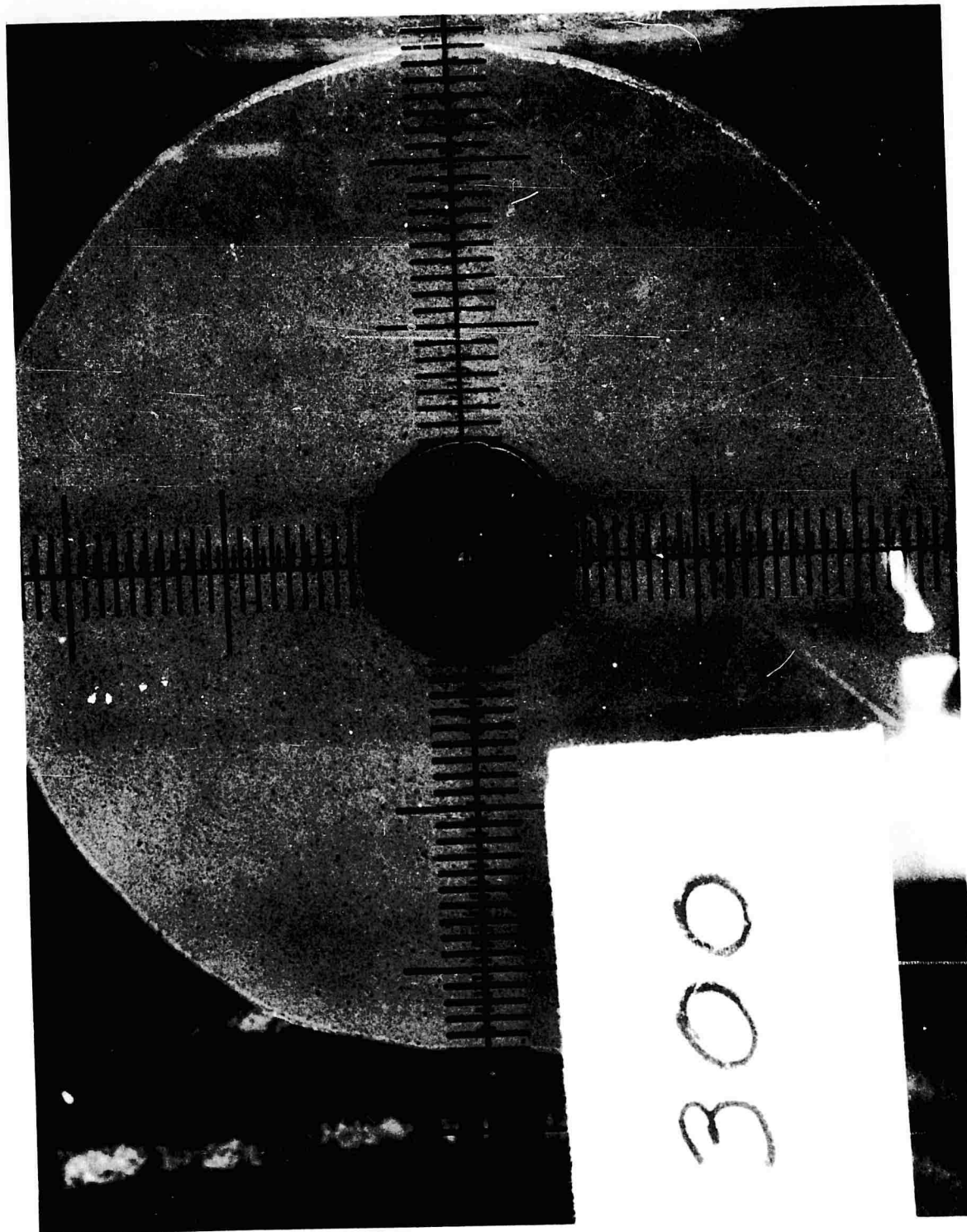
Figure 66.   End of Grain Shown in Figure 65 at Internal Pressure of 300 psig
(461 0236)

TABLE 16

REDUCED STRAIN MEASUREMENTS ON PRESSURIZED TUBULAR GRAIN

Rad., in.	$1/r^2$	100 psig $\varepsilon,\%$	100 psig ε/P	200 psig $\varepsilon,\%$	200 psig ε/P	300 psig $\varepsilon,\%$	300 psig ε/P
0.5	16.	13.0	0.13	27.0	0.135	44.4	0.148
0.6	2.78	7.5	0.075	20.8	0.104	33.4	0.111
0.7	2.04	3.4	0.034	14.3	0.072	25.3	0.084
0.8	1.56	2.8	0.028	10.3	0.052	19.0	0.063
0.9	1.23	2.0	0.020	7.8	0.039	14.1	0.047
1.0	1.00	1.1	0.011	6.7	0.034	11.7	0.039
1.1	0.83	0.6	0.006	5.0	0.025	9.3	0.031
1.2	0.69	0.5	0.005	3.2	0.016	7.5	0.025
1.4	0.51	0.5	0.005	3.0	0.015	5.5	0.018
1.5	0.44	0.3	0.003	2.5	0.013	4.9	0.014
1.6	0.39	0.3	0.003	1.8	0.009	3.9	0.013
1.7	0.34			1.5	0.008	3.1	0.010
1.8	0.31			1.1	0.006	2.8	0.009
2.0	0.25			1.0	0.005	2.5	0.008
2.5	0.16			0.8	0.004	1.9	0.006
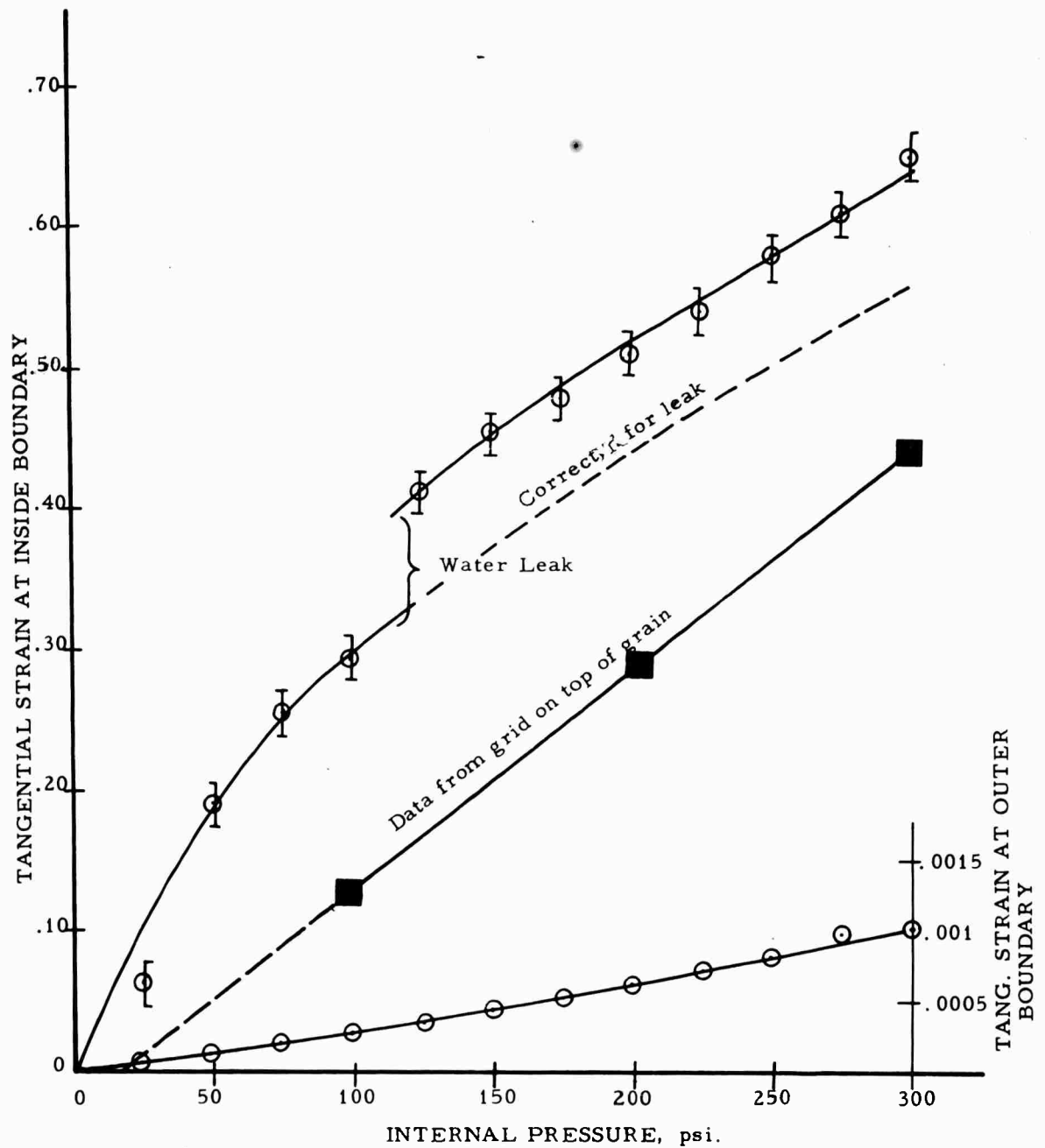
Figure 67. Tangential Strains Measured in First Test
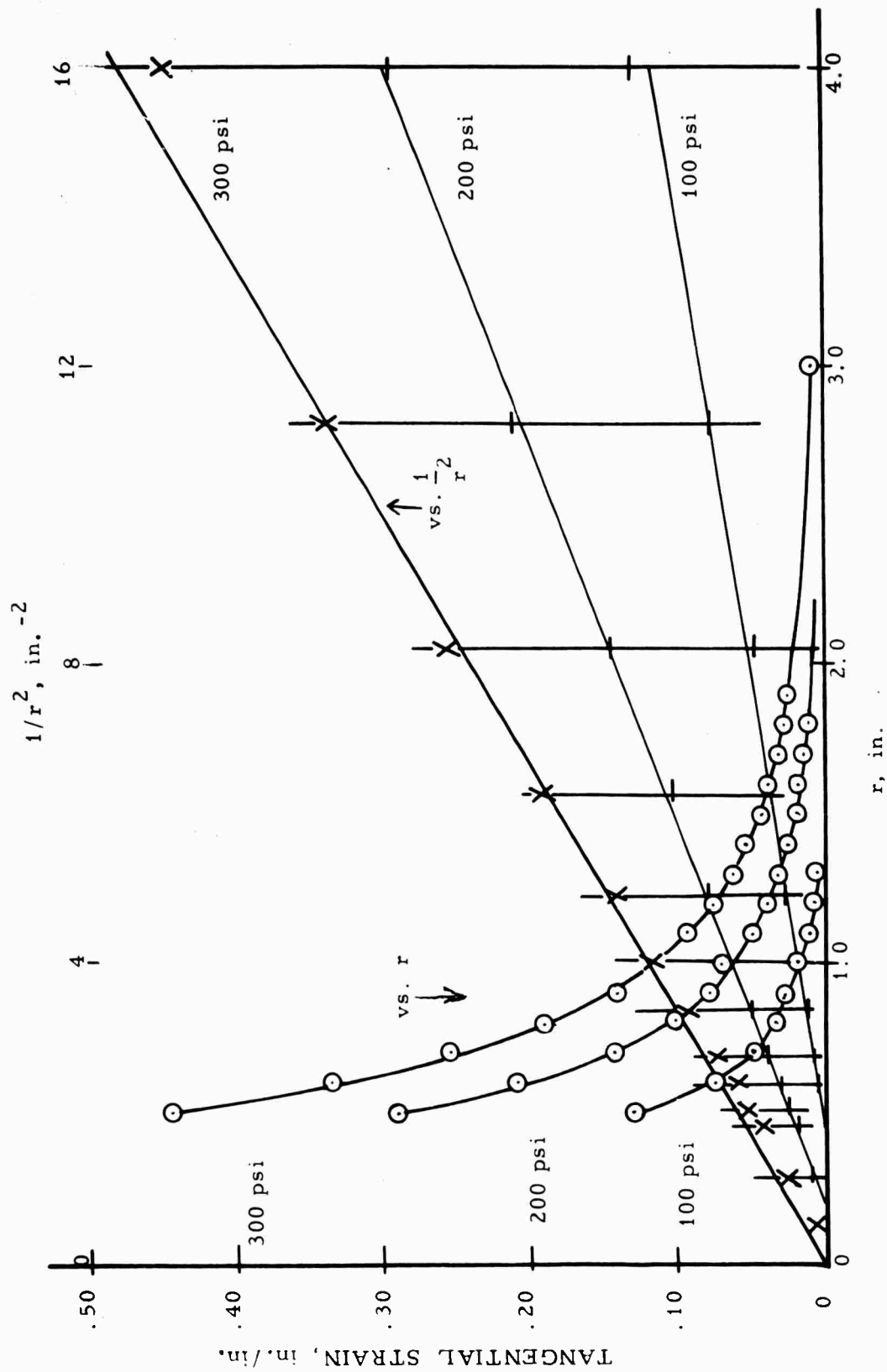
Figure 68. Distribution of Strain Through Cylinder
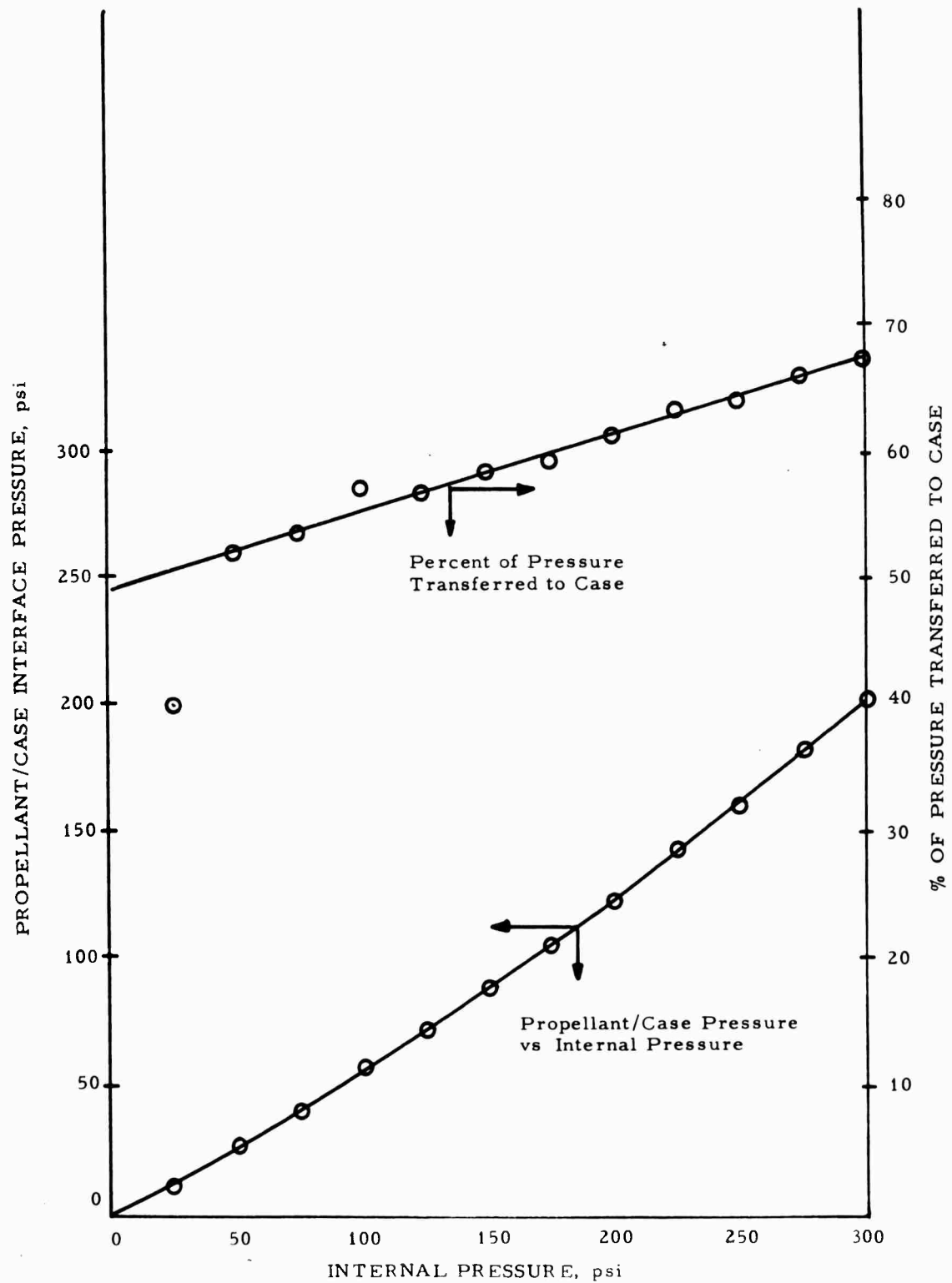
Figure 69. Percent of Pressure Transferred to Case

IV, A, Experimental Studies of Stresses and Strains in Subscale Grains (cont.)

The lack of agreement between the grid measurements and
the volume displacement data suggested that another method of measurement
be introduced. Therefore, on a second test, using a new cylinder of DP-16
propellant, in addition to measurements of radial displacement by volumetric
displacement of water and displacement of the grid on the end of the grain,
linear displacement potentiometers were inserted into the cylinder at radii of
0.5", 1", and 2". A plot showing the tangential strains as a function of radius
at 300 psi internal pressure is shown in Figure 70. It is seen that good agree-
ment is obtained between the grid and the linear transducers for measuring
radial displacement, with the volumetric measurement again too high. The
maximum strain was 18% at 300 psi on this second cylinder compared with
44% for the first cylinder at this pressure. The strain distribution was of the
same type as observed in the first test, and it was believed that the difference
in maximum strains was caused by changes in void volume, as discussed in an
earlier section. A third cylinder was tested because of the large difference in
maximum strains of the first two tests. The same behavior of strain with
pressure and with radius was observed, with the maximum strain by the grid
method being 49%. The related data for solution of Equation 13 were measured
for this third cylinder, e.g., $\mu = E/3 = 550/3$ psi, and by density the fractional
void volume $\delta = 0.0507$. The resulting calculated curve is compared with the
observed volume change of the propellant based on end-grid data for all of the
cylinder tests in Figure 71. The equation predicts the general behavior reason-
ably well. The volume increases observed in all tests are much higher than
were observed in bulk modulus test of other samples of DP-16.

The possible use of this technique for studying stress con-
centration effects led to a fourth test. A specimen of Class 2 live poly-
urethane propellant cast into a steel case of 1/4 in. wall thickness with the
oval configuration shown in Figure 72 was tested under internal pressure.
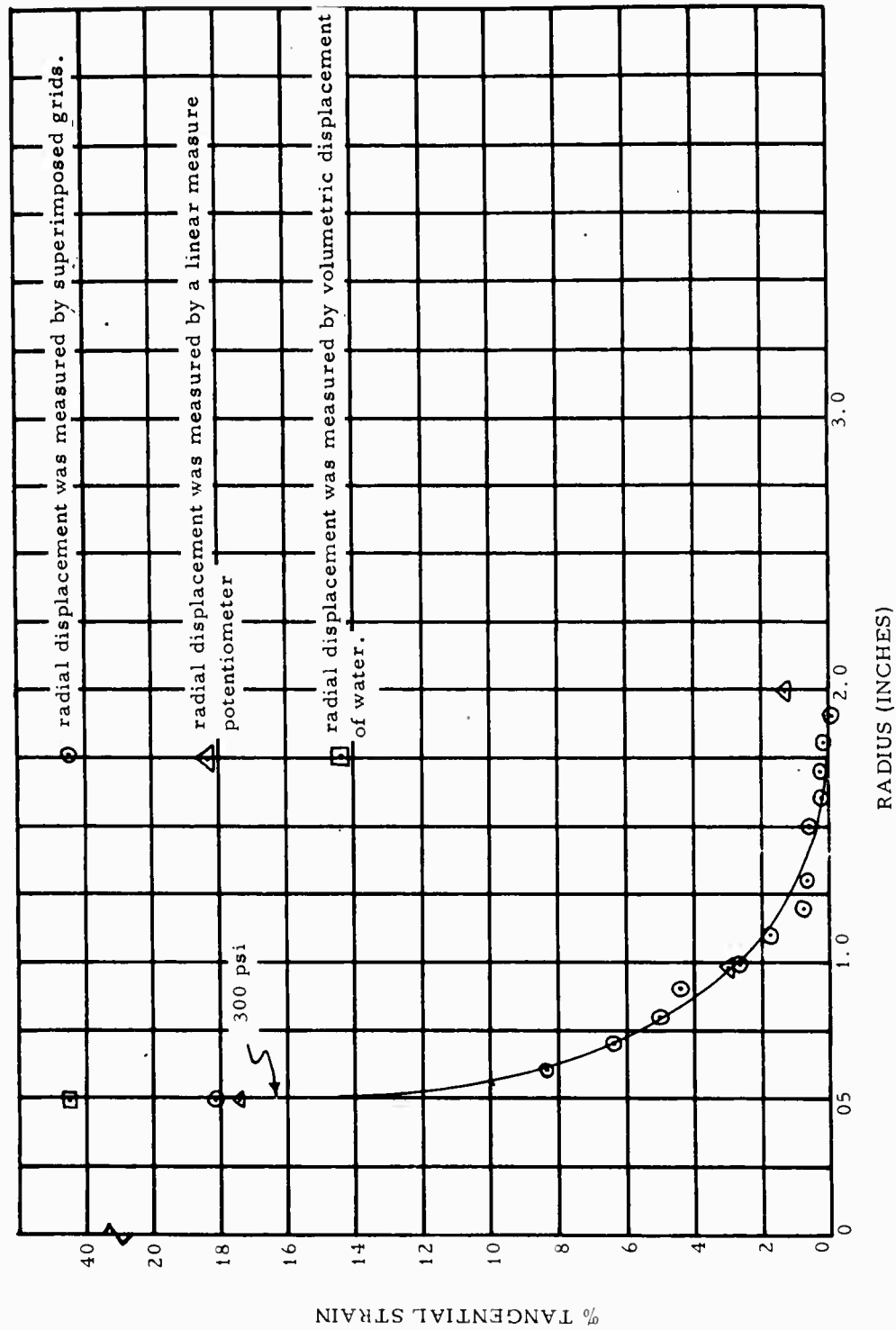
Figure 70. Tangential Strains at Various Radii in a Case-Bonded Propellant Cylinder Measured at 300 psig Internal Pressure
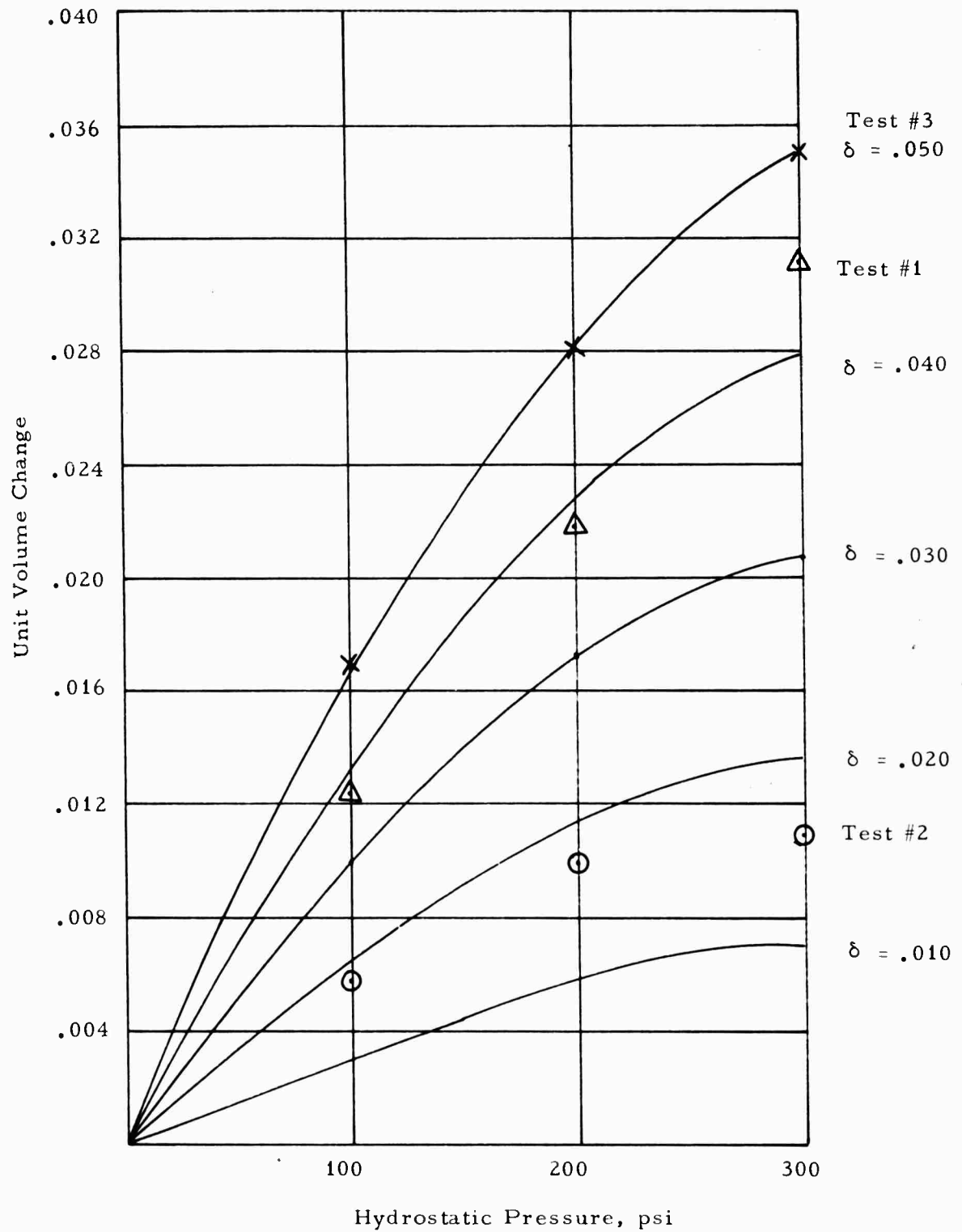
Figure 71. Effect of Hydrostatic Pressure on Unit Volume Change of Inert Propellant in Internally Pressurized Cylinder
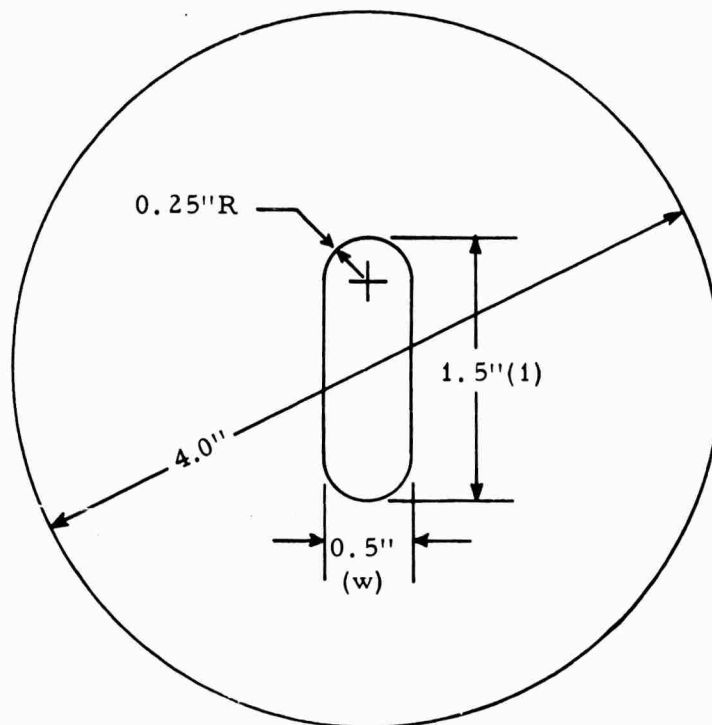
Figure 72. Simplified Oval Configuration for Propellant Pressurization Tests

IV, A, Experimental Studies of Stresses and Strains in Subscale Grains (cont.)

As in previous tests, the measurements of radial displacement were made by observing photographically the displacement of superimposed grids. A summary of the strains observed throughout the sample are given in Table 17. Figures 73 and 74 show the end of the grain at zero and at 300 psi internal pressure.

The amount of area increase of the perforation, obtained by graphically integrating the photograph, is shown in Figure 75. At 300 psi the volume increase of the bore was 19.4%, compared to an increase for the tubular grain at 300 psi of 107%, 39%, and 122% for the three tests. These correspond to a reduction in volume of the propellant for the oval of 1.0%, compared to decreases for the three tests of the tubular grain of 3.2%, 1.1%, and 3.5%. The oval is not increased the same amount in length, 0.088 in., as in width, 0.114 in., due in part to the greater thickness of propellant to compress in the width direction; the relative web reductions are 0.088/2.5 = 0.035, and 0.114/3.5 = 0.033; so these are nearly the same. (The relative web reduction of the second tubular grain test, which showed the same compressibility of propellant as the oval, was 0.18/5 = 0.036). The oval thus becomes somewhat elliptical as the pressure increases. The tangential strains at the star tips can be estimated as the circular fillets remain circular with increase of pressure, within the accuracy of measurement. The strain concentration then is the ratio of the web radius to the fillet radius, or 3, and the tangential strain at 300 psi is 3 x 5.83 or 17.5%.

The data were further analyzed by dividing the strains by the pressure and plotting vs $1/r^2$, as shown in Figure 76. It can be seen that the detailed strain behavior in the propellant is complex. It can be seen that the star points reduce significantly the strains in the rays starting essentially at the web radius. It is also of interest that the radial strains

TABLE 17

SUMMARY OF STRAIN MEASUREMENTS ON OVAL CONFIGURATION PRESSURIZED IN PLANE STRAIN

Distance, in., from Surface	Center	$1/r^2$	50 ϵ,%	50 ϵ/P	150 ϵ,%	150 ϵ/P	200 ϵ,%	200 ϵ/P	250 ϵ,%	250 ϵ/P	300 ϵ,%	300 ϵ/P
					WIDTH							
0	0.25	16.	2.20	.0440	12.32	.0820	17.25	.0862	18.03	.0721	22.70	.0757
0.10	0.35	8.2	1.17	.0234	7.70	.0513	9.48	.0474	14.81	.0593	16.92	.0565
0.30	0.55	3.3	0.826	.0165	4.57	.0304	7.01	.0350	8.50	.0340	9.24	.0308
0.50	0.75	1.78	0.596	.0120	3.58	.0239	4.93	.0247	6.48	.0259	7.47	.0249
0.70	0.95	1.11	0.468	.0094	2.18	.0145	3.15	.0158	4.49	.0180	5.30	.0177
0.90	1.15	0.76	0.112	.0082	1.47	.0098	2.21	.0110	3.01	.0121	3.63	.0121
1.10	1.35	0.55	0.327	.0065	0.653	.0044	1.81	.0090	2.46	.0098	2.74	.0091
1.30	1.55	0.42	0.303	.0060	0.645	.0043	1.42	.0071	2.14	.0086	2.56	.0085
1.50	1.75	0.33	0.236	.0047	0.688	.0046	1.24	.0062	1.71	.0068	2.03	.0068
					LENGTH							
0	0.75	1.78	0.713	.0142	3.33	.0222	3.83	.0192	4.98	.0193	5.83	.0194
0.10	0.85	1.39	0.208	.0041	0.453	.0030	1.46	.0073	2.81	.0112	3.96	.0132
0.30	1.05	0.91	0.224	.0044	0.364	.0024	1.06	.0053	1.88	.0075	2.30	.0093
0.50	1.25	0.64	0.141	.0028	0.141	.0009	0.729	.0036	1.46	.0058	2.40	.0080
0.70	1.45	0.48	0.263	.0032	0.263	.0017	0.890	.0045	1.33	.0053	2.25	.0075
0.90	1.65	0.37	0.160	.0032	0.445	.0030	0.605	.0031	1.03	.0043	1.97	.0066
1.10	1.85	0.29	0.506		0.459	.0031	0.583	.0029	0.949	.0038	1.66	.0055

Internal pressure, psig

Figure 73. Initial Appearance of Specimen Showing Grid on Lucite Plate in Black, and White Grid on Surface of Propellant
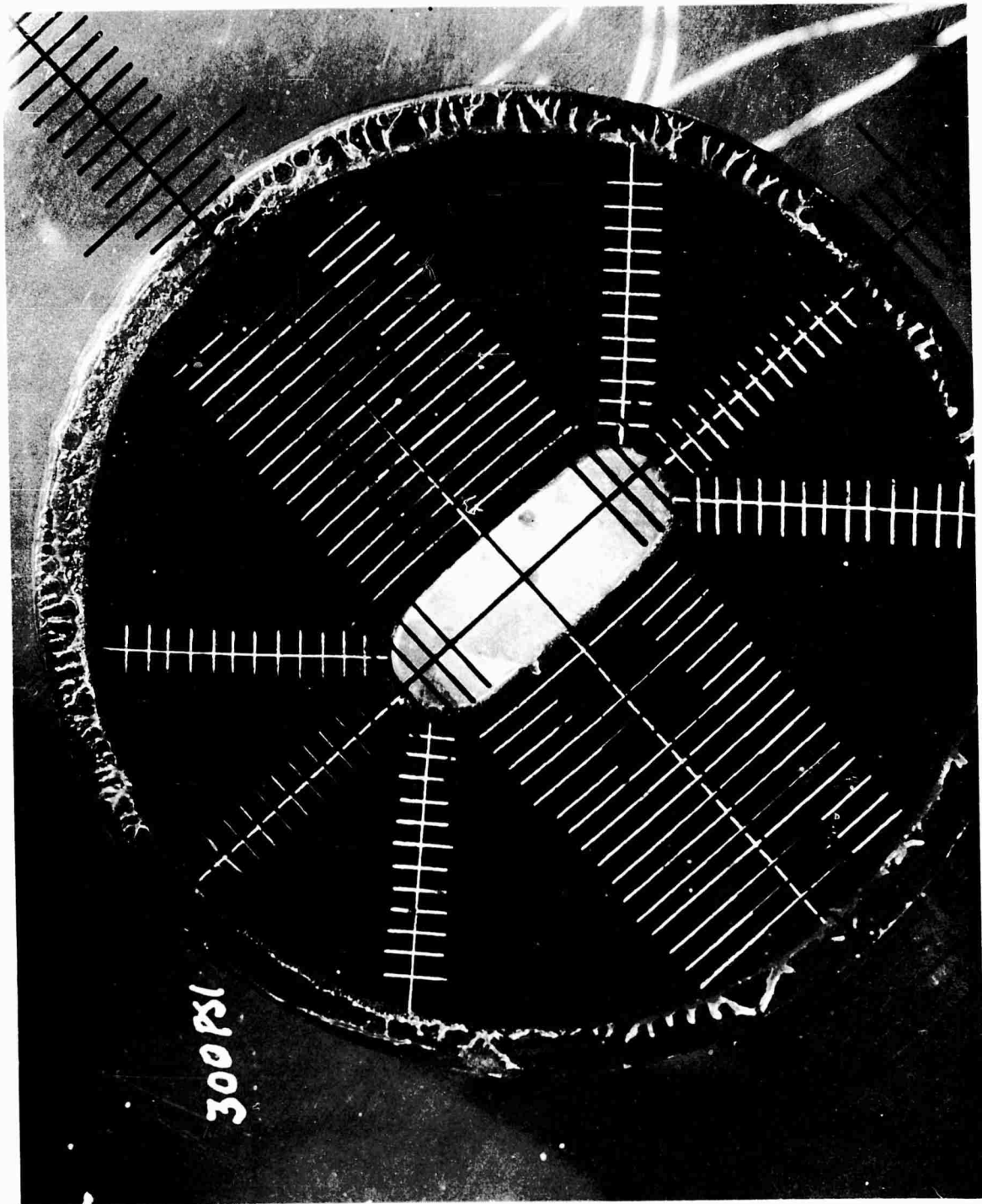
Figure 74. Effect of Pressurization to 300 psig on Propellant Specimen
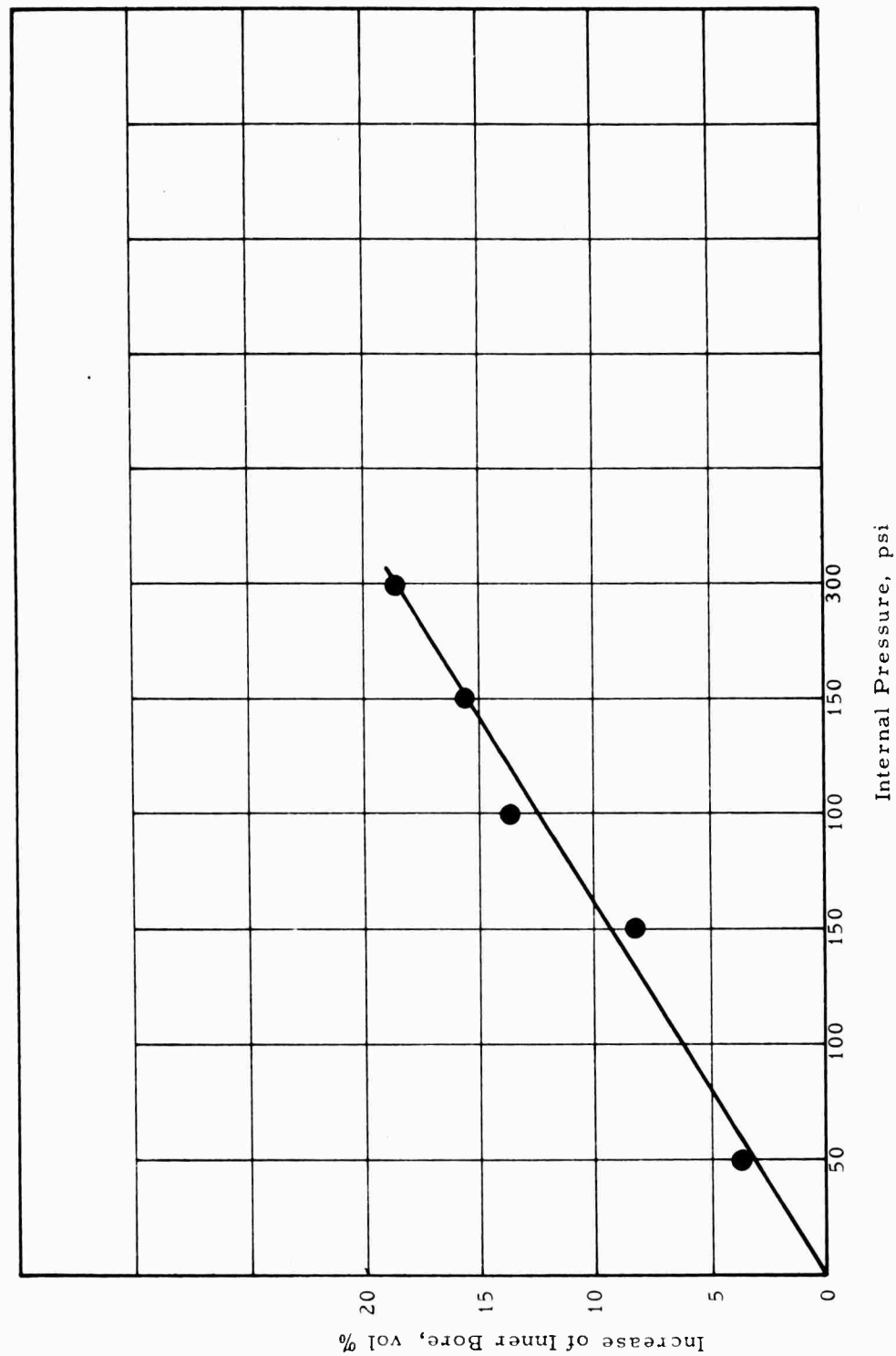
Figure 75. Area Increase With Pressure of Perforation in Oval Grain
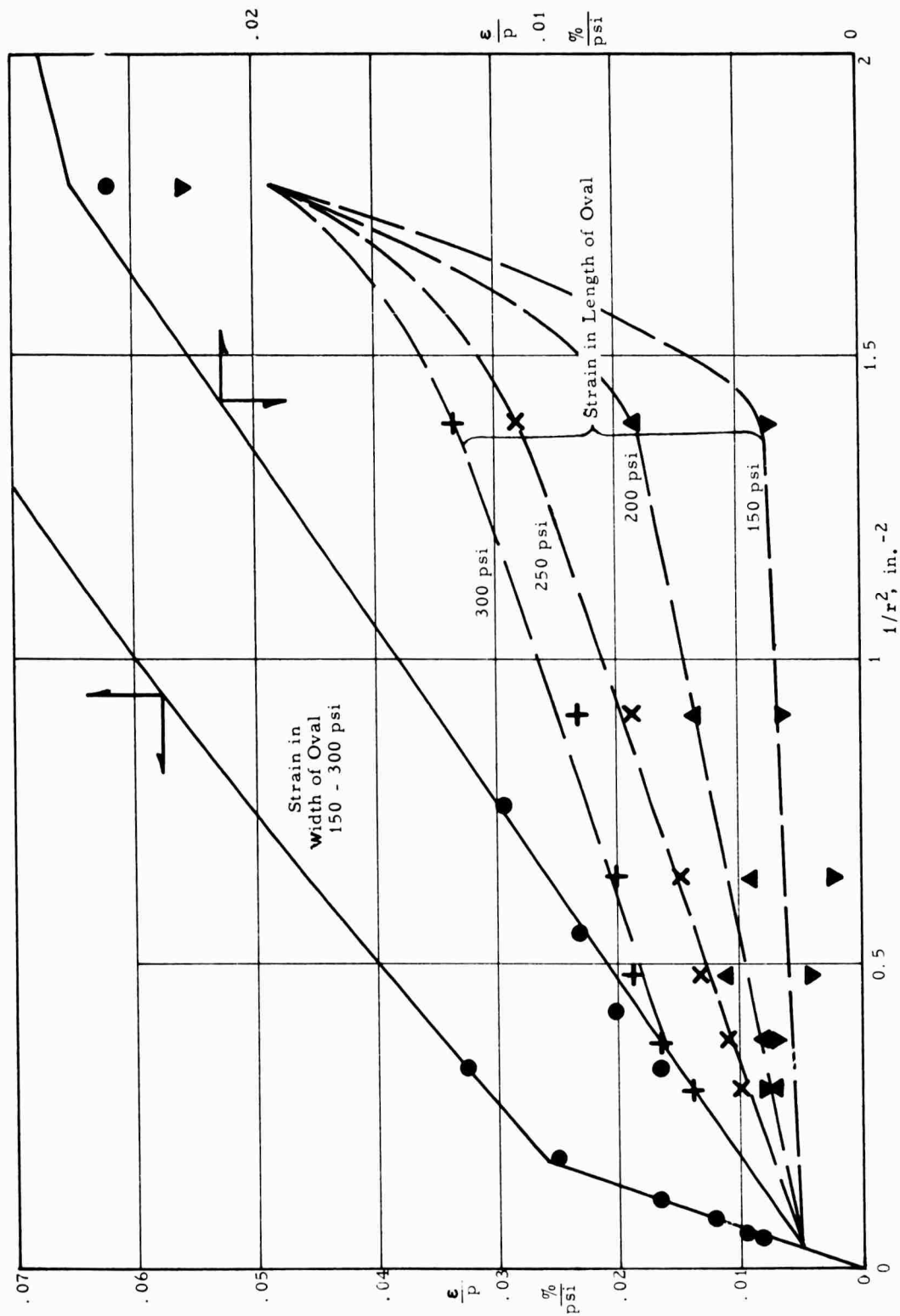
Figure 76. Analysis of Strains in Oval Configuration

IV, A, Experimental Studies of Stresses and Strains in Subscale Grains (cont.)

through the web opposite the star tip are lower, except at the surface, than those for the equivalent tube of web radius and follow a complex pattern. The data suggest that at higher pressures, the web strains would approach those in the equivalent tube of web radius.

An attempt was made to analyze the strains along the 45° diagonals. The center of the radius for the oval ends is not a clearly defined point with pressure change so measurements were made between points on the diagonals equidistant from the surface. The values reported in Table 18 give the difference of such readings between the pressure reading and the zero pressure reading; since a zero photograph was taken before and after the pressurization series, two values are reported, one the difference from the "before" pressurization and the other, the "after" pressurization photograph. The diagonals were numbered 1, 2, 3, and 4, reading clockwise. Since the readings were for the hypotenuse of a triangle whose side is the radius to the point, the readings were divided by $\sqrt{2}$ to give the values in Table 18. At the bottom of the table, the values are converted to strain by dividing by the appropriate radius in each case, and then by pressure to give ε/P. Also shown are the ε/P values for the width and length (based on radius) for the three pressures, 200, 250, and 300 psi. As can be seen from the table, the variability of the diagonal data were quite large, and no significant difference of data with pressure on ε/P was observed; in this respect of showing no pressure effect, the data behaved as did the width measurements. Figure 77 shows a comparison of the three sets of measurements. The diagonal data show the same general behavior but show much lower surface strains than would be predicted by either the width or length measurements on the oval.

B. PHOTOELASTIC STUDIES OF SOLID PROPELLANT GRAIN STRESS DISTRIBUTION

Case-bonded solid propellant grains are strongly restrained from thermal contraction. In addition, many propellants exhibit a Poisson's ratio

TABLE 18

EFFECT OF PRESSURE ON DIAGONAL READINGS

AS CALCULATED FROM READINGS BETWEEN DIAGONAL POINTS

Pressure psi	Diagonals Used For Reading	Time Taken	$\Delta r/\sqrt{2}$, in. x 1000						
			Distance From Center, in.						
			0.25	0.35	0.55	0.75	0.95	1.15	1.35
200	3 to 4	Before	27	68	75	63	62	65	65
		After	80	67	75	68	58	80	58
	4 to 1	Before	62	92	55	87	38	85	85
		After	45	92	75	103	78	117	107
	2 to 3	Before	68	70	88	65	63	67	68
		After	42	58	92	88	78	78	68
		Average	54	74	77	79	63	82	75
		Range	53	34	37	40	40	52	49
		ε/P	27	37	38	40	32	41	38
250	3 to 4	Before	50	98	98	82	77	77	93
		After	103	97	98	87	73	92	87
		Before	145	138	120	122	105	132	133
		After	128	138	140	138	130	163	155
	2 to 3	Before	125	132	153	111	105	123	107
		After	100	120	157	135	120	135	107
		Average	108	120	131	113	102	120	114
		Range	95	41	59	56	57	86	68
		ε/P	43	48	52	45	41	48	45
300	3 to 4	Before	68	120	130	107	108	73	107
		After	122	118	130	111	105	88	100
		Before	65	143	110	111	90	82	60
		After	48	143	130	128	130	41	82
		Before	110	142	113	115	85	75	48
		After	85	130	117	138	100	87	48
		Average	83	150	121	118	103	74	74
		Range	74	25	20	31	45	47	59
		ε/P	28	50	40	37	34	25	25
			Reduced Strain, ε/P, %/psi x 1000						
200		Width	86	47	35	25	16	11	9
		Length	58	22	16	11	13	9	9
	Av. Diagonal		27	26	17	13	8	9	7
250		Width	72	59	34	26	18	12	10
		Length	58	34	22	18	16	13	12
	Av. Diagonal		43	34	24	15	11	11	8
300		Width	76	57	31	25	18	12	9
		Length	58	40	28	24	22	20	17
	Av. Diagonal		28	36	18	12	9	5	5
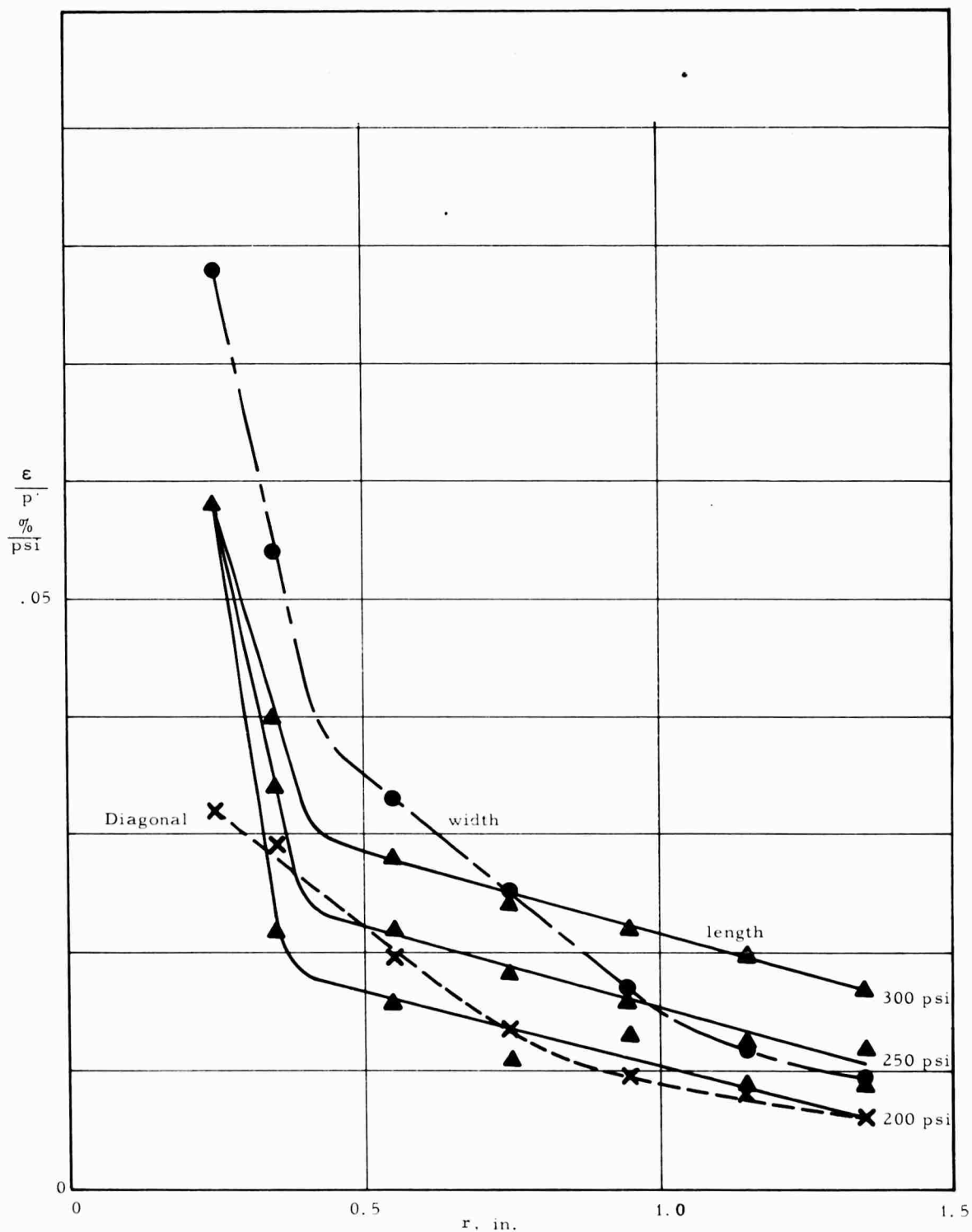
Figure 77. Decrease of Reduced Strain With Distance From Center of Fillet
Radius. Average values are used for the width and diagonal
measurements at all three pressures but separate data for each
pressure on the length data.

IV, B, Photoelastic Studies of Solid Propellant Grain Stress Distribution (cont.)

very near 0.5, particularly at the low strain levels which occur in the greater part of the propellant grain. The importance of lateral restraint and Poisson's ratio on stress induced by restraint of thermal contraction is indicated by Figure 78. This is a plot of Hooke's Law for stress-strain relations for the special condition where a relative thermal contraction, Δ, is completely restrained in the σ_1 direction. The elastic strain in the σ_1 direction is, by Hooke's Law:

$$\varepsilon_1 = \Delta = \frac{\sigma_1}{E} (1 - \nu \sigma_2/\sigma_1 - \nu \sigma_3/\sigma_1) \tag{57}$$

then,

$$\frac{\sigma_1}{E\Delta} = \frac{1}{1 - \nu(\sigma_2/\sigma_1 + \sigma_3/\sigma_1)} \tag{58}$$

The stress ratios σ_2/σ_1 and σ_3/σ_1 imply restraints on lateral contractions. The solid curves of Figure 78 represent the surface predicted for $\nu = 1/2$. Dashed curves on the right-hand plane indicate the relative values of $\sigma_1/E\Delta$ for smaller Poisson's ratios. It is seen from Figure 78 that when restraint of thermal contraction nears the triaxial hydrostatic condition, the propellant Poisson's ratio is of great importance. The model test method developed and described here makes use of a photoelastic material which has an effective Poisson's ratio approximating that of many solid propellants. The material withstands tensile strains as large as 14%, thus approaching the deformation characteristics of solid propellants.

The availability of such a photoelastic material made possible a simulated binder/oxidizer microstructure study on large scale plane models
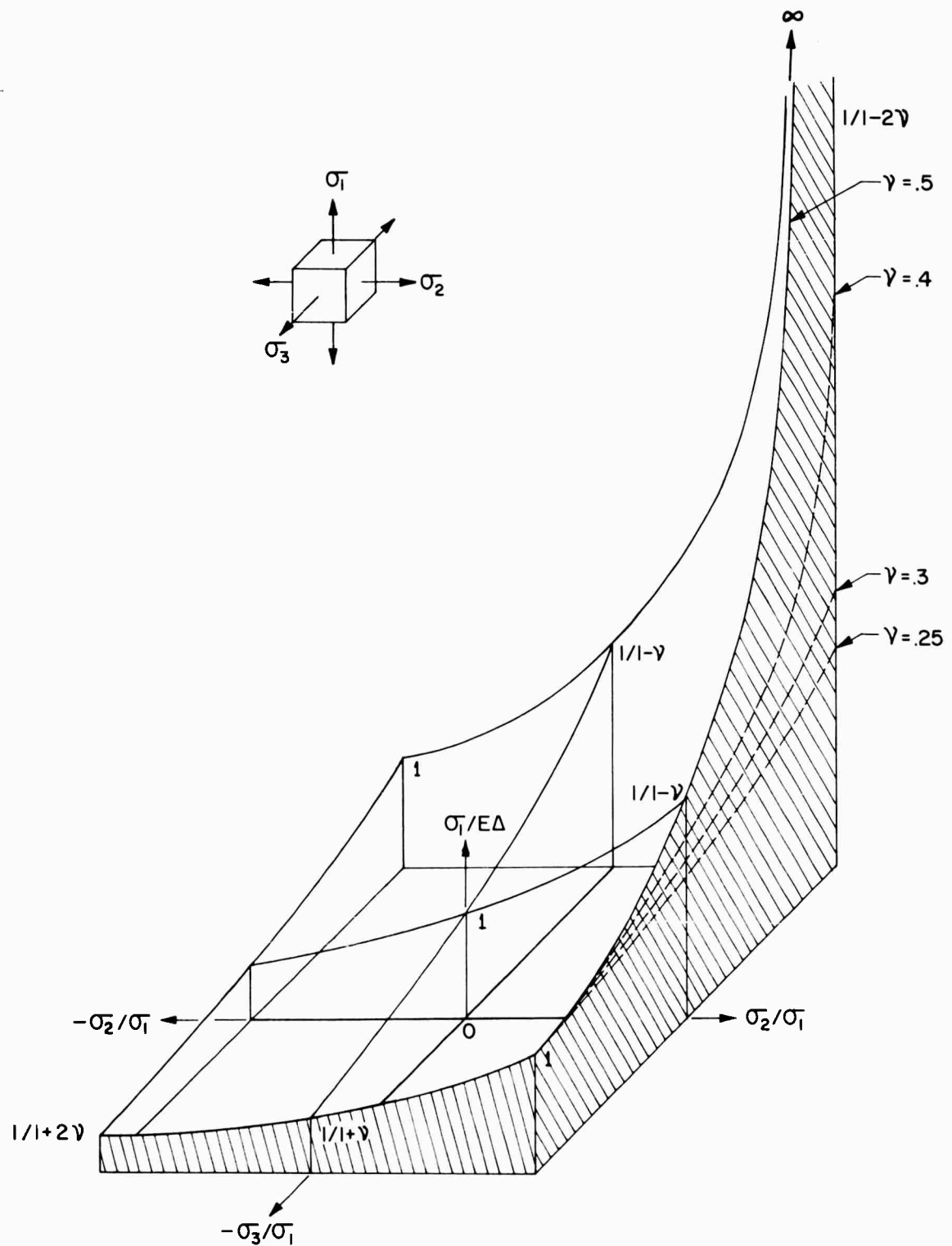
Figure 78. Variation of Restrained Thermal Contraction Stress With Lateral Restraint and Poisson's Ratio

IV, B, Photoelastic Studies of Solid Propellant Grain Stress Distribution (cont.)

of an idealized composite structure, in which it was possible to obtain the
binder stress distribution and composite effective elastic properties as a
function of the rigid inclusion packing density, the bond condition at the
binder/inclusion interfaces, and the average strain level imposed by external
loads. The photoelastic material was also used in a differential, thermal
contraction stress analysis study of the three-dimensional stress distribution
in simple case-bonded grains, and of the two-dimensional strain distribution
in a restrained grain sector designed to simulate the strain distribution of a
full cross section.

1. Development of New Photoelastic Method

a. Principles of Method

Conventional photoelastic tests, whether conducted at
room temperature or at the elevated temperature required for "stress-freezing",
require the application of constant load or constant deformation to the photo-
elastic model. With these conventional techniques, it is not possible to apply
the complex grain boundary loading conditions required for three-dimensional
photoelastic analysis o. solid rocket motor differential thermal contraction
stresses. A new photoelastic technique was developed specifically for appli-
cation to propellant grain differential contraction stress problems in two or
three dimensions. The method is applicable to any problem involving a com-
posite elastic structure in which differential contraction of the material occurs
without appreciable temperature gradients.

The new method is based upon the uniform shrinkage
that occurs during polymerization of resins. Polymerization or "cure"
shrinkage is analogous to ordinary thermal contraction in that it occurs equally

IV, B, Photoelastic Studies of Solid Propellant Grain Stress Distribution (cont.)

in all directions of an unrestrained specimen. Thus the cured, unrestrained specimen is geometrically similar to, but slightly smaller than, the mold cavity in which it was cast. If the cast specimen is permitted to bond to the mold surface, or to a solid inclusion, relative contraction is elastically restrained by the interface bond forces.

The difference in principal stresses at any point in the elastic body subjected to restrained uniform contraction can be represented by the functional relationship:

$$\sigma_1 - \sigma_2 = E \, \Delta f \, (X/L, \ Y/L, \ Z/L, \ E/E_c, \ \nu, \ \nu_c, \ \text{geometry}) \qquad (58)$$

where:

$\sigma_1 - \sigma_2$ is the difference of principal stresses in the plane of the of the stressed element, psi.

E is the effective elastic modulus of the resin, psi.

E_c is the elastic modulus of the container or inclusion, psi.

Δ is the linear, free, differential contraction per unit length of the resin and the container or the inclusion, inches/inch.

ν and ν_c are the Poisson's ratios of the resin and container, or inclusion, respectively.

X, Y, and Z are the position coordinates of the stressed element, inches.

L is a characteristic dimension of the structure, inches.

"Geometry" includes all the parameters necessary to describe the shape of the model and its container, and to delineate the areas of bonded contact.

IV, B, Photoelastic Studies of Solid Propellant Grain Stress Distribution (cont.)

If a photoelastic model is made in such a manner that all the parameters inside the brackets of Equation (59) have the same value as the corresponding parameters of the actual structure, then

$$\left[\frac{\sigma_1 - \sigma_2'}{E\,\Delta}\right]_{model} = \left[\frac{\sigma_1 - \sigma_2}{E\,\Delta}\right]_{prototype} = \beta \qquad (60)$$

where β is the value of the functional relationship indicated in Equation (59).

b.   Model Test Procedures

As the result of considerable experimentation, the following sequence of operations has been found to give the best results:

(1)   Fabricate casting molds and/or solid inclusions and degrease thoroughly.

(2)   Apply mold-release to areas where bonding is not desired.

(3)   Prepare liquid epoxy resin and hardener mixture, degassing thoroughly to remove air bubbles.

(4)   Pour resin into mold, taking care that a slight excess amount is provided to account for the shrinkage that occurs upon initial gelation. (In completely enclosed molds, risers connected to an external reservoir should be provided.)

IV, B, Photoelastic Studies of Solid Propellant Grain Stress Distribution (cont.)

(5) Permit initial gelation to occur as near to room temperature as possible.

(6) After gelation has occurred, place the model in an oven, and begin a time-temperature cure program designed to match cure shrinkage with equal thermal expansions.

(7) Hold the model at the final cure temperature until polymerization is essentially completed. Remove internal cores at this time.

(8) Regulate the oven temperature so that the model cools slowly and uniformly.

(9) Upon reaching room temperature, remove the casting mold from the model, including bonded areas. Some discretion must be used in selecting methods for parting bonded areas, since cracks may start at the interface and propagate into the model.

(10) After removal of the mold, the model may be sliced at any time. However, data should not be taken for two to three weeks, since viscoelastic deformations that were imposed during the latter part of the cooling process must be permitted to recover.

After completion of the recovery period, the "frozen" stress pattern corresponding to forces imposed during the earlier part of the

IV, B, Photoelastic Studies of Solid Propellant Grain Stress Distribution (cont.)

cooling cycle remains in the model. The processes described above are illustrated for a simple specimen by Figures 79 and 80. Figure 79 shows the observed fringe order per inch of thickness in a uniaxially restrained, cast specimen as it was cooled down from the cure temperature, point A, to room temperature, point C. Removing the specimen from the mold resulted in an immediate reduction of fringe order from $\bar{N}_C$ to $\bar{N}_D$. Subsequently, over a period of three weeks, the fringe order relaxed to the value $\bar{N}_E$. No measurable change in fringe order occurred thereafter. The manner in which the fringe order decreased with time from $\bar{N}_D$ to $\bar{N}_E$ is illustrated by Figure 80. A change of the recovery mechanism became apparent about 100 minutes after stripping from the mold.

c. Interpretation of "Frozen" Stress Patterns

The difference in principal stress is related to fringe order per unit slice thickness by the conventional photoelastic relationship:

$$\sigma_1 - \sigma_2 = N f' \tag{61}$$

where f' is the photoelastic material effective fringe value and $N = n/t$. Combining Equation (60) with Equation (61), we obtain

$$\beta = \frac{N f'}{E \Delta} \tag{62}$$

Now consider the simple uniaxial specimen shown in Figure 79. Complete restraint of axial relative contraction and freedom to contract laterally, produces the reference stress $\bar{\sigma}_1$:

$$\bar{\sigma}_1 = E \Delta = \bar{N} f' \tag{63}$$
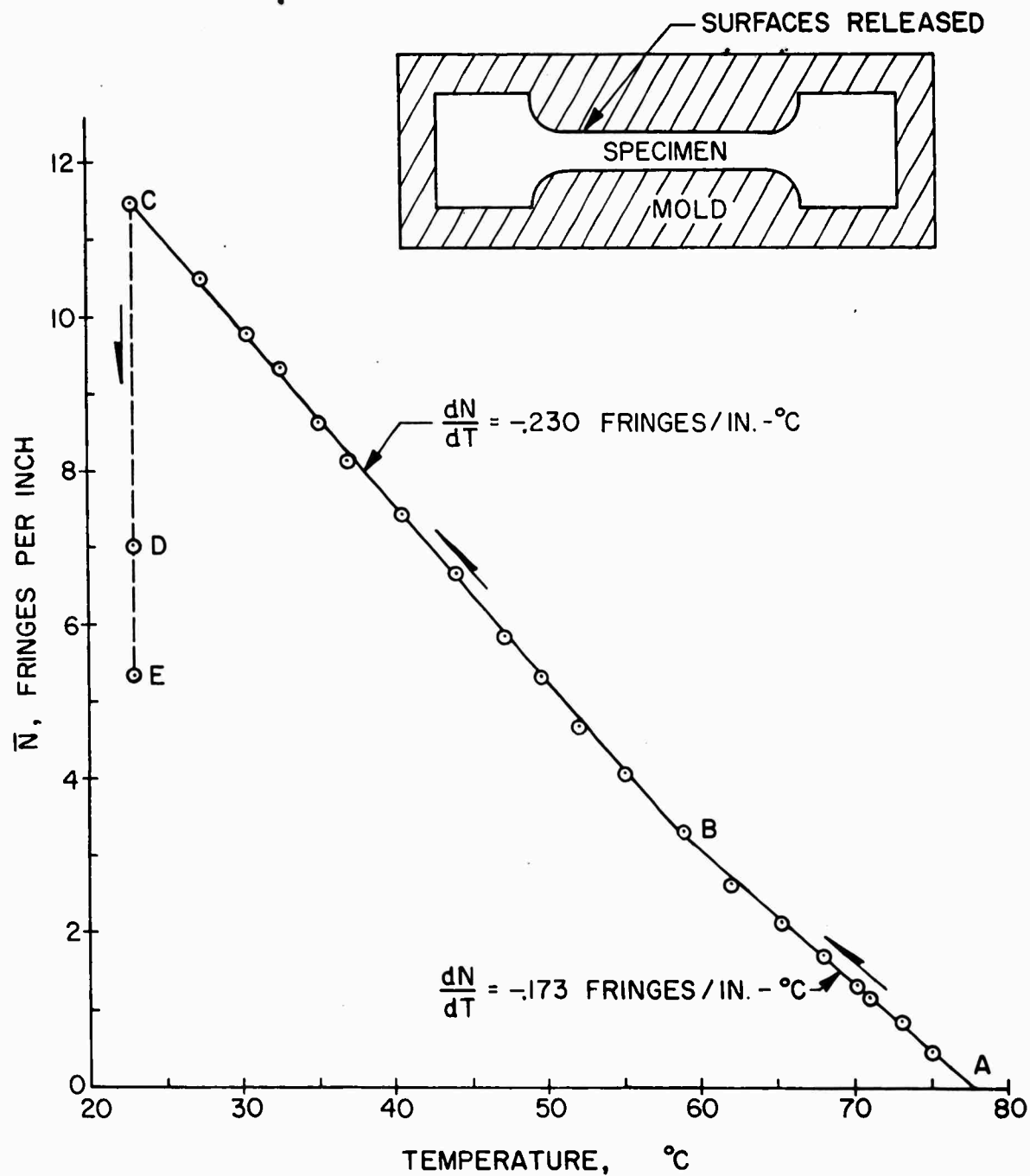
Figure 79. Characteristic Fringe Order vs Temperature Variation in Cooling of
Uniaxially Restrained Shrinkage Specimen
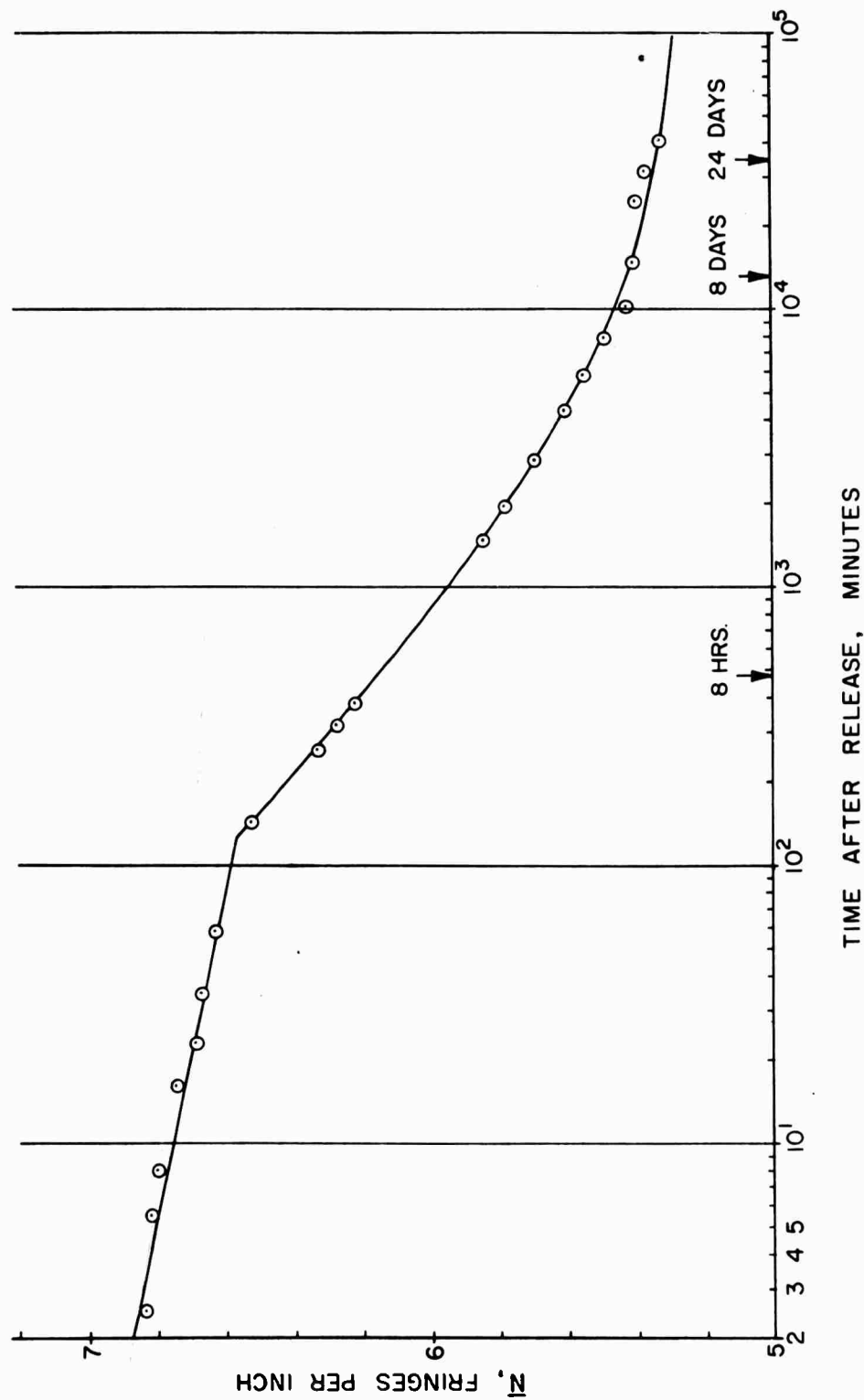
Figure 80. Decay of Fringe Order in Tensile Specimen After Release From Restraint

IV, B, Photoelastic Studies of Solid Propellant Grain Stress Distribution (cont.)

Now it should be pointed out that both E and f' vary continually with temperature during the test. However, the non-dimensional thermal stress difference in the complex model can be determined simply by substitution of Equation (63), $E \Delta = \bar{N} f'$, in Equation (62), giving:

$$\beta = \frac{N}{\bar{N}} \tag{64}$$

Substitution of Equation (64) in (60) yields:

$$\frac{\sigma_1 - \sigma_2}{E \Delta} = \frac{N}{\bar{N}} \tag{65}$$

Thus the non-dimensional stress is determined simply by the ratio of fringe order per unit thickness in the complex model slice to that in the uniaxially restrained calibration specimen. The proper calibration method is essential to determination of quantitative results. Principal stress differences in the prototype structure are determined by substitution of appropriate values of E and Δ in Equation (65). In all other respects, the photoelastic data is treated exactly as conventional "frozen" stress photoelastic data.

2.   Stress Distribution in Binder Surrounding Rigid Inclusions

a.   General Discription of Procedures

Little experimental data exists on the nature of stress distributions around rigid inclusions. Glass inclusions n paraplex and urethane rubber binders were recently employed by Durelli and Laniel (28) to estimate shrinkage stresses around circular, cylindrical inclusions subjected to differential contraction.

IV, B, Photoelastic Studies of Solid Propellant Grain Stress Distribution (cont.)

The model-making and interpretation procedures described here permit quantitative determination of such shrinkage stresses by the principles of similarity between a model and its prototype structure. Conventional photoelastic techniques then permit the stress "freezing" of additional stresses produced by external load. The principle of superposition is applied where applicable to permit separation of external load effects from relative contraction effects.

Gage marks, which are three or more inclusion pitch distances apart, were scribed on the surfaces of the multiple-inclusion models. Measurements of distances between gage marks were taken before and after stress freezing to determine average strains parallel and transverse to the load axis. From these measurements, the effective elastic modulus and Poisson's ratio of the composite were determined.

b.   Photoelastic Models

Most of the models and the molds in which they were cast are seen in Figure 81. All the models are 1/4-in. thick. The circular discs are 3-in. in diameter. The inclusions are steel cylinders of 0.250-in. diameter, and the large tensile specimens have a uniform-shank width of 1.50-in. The uniaxial tensile calibration specimen and its mold are also shown in Figure 81. Table 19 gives the nominal inclusion spacing and the conditions of bonding or release at the binder/inclusion interface for all the models.

Figure 82 shows the "row-column" convention for describing the square array inclusion locations and their spacing parameters. In addition to the square array, each of the large models incorporated a single isolated inclusion. External load was applied later in the Y-direction.
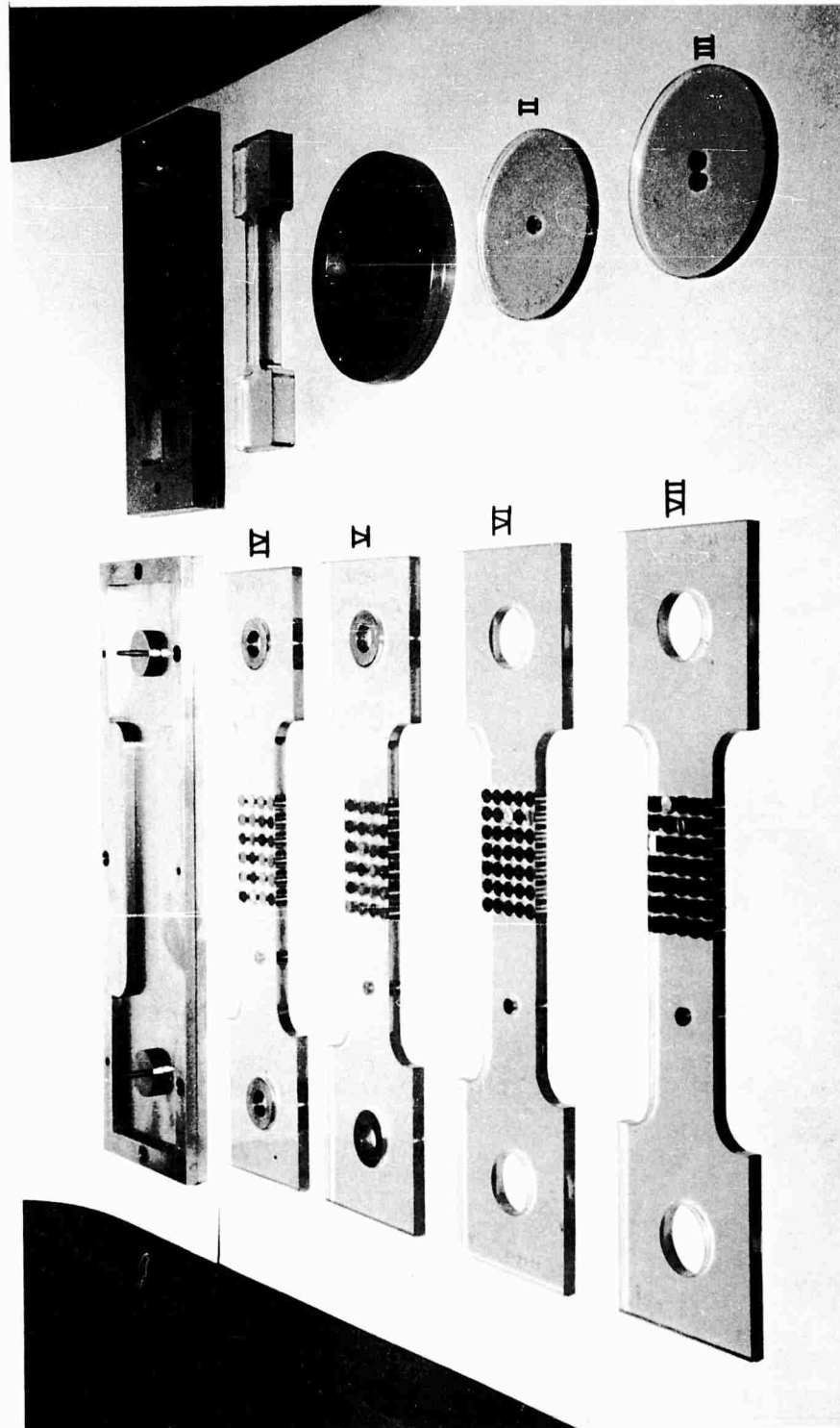
Figure 81. Models and Casting Molds for Rigid Inclusion Experiments
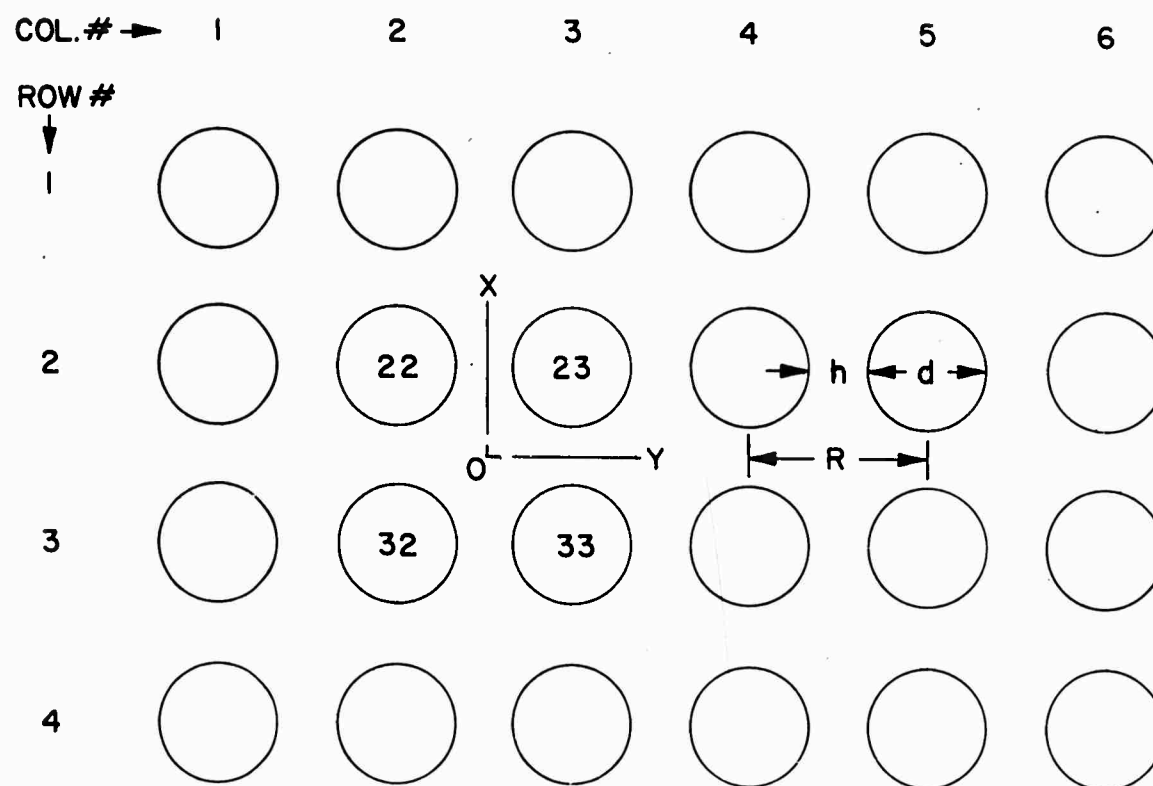
Figure 82. Convention for Describing Inclusion Locations and Spacing Geometry

TABLE 19

RESTRAINED CONTRACTION

PHOTOELASTIC MODELS

Model No.	I	II	III	IV-A	V-A	VI-A	VII-A
Inclusions	Single	Single	Double	Square Array	Square Array	Square Array	Square Array
Bonded		X	X		X		X
Released	X			X		X	
h/d	--	--	0.2	0.5	0.5	0.2	0.2
Shrinkage Calibration Fringe Order, $\bar{N}_c$ fringes/inch	9.5	9.5	11.7	9.5	9.5	11.7	11.7

IV, B, Photoelastic Studies of Solid Propellant Grain Stress Distribution (cont.)

c.   Conduct of Tests

When the models have been cast and cured with the in-
clusions in place, a shrinkage stress photoelastic pattern existed in the resin.
Since the inclusions remained in place and were never withdrawn, the stress
level corresponded to point C in Figure 79. This is the level of fringe order
maintained by continued restraint. Therefore, the calibration fringe order N_c
was used to evaluate non-dimensional thermal contraction stress distributions.

As indicated by Table 20, external load was applied
only to models No. IV and VII, inclusive. These models were hung from a
frame mounted in the oven, and dead weight was applied to the lower end of
the specimen. The "stress-freezing" cycle consisted of heating at 75°C for
one hour, then slowly cooling to room temperature. Table 20 gives the ex-
ternal load conditions and the average strains computed from gage length ex-
tension measurements.

d.   Photoelastic Fringe Patterns

Dark-field photoelastic fringe patterns for the isolated
inclusion Models I and II under restrained contraction, are shown in Figure 83.
It will be noted that the number of fringes at the bonded inclusion is nearly
double that at the released inclusion.

The dark-field pattern in the bonded, double-inclusion
Model III under restrained contraction, is shown at the top in Figure 84. The
enlarged (10X) light-field photoelastic pattern is shown below. The fringe
order at the center of the ligament is n = 9.5, while at the inclusion interface
the ligament fringe order is approximately seven.

TABLE 20

EXTERNAL LOAD PHOTOELASTIC MODEL TESTS

Model Test No.	IV-B	IV-C	V-B	V-C	VI-B	VII-B
Inclusions Bonded			X	X		X
Released	X	X			X	
h/d	0.5	0.5	0.5	0.5	0.2	0.2
Nominal Stress, $\bar{\sigma}_y$, (psi)	6.66	13.67	19.25	24.81	7.60	31.30
"Frozen" Stress Binder Fringe Value, f	1.48	1.48	1.48	1.48	1.43	1.43
"Frozen" Stress Binder Elastic Modulus, E , (psi)	1830	1830	1830	1830	1830	1830
Avg. Longitudinal Strain, $\bar{\epsilon}_y$, (in/in)	.00669	.01620	.00433	.00560	.01297	.00352
Avg. Transverse Strain, $\bar{\epsilon}_x$, (in/in)	-.00210	-.00384	-.00261	-.00300	-.00192	-.00106
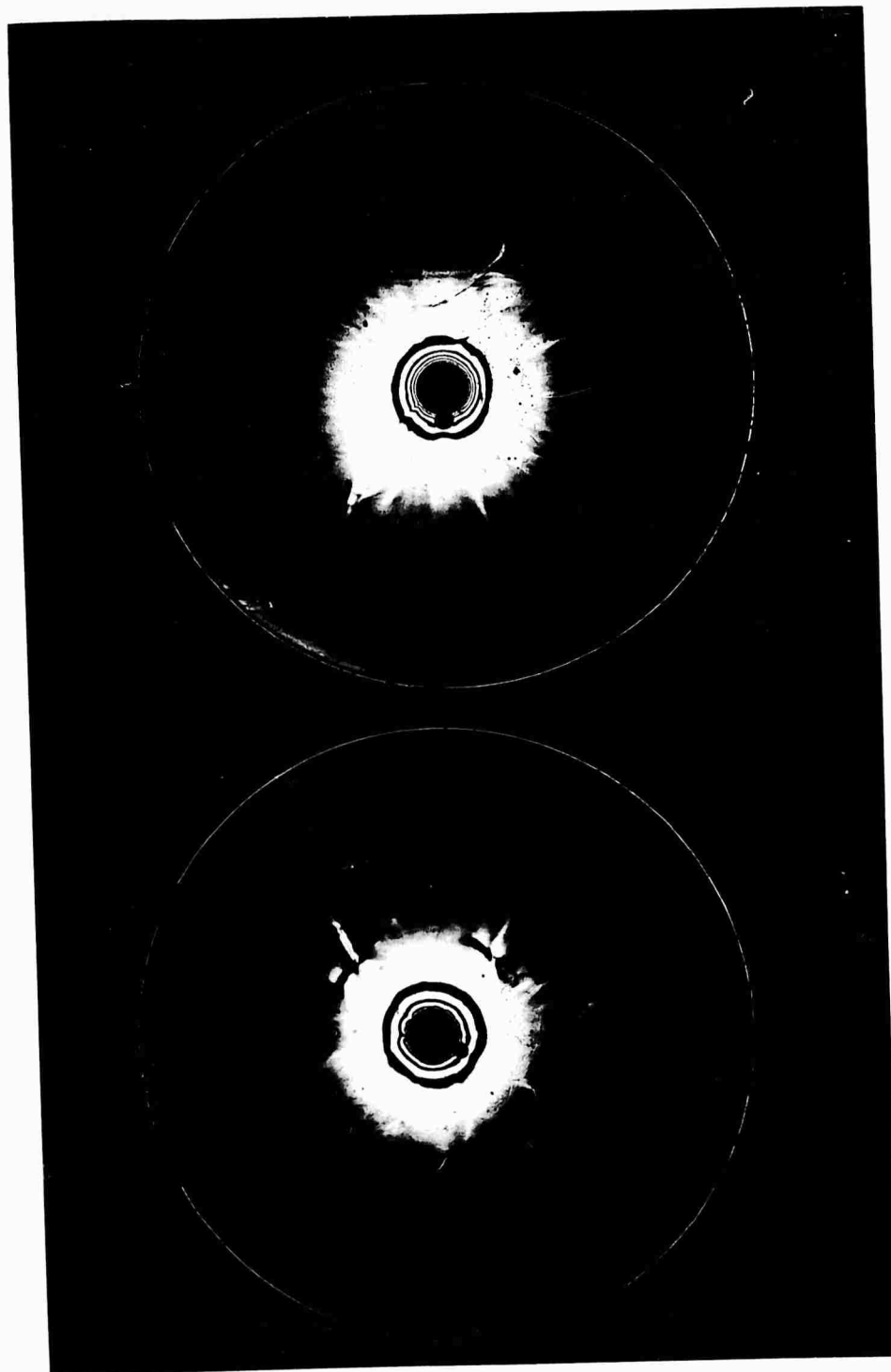
Figure 83. Dark Field Photoelastic Contraction Stress Pattern Around Released Inclusion (left) and Bonded Inclusion (right)
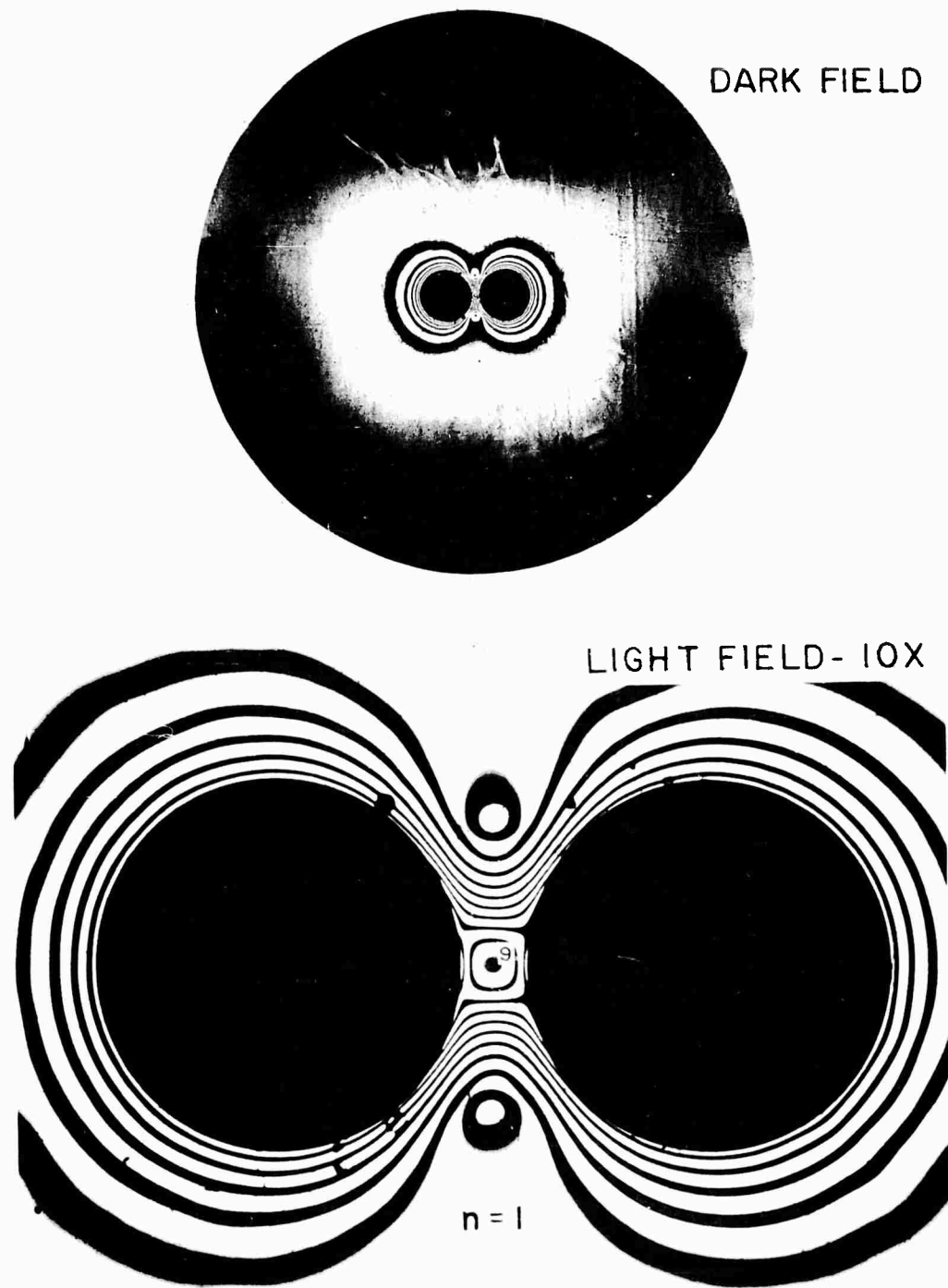
Figure 84. Contraction Stress Pattern Surrounding Pair of Bonded Inclusions. Dark Field Full View is at Top and Light Field 10 x Enlargement at Bottom

IV, B, Photoelastic Studies of Solid Propellant Grain Stress Distribution (cont.)

The dark-field photoelastic fringe pattern for the bonded square array, Model V-A under restrained contraction, is shown in Figure 85. Fringe order, n, is noted at various locations. The four inclusions shown in the enlargement are indicated by small x's in the photograph at the top of Figure 85.

The photoelastic fringe pattern under combined relative contraction and external-load "frozen" stress for Model Test No. V-B, is shown in Figure 86.

Figure 87 shows the stress pattern in Model Test VI-A under restrained contraction stress pattern, and Figure 88 shows the pattern for Model Test No. VI-B, under a combination or restrained contraction and external load.

Figure 89 shows the stress pattern in Model Test No. VII-A under restrained contraction.

Figure 90 shows the stress pattern in Model Test No. VII-B under combined contraction and external load. The enlarged photo re- veals that unbonding was initiated by the external load as evidenced by dis- turbances to the regularity and symmetry of the stress patterns.

In addition to the isochromatic fringe patterns shown here, isoclinics (lines of constant principal stress direction) were recorded for the localized areas shown in the enlarged photographs. These data were used later in the separation of stresses.
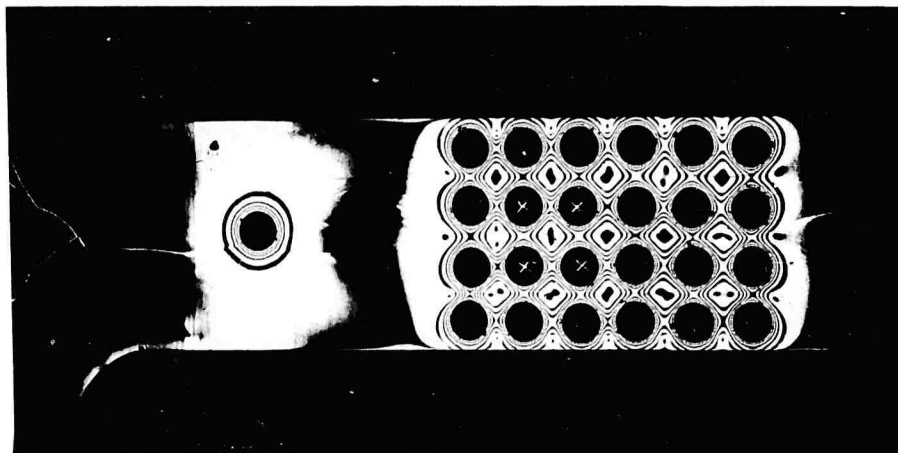
Figure 85. Dark Field Contraction Stress Pattern From Model Test V-A.
Bonded Square Array. h/d = 0.5
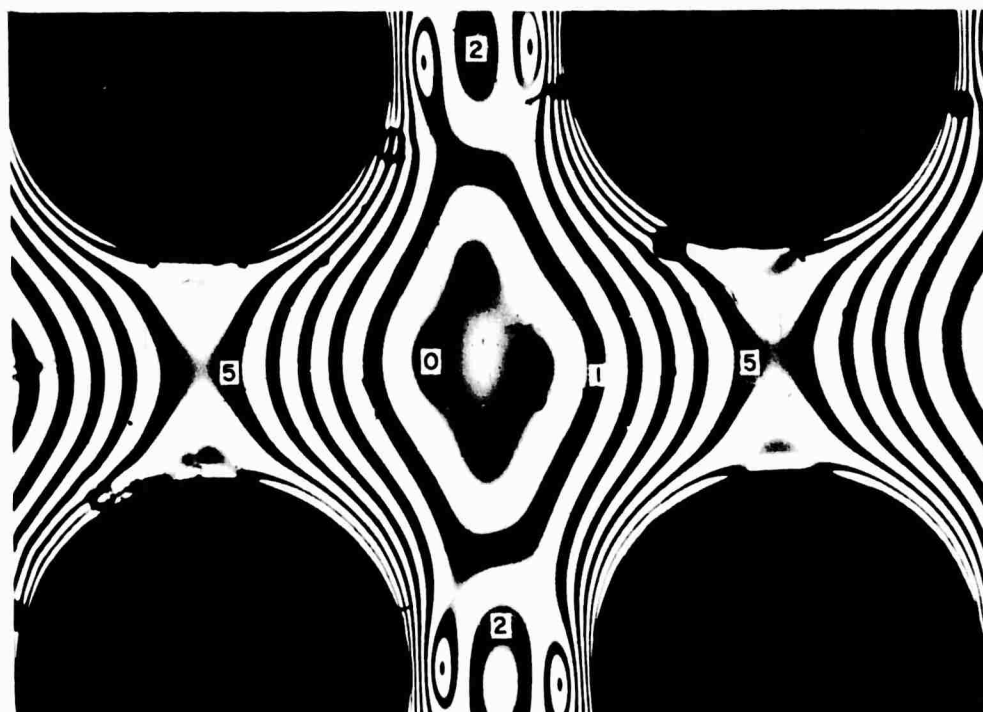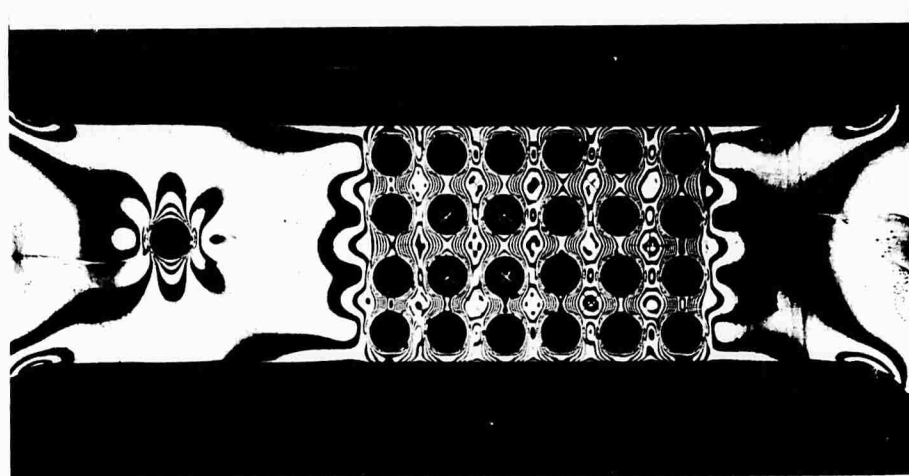
Figure 86. Dark Field Contraction and External Tension Stress Pattern From Model Test V-B. Bonded, $h/d = 0.5$, $\overline{\sigma}_v = 19.25$
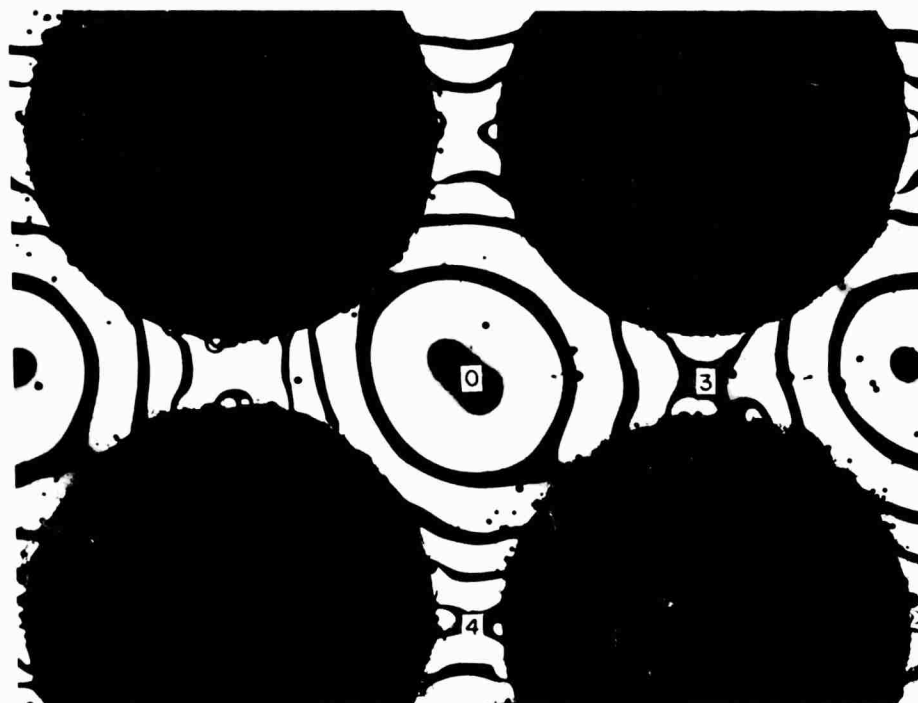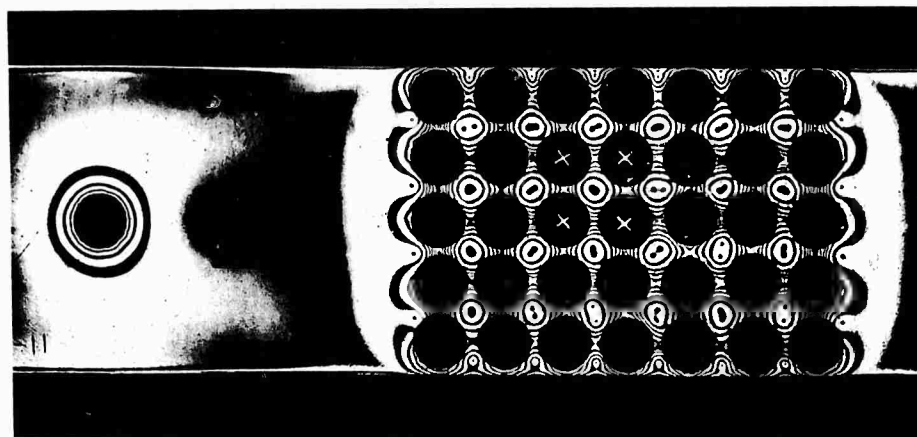
Figure 87. Dark Field Contraction Stress Pattern From Model Test VI-A.
Released, h/d = 0.2
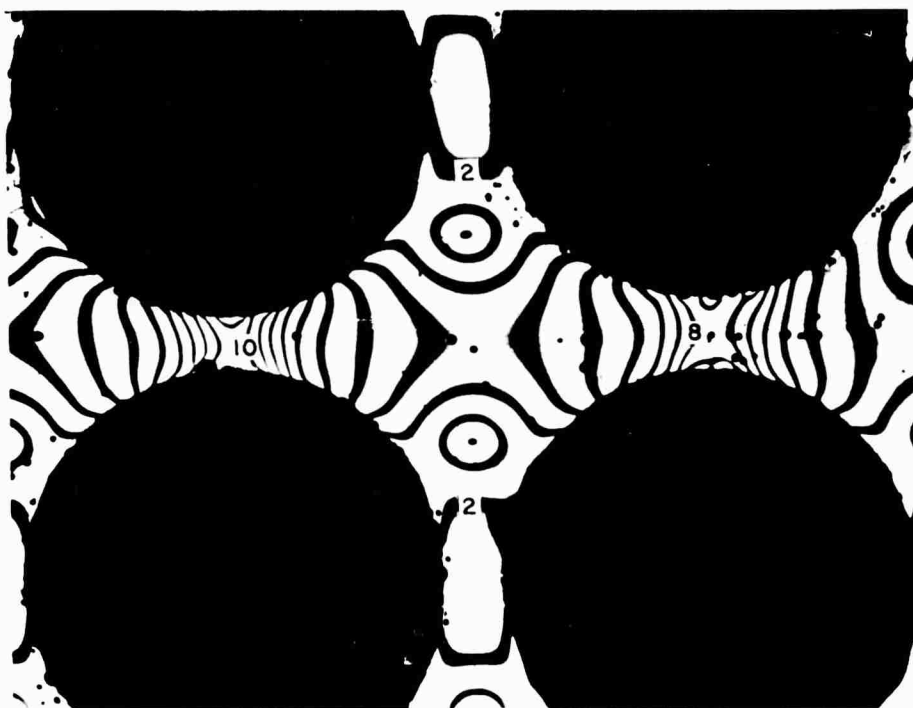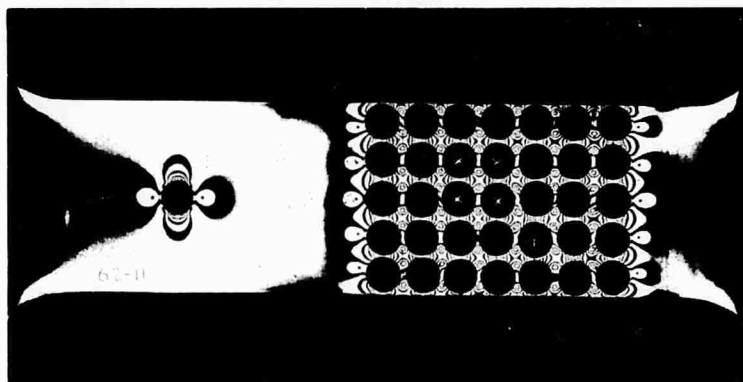
Figure 88. Dark Field Contraction and External Tension Stress Pattern From
Model Test VI-B.   Released, h/d = 0.2, $\bar{\sigma}_y$ = 7.60 psi
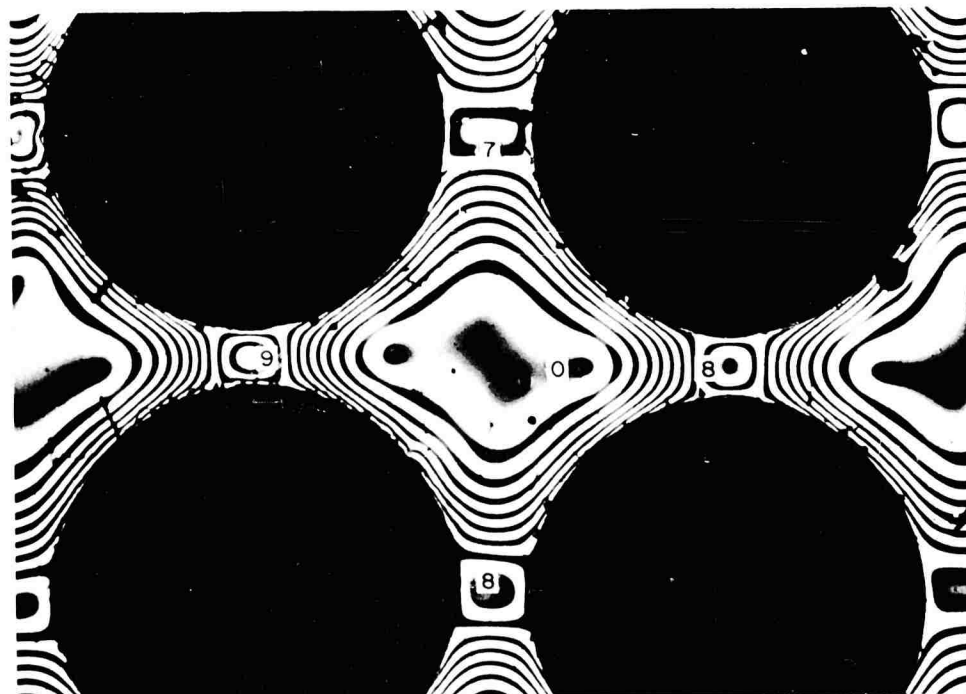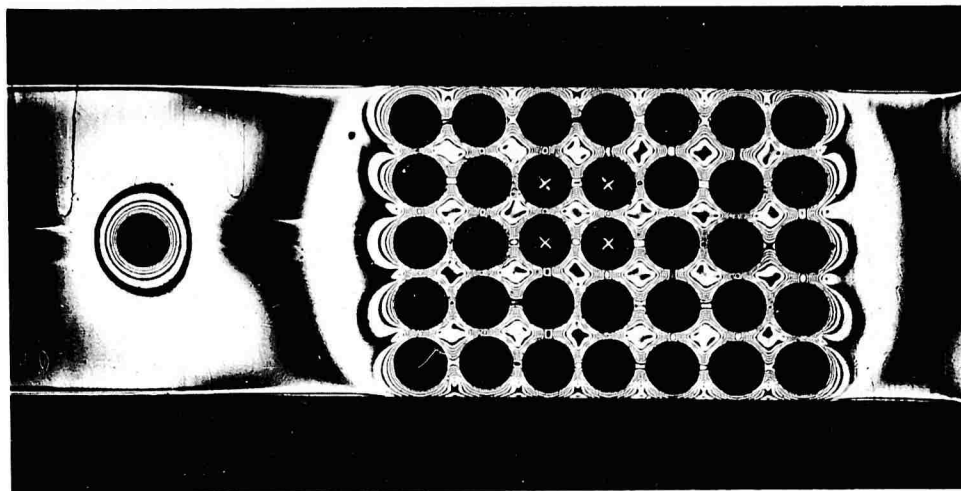
Figure 89. Dark Field Contraction Stress Pattern From Model Test VII-A.
Bonded, h/d = 0.2
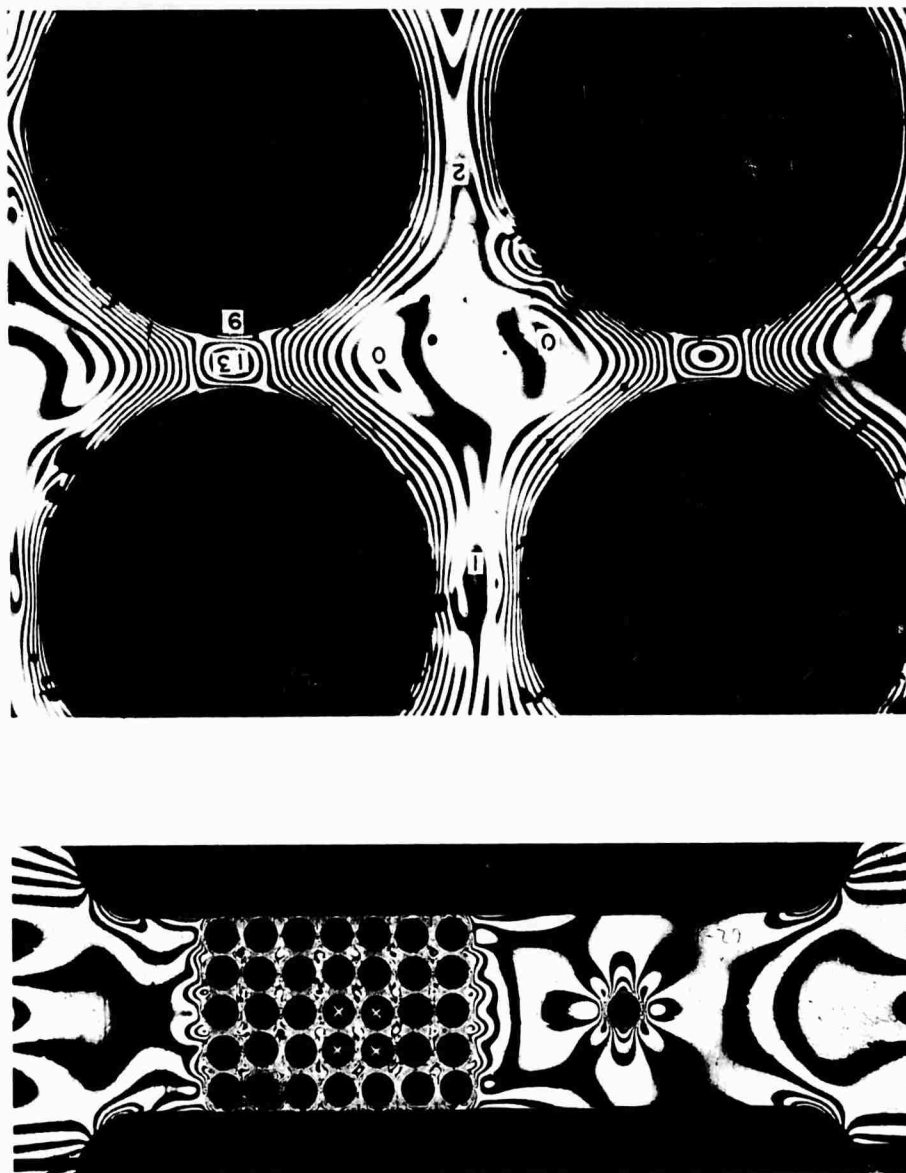
Figure 90. Dark Field Contraction and External Tension Stress Pattern From Model Test VII-B. Bonded, h/d = 0.2, $\bar{\sigma}_y$ = 31.30 psi

IV, B, Photoelastic Studies of Solid Propellant Grain Stress Distribution (cont.)

e. Separation of Stresses

The principle of superposition was applied to the separation of stresses caused by restrained contraction and by external load. The first step was to utilize standard methods for determination of stresses on the axes of symmetry in the restrained-contraction models. These stress components were first obtained in terms of photoelastic fringe order. The same process was then performed for the combined contraction and external-load photoelastic patterns. The stress components attributable to external load were then determined by algebraic subtraction of the individual stress components, still in terms of photoelastic fringe order. Then each component obtained in this manner was interpreted according to the photoelastic calibration process appropriate to the test procedure. Reduction of restrained-contraction fringe order to non-dimensional form was accomplished by the equation,

$$\frac{\sigma}{E \Delta} = \frac{N}{\bar{N}_c} \tag{66}$$

where σ is the stress component, psi. N is the fringe order per unit model thickness, fringes/in.

The fringe order components attributable to external load were transformed into non-dimensional stress values by the relationship indicated in Equation (61).

$$\frac{\sigma}{\bar{\sigma} \, y} = \frac{N \, f \, W \, t}{P_y} \tag{67}$$

IV, B, Photoelastic Studies of Solid Propellant Grain Stress Distribution (cont.)

where $\quad$ N $\quad$ is the fringe order per unit model thickness, fringes/in.

$\qquad$ f $\quad$ is the photoelastic "frozen" stress fringe value.

$\qquad$ W $\quad$ is the model width, inches.

$\qquad$ t $\quad$ is the model thickness, inches.

$\qquad$ P_y $\quad$ is the external load exerted in y-direction, lb.

$\qquad$ $\bar{\sigma}_y$ $\quad$ is the nominal applied stress, P/W t.

$\qquad$ The equation utilized for separation of the stress components (in terms of fringe order) on an axis of symmetry, was the Filon transformation of the Lame-Maxwell equilibrium equations along a stress trajectory (32). The process was begun at the intersection of ligament axes of symmetry (point 0, Figure 82) and proceeded in the y-direction, assuming an initial stress σ_{yo} of unknown value. Integration was carried out to the point $y = R/2$ on the ligament minimum section. From static equilibrium it is known that $\int_0^{R/2} \sigma_x dy = 0$; therefore, the initial value σ_{yo} can be determined from:

$$\sigma_{yo} = \frac{2}{R} \int_0^{R/2} (\sigma_x - \sigma_{yo})\, dy \qquad (68)$$

$\qquad$ By the process of numerical integration of Filon's equilibrium equations, the value of $\sigma_x - \sigma_{yo}$ at every point was obtained (in terms of fringes) as follows:

IV, B, Photoelastic Studies of Solid Propellant Grain Stress Distribution (cont.)

$$(1) \quad \sigma_y - \sigma_{yo} = 0 - \int_0^y (\sigma_y - \sigma_x) \frac{d\theta}{dx} dy \qquad (69)$$

$$(2) \quad \sigma_x - \sigma_{yo} = -(\sigma_y - \sigma_x) + (\sigma_y - \sigma_{yo}) \qquad (70)$$

where $\sigma_y - \sigma_x$ is the principal stress difference given by the photoelastic fringe order, N; and $d\theta/dx$ is the rate of change of the isoclinic parameter at position (o, y), transverse to the axis of symmetry. Then, from Equations (68), (69), and (70),

$$\sigma_y = \frac{2}{R} \int_0^{R/2} (\sigma_x - \sigma_{yo}) dy - \int_0^y (\sigma_y - \sigma_x) \frac{d\theta}{dx} dy \qquad (71)$$

$$\sigma_x = \frac{2}{R} \int_0^{R/2} (\sigma_x - \sigma_{yo}) dy - \int_0^y (\sigma_y - \sigma_x) \frac{d\theta}{dx} dy \qquad (72)$$

$$- (\sigma_y - \sigma_x)$$

IV, B, Photoelastic Studies of Solid Propellant Grain Stress Distribution (cont.)

The foregoing procedure was used for both the contraction stress pattern and the combined contraction plus external-load stress pattern. Stress components attributable to external load alone were determined by simple superposition:

$$\sigma_{Load} = \sigma_{Load + Contraction} - \sigma_{Contraction} \qquad (73)$$

Since Equation (73) assumes implicitly that the contraction stress remains the same during application of external load, it can be applied with confidence only to the bonded inclusion test results.

Time limitations permitted the application of the foregoing stress separation procedures only to Model Tests V-A and V-B.

f.   Effective Elastic Properties

The variation of effective elastic modulus ratio, E'/E, as a function of ligament width and interface bond condition is shown in Figure 91. Similar curves for the effective Poisson's ratios of the composite specimens is shown in Figure 92. As indicated in Table 20, two tests at different external load levels were run on the specimens having the larger ligament width, $h/d = 0.5$. The effective elastic modulus was determined by the ratio of average applied stress to average longitudinal strain (see Table 20);

$$E' = \bar{\sigma}_y / \bar{\epsilon}_y \qquad (74)$$

Effective Poisson's ratio was determined from the ratio of average transverse strain to the average longitudinal strain:

$$\nu' = -\bar{\epsilon}_x / \bar{\epsilon}_y \qquad (75)$$
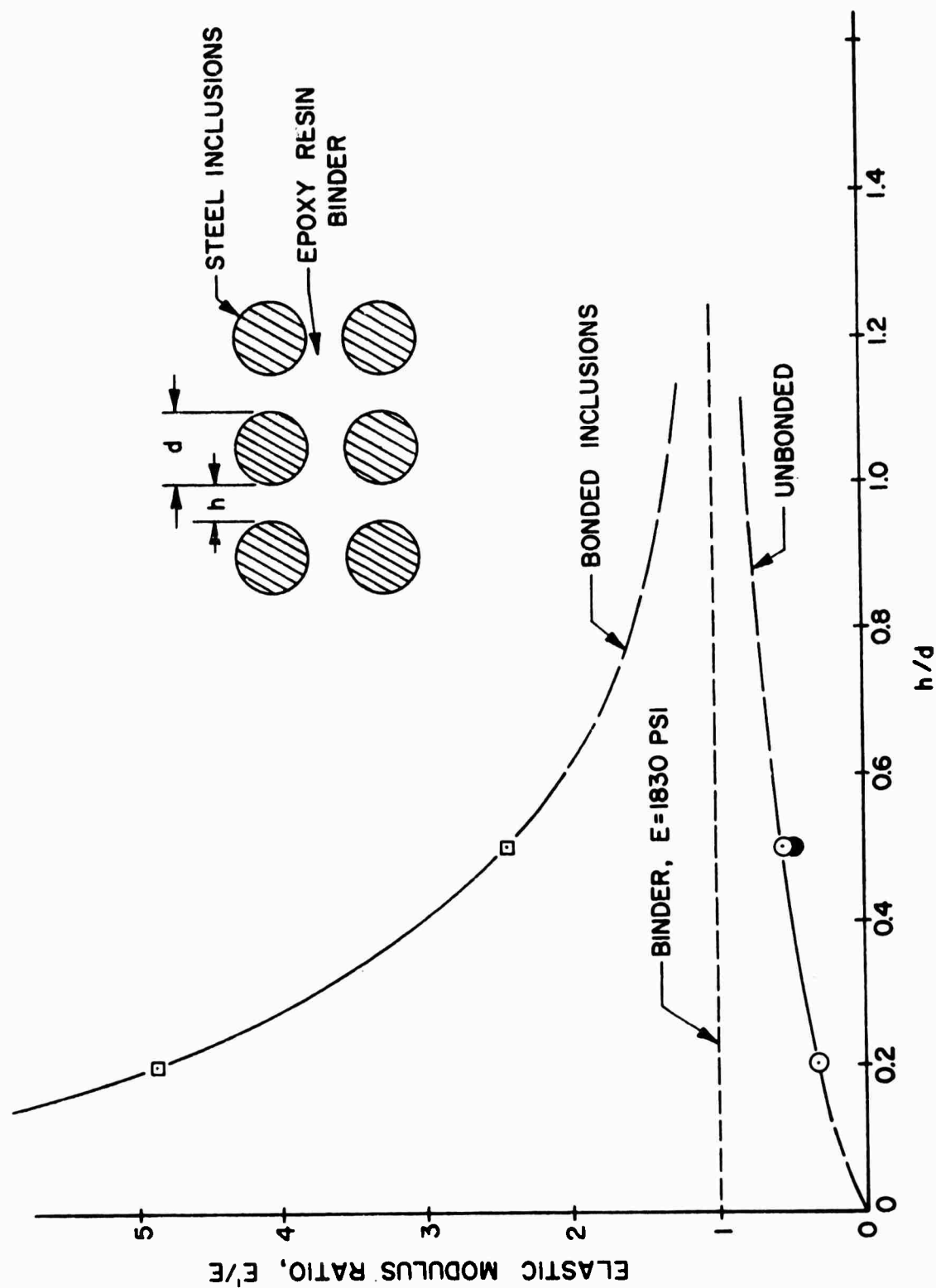
Figure 91. Effective Elastic Modulus Variation With Inclusion Spacing and Bond Condition
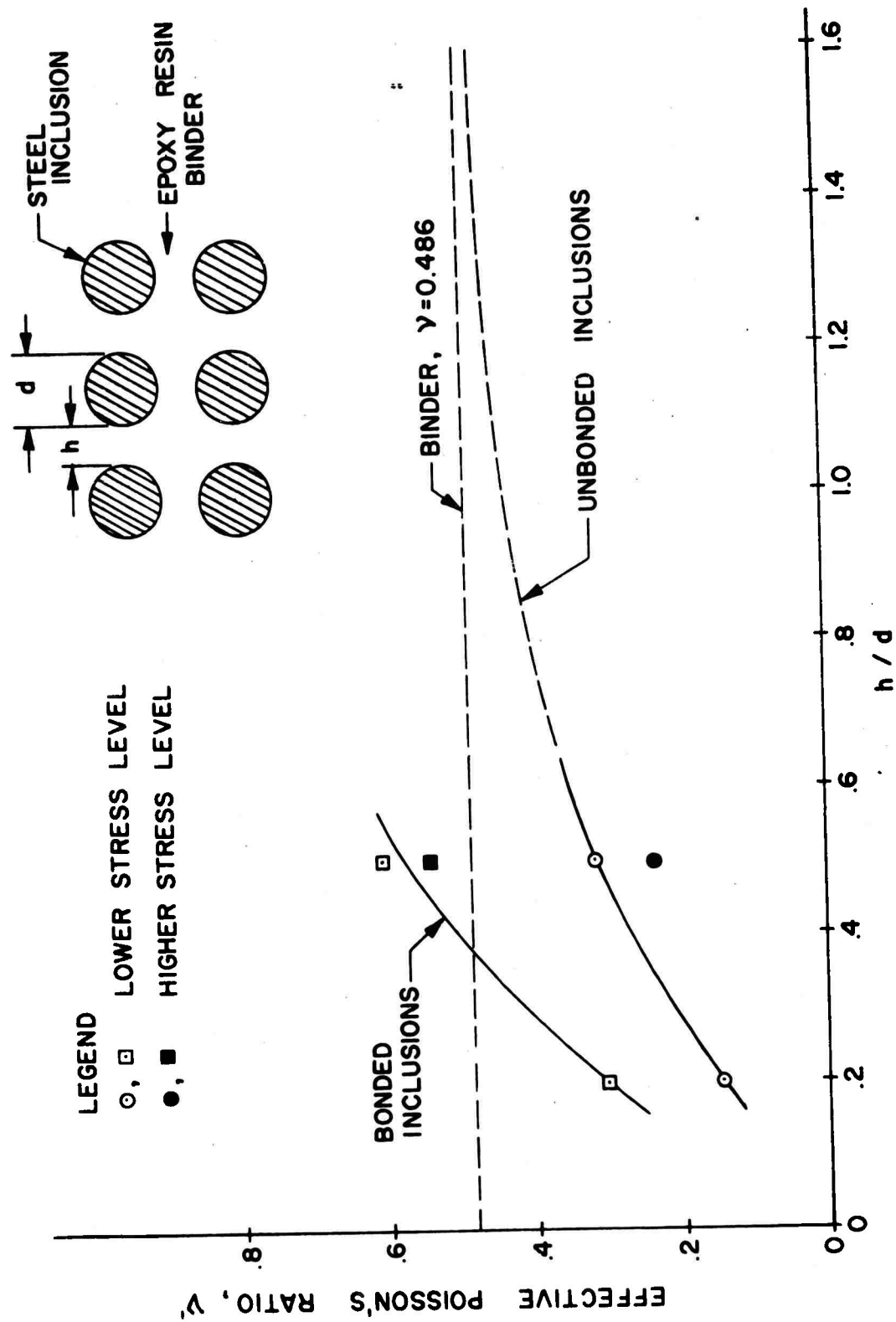
Figure 92. Effective Poisson's Ratio Variation With Inclusion Spacing and Bond Condition

IV, B, Photoelastic Studies of Solid Propellant Grain Stress Distribution (cont.)

It is seen from Figure 91 that the bonded inclusion composite material becomes more rigid, as the inclusions become more closely packed, while the unbonded inclusion composite material becomes more flexible. Figure 92 shows that the effective Poisson's ratio decreases more rapidly in the bonded composite as the ligament width, h, is reduced. The nature of the curves between $0 < h/d < 0.20$ has not been established, and extrapolation of the curves into that region is not recommended.

g. Restrained Contraction Stresses in Binder

The restrained contraction stresses in the binder surrounding a single unbonded inclusion, Model I, are shown in Figure 93. The radial and circumferential stresses were very nearly equal, and are indicated as such in Figure 93.

Binder stresses in the vicinity of an isolated bonded inclusion, Model II, are shown in Figure 94.

Shrinkage stresses on the two intersecting ligament axes of symmetry in Model III are shown in Figure 95. Tangential shear and principal stress difference variation on the inclusion boundary is also shown. The σ_x stress in the ligament reaches a compressive peak at its center. Similarly, the σ_y stress reaches a tensile maximum at the center. A shear peak at the inclusion boundary is located approximately $20°$ from the reference axis.

Contraction stress components on each leg of two intersecting ligament centerlines were determined and the results were averaged. In principle, the stresses on the ligament centerlines should have been identical;
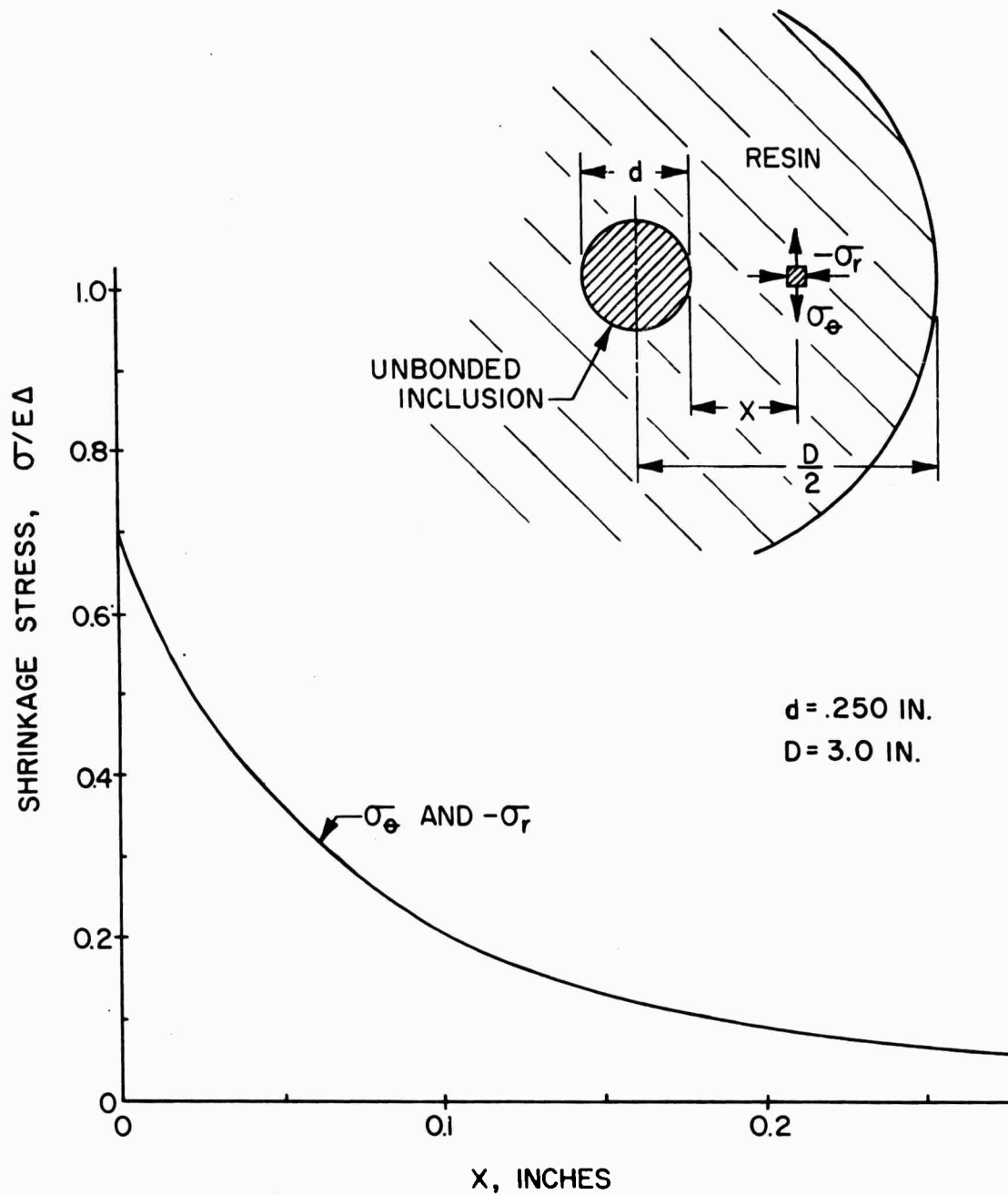
Figure 93. Stress Distribution Near Isolated, Unbonded, Single Inclusion
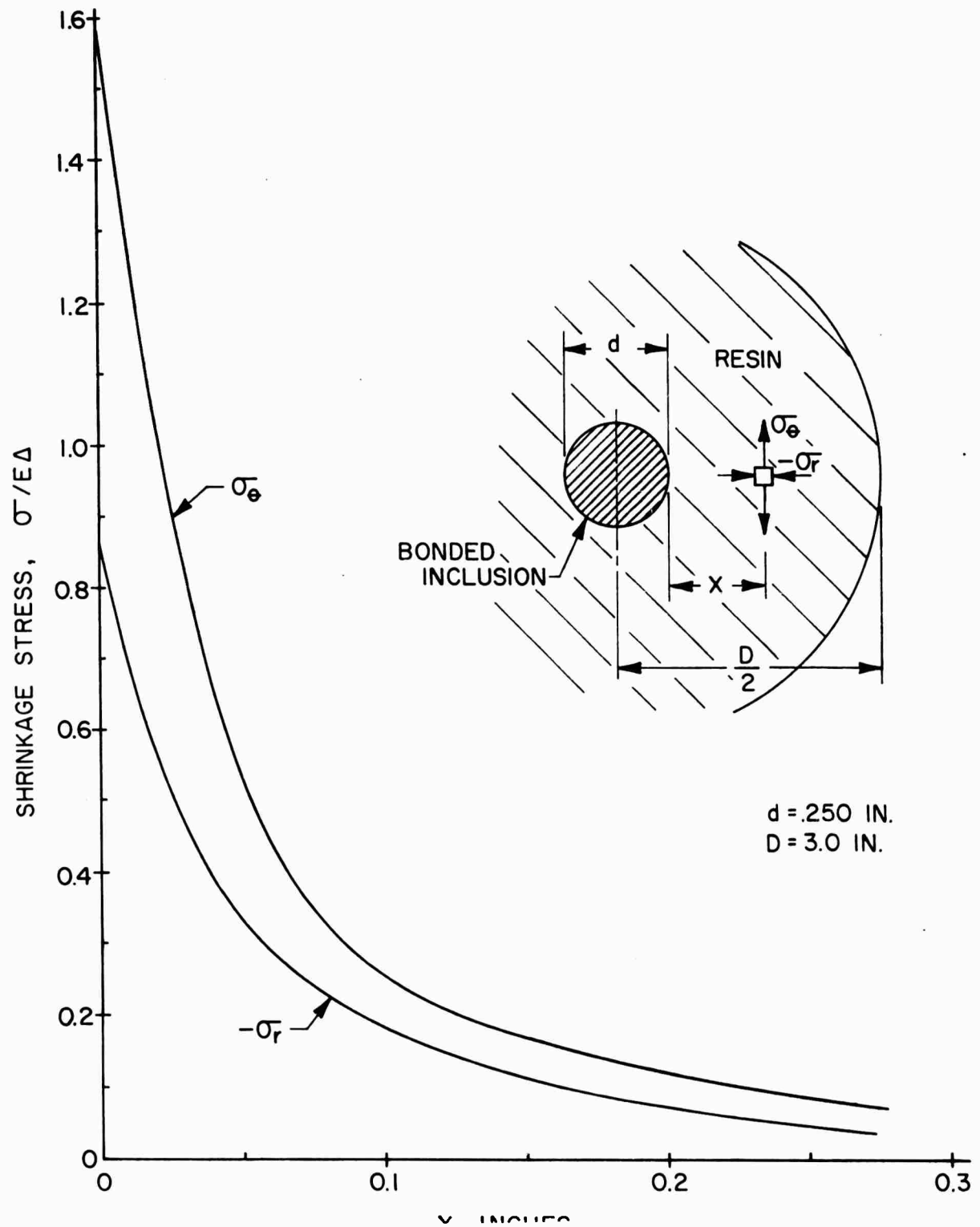
Figure 94. Stress Distribution Near Isolated Bonded Inclusion
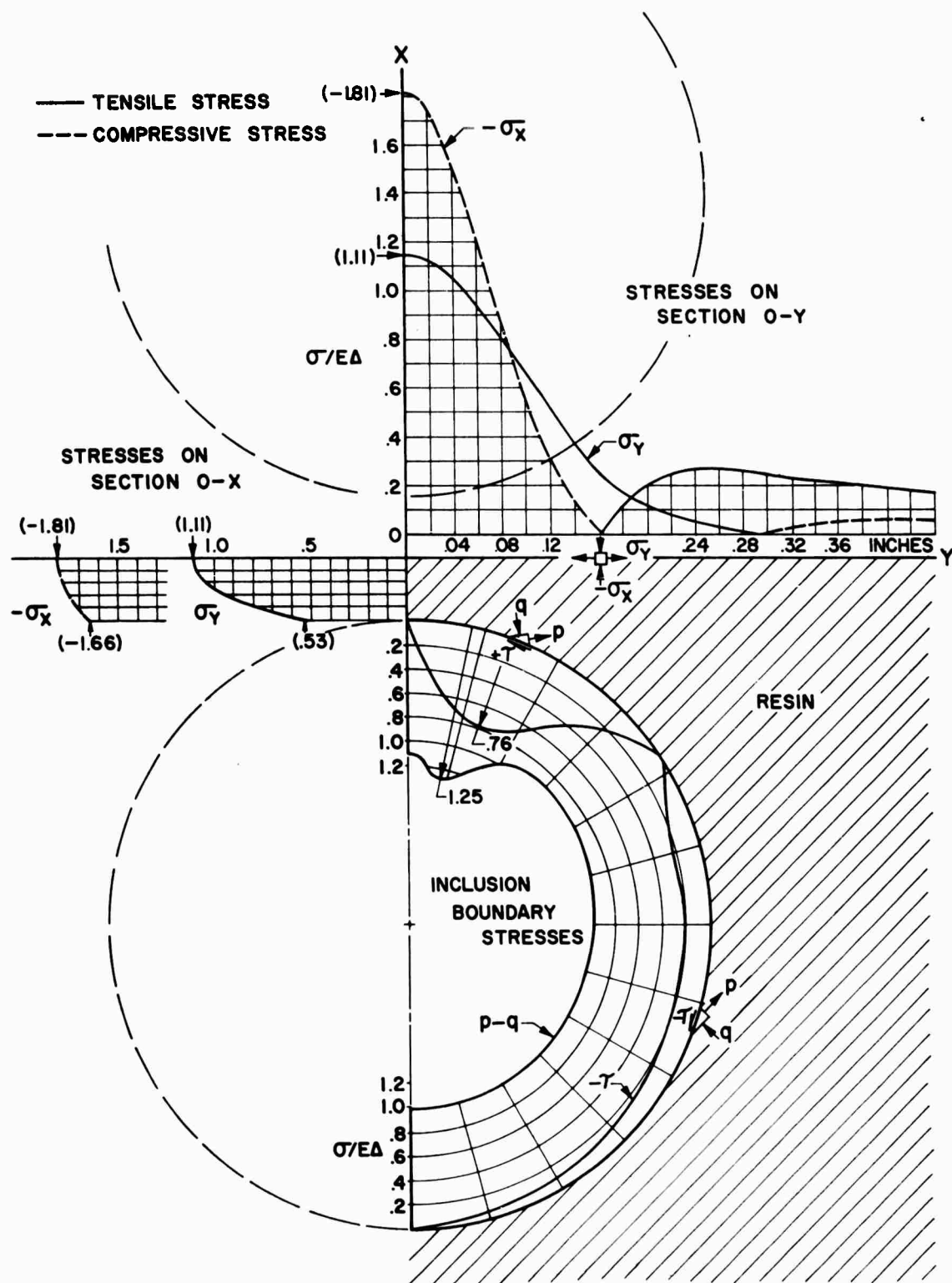
Figure 95. Stresses in Vicinity of Isolated Pair of Bonded Inclusions (h/d = 0.2)

IV, B, Photoelastic Studies of Solid Propellant Grain Stress Distribution (cont.)

however, there were differences in spacing of the cylindrical inclusions which introduced differences in the stress distribution. The average curves, believed to best represent the stresses when inclusions are more accurately spaced, are shown in Figure 96. Stress components are denoted by σ_a (axial stress, parallel to the ligament centerline) and σ_t (transverse to the ligament center-line). From the same model, the stresses across the ligament minimum sections are shown in Figure 97. The data for both figures were obtained from Model V-A. Again the results presented are the average of data obtained separately on two adjacent ligaments. Stresses in Figure 97 at $x/h = 0.5$ do not coincide with stresses shown at $Y/R = 0.5$ in Figure 96. The reason for this discrepancy is that averaged data from all four ligaments was used to obtain Figure 96, but for Figure 97, only the data from ligaments 22-23 and 23-33 were employed.

Stresses along the ligament centerline O-X of Model V, induced by a load applied in the y-direction, are given in Figure 98. Stresses across the ligament No. 22-23 minimum section are given in Figure 99. These data are from Model Tests V-A and V-B. Stresses in the same model along ligament centerline O-Y are shown in Figure 100. Ligament No. 23-33 minimum section stresses are shown in Figure 101.

h.   Discussion

The process of separating stress components attributable to contraction and to external load is quite tedious, and many opportunities exist for accumulating error. Nevertheless, the requirements of static equilibrium have been reasonably well met; consequently, the experimental stress distributions provide a valid indication of the true stress distribution.
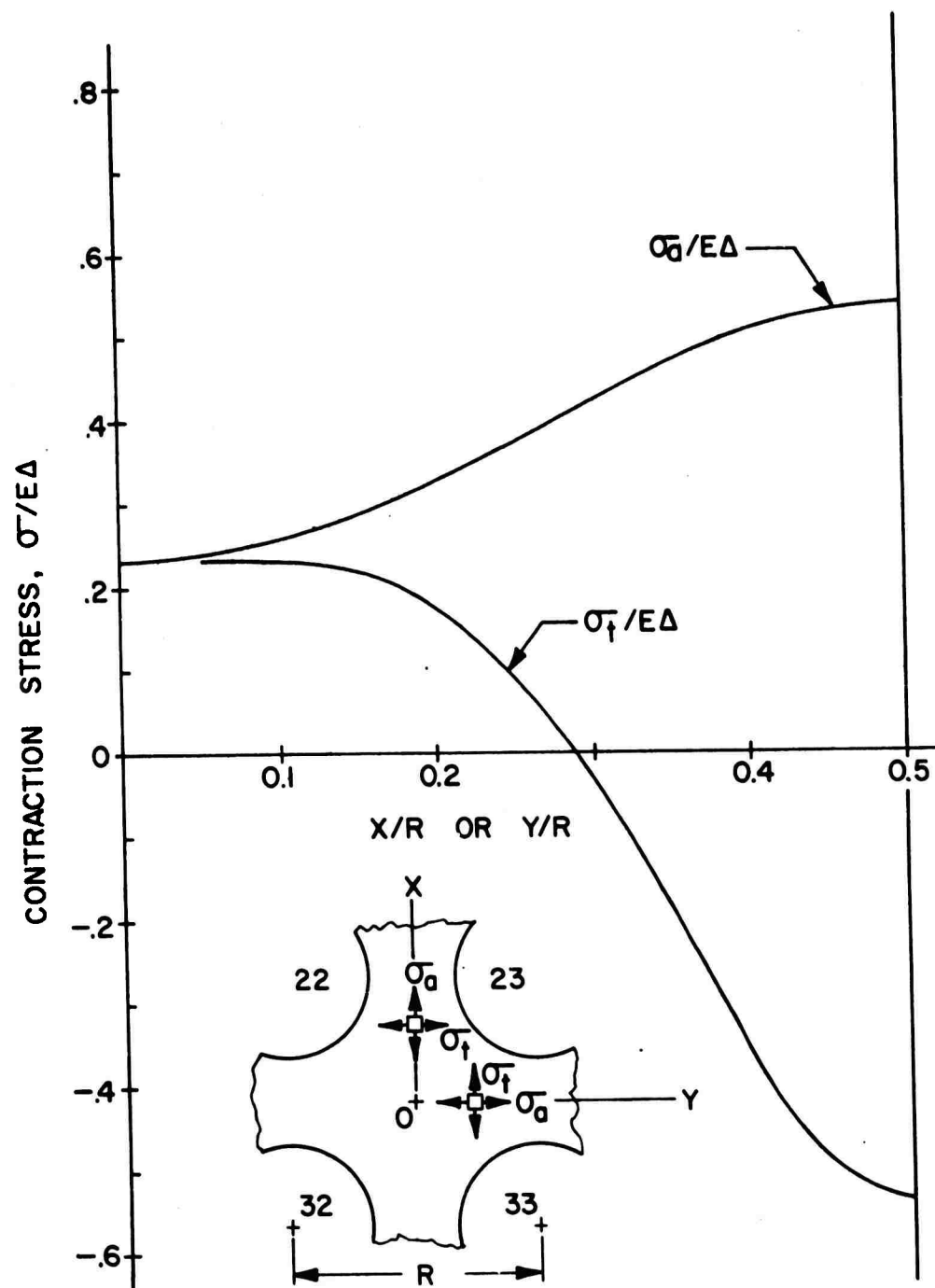
Figure 96. Contraction Stresses Along Ligament Centerlines, Model Test V-A
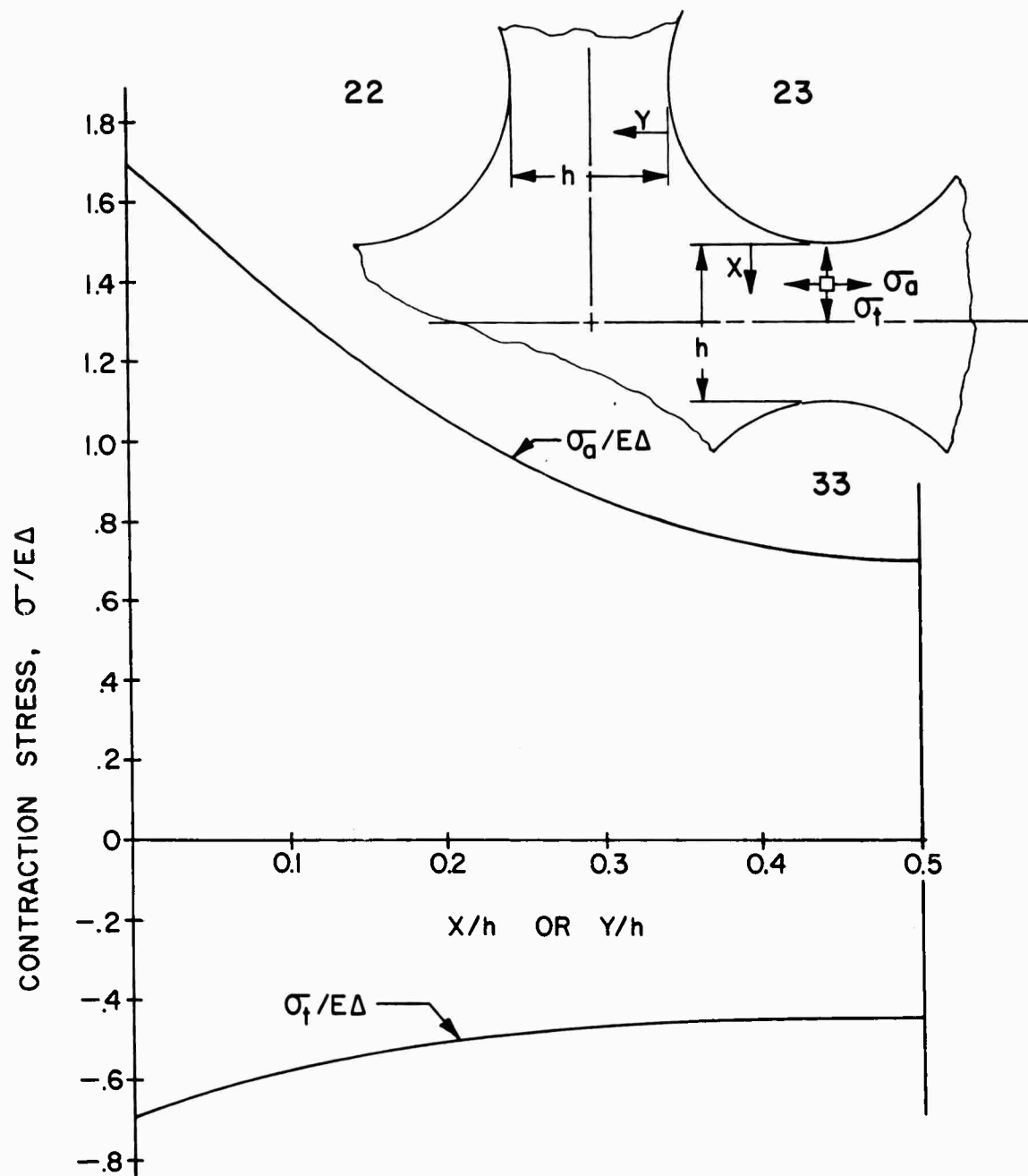
Figure 97. Contraction Stress Across Ligament Minimum Section, Model Test V-A
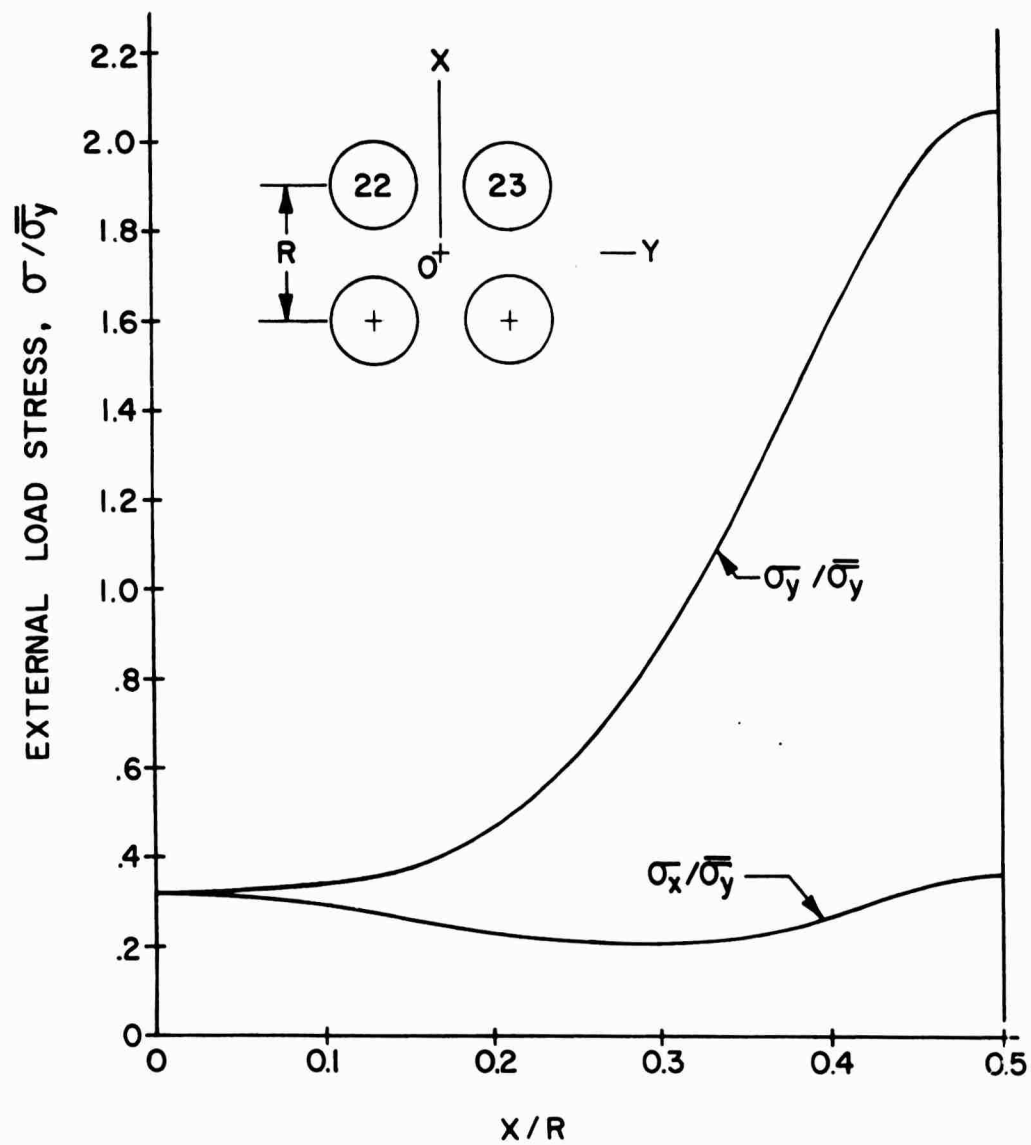
Figure 98. External Load Stress Along Centerline of Ligament Transverse to Direction of Applied Load, Model Test V-B
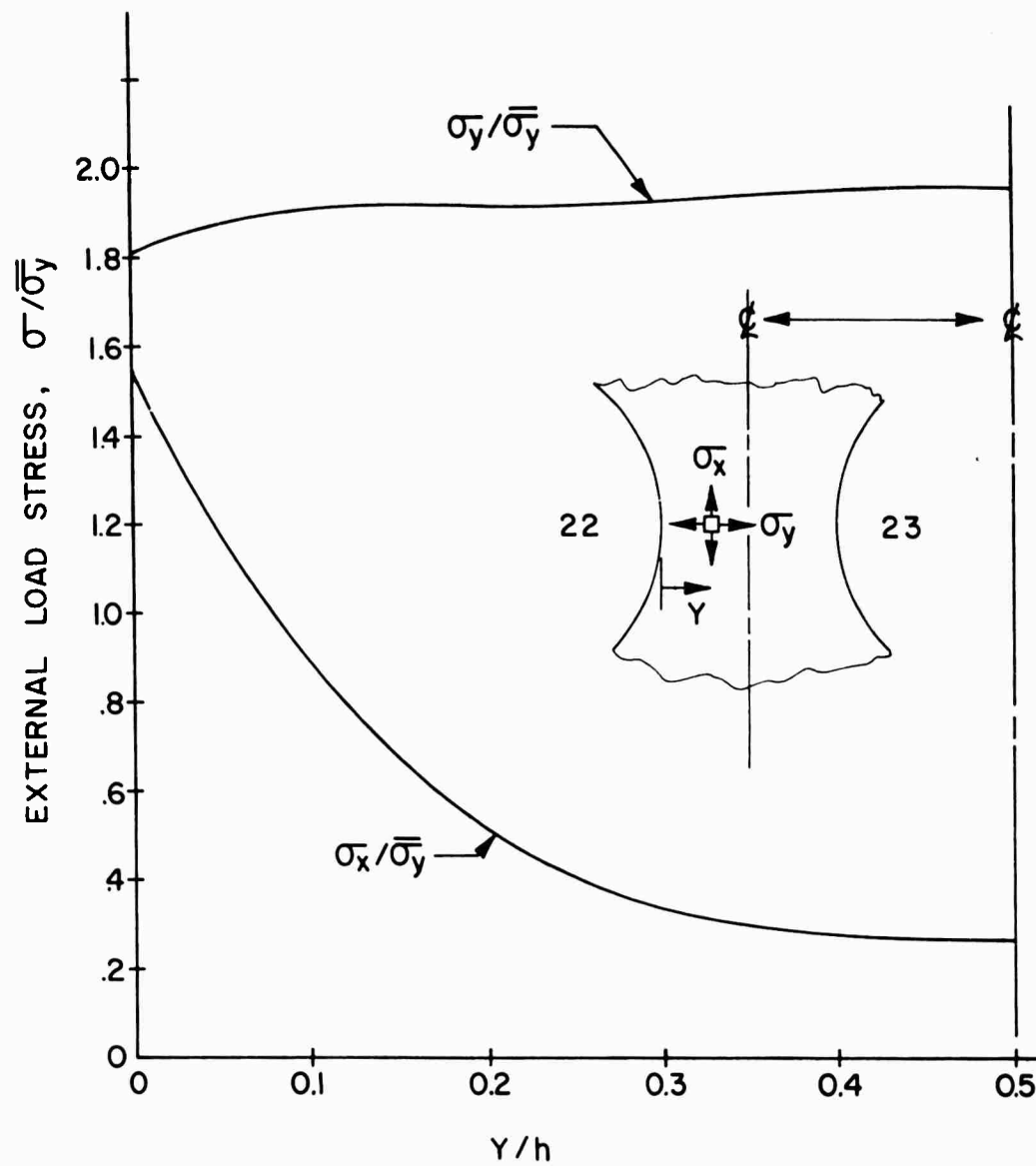
Figure 99. External Load Stress Distribution Across Ligament Transverse to
Direction of Applied Load, Model Test V-B
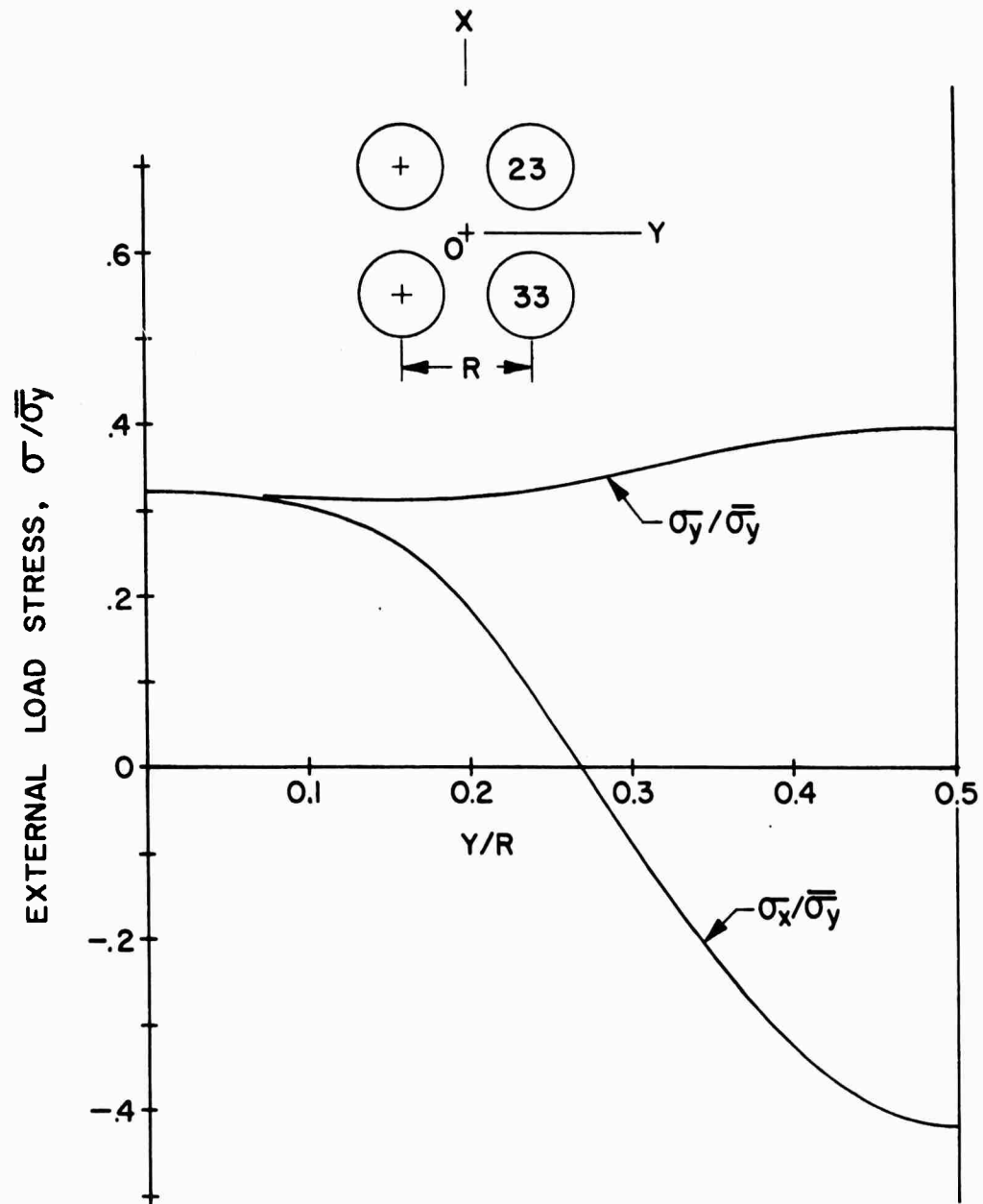
Figure 100. External Load Stress Along Centerline of Ligament Parallel to
Direction of Applied Load, Model Test V-B

#23

#33
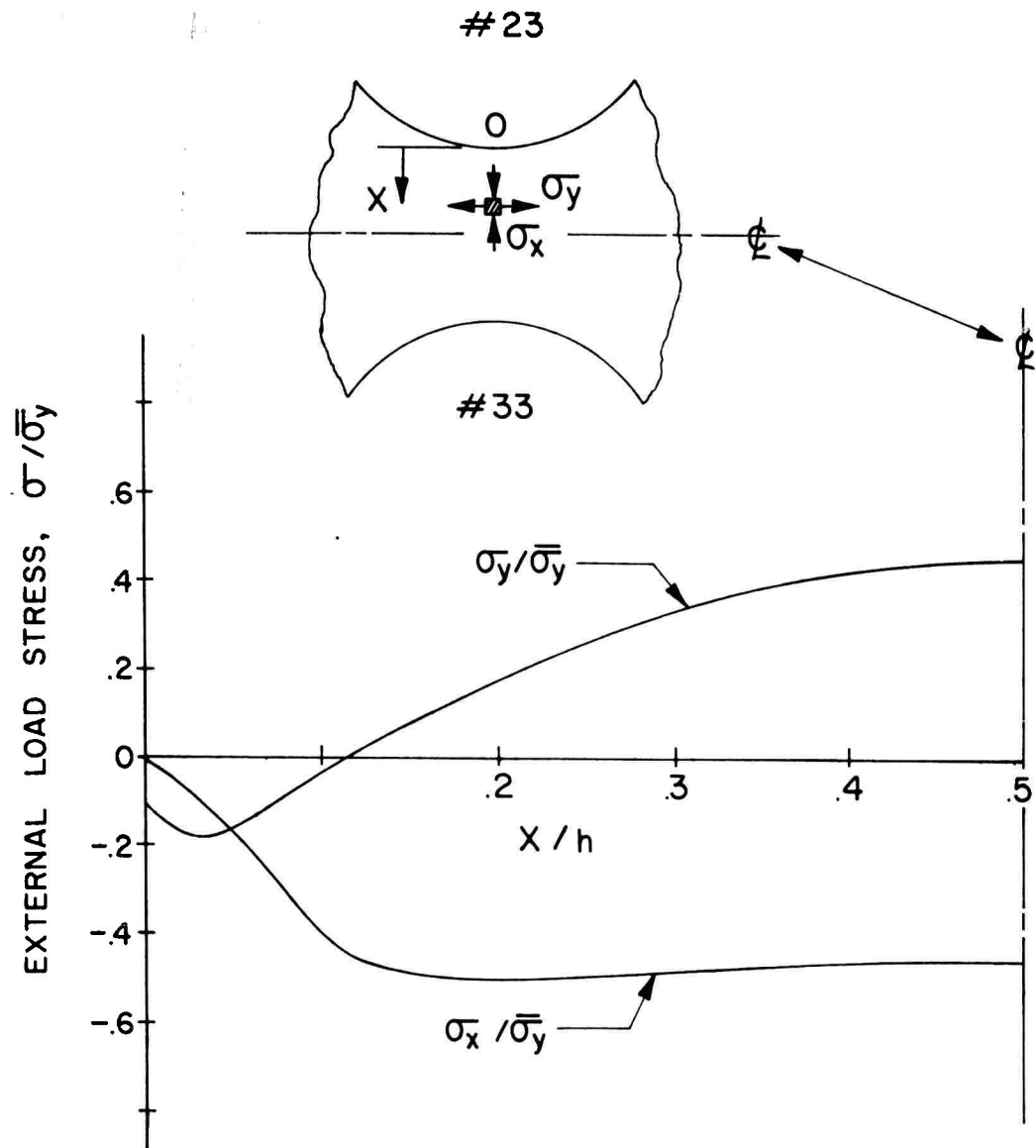
IV, B, Photoelastic Studies of Solid Propellant Grain Stress Distribution (cont.)

In the relatively broad ligaments of Model V-A, contraction stresses did not appreciably exceed values found near the isolated bonded inclusion. In the thinner ligaments of Models III and VII-A, however, it is to be noted that higher shrinkage fringe order at the ligament minimum section is produced. This is a consequence of higher lateral pressures between cylinders, and higher axial tensions in the ligaments. It is not known to what extent this trend continues as ligament widths are further reduced, but there was sufficient accidental variation of ligament width in Model VII-A (see Figure 85) to provide some indication. Maximum fringe order at the ligament minimum section varied from 7 to 11 fringes, the higher values being associated with the thinner ligaments.

Figure 99 shows that the maximum tensile stress caused by external load occurs at the minimum section of a ligament oriented transverse to the direction of load. This stress, σ_y, is oriented parallel to the load direction, and it remains essentially constant across the ligament minimum section. The other principal stress, σ_x, along the same section is nearly equal to σ_y at the bonded inclusion interface, but decreases appreciably toward the center of the ligament. Thus, one would expect the maximum local strain caused by uniaxial load to occur in the binder at the center of a transversely oriented ligament. In the bonded composite, ligaments oriented parallel to the load direction sustain axial stresses that are less than the nominal applied stress. In such ligaments, there is essentially no stress carried by the binder at the inclusion interface. If the principle of superposition is applied to the stress distributions on the minimum sections of the two orthogonal ligaments, it is found that equal biaxial external tension results in lower maximum binder stress than the application of uniaxial tension.

IV, B, Photoelastic Studies of Solid Propellant Grain Stress Distribution (cont.)

Similar photoelastic experiments with spherical particles could be performed, but the prospects for obtaining quantitative analysis of the three-dimensional state of stress throughout are very limited. Maximum shear stress distributions, as represented by the photoelastic isochromatic fringes, would be relatively simple to determine.

3. Three-Dimensional Solid Rocket Grain Thermal Cycle Stress Analysis

The procedures followed in the model test and the calibration test specimen are the same as before. The calibration fringe order observed after stripping the mold and permitting complete recovery of viscoelastic deformations is used.

A five-piece casting mold was employed, Figure 102. The cylindrical case has a 3.00 I.D. and .025-in. wall thickness. The core is 0.750-in. diameter and forms the cylindrical inner bore of the model when it is cast. When assembled, the mold has a completely enclosed, hollow, cylindrical cavity that is 1.75-in. long. The cylindrical core and the end plates are coated with a mold release agent to prevent adhesion of the liquid resin. The top-end closure of the casting mold is made slightly conical to encourage migration of entrapped air bubbles in the liquid resin toward the cylindrical core. Riser slots in the end closure bore then permit escape of the air. The riser slots also permit the transfer of liquid resin into the mold cavity to compensate for initial shrinkage of the resin. A small cylindrical reservoir, atop the end closure, provides liquid resin for that purpose. After completion of the model preparation and test procedures, the slices taken from the model were analyzed.

.750 D

RESERVOIR

RISER SLOTS

CYLINDER
3.00 I. D.
0.025 WALL

1.75
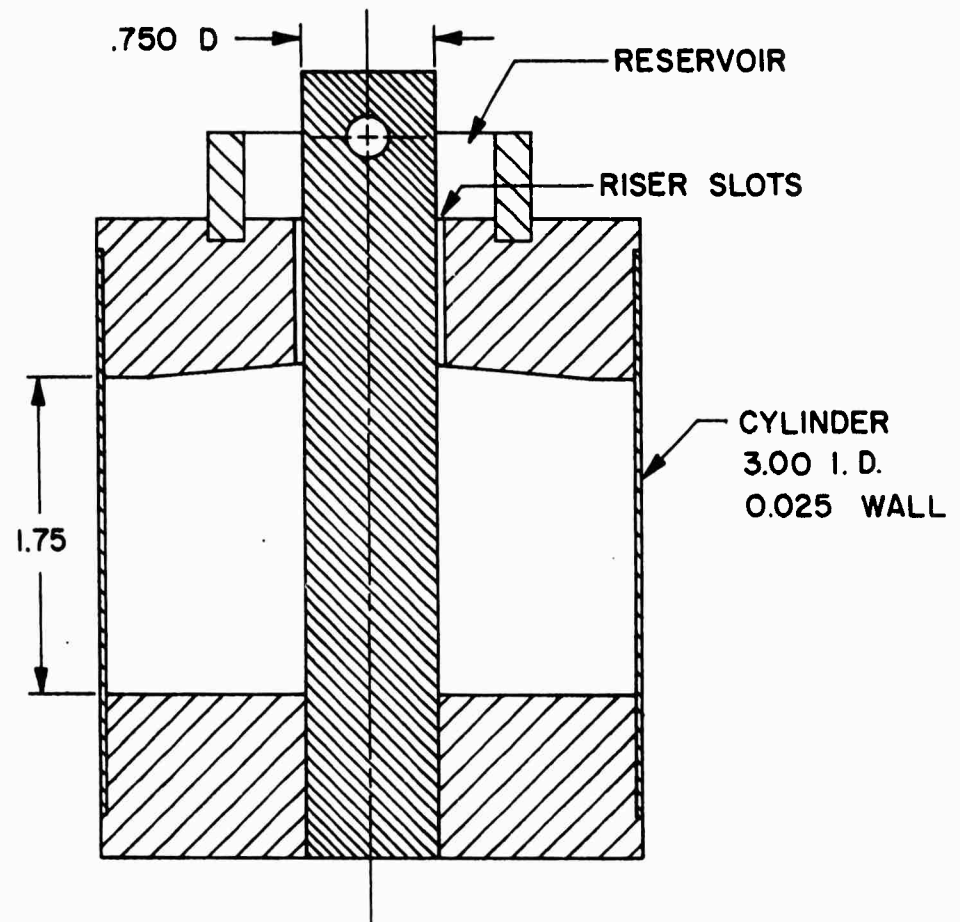
Figure 102. Cross-Section of Mold for Casting Case-Bonded Grain Model

IV, B, Photoelastic Studies of Solid Propellant Grain Stress Distribution (cont.)

a. Photoelastic "Frozen" Stress Patterns

Several slices were removed on meridional and transverse planes. The dark-field, isochromatic "frozen" stress patterns in three meridional slices, from planes about 120° apart, are shown in Figure 103. The close similarity of the three patterns illustrates the symmetry of the three-dimensional "frozen" stresses. Fringe order, n, is noted at one location. Three transverse slices from one portion of the model are also shown in Figure 103. The relative axial position of each slice is indicated on the meridional slice photograph, and fringe order is noted at several locations. The thickness of transverse slice No. 3 is 0.143-in. All other slices are 0.098-in. thick.

The fringe order data were converted to non-dimensional contraction stress differences, using Equation (65). Complete isoclinic parameter (principal stress direction) maps were also obtained for the meridional slice. Because of the rotational symmetry of the specimen, the isoclinic parameters in transverse slices were determined by geometric considerations alone.

b. Separation of Stresses

The method of numerical integration of the differential equations of equilibrium was chosen for separation of the components of stress. Two alternative approaches to the problem were available, and each was employed where it was the most appropriate. The three-dimensional "shear-difference" method of Frocht and Guernsey (29) is the most generally versatile method. The development by Jessop (30) of the three-dimensional differential equations of equilibrium along a stress trajectory is preferable for the particular case where the stress along the intersection of two planes of symmetry is to be determined.
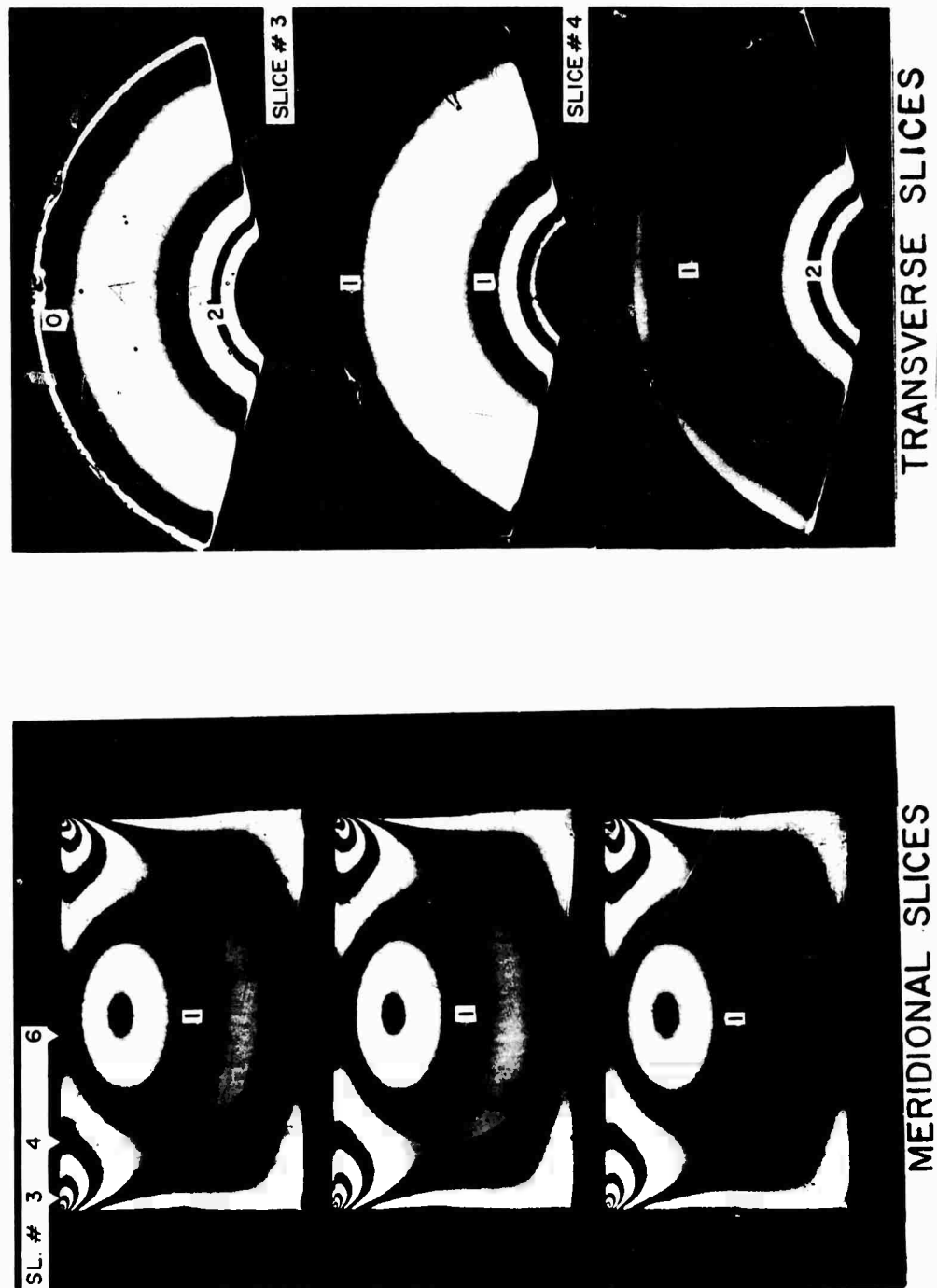
Figure 103. "Frozen" Stress Photoelastic Patterns in Meridional and Transverse Slices

IV, B, Photoelastic Studies of Solid Propellant Grain Stress Distribution (cont.)

c. Stress Distributions

Two sections were selected for determination of the three components of principle stress. The first, shown in Figure 104, is a radial line in the transverse plane of symmetry; the points represent the stresses determined from the photoelastic "frozen" stress data. The solid and dashed curves represent the calculated results obtained by the method of Messner (31) for two values of Poisson's ratio. It is seen that the experimental data agree quite well with the calculated result for a Poisson's ratio of 0.5.

Stresses along the longitudinal line of the bonded grain-case interface are shown in Figure 105. The agreement of the test points with the calculated curves for $v = 0.5$ is again evident. The experimental points indicate extremely high stresses normal to and tangential to the bond very near the corner. Bond shear stresses, which are not shown, also exhibit a high peak near the corner.

Qualitative evidence of overall agreement between theory and experiment is given by Figure 106. At the top is a plot of the calculated principal stress differences for an arbitrarily assumed thermal cycling condition in a real propellant. The "fringes" thus formed are strikingly similar in their distribution and shape to the photoelastic "frozen" stress fringes shown in the meridional slice photograph at the bottom of the figure. The uniform thickness of this slice was deliberately chosen so as to produce approximately the same order of fringes in the two patterns, and visually demonstrates the agreement. The agreement between theory and experiment indicates that the new photoelastic technique can be applied effectively to practical problems of case-bonded grain thermal cycle stress analysis.
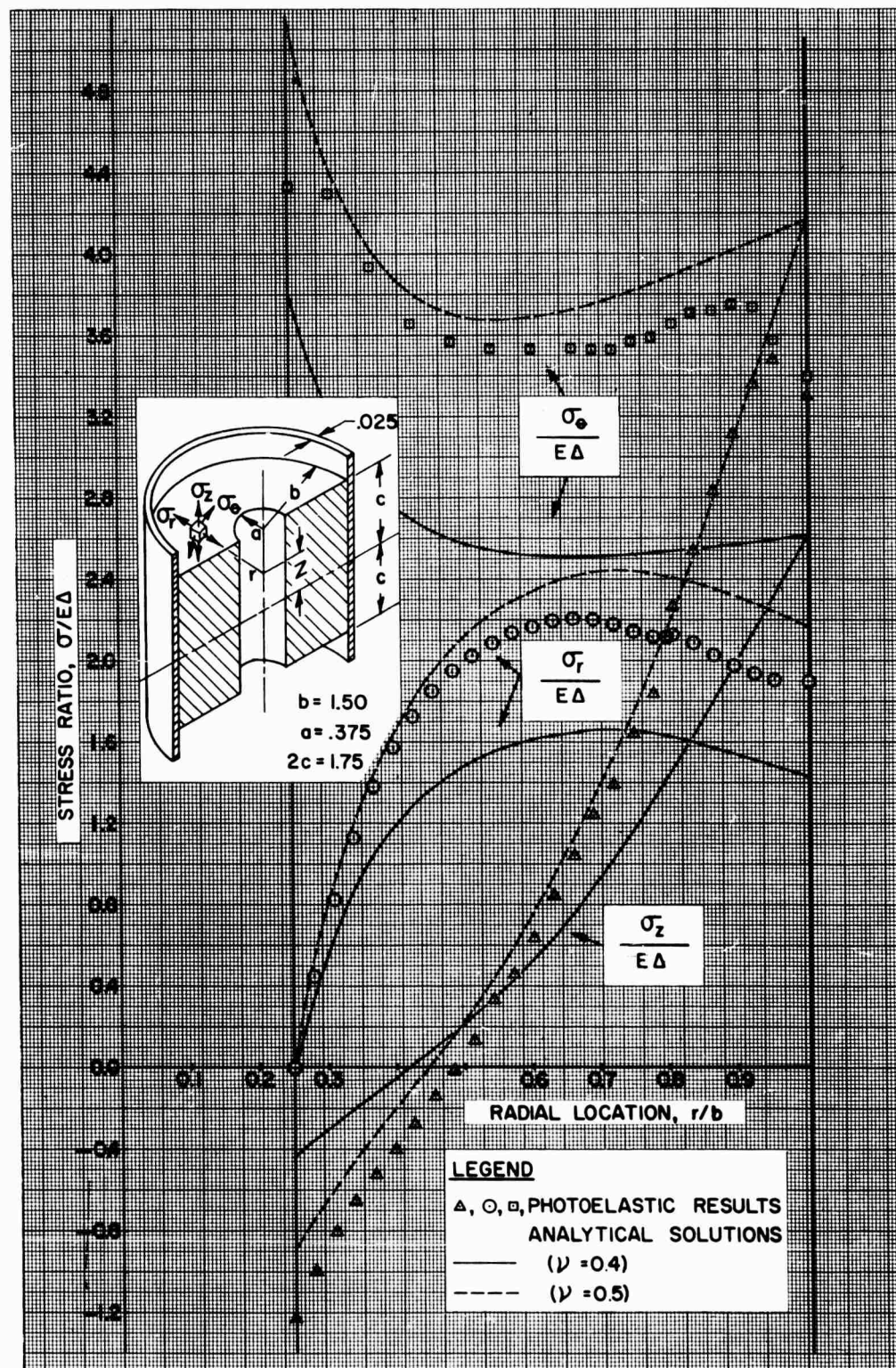
Figure 104. Stress Distribution on the Plane of Symmetry, Z = 0, in a Case-Bonded Cylindrical Bore Grain Subjected to Thermal Cycling Stresses
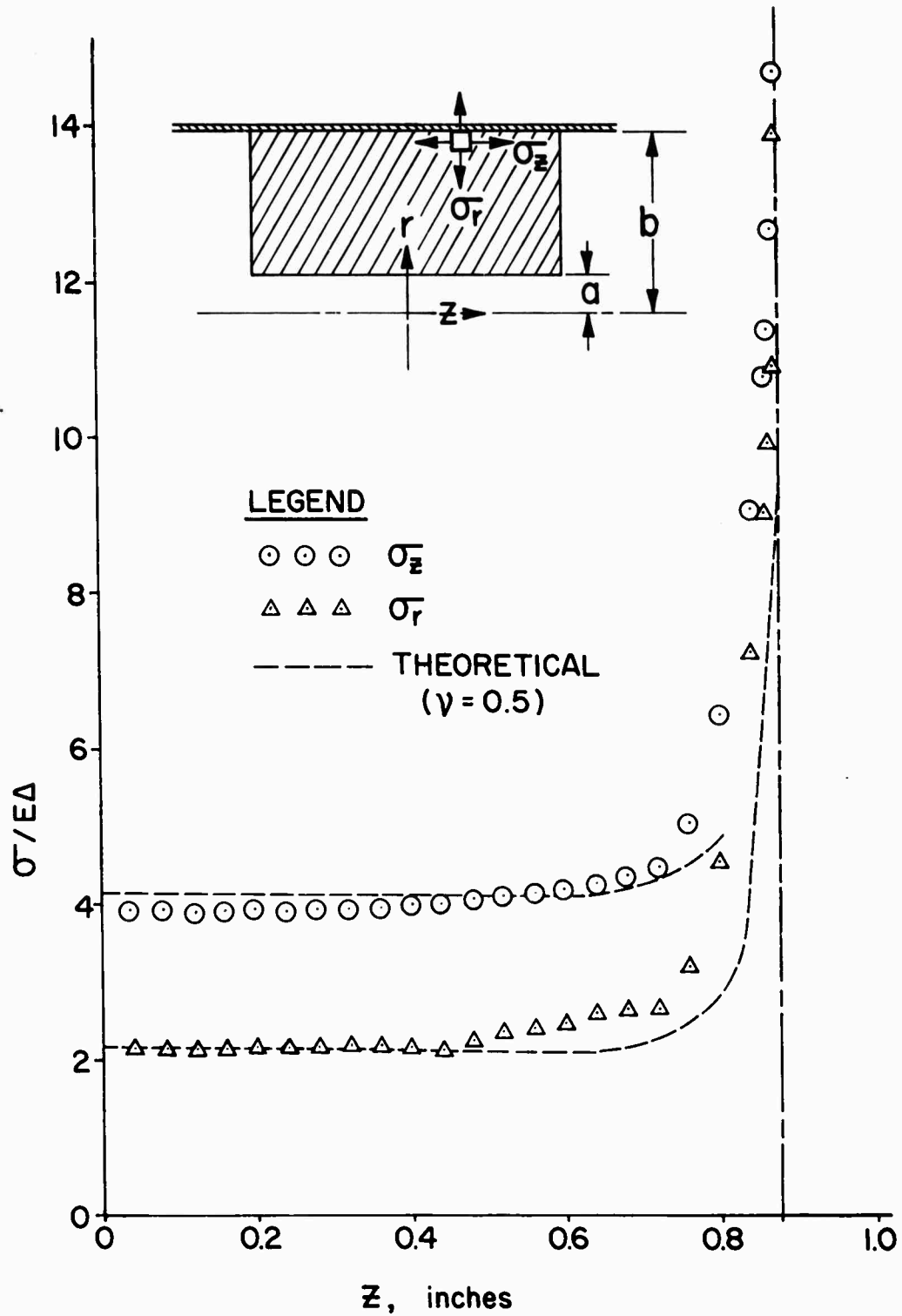
Figure 105. Normal Stress Distribution at r = b in a Case-Bonded Cylindrical Bore Grain Subjected to Thermal Cycling Stresses

ANALYTICAL SOLUTION

PHOTOELASTIC FRINGE PHOTOGRAPH
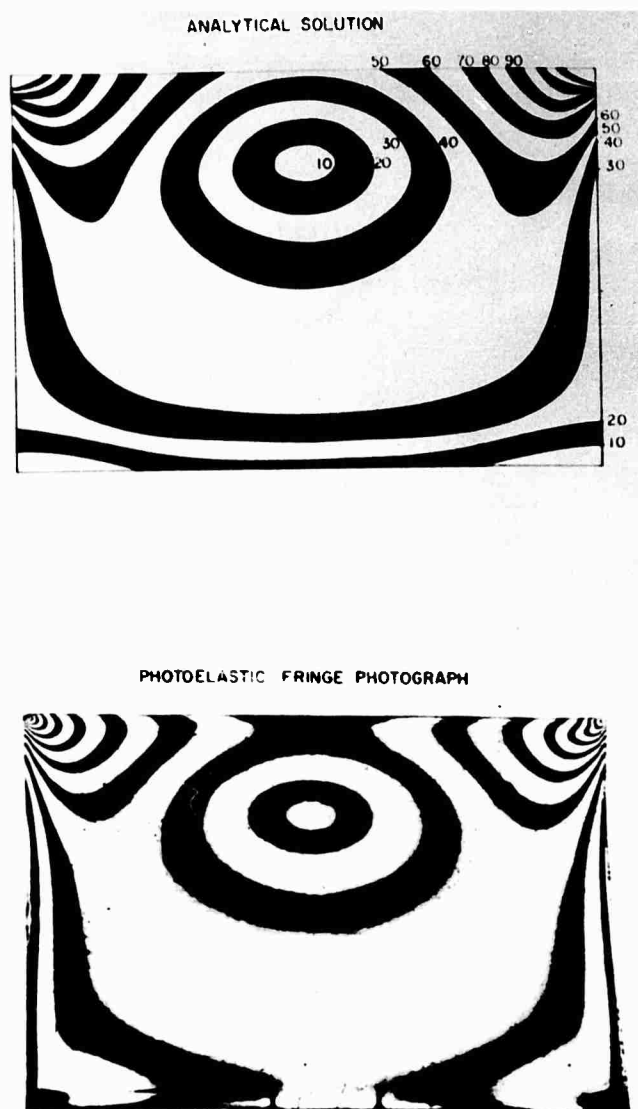
Figure 106. Comparison of Experimental and Analytical Contours of Constant
Principal Stress Difference   (11-61S 29387)

IV, B, Photoelastic Studies of Solid Propellant Grain Stress Distribution (cont.)

4. Photoelastic Analysis of a Grain Sector

A comparison of the stresses in a grain model using normal circumferential pressure loading was made with those of a segment of a grain model loaded in tension along the edges of the segment. A six-point star grain model of rigid photoelastic material (C.R.39) was tested under the normal loading method of applying a uniform external pressure to the circumference of the model. A 60° segment was cast of urethane rubber the same size and shape as one sector of symmetry of the original model. A sheet of plate glass cemented to each edge of the segment formed lips along the edges of the segment. The load was applied to the specimen by wedging the glass plates apart with two lucite wedges cut to a 60° angle to fit the edges of the segment model. One wedge was placed on each side of the model to put the model in tension without bending or changing the angle of the segment. A schematic drawing of the method used is shown in Figure 107.

Figure 108 shows the star point stress pattern in a portion of the full six-point star model under uniform external pressure. Figure 109 shows the resulting stress pattern in the grain segment model. Figure 110 is a graph comparing the fringe order variation taken from these two models at the star point web. The test results indicate that the new method produces photoelastic stress patterns which are very nearly those of full grain model subjected to uniform pressure. This significant result gives a technique for checking embedded gages and other remote devices against optical surface methods made easily accessible in the critical region of the star point.

APPLIED LOAD

LUCITE
WEDGES
(FOR LOADING)

URETHANE RUBBER
SPECIMEN

GLASS PLATE

GLASS PLATE
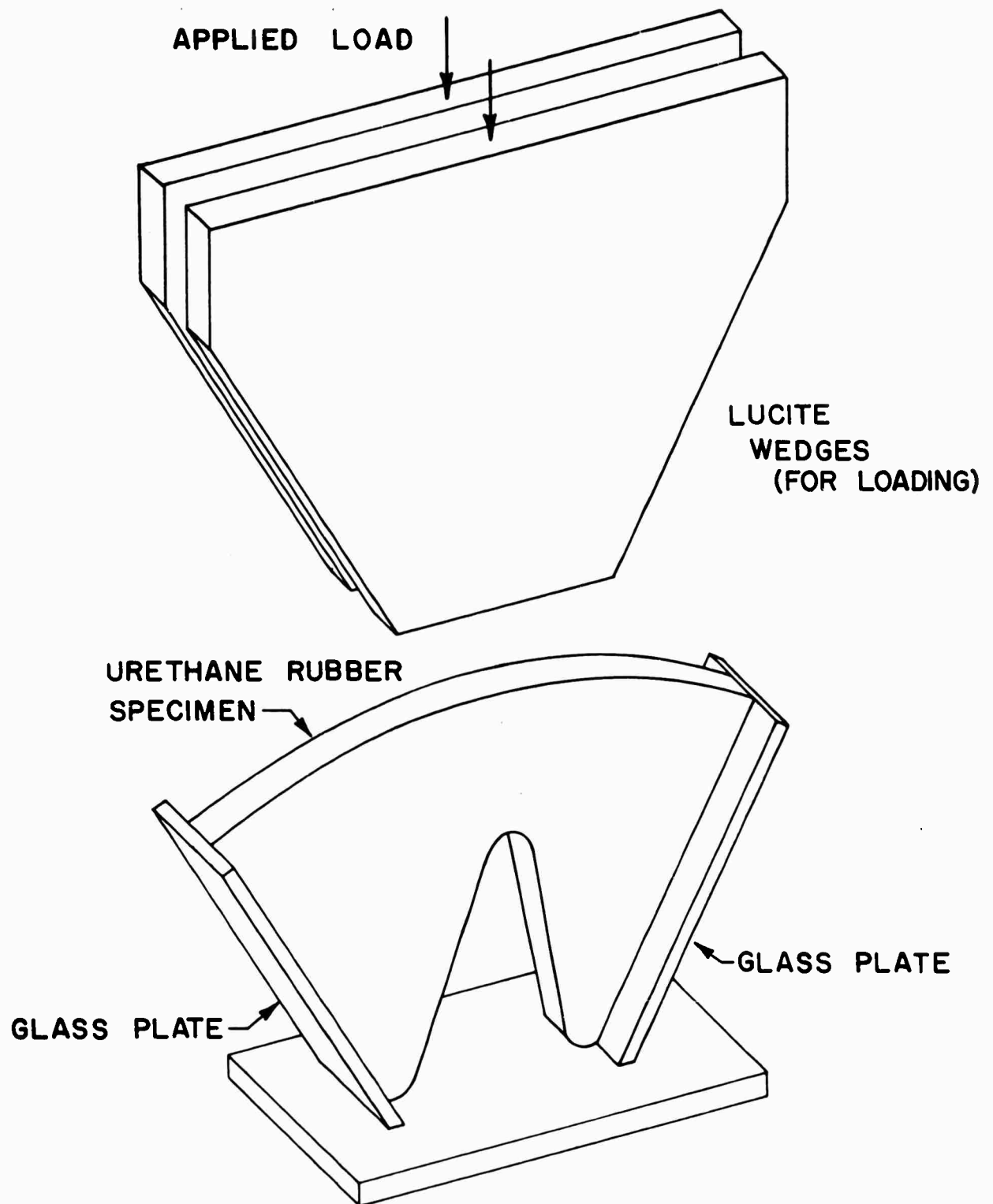
Figure 107. Loading Method
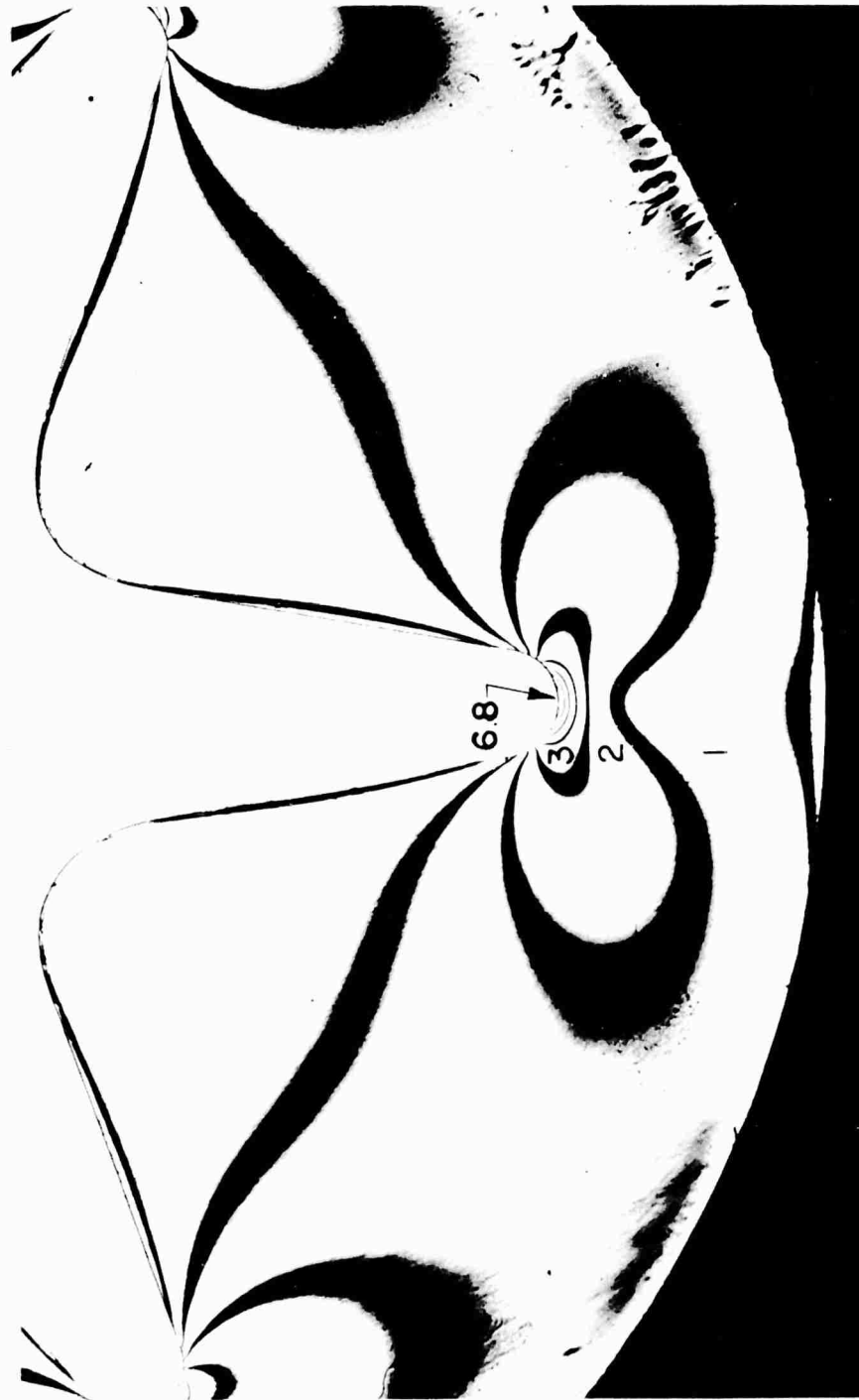
Figure 108. Fringe Pattern at Star Point of Full Grain Model
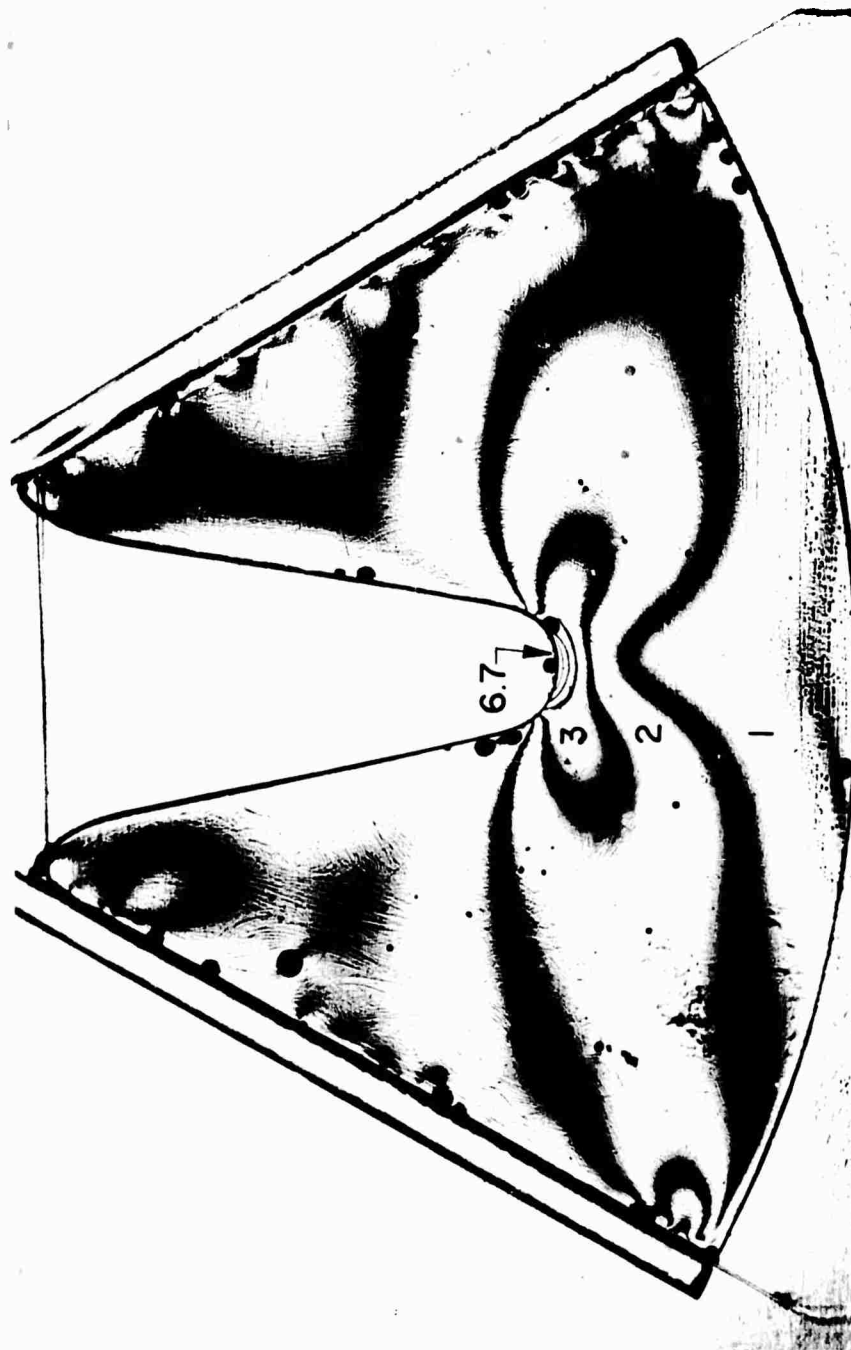
Figure 109. Fringe Pattern at Star Point of Segment Grain Model

FULL GRAIN	
n	X
6.8	0.0000
6.5	0.0083
5.5	0.0213
4.5	0.0393
3.5	0.0653
2.5	0.1066
1.5	0.2200
0.5	0.8966
0.4	1.0000

SEGMENT	
n	X
6.7	0.0000
6.5	0.0065
5.5	0.0242
4.5	0.0424
3.5	0.0685
2.5	0.1121
1.5	0.2424
0.5	0.8685
0.3	1.0000
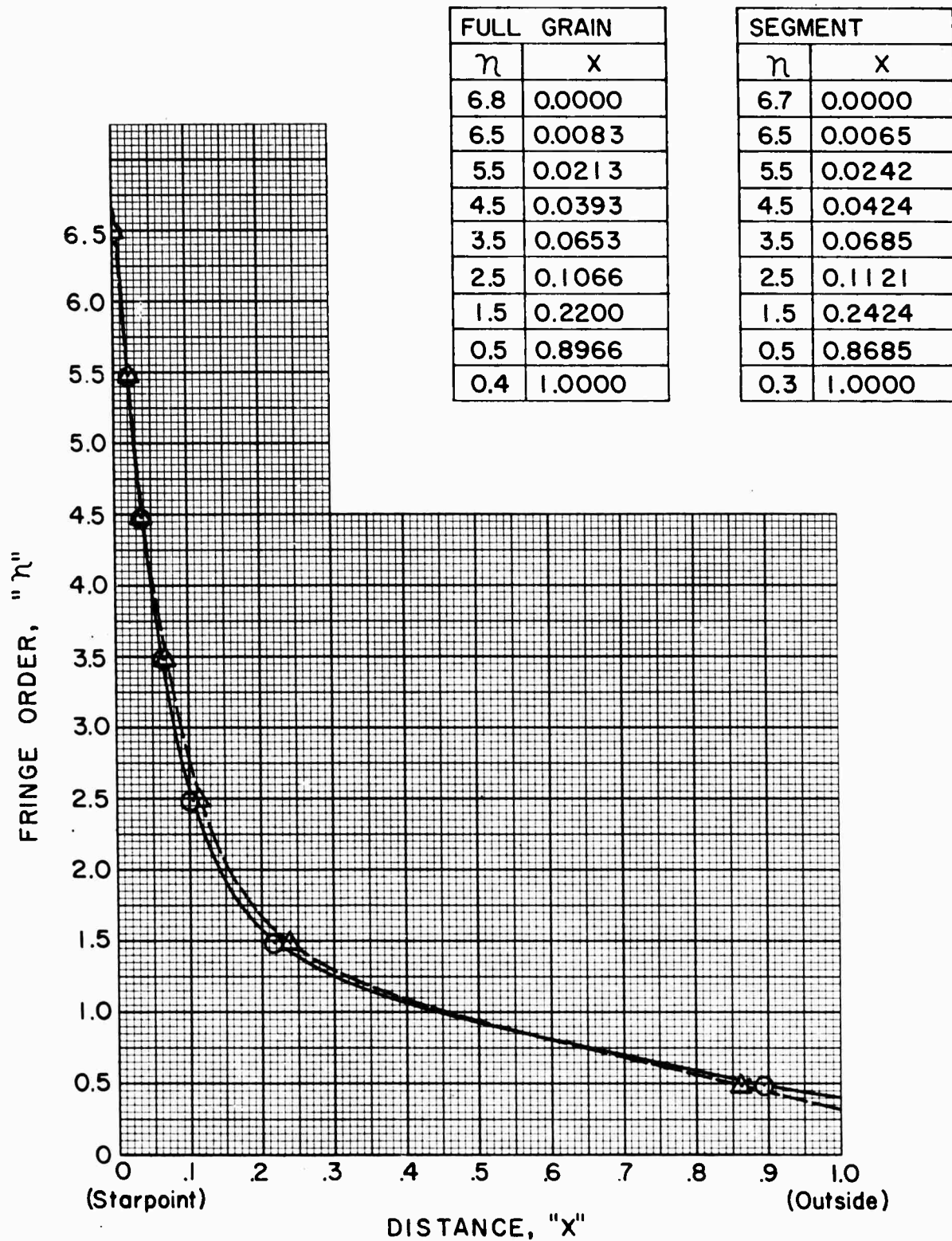
Figure 110. Fringe Order

Page 217

IV, Phase 3—Theoretical and Experimental Stress Analysis (cont.)

C.   DEVELOPMENT OF NEW METHODS OF STRAIN MEASUREMENT

Calculation methods are available, as well as photoelastic tech-
niques, for the determination of strains and stresses in simple grain shapes.
The verification of the applicability of these methods to real propellant grains,
the determination of the limits of applicability due to non-linearity, viscoelas-
ticity, and the measurement of change of volume with strain, all require ade-
quate methods of measuring strains and stresses. Recognizing the difficulty of
the measurement problem, a subcontract with Dr. Durelli, now at Catholic
University, was placed with emphasis upon measurement in localized high strain
regions. Studies also proceeded at Aerojet-General Corporation, where two
methods of electronic remote measurement of strain were developed, the spring
clip gage and the bore spring gage. The suitability of the Moire fringe technique,
studied by Dr. Durelli for other uses, was confirmed where the surface is avail-
able for visual study. Transducers for normal force, or strain, shear were
shown promising but final development for motor use will require much further
work.

1.   Survey and Development of Methods for the Determination of Strains in Solid Propellants (Catholic University)

The determination of strain requires the precise measurement
of length. Four types of measuring devices are suggested: (1) an attachment
to the propellant which will record changes in length, (2) embedding a pre-
prepared gage in the propellant with similar mechanical properties to those of
the propellant, (3) measurement of deflections inside the core opening, or
(4) marks on the propellant that can be recorded without the use of an attachment.
The first two alternatives introduce the problem of reinforcement. The pro-
pellant material is so soft that any known strain measuring device which must be

IV, C, Development of New Methods of Strain Measurement (cont.)

attached to, or embedded in, the specimen will have some influence on the stress and strain present in the material. Thus, it is necessary to somehow relate the recorded strain to that strain that would have been present had the strain measuring device not been there. The third alternative is an indirect method that requires some assumption to establish the relationship between strains in fillets and displacements inside the perforation. The fourth alternative suggests an optical system, although there are other methods to record marks on the surface.

The problems associated with these types are discussed in Appendix B and experiments on several devices are described. It would appear that optical methods are still the best available and electronic remote recording is not yet practical. Further work on this problem is urgently needed to develop apparatus suitable for use on large motors.

2. Moire Fringe Technique

A technique discussed in Appendix B for measuring plastic deformation in metals and plastic materials, which shows promise for polymers, is the Moire fringe effect. This method has the advantage over the photoelastic method in the data reduction is not tedious, that special materials (birefringent polymers) are not required, and that with the use of sufficiently fine screens it is possible to measure elastic as well as plastic strain regions.

The Moire effect is an optical phenomenon produced when two somewhat similar arrays of dots or lines are superimposed optically, resulting in the formation of alternating light and dark fringes. In practice, if one places fine, regularly spaced lines or an undeformed propellant specimen and also on a transparent overlay screen and then deforms the test piece, Moire fringes will be formed. This provides the basis from which the amount of deformation may be calculated.

IV, C, Development of New Methods of Strain Measurement (cont.)

The procedure for measuring incremental strain fields by the Moire effect is as follows: The propellant specimen (with grid) is deformed under load and at each incremental deformation step, pictures are taken of the Moire fringes. The master screen is superimposed on the specimen with the lines of the screen parallel to the original direction of the lines on the undeformed specimen. Strain measurements are then made from the prints by choosing a convenient coordinate system and drawing coordinate lines on the pictures. The distance between the interference fringes are measured along these coordinate lines in both directions.

A schematic diagram showing the Moire fringes on a sample strained uniformly in tension in a direction perpendicular to its screen lines, with the master screen superimposed onto it without rotation, is shown in Figure 111.

To obtain the necessary interference fringes, each nth line of the undeformed master screen must interfere with every $(n-1)^{th}$ line of the elongated specimen grid or with every $(n+1)^{th}$ line of the compressed specimen grid. From the distance between two neighboring screen lines, a, and d, the distance between two neighboring interference fringes in Figure 111, the conventional elongation ε is expressed by

$$n a = d = (n-1) a (1 + \varepsilon) \tag{76}$$

hence

$$\varepsilon = \frac{a}{d - a} \tag{77}$$
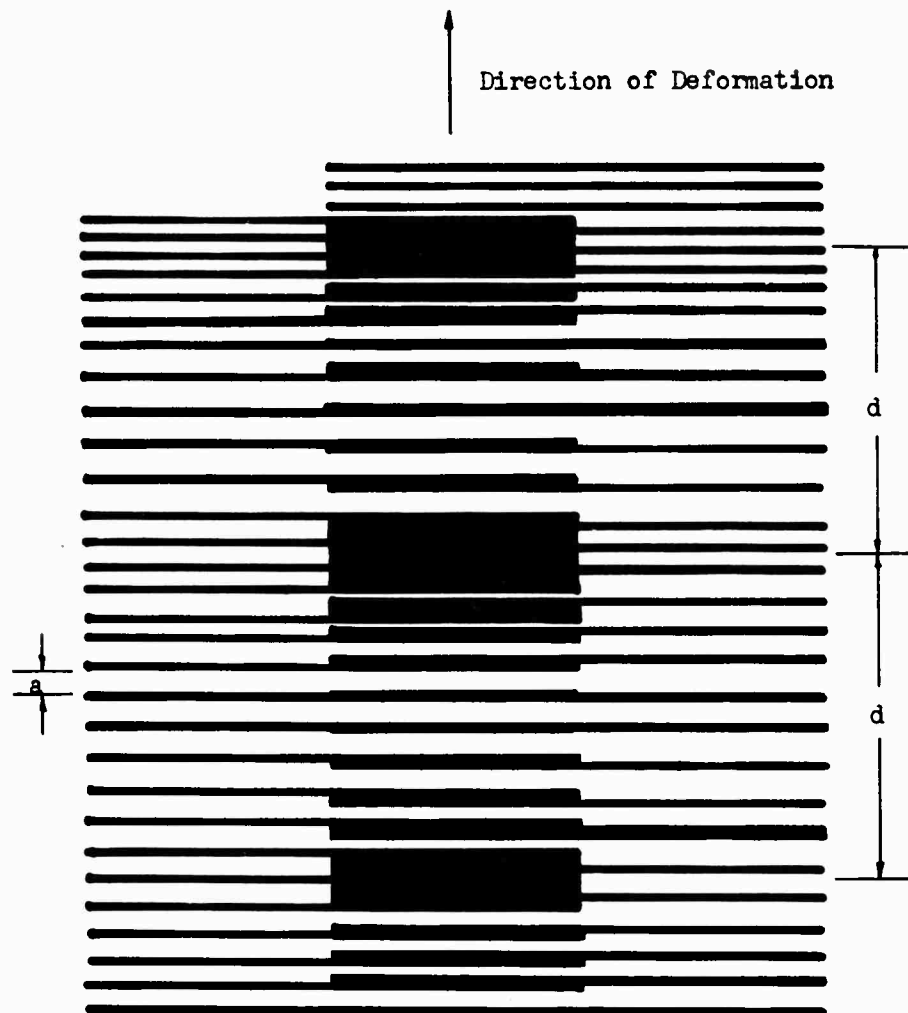
Figure 111. Schematic Diagram of the Moire Fringe Effect

IV, C, Development of New Methods of Strain Measurement (cont.)

in the case of compression

$$\varepsilon = \frac{a}{d + a} \qquad (78)$$

It is not always possible to determine at once at every point whether the strain is elongation or compression. If, however, the nature of the test or the sign of the deformation is known at one point, it is possible to determine the state of deformation at all neighboring points.

The Moire fringe method was used on a standard JANAF tensile specimen and a simple tension tear specimen. A grid of 70 lines per inch was printed on each of the specimens by the silk screen process. Care was taken to ensure that the propellant surface was smooth and defect-free. A corresponding master grid was prepared, by the same process, on a sheet of 1/8 in.-thick plexiglass. The tensile bars were tested at a crosshead displacement speed of 2 and 20 inches per minute and color photographs were taken at various sample displacements. Experiments have shown that a better black and white edge definition is obtained when the photographs are taken in color than in black and white.

Representative strain patterns at 7.5 and 22.5% strain, as calculated by standard JANAF data reduction methods, are shown in Figure 112, where the non-uniformity of fringe distance caused by non-uniform dewetting can be seen. The local strains were calculated at four places on the sample. A comparison of these strains at each overall sample strain level is shown in the following table:

A - Strain 1   B - Strain 2

Figure 112. Distribution of Moire Fringes on Standard JANAF Specimen During
Deformation

IV, C, Development of New Methods of Strain Measurement (cont.)

Overall Sample Strain, %	Position	Fringe distance, in.	Local Strain, %
7.5	1	.240	6.3
	2	.240	6.3
	3	.200	7.6
	4	.185	7.5
22.5	1	.091	18.9
	2	.080	22.7
	3	.061	28.6
	4	.105	15.7

These data demonstrate that the technique is applicable to propellant systems as well as metals and plastics. By proper selection of grids (large spaces between lines for large strains and fine lines for small strains) accurate measurements should be possible at any level of anticipated strain.

Testing of the simple tension tear specimens gave a more complicated condition of strain. Upon initial straining, fringes perpendicular to the direction of straining were observed. Upon initiation of a tear front, shear-type fringes were noted, as shown in Figure 113. An analysis of the strain pattern was not made as the picture was further complicated by the rotation of the sample as it tore. Therefore, part of the fringe pattern is due to this rotation. Methods for calculating the strain pattern when one of the grids is rotated are available.

3. Spring Clip Gage

An external clip gage has been developed for measuring linear deformations without applying significant force to the propellant surface. The gage consists of a 0.5-in.-wide strip of .002-in.-thick feeler gage stock bent into a half circle of approximately 0.5-in. radius. Strain gages are glued, two on the inside and two on the outside, of the curve of the clip to form the standard
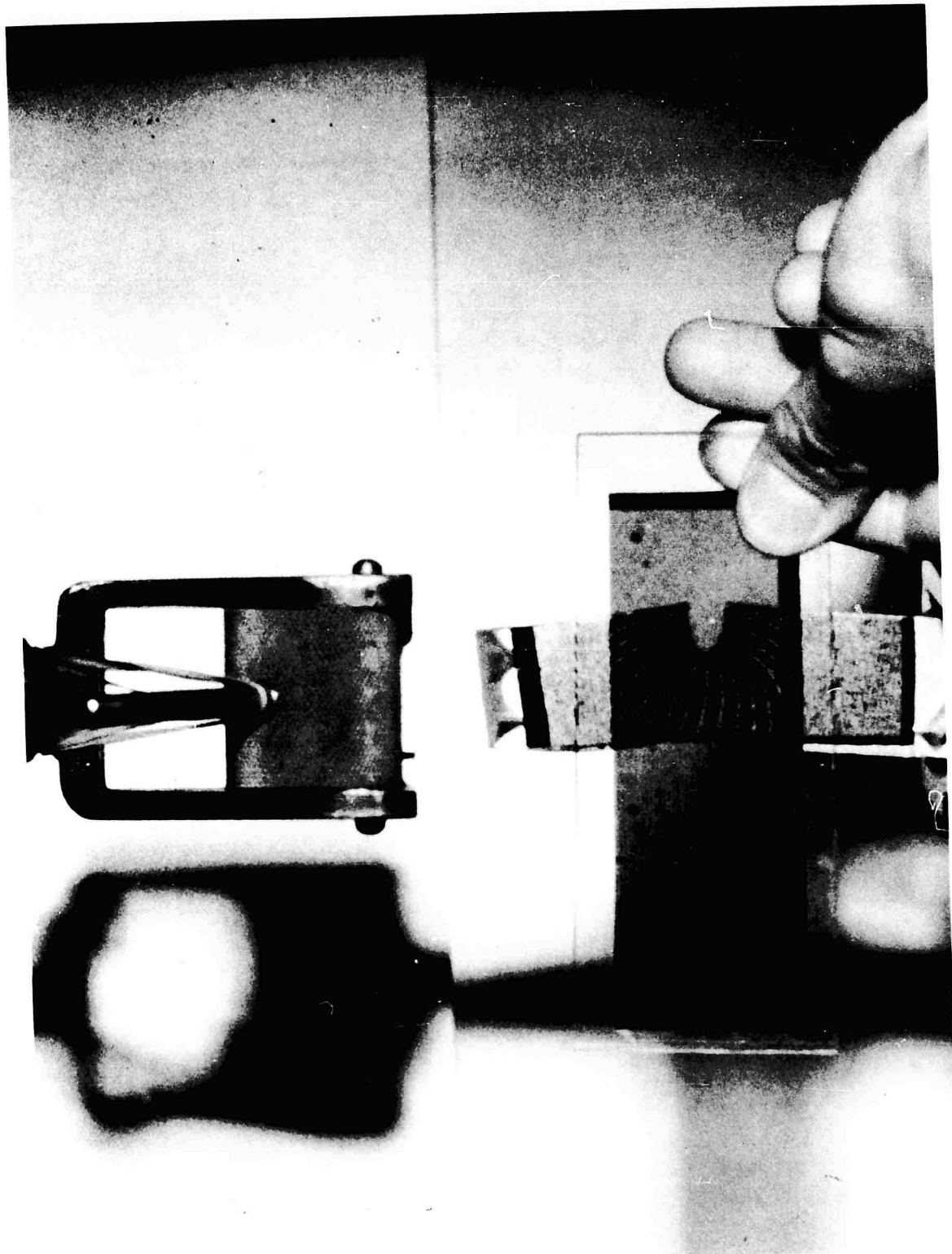
Figure 113. Moire Fringe Effect Produced Around Tear Front (262 221)

IV, C, Development of New Methods of Strain Measurement (cont.)

strain gage bridge configuration of two gages in compression and two in tension. The gage is shown in Figure 114. The clip is designed so that the tips of the gage will spring outwards from its centerline in order to follow the motion of a stretching specimen. When not in use, the gage is restrained by a safety clip; it is also provided with a limiting wire to prevent overstraining on failure of the specimen.

Calibration of the gage is performed by setting it between the jaws of a bench micrometer, and the span of the recorder set to correspond to the maximum extension desired. Although the clip gage tested was not linear, the calibration was repeatable to about 0.02% of full scale, and hysteresis was not detectable. The gage was wired into a four-prong plug and plugged directly into an Instron load cell plug so that the Instron recorder could be used to record extension. Until the clip gage broke a strain wire after two week's use, it performed as expected.

4. Force Transducer

Initial development of a force transducer was along the line of a hollow column of rubber having a multiple-wrap circumferential strain gage measuring the transverse expansion of the column when subjected to axial load, as shown in Figure 115. Testing showed that this design was not practical for the use desired. In obtaining the necessary deformation of the transducer, to match the modulus of elasticity of the propellant, the rubber expanded sufficiently to force the strain gage wire to embed itself into the sides of the rubber column rather than expand with it and give a true indication of the deformation to which the transducer was being subjected.

Figure 114. Spring Clip Gage With Safety Clip in Place (7-61S 18664)
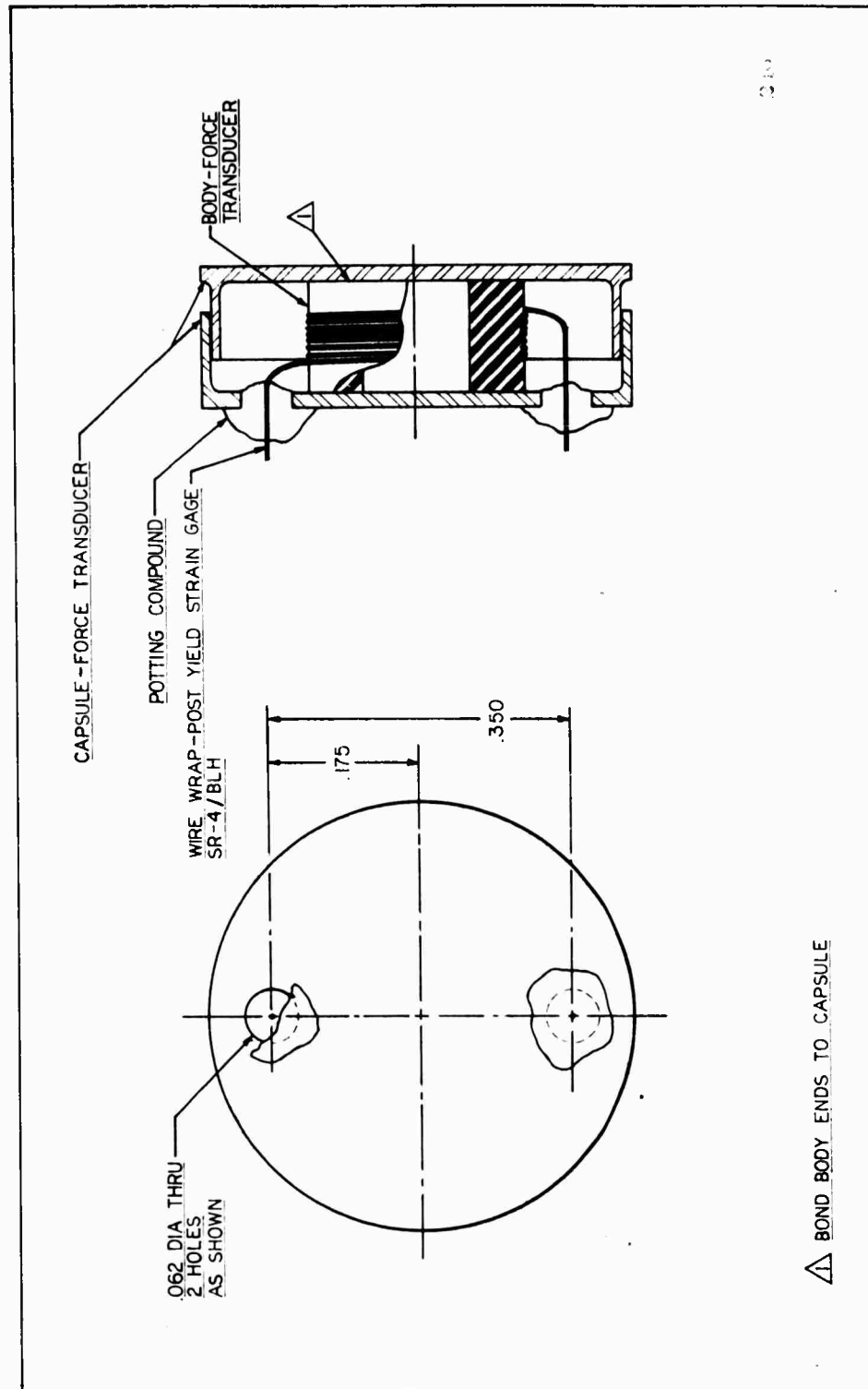
Figure 115. Force Transducer

IV, C, Development of New Methods of Strain Measurement (cont.)

The second type of force transducer consisted of a strain-gaged cantilever beam mounted in a capsule to form a transducer having sufficient deformation to match the modulus of elasticity of the propellant. The over-all size of this transducer was approximately 0.50 inch in diameter by 0.17 inch long and having the capability of shortening by approximately .035 inch. This transducer, shown in Figure 116, was manufactured as a metallic capsule with telescoping sides and the strain-gaged beam mounted inside with the spring constant of the transducer being formed by rubber blocks cemented to the ends of the capsule. The telescoping eliminated the shear effect and thus caused the transducer to sense only normal forces applied to it by the propellant. The small size of the transducer significantly reduces the stress field disruption caused by larger transducers. Preliminary data were promising but time did not permit complete development of the gage.

The third type of transducer consisted of a fluid-filled bellows embedded in the propellant grain and inter-connected to a crystal pressure transducer by a very small diameter tube. It was found that in order to account for absorbed air and tube expansion it was necessary to pre-pressurize this system to approximately 85 psi prior to installation in the chamber. A preliminary model was cast in a silicone rubber block (VT601) and worked satisfactorily with linear response for many cycles. Temperature effects were not investigated due to lack of time but the gage looks promising for further study.

5.   Embedded Strain Transducer

A number of tests were performed to evaluate a helical strain gage built by Baldwin-Lima-Hamilton for use in propellant. This gage consisted
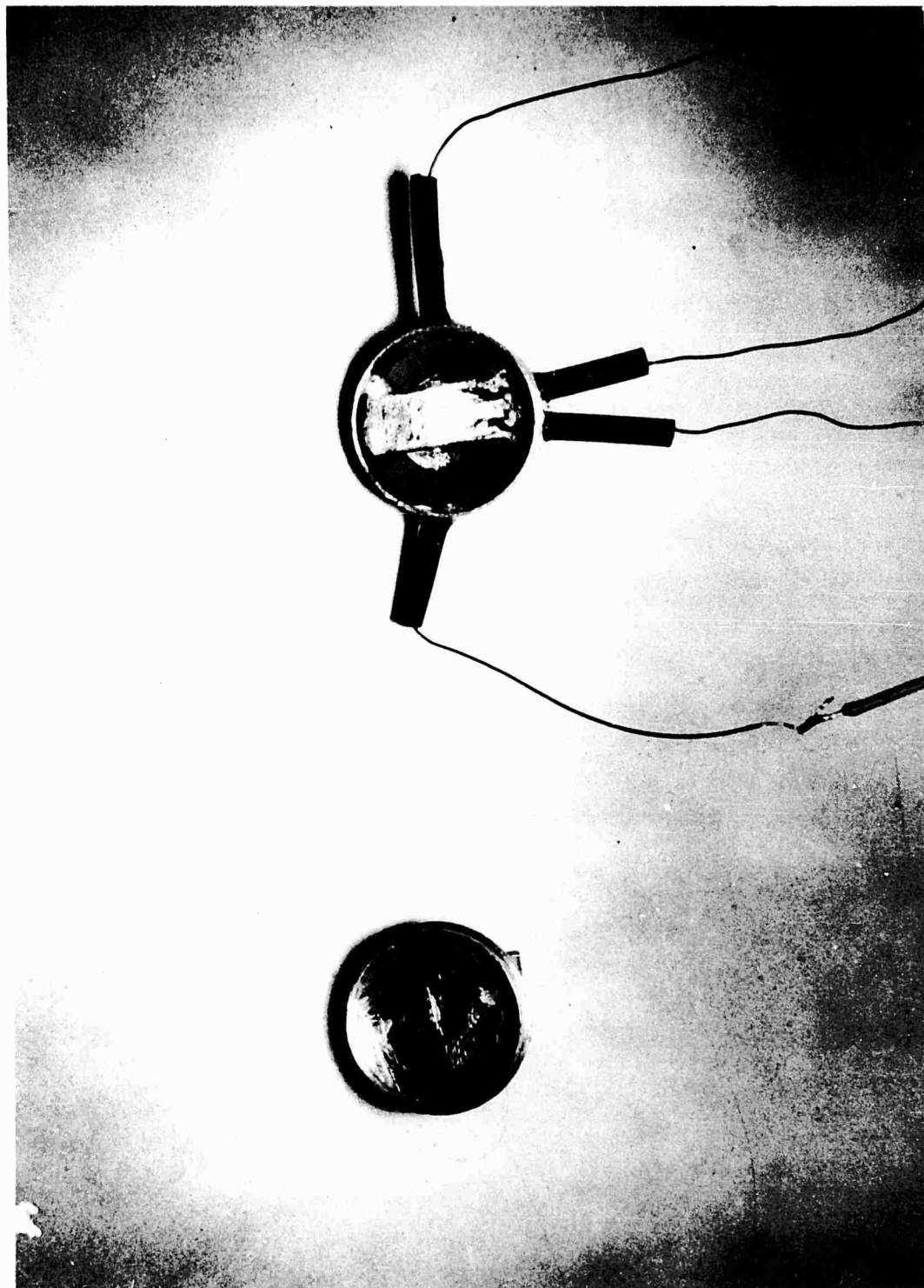
Figure 116. Cantilever Beam Mounted in Capsule for Force Gage (12-60S 33167)

IV, C, Development of New Methods of Strain Measurement (cont.)

of a half bridge formed by a foil strip mounted on a helically wound backing. The diameter of the helix was approximately 0.25-in. and the length 1.0-in. In air the gage showed approximately 500 microinch strain for a deflection of 50%. When cast into propellant or inert polyurethane rubber it showed a strain of approximately 6000 microinches for a deflection of 25%. Repeatability and sensitivity appeared reasonable, but the gage was very difficult to calibrate and the lead attachments were hard to make. As a gage was sought with the capability of 70% deformation, this gage was dropped from further investigation.

D. CALCULATION OF STRESSES AND STRAINS

Present propellant grains were designed initially to meet ballistic requirements; the necessary structural characteristics for successful operation having subsequently evolved by trial and error. As higher performance motors are developed and attempts are made to improve the reliability of existing motors, a more detailed knowledge of the stresses developed in the various configurations becomes increasingly important. The inadequate consideration given to structural characteristics in propellant grain design has not been due to a lack of interest in the problem but to a lack of ability to calculate the stresses and strains in these configurations. Attempts to solve these problems by a simple technique have met with failure and it has been necessary to develop elaborate analytical methods and to use digital computers to obtain adequate solutions.

The stress analysis of complex geometries can be considered as two distinct steps. These are first, the problem formulation or setting up of determining differential equations to be satisfied; and second, the solution of the equations. As an example illustrating the options available in each of these

IV, D, Calculation of Stresses and Strains (cont.)

steps consider the stress analysis of an axisymmetric finite cylinder: First, the problem formulation can be done by setting up a pair of second order differential equations in terms of either displacements, with the advantage of enabling the satisfaction of displacement, stress, or strain boundary conditions; or stress functions, with the advantages of removing the $1/r$ dependence from the partial differential equations, thus yielding a smoother function to find, and the stresses can be found for incompressible materials. Second, the solution of the above formulated equations can be approached using several methods. Two of these methods are first, Fourier series or other infinite series solution, and second, finite difference numerical solution using a suitable grid spacing. Three grid spacings can be used: equal spacing of straight grid line in each direction, for which a good error analysis is available; variable spacing of straight grid lines, which can make the boundary pass through grid points; or one set of straight and one set of curved grid lines, which allows one to follow a curved boundary with the grid lines. The advantages of the various grid spacings have not been fully evaluated, as all of the mentioned methods have not been compared on the same problem having a known analytic solution.

1. Parametric Analysis of Tubular Changes Under Pressurization, Thermal Cycling, and Acceleration Using Stress Functions

One analysis, applied with considerable success to a number of propellant grain problems, is based on classical elasticity theory and stress functions, using finite difference techniques to obtain computer solutions (31). This computer technique requires a different solution for each case and the required time and expense to obtain solutions is not always warranted for preliminary designs. Propellant grain stress analysis solutions were therefore made for a selected set of geometrics and loading conditions so that the stresses and strains in any particular motion can be quickly estimated by interpolating between the solutions presented. The results offer a convenient method of

IV, D, Calculation of Stresses and Strains (cont.)

estimating the stresses and strains in propellant grains where the more precise results of a computer solution of the detailed configuration is not required. The several configurations considered are tubular grains with length to outer radius, L/B, ratios of 2, 3, and 4. The loading conditions and the pertinent properties of the propellant and case are as follows:

PROPERTIES AND LOADING CONDITIONS USED IN ANALYSIS

The following mechanical properties, constants, and loading conditions were used throughout the analysis:

Linear Coefficient of Thermal Expansion for Case	$c = 589 \times 10^{-8}$ in/in°F
Linear Coefficient of Thermal Expansion for Propellant	$p = 630 \times 10^{-7}$ in/in°F
Poisson's Ratio of Case	$c = .3$
Poisson's Ratio of Propellant	$p = .5$
Modulus of Elasticity of Case	$E_c = 30 \times 10^6$ psi
Modulus of Elasticity of Propellant	$E_p = 1000$ psi
Thickness of Case to Diameter Ratio	$\frac{t}{D} = .00195$ in/in
Pressure Loading	$P = 500$ psi
Acceleration Loading (axial)	$A = 10$ g
Temperature Cycling (equivalent to a cure shrinkage of .5% in linear dimension)	$\Delta T = -79°F$

IV, D, Calculation of Stresses and Strains (cont.)

The structural problems encountered in solid propellant grains can best be explained in Figure 117, which exaggerates the deformations obtained. The figures shown are longitudinal sections of a circular inner bore segment subjected to thermal, pressure, and acceleration loading conditions. The propellant solidifies at its cure temperature and is then stress free in the configuration shown in Figure 117-a. When this motor is cooled down to some operating temperature the propellant tries to assume the shrunken configuration shown in Figure 117-b.

(a) PROPELLANT AT CURE TEMPERATURE

(b) UNBONDED PROPELLANT AT LOWER THAN CURE TEMPERATURE

INTERFACE RADIAL STRESS

(c) CASE BONDED MOTOR AT LOW TEMPERATURE

INTERFACE SHEAR STRESS

(d) PRESSURIZED MOTOR

(e) MOTOR SUBJECTED TO AXIAL ACCELERATION
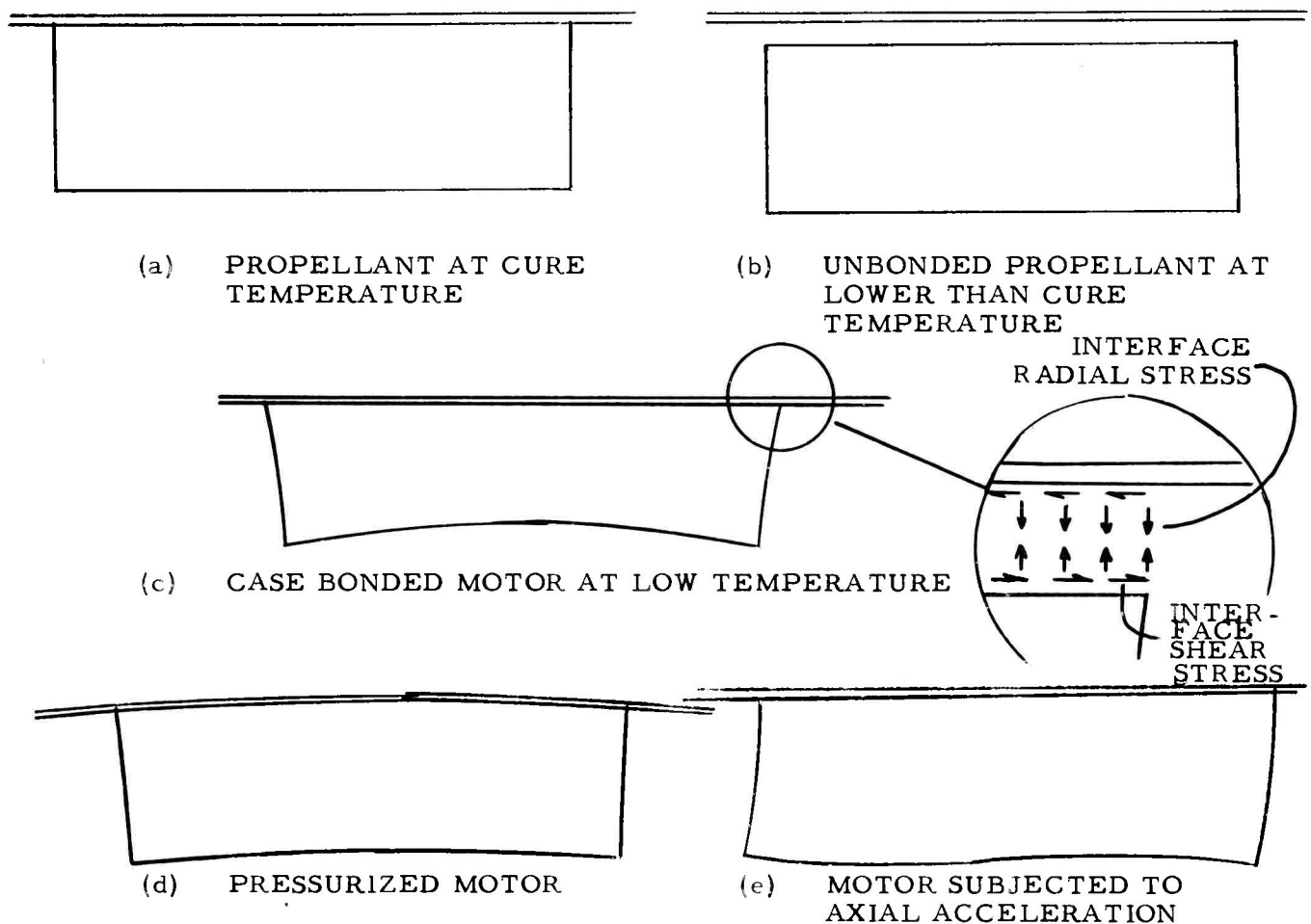
Figure 117 - EFFECT OF THE LOADING CONDITIONS AT SIMPLE GRAIN

IV, D, Calculation of Stresses and Strains (cont.)

Figure 117-c shows the low temperature configuration that results because the propellant is bonded to the case and cannot assume the stress free geometry of 117-b. The inner bore hoop strain is a measure of the percent increase in inner bore radius from Figure 117-b to Figure 117-c. It is important to note that strains are measured from the stress free configuration and not from the initial dimensions. A plot of inner bore hoop strain vs length presents percent change in radius and will have the same shape as the inner bore of the grain.

The circled area of Figure 117-c is redrawn as a separate section to illustrate the meaning of the interface shear stress and the interface radial stress. These two stresses along with the inner bore hoop strain were determined for each configuration and loading condition analyzed in this report. Figures 117-d and 117-e are the deformed shapes obtained by pressurization and acceleration loading conditions, respectively.

It was not possible to include every configuration and loading condition, so it is necessary to interpolate and extrapolate the results to fit a specific case. The loading conditions can be scaled in a linear manner, that is, doubling the change in temperature, pressure, or acceleration will double the stresses and strains presented. The effect of simultaneous loading conditions can be obtained by superpositioning results; thus, the effect of pressure plus temperature can be obtained by adding the pressure solution to the temperature solution. *
The modulus of elasticity cannot be scaled in all instances and where the results are proportional to this parameter it is indicated on the graphs. Where no such information is shown, the results are independent of the modulus. The results were obtained for steel cases and titanium or fiberglass cases would alter the

---

* The maximum strains in star shaped grains can be estimated by superimposing the stress concentration factor on the bore strain of the tube whose radius ratio is the same as that for the web of the star configuration. The estimate thus obtained appears reasonable where large strains producing localized dewetting are not obtained.

IV, D, Calculation of Stresses and Strains (cont.)

results in some instances. Acceleration is the only loading condition dependent on the actual size of the motor and additional acceleration solutions are presented to aid in evaluating the size effect. The detailed curves and the method of uses are given in Appendix C. The maximum bore hoop strains are summarized in Table 21. The strains for temperature cycling are shown in Figures 118 and 119, and for pressurization in Figures 120 and 121.

The maximum shear interfacial stresses and the radial interface stresses at the centerline are given in Table 22 but are not plotted because of the relatively small ranges of values obtained. Interpolation directly from the table would appear adequate.

TABLE 21

MAXIMUM BORE HOOP STRAINS AT ANY POINT

Strain, %

Outer/Inner Radius		2			3			4		
Length/Outer Radius		2	4	8	2	4	8	2	4	8
					Temperature Cycling, $\Delta T = -79°F$					
Ends Bonded	0	1.8	2.3	2.5	2.8	4.2	5.3	3.3	5.7	8.6
	1	2.5	2.6	2.7	4.6	6.0	6.2	6.1	9.4	10.8
	2	2.8	2.8	2.7	7.0	6.4	6.2	12.2	11.1	10.8
					Pressurization, $P = 500$					
	0	1.3	1.5	1.6	2.1	2.7	3.3	2.5	3.7	5.3
	1	1.6	1.8	1.7	3.0	3.8	4.0	4.0	6.0	6.7
	2	1.9	1.8	1.8	4.4	4.1	4.0	7.8	6.9	6.8
					Under 10g Acceleration, $B = 18$-in.					
	0	0.21	0.22	0.22	0.47	0.46	0.44	0.62	0.62	0.59
	1 (aft)	-0.03	-0.01	-0.00	-0.13	-0.06	-0.00	-0.23	-0.12	-0.02
	2	0.12	0.14	0.14	0.29	0.43	0.49	0.40	0.71	0.86
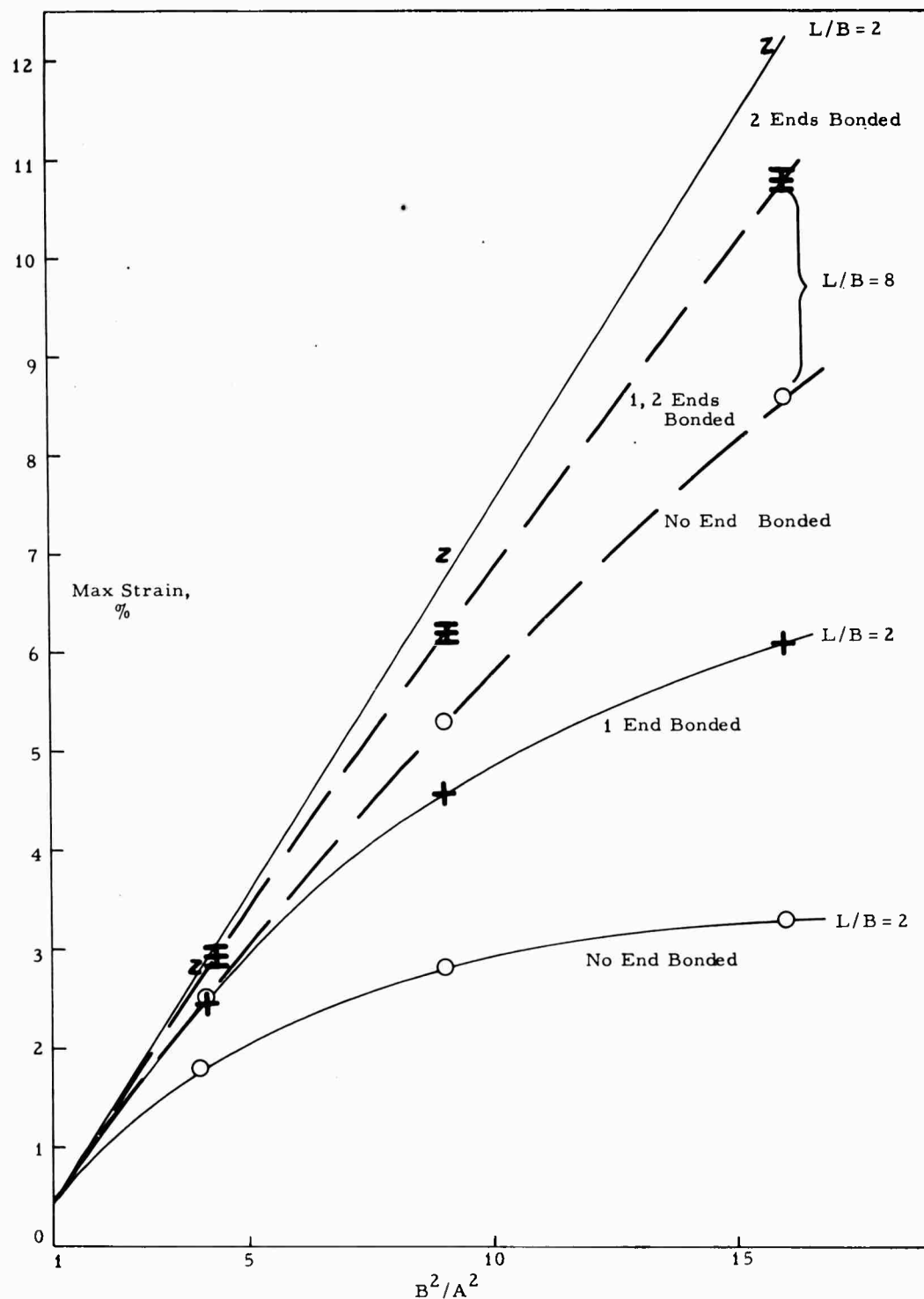
Figure 118. Effect of B^2/A^2 at $L/B = 2$ and 8 on Maximum Bore Hoop Strains by Cooling 79°F
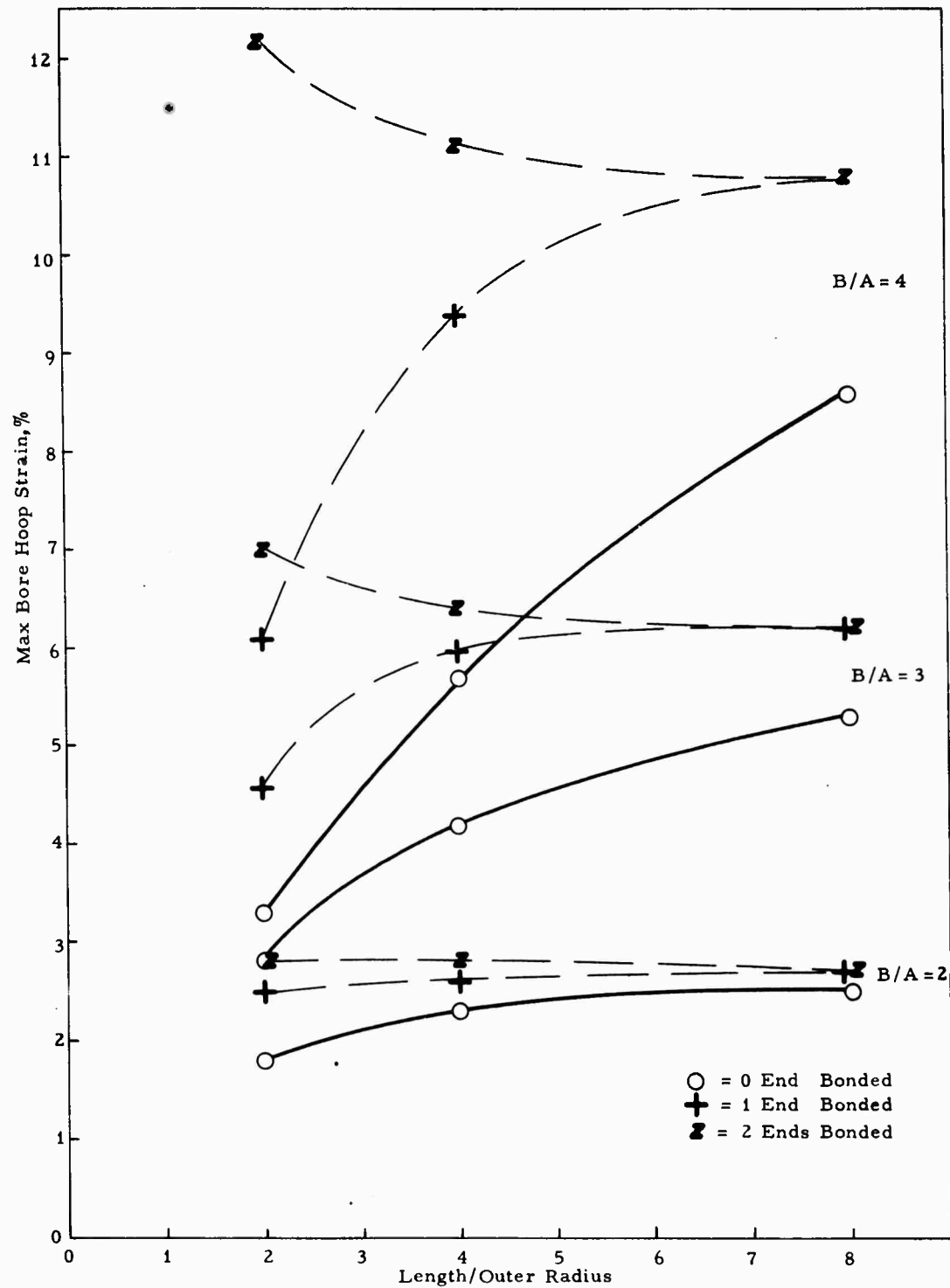
Figure 119. Effect of L/B on Maximum Bore Strain Produced by Temperature Cooling of 79°F for $a_p = 63 \times 10^{-6}$, $a_c = 6 \times 10^{-6}$ in./in./hr
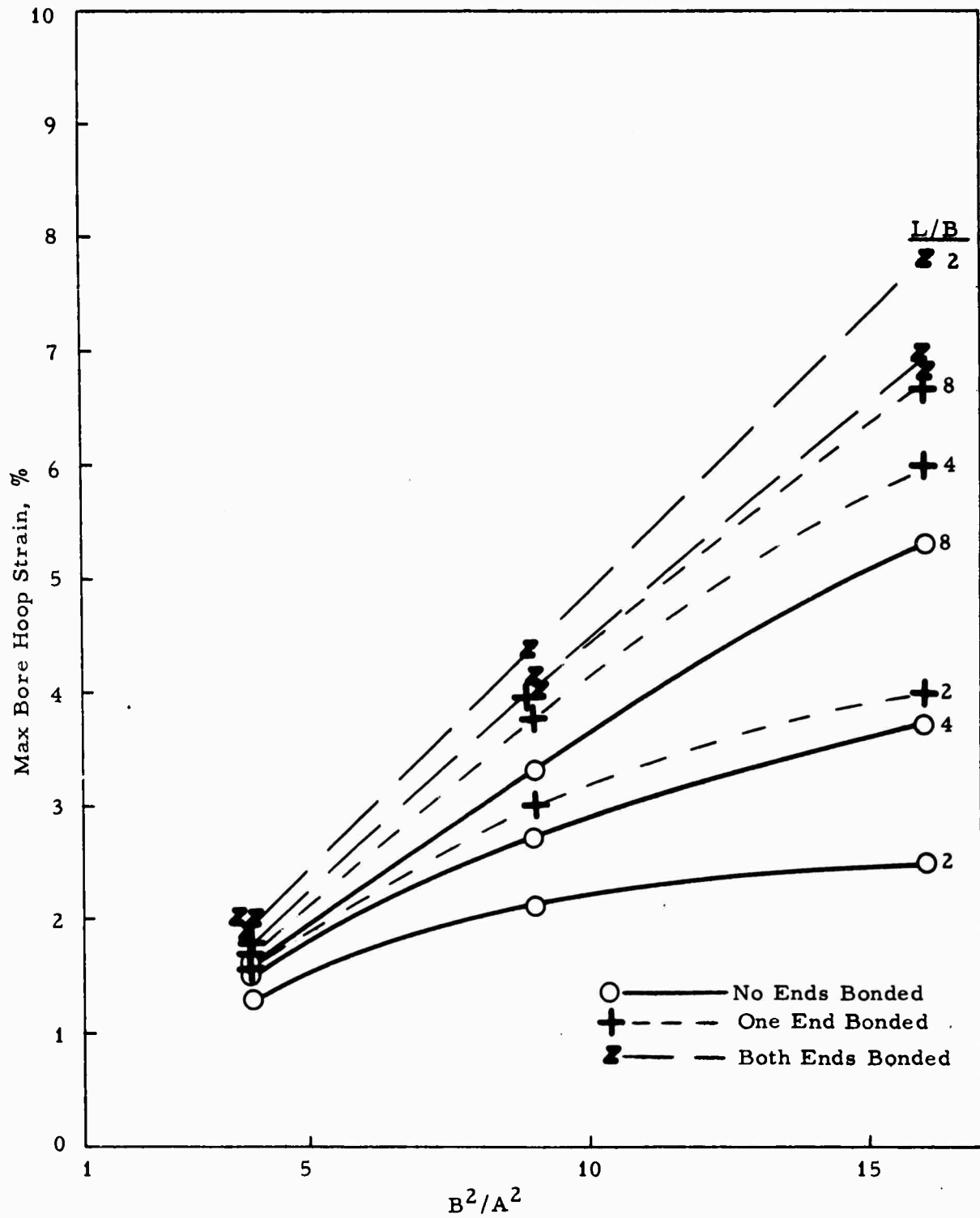
Figure 120. Effect of B^2/A^2 Ratio on Maximum Bore Hoop Strain Produced by a Pressure of 500 psi
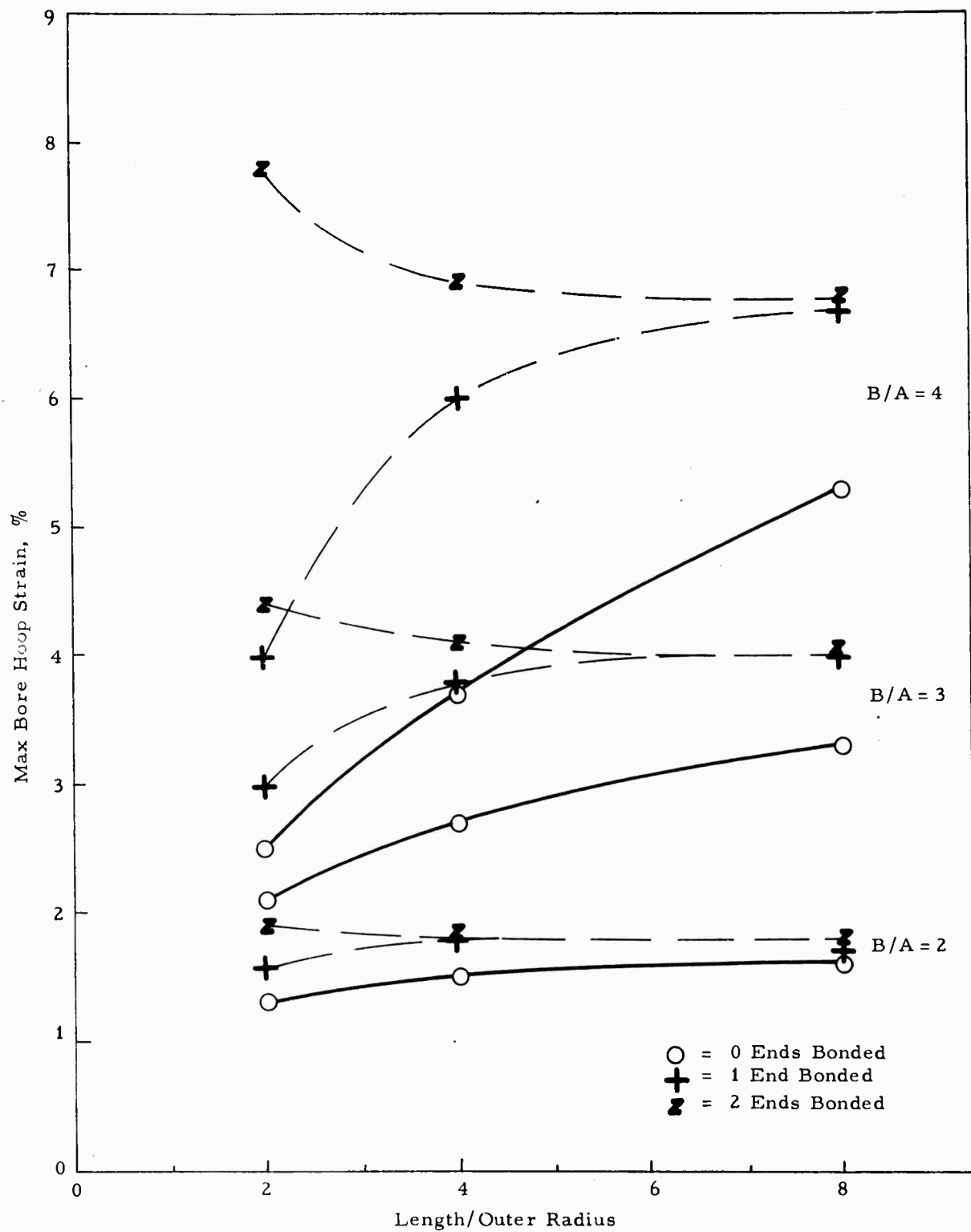
Figure 121. Effect of L/B Ratio on Maximum Bore Strain Produced by Pressurization to 500 psi

TABLE 22

MAXIMUM SHEAR AND RADIAL INTERFACIAL STRESSES ALONG WALL

Stress, psi

B/A		2			3			4		
L/B		2	4	8	2	4	8	2	4	8
Shear[***]; Pressurization, P = 500 psi[*]										
Ends Bonded										
**	0	6.1	6.8	7.0	7.7	11.3	11.2	8.8	13.0	14.8
	1	6.7	6.3	6.5	11.5	11.2	11.0	14.3	15.0	14.8
**	2	4.3	4.3	4.3	4.2	4.2	4.2	4.1	4.2	4.3
Radial[****]; Pressurization, P = 500 psi[*]										
	0	-495	-493	-490	-491	-486	-479	-488	-480	-467
	1	-493	-492	-492	-485	-480	-480	-481	-470	-464
	2	-490	-492	-492	-473	-477	-480	-449	-457	-461
Shear[***]; Temperature Cycling, $\Delta T = -79°F$										
***	0	11.7	13.1	13.5	14.8	18.8	20.2	16.2	22.7	25.5
	1	13.5	13.3	13.3	20.2	20.3	20.2	24.2	26.0	26.3
***	2	5.5	5.4	5.4	5.5	5.6	5.5	5.3	5.4	5.3
Radial[****]; Temperature Cycling, $\Delta T = -79°F$										
	0	7	12	13	11	24	32	14	32	53
	1	10	13	14	20	30	34	29	48	59
	2	15	14	12	43	35	35	78	68	64
Shear[***]; Acceleration of 10g, B = 18-in.										
	0	4.5	4.4	4.4	5.4	5.2	5.3	5.7	5.6	5.6
	1	4.3	4.4	4.4	4.1	5.1	5.3	3.9	5.1	5.6
	2	3.4	4.0	4.2	3.2	4.1	4.8	2.9	3.8	4.8
Radial[****]; Acceleration of 10g, B = 18-in.										
	0	0	0	0	0	0	0	0	0	0
(aft)	1	-0.8	-0.2	0	-2.0	-1.0	0	-3.4	-2.3	-0.5
	2	0	0	0	0	0	0.1	0	0	0.4

[*]   For other than 500 psi, stress = value given x E/1000.

[**]   Values are positive at one end, negative at other.

[***]   Maximum shear stress values are calculated at same fraction of outer radius, B, from end of grain for all cases, the point at which the computation stopped. The true maximum can not presently be calculated, but it is believed these are in the same proportion to each other as are the true maxima.

[****] For radial stresses, the values are read at the center line maximum. The end maxima cannot presently be calculated and the end points on the graph are indicative of the relative trend only. For a true square corner discontinuity, the analysis gives the end value as infinite, whereas the real properties of the material would prevent such a value from occurring.

IV, D, Calculation of Stresses and Strains (cont.)

2. Stress Analysis Using Displacement Equations

Stress and strain fields in a short, thick-walled, cylindrical propellant grain were also investigated by solving the displacement equations of equilibrium with appropriate boundary conditions. The analysis was performed within the framework of the theory of infinitesimal elasticity. The propellant was assumed to be a homogeneous, isotropic, elastic solid and all strains, rotations and displacements were assumed to be small. Cylindrical grains with concentric, circular bores and flat ends were considered in the analysis. Two methods of solution were studied, the first an analytic solution and the second a finite difference solution. The equations and the results for several cases computed with the finite difference solution are presented in Appendix D.

3. Computer Solution of Ordinary and Partial Differential Equations Used in Stress Analysis

The solution of the differential equations of stress analysis was studied and general computer programs were written covering cases of interest. This allowed the construction of finite difference equations to be mechanized and thus avoid the hand generation of these equations. The methods are applicable to ordinary differential equations which have boundary conditions specified at more than one point and to partial differential equations of elliptic type. Several programs were written applying the methods to problems with known analytic answers to evaluate the use of high order difference approximation and difference correction so that the accuracy in application could be assessed. The methods are described in Appendix E and the application to several engineering proglems is shown there.

IV, D, Calculation of Stresses and Strains (cont.)

4. Nomograph for Calculation of Stresses and Strains

A nomographic method for analyzing stresses and strains in an internally pressurized long cylindrical propellant grain with a circular bore was developed and a report written describing its utilization [33]. The possibility of using a nomograph became evident when the results of an analysis based on a large deformation theory proposed by Blatz were being examined; it was found that the differential equations derived by Blatz could be cast into a particularly useful dimensionless form, thus facilitating the use of a nomograph for their solution. The theory used is based on a parameter, ν_B, which can be measured photographically during the conventional tensile testing of propellant samples. If the longitudinal strain of a propellant sample in an Instron test is denoted by ε and the concurrent lateral contraction by ε_1, then the experimental quantities

$$\lambda = 1 + \varepsilon \tag{79}$$

$$\lambda_1 = 1 + \varepsilon_1 \tag{80}$$

can be related by a relationship of this type.

$$\lambda^2_1 = \frac{1}{1 + 2\nu_B (\lambda - 1)} \tag{81}$$

where ν_B is an experimental constant somewhat akin to a Poisson's ratio; ν_B differs from the conventional Poisson's ratio in that in remains relatively constant up through large strains.

When this concept is applied to an internally pressurized, infinitely long cylinder of propellant with a circular bore and the large deformation strain energy function theory of Rivlin is applied [8], the following differential equation, connecting tangential and radial strains, results:

IV, D, Calculation of Stresses and Strains (cont.)

$$\frac{d\lambda_r}{d\lambda_\theta} = - \frac{\lambda_r}{\lambda_\theta} \cdot \frac{1 + (1 - 2\nu_B)\lambda_r\lambda_\theta}{1 + (1 - 2\nu_B)\lambda_r^2} \tag{82}$$

with $$\lambda_r = 1 + \varepsilon_r = 1 + \frac{du}{dr} \tag{83}$$

$$\lambda_\theta = 1 + \varepsilon_\theta = 1 + \frac{u}{r} \tag{84}$$

where u is the radial displacement of the cylindrical surface originally at r. If a number B is introduced, defined as the Blatz Number,

$$B = 1 - 2\nu_B \tag{85}$$

then the differenctial equation given above can be put in the dimensionless form and independent of propellant-property,

$$\frac{d\lambda_r^*}{d\lambda_\theta^*} = - \frac{\lambda_r^*}{\lambda_\theta^*} \cdot \frac{1 + \lambda_r^* \lambda_\theta^*}{1 + \lambda_r^{*2}} \tag{86}$$

with $$\lambda_r^* = \sqrt{B} \cdot \lambda_r \qquad \text{Blatz radial extension measure} \tag{87}$$

$$\lambda_\theta^* = \sqrt{B} \cdot \lambda_\theta \qquad \text{Blatz tangential extension measure} \tag{88}$$

The nomograph is based on this demensionless strain equation.

IV, D, Calculation of Stresses and Strains (cont.)

A computer program was written to establish numerical results. A check case was run for the following values of the parameters

a = Bore Radius = 5 in.

b = Inside Case Radius = 27 in.

ν = 0.36

μ = Propellant Shear Modulus = 370 psi

t = Case Thickness = 0.10 in.

E = Case Modulus = 5×10^6 psi

ν case = 0 (filament wound)

The results contrast with those of infinitesimal elasticity theory as follows:

	Blatz Characterization	Infinitesimal Elasticity
Percent Radial Strain at Bore	-38%	-37.5%
Percent Tangential Strain at Bore	+52%	+36%
Radial Stress at Case	67 psi	37 psi

IV, D, Calculation of Stresses and Strains (cont.)

5. Nonlinear Elasticity and Anisotropic Elasticity and Viscoelasticity (University of California

Supporting analytical studies at the University of California were carried out on the general problem of anisotropic and nonlinear solids under loading conditions encountered by rocket motors. Details of the analyses are presented in the four papers of Appendix F, Parts I, II, III, and IV. A brief summary of the results follow:

a. Elastic and Viscoelastic Analysis of Orthotropic Cylinders

The equations for linear orthotropic elasticity are presented in Appendix F, Part I with applications to the thermoelastic behavior of thick-walled cylinders. Examples are given to illustrate (1) the quantitative effect of orthotropy and (2) a step by step technique for solving bilinear elastic cylinders. A solution method is given for orthotropic viscoelastic cylinders. This method does not depend on the anisotropic correspondence principle. Techniques for asymptotic solutions are discussed. A solution for the deformation of a nonlinear elastic orthotropic cylinder subjected to internal and external pressure is also presented.

b. Bilinear Elasticity with Applications to Thick-Walled Cylinders

A general bilinear elastic theory is developed in Appendix F, Part II. Representation of solid propellant mechanical properties by a bilinear model is considered. The ability of the theory to approximate the behavior of a typical propellant is investigated insofar as possible with limited experimental evidence. Analytical solutions to several problems are presented and numerical results are given.

IV, D, Calculation of Stresses and Strains (cont.)

c.   Solution Method for Nonlinear Elasticity Problems
with Applications to Thick-Walled Cylinders

A solution scheme is presented in Appendix F, Part III
for second order elastic and thermoelastic problems. To illustrate the solu-
tion method three problems occurring in solid rocket motor design are extensively
treated, i.e., pressurization, temperature effects and vertical slump of a thick-
walled cylinder. To enable one to obtain material properties in a simple manner
the uniaxial test is analyzed. The solutions are in terms of a perturbation series;
for a second order theory, only the first two terms are needed. The homogeneous
portion of the system of equations governing the behavior of each term in the
series is identical to the classical elastic equations and the nonhomogeneous por-
tion is a nonlinear function of the previous term. The method is extended to
include those problems for which only an approximate solution to the classical
problem is available.

Three classes of material behavior are considered;
compressible, incompressible and near-incompressible. The latter class of
material behavior is considered in order to refine the assumption of incompressi-
bility and to be able to examine the validity of the incompressibility assumption.

In order to be able to consider thermal effects for a
mechanically incompressible material a derivation of the constitutive equations
for such a material including thermal effects is presented.

d.   Thermal Deformation of Viscoelastic Materials

The effect of temperature on linear viscoelastic stress
analysis is investigated in Appendix F, Part IV for materials which have a
single time-temperature equivalence function. Such materials have been classified
as thermorheologically simply by Schwarzl and Staverman.

IV, D, Calculation of Stresses and Strains (cont.)

Starting from the constitutive equations in integral form
and modified for the effects of temperature, the displacement equations of
equilibrium are derived in orthogonal curvilinear coordinates. The equations
are then specialized for axisymmetric temperatures which are constant in
the axial direction. Due to nonhomogeneity in the radial direction, solutions
to this class of problems may not be readily obtained, consequently, subsequent
analysis concerns the solution of problems with uniform temperatures varying
only in time. The time dependence is shown to be obtained by solving a Volterra
integral equation. The numerical technique of solution proposed by Lee and
Rogers is introduced and numerical examples are presented for a hollow cylinder
rigidly encased at the outer boundary and stress-free at the inner boundary.
Finally, the solution of an infinite cylinder bonded to a thin elastic case is formu-
lated in terms of a Volterra integral equation, again restricted to space independ-
ent temperatures.

V. PHASE 4 -- FAILURE CRITERIA

The objective of this phase was to carry out such theoretical and experimental studies as are needed to establish failure criteria applicable to the simple charges studied in Phase 3, and to evaluate these criteria by carrying those charges to failure.

The concept of failure necessarily includes a study of the behavior of those members of the population most likely to fail. The usual measurement of properties and correlation of data, as in Phases 1 and 2 of this program, centers around consideration of mean behavior with estimates of variability being made to assess the measurement quality. Stress and strain calculations also focus on the use of mean values of the parameters and comparison with the mean of observed deflections. Failure, however, is concerned with the likelihood of a particular stress or strain occurring at the point where the material properties are least adequate. The formation of yield bands in Class 2 and Class 3 propellants gives particular point to this problem. The data on these classes suggest that as the strains increase, yield bands occur and change the distribution of strains to produce regions in which failure will occur before further strain is produced in the unyielded regions. Thus, the calculations of Phase 3 and the use of techniques such as photoelasticity, do not directly lead to predictions of failure.

By the same reasoning, the failure in Class 1 propellants would not be characterized by localized dewetting so that the overall failure strain would be the same as the local failure strain in a uniform specimen such as a tensile specimen or at the inner wall of a tubular grain. A general failure criteria for motors (such as the maximum strain at failure being greater than 1/2 of the simple strain at break on a standard JANAF test at low temperature) should then be more conservative for a Class 1 propellant than for Class 2 or Class 3 propellants displaying localized blanching. This was indeed observed and indicates why Class 1 propellants behave so well in motors for wide range performance.

V, Phase 4 -- Failure Criteria (cont.)

The conditions of manufacture, handling, storage, shipment, and use of
rocket motors can be morphologically reduced to a set of specific critical con-
ditions. Each critical condition can be analyzed and reduced to a combination
of stresses or strains and environmental conditions which, in turn, can be
reproduced with some type of laboratory test. Establishing valid failure
criteria for propellant grains can be divided into two major parts: first, the
development of theoretical criteria, and second, the evaluation of the theory
through experimentation. The work on failure has given much insight into the
probable mechanism of failure in a highly loaded polymer system. At low
temperatures and high rates, failure appears to be by brittle fracture. At low
rates and high temperatures, failure is a series of processes; first, a breaking
of the binder to oxidizer bonds, followed by tearing in the binder structure
initiated at points of stress concentration in the regions of binder-oxidizer
dewetting. The most profitable path toward establishing failure criteria appears
to be; first, using brittle fracture theory for the high-rate, low-temperature
conditions; second, using tear theory for high-temperature, low-rate condi-
tions, and third, using a modified combination of brittle and tear for interme-
diate conditions. Whatever the failure process, it is clear that analysis of a
motor should focus on the failure points and for each expected point of failure
establish a failure analysis. The comparison of simple uniaxial tensile failure
with low temperature motor failure illustrates how this approach gives the
failure problem a clear method of solution.

The work in this phase will be discussed in terms of the variability of
tensile failure behavior, the relation of tensile data to low temperature failure
in tubular grains, and the effect of rate on tensile failure over a wide temper-
ature range. Also discussed are new works on tear phenomena, on failure
under uniaxial strain, and a general analytical approach to the failure of filled
materials by workers at Massachusetts Institute of Technology.

V, Phase 4 -- Failure Criteria (cont.)

A. BATCH VARIABILITY OF FAILURE BEHAVIOR

The large variability associated with propellant properties suggests that certain batches, and certain portions of these batches, will be more suscep- tible to failure than others. A related hypothesis is immediately suggested for experimental testing -- the failure behavior under different types of stress- strain environments are related such that those batches with the highest incidence of failure in one environment will have the highest incidence in another. It is clear that we lack the knowledge at this time to define failure mechanisms in detail for different batches or even different compositions. The generalization of four classes of propellant in Phase 2 has agreed with experimental observa- tions to date in that each of these classes is consistent in the type of failure observed, and that motors using these classes show differences in failure behavior consistent with this classification system. The major problem in testing the hypothesis offered above lies in obtaining sufficient statistical infor- mation on full motors and on the same batches of propellant going into these motors. An alternative procedure is to compare property measurements with small-scale motors, and validate the results as full-scale motor data become available. It is evident that during the validation process, the small-scale motor data and the property data would become increasingly firm as a basis for acceptance criteria.

The production of propellant for several programs at the Sacramento Solid Rocket Plant of the Aerojet-General Corporation offers the possibility of taking data on different batches of propellant and determining the correlation between failure values of different mechanical property tests. Instron data at one strain rate are taken from -75°F to 180°F in these several programs. A study has been completed in this program of data on one carton from each of 40 batches of a Class 2 propellant. Figures 122 to 125 show correlation graphs of the elongation at failure at 77°F vs the same value at the other test temperatures
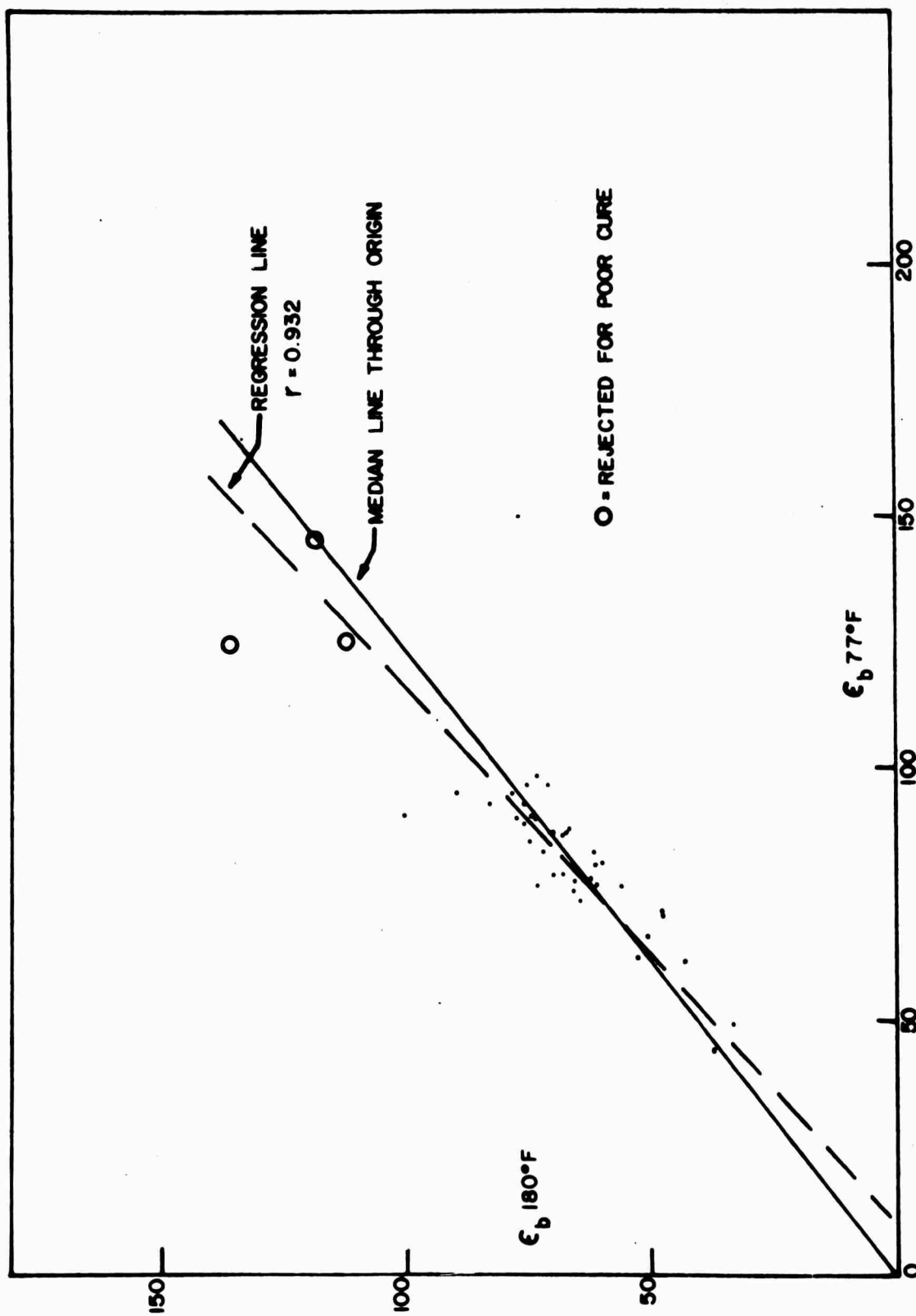
Figure 122. Failure Strain at 180°F vs That at 77°F (10-61S 27850)
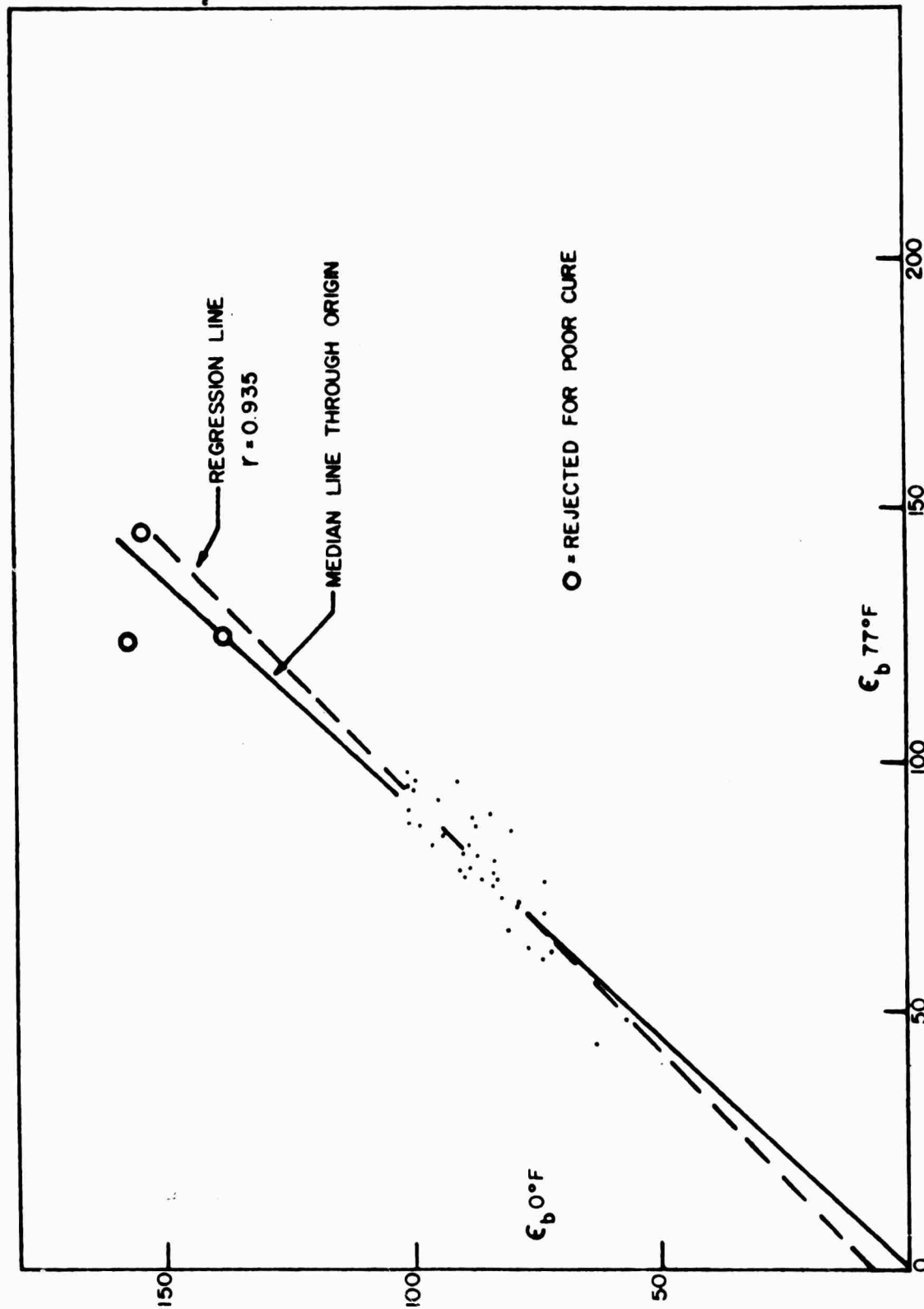
Figure 123. Failure Strain at 0°F vs That at 77°F (1-62S 02611)
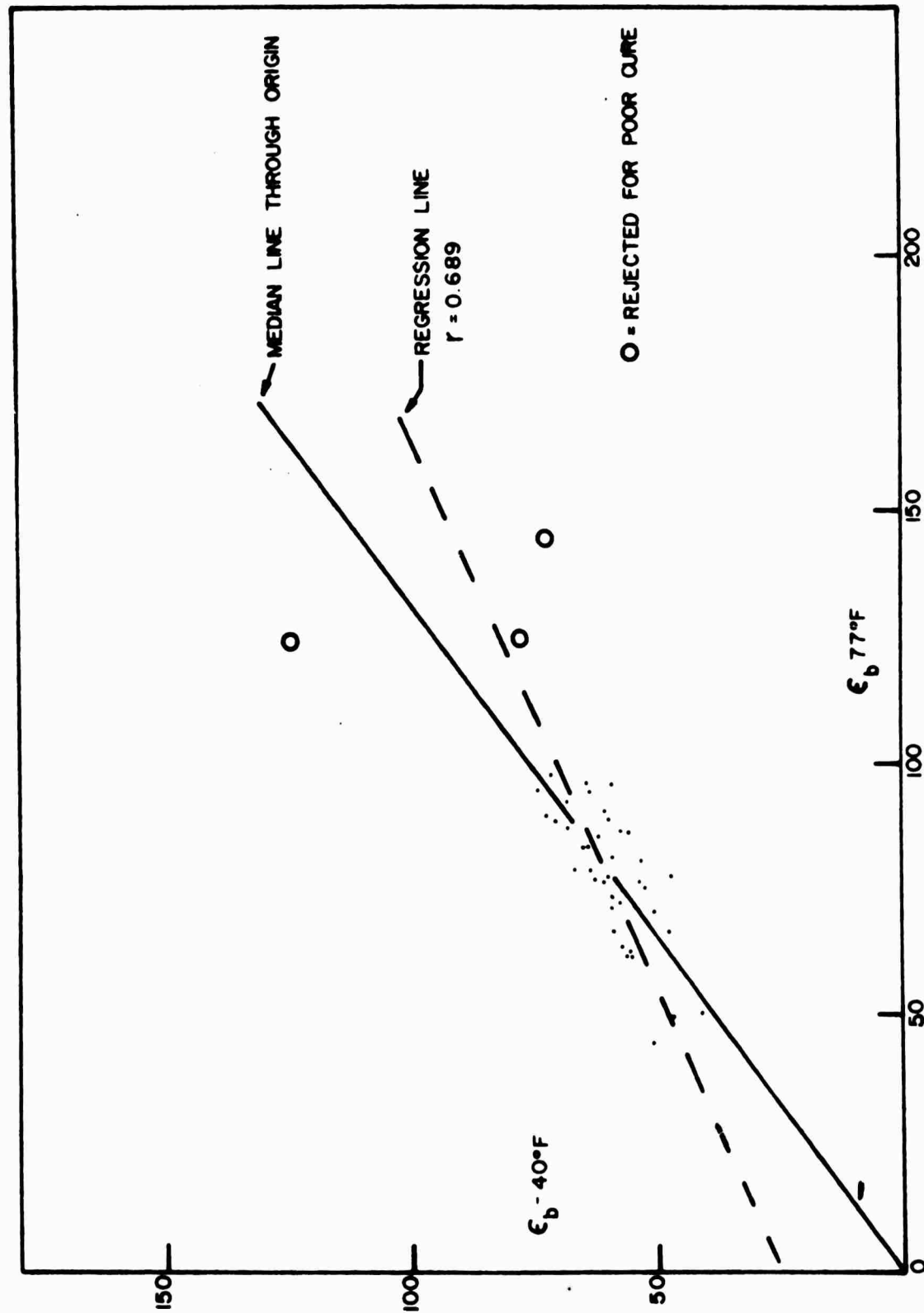
Figure 124. Failure Strain at -40°F vs That at 77°F (1-62S 02602)
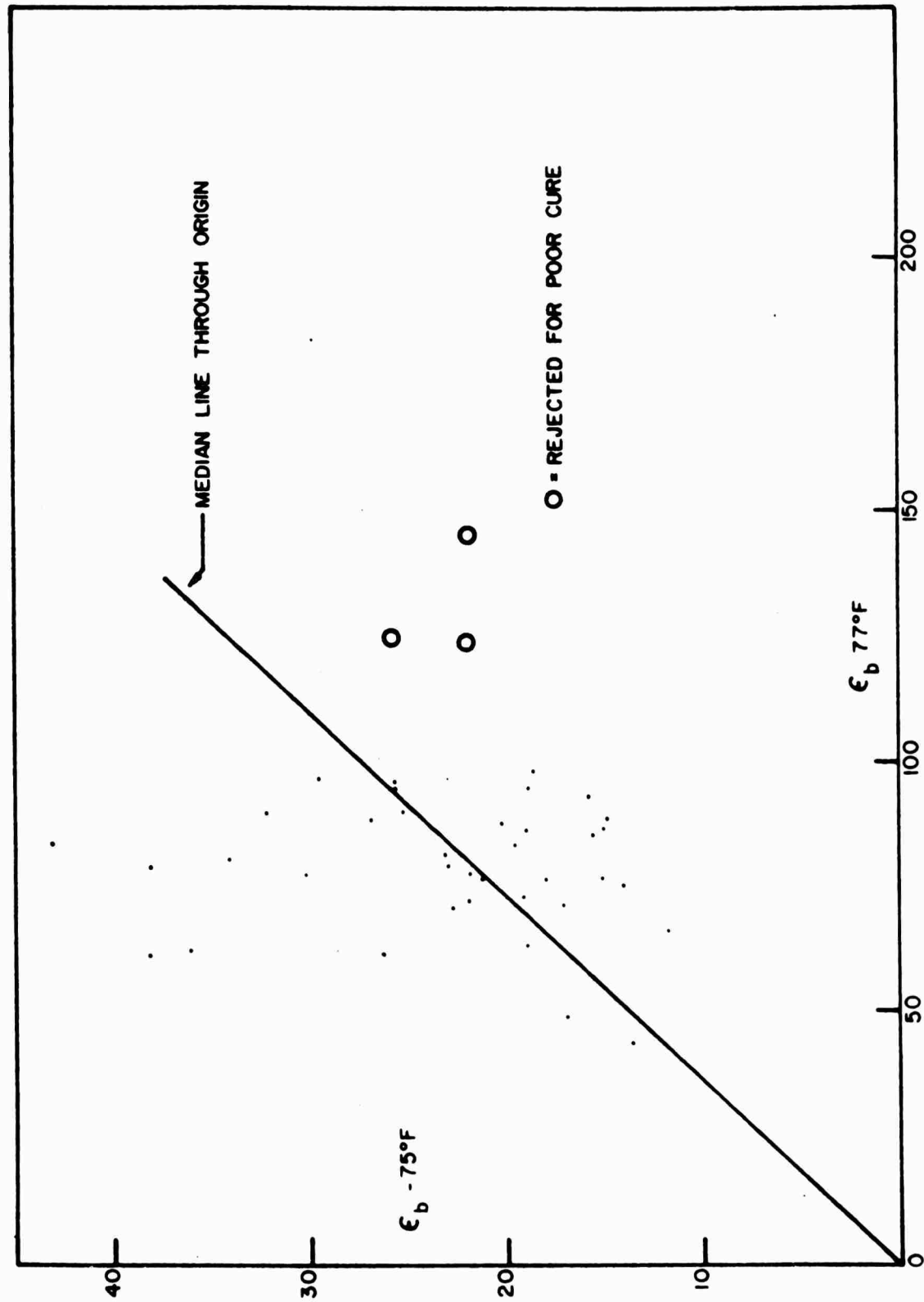
Figure 125. Failure Strain at -75°F vs That at 77°F (1-62S 02608)

V, A, Batch Variability of Failure Behavior (cont.)

for each of the cartons studied. The data were also analyzed numerically to give the correlation coefficient shown on each figure. Except for -75°F, the data gave high correlations, and in particular, the three cartons giving highest elongations and the two giving lowest elongations (except as shown in Figure 125 for -75°F) were the same in all cases. This would indicate that a test at any one of the test temperatures would have screened out the same extreme cartons of the population as any other test temperature except -75°F. The -75°F data are in question at this time because of a particularly strong effect of protest humidity exposure on -75°F test results; these tests were run on specimens experiencing a fairly wide range of humidity prior to being placed in -75°F conditioning for test.

Limited results of a different type on another Class 2 propellant are shown in Figure 126 for Instron data taken at -75°F after storage for various periods at temperatures at or near 0°F. This latter test is a measure of embrittlement which occurs to a greater or lesser degree in all composite propellants, and is characterized by an increase of modulus and a decrease of elongation at failure. The same general behavior is observed that the ordering of the batches with respect to each other was the same under both test conditions. The paucity of data for this long exposure prevents adequate statistical assessment and more data will be required.

An important further question is the relative importance of between-carton and between-batch variability, since a full evaluation of a batch of propellant requires more than one carton of propellant. The variability of the Class 2 propellant, shown in Figures 122 to 125, was analyzed in more detail for three widely different batches. It was found that the variability tended to decrease between batches and increase between cartons and within cartons as the test temperature decreased. When the three batches were considered together, coefficients of variation between batches ranged from 51% at 180°F
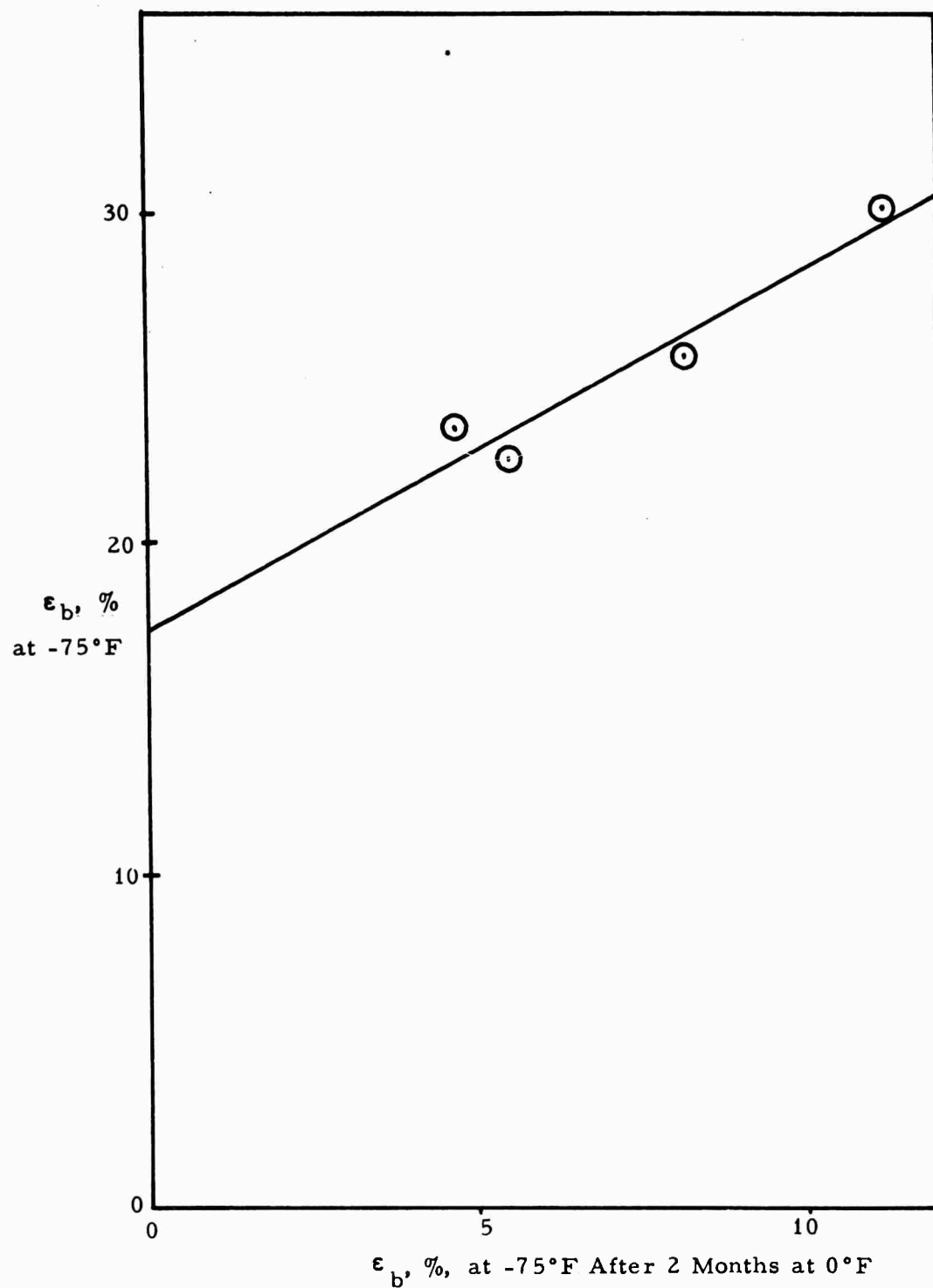
Figure 126. Effect of 2 Months Storage at 0°F on the Initial and Final Break Elongations at -75°F of Several Batches of a Class 2 Polyurethane Propellant

V, A, Batch Variability of Failure Behavior (cont.)

down to 26% at -75°F as contrasted with the between replicate variation which increased from 7% to 15% over the same temperature range. On the same three batches, there is some tendency for the between-carton variability to follow the between replicate variability excepting 0°F and -40°F, where the terms dropped out. Table 23 contains the mean values for the 3-batch, 3-carton, 3-replicate analysis and the variability analysis data are tabulated in Table 24.

An additional analysis of Batches 18-M-1 and 21-M-1 was made. In this case, test data from two additional cartons from each of these batches were available. The means of these two batches were more nearly alike at the middle temperatures and tended to diverge at the extremes, which would minimize variability at the middle temperatures. The between-carton and between-replicate values, however, followed patterns identical to those from the initial analysis of all three batches. Table 25 contains the results of the variance analysis in terms of coefficients of variation. All of the coefficients of variation listed had a significance level of 0.95 or greater, with the exception of the between-carton values for 180°F, which were from 0.80 to 0.85.

B. CORRELATION OF FAILURE DATA WITH SMALL MOTOR FAILURES

The small motors with cast-in-case cylindrical grains used for studies of strain under temperature cycling experienced failures in many cases. It appeared possible to develop a failure hypothesis by study of these failures. A survey was initially made of 41 small case-bonded motors that had been thermally cycled to -75°F; B/A ratios from 4 to 12.5 were tested. Of these 41 motors, 15 failed by longitudinal cracking of the propellant grain. The strain in the motor, as measured on the first cycle to -75°F was compared to the strain at break of the propellant at -75°F in the standard Instron test to see if there was a correlation between the propellant failure strain under the condition as seen in the motor and the failure strain as encountered in uniaxial tensile tests.

TABLE 23

MEAN VALUES OF BREAKING STRAIN
FOR THREE BATCHES OF A CLASS 2 PROPELLANT

	1	2	3
Batch	15-M-2	18-M-1	21-M-1
180°F	19.9	98.0	73.0
77°F	28.1	93.6	93.3
0°F	35.7	113.3	104.0
-40°F	33.1	69.8	61.7
-75°F	18.2	26.6	23.3

TABLE 24

COEFFICIENTS OF VARIATION FOR ALL THREE BATCHES
3 Batches, 3 Cartons, 3 Replicates

	Between Batches	Between Cartons	Between Replicates
180°F	51%	4%	7.1%
77°F	46%	8.5%	9.8%
0°F	50%	---	8.8%
-40°F	35%	---	9.8%
-75°F	26.3%	17.7%	14.9%

TABLE 25

COEFFICIENTS OF VARIATION FOR ONLY TWO BATCHES
39 DB-18-M-1 and 39 DB-21-M-1

2 Batches, 5 Cartons, 3 Replicates

	Between Batches	Between Cartons	Between Replicates
180°F	22%	3.3%	4.3%
77°F	8.9%	8.7%	7.1%
0°F	--	--	12%
-40°F	7.2%	5.5%	10.5%
-75°F	21%	13%	14%

V, B, Correlation of Failure Data With Small Motor Failures (cont.)

The propellants involved were two of Class 2 and one of Class 1 type. The propellant property used was the lowest tensile strain at break reported from the two or three tensile tests taken at -75°F. Since some of the motors had been stored for various lengths of time at 0°F before cycling to -75°F, an estimated correction for embrittlement was added to the strain at break as measured on unembrittled propellant. The strain at break corrected for embrittlement was divided by the maximum measured strain in the motor on its first cycle to -75°F, to give a ratio called $\varepsilon_b/\varepsilon_{mm}$. The data are tabulated in Table 26. The ratio of $\varepsilon_b/\varepsilon_{mm}$ is shown plotted against the percent of motors cracking at that ratio in Figure 127. When the ratio $\varepsilon_b/\varepsilon_{mm}$ was one or less, all of the motors failed; when the ratio was two or more, none of the motors failed. The region between one and two is the expected area of doubt caused by the wide distribution of propellant properties.

The success of the $\varepsilon_b/\varepsilon_{mm}$ correlation suggested that a more detailed analysis of propellants with different types of stress-strain curves would be desirable. The failures encountered in the thermal cycling experiment of Phase 3 were therefore examined, together with a more detailed study of the failures of the first group of motors.

Table 27 is a record of the grains tested during the cycling experiment. Tables 28, 29, 30, and 31 compile the various tensile and physical properties collected for the propellants tested in the grains. The failure data are summarized in Table 32.

Figure 128 shows a plot of twice the calculated motor hoop strains and the average and lowest measured tensile breaking strains plotted against temperature for the Class 2 propellant #1. The motors were thermally cycled to -75°F. Only the two motors of 1.25" core (B/A ratio of 4) survived the test which is marginal agreement for a predicted all fail of -73°F for B/A of 4.

TABLE 26

SUMMARY OF FAILURE DATA AT −75°F

Days at 0°F	ε_b embrittled %	ε_{mm} %	$\varepsilon_{be}/\varepsilon_{mm}$	Fail
		Class 1 Propellant		
20	25	19	1.3	No
21	14	19	0.7	Yes
20	25	19	1.3	No
37	51	37	1.4	Yes
37	51	36	1.4	Yes
37	38	41	0.9	Yes
37	38	38	1.0	Yes
0	40	14	2.9	No
0	40	14	2.9	No
		Class 2 Propellant		
16	22	10.5	2.1	No
16	22	10.8	2.0	No
16	24	8.9	2.7	No
26	21	8.1	2.6	No
16	25	11.5	2.2	No
16	37	13.4	2.8	No
21	35	12.0	3.1	No
16	37	13.5	2.7	No
16	61	14.4	4.2	No
21	59	11.6	5.1	No
25	36	10.5	3.4	No
25	36	6.7	5.3	No
25	36	13.2	2.7	No
20	14.2	9.0	1.6	No
20	14.2	9.9	1.4	No
20	14.2	8.0	1.8	No
19	14.2	10.3	1.4	No
19	14.2	9.0	1.6	No
19	14.2	8.7	1.6	No

TABLE 26 (cont.)

28	15.6	8.5	1.8	Yes
28	15.6	8.5	1.8	Yes
28	14.8	8.5	1.7	Yes
28	14.8	8.5	1.7	Yes
28	14.8	8.5	1.7	Yes
28	14.8	8.5	1.7	Yes
28	14.8	8.5	1.7	Yes
28	11.2	8.5	1.3	Yes
28	11.2	8.5	1.3	Yes

Class 3 Propellant

1.5	26.1	13.9	1.9	No
1.5	26.1	13.6	1.9	No
18	8.4	16.9	0.5	Yes
7	8.4	16.9	0.5	Yes
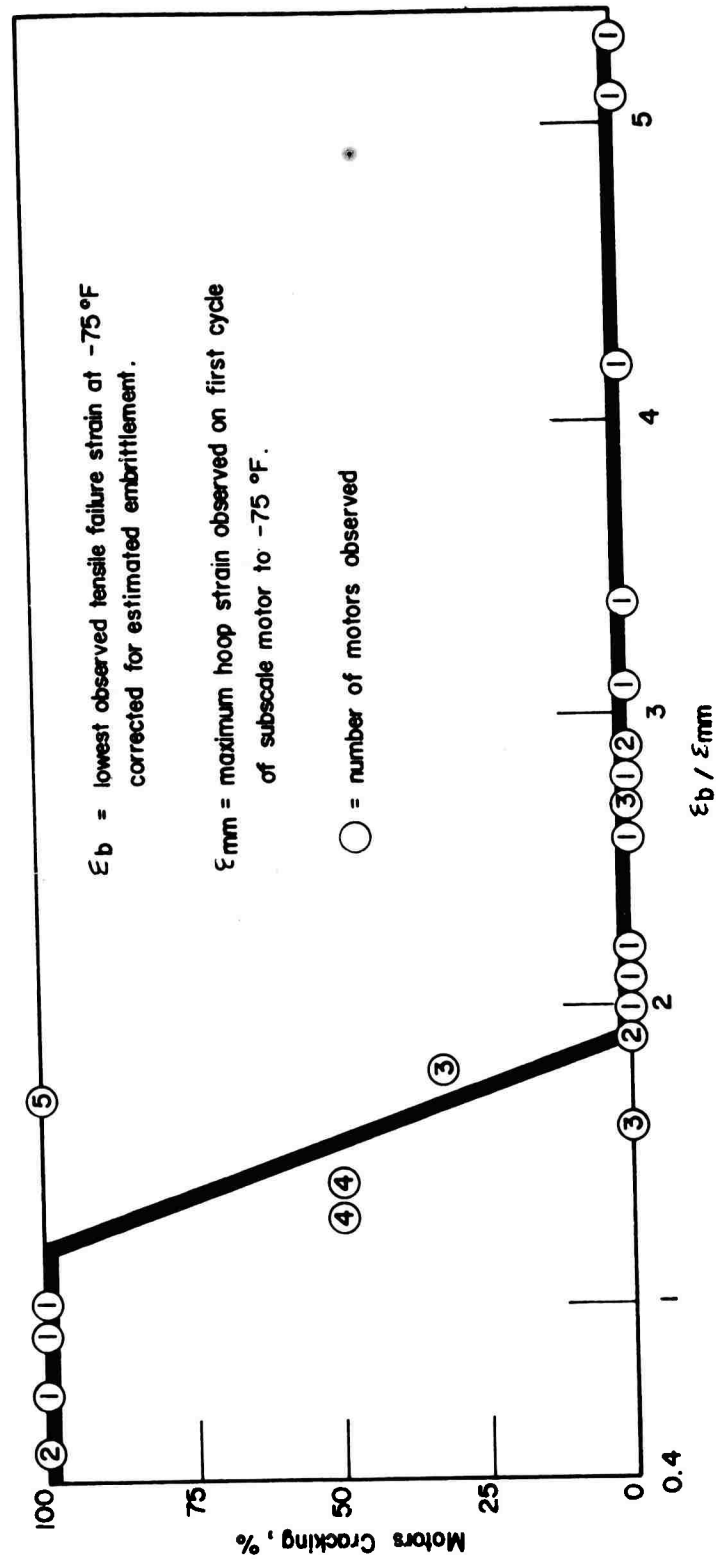
Figure 127. Relation of Failure in Tensile Specimens to Subscale Grain Cracking

TABLE 27

THERMAL CYCLING HISTORY OF 5" SUBSCALE MOTORS

Grain #	Propellant	Batch #	Length In.	Bore In.	B/A	Lowest Temp °F	Max. OBS Strain %	Remarks
23	Class 2 #1	39DB47M2	11	0.4	12.5	-75	37.5	Some end release and longitudinal crack 1st temperature drop.
13	"	"	12.75	0.5	10	-75	40	Some end release first temp. drop, crack developed on second drop.
27	"	"	18.5	0.625	8	-75	---	Some end release first temp. drop, crack developed on second drop.
14	"	"		0.853	6	---	---	Burned up in lathe.
25	"	"	13.5	---	Star	-75	---	No failure, 2 drops.
17	"	"	11	---	Solid	-75	---	Considerable release from case starting about 0°F.
18	"	"	14.5	0.4	12.5	-75	---	Some end release on 1st drop. Internal release and longitudinal crack on 2nd drop.
16	"	"	12.5	0.5	10	-75	36	Ends released to 1/2". Crack appeared on 2nd drop.
22	"	"	14.25	0.625	8	-75	---	Ends released to 1/2". Crack appeared on 1st drop.
20	"	"	13.5	0.833	6	-75	---	Ends released to 1/2". Crack appeared on 2nd drop.
26	"	"	14.25	---	Star	-75	---	No failure, 2 drops.
24	"	"	14	---	Solid	-75	---	Considerable release from case about 0°F.
101	"	39DA18M2	10.5(2)	1.25	4	-75	12.6(1)	8 days at 0°F then drop temp, no failure.
102	"	"	10.5(2)	1.25	4	-75	13.7(1)	8 days at 0°F then drop temp, no failure.

TABLE 27 (cont.)

Grain #	Propellant	Batch #	Length In.	Bore In.	B/A	Lowest Temp °F	Max. OBS Strain %	Remarks
31	PBD	17DK164	13	1.25	4	-75	11.6(1)	100%RH at 110°F 2 days. Longitudinal crack at about -65°F.
35	"	"	13	1.25	4	-75	8.5(1)	0%RH at 110°F 2 days. Release from case at about -70°F on first cycle.
36	"	"	13.25	1.25	4	-75	11.7(1)	0°F ambient RH for 8 days. Release from case at about -55°F on first cycle.
26	Class 2#2	17DD224	15	0.4	12.5	-75	33	No cracks, no releases, 2 cycles. After 0°F for 8 days, crack developed at about -60°F on 3rd drop.
27	"	"	14.75	0.5	10	-75	27	same
25	"	"	14.25	0.625	8	-75	---	No cracks, no releases, 2 cycles. After 0°F for 8 days end release but no cracks on 3rd drop. (2)
23	"	"	16	0.833	6	-75	---	same, no failures (2)
28	"	"	14.75	1.00	5	-75	---	same, no failures (2)
22	"	"	14	---	solid	-75	---	Circumferential crack 1/2" from case developed about -60°F (2)
24	"	"	15.5	0.4	12.5	-100	31	Time limitations allowed only 1 cycle. No visible failure evidence. (2)
32	"	"	15	0.5	10	-100	44	same (2)
20	"	"	15	0.625	8	-100	---	same (2)
29	"	"	16.25	0.833	6	-100	---	same (2)
21	"	"	15.75	1.00	5	-100	---	same (2)
34	"	"		---	solid	-100	---	No visible evidence of failure (2)

p. 3

TABLE 27 (cont.)

Grain #	Propellant	Batch #	Length In.	Bore In.	B/A	Lowest Temp °F	Max. OBS Strain %	Remarks
1	Class 1	61-3208M	19.5	---	12.5	-75	---	Kept dry with desiccant, no evidence of failure after 3 cycles 110°F to -75°F. (2)
2	"	"	14.25	---	8	-75	---	same
3	"	"	13.5	---	12.5	-75	---	same
4	Class 2	61-3210M	13.5	0.4	12.5	-75	24	Longitudinal cracks visible on 3rd drop.
5	"	"	12.5	---	8	-75	18	same

Footnotes:

(1) 1.25" bores required mechanical measurement gages. All other maximum strains reported were measured with electrical recording clip gages.

(2) Grains from Class 2 #2 Batch 17DD224 were allowed to stand about 2 weeks at ambient temperature and RH after the measurements reported in Table 27. %RH levels between 30% and 80% were recorded. Temperatures ranged from 40°F to 75°F. Attempts to obtain further measurements by cooling to about 0°F resulted in failure of the remaining grains by cracking.

TABLE 28

PROPELLANT PROPERTIES - CLASS 2 PROPELLANT #1

BATCH NO. 39DB-47(M-2)

Mechanical Properties:

Strain Rate = 0.74 min^{-1}

Temp., °F	S_{nm} psi	S_{nb} psi	ε_m %	ε_b av. %	Lowest Observed Value ε_b min. %	E psi
150	94	90	34	40	38	409
110	104	101	39	47	46	420
77	126	119	42	56	52	508
40	152	136	42	60	55	641
20	171	156	38	58	54	822
0	203	182	39	54	53	1030
-20	228	188	33	50	48	1410
-40	354	310	24	36	35	2240
-75	758	686	10.2	15.4	11.4	14500
0/-20	292	248	24.7	41	31	1940
0/-40	354	296	22.6	36	31	2880
0/-75	848	807	9.1	12.1	10.7	13500
0/-85	1007	978	6.6	7.7	7.3	21000

Strain Rate = 0.00059 min^{-1*}

Temp., °F				ε_b av. %	ε_b min. %	
0				45	43	
-20				47	46	
-40				46	45	
-75				28	27	

40°F Constant Strain: Held 7 days at 10% strain

Thermal Properties

Density	$.0628$ LB/IN^3
Coefficient Thermal Expansion	1.89×10^{-4} IN^3/IN^3/°F
Thermal Conductivity	$.250$ BTU ft^{-2}hr^{-1}(°F/ft)$^{-1}$
Thermal Diffusivity	7.50×10^{-3} ft^2/hr
Specific Heat	$.307$ BTU/LB m °F

* Load cells and recording system on very slow rate tester was not stable
  enough for stress-strain curves.

TABLE 29

PROPELLANT PROPERTIES – CLASS 2 PROPELLANT #2

BATCH NO. 17DD224(M-5)

Mechanical Properties:

Strain Rate = 0.74 min^{-1}

Temp., °F	S_{nm} psi	S_{nb} psi	ε_m %	ε_b av. %	Lowest Observed Value ε_b min. %	E psi
77	148	131	42	57	40	721
0	409	310	21.5	35	29	4880
-40	747	681	4.0	6.7	4.8	37800
-75	1342	1342	.6	.6	0.3	366000
0/-75	1556	1556	1.5	1.5	1.5	125000

Strain Rate = $.00059$ min^{-1}

0				38	37	
-40				20.7	19.9	
-75				4.0	4.0	

40°F Constant Strain: Held 7 days at 15% strain

Thermal Properties

Density	$.0635$ LB/IN^3
Coefficient of Thermal Expansion	1.91×10^{-4} IN^3/IN^3/°F
Thermal Conductivity	$.252$ BTU ft^2 hr^{-1} (°F/ft)$^{-1}$
Thermal Diffusivity	7.47×10^{-3} ft^2/hr
Specific Heat	$.306$ BTU/lb m °F

TABLE 30

PROPELLANT PROPERTIES - CLASS 1 POLYURETHANE PROPELLANT - BATCH NO. 61-3208M

Mechanical Properties

Strain Rate = 0.74 min^{-1}

Temp., °F	S_{nm} psi	S_{nb} psi	ε_m %	ε_b av. %	Lowest Observed Value ε_b min. %	E psi
0	311	297	79	86	65	967
-20	395	379	83	92	89	1640
-40	444	439	81	85	78	2260
-75	736	723	30	35	31	8870

Strain Rate = 0.00059 min^{-1}

0					43	40
-40					48	44
-75					51	48

40°F Constant Strain: Failed after 2 to 5 days at 10% strain

Thermal Properties

Density   .0578 LB/IN^3

Coefficient of Thermal Expansion 2.15 x 10^{-4} IN^3/IN^3/°F

TABLE 31

PROPELLANT PROPERTIES - CLASS 2 POLYURETHANE PROPELLANT #3 - BATCH NO. 61-3210 M

Mechanical Properties

Strain Rate = 0.74 min^{-1}

Temp., °F	S_{nm} psi	S_{nb} psi	ε_m %	ε_b av. %	Lowest Observed Value ε_b min.	E psi
0	175	160	36	43	34	722
-20	223	200	38	49	42	1040
-40	254	219	36	48	41	1640
-75	506	383	18	39	32	6030

Strain Rate = 0.00059 min^{-1}

-40				47	42	
-75				32	21	

40°F Constant Strain: Failed after 1 day at 10% strain

Thermal Properties

Density	$.0580$ LB/IN^3
Coefficient of Thermal Expansion	2.05×10^{-4} IN^3/IN^3/°F

TABLE 32

SUMMARY OF FAILURE DATA
CLASS 2 PROPELLANT #1

GRAIN	B/A	ε_{mm}*	$\varepsilon_m/\varepsilon_{mm}$	$\varepsilon_b\ min/\varepsilon_{mm}$	End Release		Cracked
23	12.5	37.5	.27	.304	yes	yes	1st drop
18	12.5	37.5	.27	.304	"	"	2nd drop
13	10	35.5	.28	.32	"	"	" "
16	10	35.5	.28	.32	"	"	" "
27	8	30.5	.33	.374	"	"	" "
22	8	30.5	.33	.374	"	"	1st "
20	6	23	.435	.495	"	"	2nd "
101	4	13	.77	.875	no	no	
102	4	13	.77	.875	"	"	

CLASS 2 PROPELLANT #2

GRAIN	B/A	ε_{mm}		$\varepsilon_b\ min/\varepsilon_{mm}$ (A)	End Release				Cracked
124	12.5	37.5	.008	.77	no	no	1st drop	yes	3rd drop
126	12.5	37.5	.008	.77	"	"	"	"	note (B)
127	10	35.5	.0085	.82	"	"	"	"	"
132	10	35.5	.0085	.82	"	"	"	"	"
120	8	30.5	.01	.95	"	"	"	"	"
125	8	30.5	.01	.95	"	"	"	"	"
123	6	23	.013	1.25	"	"	"	"	"
129	6	23	.013	1.25	"	"	"	"	"
128	5	19	.016	1.52	"	"	"	"	"
121	5	19	.016	1.52	"	"	"	"	"

(A) Values based on retest of fresh propellant after humidity exposure.

(B) All were cracked on dropping temperature to 0°F after 2 weeks standing at ambient (approximately 60°F and 40%RH)

3 motors - Batch 61-3208 M

	B/A	ε_{mm}		End Release		Cracked
1	12.5	37.5	.83	no	no	14 cycles from
2	8	30.5	1.02	"	"	110°F to -75°F
3	12.5	37.5	.83	"	"	no failure (maintained with desicant)

2 motors - Batch 61-3010 M

| 4 | 12.5 | 37.5 | .85 | " | yes | 3rd drop |
| 5 | 8 | 30.5 | 1.05 | " | " | " " |

---

* $\dot{\varepsilon}_{mm}$ was interpolated from Table 13.
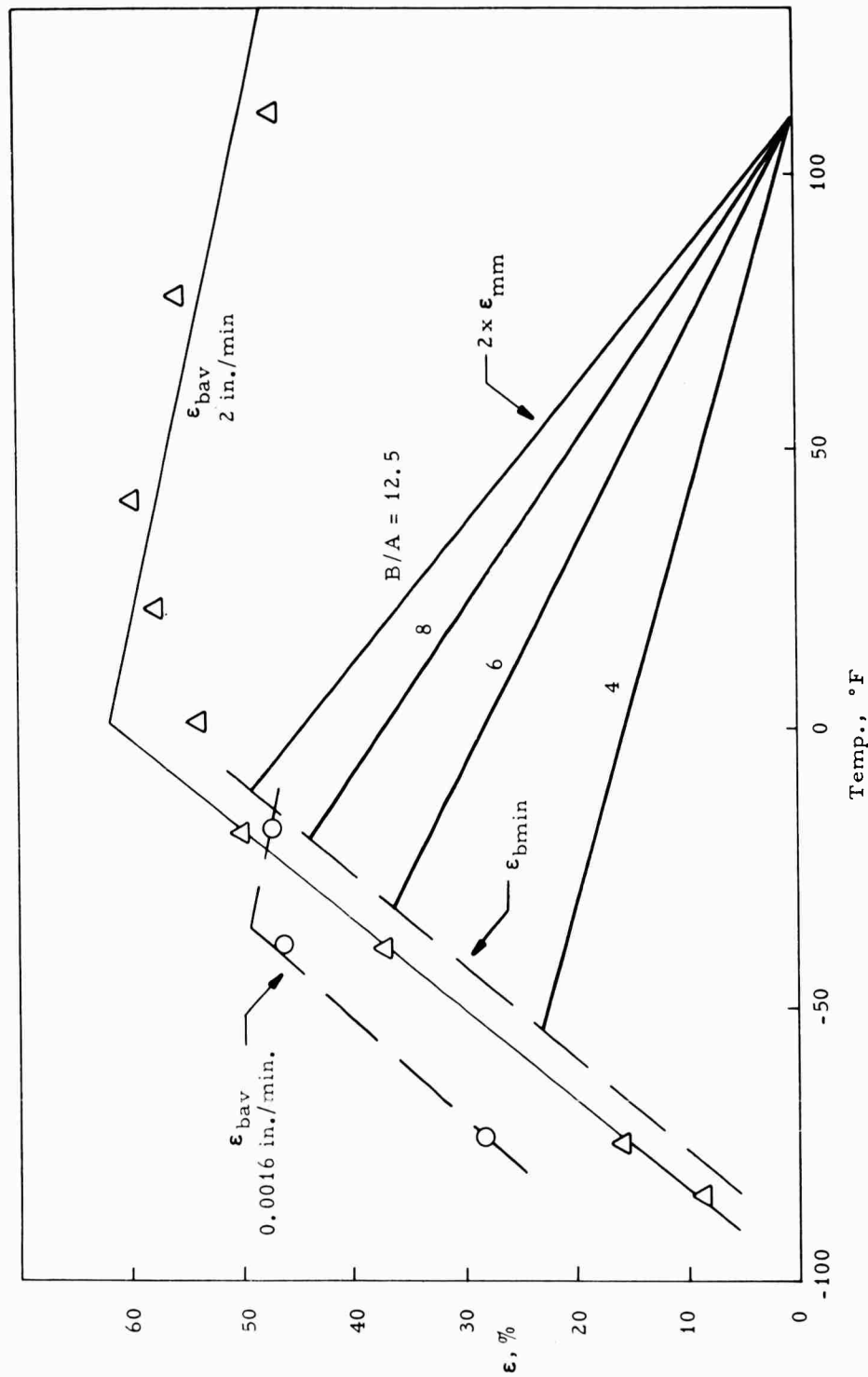
Figure 128. Comparison of 2 x Calculated Motor Hoop Strain With Observed
Tensile Failure Strains for Class 2 Propellant No. 1

V, B, Correlation of Failure Data With Small Motor Failures (cont.)

Figure 129 shows a similar plot for the Class 2 propellant #2. The initial thermal cycling results for this propellant were surprising. Failure was expected to start at about +15°F for the high B/A ratios of 12.5 and at about -7°F for the lowest B/A ratio of 5. On the first two cycles there was no visible evidence of failure in any of the motors. A third cycle after 0°F storage caused a failure in one grain at -60°F; still far below the predicted failure region. The mtors were then set aside at ambient moisture and temperature levels for three weeks while other parts of the experimental plan were carried out. After the three week storage, a mechanically measured bore profile of these motors was desired. The entire set of motors was placed in a 0°F box overnight fully expecting to make the desired measurement the following morning. The next morning observation showed that every one of the motors had failed by longitudinal cracks during the night.

Careful examination of the records concerning these particular motors showed that they had come directly from 110°F cure into the experiment. No moisture exposure or ambient aging intervened between 110°F cure and the temperature cycling in the dry CO_2 atmosphere produced by the evaporation of liquid CO_2 for refrigeration. The propellant specimens tested for mechanical properties were exposed to ambient humidity for some time before test. To determine if this propellant was sensitive to these conditions, some freshly cured propellant of this formulation was compared with propellant exposed to ambient conditions for one week. The tensile properties obtained from this test are tabulated in Table 33. The freshly cured propellant had nearly double the breaking strain of the material stored at ambient for only one week. This difference in the tensile properties between the freshly cured and aged propellant can perhaps explain part of the unusual cycling results. The failure criteria applies adequately if the conditioned motors are considered but not for these motors fresh from cure.
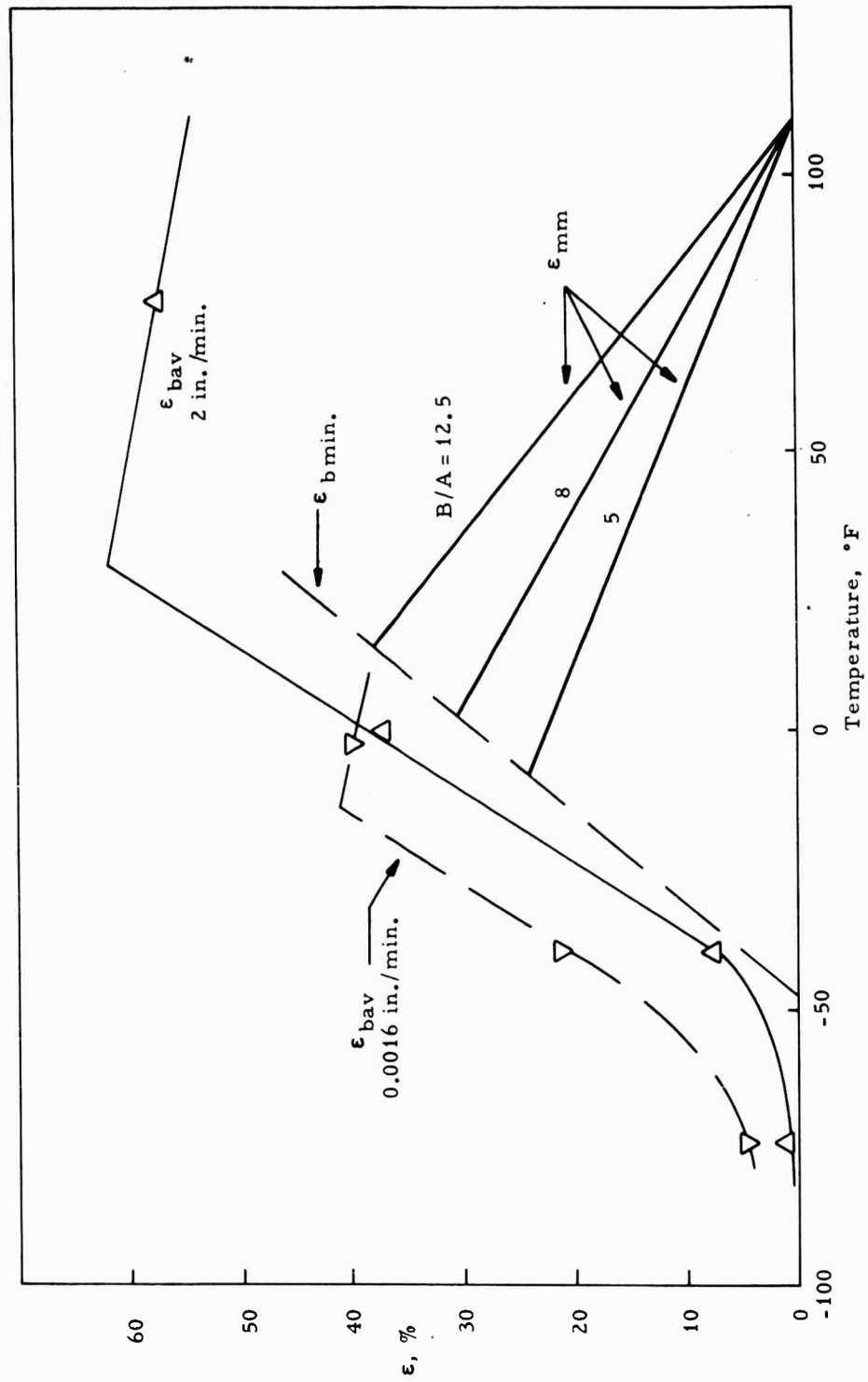
Figure 129. Comparison of 2 x Calculated Motor Hoop Strain With Observed
Tensile Failure Strains for Class 2 Propellant No. 2

TABLE 33

EFFECT OF AMBIENT HUMIDITY AND 1 WEEK AGING ON
PROPERTIES OF A BATCH OF CLASS 2 PROPELLANT #2

	Time to Test After Cure	Test Temp., °F	Sample No.	S_{nm} psi	S_{nb} psi	γ_m %	γ_b %	E psi
Batch No. 17DD235-1 M-1	10 min.	77°	1	154	148	43	47	240
			2	157	154	45	48	260
			3	157	148	46	57	260
			av.	156	150	45	50	253
	4 hours	-40°	1	674	656	16.3	18.6	8150
			2	638	633	16.5	18.7	7630
			3	706	same	15.2	same	8560
			4	707	669	15.0	17.8	9360
			av.	681	666	15.8	17.6	8430
	7 days at Amb. temp. ∉ Amb. RH	-40°	1	767	same	12.0	same	12200
			2	753	736	9.8	10.2	15000
			av.	760	752	10.9	11.1	13600
Batch No. 17DD235-1 M-2	10 min.	77°	1	27.7	25	64	84	136
			2	29	26	60.7	82.8	160
			3	30	25	58.2	85	163
			av.	28.9	25	60.9	83.9	153
	4 hours	-40°	1	648	642	13.2	15	7780
			2	637	626	16.6	23.6	7940
			3	647	642	16.9	20.5	9630
			av.	644	637	15.6	19.7	8440
	7 days at Amb. temp ∉ Amb. RH	-40°	1	821	791	9.8	11.5	19800
			2	653	same	6.9	same	12700
			3	786	747	8.3	10.7	22100
			4	779	same	8.2	same	23400
			av.	760	743	8.3	9.3	19500

V, B, Correlation of Failure Data With Small Motor Failures (cont.)

The two propellants, Class 1, Batch 61-3208M and Class 2, Batch 61-3210M, were 100 lb. batches made especially for this experiment. Special effort by the formulating chemist* produced two propellants with superior low temperature properties (ε_b = 35%) but with different shapes to the stress-strain curves at 2"/min., as shown in Figure 130. The Class 1 gave a stress-strain curve steadily rising to a maximum, so that ε_m and ε_b are relatively close together. The Class 2, Batch 61-3210M has a higher ε_b at -75°F but had a downward slope to the stress curve following the maximum, characteristic of localized dewetting. The intent of the experiment was to determine whether repeated thermal cycling would show a difference in a motor failure between the two propellants; such a difference appears to be demonstrated as the Class 2, Batch 61-3210M failed after three cycles of +110° to -75°F, while the Class 1, Batch 61-3208M showed no evidence of failure after twelve such cycles.

Figure 131 shows the failure criteria graph of the Class 1, Batch 61-3208M propellant, which indicates failure should have have occurred before -75°F for B/A of 12.5 and probably failed at about -75°F for B/A of 8. The grains were maintained dry with desiccant during the entire experiment. Figure 132 is a similar plot for the Class 2, Batch 61, 3210M. For this propellant also failure should have occurred before -75°F for B/A of 12.5 and at about -75°F for B/A of 8. The two motors did not survive three cycles.

All of the failure data are plotted on Figure 133, and it can be seen that no failures were observed above $\varepsilon_{b\,min}/\varepsilon_{mm}$ = 1.8, and no successful cyclings were performed (except for the unusual behavior described for the

---

* Dr. A. Oberth kindly provided the samples tested.
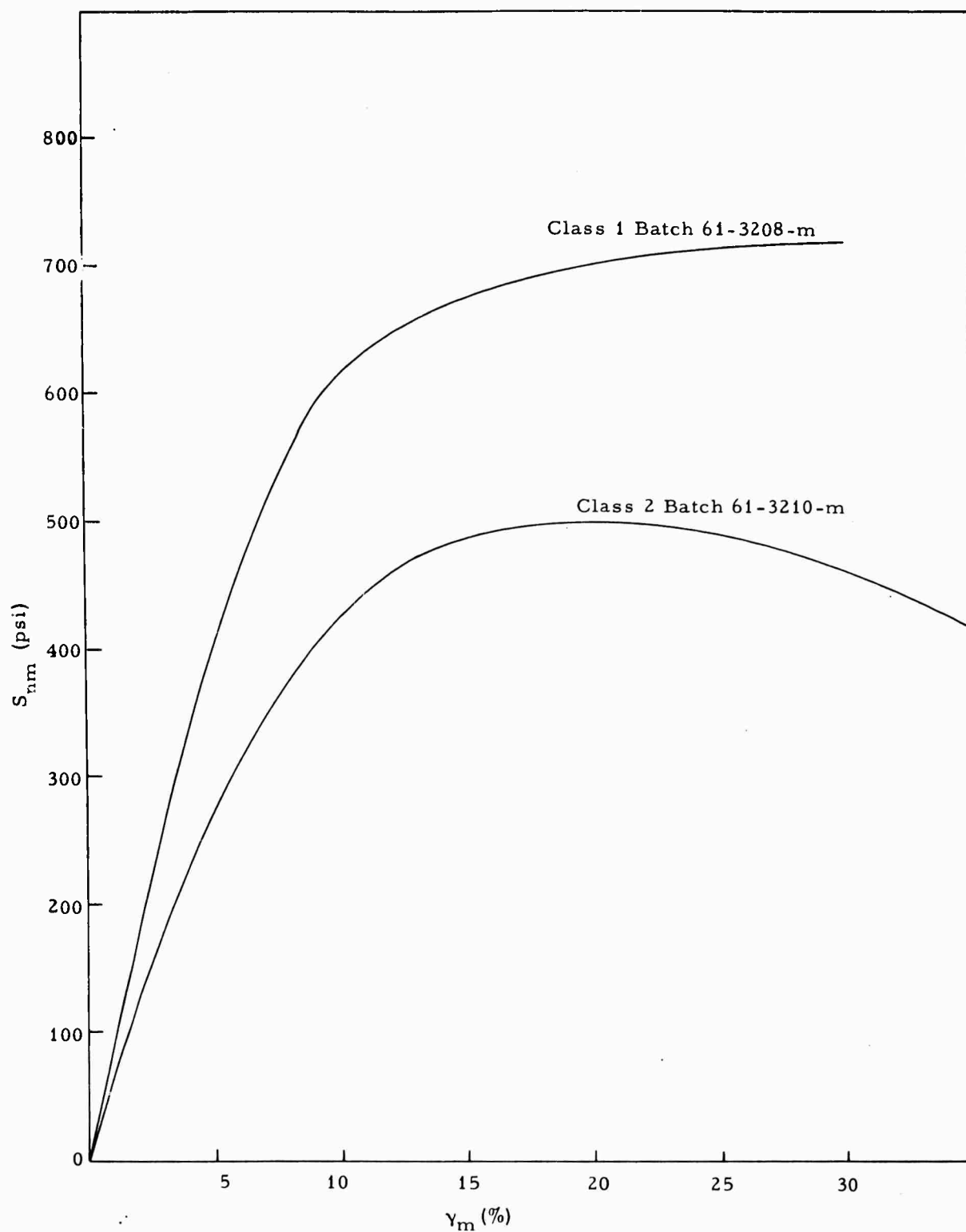
Figure 130. Instron Tensile Curves at -75°F
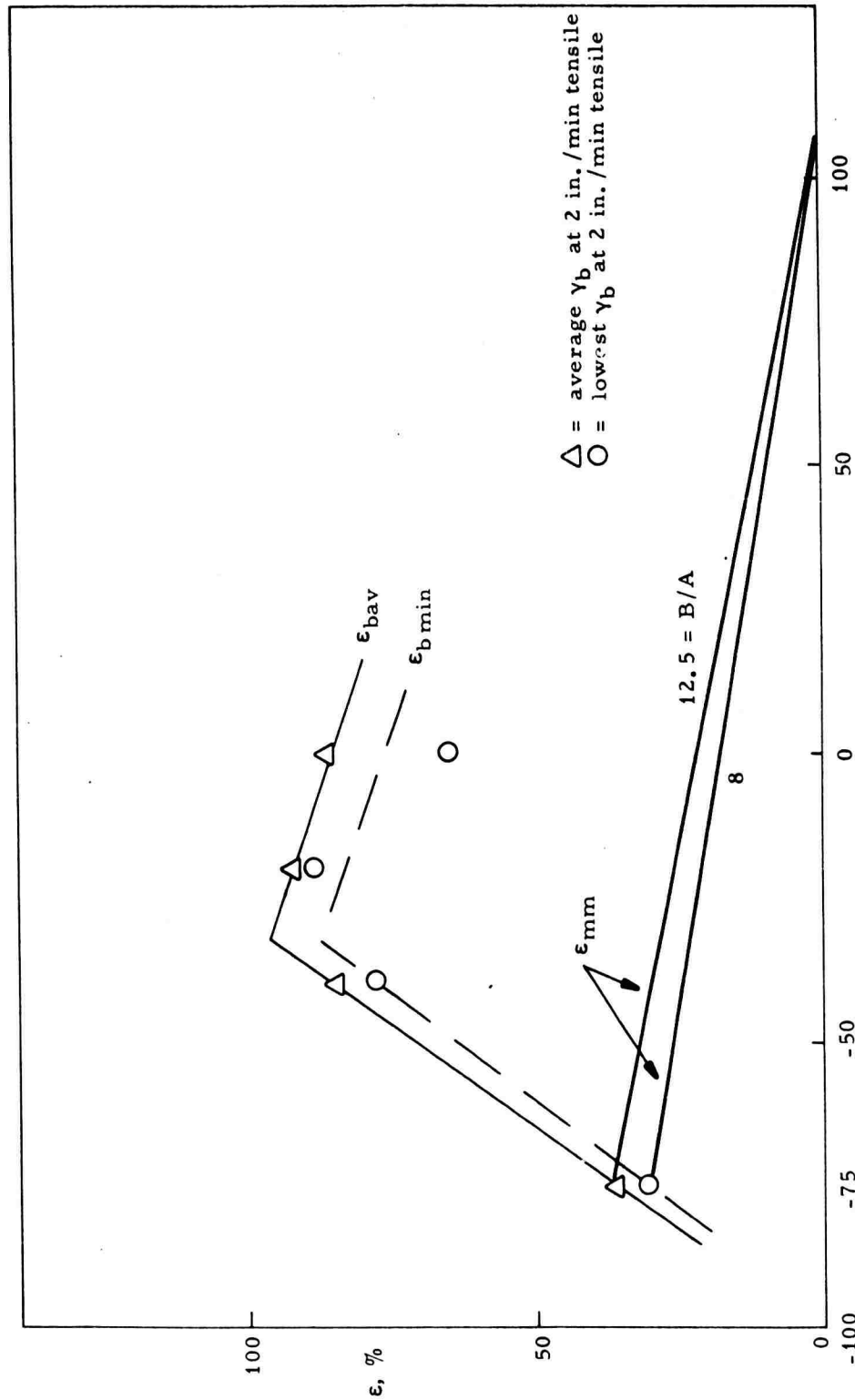
Figure 131. Comparison of Calculated Motor Hoop Strains With Observed Tensile Failure Strain for Class 1, Batch 61-3208M
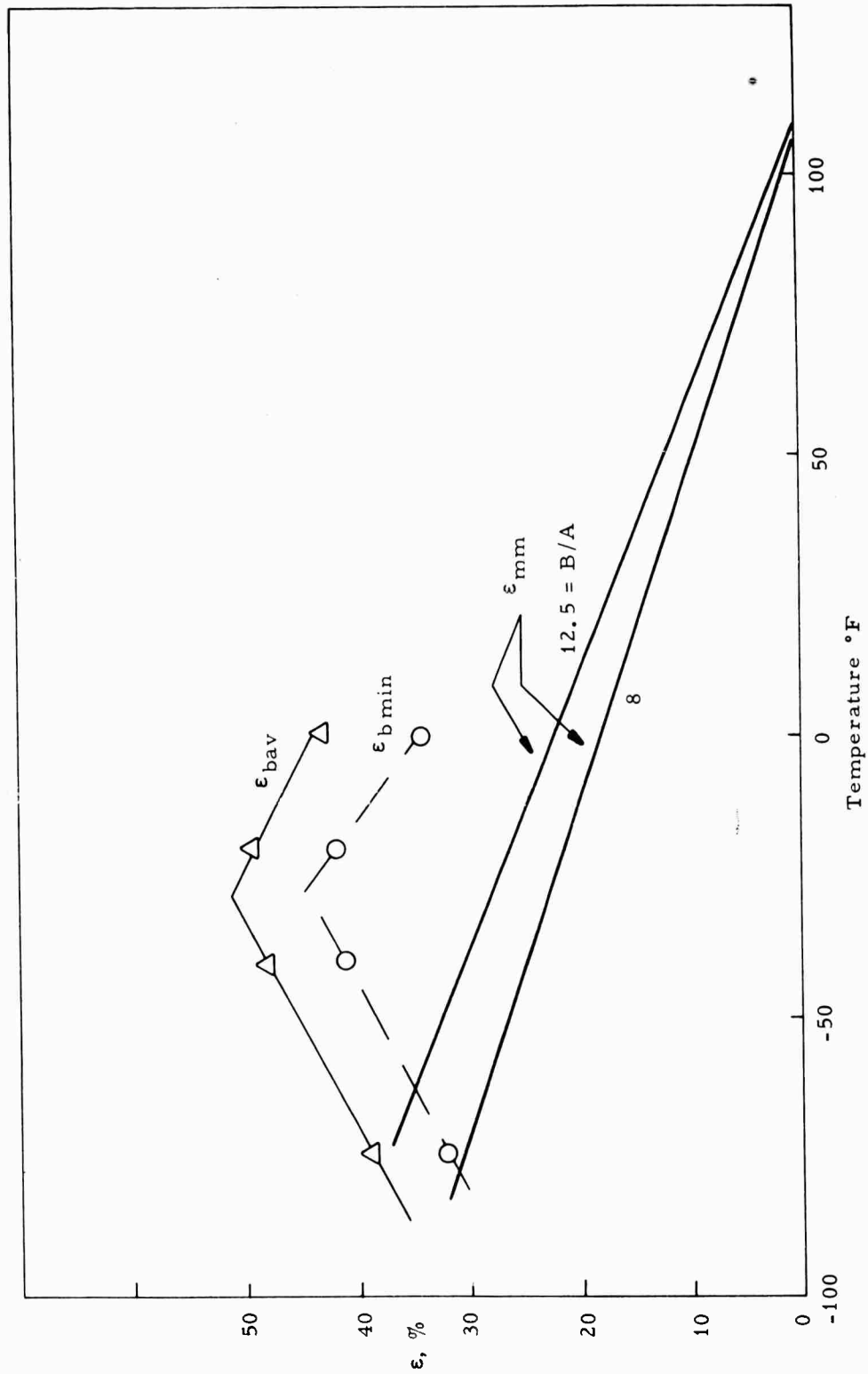
Figure 132. Comparison of Calculated Motor Hoop Strains With Observed Tensile Failure Strains for Class 2, Batch 61-3210M
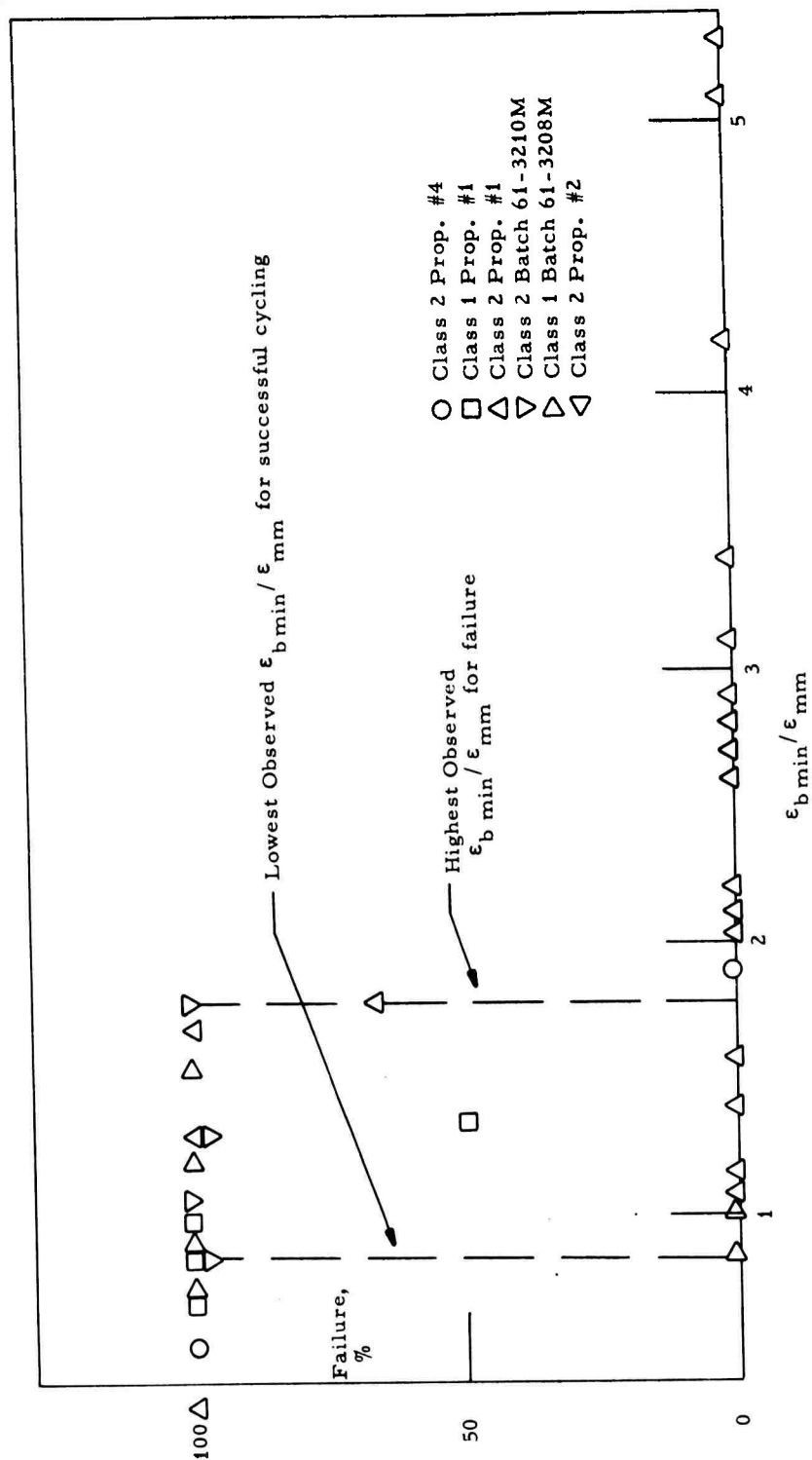
Figure 133. Summary of Failure Criteria Data

V, B, Correlation of Failure Data With Small Motor Failures (cont.)

Class 2 propellant #2 unaged and dry) below a value of 0.85. In view of the effects of rates of loading on standard testing with the wide variety of much slower rates encountered in motor cycling, the correlation continues to appear promising if used for conservative estimation. The effect of a non-uniform stress-strain field, as in a star configuration, on the failure distribution remains to be seen.

C. FAILURE AT VERY LOW STRAIN RATES

The requirement for failure studies covering larger numbers of specimens and under environmental conditions similar to those in the motor has led to the development of the very low rate tester (VLRT) shown in Figure 134. Through gear reduction, a speed range of 0.002 to 0.0005 in./min. can be obtained, equivalent to a time of failure range of 5 to 30 hr. Provision for mounting up to eleven standard specimens is provided. Break time of individual specimens can be measured from the steps in the total load time curve. For greater precision, separate instrumentation could be set up to measure individual break times.

A photograph of the apparatus is shown in Figure 135. The load time record of a test of ten machined specimens simultaneously of a Class 2 propellant performed at 20°F and crosshead rate of 0.002 in./min. is shown replotted in Figure 136. Failure could be clearly distinguished for the first seven specimens, but difficulties with the recording pen ink caused the last three failure points to be lost. The machine has gear sets to permit operation at crosshead rates of 0.002, 0.0015, 0.001, and 0.0005 in./min. Initial operation was at constant temperatures, but studies under changing temperatures corresponding to strain development on motor cycling can be performed also.
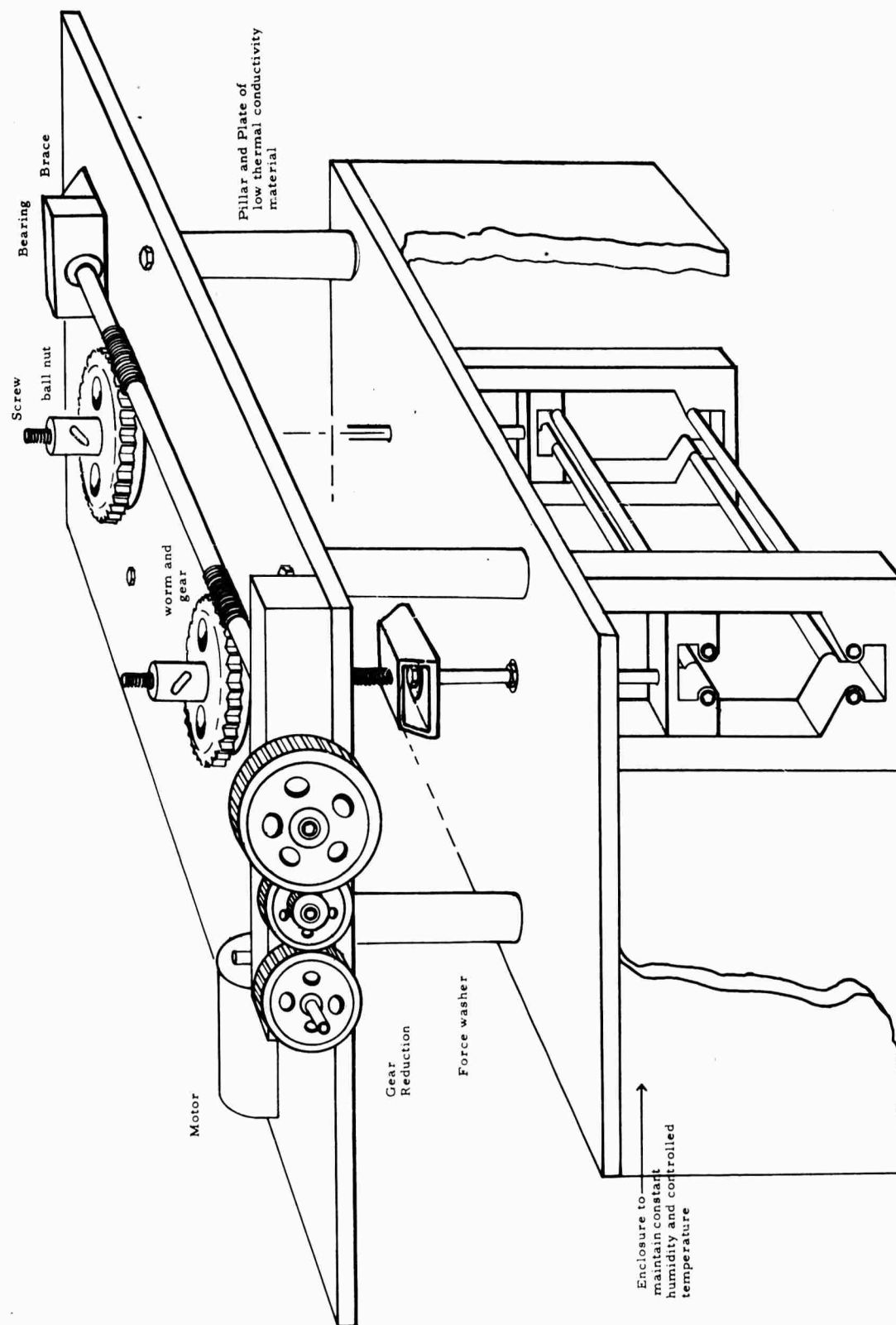
Figure 134. Sketch of Very Low Rate Tester (VLRT)
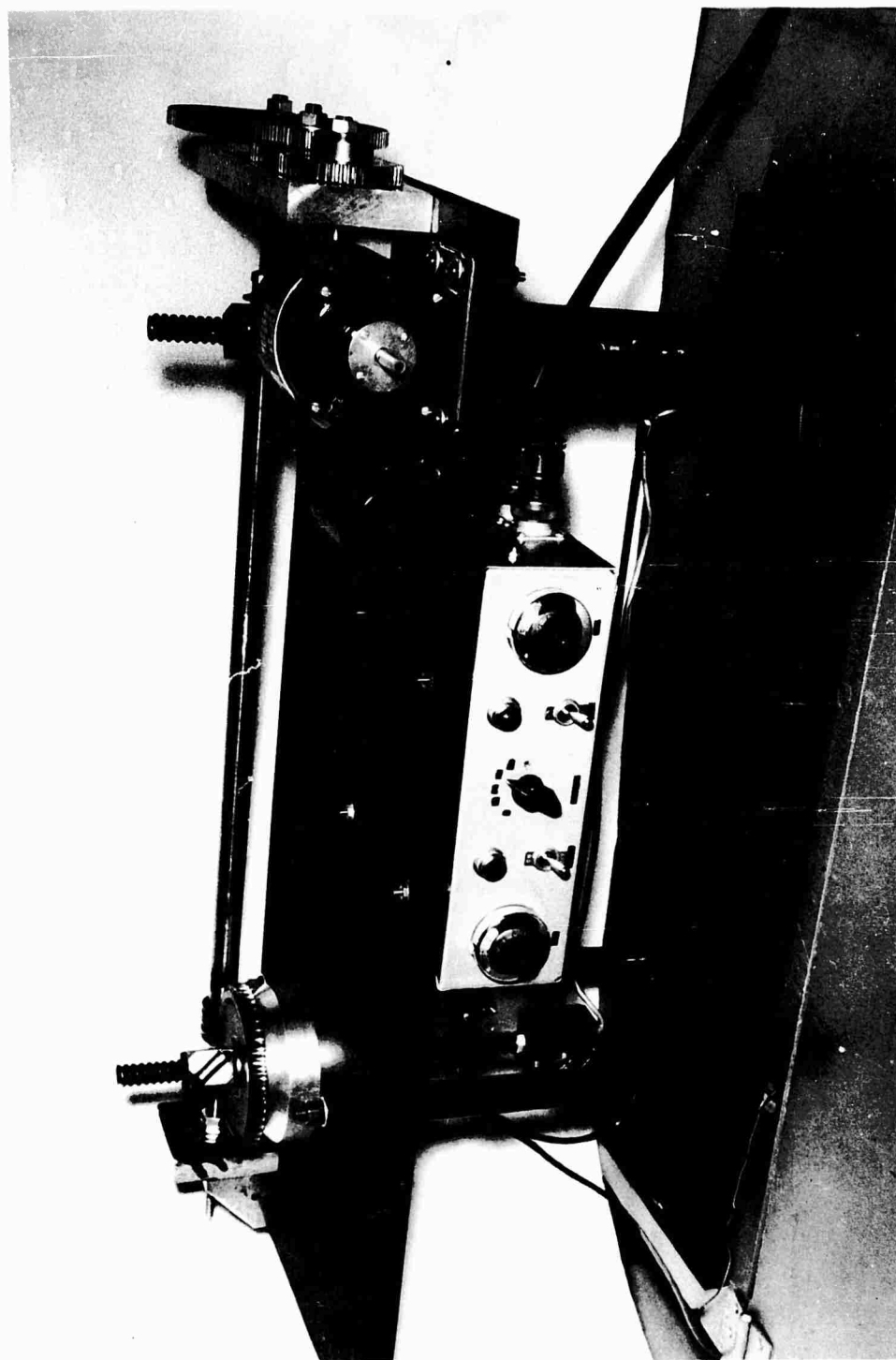
Figure 135. Upper Part of Very Low Rate Tester With Sample Holders Extending Below Lower Plate Into the Conditioning Chamber (8-61S 22318)
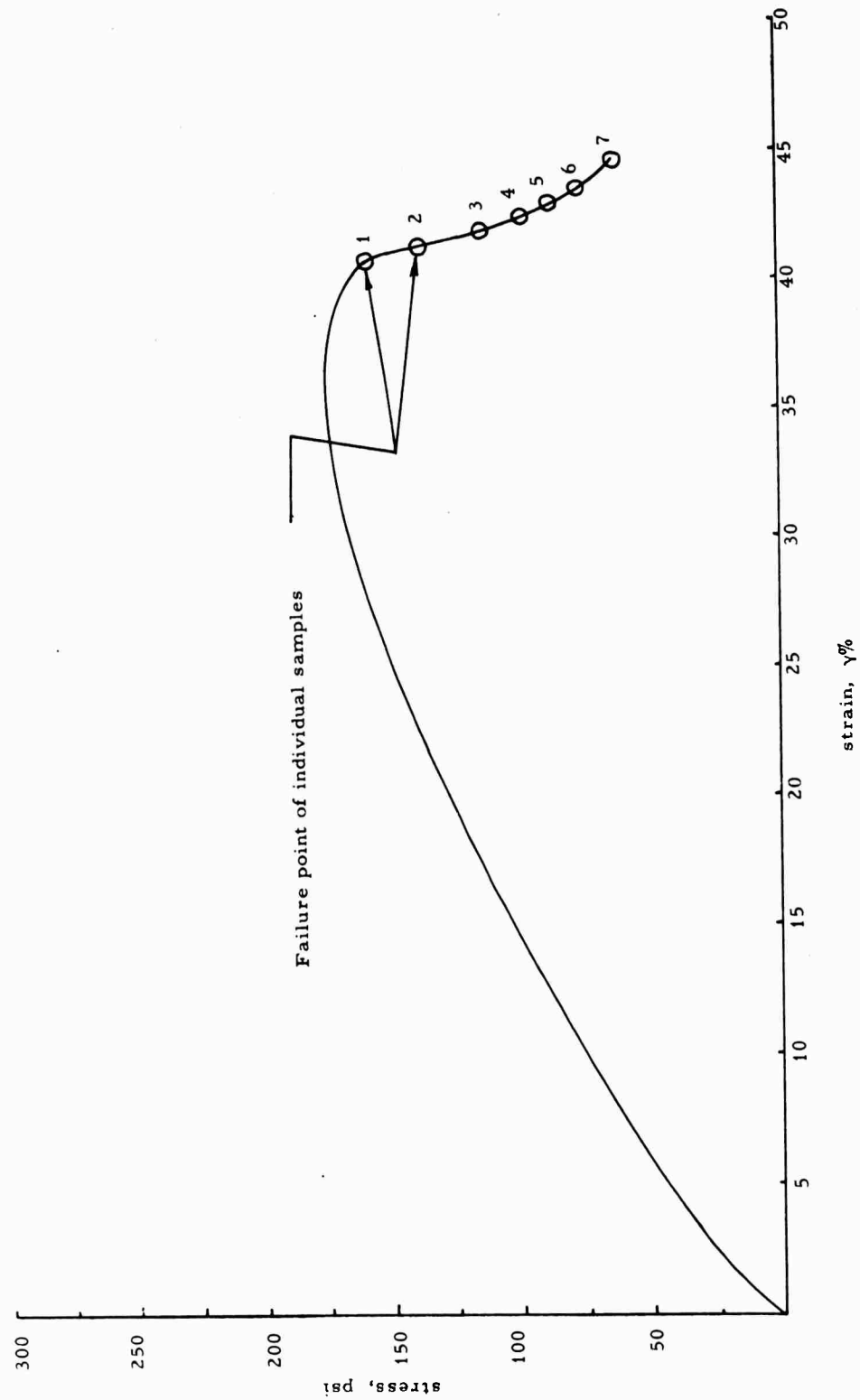
Figure 136. Ultra Slow Rate Tensile Test on Ten Specimens of Class 2 Propellant at 0.002 in./min. at 20°F

V, Phase 4 -- Failure Criteria (cont.)

D. CORRELATION OF FAILURE BEHAVIOR

1. WLF Rate Shift Factor Correlation

The correlation of mechanical property behavior at different rates and temperatures has been performed on many polymers following the shift factor technique of Williams, Landel, and Ferry (35)(WLF). Correlation of failure behavior for a rubber was shown by Smith and Stedry (34). Correlation of failure in the highly filled polyurethane systems, such as the Class 2 propellant, has not been reported in the literature. From consideration of available test data on propellants, it appeared that the maximum elongations at failure at any rate for different temperatures were not the same, this maximum decreasing as the temperature decreased. A test of the correlation is difficult since for only a few temperatures and rates generally studied, do the elongations go through a maximum, so only a portion of any set of data can provide data applicable directly to the question. Uniaxial tensile failure data for one batch of the same Class 2 propellant whose batch failure behavior are shown in Figures 122 to 125 were available at temperatures from -75°F to 180°F and strain rates from 0.074 to 1000 $min.^{-1}$. The values given in Table 34 are the average of five specimens. The analysis of the data was performed graphically using the WLF technique by shifting the points, plotted as ε_b vs log R for each temperature, horizontally and also vertically as required to produce a continuous curve of ε_b vs log Ra_T. Analysis started with the 180°F data and proceeded systematically down to -75°F. The vertical shift, not required for elastomers without filler, was done without regard to fitting a particular pattern and the results are shown in Figure 137 where the experimental locations of the point $\varepsilon_b = 0$, $R = 1$ $min.^{-1}$ are shown. The final reduced scale, log Ra_T, was selected for a shift factor based on the WLF equation, as discussed below. The vertical shift required, described by the term ε_T, was

TABLE 34

UNIAXIAL TENSILE FAILURE STRAINS, %, FOR A CLASS 2 PROPELLANT

Temp.,	Strain Rate, min. $^{-1}$						
°F	0.074	0.74	7.4	100	500	1000	2000
180	46.4	52.4	65.0	81.8	92.5	92.2	90.1
140	50.8	56.9	66.5	85.4	88.6	100	92.7
110	55.8	67.8	71.4	84.9	88.6	91.4	107
80	66.4	66.1	81.4	92.2	95.3	98.8	99.9
40	71.1	76.4	79.6	98.1	91.8	90.0	88.1
0	70.6	84.2	79.2	76.0	65.8	62.5	68.1
-40	58.3	56.4	47.6	65.8	44.4	26.2	22.8
-60	50.2	53.0	48.4	- - -	23.9	15.5	14.8
-75	35.1	27.0	17.0	9.4	8.9	5.2	3.5
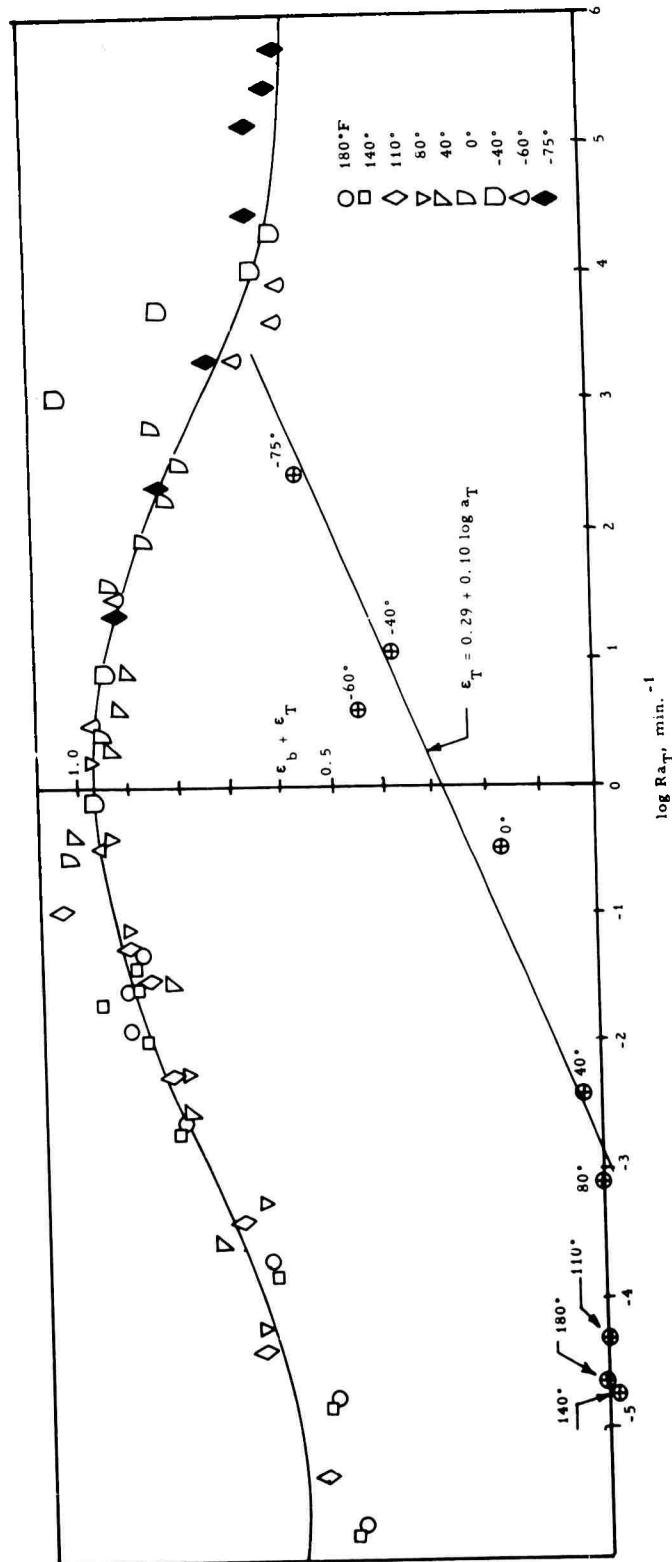
Figure 137. Variation of Failure Strain of Class 2 Propellant With Reduced Rate, ε_T, Showing Symmetry of Curve Obtained With Vertical Shift Factor, ε_T, Using $t_s = -36°F$
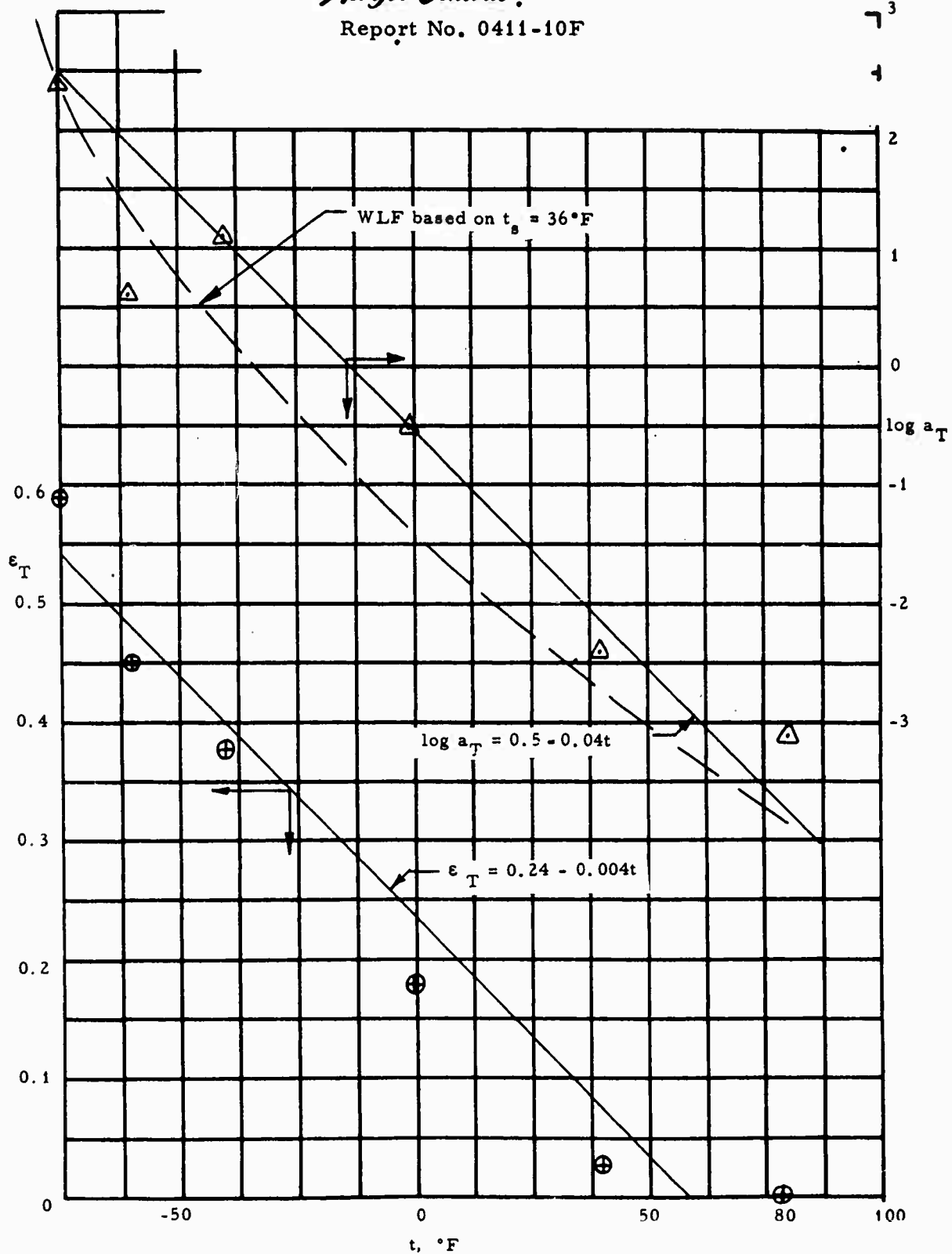
Figure 138. Relationships of Log A_T, ε_T, and Temperature From Figure 137

V, D, Correlation of Failure Behavior (cont.)

apparently zero for temperatures of 80°F and above, but became increasingly large as the temperature approached -75°F. The equation shown on Figure 137 describing the line drawn for ε_T is

$$\varepsilon_T = 0.29 + 0.10 \log a_T \tag{89}$$

The same points used to define the line given by Equation (89) are shown in a different way on Figure 138, e.g., the vertical shift, ε_T, vs temperature, and the corresponding value of the shift factor, $\log a_T$, vs temperature, and the corresponding value of the shift factor, $\log a_T$, vs temperature. The equations are

$$\varepsilon_T = 0.24 - 0.004t \tag{90}$$

and

$$\log a_T = 0.5 - 0.04t \tag{91}$$

The selection of line positions was chosen to make the constants of Equations (80), (90), and (91) consistent among themselves, e.g., any two of the equations will define the third.

Considering now the usual WLF shift factor, the WLF equation can be rearranged to give

$$T = T_s - 101.6/(1 + \frac{8.86}{\log a_T}) = T_s - A_T \tag{92}$$

In this form, it can be seen that a graph of T vs A_T will be a straight line of unit slope. Such a graph is shown in Figure 139, with a graph of $\log a_T$ vs A_T
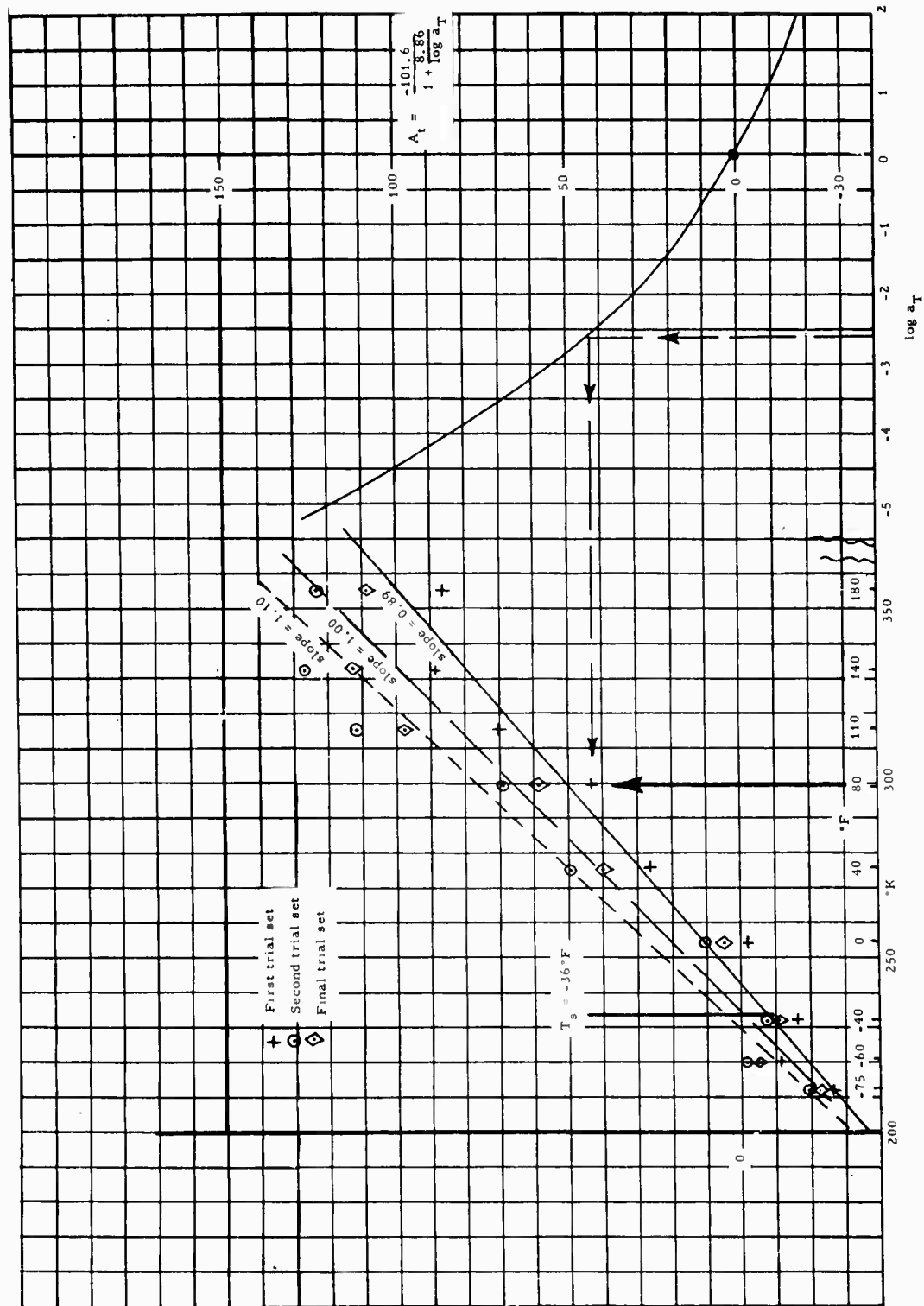
Figure 139. Location of T_s Using Shift Values A_T From Figure 137 and Linearized Shift Function

V, D, Correlation of Failure Behavior (cont.)

shown at the right for convenience. Using the data of Figure 137, before T_s was selected and the data normalized, an arbitrary shift was made by assuming a value of log a_T at -75°F and thus determining the relative value of log a_T for all the other reference data points on Figure 137. Plotting these on Figure 139, the data gave a line of slope 0.89, and T_s = 243°K. Selection of a second esti- mate of log a_T -75°F gave a second line of slope 1.10 and T_s = 230.°K. Inter- polation, which was found to be nonlinear, finally gave data that produced a line of slope 1.00 and T_s = 235°K (t_s = -36°F).

If a WLF shift factor relation holds in this case for the low temperature data, then the straight line relation of Equation (91) would not be expected to apply. Comparison of the straight line with the WLF curve for t_s = -36°F from Figure 139 is shown in Figure 138.

2. Temperature Shift Correlation

The scatter of the shift data for this propellant system led to an examination of the data when plotted vs temperature at each rate. It was discovered that the data could be superimposed to give a lower variability when an arbitrary origin was shifted both horizontally and vertically as shown in Figure 140. Not only do the data show good agreement with two straight line segments, but the shift points of the origin -- selected at 0°F and zero strain -- are remarkably consistent and show none of the scatter characteristic of the rate shift data of Figure 137. When plotted as log R vs the temperature shift required in Figure 141, a good straight line is obtained having the equation

$$\log R = 3.1 - 0.057t \tag{93}$$
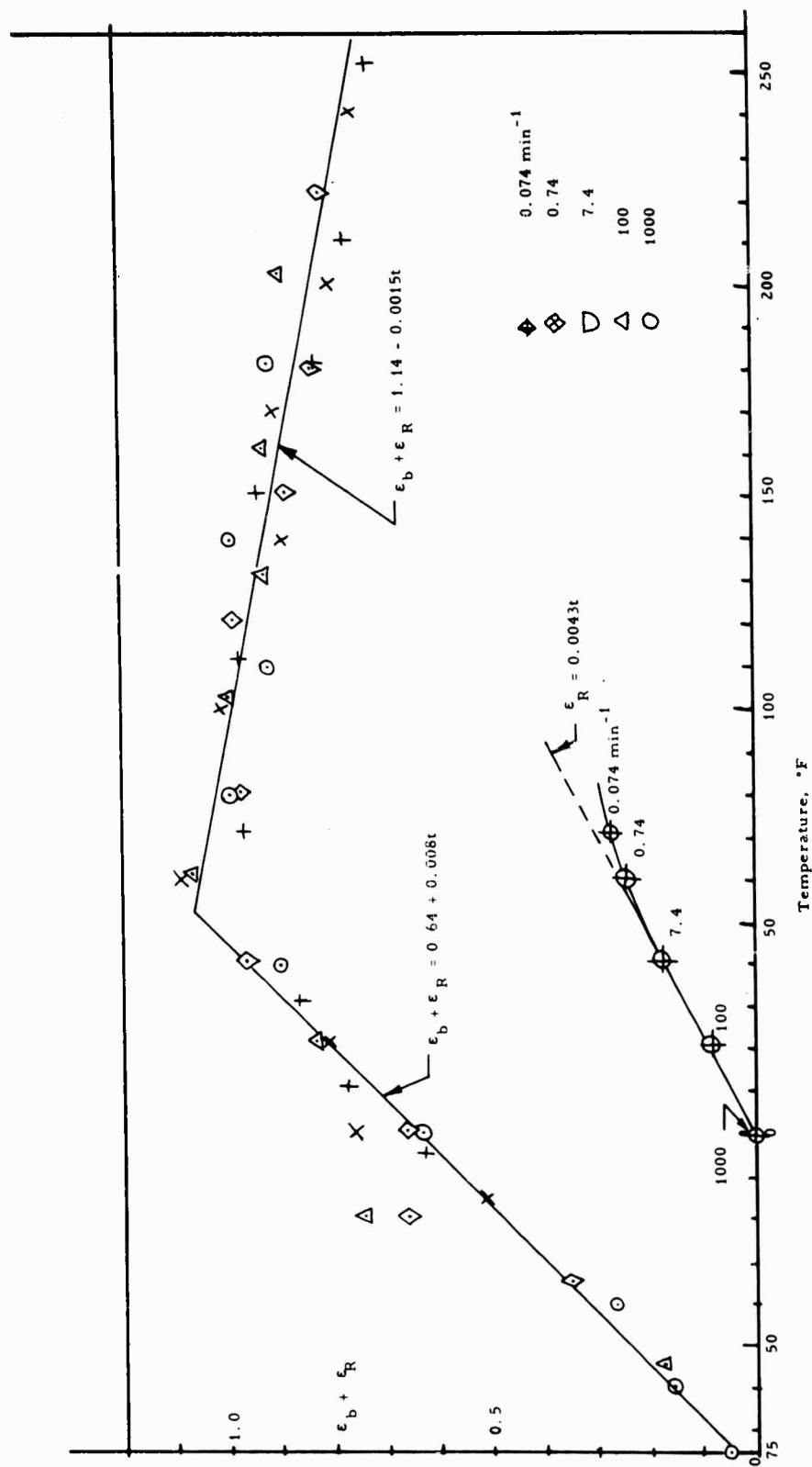
Figure 140. Variation of Failure Strain of a Class 2 Propellant With Temperature Using Diagonal Shift
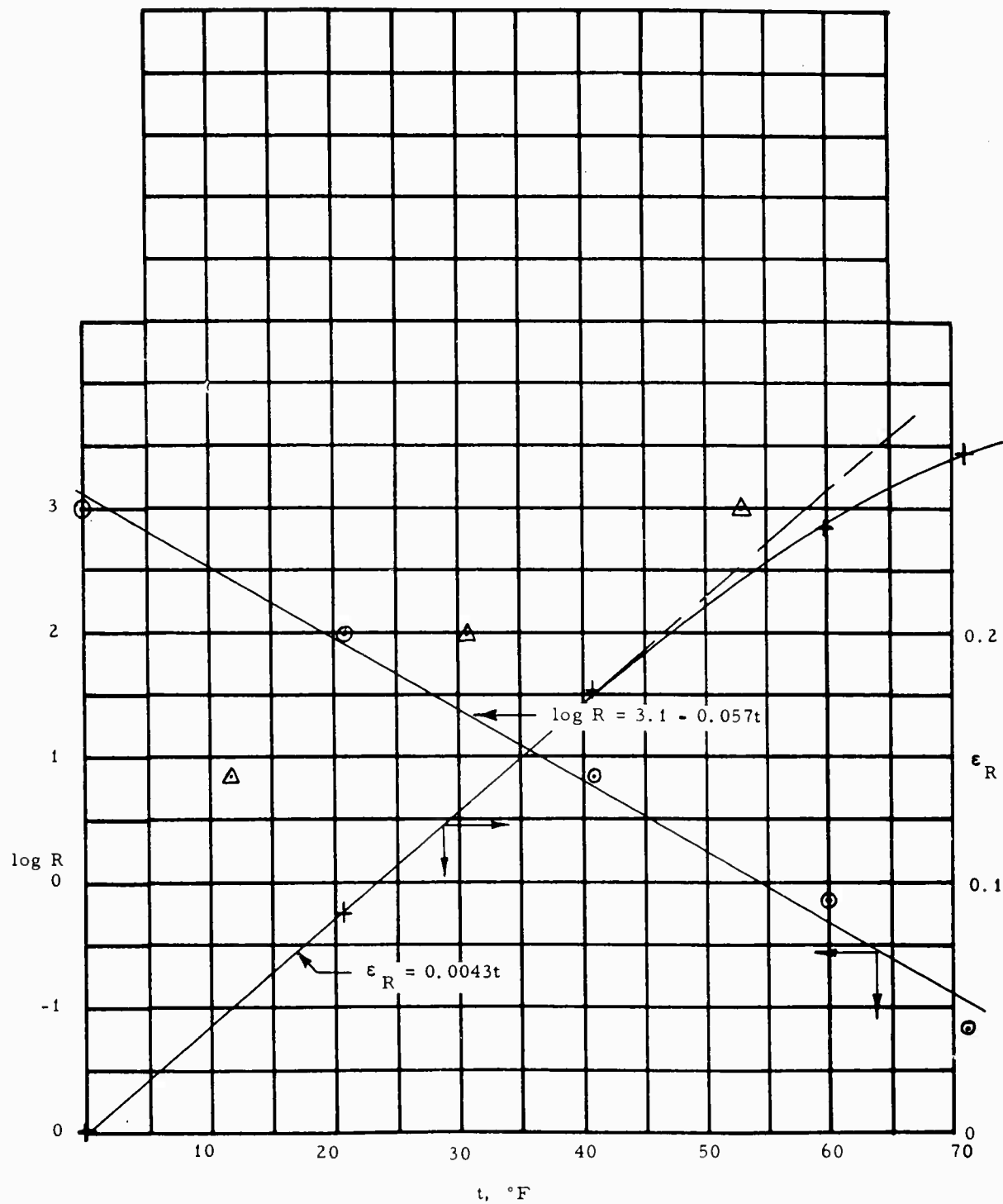
Figure 141. Relation of Log R and ε_R to Temperautre for Shift Data of Figure 140

V, D, Correlation of Failure Behavior (cont.)

Plotting the ε_R value at each shift point vs the temperature does not, however, give a straight line but rather a curve suggesting that ε_R does not increase above some limiting value even for very low rates of testing. This possibility may be evaluated by tests on the Very Low Rate Tester, but is already suggested by the values obtained in constant strain failure testing, equivalent to extremely low rates of loading.

The two straight line segments of Figure 140 give

$$\varepsilon_b + \varepsilon_R = 0.65 + 0.008t, \quad t < 50°F \text{ at } 1000 \text{ min.}^{-1} \tag{94}$$

$$= 1.14 - 0.0015t, \quad t > 50°F \text{ at } 1000 \text{ min.}^{-1} \tag{95}$$

It is of interest to note that the maximum occurs near $0°F$ for $R = 0.74$ min.$^{-1}$, a general characteristic of many polyurethane propellant systems.

E.   TEAR PHENOMENA

The complex failure behavior of solid propellants is confounded by many variables and is not understood. It is not surprising since a precise understanding of the failure modes of unfilled rubbers and related systems has been the subject of study for a number of years and is still not clearly defined. Therefore, this apparently complicated nature of failure in polymer system is only further complicated by the addition of fillers, such as oxidizers, which are used in current solid propellant applications.

The ultimate strength of a solid propellant is associated with two important areas: (1) inherent strength of the binder, and (2) the binder-filler bond. The behavior of these two areas under static and dynamic loading conditions predicts the integrity of the propellant grain to withstand failure.

V, E, Tear Phenomena (cont.)

Many studies have been made to assess the importance of rate of loading, filler type, and temperature upon the tensile, creep and stress relaxation properties of solid propellants. However, another parameter which is just as important and is associated with both static and dynamic effects is the tear behavior of the propellant grain.

Tear strength is frequently associated with overall tensile properties of the propellant and thus very little work in this specific area has been accomplished. Tearing, however, frequently occurs under conditions in which pure tensile failure would not occur. Principally, the study of tensile behavior in localized stress regions may be more precisely defined as the study of tear.

1. Literature Survey

A survey of the unclassified literature on the subject of tearing in filled and unfilled elastomers has been made. An analysis of the general conclusions of the various authors has been compiled in order to correlate their views on the different areas of study in this field.

a. Test Specimens

In general, tear resistance is usually determined by loading in a specified manner a test-piece of the elastomer of standard shape. A variety of shapes have been recommended and yield results which are characteristic of the method of test as well as of the particular type of test-piece used. Specifically, four main types of specimen have been evaluated (37, 44, 77). A fifth specimen type was used by Bussee (51) in his studies but comparisons with other specimens were not obtained. Inconsistent conclusions are made between the Delft specimen and ASTM Specimens A (Crescent), B (Crescent),

V, E, Tear Phenomena (cont.)

and C (Angular) as shown in Figure 142. Chiesa (37), Graves (38), and
Morris (41) obtained equal or better results with the standard angular type
specimen when compared with the other standard types while Nijveld (39)
and Buist (40) found better results with the Delft and crescent-shaped specimen.
It was found by Chiesa, however, that the crescent-shaped-test piece with a cut
appeared to give precise tear propagation tests although no difference was noted
with the angle-tear-test piece with or without an initial cut.

Considerable experimental evidence has shown that the
crescent-shaped specimen and the angle-tear specimen measure different com-
binations of physical stresses (42). With crescent-shaped specimens, the
results are governed chiefly by the modulus and extensibility of the material.
The angle test method indicates that resistance to tearing is a complex function
of tensile strength and extensibility. In all cases, however, it was shown that
careful specimen preparation was necessary to give more accurate test results
and thus eliminate large variability in data (43, 44).

b.   Test Method

In general, tear tests include two major areas of
measurement: (1) dependence of tear propagation velocity upon the speed of the
testing machine, and (2) spontaneous tear propagation. Various methods of
testing the resistance to tear of filled and unfilled elastomers have been inves-
tigated (37, 39, 40, 45, 54). Chiesa (37) found that the static method gives a
fair correlation between load at start of spontaneous tear propagation to initial
load, and length of the cut when tearing started to the original width of test
piece. No proportionality between remaining cross section and the load was
observed, however. The relationship between the slow dynamic method and
fast dynamic method with a tensile testing machine was also studied by Chiesa.

← 1.65" →

Nick 0.02" deep

CRESCENT TYPE A (ASTM)

|← 4.3" →|

Nick 0.02" deep

CRESCENT TYPE B (ASTM)

Note: No Nick

← 4.0" →|

ANGLE TYPE C (ASTM)

DELFT SPECIMEN ↗
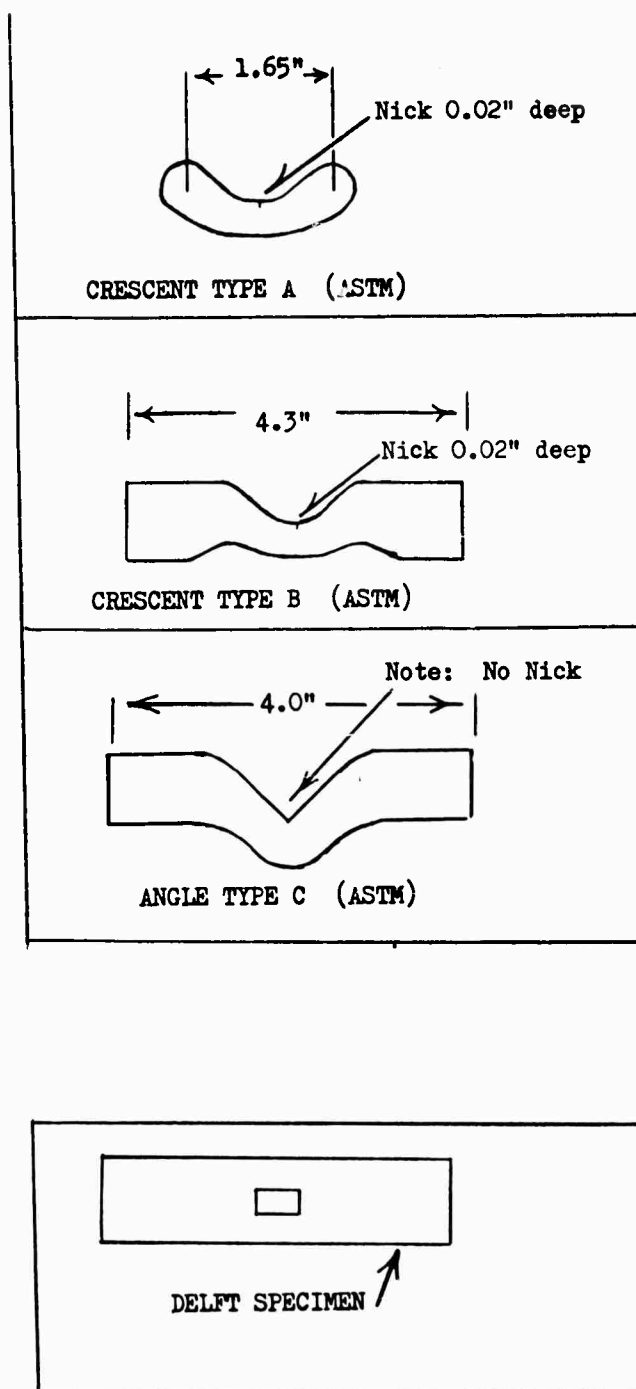
Figure 142. Schematic Drawing of Different Types of Tear Specimens Used by Various Investigators in Tear Studies

V, E, Tear Phenomena (cont.)

In these methods the standard ASTM specimens A and C were used. It was found that the slow dynamic method was the most informative. Conditions with the fast dynamic test are entirely different from those with the slow test because the velocity of stretching in the fast dynamic test is comparable to the tear propagation velocity. The results between the two did not differ greatly and hence, the fast dynamic method was not considered to be advantageous.

Kainradl (45) observed that for thin specimens the breaking extension at the notch of a vulcanizate was about the same as the breaking extension of the unnotched test specimen. The breaking extension, however, decreased with increasing thickness of the notched test specimen. The decrease in breaking extension at the base of the notch was studied in relation to other test variables. The essential difference between a tear test and a tensile test is the occurrence of a lower breaking elongation at the notch. Tear strength differences can be accounted for on the basis of differences in modulus, breaking elongation, and plastic flow.

c.   Tear Rate and Resistance

The rate of propagation of tear and the tear resistance of unfilled and filled elastomers is dependent on many variables. These variables have been assessed by a number of investigators during the last forty years (45, 46, 49, 55-65, 79, 80, 83, 85, 86). Kainradl (45) showed that the values of the tear strength for a variety of vulcanizates first declined as the tear test velocity was increased, went through a minimum and then mounted rapidly at higher velocities. The explanation of these phenomena was considered to lie in the molecular processes of orientation and crystallization on the one hand and plastic flow on the other. The reciprocal relation between the effects of increasing the temperature and increasing the tear test velocity observed by Gul (56), Greensmith (57), and Epstein (61) were consistent with Kainradl's observations.

V, E, Tear Phenomena (cont.)

The effect of depth of nick, test piece width and number of nicks have important effects on the resistance to tearing (46, 49, 60). Particularly, Chasset (46) reports that tear strength increases with test piece width. Buist (60) performed a systematic study of the resistance to tearing of unloaded and carbon black mixtures of elastomers. The method specified by ASTM D624-41T was followed, and the resistance to tearing at six different depths of nick and at four temperatures was measured. The data show the importance of the depth of nick, and that a nick 0.02 in. deep gives in general the least variable tear resistance.

Tear resistance, like most other mechanical properties, has also been found to be a function of the state of cure of the test specimen and, therefore, sensitive to aging effects (55, 62 - 64). Talalay (62) in his studies on the influence of the state of cure and of various fillers on the resistance of vulcanized rubber to tearing found that all mixtures had a maximum resistance to tearing at a definite state of cure, in general at a lower state of cure than that corresponding to the maximum tensile strength. The work of Zimmerman (55) is substantiated by these data. In addition, the resistance to tear was also found to decrease with overcure (63).

The tear resistance of vulcanized latex films is much higher than that of masticated vulcanized dry compounds (65). However, the work of van't Wont and de Vries (64), described as unreported data, shows that on aging in air at 70°C, or in compressed oxygen at 70°C, the tear resistance of vulcanized latex films decreases relatively rapidly to the values of masticated vulcanized sheets. Even at room temperature the tear resistance decreases slowly. Other properties, e.g., tensile strength, modulus, and elongation at rupture, do not show this abnormal behavior. Hence, the use of tear testing as a method for following aging may prove useful.

V, E, Tear Phenomena (cont.)

Examination of the rate of cut growth of filled and
unfilled elastomers has been investigated by Thomas (58) and Hampe (59). In
natural rubber vulcanizates (58) the tip of the cut under repeated loading
becomes rough and the rate of cut growth decreases to a final steady value. For
filled elastomers (59), the growth rate is a function only of the cut depth attained
and is independent of the size of the initial cut. A plot of cut length versus cut
depth approaches a limiting curve for a sufficiently long testing time independent
of the initial ratio of length to depth.

d.   Specific Effect of Fillers

The specific effect of fillers on the tear properties of
vulcanizates has been studied by a number of investigators (48, 55, 61 - 63,
66, 67, 68, 84).

It was found that different types of fillers produce differ-
ences in the mechanism of tearing of vulcanizates (48). Tests with different
proportions of filler in rubber mixtures at different states of cure showed that
there is no simple relation between the effect on the tear resistance and the
reinforcing power of the fillers. C and ZnO increased the resistance, while
$MgCO_3$ and clay diminished it (61, 62, 63, 67).

Interfacial affinity of rubber for fillers is suggested as
being chiefly responsible for the phenomena of resistance to tear, whereas
reinforcement is caused in part by mechanical effects such as friction and thin
film formation. Anisotropic fillers are particularly likely to develop these
mechanical effects, and thus to bring about a type of reinforcement which need
not involve an increased resistance to tear.

V, E, Tear Phenomena (cont.)

The electron microscope investigation of the rupture
process in carbon-loaded rubbers by Andrews and Walsh (66) sheds light on
this phenomenon. The deviation of the rupture path in filled rubbers, evidenced
by surface roughness and excess total filler, is explained in terms of multiple
internal failure occurring around filler particles just ahead of the advancing
rupture. The adhesion of filler to rubber is a surface-specific quality and is
related to the energy required to propagate rupture.

e.   Mechanism and Theory of Tear

Mechanism of tearing in unfilled and filled elastomers
has been postulated by many authors and experimental data have been produced
to substantiate theoretical considerations (48, 51, 68, 53, 75, 85). Perhaps
the greatest amount of work has been done by Gent, Rivlin, Thomas and
Greensmith (47, 57, 58, 78, 82, 87 - 91) on the characteristic energy criterion
for tear in rubbers, under various conditions, based on modifications of the
flaw theory proposed by Griffith (71) for brittle materials. In addition, Gul (73)
provides a comprehensive review of work done on the mechanism of rupture of
high polymers as well as theoretical and experimental data.

f.   Tear of Foamed Materials

Very little work has been done on the tear properties
of foamed materials. In their work with foams, Gent and Thomas provide a
theoretical treatment which predicts the tear of a foamed elastic material (74).

V, E, Tear Phenomena (cont.)

g.   Summary of Survey Conclusions

(1)   Inconsistent conclusions have been drawn by various workers using the Delft specimen, the ASTM Type A (Crescent), B (Crescent), and Type C (Angular) in tear studies.

(2)   Slow dynamic testing was considered to be more informative than fast dynamic testing.

(3)   The tear strength of a variety of vulcanizates first declined as the tear test velocity was increased, passed through a minimum and then increased rapidly at higher velocities. The explanation of these phenomena was considered as being associated with the molecular processes of orientation and crystallization on the one hand and plastic flow on the other.

(4)   Tear resistance, like most other mechanical properties, has also been found to be a function of the state of cure of the test specimen and, therefore, sensitive to aging effects.

(5)   A variation in the type of fillers has produced differences in the mechanism of tearing of vulcanizates. Tests show there is no simple relation between the effect on the tear resistance and the reinforcing power of the fillers.

(6)   Interfacial affinity of the rubber for fillers has been suggested as being chiefly responsible for the phenomena of resistance to tear, whereas reinforcement is caused in part by mechanical effects such as friction and thin film formation.

V, E, Tear Phenomena (cont.)

(7)   A characteristic energy criterion for tear in rubbers
has been developed based on modifications of the flaw theory for brittle materials.

2.   Experimental

Initial studies were performed to determine the resistance of
inert propellant formulations, containing 50 volume % glass beads with Class 2
and 3 binder systems, to tear as a function of binder type and filler size. These
measurements were made at a constant elongation rate of 0.22 min.$^{-1}$, over the
temperature range -60° to 180°F in 60° increments. A simple sample type,
shown in Figure 143-a, after Busse (51) was used to facilitate specimen prepa-
ration and provide as many samples as possible from the existing prepared
materials. It may be seen in Figures 144 through 147 that in both filled binder
systems the tear rate is affected by test temperature, as observed by other
investigators, and particle size, while work to produce initial tear increases
with a decrease in test temperature and is not materially affected by particle
size. This latter observation may be expected in light of the work of Buist (48).
The increased tear rate at -60°F is associated with a change in tear mechanism
at low temperature (45). Similar measurements were also performed on the
pure binder systems. These binders exhibited the same temperature behavior
as observed in the filled systems.

These preliminary studies using several sample types to
determine the tear resistance of two polyurethane polymers loaded with various
types of filler lead to the conclusions that the tear rate for both binder systems
is a function of both test temperature and filler size, the work to produce
initial tear increases with a decrease in test temperature but is not appreciably
affected by particle size, and the rate of cut growth with change in cut angle
and the remaining stress appear to be related in a pure shear sample.
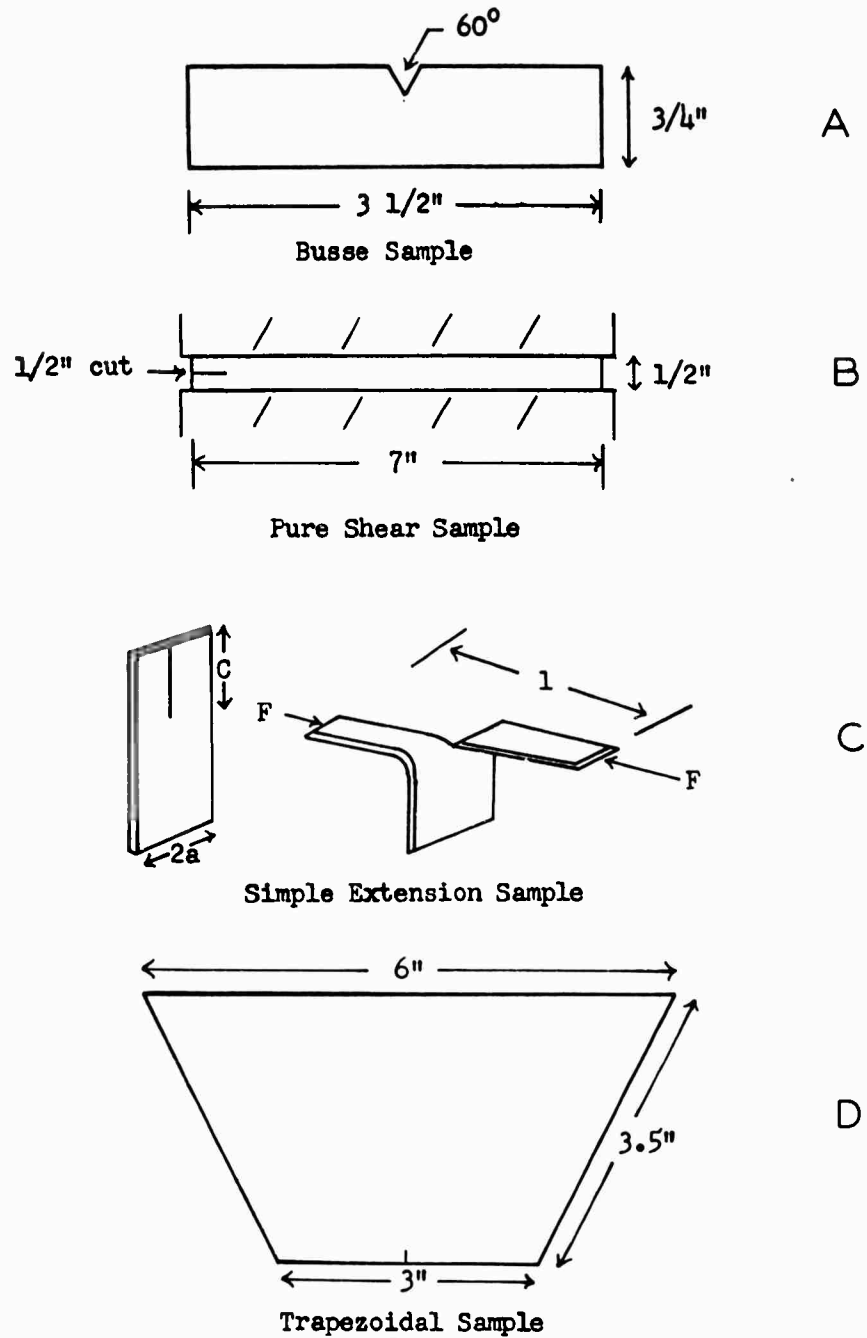
Figure 143. Schematic Drawing of Different Types of Tear Specimens Used by Various Investigators in Tear Studies
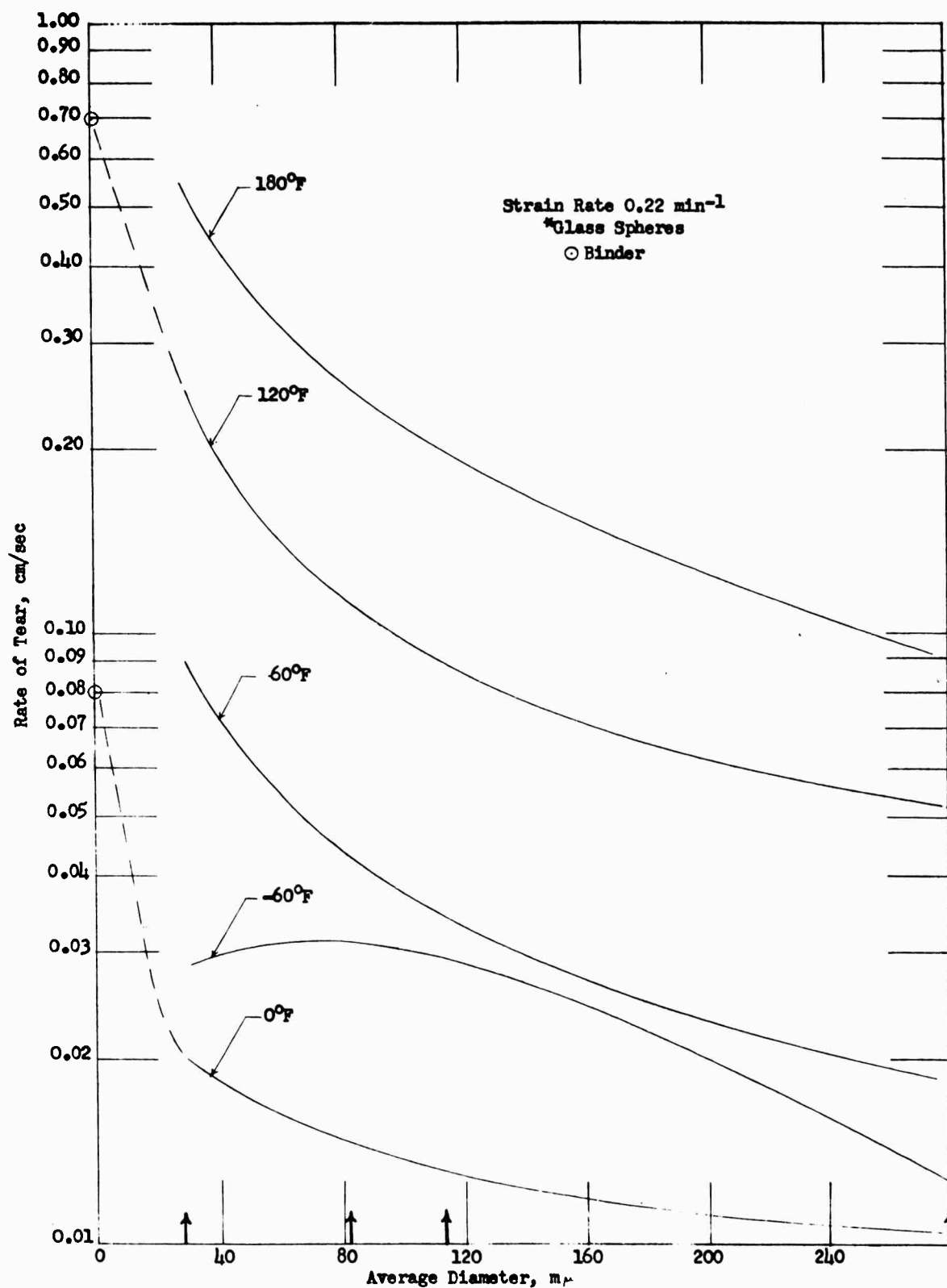
Figure 144. Effect of Particle Size and Temperature on Tear Rate of Filled Class 2 Binder
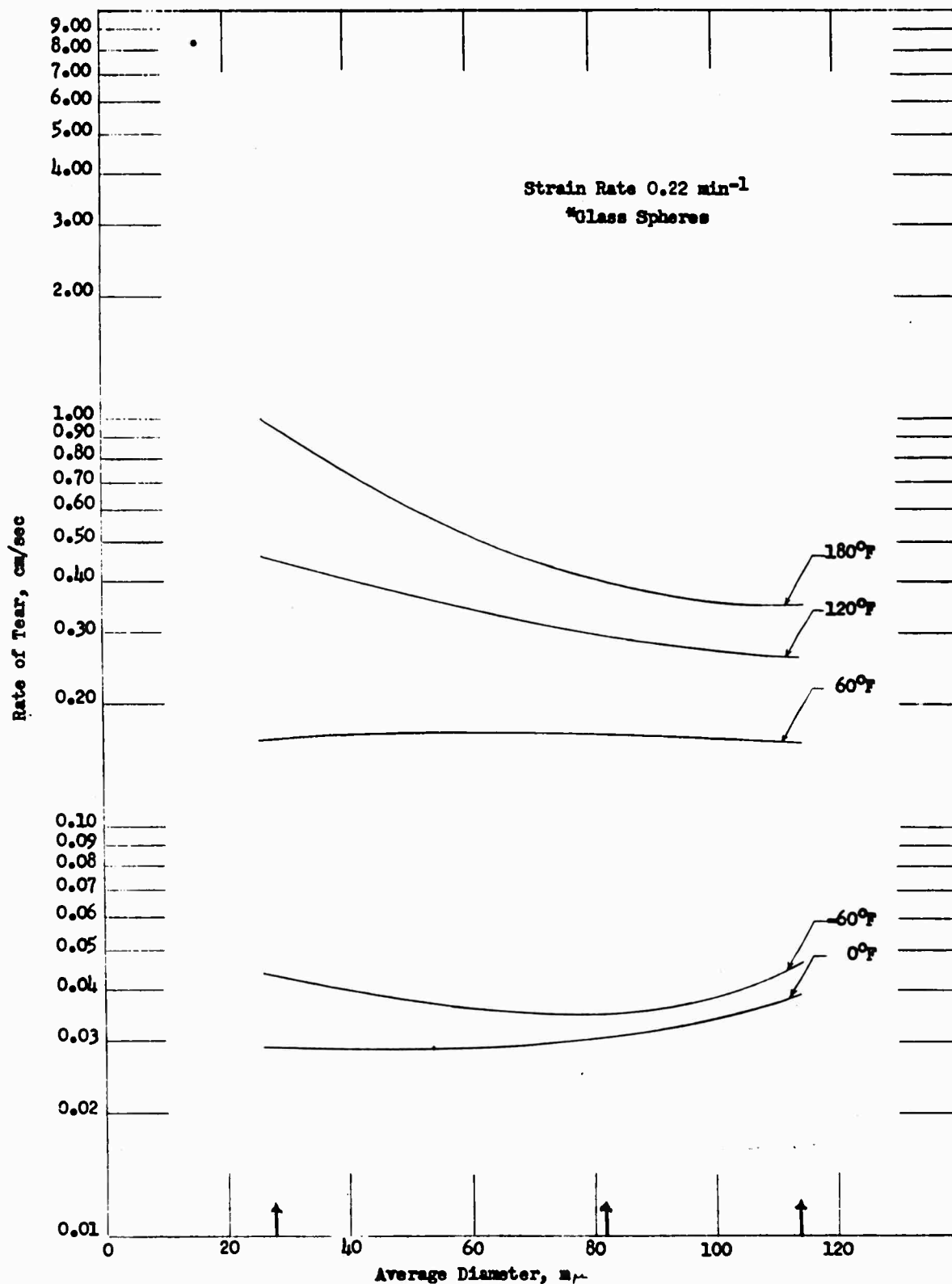
Figure 145. Effect of Particle Size and Temperature on Tear Rate of Filled Class 3 Binder.
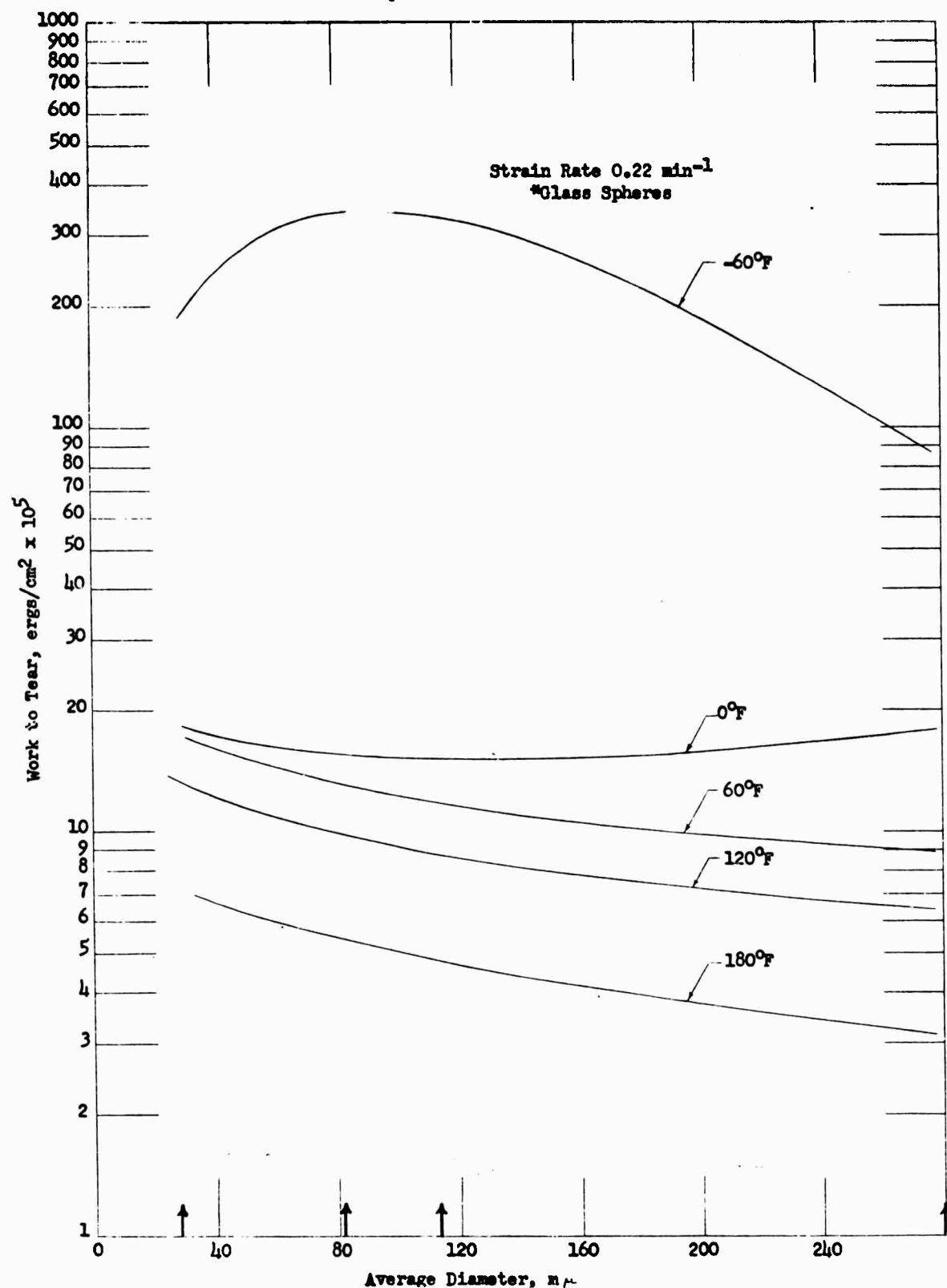
Figure 146. Work to Produce Tear in Filled Class 2 Binder as a Function of
Particle Size and Temperature
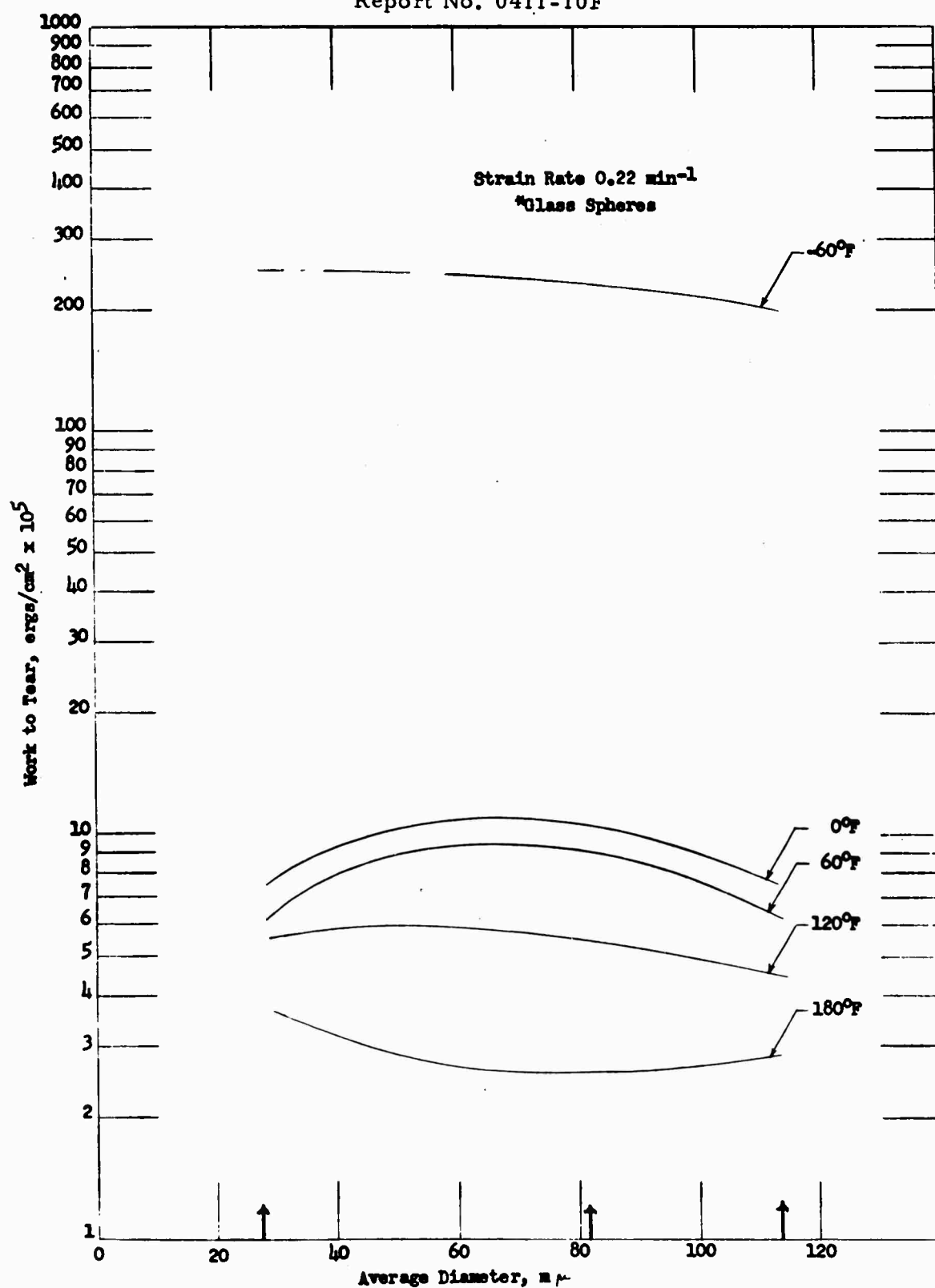
Figure 147. Work to Produce Tear in Filled Class 3 Binder as a Function of Particle Size and Temperature

V, E, Tear Phenomena (cont.)

Additional tear studies were then performed on the Class II
binder system with "pure shear" samples similar to those used by Rivlin and
Thomas (81) and shown in Figure 143-b. The rate of tear of this specimen
type with extension at 40°, 80°, and 110°F is shown in Figure 148. Initial
studies with filled systems using this type of specimen were not successful be-
cause of gross nonuniform tearing produced by the filler particles. In order to
apply the characteristic energy criterion for tearing discussed by Rivlin and
Thomas (81) and substantiated by Thomas, Greensmith, and Mullins (88, 91),
the second type of sample used in their studies, a form which is applicable to
both filled and unfilled systems, was used. This test-piece is shown in
Figure 143-c.

If a tearing force, F, is applied to the arms of the sample
to produce tearing along the central axis and if the arms are sufficiently long
in comparison with their widths (a), there will be a region of each arm which
is substantially in simple extension, with an extension ratio, λ, determined
by the force, F. For an increase, dc, in the length of the tear, the region of
simple extension in the arm is increased in volume by 2a x h x dc at the expense
of the undeformed region ahead of the tear; a, h, and dc being referred to the
undeformed state. The separation, 1, of the grips by which the force is applied
is thereby increased an amount, dl, given by:

$$dl = 2\lambda \, dc \tag{96}$$

From simple energy considerations, as described by Rivlin and Thomas (55),
the energy for tearing, T, is given by:

$$T \, h \, dc = F \, 2\lambda \, dc - W_o = a \, h \, dc \tag{97}$$

Where W_o is the work done/unit volume in deforming the vulcanizate in simple
extension to an extension ratio, λ. Rivlin and Thomas also show that if the
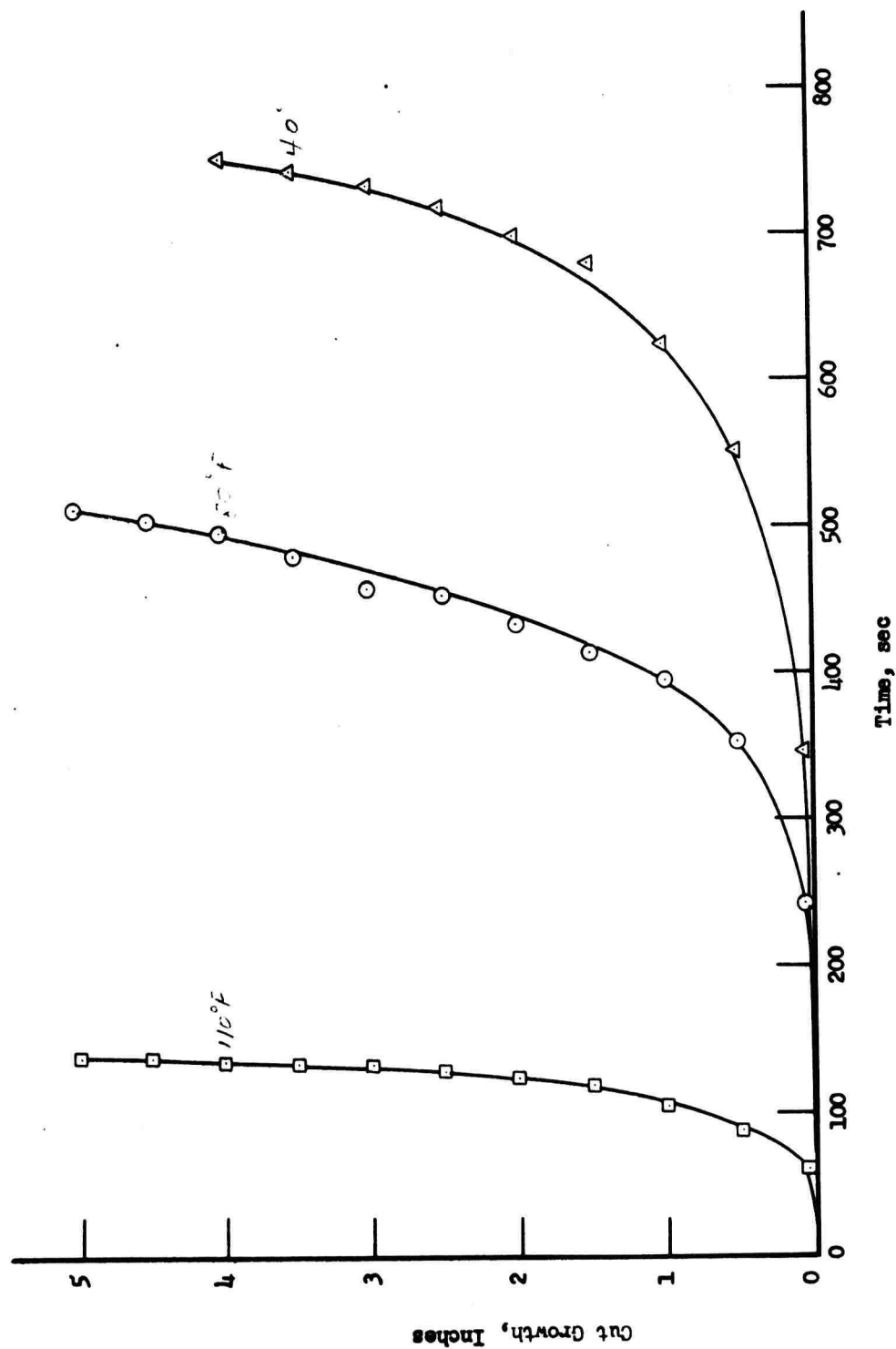
Figure 148. Effect of Temperature Upon the Tear Rate of Representative Pure
Shear Specimens (Prepared From a Class 2 Binder) at a Constant
Rate of Loading (0.2 min^{-1})

V, E, Tear Phenomena (cont.)

width, 2a, of the test piece is sufficiently large, $\lambda \approx 1$ and $F \gg W_o ah$. Equation (97) then reduces to:

$$T h = 2F \tag{98}$$

therefore, for test-pieces whose width is sufficiently large, the energy for tearing, T, may be derived from the tearing force, F, by Equation (98).

Test pieces (1.5 x 3.5 x 0.25") were prepared from filled and unfilled samples of the binder systems described above. The arms were formed by an initial razor cut of 1.5 inches. Inasmuch as the specimens were highly extensible, corrections in Equations (97) and (98) were made to allow for the extension of the arms.

The effect of test temperature upon the average tear energy (T) of the unfilled binder is seen in Figure 149. A decrease in T with an increase in temperature is noted. Tearing force versus time plots were made for this binder with various fillers and shown in Figures 150 to 156. A nearly steady state of tearing to failure is noted after the maximum tear energy is reached. The effect of these fillers on the average tear energy (T) at an extension ratio (λ) of 2, is shown by the following table.

Filler	Amount of Filler	Size of Filler, Av. Dia., μ	Average Tear Energy at $\lambda = 2$, lb/in.	Figure No.
control	0	- - -	36.0	150
glass	50 vol %	(280/28)	20.0	151
glass	50 vol %	84	14.8	152
glass	50 vol %	114	18.8	153
glass	50 vol %	280	25.2	154
Al	20 wt %	28	36.0	155
Carbon-Black	1 wt %	- - -	30.4	156
foam		300μ pore size	36.4	157
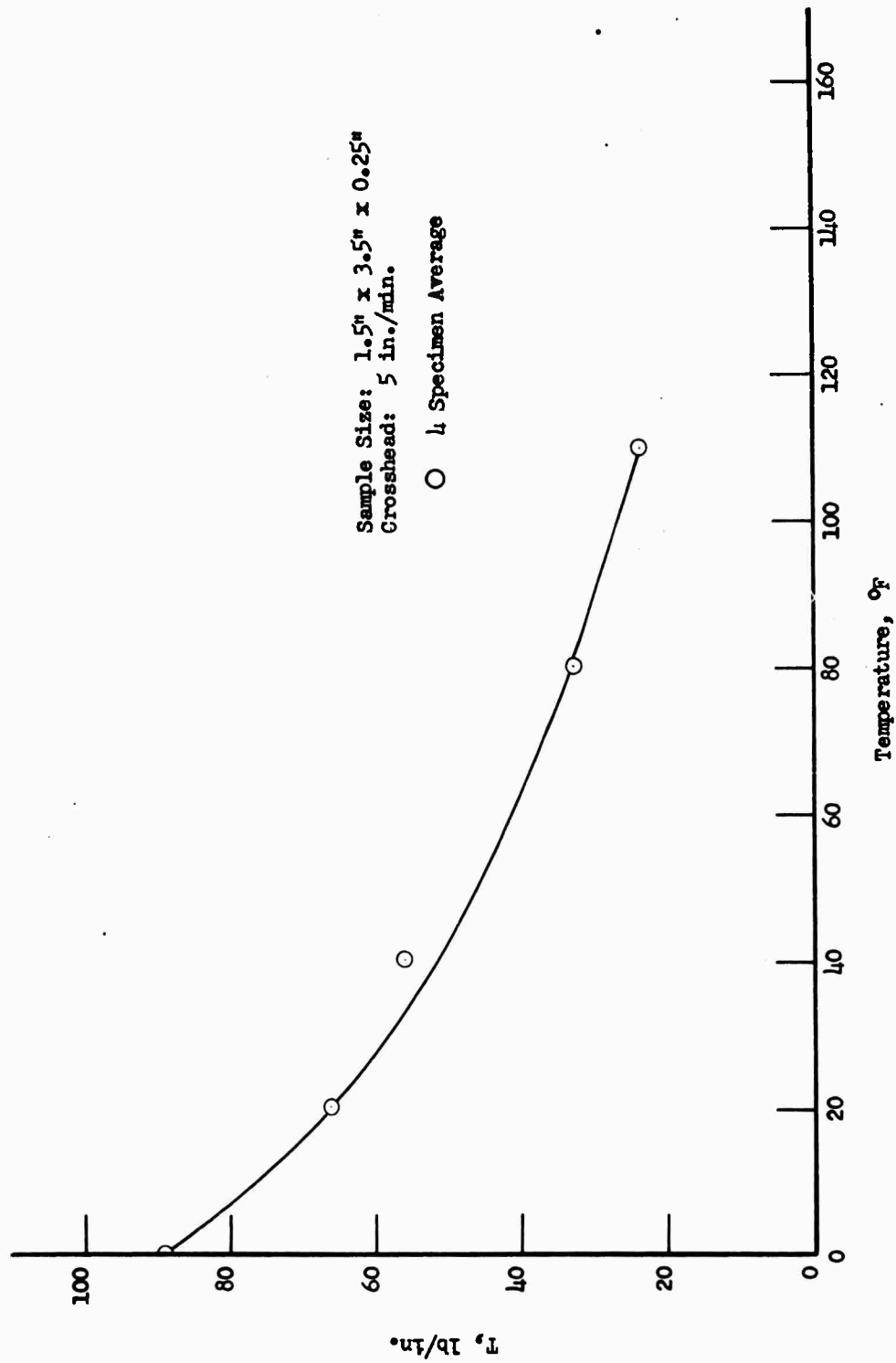
Figure 149. Temperature Dependence of Characteristic Tear Energy of Class 2
Binder in Simple Extension

Sample Size: 1.5" x 3.5" x 0.25"
Test Temperature: 80°F
Crosshead: 5 in./min.
Average Tear Energy (T) 36.0 lb/in. at $\lambda = 2$

$$T = F \frac{2 \lambda}{h}$$

Time, sec

Force, lb
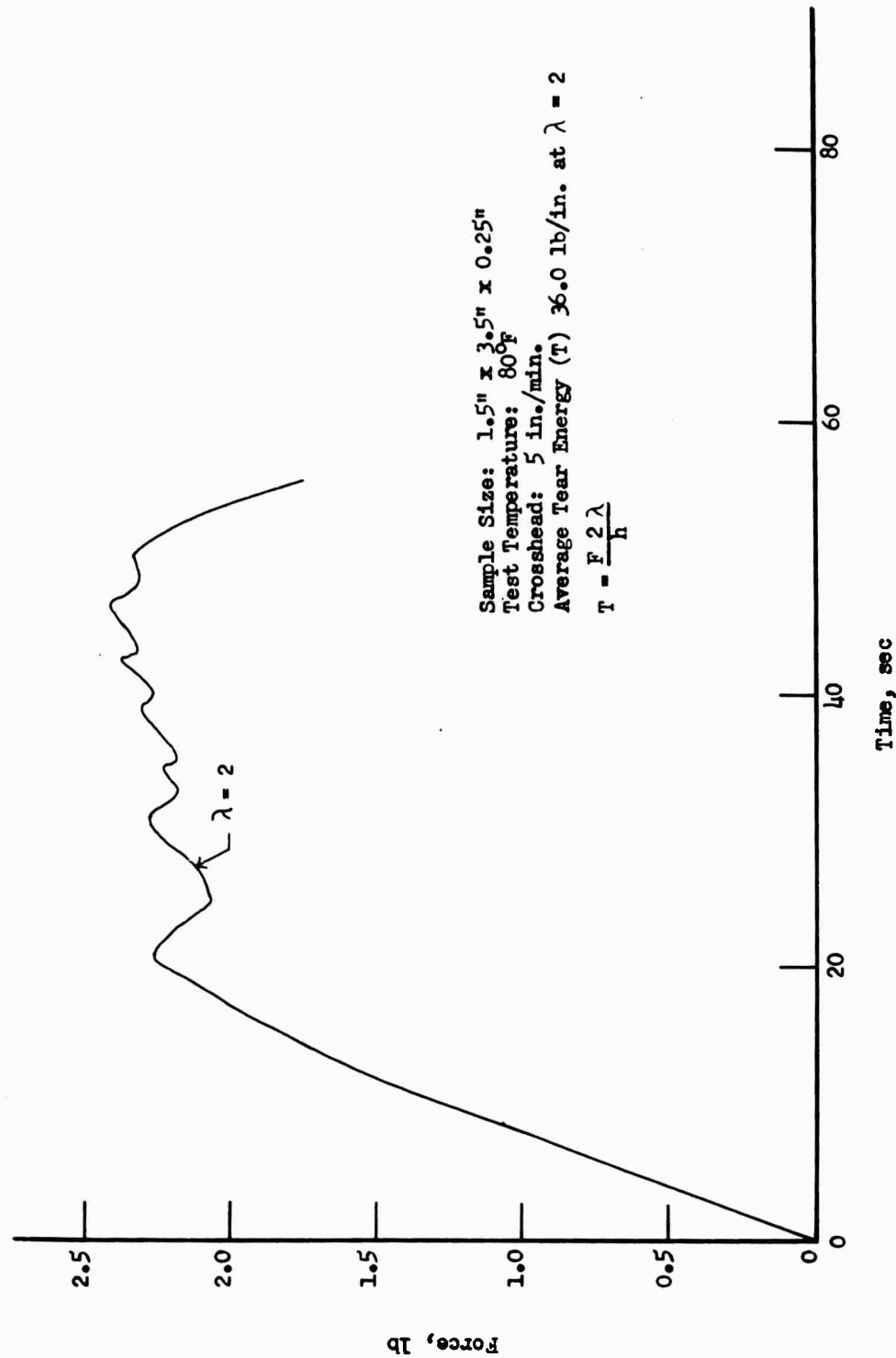
Figure 150. Characteristic Tear Behavior in Simple Extension of a Class 2
Binder System

Sample Size: 1.5" x 3.5" x 0.25"
Test Temperature: 80°F
Crosshead: 5 in./min.
Average Tear Energy (T) 20.0 lb/in. at $\lambda = 2$

$$T = F \frac{2\lambda}{h}$$

$\lambda = 2$

Time, sec

Force, lb
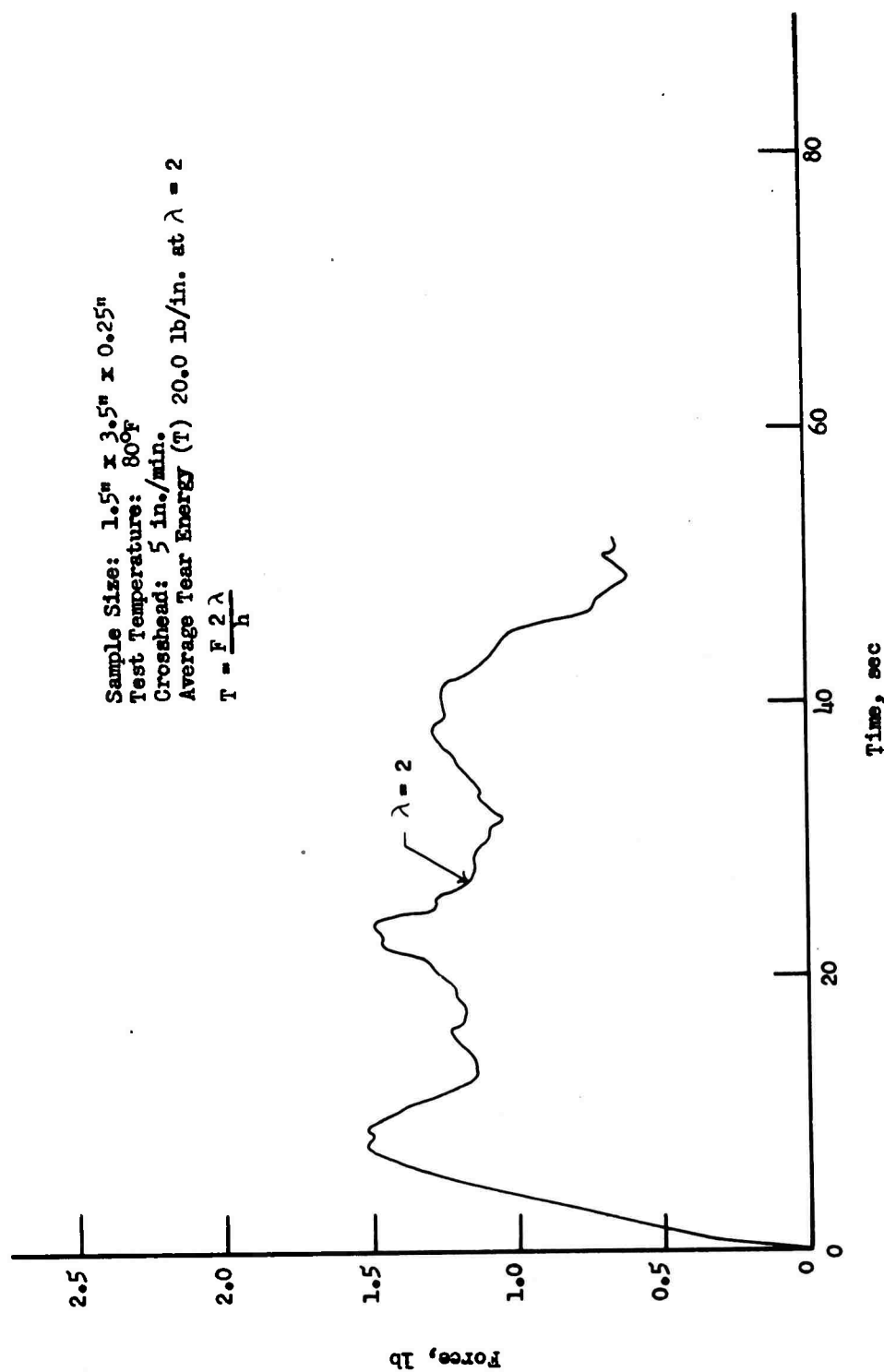
Figure 151. Characteristic Tear Behavior in Simple Extension of a Class 2 Binder Containing 50 Volume % Glass Beads (70% 280 μ/ 30% 28 μ)

Sample Size: 1.5" x 3.5" x 0.25"
Test Temperature: 80°F
Crosshead: 5 in./min.
Average Tear Energy (T) 14.8 lb/in. at λ = 2

$$T = \frac{F\ 2\ \lambda}{h}$$
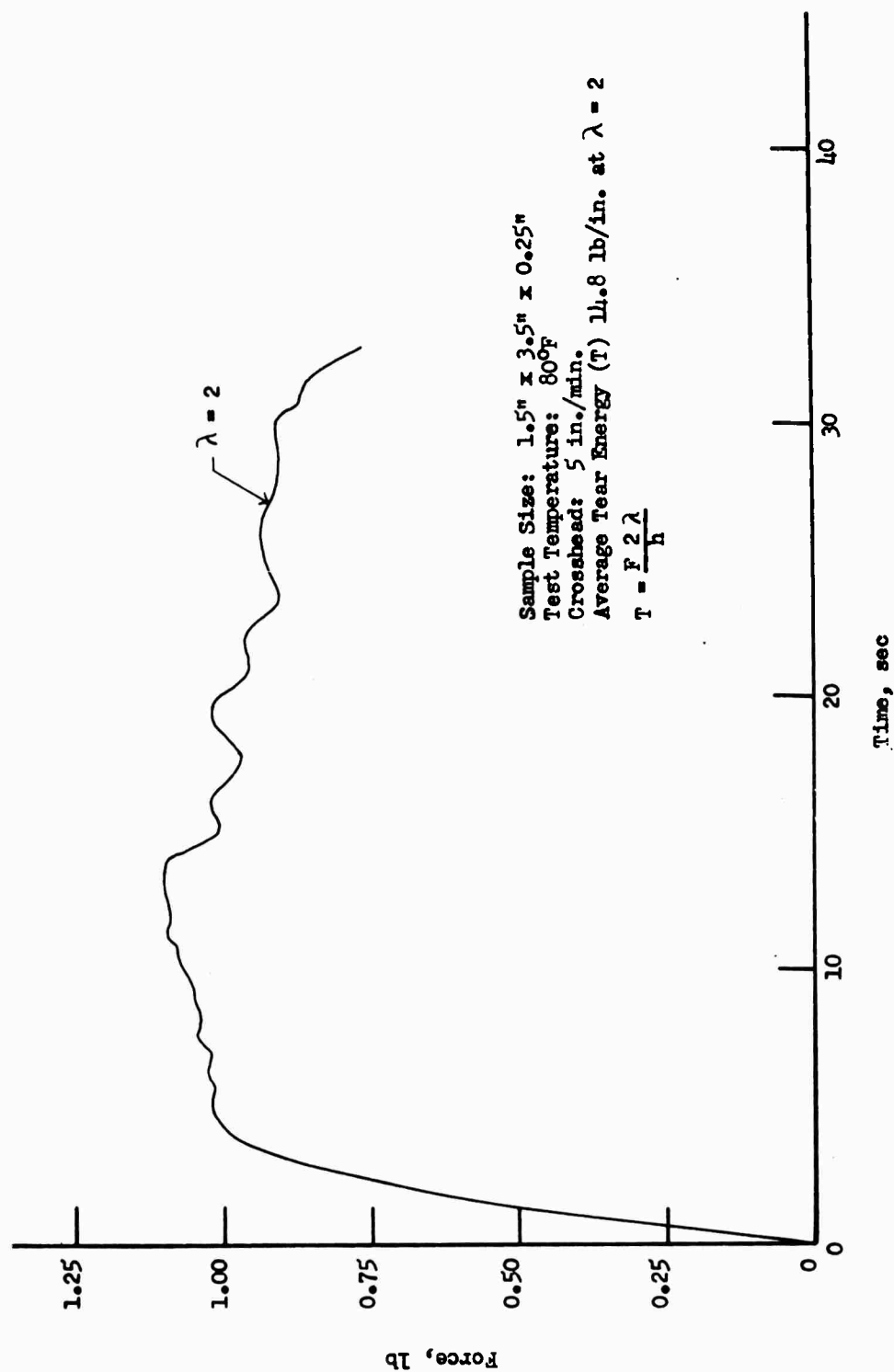
Figure 152.   Characteristic Tear Behavior in Simple Extension of a Class 2 Binder
Containing 50 Volume % Glass Beads (84 μ)
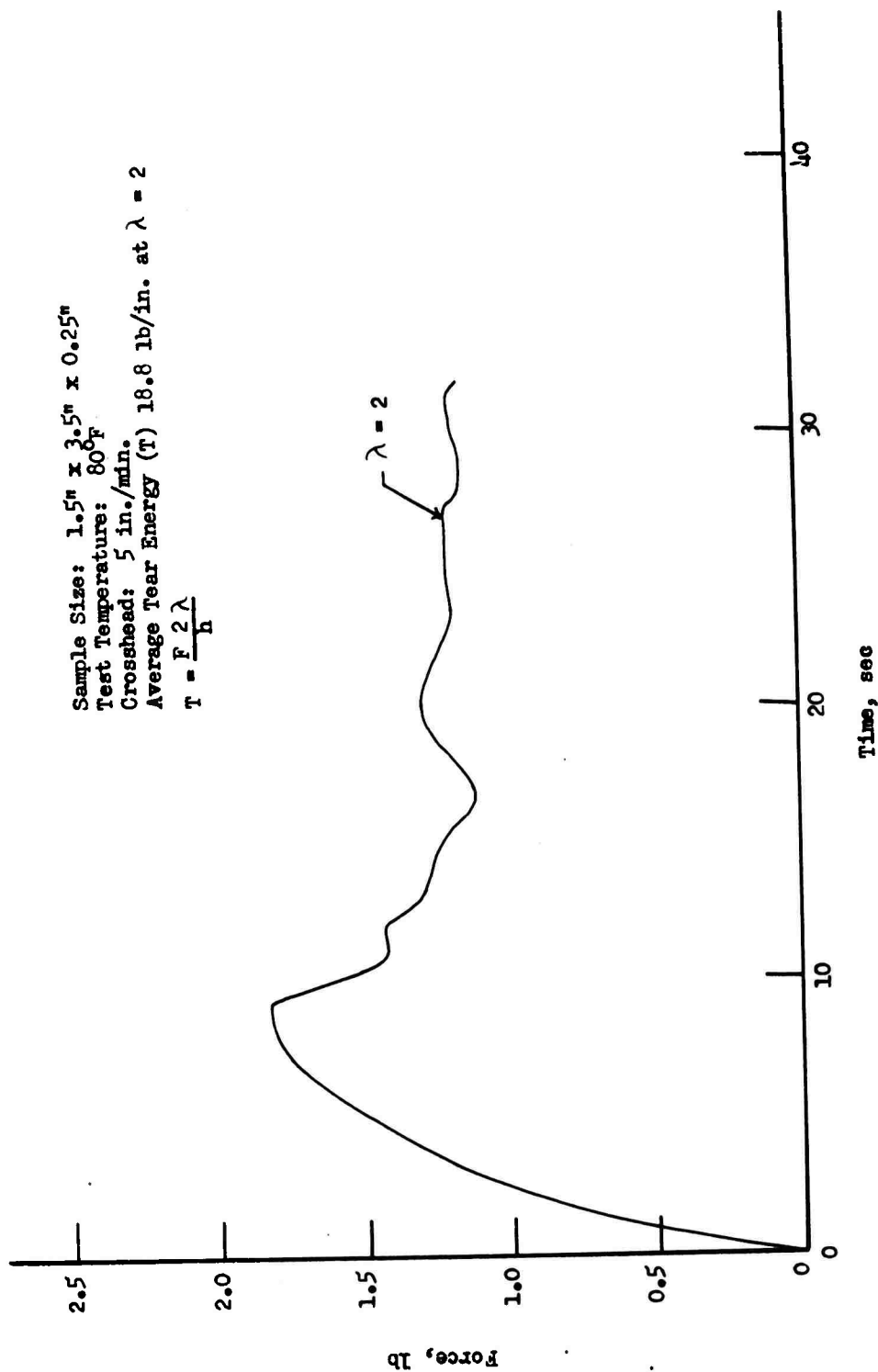
Figure 153. Characteristic Tear Behavior in Simple Extension of a Class 2 Binder Containing 50 Volume % Glass Beads (114 μ)

Sample Size: 1.5" x 3.5" x 0.25"
Test Temperature: 80°F
Crosshead: 5 in./min.
Average Tear Energy (T) 25.2 lb/in. at $\lambda = 2$

$$T = F \frac{2 \lambda}{h}$$
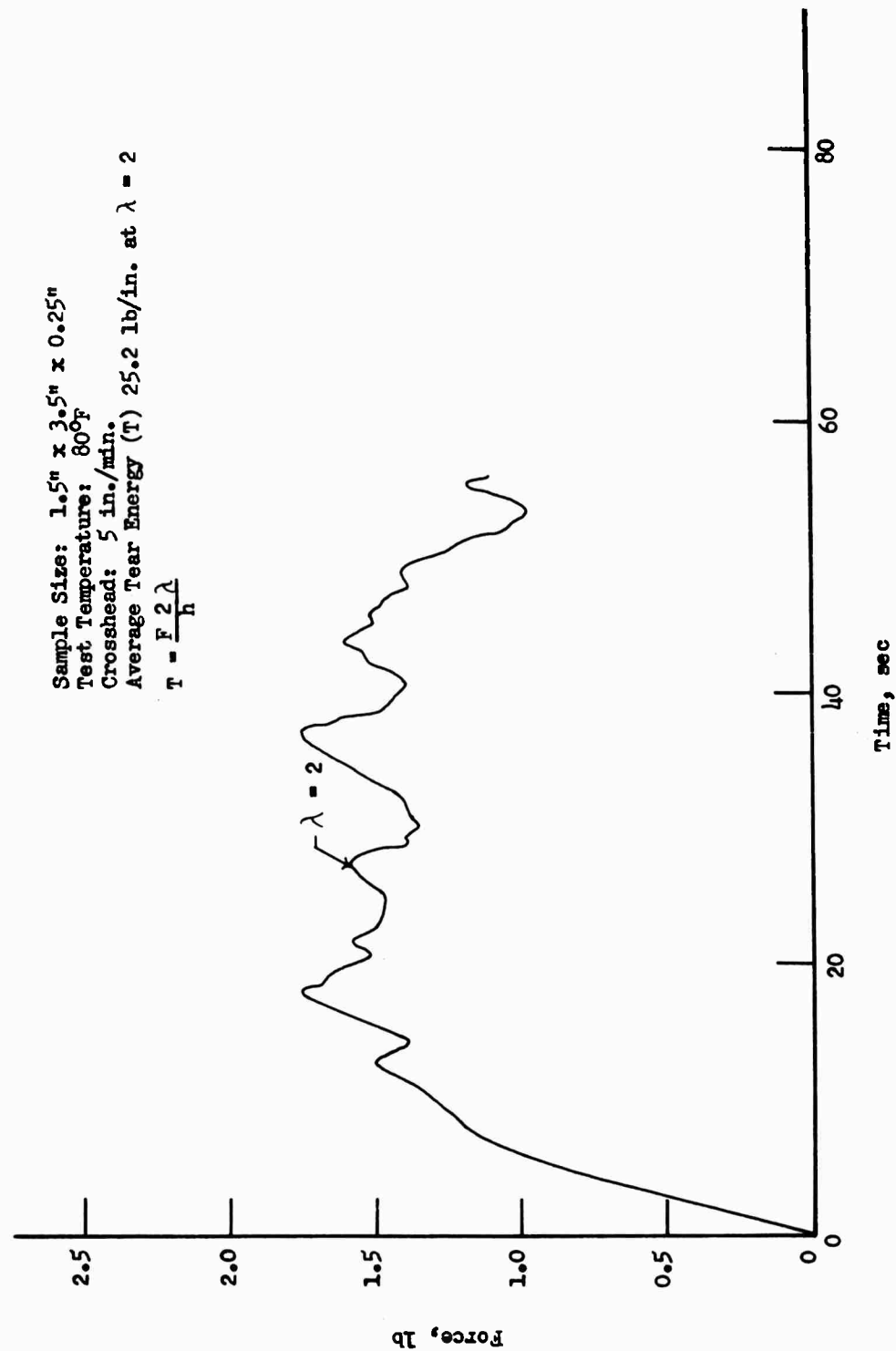
Figure 154. Characteristic Tear Behavior in Simple Extension of a Class 2 Binder Containing 50 Volume % Glass Beads (280 μ)
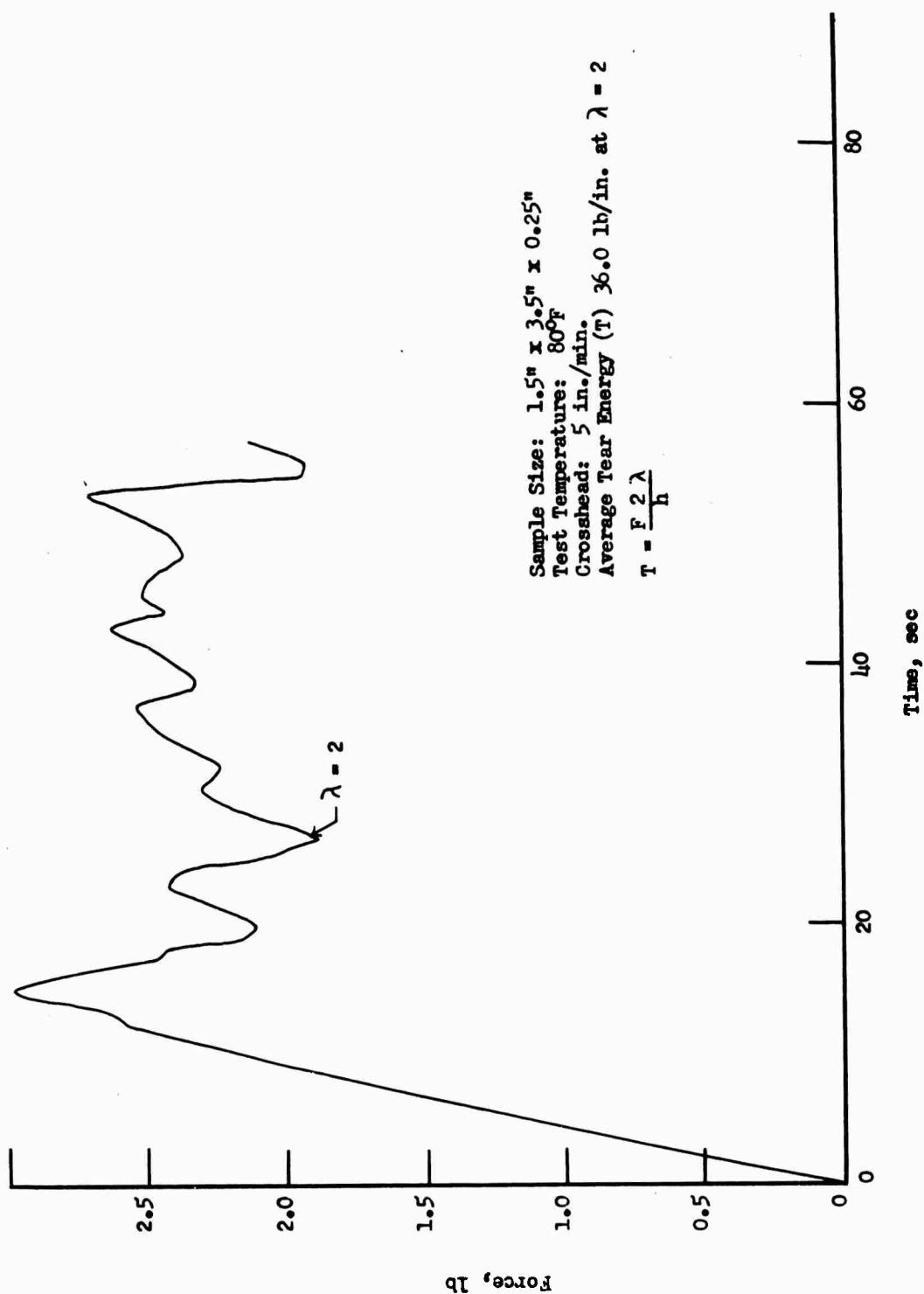
Figure 155. Characteristic Tear Behavior in Simple Extension of a Class 2 Binder
Containing 20 Weight % Al (28 μ)
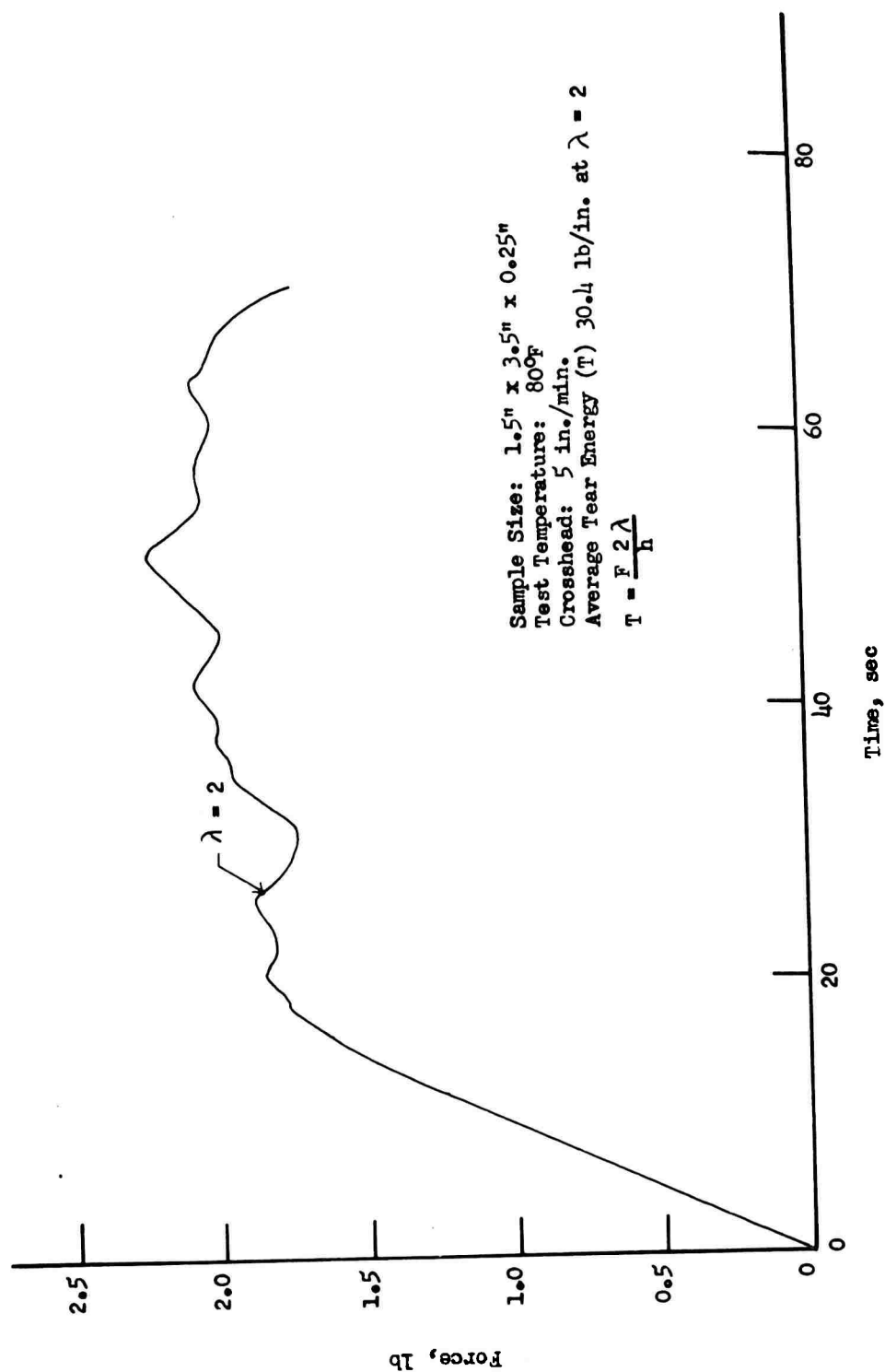
Figure 156. Characteristic Tear Behavior in Simple Extension of a Class 2 Binder Containing 1 Weight % Carbon Black

V, E, Tear Phenomena (cont.)

It is noted that the addition of glass filler decreases the tearing energy of the system. Further, a smaller size of glass beads gave lower values of the tear energy. The addition of aluminum and carbon black show no significant change in the tear energy of the system. It should be noted that the average of the maximum value of the knotty (non-uniform) tearing curve for the aluminum-filled system was assumed to be representative of the tearing properties. This knotty tearing behavior was also noted by Greensmith (89) in his studies of carbon black filled vulcanizates. A similar method analysis was used.

The change in tear energy with a low filler-to-binder bond (glass beads) and a high filler-to-binder bond system (Al) is to be expected with fillers of this size. The voids (dewetting) formed by the presence of prematurely released fillers (glass) enhances tearing and thus decreases the tearing energy, while highly bonded fillers (Al) delay void formation and a higher tear energy is required to produce failure. At failure, however, both systems may be described as behaving essentially like a filled foam. As a comparison, a foam (300 pore size) similar to the Class II binder formulation gave a tear energy value of 26.4 lb/in. The force-time curve for the foam is shown in Figure 157.

Preliminary measurements have been obtained on a new type tear sample (Figure 143-d) which has been used by Gruber at the General Tire Laboratories, Akron, Ohio. This trapezoidal design provides the same conditions, as does the simple extension piece (Figure 143-c) which are necessary for direct determination of tear energy, namely material changing in extension from an unstrained to a strained state. A tear energy of 29 lb/in. was obtained by this method as compared to 36.0 lb/in. obtained by the simple extension sample. Further studies are required.

Aerojet-General CORPORATION
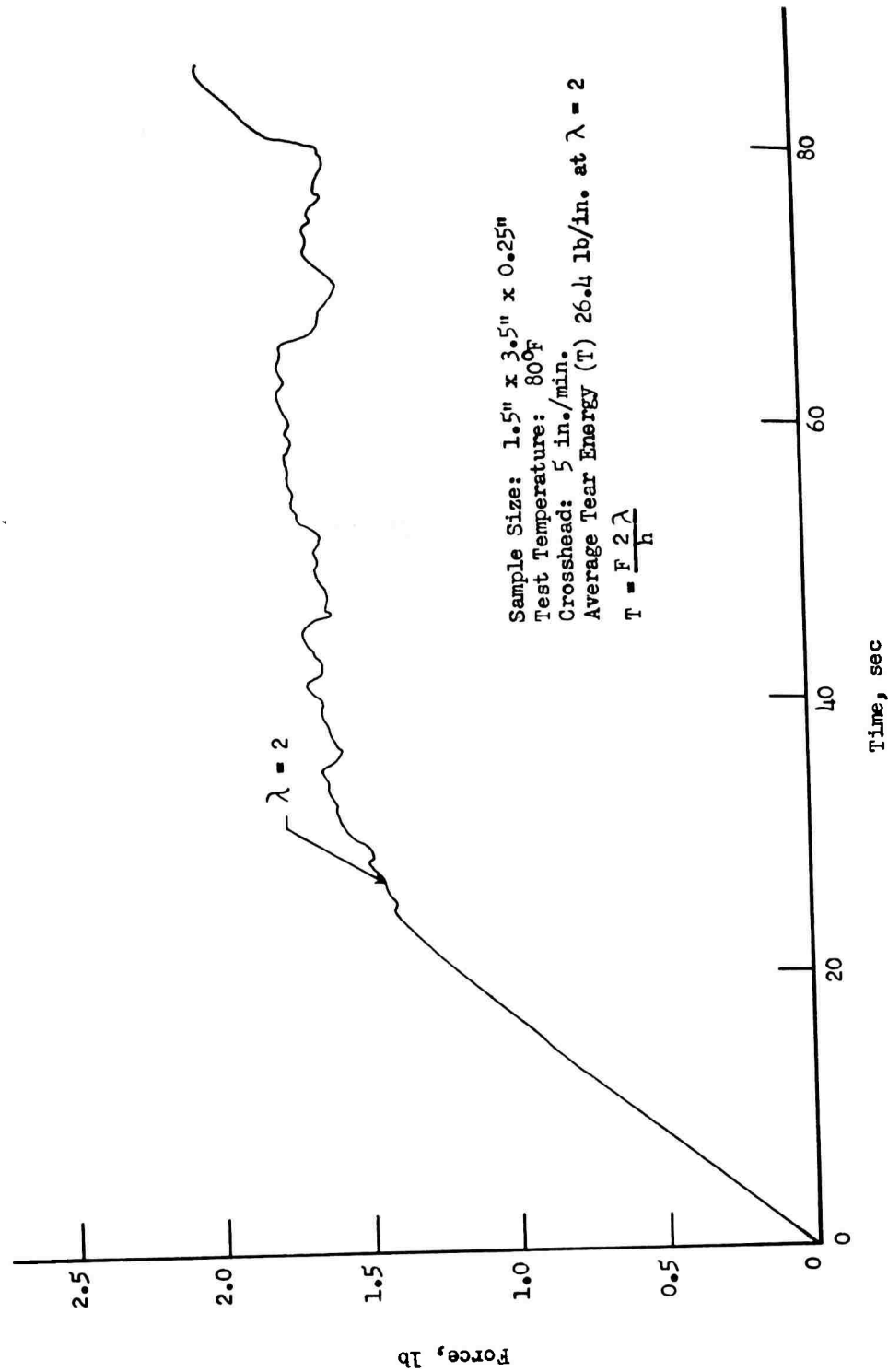
Figure 157. Characteristic Tear Behavior in Simple Extension of a Foam Material (300 μ Pore Size) Prepared From a Class 2 Binder

V. E. Tear Phenomena (cont.)

3. Examination of Tear Front

It is expected that for a flaw contained within a filled or un-
filled binder system, two boundary conditions exist which control the initiation
of tear within the sample. The first condition is represented by a very narrow
longitudinal slit perpendicular to the applied load with rupture occurring at the
ends of this slit. The second is represented by a very narrow longitudinal slit
parallel to the applied load which exhibits rupture only when the ultimate tensile
properties of the sample are reached.

Tearing has been defined by Busse (51) as the formation of
new surfaces by the application of a small force in such a way that it is con-
centrated at the tip of a sharp indentation or cut in the sample. The tear
begins when the stress and strain ahead of the cut reach the tensile strength
and ultimate elongation of the material. However, it is pointed out by Busse
that the tensile strength and ultimate elongation of tearing stresses are not
necessarily the same as those found in the standard tensile tests.

An examination of several conditions of flaw geometry and
resulting tear behavior in a binder system and measurement of the local
strains versus overall extension in a filled system (Class II) was accomplished
to assess their importance on tear initiation in the system. Modified "pure
shear" specimens were prepared from a Class II binder and initial flaws were
incorporated within the binder, as shown in Figure 158.

A marked difference in ultimate extension before tear is
noted between the flaw types (I, III, IV) with intermediate extensions prior
to tear seen for Type II. This behavior suggests that a critical angle-extension
load relationship controls the tear behavior.
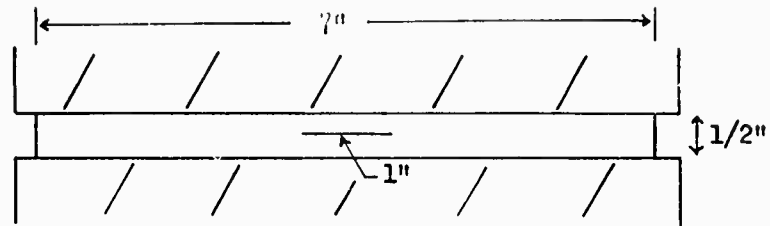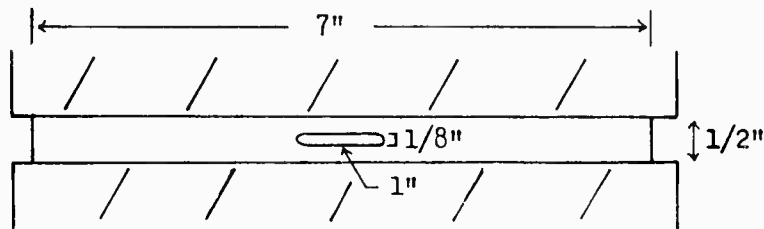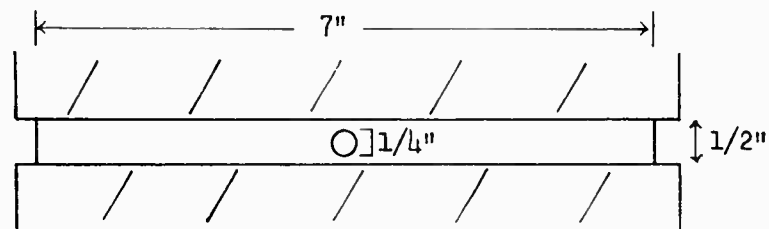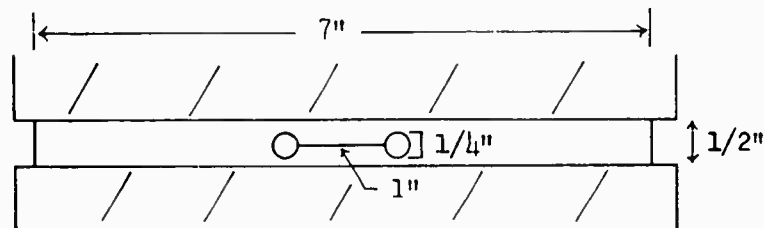
Figure 158. Modified Pure Shear Specimens for Determination of Effect of Flaw
Geometry on Tear Initiation

V, E, Tear Phenomena (cont.)

The conditions leading to failure in the localized regions, described by Busse above, were investigated in detail on a Class II propellant system. Four sets of specimens containing flaws (radius .075 to .218) were marked with fine bench marks perpendicular to the load within the flaw, and on the sample. The measurement of change in elongation within different areas was obtained from photographic film. Similar behavior within all four sets (Figures 159 to 162) is noted. In all cases, the elongation at test initiation within the critical area exceeds the overall elongation by approximately 10:1. Maximum elongations in the figures represent points at which tear initiated and not ultimate failure.

4.   Mechanism of Tear

Propellant failure can be considered to occur in two steps. First, upon application of strain, separation of the binder from the oxidizer or "dewetting" takes place. Secondly, a tear is initiated in the binder and propagates until the stress is minimized. Therefore, for the development of better propellants it is necessary to have binder systems of superior tear resistance.

A mechanism for this tearing process has been suggested. First, upon the application of strain, a number of short molecular chains between crosslinks or branch points undergo cleavage resulting in dangling chains terminated by free radicals. If a critical concentration of radicals is achieved, a transfer reaction of the radicals to adjacent chains may occur causing their cleavage. This process rapidly proceeds resulting in tearing until some minimum stress level is reached.

Further, a finite period of time is required for the propagation reaction to occur. If the binder components are of proper structure,
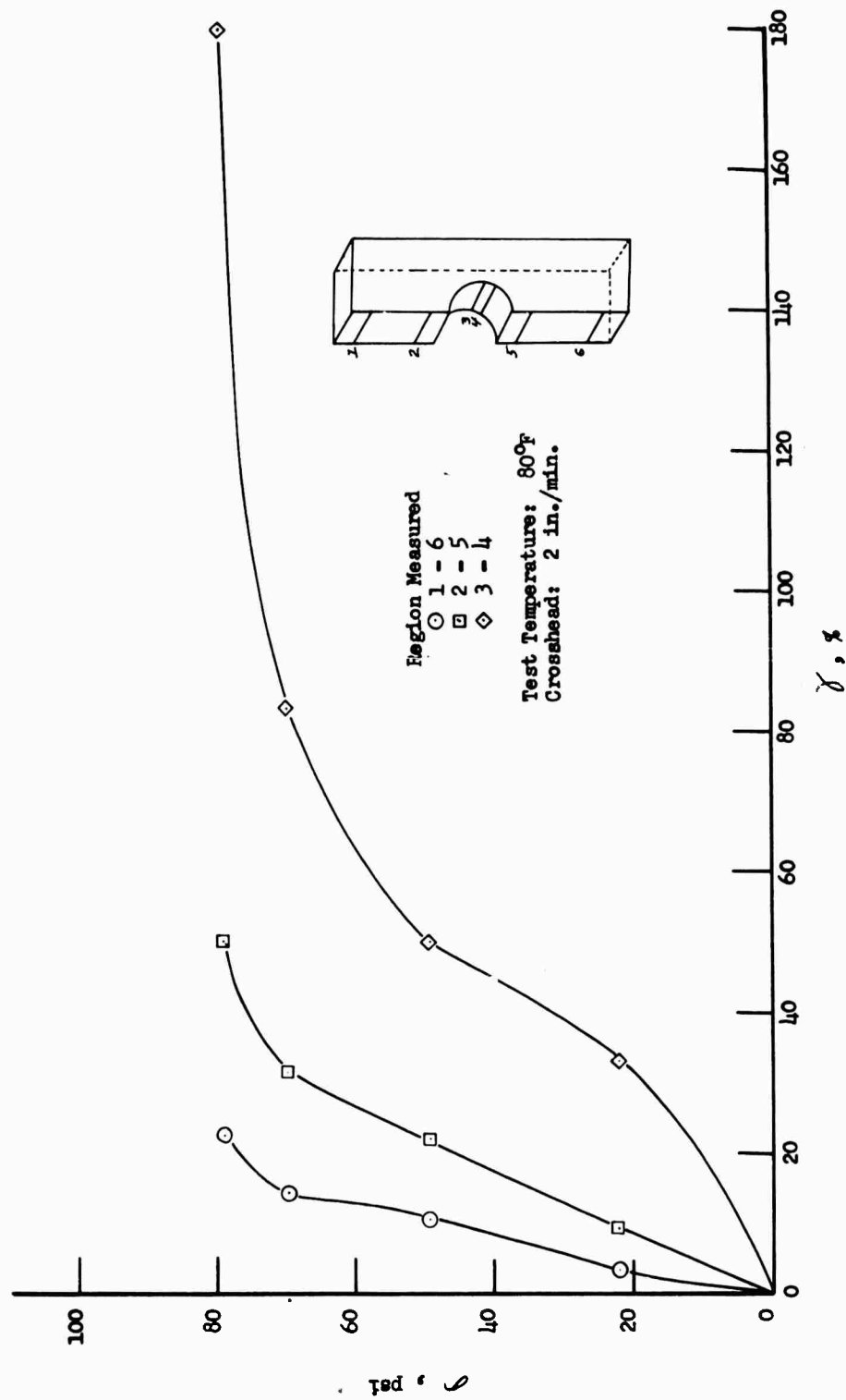
Figure 159. Effect of Failure in Localized Regions on the Overall Failure Properties
of a Class 2 Propellant (Flaw Radius 0.075 in.)

Aerojet-General CORPORATION
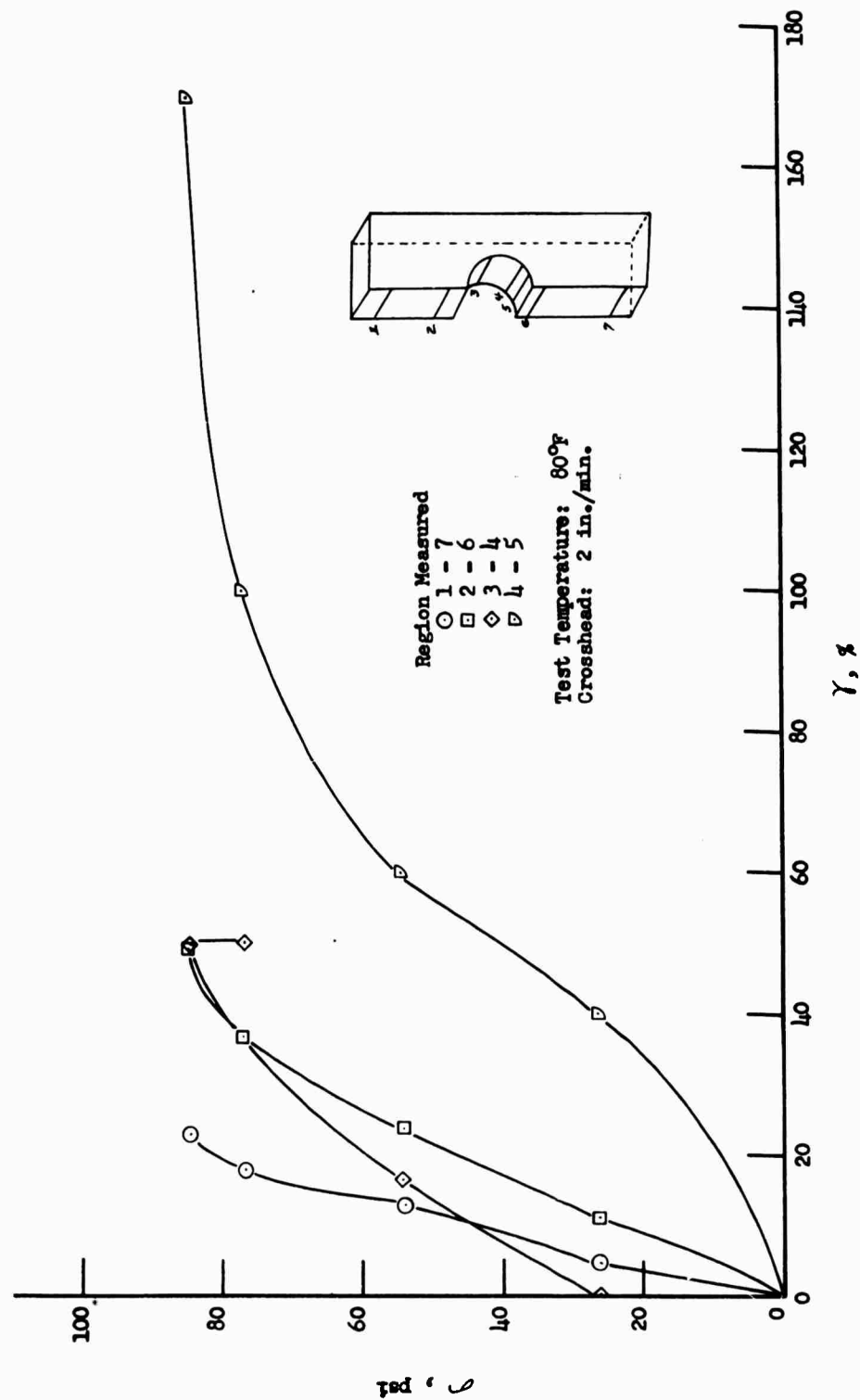
Figure 160. Effect of Failure in Localized Regions on the Overall Failure Properties of a Class 2 Propellant (Flaw Radius 0.120 in.)
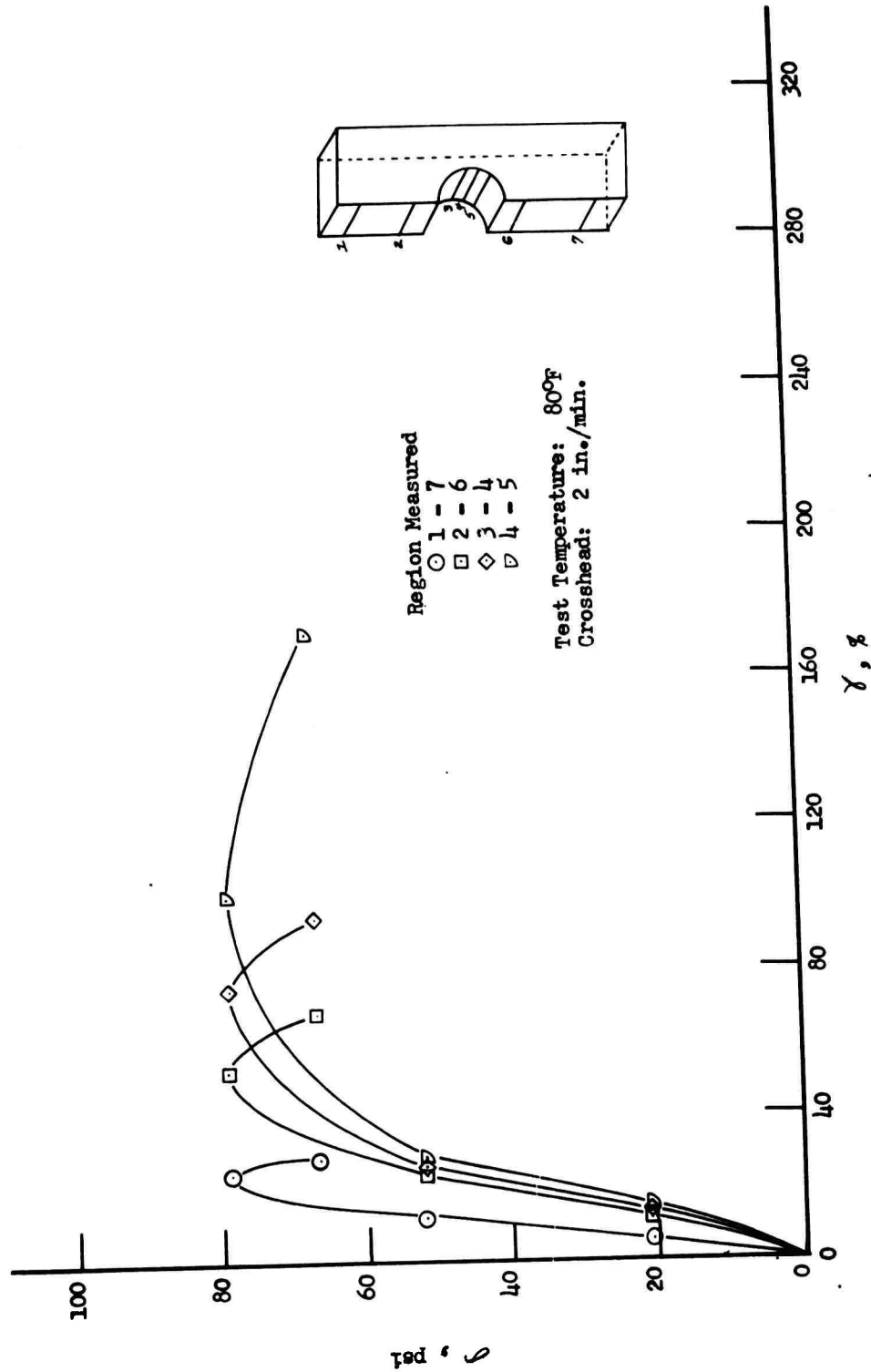
Figure 161. Effect of Failure in Localized Regions on the Overall Failure Properties of a Class 2 Propellant (Flaw Radius 0.185 in.)
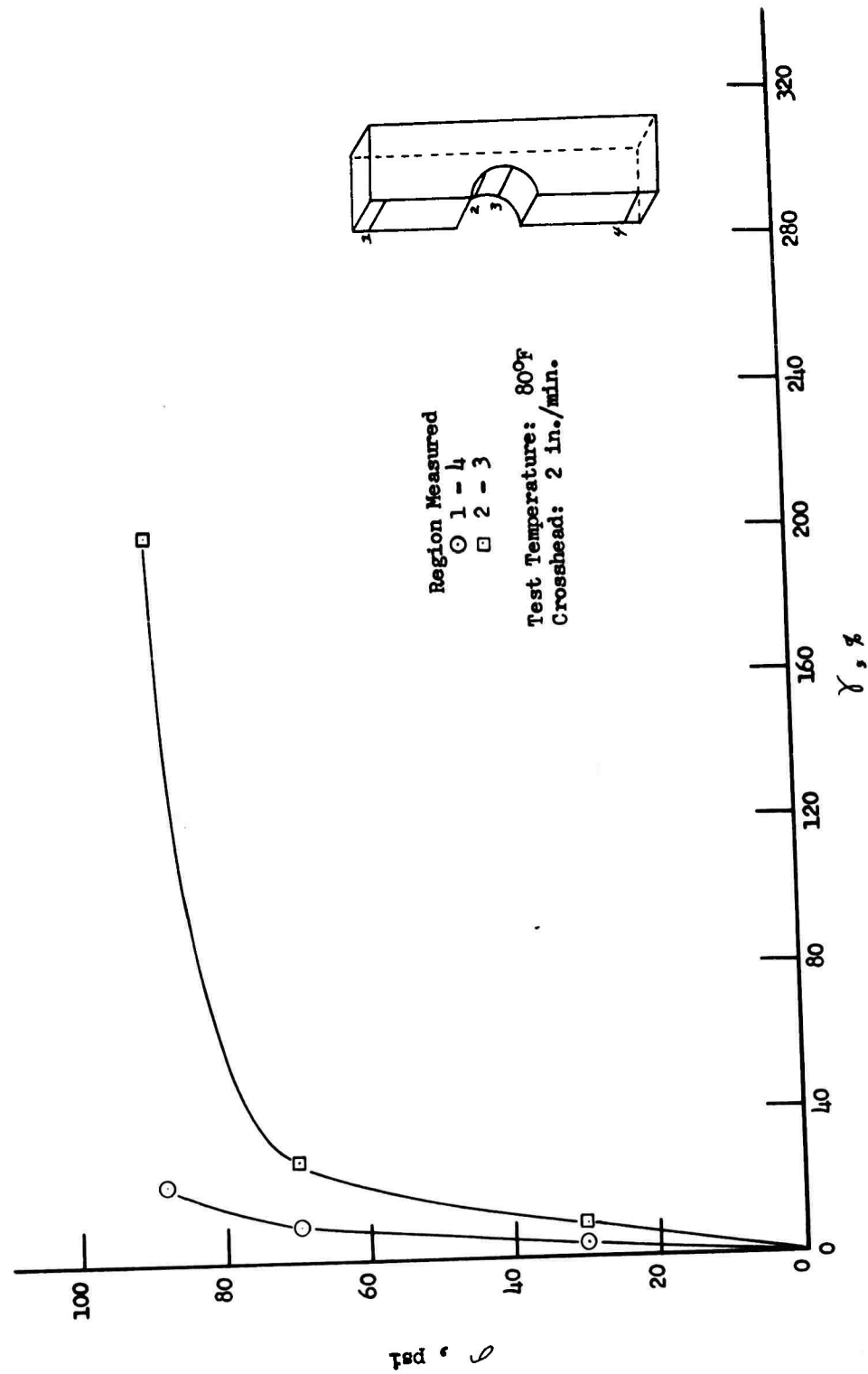
Figure 162. Effect of Failure in Localized Regions in the Overall Failure Properties of a Class 2 Propellant (Flaw Radius 0.218 in.)

V, E, Tear Phenomena (cont.)

this period may be of such length that various termination reactions of the radical could occur, thus eliminating these chain reactions. The presence of binder additives may also play a beneficial role.

This line of reasoning suggests that a narrow distribution of molecular chain lengths between "anchor points" would be desirable for the binder to have good resistance to tear initiation. Unfortunately, it is quite probable that many binder systems have a broad distribution of chain lengths due to "clumping" of the multifunctional component of the network resulting from differences in reactivity rates or incomplete miscibility of the binder components.

A method for studying this hypothesis of the tear of propellant binder was developed. Samples are cast one inch in width with one-quarter inch cast notch. These samples are then mounted between wooden blocks so as to maintain a one inch gage length and subjected to a constant load. The data are treated in a form derived by Bueche (93) and Coleman (94) for polymer failure as plots of stress versus log of time to failure.

Figure 163 shows data for two binder systems with approximately the same crosslink density as determined by swelling or by initial tensile modulus. The principal difference was the crosslinker. The Class 2 propellant contains a trifunctional monomer that is quite soluble with the other binder ingredients and has a reaction rate with the isocyanate comparable to that of the other components. The Class 3 propellant has a trifunctional monomer that is only slighly soluble in the other components and has a much higher reactivity with the isocyanate groups. This results in a "clumping" effect whereby regions of the binder exist on the micro scale of very high crosslink density and the other regions of low density. Upon application of a
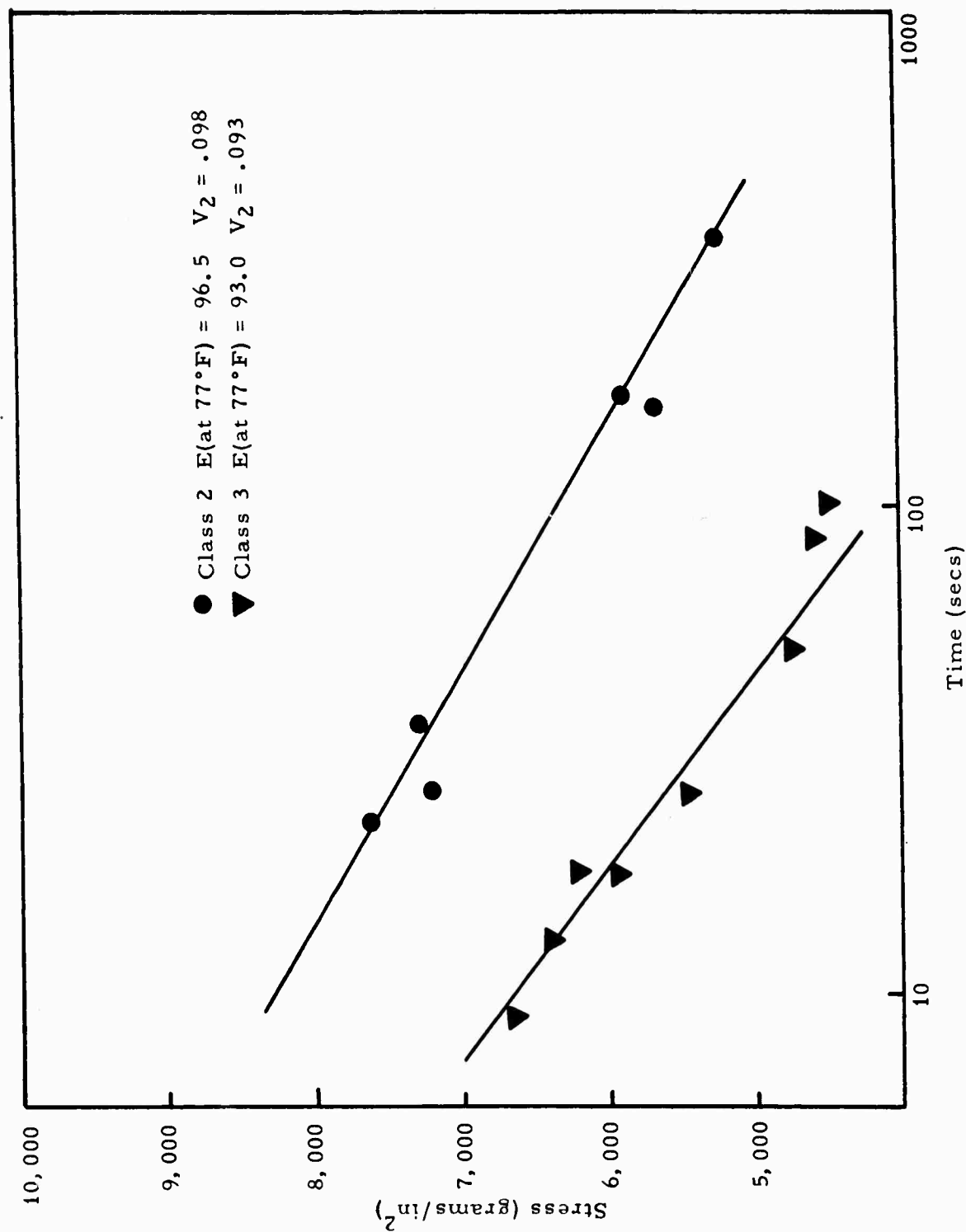
Figure 163. Effect of Crosslinker Upon Tear

Class 2 E(at 77°F) = 96.5 V_2 = .098

Class 3 E(at 77°F) = 93.0 V_2 = .093

Time (secs)

Stress (grams/in^2)

V, E, Tear Phenomena (cont.)

strain, the highly crosslinked areas quickly undergo cleavage and a tear propagates rapidly, and this is confirmed in the poorer tear resistance of this propellant.

F. UNIAXIAL STRAIN FAILURE

The strain at the wall of the motor is essentially that of uniaxial strain as the rigid case prevents lateral contraction. Failure under such conditions is difficult to observe so a new experimental technique was developed using thick transparent lucite plates to restrain a thin disc of polyurethane polymer. The experiment consisted of curing a flat, very thin disc of polyurethane rubber between rigid lucite plates and applying tensile forces normal to the plane of the disc to pull the plates apart. Since the polymer disc is very thin it cannot move radially to a significant degree and uniaxial strain results.

A typical polyurethane polymer was cast between one-inch-thick lucite plates using a rubber O-ring as a mold. The composite was placed in a 110°F oven and cured to give a strong bond to the lucite plates. As the plates were pulled apart, the sample was observed and photographed through the lucite plates. The samples were tested on the Instron tensile tester, as shown in Figure 164. Strain measurements were made by the displacement of a linear variable differential transformer measuring the movement of one axis of the Instron recorder. Records on three specimens are shown in Figure 165.

The rupture process consisted of the sudden appearance of internal flaws at a well-defined and comparatively small tensile load. Their occurrence was marked by a discontinuity in the curve relating the applied tensile load to the deflection, as shown in Figure 165. The behavior observed is similar to that reported by Gent and Lindley (95) on rubber vulcanizates. The small cracks that are formed were found to be uniformly distributed across the section and totally enclosed. Estimates of the bulk modulus, K, and the Poisson's ratio ν, are shown in Figure 165.
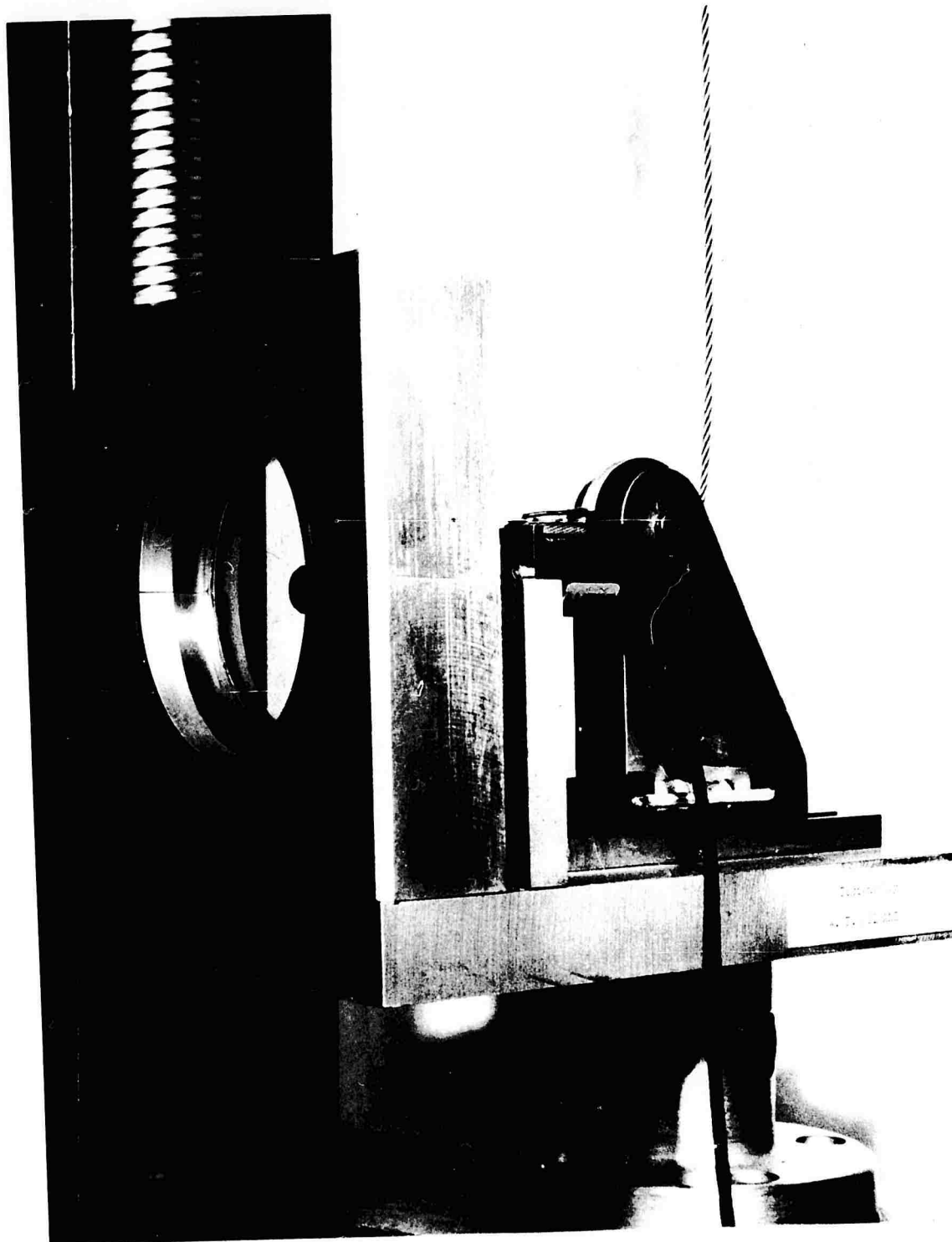
Figure 164. Triaxial Tensile Test Fixture Mounted in Instron

Sample No.	Thickness	Diameter	K, psi	ν
1	0.103	1.046	42,000	0.49960
2	0.139	1.046	64,000	0.49981
3	0.139	1.609	125,000	0.49999
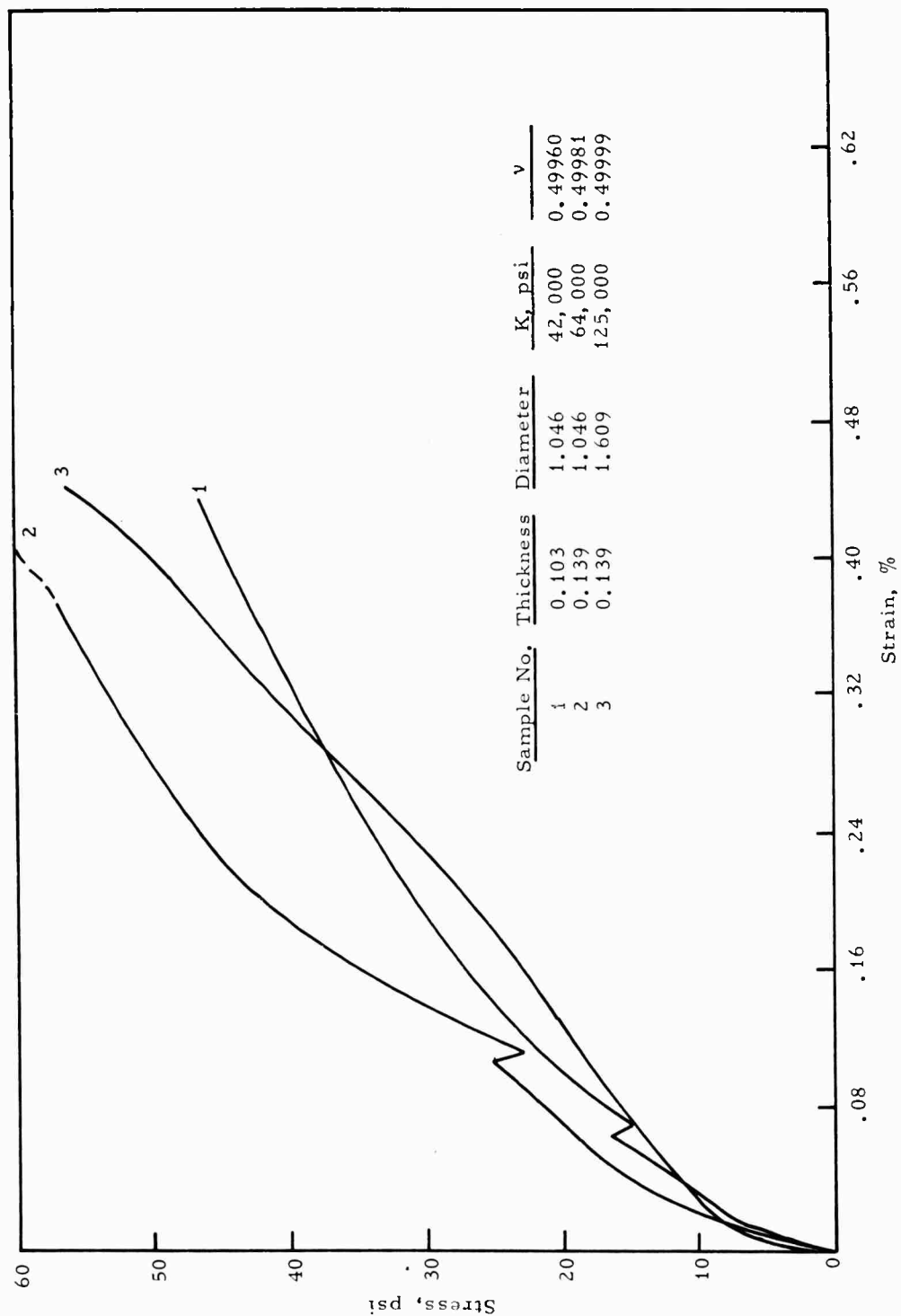
Figure 165. Uniaxial Strain Curves for Samples of Polyurethane Polymer at 80°F and 0.2 min⁻¹ Strain Rate

V, Phase 4 -- Failure Criteria (cont.)

G. THE FAILURE OF FILLED BINDERS UNDER COMBINED STRESS-- MASSACHUSETTS INSTITUTE OF TECHNOLOGY

The mechanism of failure of a filled binder was investigated theoretically and an experimental apparatus constructed at the Massachusetts Institute of Technology. A stress analysis was performed on the ligaments between filler particles in a simple cubic and a more realistic face-centered cubic array. The stiffness and load for a critical fracture were determined, together with the corresponding elastic constants. The resulting fracture locus indicates that the maximum normal stress should decrease linearly with increasing hydrostatic pressure. The results suggest that in the realistic case of nonuniform particle spacing, local clusters of particles could lead to localized unbonding which would then propagate depending on the relative strength of adjoining regions. The details of the analysis are presented in Appendix G.

Equipment was designed to investigate the effect of hydrostatic stress, both tensile and compressive, on the stress-strain and fracture behavior of inert solid fuels under shear strains. The shear strain and compressive hydrostatic stress are obtained by conventional means, that is a solid cylindrical specimen twisted under hydrostatic pressure. The hydrostatic tension is obtained by rotating the specimen. Due to the relatively high bulk modulus of the material, a practically pure hydrostatic tension results when the cylinder is rotated about its axis while its length is held constant. This can be demonstrated in a number of ways.

Using the solution for a rotating cylinder under plane strain given by Love (96) and superimposing a uniform axial tension to give zero axial strain gives:

V, G, The Failure of Filled Binders Under Combined Stress--Massachusetts Institute of Technology (cont.)

$$\sigma_r = \frac{\omega^2 \rho (a^2 - r^2)}{8} \left(\frac{3 - 2\nu}{1 - \nu} \right) \tag{99}$$

$$\sigma_\theta = \frac{\omega^2 \rho}{8} \left[\left(\frac{3 - 2\nu}{1 - \nu} \right) a^2 - \left(\frac{1 + 2\nu}{1 - \nu} \right) r^2 \right] \tag{100}$$

$$\sigma_Z = \frac{\omega^2 \rho (a^2 - 2r^2)}{4} \left(\frac{\nu}{1 - \nu} \right) + \frac{\omega^2 \rho a^2 \nu}{2} \tag{101}$$

where ω is the angular velocity, ρ is the density, and ν is the Poisson's ratio. As $\nu \rightarrow 1/2$ these reduce to:

$$\sigma_r = \frac{\omega^2 \rho}{2} (a^2 - r^2) = \sigma_\theta = \sigma_Z \tag{102}$$

This is a hydrostatic stress, uniform along the length, and varying with the radius, being greatest at the center and zero at the outer radius.

The design is shown in cross section in Figure 166 and a photograph of the completed apparatus in Figure 167. A cylindrical specimen 2-in. in diameter is bonded to two end plates which are, in turn, fastened to matching piloted plates on the shafts. An outer cover holds the specimen length constant during tests. An alternate cover with an O-ring seal arrangement is used when the specimen is under hydrostatic pressure and not rotated. The drive for rotating the specimen is provided by a series wound motor, shown at the left of Figure 167, with a variable speed control to regulate the stress level.

The entire assembly is mounted on a lathe bed for rigidity, and to permit the drive shaft to be backed off for installation of the specimen. The lathe bed ways provide an accurate means of maintaining alignment of the components during this operation. Inner and outer shafts, shown at the right of Figure 167, are connected by an intermediate quill shaft which can move

LUBRICATION BY OILMIST-NOT SHOWN. CAN BE SEEN IN PHOTOGRAPH ON LEFT HAND SIDE.
SPEED CONTROL   - "   "   "   "   "   " RIGHT "   " UNDER TABLE.
  "   "   FOR HIGH SPEED MOTOR   "   "   "   "   " LEFT   "   " AT THE BACK.

POSITIVE HYDROSTATIC STRESS OBTAINED BY SPINNING
WITH HIGH SPEED MOTOR.
NEGATIVE HYDROSTATIC STRESS OBTAINED BY PRESSURIZING
SPECIMEN HYDROSTATICALLY, USING ALTERNATE SPACER
(NOT SHOWN) WITH O-RINGS FOR SEALING - HIGH
SPEED MOTOR NOT ROTATING.
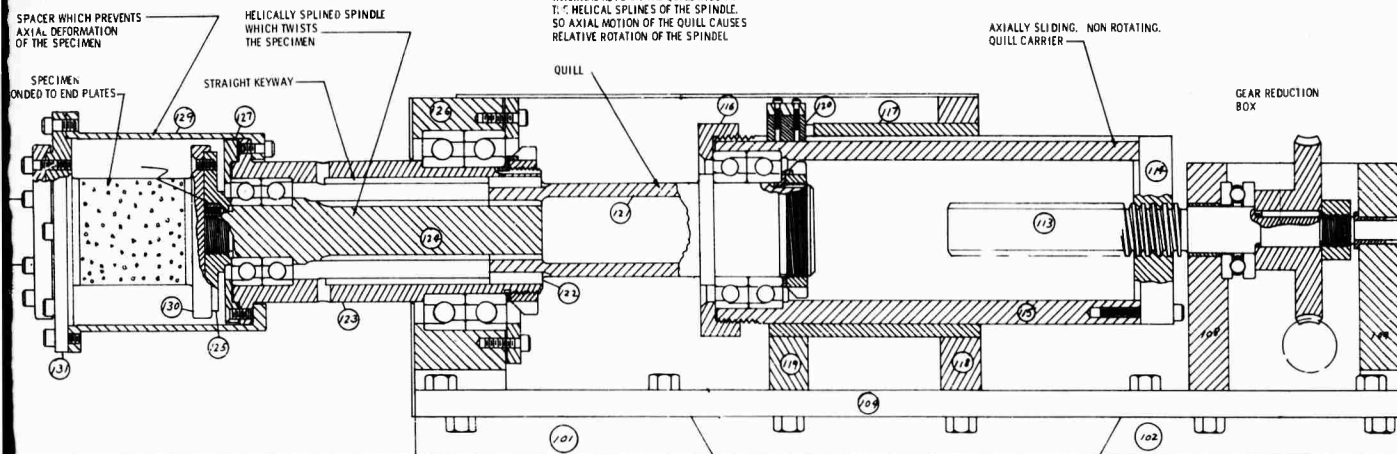
N.B. THIS IS THE WORKING GENERAL LAYOUT DRAWING
ACTUAL MACHINE DIFFERS IN SOME DETAILS.

VARIABLE HIGH SPEED DRIVING MOTOR

FLEXIBLE COUPLING

SPACER WHICH PREVENTS
AXIAL DEFORMATION
OF THE SPECIMEN

HELICALLY SPLINED SPINDLE
WHICH TWISTS
THE SPECIMEN

INTERNAL KEYS ON T
THE HELICAL SPLINE
SO AXIAL MOTION O
RELATIVE ROTATION

SPECIMEN
BONDED TO END PLATES

STRAIGHT KEYWAY

QUILL

Figure 166.   Spinning Rig for Testing Fill
Tension and Torsion

Figure 166. Spinning Rig for Testing Filled Polymers Under Combined Hydrostatic
Tension and Torsion
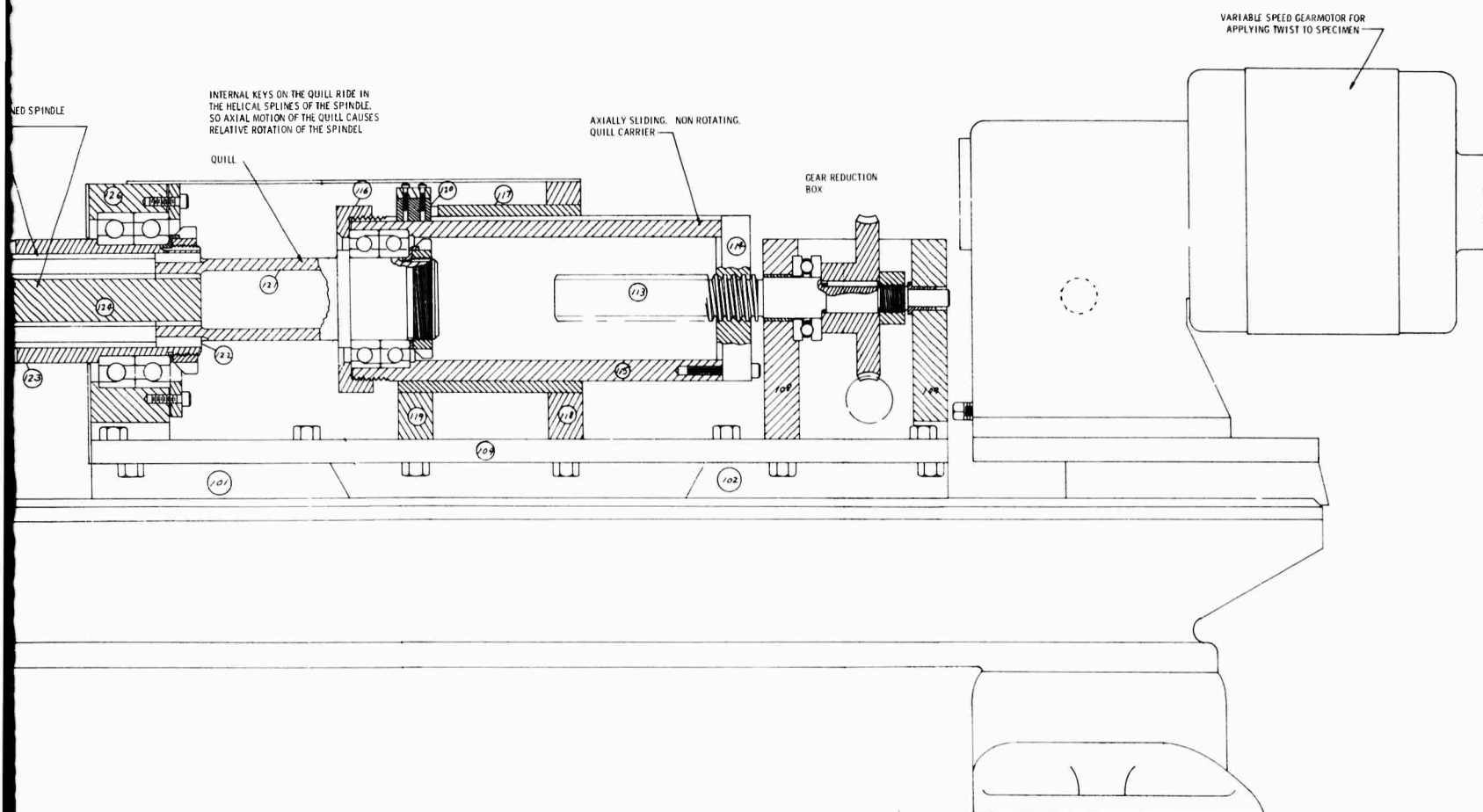
VARIABLE SPEED GEARMOTOR FOR
APPLYING TWIST TO SPECIMEN

INTERNAL KEYS ON THE QUILL RIDE IN
THE HELICAL SPLINES OF THE SPINDLE.
SO AXIAL MOTION OF THE QUILL CAUSES
RELATIVE ROTATION OF THE SPINDEL

QUILL

NED SPINDLE

AXIALLY SLIDING. NON ROTATING.
QUILL CARRIER

GEAR REDUCTION
BOX

g Rig for Testing Filled Polymers Under Combined Hydrostatic
and Torsion

Page 338
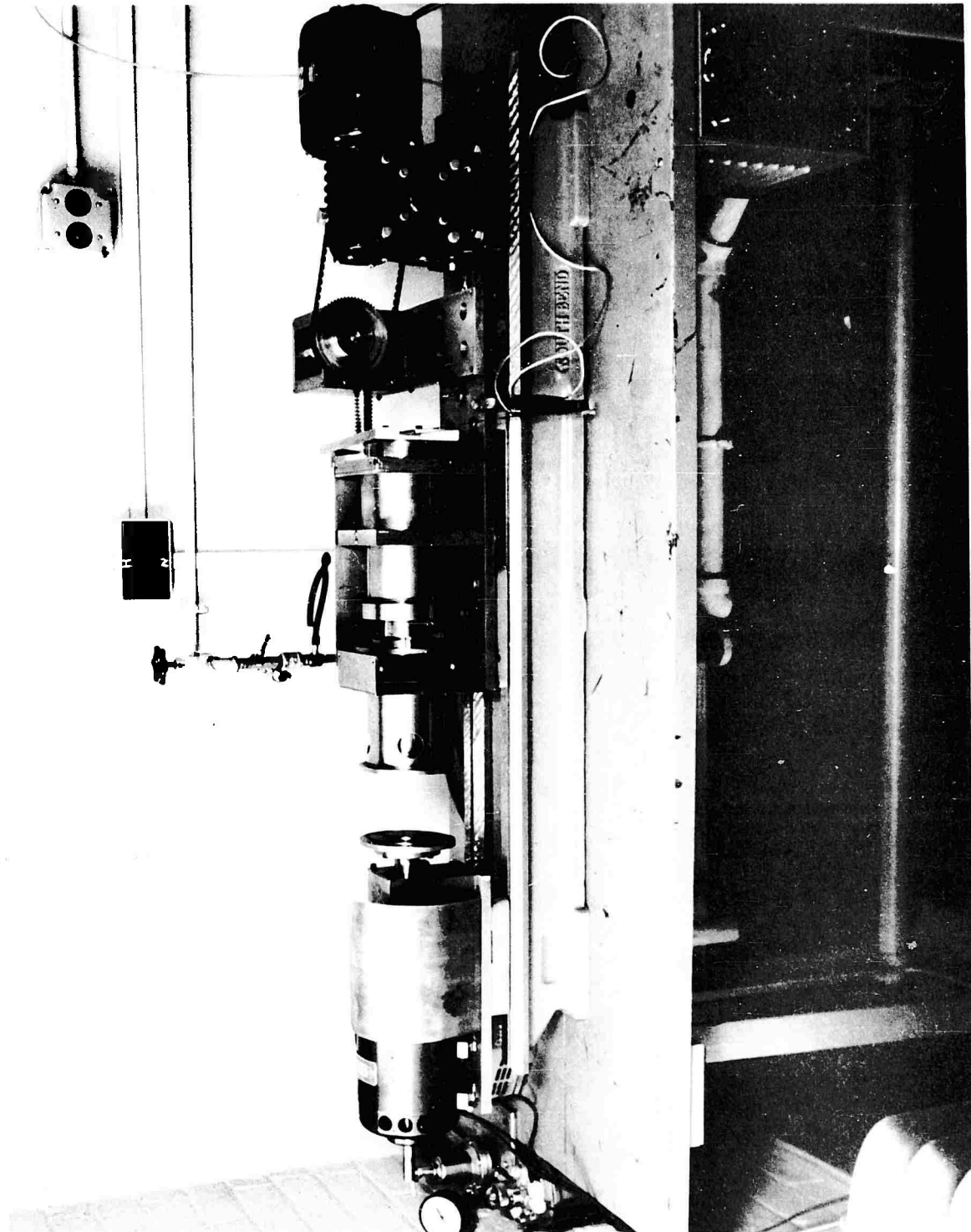
Figure 167. Experimental Apparatus for Investigating Effect of Tensile and Com-
pressive Hydrostatic Forces on Filled Binder Specimens (4-62S 09748)

VI.   PHASE 5—INTEGRATED DESIGN APPROACH

The objective of this phase was to integrate the methods of the first four phases with propellant development and charge design and develop a philosophy for optimum development of a solid propellant charge capable of meeting both structural and ballistic requirements.   In seeking a method of approach to this problem, the Program Evaluation Research Task (PERT) method of network analysis appeared promising, and the PERT concept was used as a basis of discussion for this phase of the program*.

A.   APPLICATION OF PERT TO INTEGRATED DESIGN

The difficulties of program evaluation and analysis for this type of activity are recognized by the Special Projects office of the Bureau of Naval Weapons; "three factors, however, set research and development programing apart.   First, we are attempting to schedule intellectual activity as well as the more easily measurable physical activity.   Second, by definition, research and development projects are of a pioneering nature.   Therefore, previous, parallel experience upon which to base schedules of a new project is relatively unavailable.   Third, the unpredictability of specific research results inevitably requires frequent change in program detail.   These points are acknowledged by all experienced research people.

"Yet, even though it be ridiculous to conceive of scheduling research and development with the split-second precision of an auto assembly line, it is clear that the farther reaching and more complex our projects become, the greater is the need for procedural tools to aid top managers to comprehend and control the project.   At the very least, such a method can improve over the random 'how goes it' examination if only by providing

---

* The discussion on PERT in this report is not primarily concerned with the derived Performance Evaluation and Review Technique which describes the mechanics of monitoring a program, but rather with the basic philosophy of the original research task.

VI, A, Application of PERT to Integrated Design (cont.)

"First, it (PERT) represents a fundamental operational approach to R and D
planning by describing the R and D process as a network of interrelated activities.
This will cause a very pervasive change in our planning methodology since it faces
up to the coordination problem involved in an R and D program. Secondly, PERT
has focused attention on and offers the promise for better integrated planning
methods in the cost and performance areas."[97] Malcolm further states that
the orderly application of PERT involves the following steps: (with additional
steps believed necessary in this program inserted in parentheses)

1. "Section of specified identifiable events."

2. "Determine activities necessary to achieve events."

3. (Determine kinds and quality of talent needed).

4. (Determine major characteristics of activities and the input,
    output requirements and pertinent interrelationships).

5. "Develop project network of activities and events by properly
    sequencing events and establishing inter-dependencies."

6. (Review network for completeness to assure that all necessary
    activities are present).

7. "Estimate time to complete activities, together with a measure
    of uncertainty," (including effect of quality of the talent available).

8. "Design and analysis or evaluation procedure to process and
    manipulate these date."

9. (Determine necessary control and decision points on the several
    decision lines to ensure effectiveness of interrelationship).

10. "Establishment of information channels to bring actual achieve-
    ment data and change data to the evaluation center."

VI, A, Application of PERT to Integrated Design (cont.)

11.   "Application of Electronic Data Processing equipment to the analysis procedure."

12.   "Display and use of the data by management - - ."

13.   "Maintenance and updating of the planning information to keep up with dynamics of program."

14.   (Establish basis for review to assess schedules, assess individual performance, and assess the program strategy and decisions used).

If one considers the development of a propellant charge for a particular application, the process can be visualized in general as shown in Figure 168. Assuming adequate knowledge is available on existing propellants, a morphological analysis of the possible ballistic designs will indicate which, if any, of these propellants can be used, and ballistic calculations will show the performance of the several possible designs. The compatability of these designs with the environmental conditions can then be estimated by structural analysis using the mechanical properties of the several propellants (assuming the method for doing this is available for each condition). Selection of the best of these designs would require a series of trade-offs, such as stress concentration against sliver loss in selecting fillet radii, and allow evaluation of deficiencies needing developmental correction.

The original analysis may indicate that only modest changes are required, which can be easily handled by introducing available technology into the specific propellant system. Such a change requires only confirmation and little interrelationship of activities is required. For major advances in propulsion systems, however, the chief effect of the initial morphological, ballistic, and structural analyses is to indicate the inadequacy of existing propellant systems and point up specific deficiencies as objectives for a major development program.
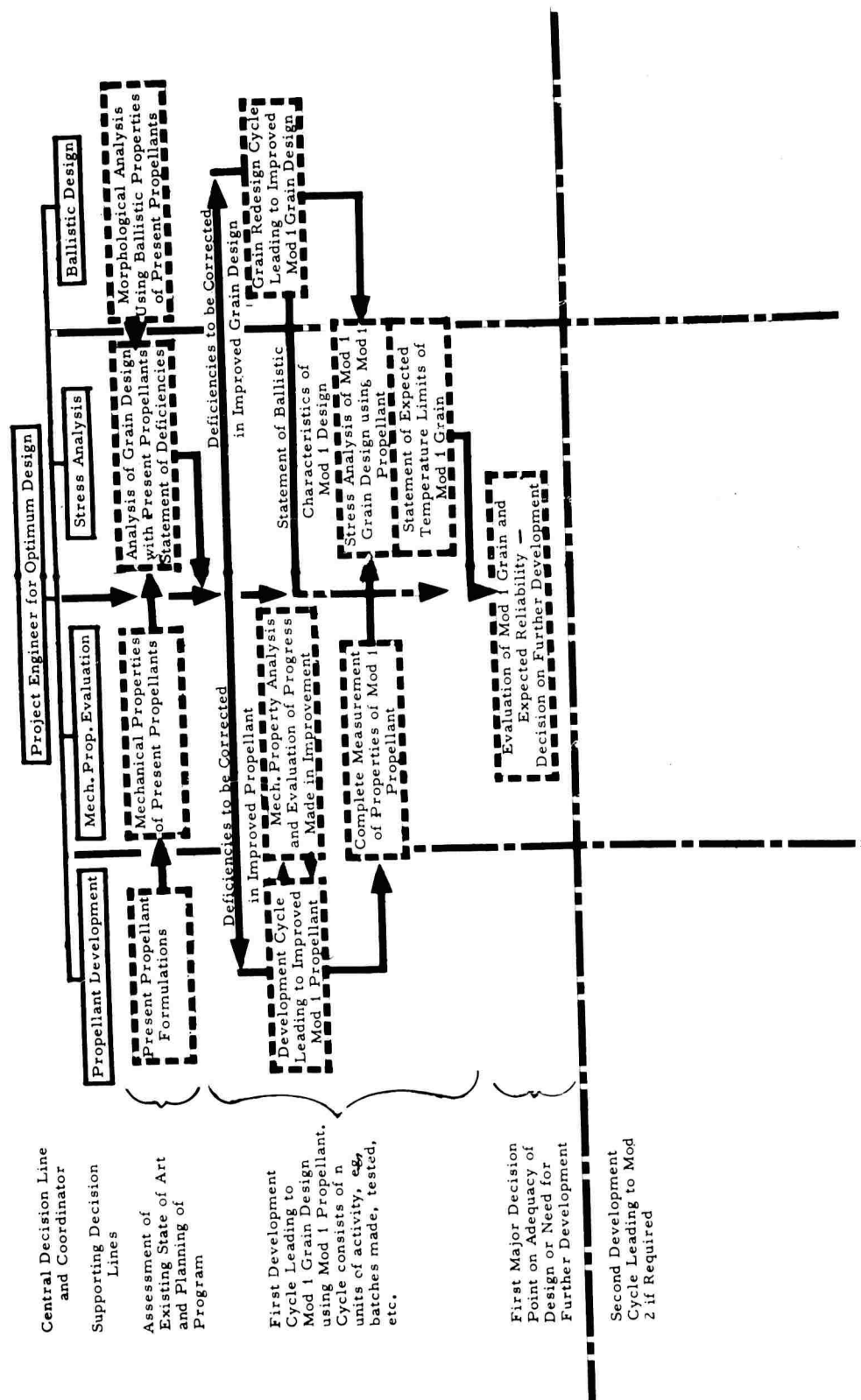
Figure 168. Diagram of General Process of Grain Development Showing Inter-relation of Major Development Efforts

VI, A, Application of PERT to Integrated Design (cont.)

The first trial solution of the problem thus defines the needed areas for study. It is evident that the process to this point is the same as that required in preparing a proposal and such an analysis is essential if the program proposed is to be adequate and describe the requirements for men, money, and materials realistically.

If the program proposed is accepted and work is started, the several lines of research and development work become continuous streams of physical and intellectual activity from which specific products may be removed from time to time for use in the several stages of motor system development. The first of these products might be the Mod 1 propellant formulation for use in the Mod 1 grain design. Both of these will be modifications of previous items and will be the result of one cycle of the charge development activity.

The removal of the Mod 1 products does not generally stop the stream of activity (assuming funding and related problems are not governing) for several reasons. First, the first modification will generally not accomplish all of the desired objectives, as was presumably forecast in the proposal, particularly under the collapsed time scales prevalent in development work on missiles. Second, a backup effort is generally initiated and continued at a reduced pace to overcome expected secondary problems of processing, reproducibility, etc., as Mod 1 goes into scale up and production. Third, a development activity once initiated requires teams of professional personnel that cannot be turned on and off abruptly, though they can be redirected, without serious effect on the development structure as a whole. Finally, the work done to reach Mod 1 has in turn generated new ideas, produced new data, and generally set the stage for further work. Thus even if Mod 1 were to be the final product of this system, it would in turn generate new work on another system for which the Mod 2 of the first system would become the Mod 1 of the second.

VI, A, Application of PERT to Integrated Design (cont.)

This concept of a continuous stream of activity is an essential basis
since a program team does not suddenly spring into being but already exists
in the continually developing skills of its members. It is essential at the
outset to assess the improvement in reliability probably resulting from the
proposed units and cycles of activity and predict the number of cycles of
activity required in a program to produce the target reliability specified.
The improvement in performance or reliability in a particular environment
due to cycles of activity is determined by the positions of the starting and
target points on the reliability curve, and the probable improvement expected
for each cycle of activity, as illustrated in Figure 169. In some cases the
target reliability may be higher than the ultimate reliability limit of the sys-
tem in the development stream; it is then essential to recognize that a break-
through to a new system with greater reliability is required. An example
of this was the limitation on low temperature performance for the conventional
composite solid propellents used in thick web case-bonded designs due to
the low failure elongations achievable at low temperatures. The breakthrough
of developing controlled dewetting behavior established a new reliability growth
curve for use.

An examination of the propellant and motor development process
reveals, however, a serious obstacle to full implementation of an intergra-
ted design approach. This obstacle is the inherent specialization of the several
members of the ultimate design and development team which prevents a
real integration of the team as a whole, but requires rather that each member
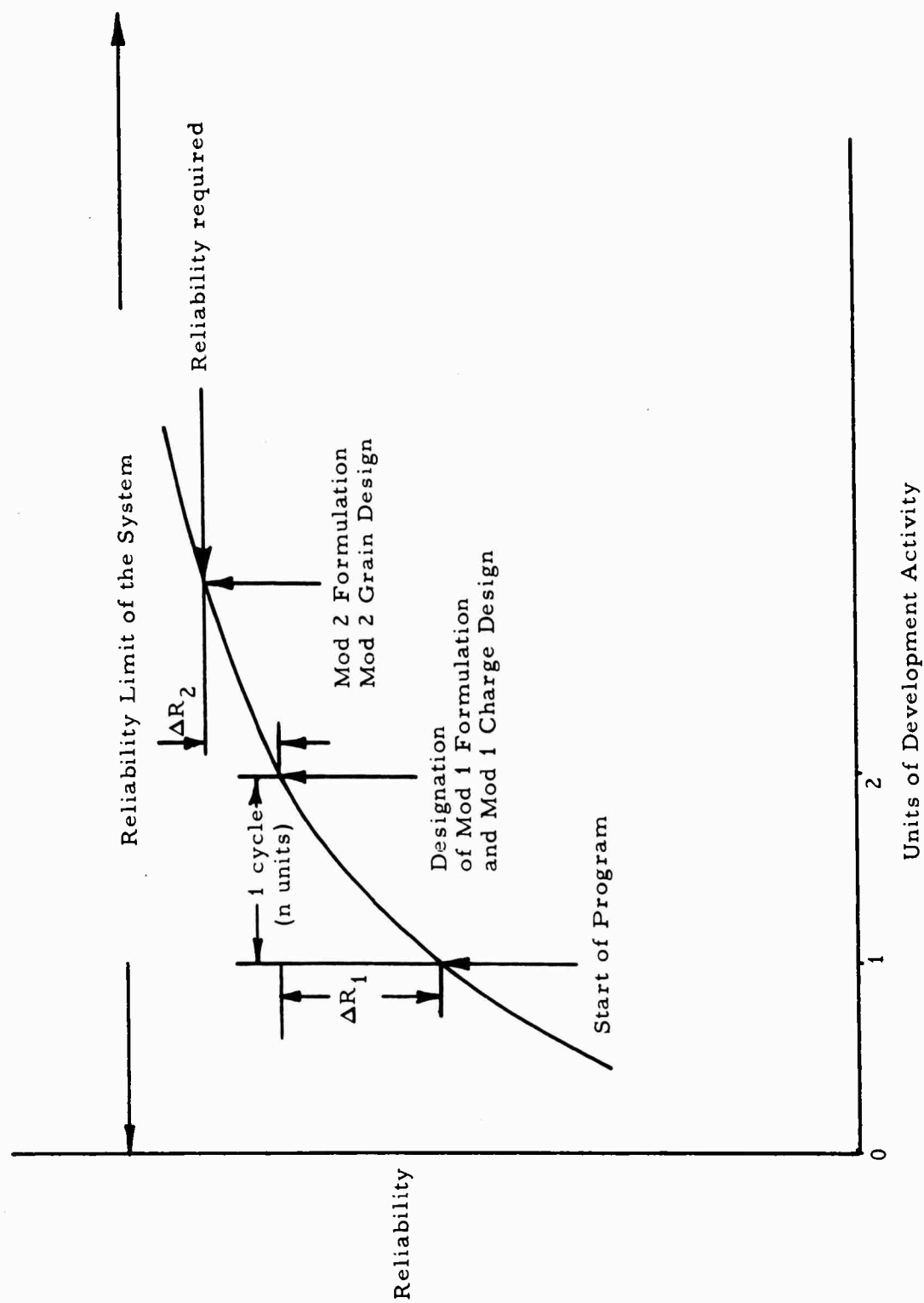
Figure 169. Growth of Reliability (or Performance) of a Given Propulsion System

VI, A, Application of PERT to Integrated Design (cont.)

operate in a limited sphere of understanding. The problem is one of semantics, of differences in the formal course work given at universities for different fields, and even of differences in the approach to problem solution. This problem is discussed by Williamson who defines "simuldisciplinary research" as the process of "analyzing the primary problem into separate problems which can then be attacked by experts", as opposed to true "interdisciplinary research" where each member of the team "works with every other member on the same overall problem. Thus, we find that the metallurgist must be able to understand the solid state physicist, the physical chemist, and the electrical engineer. Each must follow the other's reasoning and must adopt, for the time being perhaps, quite a different approach to that which is congenial to his own discipline" (92). Even in the case of "simuldisciplinary" programs, the team leader must operate in the interdisciplinary sense if he is to set up the problems properly and synthesize the several individual products into one whole product.

B.   CLASSIFICATION OF GRAIN DESIGNS BY WEB TO RADIUS RATIO

Solid propellant rocket grains can be divided roughly into five classes on the basis of their ratio of burning web thickness to chamber radius, or "reduced web."

(1)   Less than 1/3:   star, wagonwheel, dendrite, anchor
multiperforated, multitublar
Primary tactical weapons

(2)   From 1/3 to 2/3:   shell and rod, star with end-
effects,
bipropellant
Primarily booster, lower stage ballistic
missiles

VI, B, Classification of Grain Designs by Web to Radius Ratio (cont.)

(3) From 2/3 to 9/10: slot, conocyl, segmented shell

Primarily ALBM, MRBM, upper stage
ballistic missiles

(4) 0.9 to 2: unconventional designs for special
applications

(5) 2 to 10: i.e., burning path 1 to 5 diameters,
actually end-burning grains
Mostly in atmospheric sounding rockets
where aspect ratio is dominant.

This classification assumes a burning rate at standard conditions
(60°F, 1000 psia) of 0.2 - 0.5 in./sec, as typical of composite propellants
based on ammonium perchlorate. Slightly higher burning rates may be obtained
by using burning rate catalysts, but these materials do not contribute energy
to the system and their use is practically limited to a few percent without serious
sacrifice of specific impulse and other total-solids-dependent properties such
as castability and mechanical behavior of the propellant. Lower burning rates
are also obtainable by variations in the propellant formulation, but this is
usually by reduction in concentration of high energy ingredients, and this is again
limited by specific impulse considerations.

It is evident that for any given duration of burning, and a given diame-
ter of motor, a compromise must be made between selection of web thickness
of the grain and the burning rate of the propellant. If it is assumed that burning
rates are limited as above, then the choice of configurate or formulate reduces

VI, B, Classification of Grain Designs by Web to Radius Ratio (cont.)

to a selection, as between a grain design of web in one class with the higher
value of the burning rate range, and a grain design of web in the next higher web
class using the lower end of its practical burning rate range, etc. The most
available propellant is generally near the middle of the burning rate range, when
all factors of maximum specific impulse, ease of castability and mechanical
properties are favored. This may however, be biased on either side of the
range, as low side values for relatively long duration missiles in contrast to
high values for tactical or antimissile missiles.

Accepting the premise of a narrow range of burning rates of maxi-
mum availability, and practical diameter and duration restraints imposed by
overall missile design, the reduced web and therefore grain class becomes
uniquely determined. It may however be possible that different grain configura-
tions become "optimum" in different propellant systems for the same motor, if
their burning rate availability differs appreciably due to the chemical base of
the propellant, extensive development effort, etc.

The fraction of the chamber wall employed as a burning surface
area control, that is the exposure index of the grain*, however increases rapidly
as the reduced web is increased, and thus the cost of fabrication in terms of
complex cores and/or extensive insulation may be less favorable in the high web
ratio designs. The grain design decision, which appeared at first as a simple
trade-off of configuration or formulation is seen to be a more complex weighting

---

*Ratio of non-propellant confining surface (insulation or chamber wall) to
propellant burning area as illustrated in the sequence from fully case-bonded
to partially slotted to free-standing grains.

VI, B, Classification of Grain Designs by Web to Radius Ratio (cont.)

of factors reducing to a configurate-formulate-or-insulate decision. It is clear that the grain configuration for a given motor is a specialized custom design, and that success or familiarity with one configuration does not justify its imposition on other motor requirements of different proportion of duration to diameter, or ratio of length to diameter, unless the concomitant differences in burning rate and/or insulation requirement are realized.

It is fortunate that there are few scale effects in interior ballistics of solid propellants, when the design is based on determining the total burning response of the entire grain by stepwise integration of the differential elements of grain geometry and flow space.

This method of calculation is free of the restraints of artificial average conditions or approximations used in less developed computation procedures, and actually duplicates on the digital computer the complex flow and propellant consumption processes occurring in all detail parts of the motor. By analysis of known elements, minimum lead time and predictibility of performance are obtained at minimum cost by consciously changing the superficial design of the propellant configuration to minimize new problems in propellant formulation or insulation and grain support techniques. This is not to say that any diminution of effort on new propellants, or improved insulation and support techniques is justified, rather on the contrary, advances in this field will broaden the capability of grain design to yield maximum performance in a power plant and must be continuously pursued. However, in the minimum lead time development sense, versatile grain design based on most available propellant and insulation is the cheapest and most certain approach, based on analytical reproducibility of the grain configuration by mathematical means.

VI, Phase 5 -- Integrated Design Approach (cont.)

C.   THE INTEGRATED DESIGN PROCEDURE USING COMPUTERS

The principle of the integrated design procedure is that no single design consideration can dominate the selection of a propellant charge for a given propulsive mission, but that simultaneous and balanced consideration of many disciplines, including propellant properties, ballistic and stress analysis of the geometrical configuration of the charge, and the requirements of insulation, support, environmental capability, flight optimization, etc., must be made.

In earlier design decisions all of these factors were taken into account intuitively by an experienced rocket designer, and a balanced design resulted from his mental integration. However, the cost of a motor of that time could be measured in man-months of effort, and successive evolution of many design interactions could be done by trial-and-error during the developmental firings.

Today, the rocket motor is not just an independent and self-sufficient propulsion unit, definable by a thrust, duration, envelope and weight, but an intimately related part of an overall missile system, both structurally and economically, as well as in propulsion characteristics.

At the same time, as the cost of turnaround, in tooling requalification, and lost schedule has become equivalent to many man-years, the effort has intensified in the specialized disciplines to obtain rigorous predictability and accountability in all design aspects and lead by quantitative research all expensive development tests of new components and the corresponding firing analyses.

VI, C, The Integrated Design Procedure Using Computers (cont.)

As the effort in each such area has accumulated, and rule-of-thumb correlations have been replaced by highly exacting mathematical analyses, it is found that the complex interactions of many conflicting and overlapping physical functions result in processes of highly nonlinear and conditional nature, not practical for expression in conventional engineering estimate calculations. Electronic computers are ideal for this purpose, since they can be equipped by flexible computational programs capable of "remembering" a great number of alternatives, using trial-and-error sequences for nonlinear and transcendental expressions, and testing on-the-spot on the basis of tentative results the most applicable of various calculating approaches or design selections. To this extent they are free of bias, or habit from prior solutions where the designer of the program has provided them with the necessary test rationale or decision making process.

Of course this makes a great deal of bridge-crossing considerations before actually coming close enough to see the bridge, which is somewhat different from the intuitive design process which permits design decision at the point of arrival at a dilemma in terms of multiple and unresolved criteria. For computer usage, all decisions must be made on the basis of single quantitative differences, as the only elemental decision command is "equal to, greater than, or less than" in comparing two quantities. However, this is also the basis of human logic, and the computer can pyramid these branch commands to obtain twenty-seven alternatives in three successive decisions, with an executability of milli-seconds and a reproducibility of 100%. By use of index numbers, extract of key digits, conditional shift commands, etc., this decision making power can be made extremely complex to account for qualifying factors such as conditions of fabrication, work loads, raliability emphasis, prior usage, etc., which are usually considered subjective factors in decision making.

VI, C, The Integrated Design Procedure Using Computers (cont.)

Integrated rocket design thus becomes a summation of conditional and unconditional computations, on which a building block approach of fixed subroutines of single meaning and a monitor or master logic of sorting and selecting and redirecting capability is superimposed.

Typical of such subroutines would be the specific impulse of a specific propellant composition under ideal conditions, the burning surface area sequence of a particular grain configuration, the temperature distribution in a multilayer insulation composite under specified thermal duty conditions, the performance of a defined nozzle contour with an ideal gas, the structural analyses of an isolated case element, or the trajectory of a defined propulsion unit. In general, only one answer is obtainable for each of these separate problems, given thorough agreement on the conditions of input data, and consistency in acknowledgment of the state-of-the-art. There is therefore little judgment required for the evaluation except skill in the appropriate computation procedure, and knowledge of appropriateness of the physical processes represented. These routines are thus analogous to machine tools, in that they will reproduce precise articles in skilled hands, but do not in themselves produce a final assembly. Such routines should then be manufactured on a continuous basis, continuously upgrading to represent the current state-of-the-art in physical knowledge and interactions, and storable for application at time of need.

The appropriate computing approach to such a multifacet problem is analogous to a refinery process flow, where a change in the value or availability of a component may reverse the flow or control significance of a given part. This is done in the integrated design procedure on the computer by means of index registers, which record prior usage, condition values, emphasis, etc., as points on a numerical scale, and can cause skip, reversal, or alternative flow in the calculation sequence by composition of a logical test structure.

VI, C, The Integrated Design Procedure Using Computers (cont.)

Examples of secondary computer systems of this type are the
Aerojet program Beta (exterior ballistics and component optimization) (99),
the ACP-564B Interior Ballistics and Performance Predictor (cylindrical,
single-propellant grain design with end effects) (100), and the Aerojet Pro-
pellant Thermodynamics and Specific Impulse Calculation (102). These pro-
grams contain many subsidiary options, each of which has been developed over
a number of years and tested against a variety of actual motors, which are
thus used as the reference basis or standard for the computer program. Com-
puter programs of this type should not be considered as purely theoretical,
simply because they are based on mathematical calculations, since they are
tested regularly against relevant actual motors. The necessary basing factors
or physical conditions must be built into such programs, so that predictability
of results is assured. Thus within the confines of the program applicability,
future designs are expected to perform in close simulation of calculated results,
with a minimum of scale effects, design factors, etc.

D.   SOLID PROPELLANT COMPUTER SELECTOR SYSTEM, ACP-735

Propellant data for grain design requires estimation of future pro-
perties based on limited past data. When a propellant is sure in its ballistic
and mechanical properties, it is of little value in preliminary design for future
motors.

At the same time, it is essential that data of described confidence
levels be used in a computer ballistic prediction system; since neither the
accuracy nor the thoroughness of the 564 ballistic computer program is justified
if based on inadequate or wrong data. Since the value of a computer system
is its timeliness, it is necessary to include data of various levels of confidence
or experience rating, and to identify each item according to source and the level
of assurance at which it should be used. To be too highly restrictive on the

VI, D, Solid Propellant Computer Selector System, ACP-735 (cont.)

experience level of the data would preclude early use of data on advanced pro-
pellants, and result in either unwarranted extrapolations or too conservative an
estimate of future propulsion capabilities. Therefore, a system of "availability"
coding of propellant, based on the position of the propellant on the reliability
growth curve, has been devised to allow systematic separation of data into
production, limited experience, laboratory experimental, or future theoretical
categories. A scale of nine points is thus used to denote the size and quantity of
propellant processed in setting the experience level. In general, a year of work
raises a propellant one point on this scale. It is no coincidence that most pro-
pellants of unlimited availability, or code 1 are about 10 years removed from
their origin as a chemical suggestion.

1.   The Propellant Properties Card Deck

The actual end card deck now contains data on over 200 pro-
pellant formulations ranging from full production-proven compositions to a
few highly experimental current laboratory formulations. In most cases, the
data becomes less complete as the availability is lessened from 1 to 9, since
mechanical properties data are usually not available from small laboratory
specimens, and ballistic properties improve in confidence as the quantities for
testing enlarge.

Each propellant is described by two punched cards, the first
consisting primarily of propellant composition data; the second, ballistic and
mechanical properties. The following paragraphs are numbered to correspond
to the card columns for ease of reference.

VI, D, Solid Propellant Computer Selector System, ACP-735 (cont.)

CARD I:

Card Column No.	
1-4	Propellant designation number.
5-6	Oxidizer blend code.
7	Mod number is a designation identifying specific changes in processing which are believed to have no significant ballistic or structural effect on the propellant which can thus carry the experience rating of the basic designation.
8	Availability code.
9-10	Weight fraction of total ballistic solids, or total of all solids having ballistic significance such as oxidizer salts, metallic fuels, burning rate additives, etc.
11-12	Weight fraction fuel.
13-16 17-20 21-24 25-28 29-32 33-36	Additives: a space for four digit code of up to six (6) additives which are arbitrarily designated by a two letter code and the weight fraction.
37-40 41-44 45-48 49-52 53-56 57-60 61-64	Binder components: A space for four digit code of up to seven (7) fuel or binder ingredients using two letters and two digits, the latter representing concentration equivalent to nearest whole number.
65-68	Fuel identification code - a four letter designation of common fuel compositions used.

VI, D, Solid Propellant Computer Selector System, ACP-735 (cont.)

69-72	Oxidizer identification code: A four letter designation for various oxidizer compositions, such as blends of ammonium perchlorate and potassium perchlorate.

CARD II

1-4 5-6 7-8	Repeat the propellant designation, oxidizer blend, Mod number, and availability codes of the first card.
9	Mechanical properties code: to be discussed later. (See below)
10-12	M Bar - the molecular weight of the propellant gas combustion products averaged over the isentropic nozzle expansion process.
13-15	Density - the propellant density, in lbs/cu. in., scaled times 10^4.
16-17	Chamber flame temperature - the calculated adiabatic flame temperature of the propellant (°F), scaled times 10^{-2}.
18-19	Exhaust flame temperature - the calculated isentropic exhaust temperature for expansion from 1000 psia to the atmosphere (°F), scaled times 10^{-2}.
20-22	Measured I_s - the specific impulse of propellant as measured specifically in the standard I_s motor 10KS-2500 size expanding 1000 psia to atmosphere (1000/14.7) without correction of 15° half angle by Tsien divergence factor, units of lbf sec/lbm.
23-25	Mass flow coefficient (C_w) - the corresponding value to the I_s calculated as above from 10KS-2500 motor firings, scale $X10^5$.

VI, D, Solid Propellant Computer Selector System, ACP-735 (cont.)

26-29	Burning rate - the measured burning rate in units of in/sec scaled $X10^3$, corrected to 1000 psia and 60°F.
30-31	Pressure exponent - the burning rate - pressure exponent.
32-33	Test device code designating the source of the burning rate data.
34-35	Temperature sensitivity - the temperature sensitivity of pressure at constant K-ratio (π_K) or (d ln p/dt)K, scaled $X10^4$, for above 60°F.
36-37	Temperature sensitivity - ditto for the region below 60°F.
38-65	Mechanical properties data. (See below)
66-67	Isentropic flow coefficient gamma, scaled $X10^2$.

2. Propellant Selection in the Computer

In the general concept of the integrated design procedure, it will be necessary in optimization of loading, duration and web thickness to alter burning rate systematically, which requires automatic propellant substitution to maintain discreet design validity in each case. This could be performed by requesting alternate propellants, of common levels of availability, specific impulse, and within a reasonably narrow range of burning rate. Since burning rate data is stored generally at standard conditions (such as 1000 psia, 60°F), and has differing pressure exponent and temperature sensitivity in various types of formulations, it is necessary that this search be conducted on the basis of burning rate values corrected to operating conditions. This capability is provided in the propellant selector option of the ACP-735 computer program.

When preparing for propellant data input, up to six propellant designation numbers may be entered in sequence, as when it is desired to check

VI, D, Solid Propellant Computer Selector System, ACP-735 (cont.)

the performance available from a given core and configuration for various avail-
able propellants. The ballistic properties for all propellants listed are sequen-
tially brought from tape or card storage, as appropriate, by the data control
card preceding the propellant call card, and used with the same grain geometry.

In the alternate type input, where specific propellants have not
been selected, it is necessary to input the availability code to assure recourse
only to propellants obtainable in the time span of the motor development, the
minimum specific impulse to assure adequate total impulse in the confines of
fixed chamber cited at a reasonable loading factor, and the minimum and maxi-
mum burning rate allowed. The latter may be input arbitrarily, or may result
from an internal setup obtained in the web -- loading factor -- duration tradeoff
of the overall motor optimization cycle. In any case, temperature (T) is assumed
60°F if not input, and the pressure (P) is taken as 1000 psia if not otherwise
input.

Propellants which satisfy all the above conditions are then
called up for active storage and printed for examination. Burning rate is often
the most critical propellant property in selection of grain design, since it deter-
mines the web thickness, and thus all other propellants which satisfy the burning
rate condition, even though they fail on other criteria, are reported as supple-
mentary information. This will save time in reinstitution of the problem if no
primary propellant is satisfactory for reasons, such as castability, not listed
in the original selection criteria.

If, on the other hand, more than six propellants are obtained
which satisfy all conditions, the six with the highest specific impulse are
retained.

VI, D, Solid Propellant Computer Selector System, ACP-735 (cont.)

Present computer operations also allow the use of write-in propellant data, as may be necessary where specific properties have been obtained in prior data reduction operations, or where intentionally varied values are used, as in tolerance control studies. However, every effort is being made to provide for automatic up-dating of the existing propellant data card deck as each firing is conducted, so that the data file will be current and closest to actual firing performance for each propellant at all times. Since a source code is carried in the cards (Card 2 Columns 32-33), it is possible to carry simultaneously data on the same propellant from various sizes and types of motors. This will eventually permit a complete closed loop in design, performance prediction, data reduction, and up-dating of propellant data file, so as to obtain maximum consistency throughout the entire ballistics operation.

3. Mechanical Properties

The introduction of mechanical properties in propellant selector routines was initially attempted in a simple summary sense, such as modulus, nominal maximum stress, and elongation at this stress, all at the standard test temperature of 77°F. It became clear that decisions on the structurability of a grain design could not be made on the basis of these values, and much thought has been given to defining a limited set of values which would characterize any solid propellant. The need for a minimum set of values, required because of card space limitations on IBM cards, reflects the general desire of users of information for sufficiently few critical parameters that trends can easily be seen.

The problem in mechanical property description is that there are different modes of failure of solid propellant charges under the different use conditions and not all motors are subject to the same set of conditions. An example of a critical condition listing is shown in Table 35, which shows single

TABLE 35

CRITICAL CONDITIONS OF USE AND CRITICAL COMBINATIONS

	Low-temperature cycling	High-temperature cycling	High-temperature stowage	Low-temperature stowage	High humidity exposure	Vibration	High acceleration	Impact loading	Ignition pressurization
Low-Temperature cycling	α ϵ_{40} ϵ_e ϵ_b								
High-temperature cycling	α ϵ_{40} ϵ_b	E_c S_c n							
High-temperature stowage	α ϵ_{40} ϵ_e	E_c S_c n	E_c S_c n						
Low-temperature stowage	ϵ_{40} ϵ_e α	α ϵ_{40}	α ϵ_{40} ϵ_b	α ϵ_{40} ϵ_e					
High humidity exposure	ϵ_{40} ϵ_e	E_c S_c n	E_c n	ϵ_{40} ϵ_e	E_c n S_c ϵ_{40}				
Vibration	?	?	?	?	?	?			
High acceleration	α ϵ_b	E_c S_c n	E_c S_c n	?	?	?	E_c S_c n		
Impact loading	ϵ_b	O	O	ϵ_b	O	O	O	ϵ_b	
Ignition pressurization	ϵ_e	O	O	ϵ_b	O	O	O	O	ϵ_b

Description of Values Used

ϵ_e — Embrittled const. rate fail elong, -40°F and 80% R.H.

ϵ_b — Const. rate failure elong, -40°F and 20% R.H.

E_c — Creep modulus at high temp. and 20% R.H.

n — Creep rate at high temp.

S_c — Creep failure stress, high temp. and 20% R.H.

ϵ_{40} — Constant strain failure, 40°F and 80% R.H.

α — Coeff. thermal expansion

O — Not believed critical

? — Critical test not yet determined

VI, D, Solid Propellant Computer Selector System, ACP-735 (cont.)

and paired sets of conditions expected to give problems, together with a
minimum set of test values to characterize the propellant suitability. The
liner and liner-bond are also involved, but no attempt is made here to
characterize that important problem. Five tests resulting in seven values
would be required to cover all of the conditions except vibration, even assuming
that constant rate tests at -40°F and one rate characterize relative quality at
other rates, etc. (The complex effect of humidity on different types of pro-
pellants may not be adequately determined by the use of one high humidity,
80% RH, and one low value, 20%.) One may argue with the particular choice
of values, and certainly there are other multiple combinations of conditions
which are serious, but it is doubtful if a smaller set of values can be obtained
for this problem as yet. It is also clear that not all motors will be subjected
to all of these conditions, and a comparison with the ballistic ranges of use
and the corresponding web fractions will show a considerable simplification
in many cases. However, if a propellant is being considered in the most
general sense, all of the properties pertinent to critical use conditions would
have to be included. This would suggest a set of minimum tests to which all
propellant formulations were subjected. Further, the value finally reported
for card use would be the worst value expected or observed in production use;
this implies assuming a standard deviation for each property based on expe-
rience for propellants low on the availability scale.

Such summarized critical values are of use whether the full
computer optimization is used or whether screening of propellants during
development is underway. This is not to say that only these minimum values
should be measured nor that complete rheological characterization is unde-
sirable, but rather that an attempt should be made to focus on the critical
values for screening and preliminary selection. Full range characterization
can become so complex that presentation of results for motor decisions becomes
difficult.

VI, D, Solid Propellant Computer Selector System ACP-735 (cont.)

4. Stress Analysis

The summary of values of properties selected to represent the critical conditions relates directly to the state of the art of stress analysis. Thus for the case of low temperature failure on cycling, a simple criterion of failure ϵ_b, is paired with the thermal coefficient of expansion of the propellant, a, required by the elastic, infinitesimal analysis of an incompressible material. The close agreement reported in Phase 3 for such an analysis, and the unexpectedly good correlation of failure using ϵ_b in Phase 4, suggests that these two parameters are sufficient - certainly for screening purposes - taking account of high humidity, if expected, by including the two values taken at 80% RH, ϵ_e and ϵ_{40}.

The configuration of the grain can be though of in four parts, the web fraction, B/A, the stress concentration, the length to radius ratio, L/B, and the design of the end discontinuities. The web fraction is of prime ballistic interest, as already noted, and with L/B determines the maximum cylinder strain for a given type of end design. Each of the basic grain configurations has a characteristic stress concentration range determined by number of star points, filet radii, etc., which can be graphed or programed on the computer. Thus each ballistic choice open to the computer can be matched by a corresponding set of values from stress analysis. For those cases presently solved, such as low temperature cycling failure, the computed maximum strain can be compared with the critical property on the card to see if the propellant mechanical properties are compatible with the configuration. A complete stress analysis would still be required on the selected design when reduced to practice.

VI, D, Solid Propellant Computer Selector System ACP-735 (cont.)

A somewhat different approach would be possible if more complete information on mechanical properties is incorporated in the computer system. An example would be the direct estimation of lowest temperature of operation for a cylindrical bore configuration using a graphical solution as shown in Phase 4 by Figure 128. In such a case, the several possible propellants would be rated in terms of expected low temperature performance, which also describe the deficiencies for correction by propellant development. The much extended low temperature capability of the Class 1 propellant suggests, however, that no mechanical property deficiency exists at low temperature unless extreme filet radii, difficult end designs, or high humidities are required. In this case the ballistic optimization is independent of stress analysis, and mechanical property optimization and propellant development need only optimize ballistic behavior.

5. Integration of the Process

The several steps described above should be performed in practice with close interaction and communication. This can be seen in Figure 170, showing a portion of a modified PERT diagram which attempts to show the several steps in the planning of an idealized development program. At the end of Step 4, a proposal is submitted with a clear understanding of the specific requirements to be met. The actual methods of meeting these requirements are not yet all clearly definable and the usual process is somewhat Edisonian, with the results of each experiment helping to guide further experiments. By the same token, the methods of operation of the integrated system as a whole are not yet completely definable and require the close cooperation of groups working closely together. Experience at Aerojet-General during this program has demonstrated a growing understanding by all participants of the roles played by the other groups. This has been facilitated by regular monthly meetings at which individuals from all parts of the program have described their work in detail. As a result, problems

DOCUMENTS   OPERATIONAL STEPS PERFORMED

Ballistic and mechanical properties of Propellant A proposed as starting formulation

Ballistic and dimensional requirements

Environmental requirements

Step 1 -- Ballistic design on the computer, calculation of alternative configurations and selection of first configuration. Related design features are selected, e.g., liner, extent of bonding, and type of end design.

Grain design drawings.

Step 2 -- Stress-strain analysis of first design using environmental requirements and mechanical properties of Propellant A to estimate critical conditions of use and maximum strains expected.

Description of critical conditions and strain values expected.

Step 3 -- Failure analysis through comparison of expected strains with failure properties of Propellant A. Determination of test and test conditions for measuring each critical property.

Failure analysis with statement of deficiencies including estimated properties required in terms of probably manufacturing variability. Specification of tests to be used for each critical property.

Step 4 -- Propellant development establishes goals in terms of specific mechanical and ballistic properties values using specified tests and number of sample requirements. Proposal is prepared.

Charge Development Proposal defining Mod I design and work required. Forecasts subsequent cycles of activity to achieve specified requirements.
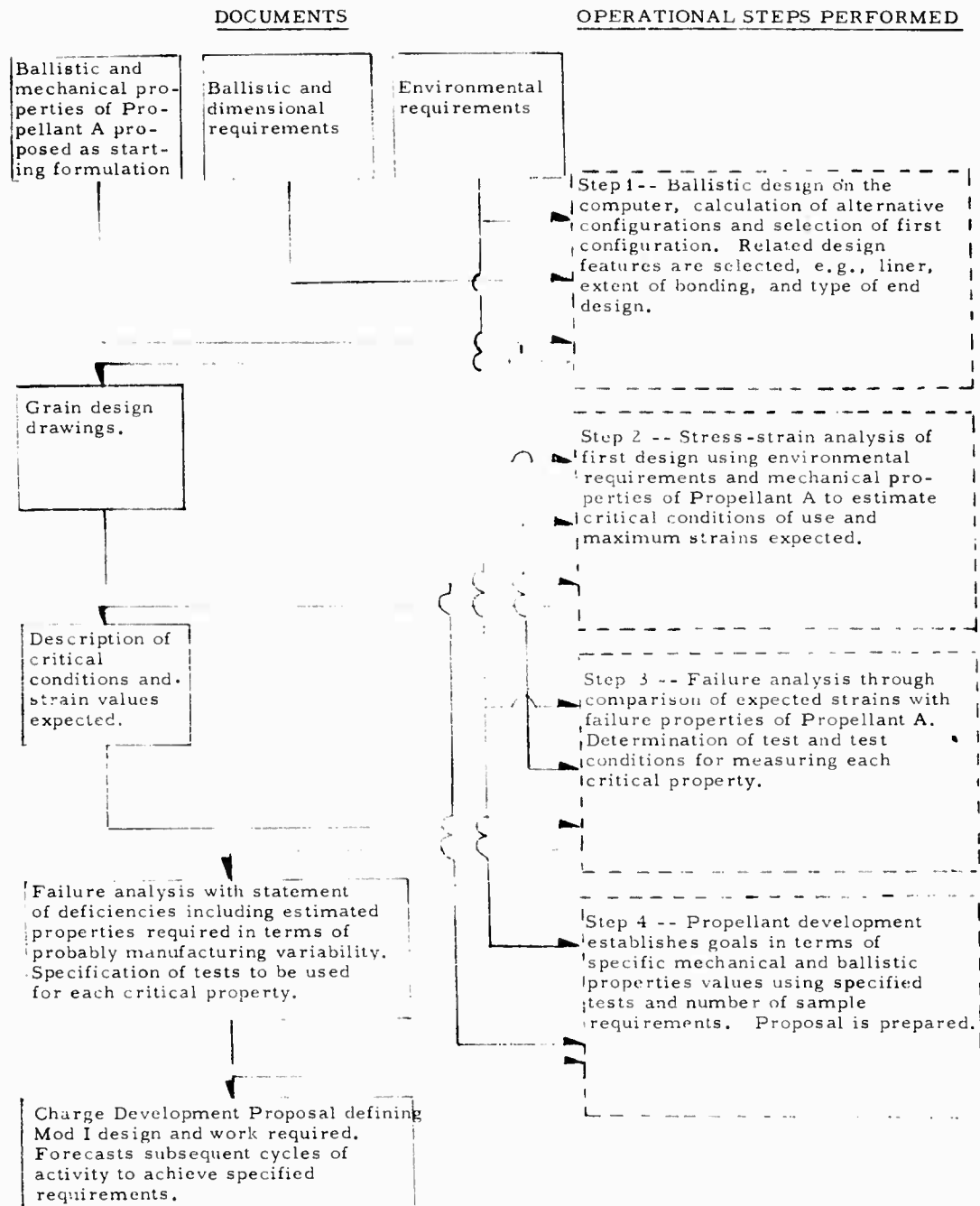
Figure 170.   Conceptual Analysis of Idealized Proposal Activity for a Propellant Charge Development Program Showing the Operations Performed and the Type of Information Used and Produced

VI, D, Solid Propellant Computer Selector System ACP-735 (cont.)

on motor-propellant interaction arising outside of this program have been handled with a steadily increasing ability in joint solution.

VII. CONCLUSIONS

Mechanical properties should be measured under conditions suitable to an experimental stress analysis and the resulting data correlated in terms of stress analysis parameters. The use of strain invariants, together with tests under several types of strain fields, offers promise of complete description of observed behavior. Description of viscoelastic behavior through models appears possible but may be too complex to cover the range of property values expected in production.

Linear elastic, infinitesimal analysis of stresses gives surprisingly close estimation of observed strains in simple tubular configurations. The strains are indendent of propellant strength for rigid cases on cycling or pressurization, which in turn means that the strains are relatively unaffected by batch-to-batch variability of the propellant.

Failure behavior of composite propellant is complex and the high batch variability of failure properties is reflected in high batch-to-batch variability of failure behavior of motors. Humidity in turn strongly affects failure behavior and, if uncontrolled, can produce additional motor failure variability. The case of low temperature cycling failure appears to be correlated well for tubular configurations by the ratio of observed failure strain in the standard JANAF constant rate tensile test to the maximum strain in the motor, both values taken at the same temperature.

VII, Conclusions (cont.)

The systematic approach to failure analysis, shown here for low temperature cycling, can be linked to systematic ballistic design on the computer and provide an intergrated design method for arriving at structurally and ballistically optimized grain designs for solid propellant motors.

BIBLIOGRAPHY

1. Vernon, J. H. C., "The Effects of Confining Pressure on the Mechanical Properties of Solid Propellants", Bulletin of the Joint Meeting JANAF Panels on Physical Properties and Surveillance of Solid Propellants, 13/SPSP-8, August 1960.

2. Surland, C. C. and Jacobs, J. M., 18th Meeting Bull. JANAF Panel on Physical Properties of Solid Prop. (1959) pp. 53-65.

3. Wise, John, "Development of a Specimen and Test Method to Provide Accurate Uniaxial Tension Mechanical Properties", to be presented at JANAF Physical Properties Panel Meeting, Nov. 1961.

4. Smith, T. L., Transactions of the Society of Rheology, 3, 113-136 (1959).

5. Rainbird, R. W. and Vernon, J. H. C., "An Instrument for the Measurement of Volume Changes Occurring in Tensile Testing", Bulletin Joint Meeting, JANAF Physical Properties and Surveillance Panels, pp. 39-44 (1960).

6. Beuche, F., Journal of Applied Polymer Science, 1961.

7. Goldhagen, S., "Study of Methods of Improving Storage Life of Solid Rocket Motors", Contract AF 33(600)-40314.

8. Rivlin, R. S., "Finite Elastic Deformations", A series of eight lectures given at California Institute of Technology, January and February 1953.

9. Blatz, P. J., Ko, W. L., and Zak, A., "Fundamental Studies Relating to the Mechanical Behavior of Solid Propellants, Rocket Grains and Rocket Motors", GALCIT SM 61-15, June 1961.

10. Blatz, P. J., and Nesheim, G. D., "Elastic Stresses in Glass Filament Wound Solid Propellant Motors", Memo 4780-2683, 9 December 1960.

11. Jones, H. C., and Yiengst, H. A., Ind. Eng. Chem., 32, 1354-9 (1940).

12. Bland, D. R., The Theory of Linear Viscoelasticity, Pergamon Press, New York, 1960.

13. Lee, E. H., Radok, J. R. M., and Woodward, W. B., "Stress Analysis for Linear Viscoelastic Materials", Trans. of the Soc. of Rheology, Vol. 3, pp. 41-59, 1959.

BIBLIOGRAPHY (cont.)

14.   Morland, L. W., and Lee, E. H., "Stress Analysis for Linear
       Viscoelastic Materials with Temperature Variation", Trans. of the
       Soc. of Rheology, Vol. 4, pp. 233-263, 1960.

15.   Williams, M. L., "The Strain Analysis of Solid Propellant Rocket Grains",
       J. of the Aerospace Sciences, Vol. 27, pp. 574-586, 1960.

16.   Williams, M. L. Blatz, P. J., and Schapery, R. A., "Fundamental
       Studies Relating to Systems Analysis of Solid Propellants", California
       Institute of Technology Report No. GALCIT SM 61-5, 1961.

17.   Hilton, H. H., Hassan, H. A., and Russell, H. G., "Analytical Studies
       of Thermal Stresses in Media Possessing Temperature Dependent Visco-
       elastic Properties", WADS TR 53-322, 1953.

18.   Hilton, H. H., and Russell, H. G., "An Extension of Alfrey's Analogy to
       Thermal Stress Problems in Temperature Dependent Linear Viscoelastic
       Media" J. of the Mechanics and Physics of Solids, Vol. 9, pp. 152-164,
       1961.

19.   Hilton, H. H., and Murthy, P. N., "The Analysis of Elastic or Viscoelastic
       Finite Length Thick-Walled Cylinders Encassed by Elastic Shells and
       Exposed to Internal Pressure, Thermal Cycling or Vertical Storage",
       Aerojet-General Corporation Report No. SP 61-1, 1961.

20.   Hilton, H. H., "Anisotropic, Nonhomogeneous, Linear Viscoelastic
       Analysis", Aerojet-General Corporation Report SD-16, 1961.

21.   Lee, E. H., and Rogers, T. G., "Solution of Viscoelastic Stress Analysis
       Problems Using Measured Creep or Relaxation Functions", Brown
       University, Division of Applied Mathematics, Interim Tech. Rept. No. 1,
       1961.

22.   Gross, B., Mathematical Structure of the Theories of Viscoelasticity,
       Hermann and Cie, Paris, 1953.

23.   Jones, J. W., Daniel, D., and Johnson, D. A., "Propellant Viscoelastic
       Characterization in Creep and Stress Relaxation Tests", 20th Meeting
       Bulletin, JANAF-ARPA-NASA Panel on Physical Properties of Solid
       Propellants, Vol. 1, pp. 193-200, 1961.

BIBLIOGRAPHY (cont.)

24. Freudenthal, A. M., "The Phenomenon of Stress-Relaxation, Proc. ASTM, Vol. 60, pp 986-999, 1960.

25. Bryant, K. C. and Bisset, D. C., Proceedings of the Third Rubber Technology Conference (1954) T. H. Messenger, ed., Heffer, Cambridge, England, p. 655.

26. Martin, G. M., Roth, F. L., and Stiehler, R. D., Trans. Inst. Rubber Ind., 32, 189-203, (1956); Rubber Chem. & Tech., 30, 876-88, (1957).

27. Jet Propulsion Laboratory, Research Summary 36-5, Vol II, Nov. 1960, pages 37-41.

28. Daniel, I. M. and Durelli, A. J. - "Photoelastic Investigation of Residual Stresses in Glass-Plastic Composites", Section 19A, 16th Annual Conference of Reinforced Plastics Division, The Society of the Plastics Industry; Chicago, Illinois.

29. Frocht, M. M. and Guernsey, R. - "Studies in Three-Dimensional Photoelasticity", Proceedings of 1st U. S. National Congress, Applied Mechanics, 1952.

30. Jessop, H. T. - "Equilibrium Equations Along Stress Trajectory in Three Dimensions", Jl. of Scientific Instruments, Vol. 26, January 1949.

31. Messner, A. - "Propellant Grain Stress Analysis", Proceedings of 17th JANAF-ARP-NASA Solid Propellant Group Meeting, 23 May 1961 at Denver, Colorado.

32. Frocht, M. M., "Photoelasticity", Vol. 1, pp 289-302.

33. Blatz, P. J. and O'Callaghan, T., Bull. 20th Meeting JANAF Panel on Physical Properties of Solid Propellants (1961).

34. Smith, Thor L., and Stedry, Paul J., "Time and Temperature Dependence of the Ultimate Properties of an SBR Rubber at Constant Elongations", Jour, Appl. Phys. 31, 1892-8 (1960).

35. Williams, Malcolm L., Landel, Robert F., and Ferry, John D., "The Temperature Dependence of Relaxation Mechanisms in Amorphous Polymers and Other Glass-forming Liquids", Jour. Am. Chem. Soc., 77, 3701-7 (1955).

36. San Miguel, A., Ibid, pp. 163-73.

BIBLIOGRAPHY (cont.)

37.   Chiesa, A., Kautschuk u. Gummi 11, WT 161, (1958).

38.   Graves, F. L., India Rubber World 122, 534, 539, (1950).

39.   Nijveld, H. A. W., Proceedings 2nd Rubber Technol, Conf. (London), 256, (1948).

40.   Buist, J. M., Geldof, H., India Rubber World 122, 291 (1950).

41.   Morris, R. E., Bonnar, R. U., Anal. Chem., 19, 436, (1947).

42.   Graves, F. L., India Rubber World 111, 305, 317 (1944).

43.   Buist, J. M., Kennedy, R. L., India Rubber Journal 110, 809. (1946).

44.   Poules, I. C., India Rubber World 103, No. 5, 41, (1941).

45.   Kainradl, P., Handler, F., Kautschuk u. Gummi 12, WT 239, (1959).

46.   Chasset, P., Thirion, P., Rev. gen. caoutchouc 35, 451, (1958).

47.   Greensmith, H. W., Thomas, A. G., J. Pol. Sci. 18, 189, (1955).

48.   Buist, J. M., India Rubber World 120, 328, (1949).

49.   Reinsmith, Gerald, India Rubber World 116, 499, 507, (1947).

50.   Patrike'ev, G. A., Melnikov, A. I., Rubber Chem and Tech. 14, 863 (1941).

51.   Busse, W. F., Ind. Eng. Chem. 26, 1194 (1934).

52.   Van Wijk, D. J., Rubber Chem. and Tech. 11, 689 (1938).

53.   Tuttle, J. B., India Rubber World 67, 150 (1922).

54.   Luttringer, A. D., Caoutchouc and guttapercha 20, 11, 733, (1923).

55.   Zimmerman, E. C., Rubber Age 12, 130 (1922).

56.   Gul, V. E., Kolloid Zhur. 20, 318 (1958).

57.   Greensmith, H. W., Rheol. Elastomers, Proc. Conf., 113 (1957).

BIBLIOGRAPHY (cont.)

58. Thomas, A. G., J. Pol. Sci. 21, 467 (1958)

59. Hampe, E. A., Kautschuk u. Gummi 10, WT 141 (1957).

60. Buist, J. M., Trans. Inst. Rubber Ind. 20, 155 (1945).

61. Epshtein, V. G., Kauchuk i. Rezina 18, 27 (1959).

62. Talalay, J., Kautschuk 9, 82, 100 (1933).

63. Evans, B. B., India Rubber Journal 64, 815, (1922).

64. van't Wout, J. W. F., de Vries, A. J., Rubber Age 77, 693, (1955).

65. Houwink, R., de Vries, A. J., van't Wout, J. W. F., Rev gen caoutchouc 30, 181 (1953).

66. Andrews, E.H., Walsh, A., J. Pol. Sci. 33, 39 (1958).

67. Lefcaditis, G. D., Trans. Inst. Rubber Ind., 9, 67 (1933).

68. Amidon, R. W., Goldfinger, G., Rubber and Plastics Age 40, 938 (1959).

69. Powell, E. F., Gough, V. E., Rubber Chem. and Tech. 19, 406 (1956).

70. Davies, B. L., Rubber Chem. and Tech. 12, 509 (1959).

71. Griffith, A. A., Phil Trans. A 221, 163 (1920).

72. Goldfein, S., Modern Plastics 37, 127, (Apr 1960).

73. Gul, V. E., Doklady Akad Nauk S.S.S.R. 123, No. 4, 713, (1958).

74. Gent, A. N. Thomas, A. G., J. Appl. Pol. Sci. 2, 354 (1959).

75. Berry, J. P., J. Pol. Sci. 50, 107, 313, (1961).

76. Fenstermacher, J. E., J. Am. Ceram. Soc. 44, 297 (1961).

77. Tichara, M., Chem. Prumysl 9, 438, (1959).

78. Thomas, A. G., J. Pol. Sci. 18, 177 (1955).

BIBLIOGRAPHY (cont.)

79.   Kaiser, R., Rubber Chem. and Tec. 29, 207 (1956).

80.   Kruse, J., Kautschuk u. Gummi 6, WT 202 (1953).

81.   Rivlin, R. S., Thomas A. G., J. Pol. Sci. 10, 291 (1953).

82.   Gent, A. N., Rivlin, R. S., Proc. Phys. Soc. 65B, 118, 487, 645, (1952).

83.   Buist, J. M., Proceedings 2nd Rubber Tech. Conf. (London), 269, (1948).

84.   Lefcaditis, G., Cotton, F. H., Trans. Inst. Rubber Ind. 8, 364 (1933).

85.   Ito, K., Purasuchikkusu 12, 39, (1961).

86.   Andrews, E. H., J. Appl. Phys. 32, 542, (1961).

87.   Greensmith, H. W., J. Pol. Sci. 21, 175, (1956).

88.   Thomas, A. G., J. Appl. Pol. Sci. 3, 168, (1960).

89.   Greensmith, H. W., J. Appl. Poly. Sci. 3, 175, (1960).

90.   Greensmith, H. W., J. Appl. Pol. Sci. 3, 183, (1960).

91.   Greensmith, H. W., Mullins, L., Thomas, A. G., Trans. Soc. Rehol. IV,
      179, (1960).

92.   Williamson, Merritt A., Research/Development, p. 69, Sept. (1961).

93.   Bueche, F., J. Appl. Phys. 29, 1231 (1958).

94.   Coleman, B. D., Trans. Soc. Rheology, 1, 153 (1957).

95.   Gent, A. N. and Lindley, P. B., Proc. Roy. Soc. A249, 195-205 (1959).

96.   Love, A. E. H., The Mathematical Theory of Elasticity, Dover, 4th
      Edition, page 146.

97.   Malcolm, D. G., "Extensions and Applications of PERT as a System
      Management Tool", Address delivered at Aerospace Industries Assn.,
      July 1940, Operations Research, Inc.

BIBLIOGRAPHY (cont.)

98. Special Projects Office, Bureau of Naval Weapons, "Program Evaluation Research Task, Summary Report, Phase 1", July 1958.

99. Alexander, R. V., "Summary Report of Program Beta, A Digital Computer Program for High Speed Analysis of Performance, Preliminary Design, and Optimization of Solid Rocket Vehicles", Aerojet-General Corporation TM 176 SRP, January 1962, (ARS Preprint 2319-62).

100. Whetstone, A. E., Threewit, T. R., Billheimer, J. S., "Basic Grain Design and the 564 Interior Ballistics Computer Program", Aerojet-General Corporation STM-143, 10 June 1961.

101. Whetstone, A. E., Threewit, T. R., Rossini, R. A., "Intermediate Grain Design and the ACP-564 B Interior Ballistics Computer Program" Aerojet-General Corporation STM-148, 20 February 1962.

102. Gordon, L. J. and Boerlin, H. E., A practical approach to computer programing for specific impulse calculations, "Kinetics, Equilibria and Performance of High Temperature Systems", Ed. by Bohn, G. S. and Zukoski, E. E., Butterworth, Inc., Washington D. C., 1960, pp 152-160.